

DOE Final Report

Project: DE-FC02-06ER41441

Massimo Di Pierro

March 15, 2012

DOE Award Number: DE-FC02-06ER41441

Name of Recipient: Massimo Di Pierro

Principal Investigator: Massimo Di Pierro

Consortium Name: USQCD Collaboration

1 License

This report and its content can be distributed without limitation.

The software developed under this grant is already posted online under version control system, always under an OSI approved Open Source License. The specific licence is different for different parts of the code and details about the licenses are included with the code.

2 Executive Summary

Our research project is about the development of visualization tools for Lattice QCD. We developed various tools by extending existing libraries, adding new algorithms, exposing new APIs, and creating web interfaces (including the new NERSC gauge connection web site). Our tools cover the full stack of operations from automating download of data, to generating VTK files (topological charge, plaquette, Polyakov lines, quark and meson propagators, currents), to turning the VTK files into images, movies, and web pages. Some of the tools have their own web interfaces. Some Lattice QCD visualization have been created in the past but, to our knowledge, our tools are the only ones of their kind since they are general purpose, customizable, and relatively easy to use. We believe they will be valuable to physicists working in the field. They can be used to better teach Lattice QCD concepts to new

graduate students; they can be used to observe the changes in topological charge density and detect possible sources of bias in computations; they can be used to observe the convergence of the algorithms at a local level and determine possible problems; they can be used to probe heavy-light mesons with currents and determine their spatial distribution; they can be used to detect corrupted gauge configurations. There are some indirect results of this grant that will benefit a broader audience than Lattice QCD physicists and explained below.

3 Achievements and Comparison of Goals

The goal of this research project is the creation of a visualization toolkit that could be used to aid physicists in the analysis of data from lattice QCD computations. This goal has been successfully achieved as described below.

Links to code, images and video can be found at:

<http://latticeqcd.org>

The original grant proposal stated:

Lattice QCD computations comprise multiple steps, creating very large datasets, but the final result is typically encompassed in a small set of numbers with the analysis performed in an automated way. While an automated procedure may be beneficial in efficiency, the ability to visualize the data being analyzed is important both as an aid to the analysis, and as a means of acquiring insight into the physics. [...]

Crucial to the success of the graphics-visualization initiative will be a close collaboration between physicists to devise and interpret visualization of physically important quantities, and computer scientists to provide the appropriate visualization toolbox. Questions that visualization might address are many: can we understand how flux-tube formation observed with infinitely heavy quarks extends to hadrons where one or more of the quarks is light; what is the distribution of charge within a nucleon; can we display the distribution of spin and magnetism within a hadron? In the longer term, can we visualize the interactions of hadrons? Currently, no general-purpose package is available tailored to the display of lattice data. Thus a software package will be developed with a general GUI capable of reading a set of four-dimensional lattice quantities, and taking their ensemble average; performing a projection into a real four-dimensional vector; interpolating the 4-D vector into a continuous four-dimensional field; taking

three-dimensional slices of a four-dimensional field; displaying the data using density plots, iso-surfaces, and 2-D projections; and displaying the evolution of data, both in simulation time for four-dimensional quantities, and as the evolution of three- and two-dimensional slices in the remaining coordinates. The software will support two types of plug-ins: type-1 plug-ins that perform specific physics measurements and output a real 4-D vector, and type-2 plug-ins that take the interpolated 3-D field and generate specific types of plots.

Most of the research underlying this project will consist of identifying a set of physical measurements suitable to be implemented as type-1 plug-ins. The visualization techniques for the type-2 plug-ins are very similar to standard techniques used for representation of 3-D geophysical data and, when possible, we will incorporate existing libraries into the development of our plug-ins.

The system will be developed in C++ and take advantage of existing graphics and visualization libraries such the Trolltech QT libraries and the Visualization Tool Kit (VTK) library. The plug-ins will be callable from C or C++ code conforming to the QCD API, and will form another component of our Level 4 QCD Toolbox. The system will be capable of reading datasets in the SciDAC/ILDG format and the MILC format.

[...]

DePaul University will lead the design and development of a visualization tool for lattice QCD. Work will be done in collaboration with physicists involved in the project and with computer scientists at the University of North Carolina. The goals for the first year of the project are to identify and catalog the types of datasets to be visualized, identify appropriate smoothing and visualization algorithms, and develop a prototype interface. In subsequent years, plugins will be developed to read in the various types of datasets produced in lattice QCD simulations, and tools for manipulating the data in increasingly sophisticated ways will be created. A total of 1.08 FTE per year is budgeted for this effort.

A QCD physics toolbox will be constructed which will contain sharable software building blocks for inclusion in application codes, performance analysis and visualization tools, and software for automation of physics work flow. New software tools will be created for managing the large data sets generated in lattice QCD simulations, and for sharing them through the International Lattice Data Grid consortium.

Our basic toolkit consists of two parts. The first part has been implemented in the form of C++ libraries which are now included within the FermiQCD toolkit which is part of the USQCD Software Suite. These API allow the project of arbitrary fields into 3D and 4D scalar

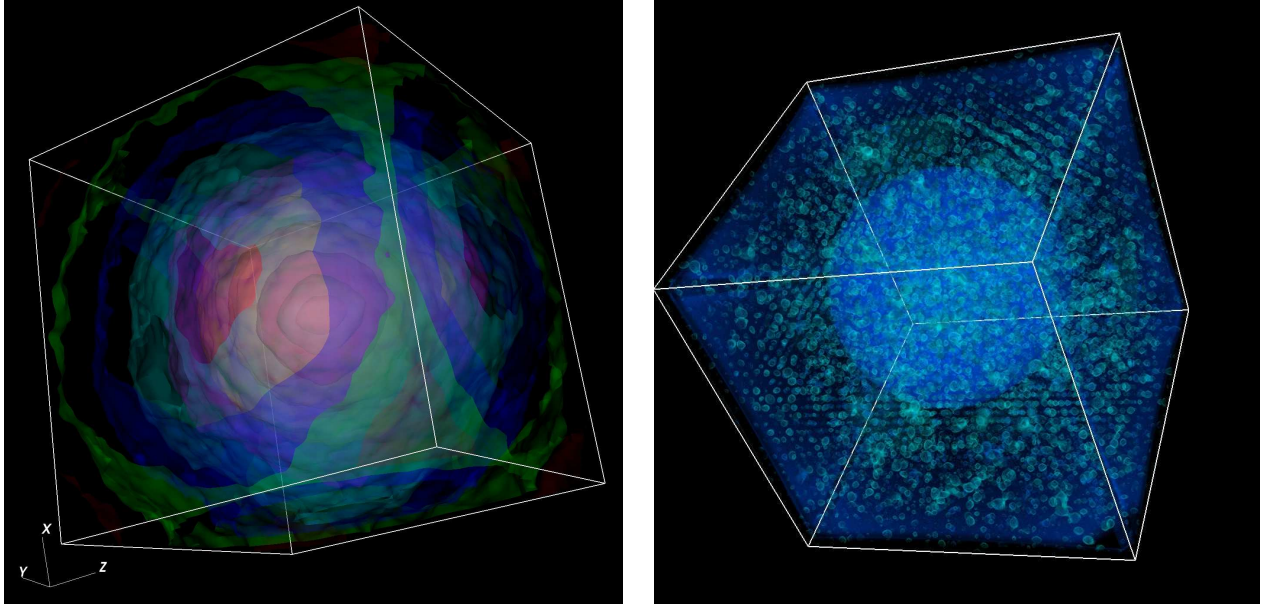


Figure 1: Example Images. The left one shows iso-surfaces for a quark wave function. The right one shows the density of HMC hits in presence of a lump of topological charge.

fields with can be visualized using open source toolkits like VisIt, Paraview, and MayaVi. The toolkit includes algorithms to project topological charge density, plaquette, Polyakov line components, quark propagators, meson propagators, and current insertions. It provides an API to create other custom operators and quark contractions and project/visualize them too. We also modified the minimum residue and the stabilized bi-conjugate inverter so that it is possible to observe the spatial effect of this algorithms and visualize their convergence for arbitrary sources. Our choice of the FermiQCD toolkit is motivated by the critical need to be able to perform visualizations for arbitrary $SU(N)$ gauge groups. FermiQCD is the only lattice QCD code, part of the USQCD Software Suite, that at this time supports arbitrary gauge groups.

The second part of our toolkit consists of a collection of Python programs that interface with the C++ programs and make the system more accessible to scientists by implementing a typical workflow. Specifically we developed 7 different programs.

The first program (as required by the original grant proposal) has the ability to convert MILC/ILDG data (as well other data formats) into the format required for visualization. On top of that, as described below, the same program has the ability to download gauge configurations from the NERSC repository, which is the largest public repository of gauge

configurations in the United States.

The second program is the main interface to the C++ algorithms. The program provides command line options to run physical algorithms such as the computation of the topological change density, plaquette, Polyakov, lines, quark propagators, meson propagators, currents, 4-quark operators. The program downloads, compiles and runs the requested algorithms. Each algorithm provides the option to save the computation steps in the VTK format for visualization. Not all the C++ algorithm are accessible via this interface and some requires explicit programming. Yet the provided code and documentation should be a sufficient example for the scientists to write their own customized code for other particular cases.

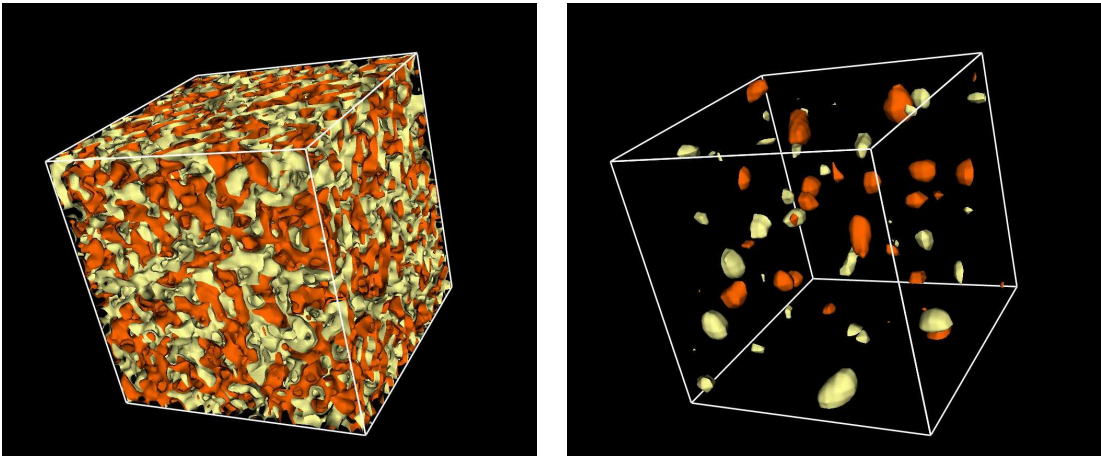


Figure 2: Example Images: They show the visualization of the topological charge at different cooling steps.

The third program perform the tasks of extracting information from the VTK files generated by the previous step, resampling them (to achieve better resolution in visualization), interpolating them (to make smooth visualizations and movies) and generating VisIt scripts. The VisIt visualization toolkit was developer by the Lawrence Livermore National Laboratory and it is a critical part of our workflow. It can be accessed via a GUI or programmatically via Python. Using a GUI to automate a workflow and process many files at once is not practical. It must be done programmatically. Our program generates VisIt scripts using meta-programming techniques so that QCD phycisists do not have to code. By running these scripts scientists can directly obtain images and movies without programming.

The fourth program we develop allows to convert 3D VTK files into interactive web pages. The program opens the VTK files, identifies optimal thresholds for the iso-surfaces, computes said iso-surfaces and generates a 3D representation of the polygons in JavaScript. The output

consists of static HTML files which embed the 3D objects. They can be visualized with any browser and the viewer can rotate them with the mouse. While VisIt is a general purpose tool is very powerful which allows many more maniputaions of the data, the possibility of generating 3D interactive web pages opens the possibility for scientists to view the data without installing VisIt and to publish the data on the web for other people to see.

The other programs we created are beyond the scope of the original grant proposal but we felt they were necessary and part of a broader interpretation of the conept of visualization. In fact, not all visualizations are spatial visualizations. There is other information that is important to visualize, which often takes the forms of simple 2D plots but often is not looked at because of the extra work involved in doing so. Examples are autocorrelations between physical measurements on different gauge configurations, moving averages, distributions of bootstrap samples. Our other programs serve this purpose. One of the programs read the output of typical QCD algorithms, extract the numerical results for each gauge configuration, and combines them into a bootstrap analysis. The user can specify the expression to bootstrap using command line arguments without programming. The code generates CSV files storing data for the intermediate steps of the computation. The other two programs can read those CSV files and generate plots and fits from them automatically. CSV files can also be read by many third party analysis and visualization programs.

Consider for example the computation of a four-quark matrix element. It involves the computation of a two-point and a three-point correlation funciton for each gauge configuration and their bootstrap analysis. Our programs can perform this analysis in the standard way but they also generate autocorrelation plots for each two-point and three-point correlation function, moving averages for the ratio on different time-slices, and bin the distribution of the bootstrap samples.

Those programs have been documented in long technical document attached to this report [1].

The main obstacle to this research has been accessibility. Visualization is indeed useful not but the way QCD physicists normally approach lattice QCD computations. We have therefore put lots of extra work in making our programs accessible by creating web interfaces that could simplify the task. Another obstacle is that no computing time was allocated to this project. While this did not prevent us from achieving the task of developeing the tools, it did not allow us to move beyond the original stated goal and utilize the tools for obtaining more abituious scientific results which would have been computing intensive.

Nevertheless we have used our toolkit to produce scientific results. Specifically we collaborated with Chulwoo Jung at Columbia University, Mike Clark and Richard Brower at Boston Universty and looked at the autocorrelation of topological charge density over short HMC trajectories [15]. It is a well known problem that global topological charge has a long auto-correlation. We found that the local topological charge instead has very short autocorrelation

and therefore there is no measurable bias in production gauge configurations.

We also were able to observe the effect of a single instanton on a quark propagator and how its presence gives mass to the quark by increasing the exponential fall off of the propagator [1].

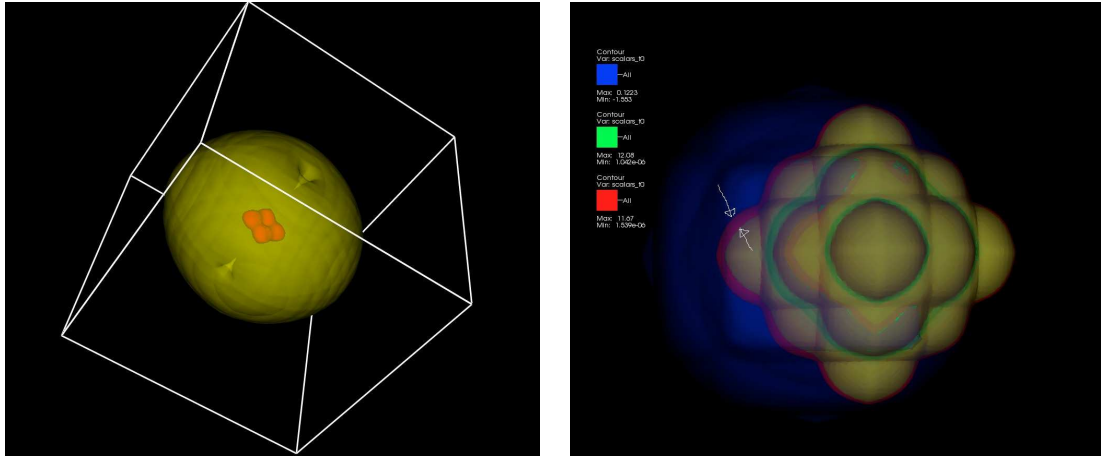


Figure 3: Example Images: left left image shows the density of a current inserted between two meson operators. The right image shows the shrinking of a quark propagator (red) in presence of a localized topological charge (blue).

Anyway, that is beyond the scope of the current grant and more visualizations will be done in the future as computing time becomes available.

In our original proposal we stated that our tools would have a GUI based on the Qt toolkit. In the very early stages of our project we have revised that decision. On the one side Nokia, owner of Qt, decided to cut support for the library. On the other site it became evident that desktop GUI have became an obsolete technology giving way to modern web based interfaces. We have therefore put lots of extra work in this direction and we have created three web applications.

The first web application (nersc) [3] was developed in collaboration with the National Energy Research Scientific Center (NERSC) to replace their previous interface to the lattice QCD archive known as “gauge connection”. The new system allows searching for gauge configuration, visualize statistics, and collaborate online by editing metadata in a wiki format. The system also allows batch downloads of the data using the program we described above. We have used our toolkit to process many ensembles from the NERSC archive and generated movies of the topological charge density. This program is designed to be very general purpose and it can be used by communities other than Lattice QCD to publish their data online.

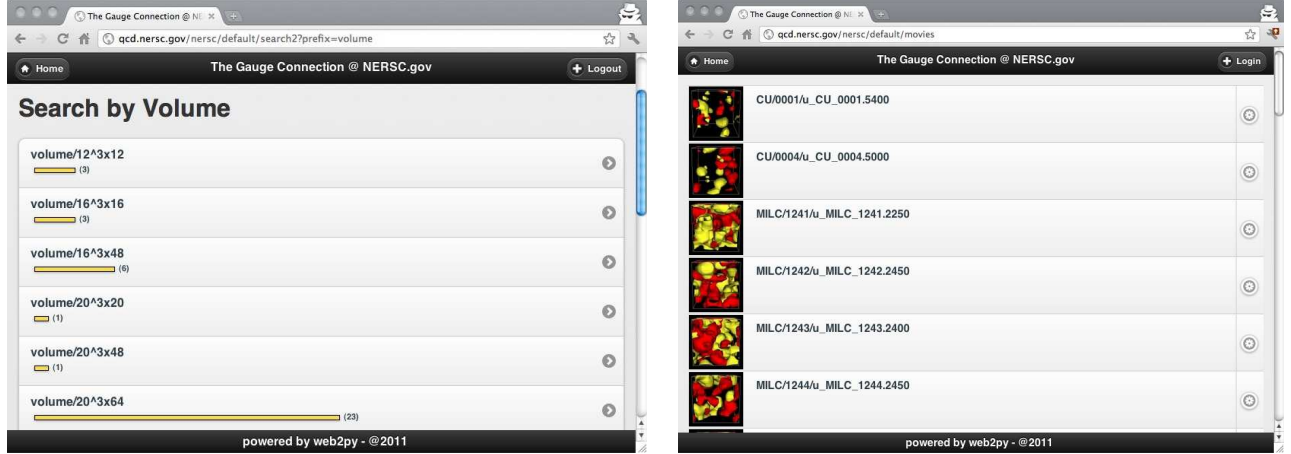


Figure 4: Screenshots from the NERSC “gauge connection” web site.

The second web application (vis) [6, 8] provides an interface to the algorithms and allows upload of gauge configurations and schedule visualization algorithms to run in background. The system provides a web interface to the Portable Batch System (PBS) and to VisIt and. It can schedule both computations and visualizations. The results are displayed in a web page.

The third web application (mc4qcd) [7, 9] is an interface to our analysis and plotting tools. It allows users to upload the log file result of a physics runs, to extract data from it using pattern matching, and to perform bootstrap analysis. The results of the analysis are stored and published online together with the reiative plots (including autocorrelations, moving averages, distribution of bootstrap samples, and fits). Scientists in a group can track results and collaborate online by sharing data and comments.

In order to develop these tools, in the eraly stages of the project we have developed a set of libraries for creating online scientific applications called web2py. This project is not part of the goal of this grant but it turned out to be an important and necessary component to replace the obsolete GUI concept with the modern web based paradigm. This project took a life on its own and found applications beyond this physics project. It was released open source and it is now used by thousands of users and businesses worldwide. It won the Bossie Award for “best open source software development tool” in 2011 and the InfoWorld Best Technology of the Year Award in 2012. This provides an example of unexpected broader impact of DOE funded research. Although we consider this very important and we are proud of the result, since it falls outside the scope of the original grant, we omitted references to it in the rest of this report. Yet references are available upon request.

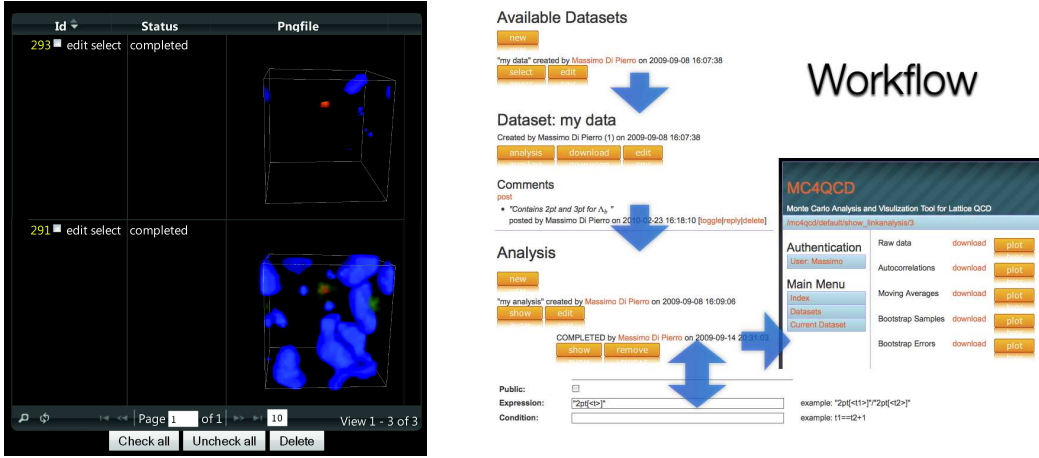


Figure 5: Screenshots from the VIS and the MC4QCD web applications respectively.

In 2010 we also contributed organize the 6th High End Visualization workshop in Obergugl, Austria.

Some of the visualization created with our tools were used for the opening video for the Lattice 2011 conference: <http://vimeo.com/25242353>

3.1 Summary of Code Created

The code written as part of this grant is published in the following repositories:

- <http://code.google.com/p/qcdutils/> It is the main toolkit, documented in [1].
- <http://code.google.com/p/fermiqcd/> This is a pre-existing C++ library for lattice QCD computations part of the USQCD Software Suite. The core visualization algorithms have been included here and distributed together. They are accessible via QCDUTILS.
- <http://code.google.com/p/nersc-data-publisher/> This is code behind the new NERSC “gauge connection” web interface. Developed in collaboration with James Hetrick (University of Pacific) and David Skinner (NERSC).
- <http://code.google.com/p/qcdvis/> This is a web interface to the visualization algorithms.

- <http://https://launchpad.net/qcdmc> This is a web interface to our analysys and plotting tools.

3.2 Published Web Sites

- <http://latticeqcd.org> This is the main front-end where we have published links to the code and some of our visualizations. More will be published as our tools is put into production. This site includes web interfaces to VIS and MC4QCD.
- <http://qcd.nersc.gov> This is the new NERSC “gauge connection” archive (developed in collaboration with NERSC). It also stores some videos created using our tools.
- <http://tests.web2py.com/ildg> This is a new proposed web site for the International Lattice Data Grid. It provides an interface for searching lattice QCD data in a visual way.

3.3 Fostered Collaborations

During this research project we have collaborated with Prof. James Hetrick from the University of Pacific and David Skinner at NERSC to re-build the new “gauge connection” web site.

We collaborated with Prof. Werner Berger from the Center for Computation and Technology, Louisiana State University and together we organized the 6th High End Visualization Workshop.

We utilized the VisIt software created by the Lawrence Livermore National Laboratory. Although we did not interact directly with the authors we interacted indirectly by using various online resources generated for that project.

Finally we interacted with the rest of the USQCD and the ILDG collaborations, from which we received constant feedback and suggestions.

3.4 Personnel

This grant has funded the PI and many graduate students:

- Nate Wilson
- Yaoquan Zhong
- Brian Schinazi

- Tony Garcia
- Vincent Havery

3.5 Published Papers

In the following bibliography we list all the papers published by the PI and supported directly by this research grant. We omitted papers and books published by the PI on other topics not directly related to the grant scope.

References

- [1] M. Di Pierro “qcdutils“ arXiv:1202.4813 [hep-lat]
- [2] M. Di Pierro “Improving Non-Linear Fits“ arXiv:1202.0988 [cs.NA]
- [3] M. Di Pierro, J. Hetrick, S. Cholia, D. Skinner “Making QCD Lattice Data Accessible and Organized through Advanced Web Interfaces“ PoS **LAT2011** (2011) arXiv:1112.2193 [hep-lat]
- [4] E. T. Neil *et al.* [for the Fermilab Lattice Collaboration and for the MILC Collaboration], “B and D meson decay constants from 2+1 flavor improved staggered arXiv:1112.3978 [hep-lat]
- [5] A. Bazavov *et al.* [Fermilab Lattice and MILC Collaborations], “B- and D-meson decay constants from three-flavor lattice QCD,” arXiv:1112.3051 [hep-lat]
- [6] M. Di Pierro, Y. Zhong and B. Schinazi, “Vis: Online analysis tool for lattice QCD,” PoS **LATTICE2010**, 326 (2010).
- [7] M. Di Pierro and Y. Zhong, “Analysis and visualization tools for Lattice QCD,” PoS **LAT2009**, 038 (2009).
- [8] M. Di Pierro, “Vis: QCD workflow and visualization tool“ in Proceedings of the 6th High End Visualization Workshop, Dec 8th - 12th, (2010), Obergurgl (Austria), Lehmanns Media, ISBN 978-3-86541-361-1
- [9] M. Di Pierro, Y. Zhong and B. Schinazi, “mc4qcd: Online Analysis Tool for Lattice QCD,” PoS A **CAT2010**, 054 (2010) arXiv:1005.3353 [hep-lat]

- [10] C. Bernard *et al.* [Fermilab Lattice Collaboration and MILC Collaboration], “Tuning Fermilab Heavy Quarks in 2+1 Flavor Lattice QCD with Application to Phys. Rev. D **83**, 034503 (2011) arXiv:1003.1937 [hep-lat]
- [11] A. Bazavov *et al.* [Fermilab Lattice and MILC Collaborations], “The Ds and D+ Leptonic Decay Constants from Lattice QCD,” PoS **LAT2009**, 249 (2009) arXiv:0912.5221 [hep-lat]
- [12] T. Burch *et al.*, “Quarkonium mass splittings in three-flavor lattice QCD,” Phys. Rev. D **81**, 034508 (2010) arXiv:0912.2701 [hep-lat]
- [13] J. A. Bailey *et al.* [Fermilab Lattice Collaboration and MILC Collaboration], “Progress on charm semileptonic form factors from 2+1 flavor lattice QCD,” PoS **LAT2009**, 250 (2009) arXiv:0912.0214 [hep-lat]
- [14] T. Burch *et al.*, “Quarkonium mass splittings with Fermilab heavy quarks and 2+1 flavors of PoS **LAT2009**, 115 (2009) arXiv:0911.0361 [hep-lat]
- [15] M. Di Pierro *et al.*, “Visualization as a tool for understanding QCD evolution algorithms,” J. Phys. Conf. Ser. **180**, 012068 (2009).
- [16] C. Bernard *et al.*, “Visualization of semileptonic form factors from lattice QCD,” Phys. Rev. D **80**, 034026 (2009) arXiv:0906.2498 [hep-lat]
- [17] C. Bernard *et al.*, “B and D Meson Decay Constants,” PoS **LATTICE2008**, 278 (2008) arXiv:0904.1895 [hep-lat]
- [18] J. A. Bailey *et al.*, “The $B \rightarrow \bar{D}^* l \nu$ semileptonic form factor from three-flavor lattice QCD: Phys. Rev. D **79**, 054507 (2009) arXiv:0811.3640 [hep-lat]
- [19] C. Bernard *et al.*, “The Anti- $B \rightarrow D^* l \bar{\nu}$ form factor at zero recoil from three-flavor Phys. Rev. D **79**, 014506 (2009) arXiv:0808.2519 [hep-lat]
- [20] M. Di Pierro, “A Visualization Toolkit for Lattice Quantum Chromodynamics“, in Proceedings of the 4th High End Visualization Workshop, June 18th - 22th, (2007), Obergurgl (Austria), Lehmanns Media, ISBN 9783865412164
- [21] C. Bernard *et al.* [Fermilab Lattice, MILC and HPQCD Collaborations], “The decay constants $f(B)$ and $f(D^+)$ from three-flavor lattice QCD,” PoS **LAT2007**, 370 (2007).

- [22] R. Todd Evans, E. Gamiz, A. X. El-Khadra and M. Di Pierro, “A Determination of the $B_0(s)$ and $B_0(d)$ mixing parameters in 2+1 lattice PoS **LAT2007**, 354 (2007) arXiv:0710.2880 [hep-lat]
- [23] M. Di Pierro, “Visualization for Lattice QCD“ PoS **LAT2007**, 331 (2007)
http://pos.sissa.it/archive/conferences/042/031/LATTICE2007_031.pdf

QCDUTILS

Massimo Di Pierro

February 23, 2012

Abstract

This manual describes a set of utilities developed for Lattice QCD computations. They are collectively called `qcdutils`. They are comprised of a set of Python programs each of them with a specific function: download gauge ensembles from the public NERSC repository, convert between formats, split files by time-slices, compile and run physics algorithms, generate visualizations in the form of VTK files, convert the visualizations into images, perform bootstrap analysis of results, fit the results of the analysis, and plot those results. These tools implement the typical workflow of most Lattice QCD computations and automate it by enforcing filename conventions: the output of one tool is understood by the next tool in the workflow. This manual is organized as a series of autonomous recipes which can be combined together.

Contents

1	Introduction	4
1.1	Resources	5
1.2	Getting the tools	6
1.3	Dependencies	7
1.4	License	7
1.5	Acknowledgments	7
2	Accessing public data with <code>qcdutils.get.py</code>	7
2.1	Searching data on the NERSC <i>Gauge Connection</i>	8
2.2	Downloading data from NERSC	10
2.3	Testing download	12
2.4	Converting to ILDG format (.ildg)	12
2.5	Using the catalog file	13
2.6	Converting gauge configurations to the FermiQCD format (.mdp)	14
2.7	Splitting gauge configurations into time-slices	14
2.8	Splitting ILDG propagators into timeslices	15
3	Details about file formats	15
3.1	NERSC file format (3x3)	16
3.2	NERSC file format (3x2)	17
3.3	MILC file format	19
3.4	FermiQCD file format	20
3.5	LIME file format	22
3.6	ILDG file format	24
3.7	SciDAC file format	25
4	Running physics algorithms with <code>qcdutils.run.py</code>	26
4.1	Running in parallel	27
4.2	General syntax	28
4.3	Creating a cold or hot gauge configuration	29
4.4	Loading a gauge configuration	30
4.5	Heatbath Monte Carlo	31
4.6	Computing a pion propagator	32
4.7	Action and inverters	34
4.8	Meson propagators	36
4.9	Current insertion	38

4.10 Four quark operators	39
5 Images and movies with <code>qcdutils_vis.py</code> and <code>qcdutils_vtk.py</code>	41
5.1 About VTK file format	42
5.2 Plaquette	43
5.3 Topological charge density	46
5.4 Cooling	48
5.5 Polyakov lines	50
5.6 Quark propagator	52
5.7 Pion propagator	52
5.8 Meson propagators	54
5.9 Current insertions	55
5.10 Localized instantons	55
6 Analysis with <code>qcdutils_boot.py</code>, <code>qcdutils_plot.py</code>, <code>qcdutils_fit.py</code>	57
6.1 A simple example	61
6.2 2-point and 3-point correlation functions	63
6.3 Fitting data with <code>qcdutils_fit.py</code>	66
6.4 Dimensional analysis and error propagation	70
A Filename conventions	71
B Help Pages	72
B.1 <code>qcdutils_get.py</code>	72
B.2 <code>qcdutils_run.py</code>	72
B.3 <code>qcdutils_vis.py</code>	75
B.4 <code>qcdutils_vtk.py</code>	77
B.5 <code>qcdutils_boot.py</code>	77
B.6 <code>qcdutils_plot.py</code>	78
B.7 <code>qcdutils_fit.py</code>	78

1 Introduction

In this manual we provide a description of the following tools:

- `qcdutils_get.py`: a program to download gauge configurations from the NERSC *Gauge Connection* archive [1] and convert them from one format to another, including to ILDG [2] and FermiQCD formats [3, 4].
- `qcdutils_run.py`: a program to download, compile and run various parallel Physics algorithms (for example compute the average plaquette, the topological charge density, two and three points correlation functions). `qcdutils_run` is a proxy for FermiQCD. Most of the FermiQCD algorithms and examples generate files that are suitable for visualization (VTK files [5])
- `qcdutils_vis.py`: a program to manipulate the VTK files generated by `qcdutils_run` which can be used to split VTK files into components, interpolate them, and generate 3D contour plots as JPEG images. This program uses metaprogramming to write a VisIt [6] script and runs it in background.
- `qcdutils_vtk.py`: a program that converts a VTK file into a web page (HTML) which displays iso-surfaces computed from the VTK file. The generated files can be visualized in any browser and allows interactive rotation of the visualization. This program is based on the “processing.js” library [7].
- `qcdutils_boot.py`: a tool for performing bootstrap analysis of the output of `qcdutils_run` and other QCD Software. It computes autocorrelations, moving averages, and distributions.
- `qcdutils_plot.py`: a tool to plot results from `qcdutils_boot`.
- `qcdutils_fit.py`: a tool to fit results from `qcdutils_boot.py`.

As the .py extension implied, these programs are written in Python [8] (2.7 version recommended).

Together these tools allow automation of the workflow of most Lattice QCD computations from downloading data to computing scientific results, plots, and visualizations.

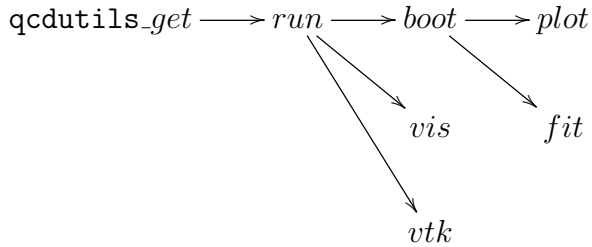
Notice that each of the utilities has its own help page which you can access using the -h command line option. The output for each is reported in the Appendix.

The data downloaded by `qcdutils_get` can be read by `qcdutils_run` which executes the physics algorithms implemented in C++. The output can be VTK files manipulated by

`qcdutils_vis` and then transformed into images and movies by VisIt, or they can be tabulated data that require bootstrap analysis. This is done by `qcdutils_boot`. The output of the latter plotted by `qcdutils_plot` and can be fitted with `qcdutils_fit`.

These files enforce a workflow by following the file naming conventions described in the Appendix but, they do not strictly depend on each other. For example `qcdutils_boot` can be used to analyze the output of any of your own physics simulations even if you do not use `qcdutils_run`.

Here is an overview of the workflow:



This manual is not designed to be complete or exhaustive because our tools are in continuous development and new features are added every day. Yet it is designed to provide enough examples to allow you to explore further. Our analysis and visualizations are created on sample data and aimed exclusively at explaining how to use the tools.

Our hope is that these tools will be useful to practitioners in the field and specifically to graduate students new to the field of Lattice QCD and looking to jumpstart their research projects.

These tools can also be used to automate the workflow of analyzing gauge configurations in real time in order to obtain and display preliminary results.

Some of the tools described here find more general application than Lattice QCD and can be utilized in other scientific areas.

1.1 Resources

`qcdutils` can be downloaded from:

<http://code.google.com/p/qcdutils>

More information FermiQCD code used by `qcdutils_run` is available from refs. [3, 4] and the web page:

<http://fermiqcd.net>

More examples of visualizations and links do additional code and examples can be found at:

<http://latticeqcd.org>

1.2 Getting the tools

There are two ways to get the tools described in here. The easiest way to get `qcdutils` is to use Mercurial:

Install mercurial from:

```
1 http://mercurial.selenic.com/
```

and download `qcdutils` from the googlecode repository

```
1 http://code.google.com/p/qcdutils/source/browse/
```

using the following commands:

```
1 hg clone https://qcdutils.googlecode.com/hg/ qcdutils
2 cd qcdutils
```

The command creates a folder called “`qcdutils`” and download the latest source files in there.

You can also download individual files using `wget` (default on Linux systems) or `curl` (default on mac systems):

```
1 wget http://qcdutils.googlecode.com/hg/qcdutils_get.py
2 wget http://qcdutils.googlecode.com/hg/qcdutils_run.py
3 wget http://qcdutils.googlecode.com/hg/qcdutils_vis.py
4 wget http://qcdutils.googlecode.com/hg/qcdutils_vtk.py
5 wget http://qcdutils.googlecode.com/hg/qcdutils_boot.py
6 wget http://qcdutils.googlecode.com/hg/qcdutils_plot.py
7 wget http://qcdutils.googlecode.com/hg/qcdutils_fit.py
```

1.3 Dependencies

These files do not depend on each other so you can download only those that you need. `qcdutils_run` is special because it is a Python interface to the `FermiQCD` library. As it is explained later, when executed, it downloads and compiles `FermiQCD`. It assumes you have `g++` installed.

`qcdutils_fit.py` and `qcdutils_plot.py` requires the Python `numpy` and `matplotlib` installed.

All the file require Python 2.x (possibly 2.7) and do not work with Python 3.x.

1.4 License

`qcdutils` are released under the GPLv2 license.

1.5 Acknowledgments

We thank all members of the USQCD collaborations for making most of their data and code available to the public, and for a long-lasting collaboration. We thank David Skinner, Schreyas Cholia, and Jim Hetrick for their collaboration in improving and running the NERSC gauge connection. We particularly thank Jim Hetrick for sharing his code for t’Hooft instantons. We thank Chris Maynard for useful discussions about ILDG. We thanks Simon Catterall, Yannick Meurice, Jonathan Flynn, and all those that over time have submitted patches for FermiQCD thus contributing to make it better. We also thank all of those who have used and who still use FermiQCD, thus providing the motivation for continuing this work. We thank the graduate students that over time have helped with coding, testing, and documentation: Yaoqian Zhong, Brian Schinazi, Nate Wilson, Vincent Harvey, and Chris Baron.

This work was funded by Department of Energy grant DEFC02-06ER41441 and by National Science Foundation grant 0970137.

2 Accessing public data with `qcdutils_get.py`

2.1 Searching data on the NERSC *Gauge Connection*

The *Gauge Connection* [1] is a repository of Lattice QCD data, primarily but not limited to gauge ensembles, hosted by the National Energy Research Science Center (NERSC) on their High Performance Storage System (HPSS). At the time of writing the Gauge Connection hosts 16 Terabytes of data and makes it publicly accessible to researchers worldwide.

The new Gauge Connection site consists of a set of dynamic web pages in hierarchical structures that closely mimics the folder structure in the HPSS FTP server. Each folder corresponds to a web page. The web page provide a description of the folder content, in the form of an editable wiki, comments about the content, links to sub-folder and links to files contained in the folder. Since folders may contain thousands of files, files with similar filenames are grouped together into filename patterns. For example all files with the same name but different extension or similar names differing only for a numerical value are grouped together. Pages are tagged and can be searched by tag. Users can search for files by browsing the folder structure, searching by tags and can download individual files or all files matching a pattern.

You do not need an account to login and you can use your OpenID account, for example a Google email account. You do not need to login to search but you need to login to download. From now on we assume you are logged in into the Gauge Connection.

Fig 1 (left) is a screenshot of the main Gauge Connection site. Each gauge ensemble is stored in a folder which is represented by a dynamic web page and tagged. You can search these pages by tag, as shown in Fig. 1 (right).

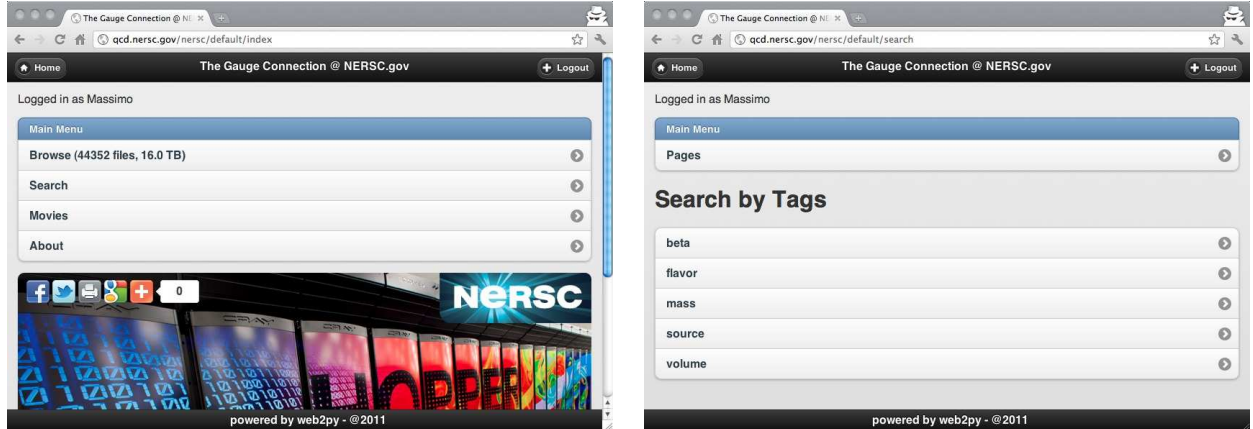


Figure 1: Main NERSC Gauge Connection web site (left) and search by tag feature (right).

Fig. 2 (left) shows statistical information about tags.

Each tag has the form “type/value” where the tag type can be:

- *source*: the name of the organization who donated the data, value can be, for example MILC [9].
- *flavor*, the flavor content of the data, value can be “0” for quenched data, “2” for two flavor unquenched data, “2+1” for three flavor unquenched where two quarks have one mass and 1 quark has another mass.
- *kappa*: the κ value
- *mass*: the quark mass

We have also processed many of the ensambles using some of the tools described here and generated animations of the topological charge densities. This is shown in fig. 2 (right).

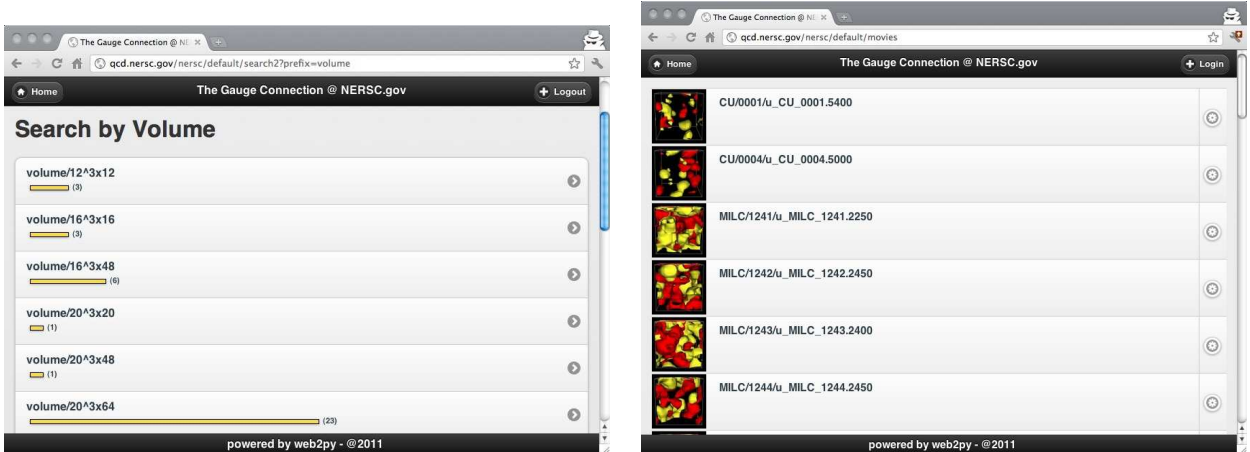


Figure 2: A page showing statitistical information (left) and list of visualzations (right).

A screenshot of a folder page is shown in fig. 3 (left)

You can see a description, a list of tags, list of file patterns in the folder, and comments. The comments are only visible to logged in users. The login link is at top left of the page.

A screenshot of a page listing the files in an ensemble is shown in fig. 3 (right)

You can download an individual files by clicking on the file.

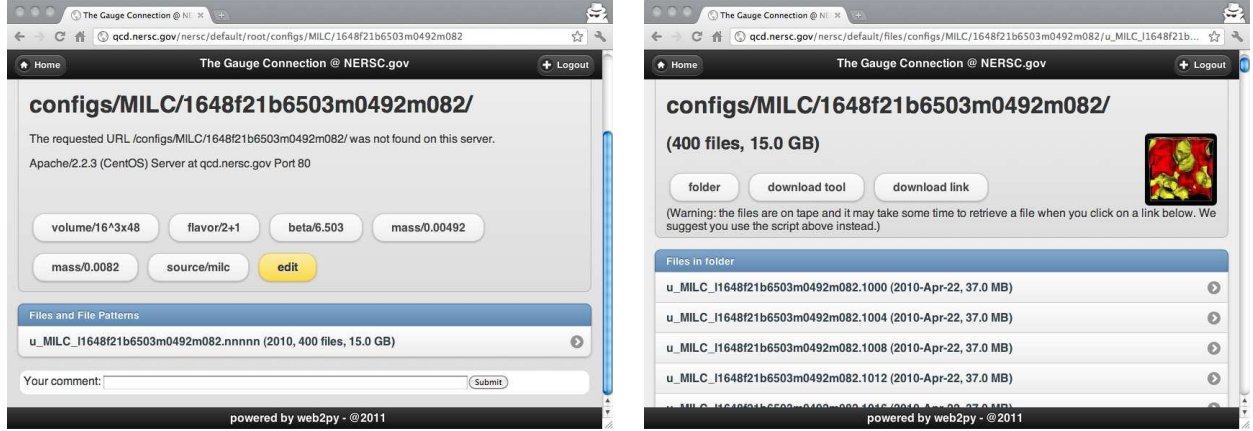


Figure 3: Folder page (left) and page listing all files in an ensamble (right).

To download files in batch you need to first download `qcdutils_get.py`. The web page above includes a link [*download tool*] that explains where to get and how to use `qcdutils_get.py`. We suggest you first read the rest of this section but also read the linked instructions which may be more updated. The page also contains a link [*download link*] which is used to reference the data for later download.

2.2 Downloading data from NERSC

Here we assume you want to download the 400 MILC gauge configurations of size $16^3 \times 48$ and $\beta = 6.503$ computed using 2+1 quarks of mass respectively 0.00492 (light) and 0.082 (heavy). These files can be found at

¹ `http://qcd.nersc.gov/nersc/default/root/configs/MILC/1648f21b6503m0492m082`

where you should notice the folder name

¹ `1648f21b6503m0492m082`

It follows the MILC filename convention

¹ `[time][space]b[beta]m[mass]m[mass]`

and the values of [beta] and [mass] omit the decimal point.

The above page links the pattern page:

```
1 http://qcd.nersc.gov/nersc/default/files/configs/MILC/1648  
f21b6503m0492m082/u_MILC_11648f21b6503m0492m082.nnnnn
```

where

```
1 u_MILC_11648f21b6503m0492m082.nnnnn
```

is the filename pattern and `nnnnn` is just a wildcard for the gauge configuration numbers in the ensemble.

The page contains a [*download link*] to a document in JSON format listing all files in the folder matching the pattern and additional meta-data about each file. You do not need to open this document. All you need to do is copy the link address and pass it to `qcdutils_get.py` as a command line argument. The program opens the URL, download the list, loop over the files in the ensemble, and download them one by one.

Copy the *download link* to clipboard and it looks something like this:

```
1 http://qcd.nersc.gov/nersc/api/files.json/.../  
u_MILC_11648f21b6503m0492m082.nnnnn
```

We have shortened the full actual path using This URL is a personal token and different users get different URLs for the same data. This allows the server to monitor usage and expire an URL in case of indiscriminate downloads from one user without affecting other users.

To download all data referenced by this link you simply paste the download link after a call to `qcdutils_get`:

```
1 python qcdutils_get.py [download link]
```

`qcdutils_get.py` performs the following operations:

Before downlaod, `qcdutils` creates a folder with the same name as the ensemble:

```
1 u_MILC_11648f21b6503m0492m082.nnnnn/
```

and then download all files in there. The files retain the original file name.

`qcdutils` also creates a file called “`qcdutils.catalog`” where it keeps track of successful downloads. This allows automatic resume on restart: if your download is interrupted, for any reason (for example network problem or server crash), you can re-issue the download command and it resumes where it stopped. `qcdutils` does not download again files that were already downloaded and are currently present on your system.

`qcdutils` can check if a file is complete by checking its size. Data integrity during transmission is guaranteed by the TCP protocol. It is still possible that data is corrupted at the source or locally after download (for example due to a bad disk sector). If a file is found to be corrupted simply delete it, run `qcdutils_get` again, and it downloads it again.

Notice that most of the files stored and served by the Gauge Connection are in either the NERSC 3x3 or the NERSC 3x2 file format, described later. If your program can read them, you do not need any conversion. Yet it is likely you need to convert them and this is the subject of the rest of the section.

2.3 Testing download

If you encounter any problem downloading real data you can try download a single small demo gauge configuration:

```
1 python qcdutils_get.py http://qcd.nersc.org/nersc/api/files/demo
```

It creates a folder called `demo` and download a single file

```
1 demo/demo.nersc
```

2.4 Converting to ILDG format (.ildg)

The `qcdutils_get.py` can also auto-detect and convert file formats. It can input NERSC3x2, NERSC3x3, MILC, UKQCD, ILDG, SciDAC, FermiQCD and it can output ILDG and FermiQCD formats. Other output formats may be supported in the future if this becomes necessary. `qcdutils` converts files using the following syntax

```
1 python qcdutils_get.py -c [target-format] [source]
```

Here [source] can be a *download link*, a *glob* pattern such as “`demo/*`”, or an individual file. [target-format] is one of the following:

- *ildg* converts a gauge configuration to ILDG
- *mdp* converts a gauge configuration to the FermiQCD format
- *slice.mdp* converts a gauge configuration (for example $12^3 \times 48$) into multiple configuration files, one for each time slice (for example 1×12^3), in the FermiQCD file format.

- *prop* like *mdp* but converts file propagators from *Scidac-ILDG format* into the FermiQCD format.
- *slice.prop.mdp* like *prop.mdp* but converts a *Scidac-ILDG* propagator into FermiQCD time-slice files.

Most gauge configuration files are very large and require physics algorithms to run in parallel. Yet some algorithms, specifically some visualization ones, can work on individual time-slices. *slice.mdp* and *slice.prop.mdp* allow you to break large files into time-slices for this purpose.

Here is an example to convert to ILDG format:

```
1 python qcdutils_get.py http://qcd.nersc.gov/nersc/api/files/demo
2 python qcdutils_get.py -c ildg demo/*
```

Or in one single line:

```
1 python qcdutils_get.py -c ildg http://qcd.nersc.gov/nersc/api/files/demo
```

If the source file is “demo/demo.nersc”, the converted file has the “.ildg” postfix appended and be called “demo/demo.nersc.ildg”. The original file is not deleted. These are the output folder/files:

```
1 demo/
2 demo/demo.nerc
3 demo/demo.nersc.ildg
4 demo/qcdutils.catalog
```

By default `qcdutils` preserves the precision of the input data, but can specify the precision of the target gauge configuration using the `-4` flag for single precision and the `-8` flag for double precision. The input precision is automatically detected. For example:

```
1 python qcdutils_get.py -c ildg -4 demo/*
```

2.5 Using the catalog file

The file “`qcdutils.catalog`” is only used internally by `qcdutils` and should not be deleted or else it loses track of completed downloads and may perform them again unnecessarily.

If can pass a `qcdutils.catalog` to `qcdutils_get` you get a report about the downloaded files.

```
1 python qcdutils_get.py demo/qcdutils.catalog
```

Notice that output files are never overwritten so make sure you delete the old one if you want to create new ones.

2.6 Converting gauge configurations to the FermiQCD format (.mdp)

This option works similarly to the previous section:

```
1 python qcdutils_get.py http://qcd.nersc.gov/nersc/api/files/demo
2 python qcdutils_get.py -c mdp demo/*
```

or in one line

```
1 python qcdutils_get.py -c mdp http://qcd.nersc.gov/nersc/api/files/demo
```

It creates

```
1 demo
2 demo/demo.nersc
3 demo/demo.nersc.mdp
4 demo/qcdutils.catalog.db
```

As in the previous case you can specify the precision of the converted file using `-4` or `-8`.

Notice you cannot specify the endianness. The FermiQCD format (.mdp) uses LITTLE endianness by convention because that is the format used internally by x386 compatible architectures.

2.7 Splitting gauge configurations into time-slices

Often we need to break a single gauge configuration with T time-slices into T gauge configurations with 1 time-slice each. You can do it using the `slice.mdp` output file format:

```
1 python qcdutils_get.py http://qcd.nersc.gov/nersc/api/files/demo
2 python qcdutils_get.py -c slice.mdp demo/demo.mdp
```

The first line creates the following files:

```
1 demo/
2 demo/demo.nersc
3 demo/qcdutils.catalog.db
```

while the second line creates:

```
1 demo/demo.nersc.t0001.mdp
2 demo/demo.nersc.t0002.mdp
3 demo/demo.nersc.t0003.mdp
4 demo/demo.nersc.t0004.mdp
```

Four files because “demo.nersc” contains 4 timeslices.

2.8 Splitting ILDG propagators into timeslices

We can play the same trick with propagators. While for gauge configurations `qcdutils` can read multiple file formats, for input propagators qcd can only read FermiQCD and SciDAC propagators.

Given a file “propagator.scidac” we can convert it into FermiQCD format:

```
1 python qcdutils_get.py -c prop.mdp propagator.scidac
```

which creates

```
1 propagator.scidac.prop.mdp
```

or split into time-slices

```
1 python qcdutils_get.py -c slices.prop.mdp propagator.scidac
```

This creates

```
1 propagator.scidac.t0000.prop.mdp
2 propagator.scidac.t0001.prop.mdp
3 propagator.scidac.t0002.prop.mdp
4 ...
```

In this case you can specify the target precision.

3 Details about file formats

In this section we show simplified code snippets that should help you understand the different file formats used in Lattice QCD. They are very similar to the actual code implemented in `qcdutils` but simplified for readability.

3.1 NERSC file format (3x3)

To better illustrate each data format we present a minimalist program to store data in the corresponding format.

We assume the input is available through an instance of the following class called `data`:

```
1 class GenericGauge(object):
2     def u(x,y,z,t,mu):
3         # u_ij below are complex numbers
4         return [[u_00,u_01,u_02],
5                 [u_10,u_11,u_12],
6                 [u_20,u_21,u_22]]
```

In this section (and only in this section) we follow the convention that $\mu = 0$ is X , 1 is Y , 2 is Z and 3 is T . Everywhere else, in particular in the input parameters of `qcdutils_run` $\mu = 0$ is T , 1 is X , 2 is Y and 3 is Z , which is the FermiQCD convention.

The following code shows how to read `data` and write it in the NERSC3x3 format:

```
1 NERSC_3x3_HEADER = """BEGIN_HEADER
2 HDR_VERSION = 1.0
3 DATATYPE = 4D_SU3_GAUGE_3x3
4 DIMENSION_1 = %(NX)i
5 DIMENSION_2 = %(NY)i
6 DIMENSION_3 = %(NZ)i
7 DIMENSION_4 = %(NT)i
8 CHECKSUM = %(checksum)s
9 LINK_TRACE = %(linktrace)f
10 PLAQUETTE = %(plaquette)f
11 CREATOR = %(creator)s
12 ARCHIVE_DATE = %(archive_date)s
13 ENSEMBLE_LABEL = %(label)s
14 FLOATING_POINT = %(precision)s
15 ENSEMBLE_ID = %(ensemble_id)s
16 SEQUENCE_NUMBER = %(sequence_number)i
17 BETA = %(beta)f
18 MASS = %(mass)f
19 END_HEADER
"""
21 def save_3x3_nersc(filename,metadata,data):
22     f = open(filename,'wb')
23     f.write(NERSC_3x3_HEADER % metadata)
24     nt = metadata['NT']
25     nx = metadata['NX']
```

```

26 ny = metadata['NY']
27 nz = metadata['NX']
28 if metadata['FLOATING_POINT']=='IEEE32':
29     couple = '>2f'
30 elif metadata['FLOATING_POINT']=='IEEE64':
31     couple = '>2d'
32 else:
33     raise RuntimeError, "Unknown precision"
34 for t in range(nt):
35     for z in range(nz):
36         for y in range(ny):
37             for x in range(nz):
38                 for mu in range(0,1,2,3):
39                     u = data.u(x,y,z,t,mu)
40                     for i in range(3):
41                         for j in range(3)
42                             c = u[i][j]
43                             re,im = real(c),imag(c)
44                             f.write(struct.pack(couple,re,im))

```

The variable `couple` determines how to pack in binary the 2 variables `re,im` using big endianness (“>”) in single (“f”) or double precision (“d”). For more info read the documentation on the Python “`struct`” package.

All common file formats used by the community to store QCD gauge configuration require two loops: one loop over the lattice sites and one loop over the link directions at each lattice site.

In the NERSC, ILDG and MILC case, the first loop is:

```

1 for t ...
2   for z ...
3     for y ...
4       for x ...

```

and the second loop is:

```

1 for mu in (X,Y,Z,T) # (0,1,2,3)

```

3.2 NERSC file format (3x2)

The NERSC 3x2 format is more common than NERSC 3x3 and here is how to write it:

```

1 NERSC_3x2_HEADER = """BEGIN_HEADER
2 HDR_VERSION = 1.0
3 DATATYPE = 4D_SU3_GAUGE
4 DIMENSION_1 = %(NX)i
5 DIMENSION_2 = %(NY)i
6 DIMENSION_3 = %(NZ)i
7 DIMENSION_4 = %(NT)i
8 CHECKSUM = %(checksum)s
9 LINK_TRACE = %(linktrace)f
10 PLAQUETTE = %(plaquette)f
11 CREATOR = %(creator)s
12 ARCHIVE_DATE = %(archive_date)s
13 ENSEMBLE_LABEL = %(label)s
14 FLOATING_POINT = %(precision)s
15 ENSEMBLE_ID = %(ensemble_id)s
16 SEQUENCE_NUMBER = %(sequence_number)i
17 BETA = %(beta)f
18 MASS = %(mass)f
19 END_HEADER
"""
20
21 def save_3x2_nersc(filename, metadata, data):
22     f = open(filename, 'wb')
23     f.write(NERSC_3x2_HEADER % metadata)
24     nt = metadata['NT']
25     nx = metadata['NX']
26     ny = metadata['NY']
27     nz = metadata['NZ']
28     if metadata['FLOATING_POINT'] == 'IEEE32':
29         couple = '>2f'
30     elif metadata['FLOATING_POINT'] == 'IEEE64':
31         couple = '>2d'
32     else:
33         raise RuntimeError, "Unknown precision"
34     for t in range(nt):
35         for z in range(nz):
36             for y in range(ny):
37                 for x in range(nx):
38                     for mu in range(0,1,2,3):
39                         u = data.u(x,y,z,t,mu)
40                         for i in range(3):
41                             for j in range(2) # here
42                             c = u[i][j]
43                             re,im = real(c),imag(c)
44                             f.write(struct.pack(couple,re,im))

```

Notice it differs from NERSC 3x3 by only two lines. One line is in the header:

```
1 DATATYPE = 4D_SU3_GAUGE
```

instead of

```
1 DATATYPE = 4D_SU3_GAUGE_3x3
```

and in the line marked by a `here`.

This file format does not store all the 3x3 matrices but only the first two rows. The third row can be reconstructed when reading the file using the condition that the third row is the (complex) vector product of the first two.

`qcdutils` can reads and rebuilds the missing rows using this code:

```
1 def reunitarize(s):
2     (a1re, a1im, a2re, a2im, a3re, a3im,
3      b1re, b1im, b2re, b2im, b3re, b3im) = s
4     c1re = a2re*b3re - a2im*b3im - a3re*b2re + a3im*b2im
5     c1im = -(a2re*b3im + a2im*b3re - a3re*b2im - a3im*b2re)
6     c2re = a3re*b1re - a3im*b1im - a1re*b3re + a1im*b3im
7     c2im = -(a3re*b1im + a3im*b1re - a1re*b3im - a1im*b3re)
8     c3re = a1re*b2re - a1im*b2im - a2re*b1re + a2im*b1im
9     c3im = -(a1re*b2im + a1im*b2re - a2re*b1im - a2im*b1re)
10    return (a1re, a1im, a2re, a2im, a3re, a3im,
11            b1re, b1im, b2re, b2im, b3re, b3im,
12            c1re, c1im, c2re, c2im, c3re, c3im)
```

3.3 MILC file format

The MILC file format is the same as the NERSC 3x3 but the header contains different information, it uses a binary format, and the endianness is not specified (although generally large endianness is used). The binary data after the header is the same as NERSC3x3.

Here is an example of code to write a MILC gauge configuration in Python:

```
1 def save_milc(filename,metadata,data):
2     f = open(filename,'wb')
3     milc_header = '>i4i64siii'
4     milc_magic = 20103
5     f.write(struct.pack(milc_header,
6                         milc_magic,
7                         metadata['NX'],
```

```

8         metadata[ 'NY' ] ,
9         metadata[ 'NZ' ] ,
10        metadata[ 'NT' ] ,
11        metadata[ 'ARCHIVE_DATE' ][:64] ,
12        metadata[ 'ORDER' ] ,
13        metadata[ 'CHECKSUM1' ] ,
14        metadata[ 'CHECKSUM2' ] )
15 nt = metadata[ 'nt' ]
16 nx = metadata[ 'nx' ]
17 ny = metadata[ 'ny' ]
18 nz = metadata[ 'nz' ]
19 if metadata[ 'FLOATING_POINT' ] == 'IEEE32':
20     couple = '>2f'
21 elif metadata[ 'FLOATING_POINT' ] == 'IEEE64':
22     couple = '>2d'
23 else:
24     raise RuntimeError, "Unknown precision"
25 for t in range(nt):
26     for z in range(nz):
27         for y in range(ny):
28             for x in range(nx):
29                 for mu in range(0,1,2,3):
30                     u = data.u(x,y,z,t,mu)
31                     for i in range(3):
32                         for j in range(3)
33                             c = u[i][j]
34                             re,im = real(c),imag(c)
35                             f.write(struct.pack(couple,re,im))

```

When reading a MILC gauge configuration, `qcdutils.get` checks for the magic number and determines the endianness from the first 4bytes of the header. `qcdutils` also determines the precision from the total file size.

3.4 FermiQCD file format

The file format used by FermiQCD is called MDP and files have a ".mdp" extensions. They are very similar to the MILC format with these differences:

- the header has a different format and stores slightly different information
- the endianness is always little-endian.
- the inner loop over mu has the same order as the outer loop

- it is designed to work for an arbitrary number of dimensions (from 1D lattices to 10D lattices and have an arbitrary site structure) and the FermiQCD code deal with this aspect in an automated way that is explored later.

For regular QCD ($SU(3)$ matrices per link and 4D lattice) a FermiQCD gauge configuration can be generated using the following code:

```

1 def save_fermiqcd_4d_su3(filename,metadata,data):
2     f = open(filename, 'wb')
3     nt = metadata['nt']
4     nx = metadata['nx']
5     ny = metadata['ny']
6     nz = metadata['nz']
7     header_format = '<60s60s60sLi10iii'
8     maginc_number = 1325884739
9     ndim,
10    if metadata['FLOATING_POINT']=='IEEE32':
11        couple = '>2f'
12        metadata['SITE_SIZE'] = 4*9*2*4
13    elif metadata['FLOATING_POINT']=='IEEE64':
14        couple = '>2d'
15        metadata['SITE_SIZE'] = 4*9*2*4
16    else:
17        raise RuntimeError, "Unknown precision"
18    f.write(struct.pack(header_format,
19                        'File Type: MDP FIELD',
20                        metadata['FILENAME'],
21                        metadata['ARCHIVE_DATE'][::60],
22                        magic_number,ndim,nt,nx,ny,nz,0,0,0,0,0,0,0,
23                        metadata['SITE_SIZE'],nt*nx*ny*nz))
24    for t in range(nt):
25        for z in range(nz):
26            for y in range(ny):
27                for x in range(nx):
28                    for mu in range(3,2,1,0):
29                        u = data.u(x,y,z,t,mu)
30                        for i in range(3):
31                            for j in range(3)
32                                c = u[i][j]
33                                re,im = real(c),imag(c)
34                                f.write(struct.pack(couple,re,im))
```

Notice the following:

- The header is binary but uses a string “File Type: MDP FIELD” to identify the file

format and version. This allows you to identify the file using an ordinary editor, like in the NERSC format.

- It still uses an integer magic number to allow the reader to check the endianness.
- It requires an `ndim` variable which is set to 4 because this manual mostly deals with 4D fields.
- It stores in `metadata['SITE_SIZE']` the number of bytes for each lattice site. For single precision this is 4 directions times 9 SU(3) matrix elements times 2 (real+complex) times 4 (4 bytes for IEEE32, single precision, float) = 288 bytes. It is 576 bytes for double precision.

3.5 LIME file format

The file formats described so far store metadata in a header which precedes the binary data.

The LIME data format is different. It is similar to TAR or MIME as scope. It is designed to package multiple files into one file.

A LIME file is divided into segments (sometime called records in the literature although it does not strictly conform to the definition of a record because LIME has nothing to do with databases). A segment is comprised of five parts: a magic number, a version number, an integer storing the size of the binary data, a segment name, and the binary data.

The magic number identifies the file as a LIME file and the version number identifies the LIME version. This information is repeated for each segment.

Notice that LIME records do not declare the type of the segments and this has to be inferred from the name of the segments. One important caveat of LIME is that some segments contain binary data, while some contain ASCII strings such as XML. Segments that contain ASCII strings are null-terminated and the terminating zero is counted in the size. Binary segments are not null-terminated. This is an important detail when reading the data.

`qcdutils` contains a class LIME that can be used to open LIME files and read/write segments in or out of order.

A minimalist implementation of the LIME file format is the following:

```
1 class Lime(object):
2     def __init__(self, filename, mode, version = 1):
3         self.magic = 1164413355
```

```

4     self.version = version
5     self.filename = filename
6     self.mode = mode
7     self.file = open(filename, mode)
8     self.records = [] # [(name, position, size)]
9     if mode == 'r' or mode == 'rb':
10        while True:
11            header = self.file.read(144)
12            if not header: break
13            magic, null, size, name = struct.unpack('!iiq128s',header)
14            if magic != 1164413355:
15                raise IOError, "not in LIME format"
16            name = name[:name.find('\0')]
17            position = self.file.tell()
18            self.records.append((name,position,size)) # in bytes
19            padding = (8 - (size % 8)) % 8
20            self.file.seek(size+padding,1)
21    def read(self,record):
22        (name,position,size) = self.records[record]
23        self.file.seek(position)
24        return (name, self.file, size)
25    def __iter__(self):
26        for record in range(len(self)):
27            yield self.read(record)
28    def write(self,name,data,size = None,chunk = MAXBYTES):
29        position = self.file.tell()
30        header = struct.pack('!iiq128s',self.magic,self.version,size,name)
31        self.file.write(header)
32        self.file.write(data)
33        self.file.write('\0'*(8 - (size % 8)) % 8)
34        self.records.append((name,size,position))
35    def close(self):
36        self.file.close()

```

The actual implementation in `qcdutils` is more complex because it performs more checks and because it can read and write segments even if they do not fit in RAM, which is not the case in the example above.

Here is an example of usage from Python:

Open a LIME file for writing

```

1 >>> from qcdutils_get import Lime
2 >>> lime = Lime('test.lime','w')

```

Write two records in it

```
1 >>> lime.write('record1', '01234567')
2 >>> lime.write('record2', 'other binary data')
```

Close it

```
1 >>> lime.close()
```

Open the file again for reading:

```
1 >>> lime = Lime('test.lime', 'r')
```

Loop over the segments and print, name size, content:

```
1 >>> for name,reader,size in lime:
2 ...     print (name, size, reader.read(size))
```

3.6 ILDG file format

The ILDG file format uses LIME to package two segments:

- One segment contains the metadata marked up in XML.
- One segment contains the binary data, in the same format as in MILC and NERSC 3x3.

The XML markup is specified by ILDG for 4D gauge files. Notice that because the first segment refers to the second, many programs that read ILDG expect the metadata segment to precede the data segment.

Here is an example of code to write an ILDG file:

```
1 def save_ildg(filename,metadata,data,lfn):
2     lime = Lime(filename, 'wb')
3     lime.write('ildg-format', """
4         <?xml version = "1.0" encoding = "UTF-8"?>
5         <ildgFormat>
6             <version>%(VERSION)s</version>
7             <field>su3gauge</field>
8             <precision>%(PRECISION)s</precision>
9             <lx>%(NX)s</lx>
10            <ly>%(NY)s</ly>
11            <lz>%(%NZ)s</lz>
12            <lt>%(%NT)s</lt>
13        </ildgFormat>
```

```

14 """ .strip() % metadata)
15     nt = metadata['NT']
16     nx = metadata['NX']
17     ny = metadata['NY']
18     nz = metadata['NZ']
19     def writer():
20         for t in range(nt):
21             for z in range(nz):
22                 for y in range(ny):
23                     for x in range(nx):
24                         for mu in range(0,1,2,3):
25                             u = data.u(x,y,z,t,mu)
26                             for i in range(3):
27                                 for j in range(3):
28                                     c = u[i][j]
29                                     re,im = real(c),imag(c)
30                                     yield struct.pack(couple,re,im)
31     self.lime.write('ildg-binary-data',writer)
32     self.lime.write('ildg-data-LFN',lfn)

```

Notice that this file takes the same arguments as `save_3x3_nersc` plus an addition one called `lfn`. `lfn` stands for *lattice file name*.

```
1 lfn://myCollab/myFilename
```

The `lfn` is intended to be a Unique Resource Identifier (URI) but it not a Universal Resource Locator (URL). The prefix `lfn` is not a protocol like `http` or `ftp`.

3.7 SciDAC file format

The SciDAC format is used primarily for storing propagators. It uses LIME and it packages the following segments:

- `scidac-binary-data`: the actual binary data
- `scidac-private-file-xml`
- `scidac-private-record-xml`

We do not describe it here because this file type is not used by the tools which are described in this manual. Yet we observe that `qcdutils_get` can convert this files into FermiQCD propagators.

4 Running physics algorithms with `qcdutils_run.py`

`qcdutils_run.py` is a program for downloading, compiling, and running FermiQCD [3, 4]. FermiQCD is a library for parallel Lattice QCD algorithms. The library has been improved over time and it now includes algorithms for visualization of Lattice QCD data. You can learn more about LatticeQCD from refs. [10, 11, 12]. You can learn more about FermiQCD from:

```
http://fermiqcd.net
```

After you download `qcdutils`, run the following command:

```
1 python qcdutils_run.py -download
```

This creates a local folder called “`fermiqcd`”, download the latest FermiQCD source from the google code repository:

```
1 http://code.google.com/p/fermiqcd
```

The source include a file “`fermiqcd.cpp`” file, which can parse command line arguments and run various physics algorithms, some described in this section. `qcdutils_run.py` compiles this source file and stores the compiled one in:

```
1 fermiqcd/fermiqcd.exe
```

Notice the `.exe` extension is used on all supported platforms.

`qcdutils_run` requires `g++` and you need to install it separately.

Now you can run physics algorithms with:

```
1 python qcdutils_run.py [options]
```

`qcdutils_run.py` internally calls `fermiqcd.exe` and pass its [options] along.

You can learn more about the FermiQCD options with

```
1 python qcdutils_run.py -h
```

The output is reported in the appendix but you are encouraged to run it yourself with the latest code.

`qcdutils_run.py` simply passes its command line arguments to “`fermiqcd.exe`” which parses and calls the corresponding algorithms. Some arguments are special (`-download`, `-compile`, `-mpi`, `-options`, `-h`) because they are handled by `qcdutils_run` directly. In particular a call

to `-options` introspects the source of “fermiqcd.cpp” and figures out which arguments are supported.

Notice that FermiQCD can do more of what `qcdutils_run` can access. For example it supports staggered fermions (including asqtad), staggered mesons, and domain wall fermions. It can do visualizations using those fields too, but that is not discussed here.

You can fork “fermiqcd.cpp” and force “`qcdutils_run`” to use your own source code:

```
1 python qcdutils_run.py -compile -source myownfermiqcd.cpp
```

4.1 Running in parallel

There are two ways to run FermiQCD in parallel with `qcdutils_run.py`. On an SMP machine you can simply run with the option `-PSIM_NPROCS=<number>`. Here is an example that loads a gauge configuration and computes the plaquette in parallel using 4 processes:

```
1 python qcdutils_run.py -PSIM_NPROCS=4 \
2   -gauge:start=load:load=demo/demo.nersc.mdp -plaquette
```

When running in parallel with `-PSIM_NPROCS`, FermiQCD uses fork to create the parallel processes and uses named pipes for the message passing. Most PCs and workstations do not allow dynamic memory allocation of more than 2GB of contiguous space and this creates problems when processing large lattices, even if there is enough total RAM available. `-PSIM_NPROCS` is designed to overcome this limitation.

FermiQCD with `-PSIM_NPROCS` enables you to run parallel processes on one machine even if there is only enough RAM to run one of them at time but not all of them concurrently. This is because only one of the parallel processes needs to be loaded in RAM at once and the OS can automatically switch between processes by swapping to disk. Communications between the parallel processes are also buffered to disk and therefore they work as expected. For example:

- `qcdutils_run.py -PSIM_NPROCS=2` forks two processes (0 and 1)
- p1 is put to sleep and p0 is executed
- If p0 sends data to p1 the data is stored in a named pipe
- When p0 is completed or attempts to receive data it is put to sleep
- When p0 is put to sleep, p1 is loaded in RAM and continues execution.

- p1 can receive the data sent from p0 by reading from the named pipe.

While this is not very efficient, it does allow to run most algorithms even when there is not enough RAM available. The communication patterns are implemented in ways that avoid deadlocks.

A better option is to use MPI and this is the preferred option for production runs. If you want to use MPI, it must be pre-installed on your system separately. On Debian/Ubuntu Linux machines this is done with:

```

1 sudo apt-get install mpich2
2 cd ~
3 touch .mpd.conf
4 chmod 600 .mpd.conf
5 mpd &
```

In order to use it from `qcdutils_run` you need to recompile FermiQCD with MPI:

```

1 python qcdutils_run.py -compile -mpi
```

This makes an mpi-based executable for FermiQCD:

```

1 fermiqcd/fermiqcd-mpi.exe
```

You can run it with

```

1 python qcdutils_run.py -mpi=4 \
2     -gauge:start=load:load=demo/demo.nersc.mdp -plaquette
```

Internally it calls `mpirun`.

4.2 General syntax

The main options of “`qcdutils_run.py`” are:

- `-gauge`: creates, loads, and saves gauge configurations
- `-plaquette`: computes the average plaquette
- `-plaquette_vtk`: generates images of the plaquette density
- `-polyakov`: computes Polyakov lines
- `-polyakov_vtk`: computes images from polyakov lines

- `-topcharge`: computes the total topological charge
- `-topcharge_vtk`: generates images of the topological charge density
- `-cool`: cools the gauge configurations
- `-cool_vtk`: cools the gauge configurations and save images of the topological charge at every step
- `-quark`: computes a quark propagator (different sources are possible)
- `-pion`: computes a pion propagator (and optionally saves images of the pion propagator)
- `-meson`: computes a meson propagator (and optionally saves images of the meson propagator)
- `-current_static`: computes a three points correlation function by inserting a light-light between two heavy-light meson operators (and optionally saves images of the current density)
- `-4quark`: computes all possible contractions of a 4-quark operator between two light mesons.

Each option takes optional attributes in the form `:name=value`. All attributes have default values. The `-pion`, `-meson` and `current_static` operators take an optional `:vtk=true` argument needed to save the VTK files for visualization.

Multple options can be listed and executed together in one run. Although we recommend separating the following operations in different runs:

- Generate gauge configurations,
- Compute propagators on each gauge configuration.
- Measure opeartors by reading previously computed gauge configurations and propagators.

The code described here should be considered and example and other cases can be dealt with by modifying the provided examples.

4.3 Creating a cold or hot gauge configuration

You can create a cold gauge configuration with the following command

```
1 python qcutils_run.py -gauge:start=cold:nt=16:nx=4:ny=4:nz=4:nc=3
```

The `-gauge` option sets the gauge parameters of FermiQCD. The option is followed by parameters separated by a colon. All parameters have default values.

`qcutils_run.py` creates a cold gauge configuration with volume `nt=16:nx=4:ny=4:nz=4`, $SU(N_c)$ with `nc=3`, and saves it with the name “cold.mdp”.

The order of the parameters is not important. All parameters have default values. The output lists all parameters which are used.

You can also run

```
1 python qcutils_run.py -gauge:start=hot:nt=16:nx=4
```

to generate a “hot.mdp” gauge configuration. Notice `nc=3` is the default.

4.4 Loading a gauge configuration

The `start` attribute of the `-gauge` option takes four possible values:

- `cold`: makes a cold gauge configuration
- `hot`: makes a hot gauge configuration
- `instantons`: makes a cold configuration containing one instanton and an, optionally, one anti-instanton at given positions.
- `load`: loads one or more gauge configurations (if more than one, it loops over them)

When not set, `start` defaults to `load`, and FermiQCD expects to load input gauge configurations.

In this case, the `load` attribute of the `-gauge` option specifies the pattern of the filenames to read.

You can specify one single gauge configuration by filename or multiple configurations using a glob pattern (for example “*.mdp”).

Here is an example that loads all gauge configurations in the “demo” folder and computes their average plaquette (`-plaquette`):

```
1 python qcutils_run.py -gauge:start=load:load=demo/*.mdp -plaquette
```

Similarly if you want to download a stream of NERSC gauge configurations and compute the average plaquette on each of them you can do:

```
1 python qcdutils_get.py -c mdp -4 http://qcd.nersc.org/nersc/api/files/demo
2 python qcdutils_run.py -gauge:load=demo/*.mdp -plaquette > run.log
3 grep plaquette run.log
```

When loading gauge configurations there is no need to specify the volume since FermiQCD reads that information from the input files.

If you peek into “fermiqcd/fermiqcd.cpp” you can find code like this:

```
1 if(arguments.have("-plaquette")) {
2     mdp << "plaquette = " << average_plaquette(U) << endl;
3 }
```

Here `arguments.have("-plaquette")` checks that the option is present and `average_plaquette(U)` performs the computation for the input gauge configuration `U`. `mdp` is the parallel output stream and it double as wrapper object for the MPI communicator.

4.5 Heatbath Monte Carlo

Whether you start form a cold, hot or loaded gauge configuration you can generate more by using the `n` attribute. In this example:

```
1 python qcdutils_run.py -gauge:start=cold:beta=4:n=10:therm=100:steps=5
```

FermiQCD starts from a cold configuration, and using the Wilson gauge action [13] (default) generates `n=10` gauge configurations. It perform 100 thermalization steps (*therm*) starting from the cold one and then 5 *steps* separating the one configuration from the next.

It saves the gauge configuration files with progressive names:

```
1 cold.mdp
2 cold.0000.mdp
3 cold.0001.mdp
4 ...
5 cold.0099.mdp
```

If you want to change “cold” prefix of numbered filename you can specify the `prefix` attribute of the `-gauge` option. When this attribute is missing, `prefix` defaults to the name of the starting gauge configuration, i.e. “cold”.

When you start from hot or cold, FermiQCD generates output files in the current working directory. If you start from a loaded file, it generates output files (gauge configurations, propagators, vtk files) in the same folder as the input files.

You can use the optional `alg` attribute to use an improved action or a SSE2 optimized action.

Here is the relevant code in “fermiqcd.cpp”:

```

1 int nconfigs = arguments.get("-gauge", "n", 0);
2 ...
3 for(int n=-1; n<nconfigs; n++) {
4     if(n>=0) {
5         int niter =(n==0)?ntherm:nsteps;
6         if (gauge_action=="wilson")
7             WilsonGaugeAction::heatbath(U,gauge,niter);
8         else if (gauge_action=="wilson_improved")
9             ImprovedGaugeAction::heatbath(U,gauge,niter);

```

Use `-options` to see which algorithms are available. For example you can declare an improved gauge action:

```
1 -gauge:action=wilson_improved:beta=...:zeta=...:u_s=...:u_t=...
```

where ζ , u_t , and u_s are the parameters of the improved un-isotropic action defined in ref. [14].

4.6 Computing a pion propagator

We define a pion propagator as

$$C_2[t_1] = \sum_{\mathbf{x}} \langle \pi(0, \mathbf{0}) | \pi(+t, \mathbf{x}) \rangle \quad (1)$$

$$= \sum_{\mathbf{x}} \sum_{ij,\alpha\beta\delta\rho} \langle 0 | \bar{q}_a^{i\alpha}(0) \gamma_{\alpha\beta}^5 q_b^{j\beta}(0) \bar{q}_b^{j\delta}(t, \mathbf{x}) \gamma_{\delta\rho}^5 q_a^{i\rho}(t, \mathbf{x}) | 0 \rangle \quad (2)$$

$$= \sum_{\mathbf{x}} \sum_{i,\alpha} |S^{ii,\alpha\alpha}(t, \mathbf{x})|^2 \quad (3)$$

where

$$S^{ij,\alpha\beta}(t, \mathbf{x}) \equiv \langle 0 | \{q^{i\alpha}(0), \bar{q}^{j\beta}(t, \mathbf{x})\} | 0 \rangle \quad (4)$$

is a quark propagator with source at $\mathbf{0}$. Here a and b label quark flavours, i and j label color indexes, α , β , δ , ρ label spin indexes. Notice we used the known identity

$$\langle 0 | \{q^{i\alpha}(t, \mathbf{x}), \bar{q}^{j\beta}(0)\} | 0 \rangle = \sum_{\rho\delta} \gamma_{\alpha\rho}^5 S^{*,ji,\delta\rho}(t, \mathbf{x}) \gamma_{\delta\beta}^5 \quad (5)$$

You can compute C2 using the following syntax:

```
1 python qcdutils_run.py \
2     -gauge:start=cold:beta=4:n=10:steps=5:therm=100 \
3     -quark:kappa=0.11:c_sw=0.4:save=false -pion > run.log
```

`qcdutils_run` calls “fermiqcd/fermiqcd.exe” which generates 10 gauge configurations and, for each, computes a quark propagators with the given values of κ and c_{SW} using a fast implementation of the clover action (another attribute that can be set) and compute the pion propagator.

The `-quark` option loops over the j, β indexes and computes the $S^{ij,\alpha\beta}(t, \mathbf{x})$. The `-pion` options loops over the i, α indexes and for every t computes the zero momentum Fourier transform in \mathbf{x} of eq. 2.

Notice that by default `qcdutils` saves all the S components. We can avoid it with `save=false`.

The pion propagator for each gauge configuration can be found in the output log file.

```
1 grep C2 run.log
```

The output of `qcdutils.run` in this case is looks like the following.

```
1 C2 [0] = 14.4746
2 ...
3 C2 [15] = 0.794981
4 C2 [0] = 14.4746
5 ...
6 C2 [15] = 0.794981
7 ...
```

For each t , `C[t]` takes a different value on each gauge configuration.

In some of the following example we rely on the output pattern:

```
1 C2 [...] = ...
```

Later we show how to use `vtk=true` option to save the propagator as function of x and visualize it. We also show tools to automate the analysis of logfiles like “run.log”.

If you peek into “fermiqcd.cpp” you find the following code that computes the pion propagator:

```

1 for(int a=0; a<4; a++) {
2     for(int i=0; i<nc; i++) {
3         psi = 0;
4         if (on_which_process(U.lattice(),0,0,0,0)==ME) x.set(0,0,0,0);
5         psi(x,a,i)=1;
6         psi.update();
7         [...]
8         mul_invQ(phi,psi,U,quark,abs_precision,rel_precision);
9         [...]
10        if (arguments.have("-pion")) {
11            [...]
12            forallsitesandcopies(x) {
13                for(int b=0; b<4; b++)
14                    for(int j=0; j<nc; j++) {
15                        tmp = real(phi(x,b,j)*conj(phi(x,b,j)));
16                        pion[(x(TIME)-t0+NT)%NT] += tmp;
17                        Q(x) += tmp;
18                    }
19            }
20        }
21    }

```

Notice the field Q which is used in the next section. It is used for 3D visualizations of the propagator.

4.7 Action and inverters

You can change the action by setting the `action` attribute of the `-quark` option to one of the following: `clover_fast`, `clover_slow`, `clover_sse2`. The first of them is the fastest portable implementation. The second is a slower but more readable one. The first two support arbitrary $SU(N_c)$ gauge groups while the latter is optimized in assembler for $N_c = 3$. All of them support clover, and un-isotropic actions. The attributes are

<code>kappa</code>	κ
<code>kappa_s</code>	κ_s
<code>kappa_t</code>	κ_t
<code>c_SW</code>	c_{SW}
<code>c_E</code>	c_E
<code>c_B</code>	c_B

If separate values for $\kappa_{s,t}$ are not specified, κ is used for both. c_E is the coefficient that multiplies the electric part of the SW term, c_B multiplies the magnetic part. c_{SW} defaults to 0.

The inverter can be specified using the `alg` attribute of the `-quark` option and it can be one of the following: `bicgstab`, `minres`, `bicgstabvtk`, `minresvtk`. The meaning of the first two is obvious. The second two perform the extra task of saving the field components and the residue at every step of the inversion as a VTK file.

The `-quark` option also takes an optional `source_type` attribute which can be `point` or `wall` and, if point, a `source_point` attribute to position the source at `zero` or the `center` of the lattice. It also takes the optional `smear_steps` and `smear_alpha` which are used to smear the sink.

The relevant code in “fermiqcd.cpp” is:

```

1   for(int a=0; a<4; a++) {
2       for(int i=0; i<nc; i++) {
3           if(source_type==''point '') {
4               psi = 0;
5               if (on_which_process(U.lattice(),t0,x0,y0,z0)==ME) {
6                   x.set(t0,x0,y0,z0);
7                   psi(x,a,i)=1;
8               }
9           }
10          [...]
11          psi.update();
12          [...]
13          if (arguments.get(``-quark '', ``load '', ``false|true '')== ``true '') {
14              phi.load(quarkfilename);
15          } else {
16              mul_invQ(phi,psi,U,quark,abs_precision,rel_precision);
17              phi.save(quarkfilename);
18          }
19          [...]
20          if(use_propagator) {
21              forallsites(x) {
22                  forspincolor(b,j,nc) {
23                      S(x,a,b,i,j) = phi(x,b,j);
24                  }
25              }
26          }
27      }

```

Notice that in FermiQCD inverters are action agnostic. A call to `mul_Q(phi,psi,U,...)` computes $\phi = Q[U]\psi$ where Q is the selected action for the type of fermion ψ (in this document we deal only with wilson type fermions but it works with staggered and domain wall too). A call to `mul_invQ(phi,psi,U,...)` computes $\phi = Q^{-1}[U]\psi$ using the same Q and the selected inverter. There is no code in the inverter which is action specific.

4.8 Meson propagators

Given a meson created by $\bar{q}\Gamma q |0\rangle$, a meson propagator can be defined as follows:

$$C_2[t_1] = \sum_{\mathbf{x}} \langle \Gamma^{source}(0, \mathbf{0}) | \Gamma^{sink}(+t, \mathbf{x}) \rangle \quad (6)$$

$$= \sum_{\mathbf{x}} \sum_{ij,\alpha\beta\delta\rho} \langle 0 | \bar{q}_a^{i\alpha}(0) \Gamma_{\alpha\beta}^{source} q_b^{j\beta}(0) \bar{q}_b^{j\delta}(t, \mathbf{x}) \Gamma_{\delta\rho}^{sink} q_a^{i\rho}(t, \mathbf{x}) | 0 \rangle \quad (7)$$

$$= \sum_{\mathbf{x}} \dots S^{ij,\beta\delta}(t, \mathbf{x}) (\Gamma^{sink} \gamma^5)_{\delta\rho} S^{*ij,\alpha\rho}(t, \mathbf{x}) (\gamma^5 \Gamma^{source})_{\alpha\beta} \quad (8)$$

The command to compute an arbitrary meson propagator and reuse the previously computed propagators (the code assumes different flavours of degenerate quarks, i.e. same mass):

```
1 python qcutils_run.py \
2     -gauge:start=cold:beta=4:n=10:steps=5:therm=100 \
3     -quark:kappa=0.11:c_sw=0.4:save=false \
4     -meson:source_gamma=1:sink_gamma=1 > run.log
```

The `source_gamma` and `sink_gamma` attributes can be specified according to the following table:

source_gamma/sink_gamma	$\Gamma^{source}/\Gamma^{sink}$
I	1
5	γ^5
0	γ^0
1	γ^1
2	γ^2
3	γ^3
05	$\gamma^0\gamma^5$
15	$\gamma^1\gamma^5$
25	$\gamma^2\gamma^5$
35	$\gamma^3\gamma^5$
01	$\gamma^0\gamma^1$
02	$\gamma^0\gamma^2$
03	$\gamma^0\gamma^3$
12	$\gamma^1\gamma^2$
13	$\gamma^1\gamma^3$
23	$\gamma^2\gamma^3$

The relevant code in “fermiqed.cpp” is described here:

```

1  if(arguments.have("-meson")) {
2      [...]
3      G1 = Gamma5*parse_gamma(arguments.get("-meson", "source_gamma", ...))
4      G2 = parse_gamma(arguments.get("-meson", "sink_gamma", ...))*Gamma5
5      forspincolor(a,i,U.nc) {
6          forspincolor(b,j,U.nc) {
7              forallsites(x) {
8                  s1=s2=0;
9                  for(int c=0;c<4;c++) {
10                      s1 += S(x,a,c,i,j)*G2(c,b);
11                      s2 += conj(S(x,c,b,i,j))*G1(c,a);
12                  }
13                  tmp = abs(s1*s2);
14                  meson[(x(TIME)-t0+NT)%NT] += tmp;
15                  Q(x) += tmp;
16              }
17          }
18      }
}

```

As before we use a scalar field Q for data visualization.

In this and the other examples the two quarks are degenerate but it is possible to change one of the quark propagators by simply replacing it in the code for a different one. We leave it

to the reader as an exercise. A next version of “fermiqcd.cpp” will have an option `-quark2` for doing this automatically.

4.9 Current insertion

We define it as follows (for two light quarks a, b and one static quark h):

$$\begin{aligned}
 C_{current}[t] &= \sum_{\mathbf{x}} \langle \Gamma_{ha}^{source}(-t, \mathbf{x}) | \bar{q}_a \Gamma^{current} q_b(0) | \Gamma_{bh}^{sink}(+t, \mathbf{x}) \rangle \\
 &= \sum_{\mathbf{x}} \sum_{\dots} \langle 0 | \bar{h}^{i\alpha}(-t, \mathbf{x}) \Gamma_{\alpha\beta} q_a^{i\beta}(-t, \mathbf{x}) \bar{q}_a^{r,\zeta} \Gamma_{\zeta\theta}^{current} q_b^{s\theta} \bar{q}_b^{j\delta}(t, \mathbf{x}) \Gamma_{\delta\rho} h^{i\rho}(t, \mathbf{x}) | 0 \rangle \\
 &= \sum_{\mathbf{x}} \text{tr}(\Gamma^{source} \gamma^5 S^\dagger(-t, \mathbf{x}) \gamma^5 \Gamma^{current} S(t, \mathbf{x}) \Gamma^{sink} H^\dagger(-t, t, \mathbf{x})) \tag{9}
 \end{aligned}$$

Here H is the heavy quark propagator according to Heavy Quark Effective Theory [15] (from $(-t, \mathbf{x})$ to (t, \mathbf{x})):

$$H(-t, t, x) = \frac{1}{2}(1 + \gamma^0)U_0(-t, x)U_0(-t + 1, x)\dots U_0(t - 1, x) \tag{10}$$

You can compute it with

```

1 python qcutils_run.py \
2   -gauge:start=cold:beta=4:n=10:steps=5:therm=100 \
3   -quark:kappa=0.11:c_sw=0.4:save=false \
4   -current_static:source_gamma=1:sink_gamma=1:current_gamma=I > run.log

```

The relevant code in “fermiqcd.cpp” is:

```

1 G1 = parse_gamma(arguments.get("-current_static", "source_gamma", ...)) *
      Gamma5;
2 G2 = parse_gamma(arguments.get("-current_static", "sink_gamma", ...));
3 G3 = Gamma5*parse_gamma(arguments.get("-current_static", "current_gamma",
      ...));
4 G4 = G2*(1-Gamma[0])/2*G1;
5 forallsites(x)
6   if(x(TIME)>=0) {
7     z.set((NT+2*t0-x(TIME))%NT,x(1),x(2),x(3));
8     forspincolor(a,i,U.nc) {

```

```

9      for spin color(b,j,U.nc) {
10         s1 = s2 = 0;
11         for(int c=0; c<4; c++) {
12             s1 += conj(S(z,c,a,j,i))*G3(c,b);
13             for(int k=0; k<U.nc; k++)
14                 s2 += S(x,b,c,j,k)*G4(c,a)*conj(Sh(x,i,k));
15         }
16         tmp = abs(s1*s2);
17         current[(x(TIME)-t0+NT)%NT] += tmp;
18         Q(x) += tmp;
19     }
20 }
21 }
```

Here Sh is the product of links from $-t$ to t along the time direction.

4.10 Four quark operators

Instead of inserting a current we can insert a 4-quark operator between two meson operators (light-light):

$$\begin{aligned}
C_3[t_1][t_2] &= \sum_{\mathbf{x}_1} \sum_{\mathbf{x}_2} \langle \Gamma^{source}(-t_1, \mathbf{x}_1) | \bar{q}_a \Gamma_A q_b \otimes \bar{q}_c \Gamma_B q_d | \Gamma^{sink}(+t_2, \mathbf{x}_2) \rangle \quad (11) \\
&= \text{tr}(\Gamma^{source} \gamma^5 S^\dagger(-t_1, \mathbf{x}_1) \gamma^5 \Gamma_A S(-t_1, \mathbf{x}_1)) \text{tr}(\Gamma^{sink} \gamma^5 S^\dagger(t_2, \mathbf{x}_2) \gamma^5 \Gamma_B S(t_2, \mathbf{x}_1)) \\
&\text{or } \text{tr}(\Gamma^{source} \gamma^5 S^\dagger(-t_1, \mathbf{x}_1) \gamma^5 \Gamma_A S(t_2, \mathbf{x}_2) \Gamma^{sink} \gamma^5 S^\dagger(t_2, \mathbf{x}_2) \gamma^5 \Gamma_B S(-t_1, \mathbf{x}_1))
\end{aligned}$$

The *or* indicates that there are two possible contractions. FermiQCD computes both of them and writes them separately in the output.

Here $\Gamma_A \otimes \Gamma_B$ is the spin/color structure of the 4-quark operator. We are also ignoring the contractions that corresponds to disconnected diagrams.

We can compute $\Gamma_A \otimes \Gamma_B$ for $\gamma_5 \otimes \gamma_5$ in spin and $\mathbf{1} \otimes \mathbf{1}$ in color (`5Ix5I`) with:

```

1 python qcdutils_run.py \
2   -gauge:start=cold:beta=4:n=10:steps=5:therm=100 \
3   -quark:kappa=0.11 -4quark:source=1:operator=5Ix5I > run.log
```

In this example, `source=1` indicates that $\Gamma^{source} = \Gamma^{sink} = \gamma^1$.

This generates the following output, repeated for each of the 10 gauge configurations:

```

1 C3 [0] [0] = 9.12242
2 C3 [0] [1] = 0.485189
3 ...
4 C3 [15] [15] = 9.12242

```

Notice the program computes the two contractions of the operator and writes one in `C3` and one in `C3x`.

Instead of `source=1` you can use any of the operators defined for mesons.

Instead of $5I \times 5I$ 4-quark operator you can use any the following other operators: $5Ix5I$, $0Ix0I$, $1Ix1I$, $2Ix2I$, $3Ix3I$, $05Ix05I$, $15Ix15I$, $25Ix25I$, $35Ix35I$, $01Ix01I$, $02Ix02I$, $03Ix03I$, $12Ix12I$, $13Ix13I$, $23Ix23I$, $5Tx5T$, $0Tx0T$, $1Tx1T$, $2Tx2T$, $3Tx3T$, $05Tx05T$, $15Tx15T$, $25Tx25T$, $35Tx35T$, $01Tx01T$, $02Tx02T$, $03Tx03T$, $12Tx12T$, $13Tx13T$, $23Tx23T$. Here the numerical part represents the $\Gamma \otimes \Gamma$ stucture of the 4-quark operator, the I or T represents its color structure. TxT stands for $\sum_a T^a \otimes T^a$ with $T^a = \lambda^a/2$, and λ^a is the $SU(3)$ generator.

Here is the relevant source code in “fermiqcd.cpp”:

```

1 mdp_matrix G = parse_gamma(arguments.get("-4quark", "source", ...));
2 forspincolor(a,i,U.nc) {
3     for(int c=0; c<4; c++)
4         for(int d=0; d<4; d++)
5             if(G(c,d)!=0)
6                 forallsites(x)
7                     for(int k=0; k<U.nc; k++)
8                         open_prop[a][b][i][j][(x(TIME)-t0+NT)%NT] +=
9                             S(x,a,c,i,k)*conj(S(x,b,d,j,k))*G(c,d);
10    string op4q = arguments.get("-4quark", "operator", ...);
11    if(arguments.have("-4quark")) {
12        for(int a=0; a<4; a++)
13            for(int b=0; b<4; b++)
14                for(int c=0; c<4; c++)
15                    for(int d=0; d<4; d++) {
16                        mdp_complex g1 = G1(b,a);
17                        mdp_complex g2 = G2(d,c);
18                        if(g1!=0 && g2!=0)
19                            for(int i=0; i<U.nc; i++)
20                                for(int j=0; j<U.nc; j++)
21                                    if(!rotate) {
22                                        c3a+=abs(open_prop[a][b][i][j][t1s]*g1*
23                                                 open_prop[c][d][j][j][t2s]*g2);
24                                        c3b+=abs(open_prop[c][b][j][i][t1s]*g1*
25                                                 open_prop[a][d][i][j][t2s]*g2);
26                                    } else

```

```

27             [...]
28         }
29     }
30 }
31 }
```

Notice the two contractions are computed separately. The case `rotate==true` corresponds to the TxT color structure.

5 Images and movies with `qcdutils_vis.py` and `qcdutils_vtk.py`

In this section we describe how to make 3D visualizations using VisIt [6] and how to embed visualizations into web pages using “processing.js” [7].

VisIt is a visualization software developed at Lawrence Livermore National Lab based on the VTK toolkit. It provides a GUI which can be used to open the VTK files created by FermiQCD (or other scientific program) in interactive mode, but it can also be scripted using the Python language.

“processing.js” is a lightweight javascript library that allows drawing on an HTML canvas using the *processing* language or the javascript language.

`qcdutils` uses meta-programming to generate VisIt scripts (`qcdutils_vis`) or processing.js scripts (`qcdutils_vtk`). The former is more flexible and is more appropriate for making high resolution images. The latter makes it easy to embed 3D visualizations into web pages.

Using VisIt is intuitive but there are certain tasks which can be repetitive. For example if you have multiple VTK files containing topological change density (or any other scalar field), you have to determine the optimal threshold values for the contour plots. If you have many files you may want to interpolate between them for a smoother visualization. `qcdutils_vis` helps with these tasks. In particular it can:

- Split VTK files containing multiple time-slices into separate VTK files, one for each slice.
- Interpolate each couple of consecutive VTK files and make new ones in between. This is necessary for smoother visualizations.
- Compute automatic thresholds values for contour plots.
- Resample the points by interpolating between the.

- Generate VisIt scripts which converts VTK files to JPEG format (these script can be saved, edited, and reused).
- Pipe the above operations and run them for multiple files.

Images generate in this way can be assembled into mpeg4 (or quicktime or avi) movies using ffmpeg (an open source tool that is distributed with VisIt) but there are other and better tools available. We strongly recommend “MPEG Streamclip”. It is much faster, robust, and much easier to properly configure than ffmpeg.

5.1 About VTK file format

There are many VTK file formats. `qcdutils` uses the binary VTK file format described below to store scalar fields, usually by timeslices.

A typical file has the following content:

```

1 # vtk DataFile Version 2.0
2 filename.vtl
3 BINARY
4 DATASET STRUCTURED_POINTS
5 DIMENSIONS 4 4 4
6 ORIGIN      0 0 0
7 SPACING     1 1 1
8 POINT_DATA 64
9 SCALARS scalars_t0 float
10 LOOKUP_TABLE default
11 [binary data]
12 SCALARS scalars_t1 float
13 LOOKUP_TABLE default
14 [binary data]
15 ...

```

It consists of an ASCII header declaring the 3D dimensions (4 4 4) and the total number of points ($4 \times 4 \times 4 = 64$). This is followed by blocks representing the time-slices. Each block has its own ASCII header:

```

1 SCALARS scalars_t0 float
2 LOOKUP_TABLE default

```

followed by binary data (64 floating point numbers).

`scalars_t0`, `scalars_t1`, etc. are the names of the fields as stored by FermiQCD. When time-slices are extracted by `qcdutils_vis` the slices are renamed as `slice`.

Given any VTK file, for example `demo.vtk` we can visualize it using `qcdutils_vis.py` using the following syntax:

```
1 python qcdutils_vis.py -r 'scalars_t0' -p default demo.vtk
```

`qcdutils_vis.py` generates images in JPEG format.

Similarly we can visualize by creating an interactive 3D web page:

```
1 python qcdutils_vtk.py -u 0.10 -l 0.90 demo.vtk
```

If the filename is a glob pattern (`*.vtk`), both tools loop and process all files matching the pattern.

`qcdutils_vtk` computes the range of values in the scalar field from the maximum to the minimum. `-u 0.10` indicates we want an isosurface at 10% from the max and `-l 0.90` indicates we want another isosurface at 90% from the max (10% from the min). It is also possible to specify the colors of the iso-surfaces.

`qcdutils_vtk` generates HTML files with the same as the input VTK files followed by the `.html` postfix. The isosurfaces are computed by the Python program itself but the representation of the isosurfaces is embedded in the html file, together with the “processing.js” library, and with custom JS code. These files are not static images. You can rotate them in the browser using the mouse.

5.2 Plaquette

As an example, we want to make a movie of the plaquette as function of the time-slice. We follow this workflow:

- Load a gauge configuration.
- Compute the plaquette at each lattice site.
- Save the plaquette as a VTK file.
- Split the VTK file into one file per time-slice.
- Interpolate the timeslices to generate more frames.
- Generate contour plots for each frame and save them as JPEG files.

This can be done in two steps. Step one:

```
1 python qcdutils_run.py \
2     -gauge:load=demo/demo.nersc.mdp \
3     -plaquette_vtk
```

This command uses FermiQCD to load the gauge configurations. For each of them it computes the trace of the average plaquette at each lattice site, and generates one VTK file contain the 4D scalar for the plaquette. This file is saved in a new file with the same prefix as the input but ending in “.plaquette.vtk”.

Step two:

```
1 python qcdutils_vis.py -s '*' -i 9 -p default 'demo/*.plaquette.vtk'
```

It reads all files matching the pattern “demo/*.plaquette.vtk”, extracts all time-slices with names matching “*” (all time slices), and interpolates each couple of VTK files by adding 9 more frames (-i 9), then generates a VTK script that reads each VTK file, resamples it, and stores contour plots in JPEG files with consecutive file filenames..

The generated script has a unique name which looks like this:

```
1 qcdutils_vis_2fac1b86-5b86-42ee-8552.py
```

qcdutils_vis writes and runs the script. It saves it for you in case you want to read and modify it.

When it runs, it loops over all the frames, resamples them, computes the contour plots and saves each frame into one JPEG image:

```
1 qcdutils_vis_2fac1b86-5b86-42ee-8552_0000.00.jpeg
2 qcdutils_vis_2fac1b86-5b86-42ee-8552_0001.01.jpeg
3 ...
4 qcdutils_vis_2fac1b86-5b86-42ee-8552_0003.00.jpeg
```

Here 0000, 0001, 0002, 0003 are the original frames (timeslices) and the. .01, .02, ..., .09 are the interpolated ones.

Notice that the -i 9 option is very important to obtain smooth sequences of images to be assembled into movies.

The option

```
1 -p default
```

is equivalent to

```
1 -p 'AnnotationAttributes [] ; ResampleAttributes [] ; ContourAttributes [] '
```

Here `Annotation`, `Resample` and `Contour` are VisIt functions. Using `-p` you can set the attributes for each functions.

For example, to remove the bounding box you would replace

```
1 AnnotationAttributes []
```

with

```
1 AnnotationAttributes [axes3D.bboxFlag=0]
```

To increase the re-sampling points from 100 to 160 you would replace:

```
1 ResampleAttributes []
```

with

```
1 ResampleAttributes [samplesX=160; samplesY=160; samplesZ=160]
```

To change the color of the 9th contour to Orange, you would replace:

```
1 ContourAttributes []
```

with

```
1 ContourAttributes [SetMultiColor(9,orange)]
```

The argument of the `<function>Attributes[...]` are VisIt attributes and they are described in the VisIt documentation.

The relevant page of code in “fermiqcd.cpp” that computes the VTK plaquette is here:

```
1 void plaquette_vtk(gauge_field& U, string filename) {
2     mdp_field<mdp_real> Q(U.lattice());
3     mdp_site x(U.lattice());
4     forallsites(x) if(x(0)==0) {
5         Q(x)=0;
6         for(int mu=0; mu<4; mu++)
7             for(int nu=mu+1; nu<4; nu++)
8                 Q(x)+=real(trace(plaquette(U,x,mu,nu)));
9     }
10    Q.save_vtk(filename,-1);
11 }
12 [...]
13 if (arguments.have("-plaquette_vtk")) {
```

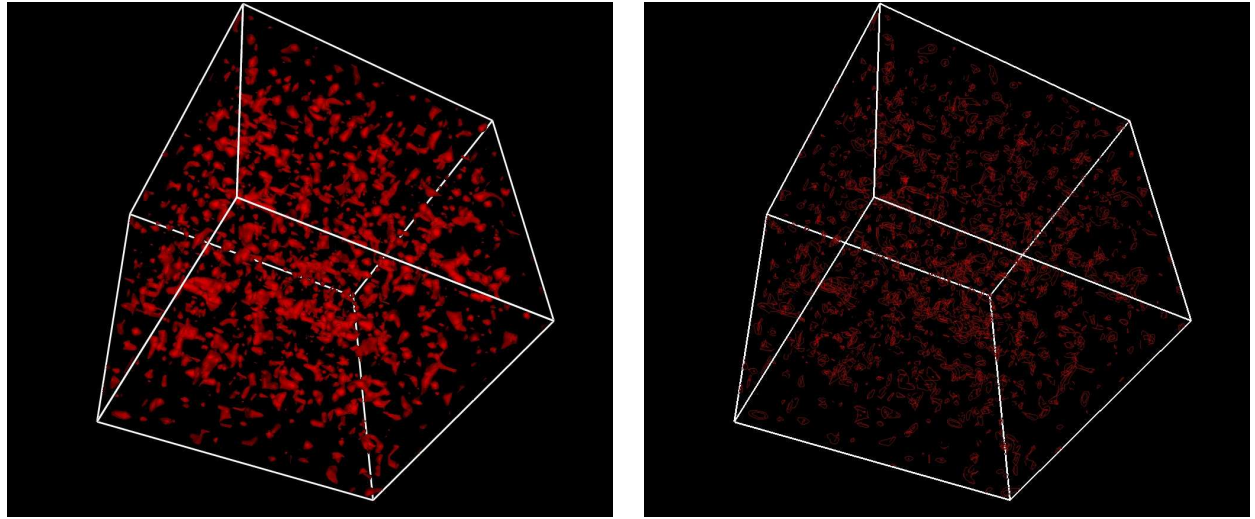


Figure 4: Visualization of a contour plot for the average plaquette (left) and the intersection of the contours with the bounding box (right)

```
14     plaquette_vtk(U,newfilename+" .plaqette.vtk");
15 }
```

Notice how the plaquette is computed for each x , summed over μ, ν , stored in a scalar field $Q(x)$, and then saved in a file. This strategy can be used to visualize any FermiQCD scalar field with minor modifications of the source.

5.3 Topological charge density

Similarly to the average plaquette we can make images corresponding to the topological charge density.

To generate the topological charge density we need to cool the gauge configurations (`-cool`) and then compute the topological charge (`-topcharge_vtk`):

```
1 python qcutils_run.py \
2     -gauge:load=demo/demo.nersc.mdp \
3     -cool:steps=20 -topcharge_vtk
1 python qcutils_vis.py -s '*' -i 9 -p default 'demo/*.topcharge.vtk'
```

The relevant code in “fermiqcd.cpp” is below:

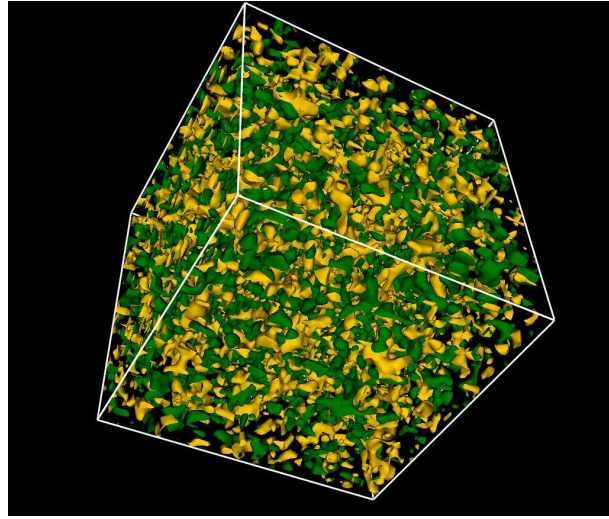


Figure 5: Visualization of the topological charge density.

```

1 if (arguments.have("-topcharge_vtk")) {
2     float tc = topological_charge_vtk(U,newfilename+".topcharge.vtk",-1);
3     mdp << "topcharge = " << tc << endl;
4 }
```

`topological_charge_vtk` is defined in “`fermiqcd.topological_charge.h`”. The `-1` arguments indicates we want to save all time slices. The actual code to compute the topological charge density is:

```

1 void topological_charge(mdp_field<float> &Q, gauge_field &U) {
2     compute_em_notrace_field(U);
3     mdp_site x(U.lattice());
4     forallsitesandcopies(x) {
5         Q(x)=0;
6         for(int i=0; i<U.nc; i++)
7             for(int j=0; j<U.nc; j++)
8                 Q(x)+=real(U.em(x,0,1,i,j)*U.em(x,2,3,j,i)-
9                             U.em(x,0,2,i,j)*U.em(x,1,3,j,i)+
10                            U.em(x,0,3,i,j)*U.em(x,1,2,j,i));
11     }
12     Q.update();
13 }
```

Here `U.em` is the electro-magnetic field computed from `U`.

5.4 Cooling

Sometimes we may want to see the changes in the topological charge density as the configuration is cooled down. This requires computing the topological charge density at every cooling step. This can be done with the `-cool_vtk` option:

```
1 python qcdutils_run.py \
2     -gauge:start=load:load=demo/demo.nersc.mdp \
3     -cool_vtk:cooling=10 > run.log

1 python qcdutils_vis.py -r 'scalars_t0' -i 9 -p default 'demo/*.cool???.vtk'
```

The `-cool_vtk` option creates VTK files ending in “cool00.vtk”, “cool01.vtk”,..., “cool49.vtk”. To make a smooth movie we do not break files into time-slices (no `-s` option) but instead we extract the same slice for every file (`-r 'scalars_t0'`). Then we interpolate the frames (`-i 9`).

The above code generates JPEG images showing different stages of cooling of the data. You can see some of the images in fig. 6

The relevant code in “fermiqcd.cpp” is here:

```
1 void cool_vtk(gauge_field& U, mdp_args& arguments, string filename) {
2     if (arguments.get("-cool","alg","ape")=="ape")
3         for(int k=0; k<arguments.get("-cool_vtk","n",20); k++) {
4             ApeSmearing::smear(U,
5                 arguments.get("-cool_vtk","alpha",0.7),
6                 arguments.get("-cool_vtk","steps",1),
7                 arguments.get("-cool_vtk","cooling",10));
8             topological_charge_vtk(U,filename+".cool"+tostring(k,2)+".vtk",0);
9         }
10    else
11        mdp.error_message("cooling algorithm not supported");
12 }
```

The smearing algorithm is in the “topological_charge_vtk” file:

```
1 class ApeSmearing {
2     public: static void smear(gauge_field &U,
3                                 mdp_real alpha=0.7,
4                                 int iterations=20,
5                                 int cooling_steps=10) {
6         gauge_field V(U.lattice(),U.nc);
7         mdp_site x(U.lattice());
8         for(int iter=0; iter<iterations; iter++) {
```

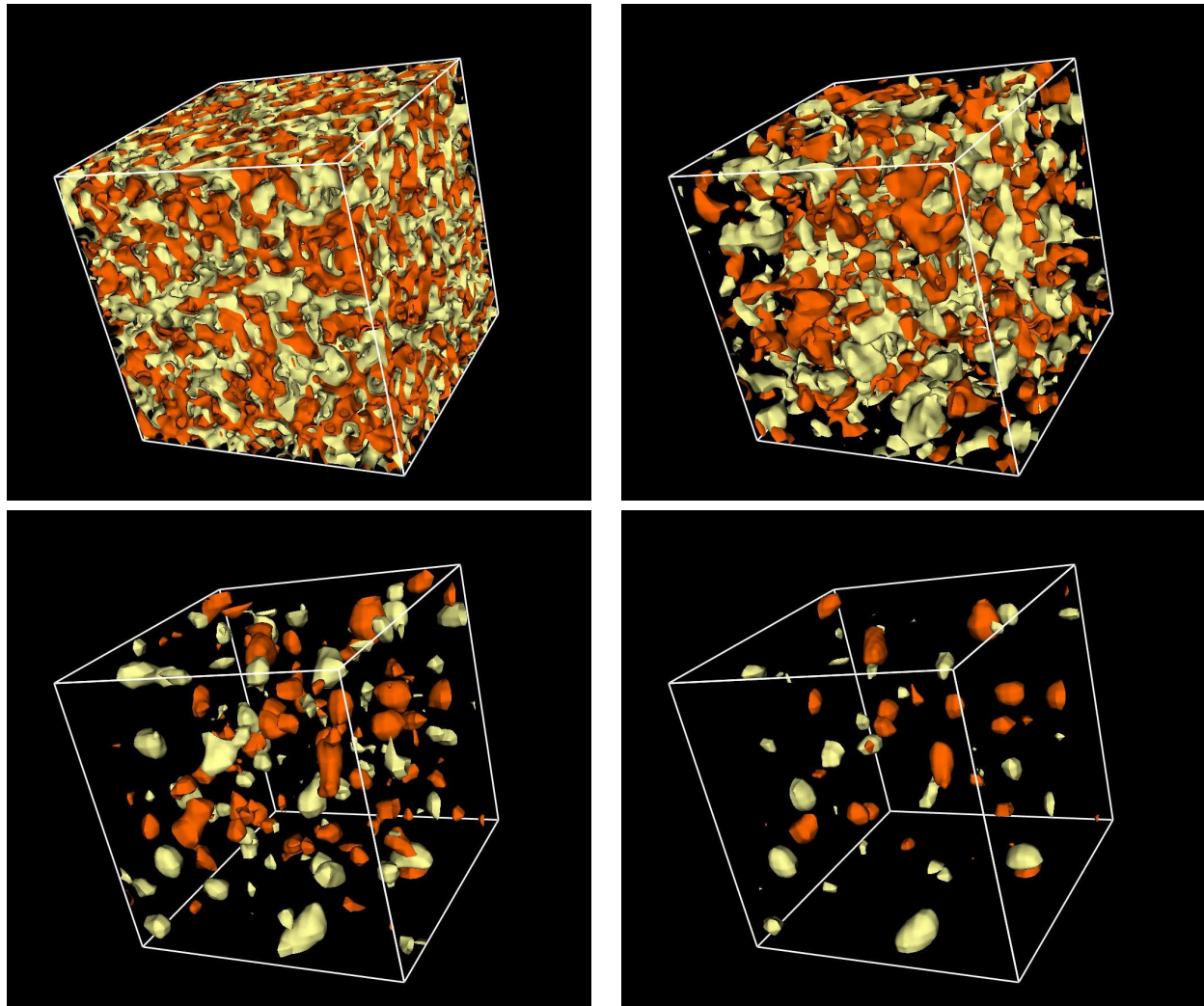


Figure 6: Visualization of the topological charge density at different cooling stages.

```

9   cout << "smearing step " << iter << "/" << iterations << endl;
10  V=U;
11  for(int mu=0; mu<4; mu++) {
12      forallsites(x) {
13          U(x,mu)=(1.0-alpha)*V(x,mu);
14          for(int nu=0; nu<U.ndim; nu++)
15              if(nu!=mu)
16                  U(x,mu)+=(1.0-alpha)/6*
17                      (V(x,nu)*V(x+nu,mu)*hermitian(V(x+mu,nu))+
```

```

18         hermitian(V(x-nu,nu))*V(x-nu,mu)*V((x-nu)+mu,nu));
19         U(x,mu)=project_SU(U(x,mu),cooling_steps);
20     }
21 }
U.update();
23 }
24 }
25 };

```

5.5 Polyakov lines

A Polyakov line is the trace of the product of the gauge links along the time direction, therefore it is a 3D complex field. Here we are interested in the real part only (the image part is qualitatively the same).

We can visualize Polyakov lines using the `-polyakov_vtk` option:

```

1 python qcutils_run.py \
2     -gauge:load=demo/demo.nersc.mdp \
3     -polyakov_vtk

```

which we can convert to images with:

```

1 python qcutils_vis.py \
2     -r 'scalars_t0' -i 9 -p default 'demo/*.polyakov.vtk'

```

The output is show in fig. 7.

Here is the relevant code in “fermqcd.cpp”:

```

1 void polyakov_vtk(gauge_field& U, string filename) {
2     int L[3];
3     L[0]=U.lattice().size(1);
4     L[1]=U.lattice().size(2);
5     L[2]=U.lattice().size(3);
6     mdp_lattice space(3,L,
7         default_partitioning<1>,
8         torus_topology,
9         0, 1, false);
10    mdp_matrix_field V(space,U.nc,U.nc);
11    mdp_field<mdp_real> Q(space,2);
12    mdp_site x(U.lattice());
13    mdp_site y(space);
14

```

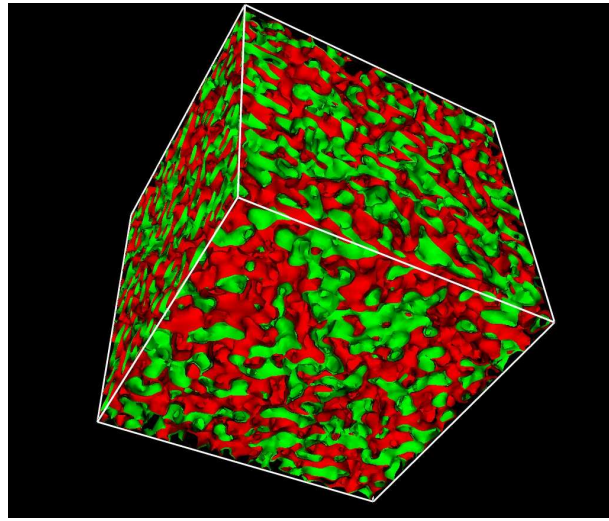


Figure 7: Visualizaition of contour plots for the Polyakov lines. Different colors represent positive and negative values of the real part of the Polyakov lines.

```

15 int k,mu=0,nu=1;
16 mdp_complex s=0;
17
18 forallsites(y) V(y)=1;
19 for(int t=0; t<L[0]; t++) {
20     forallsites(y) {
21         x.set(t,y(0),y(1),y(2));
22         V(y)=V(y)*U(x,0);
23     }
24 }
25
26 forallsites(y) {
27     mdp_complex z=trace(V(y));
28     Q(y,0)=real(z);
29     Q(y,1)=imag(z);
30 }
31 Q.save_vtk(filename,-1,0,0,false);
32 }
33 [...]
34 if (arguments.have("-polyakov_vtk")) {
35     polyakov_vtk(U,newfilename+".polyakov.vtk");
36 }
```

This code is a little different than the previous one. It creates a 3D lattice called `space` which

is a time projection of the 4D space. While x lives on the full lattice, y leaves only on the 3D space. q is a scalar field with two components (real and imaginary part of the Polyakov lines) which lives in 3D space.

5.6 Quark propagator

Given any gauge configuration we can visualize quark propagators in two ways. We can use the normal inverter and save the propagator at the end of the inversion for each source/sink spin/color component:

```
1 python qcutils_run.py \
2     -gauge:start=load:load=demo/demo.nersc.mdp \
3     -quark:kappa=0.135:source_point=center:alg=bicgstab:vtk=true > run.log
```

(here using the `bicgstab`, the Stabilized Bi-Conjugate Gradient). Alternatively we can use a modified inverter which saves the components but also VTK visualization for the field components and the residue at each step of the inversion.

```
1 python qcutils_run.py \
2     -gauge:start=load:load=demo/demo.nersc.mdp \
3     -quark:kappa=0.135:source_point=center:alg=bicgstab_vtk > run.log
```

Fig. 8 shows different components of a quark propagator on a hot and a cold configuration. From now on we assume the propagator has been computed and we reuse it.

5.7 Pion propagator

In a previous section, computed the zero momentum Fourier transform of the pion propagator. Now we want to visualize it for every point in space:

$$Q(t, \mathbf{x}) = \langle \pi_{ab}(0, \mathbf{0}) | \pi_{ab}(+t, \mathbf{x}) \rangle = \sum_{i,\alpha} |S^{ii,\alpha\alpha}(t, \mathbf{x})|^2 \quad (12)$$

This can be done using the `vtk=true` attribute of the `-pion` option:

```
1 python qcutils_run.py \
2     -gauge:start=load:load=demo/demo.nersc.mdp \
3     -quark:kappa=0.135:source_point=center:load=true \
4     -pion:vtk=true > run.log
```

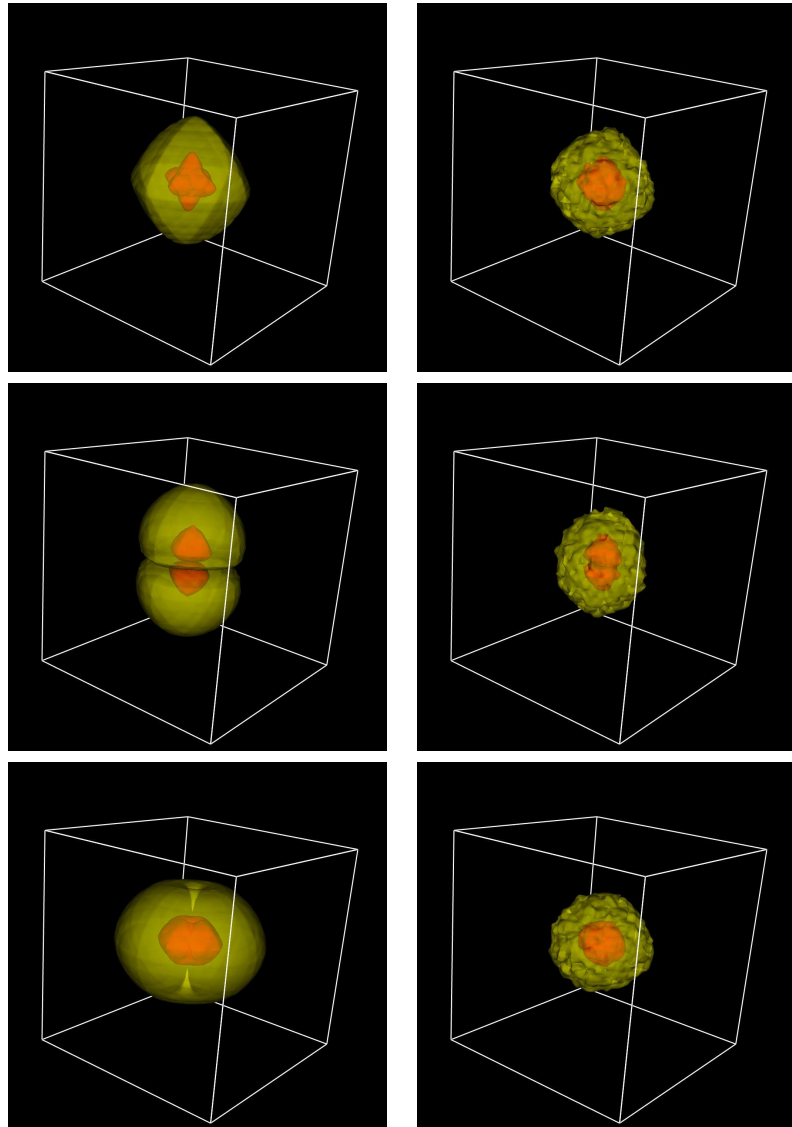


Figure 8: Different components of a quark propagator on a cold gauge configuration (left) and on a thermalized gauge configuration (right). From top to bottom, they show the magnitude of $S^{\alpha\beta ij}(t, \mathbf{x}) = S^{0000}(0, \mathbf{x})$, $S^{0200}(0, \mathbf{x})$, and $S^{0300}(0, \mathbf{x})$.

Notice the `-quark...:load=true` which reloads the previous propagator. We can now convert the pion VTK visualization into images using `qcdutils_vis`:

```
1 python qcdutils_vtk.py -u 0.01 -l 0.00001 'demo/*.pion.vtk'
```

```
2 python qcduutils_vis.py -s '*' -i 9 -p default 'demo/*.pion.vtk'
```

In this case the `-i 9` option is used to interpolate between time-slices in case the images are to be assembled into a movie.

Examples of images are shown in fig.9

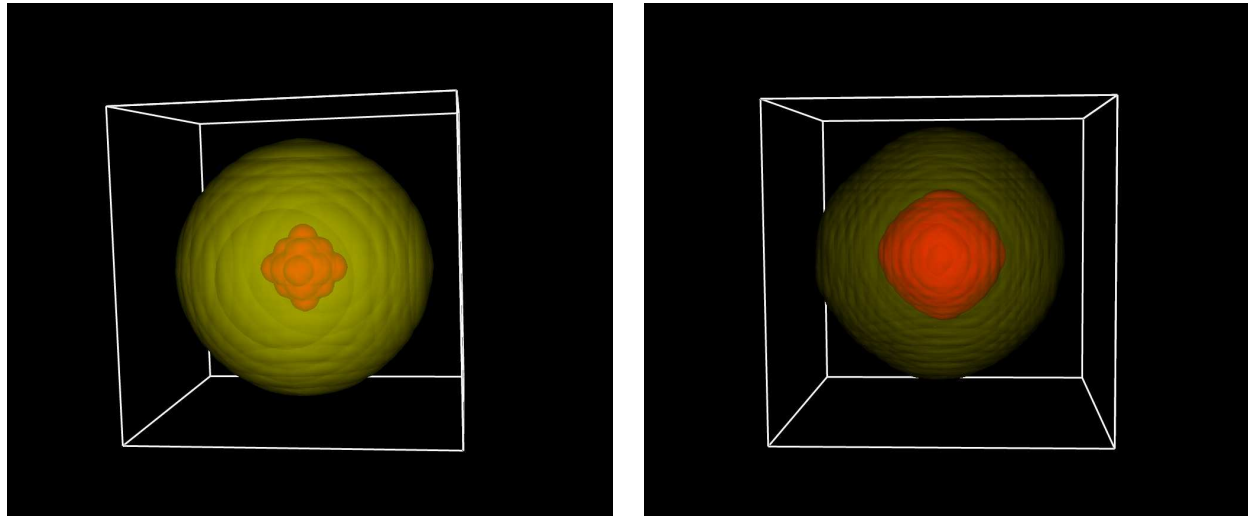


Figure 9: Contour plot for a pion propagator.

5.8 Meson propagators

A meson propagator is defined similarly to a pion propagator but it has a different gamma structure:

$$Q(t, \mathbf{x}) = \langle \Gamma_{ab}^{source}(0, \mathbf{0}) | \Gamma_{ab}^{sink}(+t, \mathbf{x}) \rangle \quad (13)$$

$$= \sum S^{ij,\beta\delta}(t, \mathbf{x}) (\Gamma^{sink} \gamma^5)_{\delta\rho} S^{*ij,\alpha\rho}(t, \mathbf{x}) (\gamma^5 \Gamma^{source})_{\alpha\beta} \quad (14)$$

...

We can visualize a Meson propagator using the following code:

```
1 python qcduutils_run.py \
2   -gauge:start=load:load=demo/demo.nersc.mdp \
3   -quark:kappa=0.135:source_point=center:load=true \
4   -meson:source_gamma=1:sink_gamma=1:vtk=true > run.log
```

and then process the VTK file as in the pion example. In this case $\Gamma^{source} = \Gamma^{sink} = \Gamma^1$ indicates a vector meson polarized along the X axis.

5.9 Current insertions

We can also visualize the mass density and the charge density of a heavy-light meson by inserting an operator ($\bar{q}q$ and $\bar{q}\gamma^0 q$ respectively) in between meson bra-kets.

$$\begin{aligned} Q(t, \mathbf{x}) &= \langle \Gamma_{ha}^{source}(-t, \mathbf{x}) | \bar{q}_a \Gamma^{current} q_b | \Gamma_{bh}^{sink}(+t, \mathbf{x}) \rangle \\ &= \text{tr}(\Gamma^{source} \gamma^5 S^\dagger(-t, \mathbf{x}) \gamma^5 \Gamma^{current} S(t, \mathbf{x}) \Gamma^{sink} H^\dagger(-t, t, \mathbf{x})) \end{aligned} \quad (15)$$

Here we measure the mass distribution for a static vector meson:

```
1 python qcutils_run.py \
2   -gauge:start=load:load=demo/demo.nersc.mdp \
3   -quark:kappa=0.135:source_point=center:load=true \
4   -current_static:source_gamma=1:sink_gamma=1:current_gamma=I:vtk=true \
5   > run.log
```

Using the same diagram we can compute the spatial distribution of $B^* \rightarrow B\pi$ by inserting the axial current ($\bar{q}\gamma^5 q$) in between a static B ($\bar{q}\gamma^5 h$) and a static B^* ($\bar{q}\gamma^1 h$):

```
1 python qcutils_run.py \
2   -gauge:start=load:load=demo/demo.nersc.mdp \
3   -quark:kappa=0.135:source_point=center:load=true \
4   -current_static:source_gamma=1:sink_gamma=5:current_gamma=5:vtk=true \
5   > run.log
```

A sample image is shown in fig. 10.

5.10 Localized instantons

FermiQCD allows the creation of custom gauge configurations with localized topological charge. Here we consider the case of a pion propagator on a single gauge configuration in presence of one t'Hooft instanton (localized lump of topological charge). Here is the code:

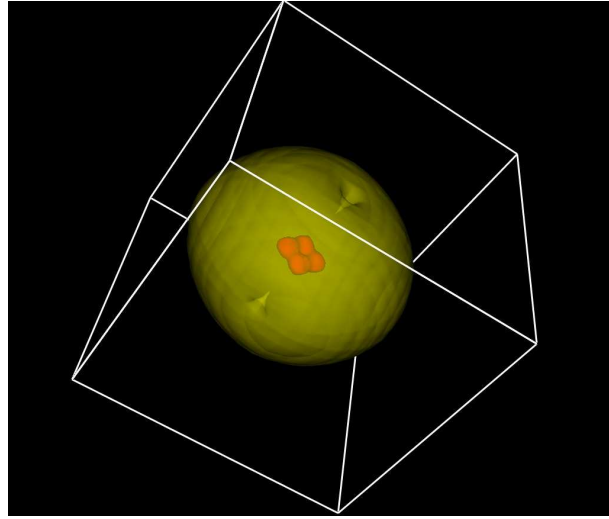


Figure 10: Contour plot for a three points correlation function.

```

1 python qcdutils_run.py \
2     -gauge:start=instantons:nt=20:nx=20:t0=0:x0=4.5:y0=10:z0=10 \
3     -topcharge_vtk \
4     -quark:kappa=0.120:source_point=center \
5     -pion:vtk=true > run.log

```

This code places the center of the instanton at point $(t_0, x_0, y_0, z_0) = (0, 4.5, 10, 10)$ and then computes a pion propagator with source on time slice 0 but spatial coordinates $(x, y, z) = (10, 10, 10)$ (center).

Fig. 11 show the pion propagator in presence of the instanton as the instanton nears the center of the propagator. Each image has been generated using the above command by placing the instanton at different locations. The last image shows a superposition of the pion propagator with and without the instanton in order to emphasize the difference. The difference is small but visible. The propagator retracts as the instanton nears. One may say that the quark interacts with the instanton and acquires mass thus making the propagator decrease faster when going through the instanton. Fig. 12 shows the effect of the instanton on individual components of the quark propagator.

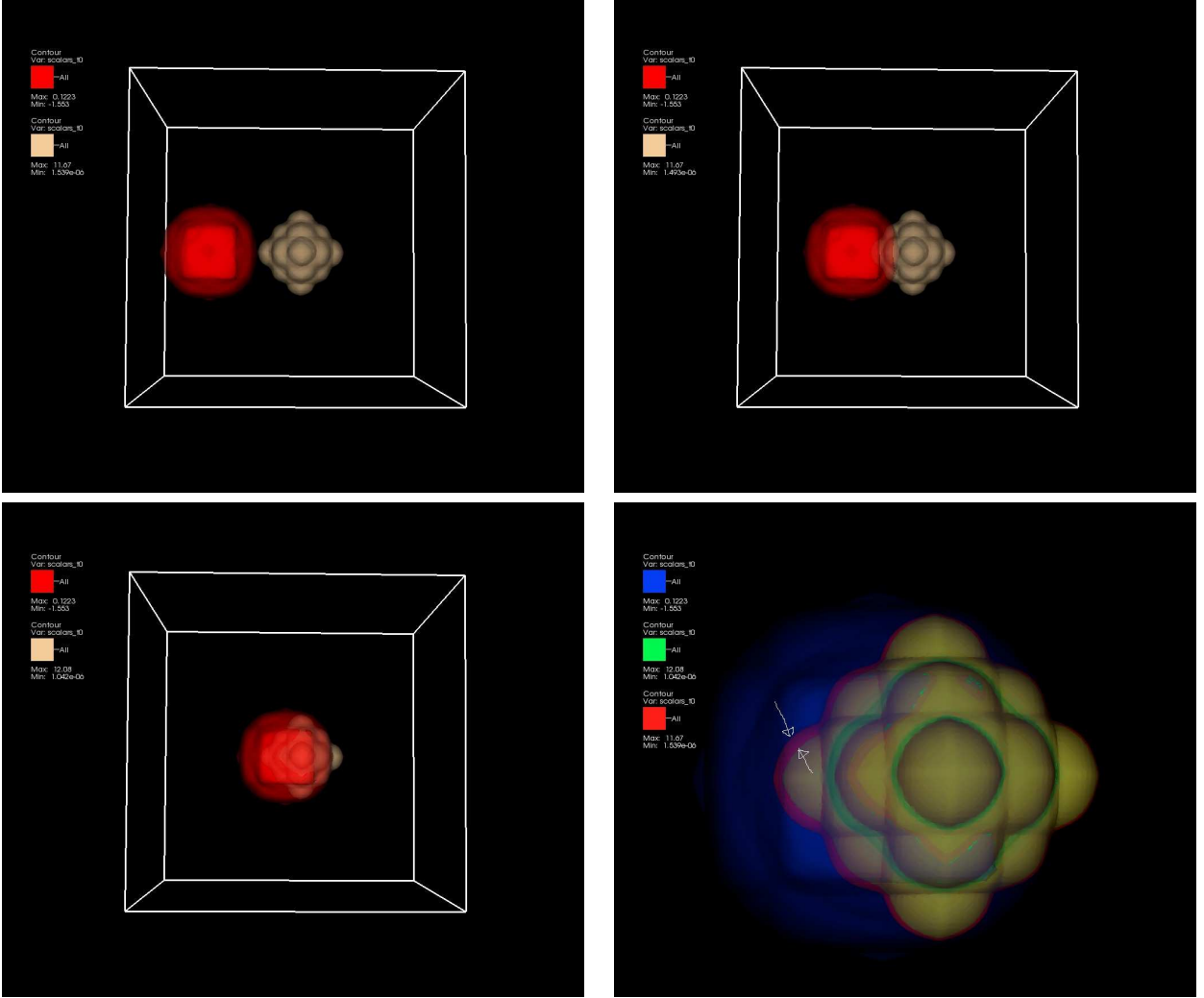


Figure 11: Pion propagator on a semi-cold configuration in presence of one localized instanton. The bottom right image shows the instanton (in blue) and an overlay of the pion propagator with and without the instanton. The difference shows that propagator shrinks as the instanton nears.

6 Analysis with `qcdutils_boot.py`, `qcdutils_plot.py`, `qcdutils_fit.py`

The console output of the `qcdutils_run` program consists of human readable text with comments and results of measurements performed on each gauge configuration. Here are some

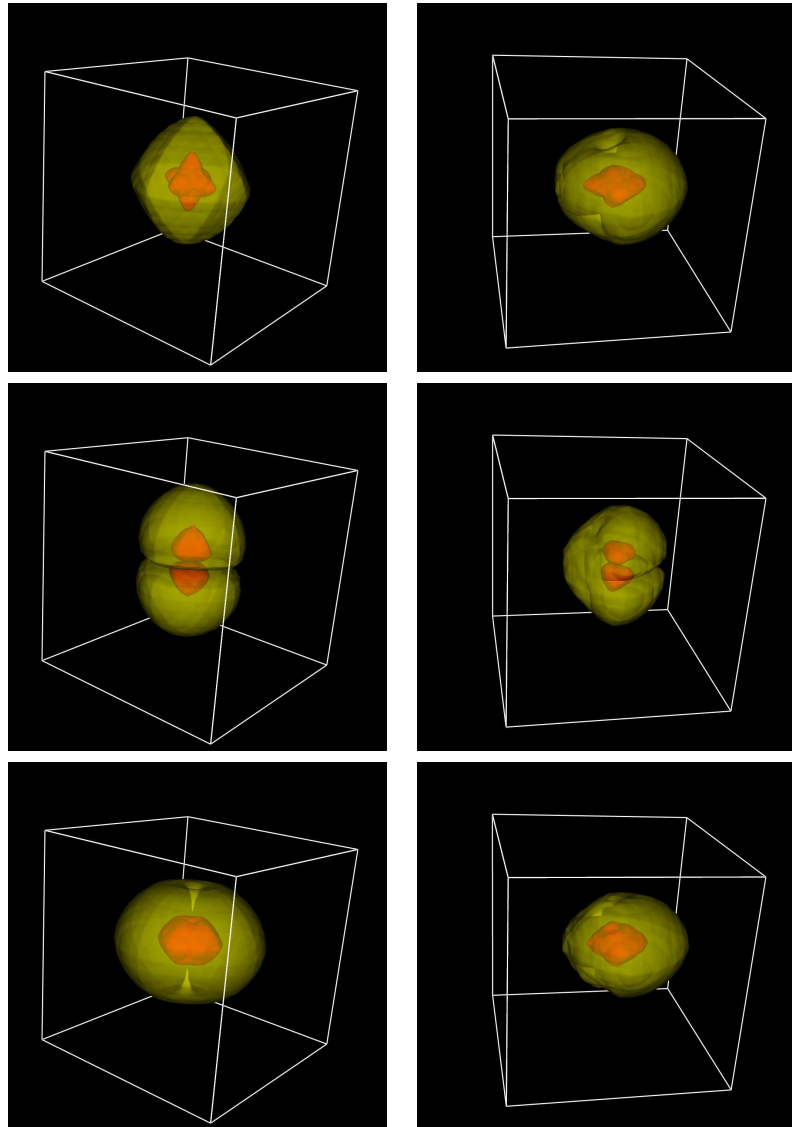


Figure 12: Comparison of quark propagator components on a cold configuration (left) and in presence of a localized instanton (right). The instanton is located as in fig. 11 (bottom-right).

examples of measurements logged in the output:

```

1 ...
2 plaquette = 0.654346
3 C2[0] = 14.5234

```

```

4 C3 [0] [0] = 1.214321
5 C3 [0] [0] = 1.123425
6 ...

```

`qcdutils_boot.py` is a tool that can extract the values for these measurements, aggregate them and analyze them in various ways. For example it computes the average and bootstrap errors [16] of any function of the measurements. `qcdutils_plot.py` is a tool to visualize the results of the analysis. It uses the Python `matplotlib` package, one of the most powerful and versatile plotting libraries available, although `qcdutils_plot.py` uses only a small subset of the available functionality.

Now, let us consider a typical Lattice QCD computation where one or more observables are measured on each Markov Chain Monte Carlo step (on each gauge configuration). We label the observables with Y_j (gauge configuration, 2-point correlation function for a given value of t , etc.)

We also refer to each measurements with y_{ij} where i labels the gauge configuration and j labels the observable (same index as Y_j). y_{i0} could be, for example, the plaquette on the i th gauge configuration.

The expectation value of each one observable is computed by averaging its measurements over the MCMC steps:

$$\bar{Y}_j = \langle 0 | Y_j | 0 \rangle = \frac{1}{N} \sum_i y_{ij} \quad (16)$$

Here N is the number of the measurements. The statistical error on the average for this simple case can be estimated using the following formula:

$$\delta Y_j \simeq \sqrt{\frac{1}{N(N-1)} \sum_i (y_{ij} - \bar{Y}_j)^2} \quad (17)$$

Usually we are interested in the expectation value of non-trivial functions of the observables:

$$\bar{f} = \langle 0 | f(Y_1, Y_2, \dots, T_M) | 0 \rangle = f(\bar{Y}_1, \bar{Y}_2, \dots, \bar{Y}_M) \quad (18)$$

Often the y_{ij} are not normal distributed and may depend on each other therefore standard error analysis does not apply.

The proper technique for estimating the error on \bar{f} is the bootstrap algorithm. It consists of the following steps:

- We build K vectors b^k of size N . The elements of these vectors b_i^k are chosen at random, uniformly between $\{1, 2, \dots, N\}$.
- For every k we compute:

$$\bar{Y}_j^k = \frac{1}{N} \sum_i y_{b_i^k j} \quad (19)$$

- Again for each k we compute:

$$\bar{f}^k = f(\bar{Y}_1^k, \bar{Y}_2^k, \dots, \bar{Y}_M^k) \quad (20)$$

- We then sort the resulting values for \bar{f}^k .
- We define the α percent confidence interval as $[\bar{f}^{k'}, \bar{f}^{k''}]$ where $k' = \lfloor (1 - \alpha)K/2 \rfloor$ and $k'' = \lfloor 1 + \alpha)K/2 \rfloor$.

`qcdutils_boot` is a program that takes as input $f(Y_0, Y_1, \dots)$ in the form of a mathematical expression where the Y_j are represented by their string pattern. It locates and extracts the corresponding y_{ij} values from the log files and stores them in a file called “`qcdutils_raw.csv`”. It computes the autocorrelation for each of the y_{ij} and stores them in “`qcdutils_autocorrelation.csv`”. It computes the moving averages for each of the \bar{Y}_j and stores them in “`qcdutils_trails.csv`”. It generates the K bootstrap samples \bar{f}^k and saves them in “`qcdutils_samples.csv`”. Finally it computes the mean and the 68% confidence level intervals $[\bar{f}^{k'}, \bar{f}^{k''}]$ and stores it “`qcdutils_results.csv`”.

Mind that these files are created in the current working directory and they are overwritten every time the `qcdutils_boot` is run. Move them somewhere else to preserve them.

Moreover, if the input expression for f depends on wildcards, the program repeats the analysis for all matching expressions.

`qcdutils_boot` performs this analysis without need to write any code. It only needs the input f in the syntax explained below and the list of log-files to analyze for data.

6.1 A simple example

Consider the output of one of the previous `qcdutils_run`:

```
1 python qcdutils_run.py -gauge:load=*.mdp -plaquette > run.log
```

In this case the observable is $Y_0 = \text{"plaquette"}$. We can analyze it with

```
1 python qcdutils_boot.py 'run.log' '"plaquette"'
```

This produces the following output:

```
1 < plaquette > = min: 0.26, mean: 0.32, max: 0.38
2 average trails saved in qcdutils_trails.csv
3 bootstrap samples saved in qcdutils_samples.csv
4 results saved in qcdutils_results.csv
```

Notice that `qcdutils_run` takes three arguments:

- A file name or file pattern (for example “run.log”)
- An expression (for example “plaquette”).
- A condition (optional)

Each of the argument must be enclosed in single quotes.

The represents $f(Y_0, Y_1, \dots)$ and the Y_j are the names of observables in double quotes.

In ’"plaquette"’ the outer single quote delimits the expression and the term `plaquette` between double quotes, determines the string we want to parse from the in file.

`qcdutils` uses the observable name to find all the occurrences of

```
1 plaquette = ...
```

or

```
1 plaquette: ...
```

in the input files and maps them into y_{i0} where i labels the occurrence. In this case we have a single observable (`plaquette`) so we use 0 to label it.

The program opens the file or the files matching the file patterns and parses them for the values of the “plaquette” thus filling an internal table of y s. It gives the output as the result:

```
1 < plaquette > = min: 0.26, mean: 0.32, max: 0.38
```

Here “mean” is the mean of the expression “plaquette”. min and max are the 65% confidence intervals computed using the bootstrap.

Here is example of the content of the “qcdutils_results.csv” file for the average plaquette case:

```
1 "plaquette", "[min]", "[mean]", "[max]"
2 "plaquette", 0.26, 0.32, 0.38
```

In general it contains one row for each matching expression.

You can plot the content of the files generated by `qcdutils_boot` using `qcdutils_plot`:

```
1 python qcdutils_plot.py -r -a -t -b
```

Here `-r` indicates that we want to plot the raw data, `-a` indicates we want a plot of autocorrelations, `-t` is for partial averages, and `-b` means we want a plot of bootstrap samples. `qcdutils_plot` loops over all the files reads the data in them and for each Y_j it makes one plot with raw data (y_{ij}), one with autocorrelations, one with partial averages. Then for each f it makes one plot with the bootstrap samples, and one plot with the final results found in “`qcdutils_results.csv`”.

The plots are in PNG files which have a name prefix equal to the name of the data source file, followed by a serialization of the expression for Y_j or f , depending on the case.

For example in the case of the plaquette, the autocorrelations and the partial averages are in the files:

```
1 qcdutils_autocorrelations_plaquette.png
2 qcdutils_trails_plaquette.png
```

and they are shown in fig. 13.

Similarly, if you want to bootstrap $f(Y_0) = \exp(Y_0/3)$ where Y_0 is the plaquette you would run:

```
1 python qcdutils_boot.py run.log 'exp("plaquette"/3)'
```

It produces output like this:

```
1 < exp(plaquette/3) > = min: 1.092, mean: 1.114, max: 1.145
```

Notice that again the observable Y_0 is identified for convenience by “`plaquette`”. The double quotes are necessary to avoid naming conflicts between patterns and functions.

Also notice that running `qcdutils_boot` twice does not guarantee generating the same exact results twice. That is because the bootstrap samples are random.

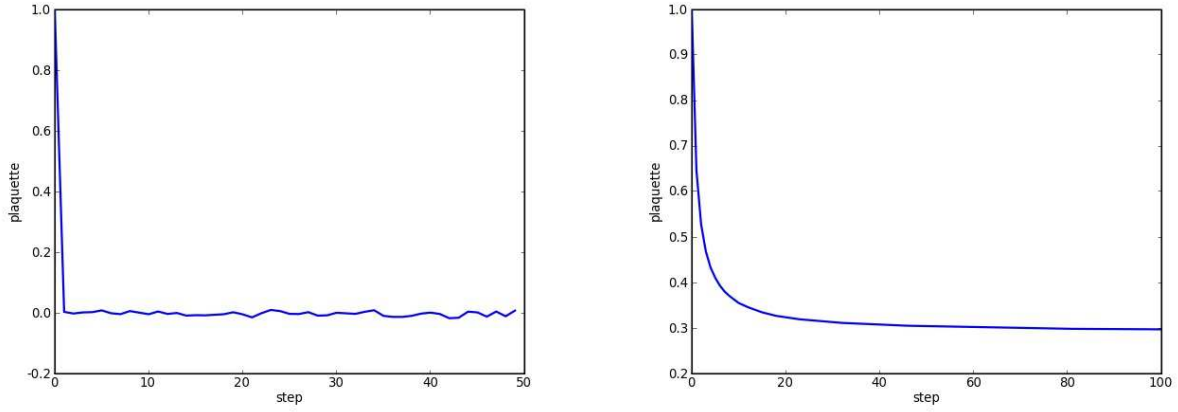


Figure 13: Example plots of autocorrelation (left) and partial averages (right).

6.2 2-point and 3-point correlation functions

In order to explain more complex cases we could generate 2- and 3- points correlation functions using something like:

```

1 python qcutils_run.py \
2     -gauge:start=cold:beta=4:n=10:steps=5:therm=100 \
3     -quark:kappa=0.11:c_sw=0.4:save=false -pion
4     -4quark:operator=5Ix5I > run.log

```

For testing purposes can also run:

```

1 python qcutils_boot.py -t

```

Where `-t` stands for test. This creates and analyzes a file called “`test_samples.log`” which contains *random* measurements for C2 and C3. Once this file is being created we can filter and study, for example, only the 2-point correlation function C2:

```

1 python qcutils_boot.py run.log '"C2[<t>]"'

```

Notice that `<t>` means we wish to define a variable `t` to be used internally for the analysis and whose values are to be determined by pattern-matching the data. The `t` correspond to the j of the previous abstract discussion. `"C2[<t>]"` matches `C2[0]` with $t = 0$, `C2[1]` matches with $t = 1$, etc.

The command above produces something like:

```

1 reading file test_samples.log
2 C2[00] occurs 100 times
3 ...
4 C2[15] occurs 100 times
5 raw data saved in qcdutils_raw_data.csv
6 autocorrelation for C2[02] and d=1 is -0.180453
7 ...
8 autocorrelation for C2[06] and d=1 is -0.0436378
9 autocorrelations saved in qcdutils_autocorrelations.csv
10 < C2[00] > = min: 1.988, mean: 1.999, max: 2.008
11 < C2[01] > = min: 1.617, mean: 1.629, max: 1.64
12 < C2[02] > = min: 1.328, mean: 1.345, max: 1.359
13 < C2[03] > = min: 1.064, mean: 1.079, max: 1.094
14 < C2[04] > = min: 0.878, mean: 0.894, max: 0.908
15 < C2[05] > = min: 0.722, mean: 0.733, max: 0.744
16 < C2[06] > = min: 0.574, mean: 0.584, max: 0.597
17 < C2[07] > = min: 0.478, mean: 0.49, max: 0.5
18 < C2[08] > = min: 0.395, mean: 0.407, max: 0.419
19 < C2[09] > = min: 0.322, mean: 0.331, max: 0.339
20 < C2[10] > = min: 0.268, mean: 0.277, max: 0.286
21 < C2[11] > = min: 0.225, mean: 0.231, max: 0.237
22 < C2[12] > = min: 0.18, mean: 0.186, max: 0.192
23 < C2[13] > = min: 0.138, mean: 0.144, max: 0.151
24 < C2[14] > = min: 0.107, mean: 0.112, max: 0.118
25 < C2[15] > = min: 0.0883, mean: 0.0933, max: 0.0982
26 average trails saved in qcdutils_trails.csv
27 bootstrap samples saved in qcdutils_samples.csv
28 results saved in qcdutils_results.csv

```

which we can plot as usual with

```
1 python qcdutils_plot.py -r -a -b -t
```

This produces about 60 plots. Some of them are shown in fig.14.

We can as easily compute the log of C2 (for every t):

```
1 python qcdutils_boot.py test_samples.log 'log("C2[<t>]" )'
```

or the log of the ratio between C2 at two consecutive time-slices:

```
1 python qcdutils_boot.py run2.log \
2     'log("C2[<t1>]"/"C2[<t2>]" )' \
3     't2==t1+1 if t1<8 else t2==t1-1'
```

In this case we used two implicit variables `t1` and `t2` but we used the third argument of `qcdutils_boot` to set a condition to link the two. This produces the following output:

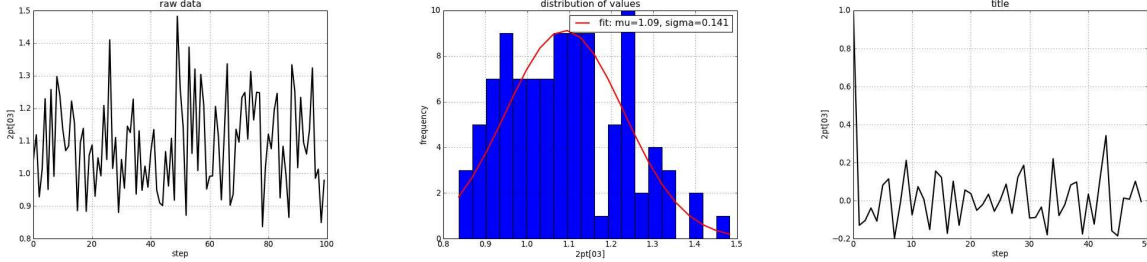


Figure 14: Example plots for the raw data (left), the distribution of raw data (center) and autocorrelations (right) for C2.

```

1 reading file test_samples.log
2 C2[00] occurs 200 times
3 ...
4 C2[15] occurs 200 times
5 raw data saved in qcutils_raw_data.csv
6 autocorrelation for C2[02] and d=1 is -0.176706
7 ...
8 autocorrelation for C2[06] and d=1 is -0.0476376
9 autocorrelations saved in qcutils_autocorrelations.csv
10 < log(C2[00]/C2[01]) > = min: 0.196, mean: 0.204, max: 0.212
11 < log(C2[01]/C2[02]) > = min: 0.18, mean: 0.191, max: 0.202
12 [...]
13 < log(C2[13]/C2[14]) > = min: 0.208, mean: 0.249, max: 0.291
14 < log(C2[14]/C2[15]) > = min: 0.147, mean: 0.189, max: 0.227
15 average trails saved in qcutils_trails.csv
16 bootstrap samples saved in qcutils_samples.csv
17 results saved in qcutils_results.csv

```

In the same fashion we can compute a matrix element as the ratio between a 3-point correlation function (C3) and a 2-point correlation function (C2):

```

1 python qcutils_boot.py test_samples.log \
2   ' "C3[<t>][<t1>]"/"C2[<t2>]"/"C2[<t3>]"' \
3   't3==t and t2==t and t1==t' > run.log
4 python qcutils_plot.py -a -t -b -r

```

Some of the generated plots can be seen in fig.19-16.

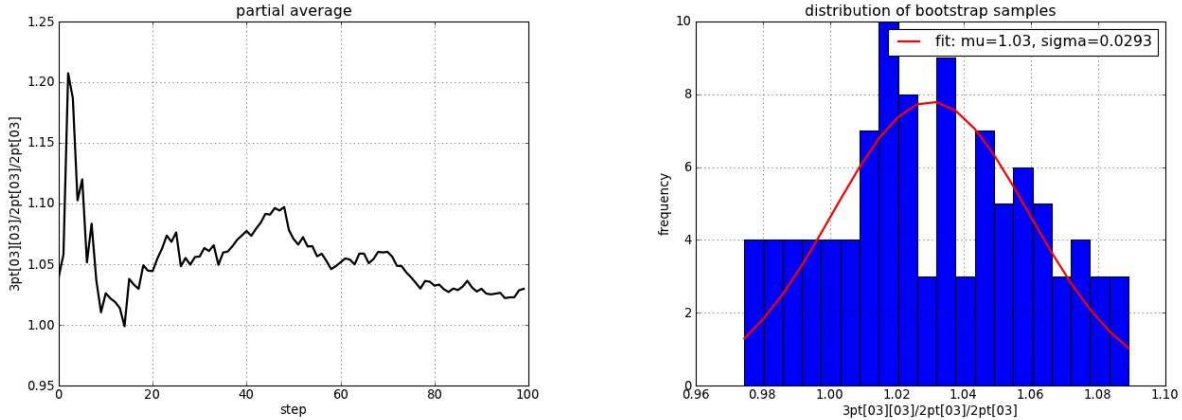


Figure 15: Example plots of moving averages (left) and distribution of bootstrap samples (right) for the ratio C_3/C_2^2 .

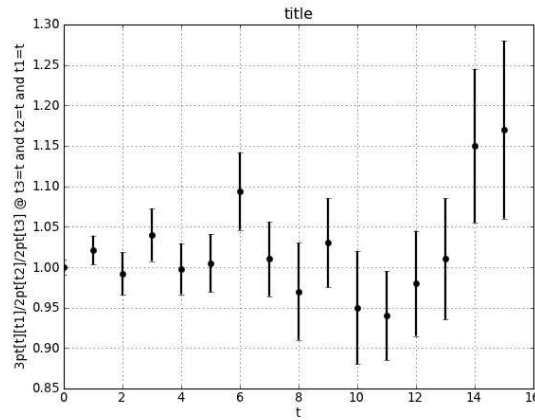


Figure 16: Example plot showing results of the bootstrap analysis.

6.3 Fitting data with `qcdutils_fit.py`

`qcdutils_fit.py` is a fitting and extrapolation utility. It can read and understand the output of `qcdutils_boot.py`. Internally it uses a “stabilized” multidimensional Newton method to minimize χ^2 . It is stabilized by reverting to the steepest descent in case the Newton step fails to reduce the χ^2 . The length of the steepest descent step is adjusted dynamically to guarantee that each step of the algorithm reduces the χ^2 . The program accepts for input any

function and any number of the parameters. It also accepts, optionally, Bayesian priors for those parameters and they can be used to further stabilize the fit [17]. A more sophisticated approach is described in ref. [18].

In Euclidean space C2 can be modeled by an exponential $a \exp(-bt)$ and b is the mass of the lowest energy state which propagates between the source and the sink. Here is an example in which we fit C2 using a single exponential:

```

1 python qcdutils_boot.py -t
2 python qcdutils_boot.py test_samples.log '"C2[<t>]"' > run.log
3 python qcdutils_fit.py 'a*exp(-b*t)@a=2, b=0.3'
```

The input data is read from the output of `qcdutils_boot`. The expression in quotes is the fitting formula. You can name the fitting parameters as you wish (in this case `a` and `b`) but the other parameters (in this case `t`) must match the parameters defined in the argument of `qcdutils_boot` (`<t>`). The `@` symbol separates the fitting function (left) from the initial estimates for the fitting parameters (on the right, separated by commas). Every parameter to be determined by the fit must have an initial value.

The output looks something like this:

```

1 a = 1.99864
2 b = 0.200645
3 chi2= 12.8048378376
4 chi2/dof= 0.984987525973
```

`qcdutils_fit.py` also generates the plot of fig. 17 (left).

If C2 is a meson propagator, b here represents the mass of the meson (of the lowest energy state with the same quantum numbers as the operator used to create the meson).

Similary we can analyze and fit the log of C2:

```

1 python qcdutils_boot.py test_samples.log 'log("C2[<t>]"' > run.log
2 python qcdutils_fit.py 'a-b*t@a=1, b=0.3'
```

which produces something like:

```

1 a = 0.69169
2 b = 0.200627
3 chi2= 12.1641201448
4 chi2/dof= 0.935701549598
```

and the plot of fig. 17 (right)

If our goal is obtaining b we can also cancel the a dependency in the analysis:

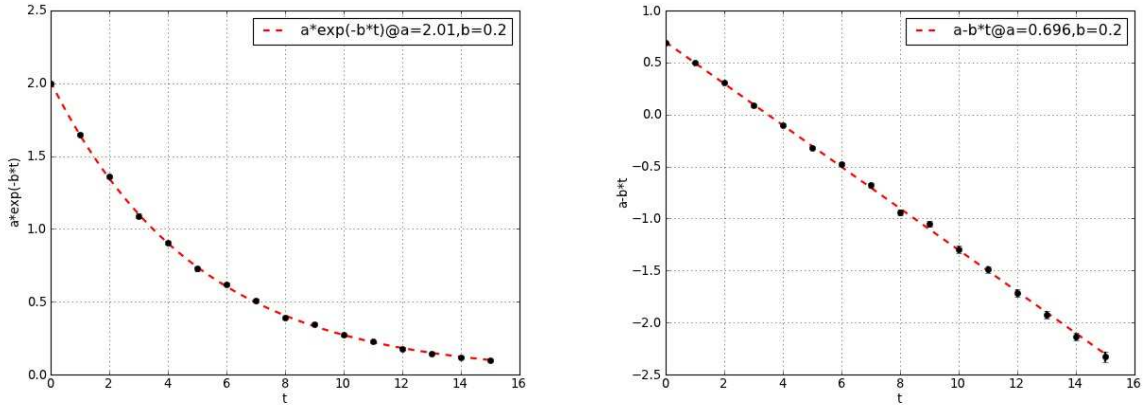


Figure 17: Example fits for a two points correlation function (left) and its log (right).

```

1 python qcdutils_boot.py test_samples.log \
2   'log("C2[<t>]"/"C2[<t1>]"' 't1==t+1' > run.log
3 python qcdutils_fit.py 'b@b=0'

```

and obtain:

```

1 b = 0.201755
2 chi2= 12.4502446913
3 chi2/dof= 0.9577111301

```

The generated plot is shown in fig. 18.

Notice that the variable names **a** and **b** are arbitrary and you can choose any name.

Similarly we can fit 3-point correlation functions:

```

1 python qcdutils_boot.py test_samples.log '"C3[<t1>][<t2>]"' > run.log
2 python qcdutils_fit.py 'a*exp(-b*(t1+t2))@a=3, b=0.3, _b=0.2'

```

In this case we have stabilized the plot with a Bayesian prior, indicated by **_b**. A variable starting with underscore indicates the uncertainty associated with our a priori knowledge about the corresponding variable without underscore. In other words **b=0.3, _b=0.2** is equivalent to **b=0.3 ± 0.2**. The result of this fit yields something like:

```

1 a = 3.78387
2 b = 0.195542
3 chi2= 2070.73759118
4 chi2/dof= 8.18473356199

```

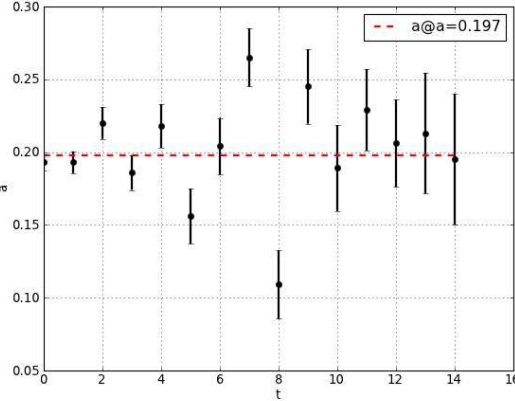


Figure 18: Example plot of fit of $\log(C2(t)/C2(t - 1))$.

A call to `qcdutils_plot.py` generates the plot of fig.19 (left)

In order to extract a matrix element (for example a 4-quark operator) we fit the ratio between C3 and C2:

```

1 python qcdutils_boot.py test_samples.log \
2   '"C3[<t>][<t1>]"/"C2[<t2>]"/"C2[<t3>]"' \
3   't3==t and t2==t and t1==t' > run.log
4 python qcdutils_fit.py 'a@a=0'

```

It produces output like:

```

1 a = 1.00658
2 chi2= 13.2075581022
3 chi2/dof= 0.943397007297

```

It produces the plot in fig. 19 (right).

You can use `qcdutils_fit.py` to perform extrapolations by using the `-extrapolate` command line option:

```

1 python qcdutils_fit.py -extrapolate x=100 'ax+b@a=1, b=0'

```

The extrapolated point will be added to the generated plot and represented by a square.

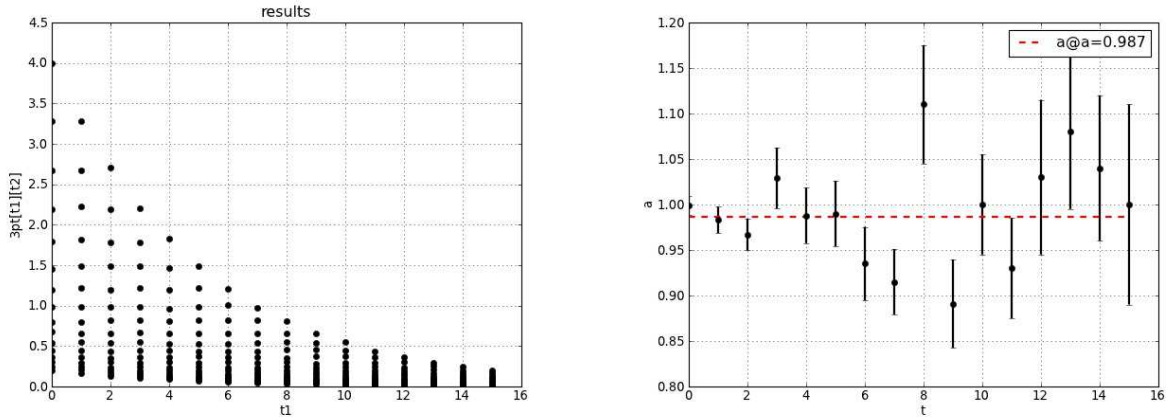


Figure 19: Example plot showing $C3[t][t1]$ (left) and the fit of $C3[t]/C2[t]c2[t1]$ (right).

6.4 Dimensional analysis and error propagation

In this section we did not discuss error propagation but we have developed a utility called *Buckingham* which is available from:

<http://code.google.com/p/buckingham/>

It provides dimensional analysis, unit conversion, and arithmetic operation with error propagation. We plan to discuss it in a separate manual but we here provide one example of usage (from inside a Python shell):

```

1 >>> from buckingham import *
2 >>> a = Number(2.0, error=0.3, dims="fermi")
3 >>> b = Number(1.0, error=0.2, dims="second^2")
4 >>> c = a/b
5 >>> print c, c.units()
6 (2.000 pm 0.500)/10^15 meter*second^-2
7 >>> print c.convert('fermi*second^-2')
8 2.000 pm 0.500
9 >>> print c.convert('lightyear*day^-2')
10 (1.578 pm 0.395)/10^21

```

(here pm stands for \pm) Buckingham supports 944 unit types (including eV) and their combinations.

A Filename conventions

```
1 Gauge configuration in NERSC format (3x3 or 3x2)
2   *.nersc
3 Gauge configuration in Fermiqcd format
4   *.mdp
5 Gauge configuration in MILC format
6   *.milc
7 Generic LIME file
8   *.lime
9 Gauge configuration in ILDG format
10  *.ildg
11 SciDAC quark propagator
12  *.scidac
13 Quark propagator in FermiQCD format
14  *.prop.mdp
15 Time slice for gauge configuration in FermiQCD format:
16  *.t[NNNN].mdp
17 Time slice for propagator in FermiQCD format:
18  *.t[NNNN].prop.mdp
19 Quark field for a given SPIN, COLOR source:
20  *.s[SPIN].c[COLOR].quark
21 Generic log file
22  *.log
23 VTK file containing real trace of plaquettes
24  *.plaqette.vtk
25 VTK file containing real part of Polyakov lines
26  *.polyakov.vtk
27 VTK file containing topological charge density
28  *.topcharge.vtk
29 VTK file containing topological charge density for a cooled config
30  *.topcharge.cool[STEP].vtk
31 VTK file contain a the norm squared of a pion propagator
32  *.pion.vtk
33 HTML file generated by qcdutils_vtk, represents a VTK file.
34  *.vtk.html
35 VisIt visualization script generated by qcdutils_vis.py
36  qcdutils_vis_[UUID].py
37 VisIt image generates by the previous script
38  qcdutils_vis_[UUID]_[FRAME].jpeg
39 Raw data extract from a log file by qcdutils_boot
40  qcdutils_raw_data.csv
41 Autocorrelations computed by qcdutils_boot
42  qcdutils_autocorrelations.csv
43 Partial averages computed by qcdutils_boot
```

```
44     qcutils_trails.csv
45 Bootstrap samples generated by qcutils_boot
46     qcutils_samples.csv
47 Means and bootstrap errors computed by qcutils_boot
48     qcutils_results.csv
```

B Help Pages

B.1 qcutils_get.py

```
1 $ qcutils_get.py -h
2 Usage:
3
4     qcutils_get.py [options] sources
5
6 Examples:
7
8     qcutils_get.py --test
9     qcutils_get.py --convert ildg gauge.cold.12x8x8x8
10    qcutils_get.py --convert mdp --float *.ildg
11    qcutils_get.py --convert split.mdp *.mdp
12
13 Options:
14     -h, --help                  show this help message and exit
15     -q, --quiet                 no progress bars
16     -d DESTINATION, --destination=DESTINATION
17                           destination folder
18     -c CONVERT, --convert=CONVERT
19                           converts a field to format
20                           (ildg,split.prop.mdp,prop.ildg,prop.mdp,split.mdp,
21                           mdp)
22     -4, --float                 converts to float precision
23     -8, --double                converts to double precision
24     -t, --tests                 runs some tests
25     -n, --noprogressbar        disable progress bar
```

B.2 qcutils_run.py

```
1 $ qcutils_run.py -h
2 qcutils_run.py is a tool to help you download and use fermiqcd from
3
4     http://code.google.com/p/fermiqcd
5
```

```

6 When you run:
7
8     python qcdutils_run.py [args]
9
10 It will:
11 - create a folder called fermiqcd/ in the current working directory
12 - connect to google code and download fermiqcd.cpp + required libraries
13 - if -mpi in [args] compile fermiqcd with mpiCC else with g++
14 - if -mpi in [args] run fermiqcd.exe with mpiCC else run it normally
15 - pass the [args] to the compiled fermiqcd.exe
16
17 Some [args] are handled by qcdutils_run.py:
18 -download force downloading of the libraries
19 -compile force recompiling of code
20 -source runs and compiles a different source file
21 -mpi for use with mpi (mpiCC and mpirun but be installed)
22
23 Other [args] are handled by fermiqcd.cpp for example
24 -cold make a cold gauge configuration
25 -load load a gauge configuration
26 -quark make a quark
27 -pion make a pion
28 (run it with no options for a longer list of options)
29
30 You can find the source code in fermiqcd/fermiqcd.cpp
31
32 More examples:
33     qcdutils_run.py -gauge:start=cold:nt=16:nx=4
34     qcdutils_run.py -gauge:start=hot:nt=16:nx=4
35     qcdutils_run.py -gauge:load=cold.mdp
36     qcdutils_run.py -gauge:load=cold.mdp:steps=10:beta=5.7
37     qcdutils_run.py -gauge:load=*.mdp -plaquette
38     qcdutils_run.py -gauge:load=*.mdp -plaquette_vtk
39     qcdutils_run.py -gauge:load=*.mdp -polyakov_vtk
40     qcdutils_run.py -gauge:load=*.mdp -cool:steps=20 -topcharge_vtk
41     qcdutils_run.py -gauge:load=*.mdp -quark:kappa=0.12:alg=minres_vtk
42     qcdutils_run.py -gauge:load=*.mdp -quark:kappa=0.12 -pion
43     qcdutils_run.py -gauge:load=*.mdp -quark:kappa=0.12 -pion_vtk
44
45 Options:
46     -cool
47         alg = ape
48         alpha = 0.7
49         steps = 20
50         cooling = 10

```

```

51 -cool_vtk
52     n = 20
53     alpha = 0.7
54     steps = 1
55     cooling = 10
56 -quark
57     action = clover_fast (default) or clover_slow or clover_sse2
58     alg = bicgstab (default) or minres or bicgstab_vtk or minres_vtk
59     abs_precision = 1e-12
60     rel_precision = 1e-12
61     source_t = 0
62     source_x = 0
63     source_y = 0
64     source_z = 0
65     source_point = zero (default) or center
66     load = false (default) or true
67     save = true (default) or false
68     matrices = FERMILAB (default) or MILC or
69                 UKQCD or Minkowsy-Dirac or Minkowsy-Chiral
70     kappa = 0.12
71     kappa_t = quark[ "kappa" ]
72     kappa_s = quark[ "kappa" ]
73     r_t = 1.0
74     r_s = 1.0
75     c_sw = 0.0
76     c_E = 0.0
77     c_B = 0.0
78 -meson
79     source = 5
80     sink = 5
81     current = I
82 -4quark
83     source = 5 (default) or I or 0 or 1 or 2 or 3 or 05 or
84                 15 or 25 or 35 or 01 or 02 or 03 or 12 or 13 or 23
85     operator = 5Ix5I (default) or 0Ix0I or 1Ix1I or 2Ix2I or 3Ix3I or
86                 05Ix05I or 15Ix15I or 25Ix25I or 35Ix35I or 01Ix01I or
87                 02Ix02I or 03Ix03I or 12Ix12I or 13Ix13I or 23Ix23I or
88                 5Tx5T or 0Tx0T or 1Tx1T or 2Tx2T or 3Tx3T or 05Tx05T or
89                 15Tx15T or 25Tx25T or 35Tx35T or 01Tx01T or 02Tx02T or
90                 03Tx03T or 12Tx12T or 13Tx13T or 23Tx23T
91 -gauge
92     nt = 16
93     nx = 4
94     ny = nx
95     nz = ny

```

```

96      start = load (default) or cold or hot or instantons
97      load = demo.mdp
98      n = 0
99      steps = 1
100     therm = 10
101     beta = 0
102     zeta = 1.0
103     u_t = 1.0
104     u_s = 1.0
105     prefix =
106     action = wilson (default) or wilson_improved or wilson_sse2
107     save = true
108     t0 = 0
109     x0 = 0
110     y0 = 0
111     z0 = 0
112     r0 = 1.0
113     t1 = 1
114     x1 = 1
115     y1 = 1
116     z1 = 1
117     r1 = 0.0
118 -baryon
119 -pion
120 -pion_vtk
121 -meson_vtk
122 -current_static
123 -current_static_vtk
124 -plaquette
125 -plaquette_vtk
126 -polyakov_vtk
127 -topcharge_vtk

```

B.3 qcdutils_vis.py

```

1 $ qcdutils_vis.py -h
2 Usage:
3 This is a utility script to manipulate vtk files containing scalar files.
4 Files can be split, interpolated, and converted to jpeg images.
5 The conversion to jpeg is done by dynamically generating a visit script
6 that reads the files, and computes optimal contour plots.
7
8 Examples:
9
10 1) make a dummy vtk file

```

```

11      qcdutils_vis.py -m 10 folder/test.vtk
12
13 2) reads fields from multiple vtk files
14
15      qcdutils_vis.py -r field folder/*.vtk
16
17 3) extract fields as multiple files
18
19      qcdutils_vis.py -s field folder/*.vtk
20
21 (fields in files will be renamed as "slice")
22 4) interpolate vtk files
23
24      qcdutils_vis.py -i 9 folder/*.vtk
25
26 tricubic Resample/Interpolate individual vtk files
27
28      visit -v 10x10x10 folder/*.vtk
29
30 6) render a vtk file as a jpeg image
31
32      qcdutils_vis.py -p 'AnnotationAttributes[axes3D.bboxFlag=0];
33          ResampleAttributes[samplesX=160; samplesY=160; samplesZ=160];
34          ContourAttributes[SetMultiColor(9, $orange)]' 'folder/*.vtk'
35
36      or simply
37
38      qcdutils_vis.py -p default 'folder/*.vtk'
39
40 Options:
41     -h, --help           show this help message and exit
42     -r READ, --read=READ name of the field to read from the vtk file
43     -s SPLIT, --split=SPLIT
44                           name of the field to split from the vtk file
45     -i INTERPOLATE, --interpolate=INTERPOLATE
46                           name of the vtk files to add/interpolate
47     -c CUBIC, --cubic-interpolate=CUBIC
48                           new size for the lattice 10x10x10
49     -m MAKE, --make=MAKE make a dummy vtk file with size^3 whete size if
50                           arg of
51                           make
52     -p PIPELINE, --pipeline=PIPELINE
53                           visualizaiton pipeline instructions

```

B.4 qcdutils_vtk.py

```
1 $ qcdutils_vtk.py -h
2 Usage: qcdutils_vtk.py filename.vtk
3
4 Options:
5   -h, --help           show this help message and exit
6   -u UPPER, --upper-threshold=UPPER
7                   threshold for isosurface
8   -l LOWER, --lower-threshold=LOWER
9                   threshold for isosurface
10  -R UPPER_RED, --upper-red=UPPER_RED
11                  color component for upper isosurface
12  -G UPPER_GREEN, --upper-green=UPPER_GREEN
13                  color component for upper isosurface
14  -B UPPER_BLUE, --upper-blue=UPPER_BLUE
15                  color component for upper isosurface
16  -r LOWER_RED, --lower-red=LOWER_RED
17                  color component for lower isosurface
18  -g LOWER_GREEN, --lower-green=LOWER_GREEN
19                  color component for lower isosurface
20  -b LOWER_BLUE, --lower-blue=LOWER_BLUE
21                  color component for lower isosurface
```

B.5 qcdutils_boot.py

```
1 $ qcdutils_boot.py -h
2 Usage: qcdutils_boot.py *.log 'x[<a>]/y[<b>]' 'abs(a-b)==1'
3   scans all files *.log for expressions of the form
4     x[<a>]=<value> and y[<b>]=<value>
5   and computes the average and bootstrap errors of x[<a>]/y[<b>]
6   where <a> and <b> satisfy the condition abs(a-b)==1.
7
8 This is program to scan the log files of a Markov Chain Monte Carlo
9 Algorithm,
10 parse for expressions and compute the average and bootstrap errors of any
11 function of those expressions. It also compute the convergence trails of
12 the
13 averages.
14
15 Options:
16   --version           show program's version number and exit
17   -h, --help           show this help message and exit
18   -b MIN, --minimum_index=MIN
```

```

17                         the first occurrence of expression to be
18                         considered
19 -e MAX, --maxmimum_index=MAX
20                         the last occurrence +1 of expression to be
21                         considered
22 -n NSAMPLES, --number_of_samples=NSAMPLES
23                         number of required bootstrap samples
24 -p PERCENT, --percentage=PERCENT
25                         percentage in the lower and upper tails
26 -t, --test
27                         make a test!
28 -r, --raw
29                         Load raw data instead of parsing input
30 -a, --advanced
31                         In advanced mode use regular expressions for
                           variable
                           patterns
-i IMPORT_MODULE, --import_module=IMPORT_MODULE
                           import a python module for expression evaluation
-o OUTPUT_PREFIX, --output_prefix=OUTPUT_PREFIX
                           path+prefix used to build output files

```

B.6 qcdutils_plot.py

```

1 $ qcdutils_plot.py -h
2 Usage: python qcdutils_plot.py
3
4 plot the output of qcdutils.py
5
6 Options:
7   --version
8   -h, --help
9   -i INPUT_PREFIX, --input_prefix=INPUT_PREFIX
10                          the prefix used to build input filenames
11   -r, --raw
12   -a, --autocorrelations
13                          make autocorrelation plots
14   -t, --trails
15   -b, --bootstrap-samples
16                          make bootstrap samples plots
17   -v PLOT_VARIABLES, --plot_variables=PLOT_VARIABLES
18                          plotting variables
19   -R RANGE, --range=RANGE
20                          range as in 0:1000

```

B.7 qcdutils_fit.py

```

1 $ qcdutils_fit.py -h

```

```

2 Usage: qcdutils_fit.py [OPTIONS] 'expression@values'
3   Example: qcdutils-fit.py 'a*x+b@a=3, b=0'
4   default filename is qcdutils_results.csv
5   ...., 'x', 'min', 'mean', 'max'
6   ...., 23, 10, 11, 12
7   ...., etc etc etc
8
9 Options:
10  --version           show program's version number and exit
11  -h, --help            show this help message and exit
12  -i INPUT, --input=INPUT
13                  input file (default qcdutils_results.csv)
14  -c CONDITION, --condition=CONDITION
15                  sets a filter on the points to be fitted
16  -p PLOT, --plot=PLOT plots the hessian (not implemented yet)
17  -t, --test             test a fit
18  -e EXTRAPOLATIONS, --extrapolate=EXTRAPOLATIONS
19                  extrapolation point
20  -a AP, --absolute_precision=AP
21                  absolute precision
22  -r RP, --relative_precision=RP
23                  relative precision
24  -n NS, --number_steps=NS
25                  number of steps

```

References

- [1] M. Di Pierro, J. Hetrick, S. Cholia, D. Skinner, PoS LAT2011, 2011
- [2] <http://www.usqcd.org/ildg/>
- [3] M. DiPierro, Comput.Phys.Commun. 141, 2001, (pp 98-148) [hep-lat/0004007]
- [4] M. Di Pierro, Nucl.Phys.Proc.Suppl.129:832-834, 2004 [<http://fermiqcd.net>]
- [5] <http://www.vtk.org/>
- [6] <https://wci.llnl.gov/codes/visit/home.html>
- [7] <http://processingjs.org/>
- [8] <http://python.org>
- [9] <http://www.physics.utah.edu/~detar/milc>

- [10] M. Creutz, *Quarks, gluons and lattices*, Cambridge University Press, 1985
- [11] I. Montvay and G. Münster, *Quantum fields on a lattice* Cambridge University Press, 1997
- [12] T. DeGrand and C. DeTar, Lattice Methods for Quantum Chromodynamics, World Scientific 2006
- [13] K. Wilson, K, *Confinement of quark*, Physical Review D 10 (8) 1974
- [14] C. Morningstar and M. Peardon, Phys.Rev.D56:4043-4061,1997
- [15] E. Eichten and B. Hill, Phys. Lett. B234 (1990) 51
- [16] B. Efron, The Annals of Statistics 7 (1), 1979
- [17] G. Lepage et al., Nucl.Phys.Proc.Suppl.106:12-20,2002 [arXiv:hep-lat/0110175v1]
- [18] M. Di Pierro, <http://arxiv.org/abs/1202.0988v2>

A Visualization Toolkit for Lattice Quantum Chromodynamics

Massimo Di Pierro

School of Computer Science, Telecommunications and Information Systems
DePaul University, 243 S Wabash, Chicago, Illinois, USA
`mdipierro@cs.depaul.edu`

Abstract

Lattice QCD is an algorithmic formulation of QCD, the mathematical model that describes how quarks bind together to form composite particles such as proton and neutron. It has been successful in predicting properties of many newly discovered particles, including their mass and decay time. Unfortunately, lattice QCD is very computationally expensive and comprises of sophisticated algorithmic manipulations of large data-structures whose interpretation is purely statistical. In this paper we provide an overview of both lattice QCD and our work to develop a visualization toolkit to extract information from those data-structures. Our toolkit consists of a set of parallel algorithms for projecting the lattice QCD data structures into 3D scalar fields (for example the topological charge of the vacuum, the energy density, the wave function of the quarks, etc.) and uses VTK for the proper visualization.

1 Introduction

Quantum Chromodynamics [1] (QCD) is the mathematical model that best describes interactions among quarks, the basic constituents of most of ordinary matter. Lattice QCD [2] is a formulation of QCD in terms of discretized space and time (lattice) that is suitable for numerical computation. Lattice QCD has been successful at explaining and predicting properties of composite

particles such as the mass and lifetime of protons, neutrons, and many other particles produced by modern particle accelerators such as the Tevatron [3] at Fermilab, LEP and LHC at CERN, and Slac at Stanford.

Lattice QCD algorithms comprise of massive parallel Monte Carlo simulations. Modern state of the art computations are performed on commercial supercomputers (such as Blue Gene [5] and the Earth Simulator), clusters of workstations (there are nearly 1000 dedicated nodes at Fermilab [7] and Jefferson Laboratory), and dedicated machines (Ape [8] in Rome, QCDOC [9] at Columbia University and Brookhaven National Laboratory).

In many Lattice QCD computations, the only published output consists of one number with two or three significative digits. At the same time, hundreds of terabytes of data are generated in the intermediate steps of the computation and are not usually looked at because their interpretation is purely statistical: they are random points in a Monte Carlo ensemble.

The goal of our project is twofold: identifying a set of projection operators that would map this data into 3D scalar fields of physical significance for the purpose of extracting information in a visual format; incorporating these operators into a visualization toolkit that will interface with existing Lattice QCD software libraries such as MILC [10], FermiQCD [11] and SciDAC [12].

In the next section we will give a brief description of Lattice QCD from a computational point of view and we will discuss examples of projection operators of physical interest. In the third section we will present the high level design of our toolkit. Finally we will draw conclusions, show some images produced by our system and discuss the current status of the project.

2 Theoretical Foundations

The ingredients of any Lattice QCD computation are the following:

- In nature, there are 6 *flavors* of *Quarks*. They are the basic constituents of protons and neutrons, as well as of other composite particles that can be produced in particle accelerators and are occasionally produced naturally by cosmic rays. Each quark flavor can best be described as a complex field $q_{x,\alpha,i}$. The index $x = (\vec{x}, t)$ labels a point on the hypercubic lattice that corresponds to a position in space \vec{x} and time t . At point x in space-time, a quark exhibits a number of local degrees of freedom that are parameterized by the indices $\alpha = 0, 1, 2, 3$ and $i = 0, 1, 2$. α is referred to as spin index and i as color index. $|q_{x,\alpha,i}|^2$

is the probability of finding the quark at a given position \vec{x} at time t , in a spin state α and color state i .

- Quarks interact with each other by exchanging *gauge bosons*, also known as *gluons*. Gauge bosons can be best described as a complex field $U_{x,\mu,i,j}$. Similarly to the case of quarks, the index x labels a point in space-time, while the indices μ , i and j parameterize the local degrees of freedom. The value of the field U is related, in a non-trivial way, to the probability of finding a given type of gauge boson in a given polarization state, at a given position in space and moment in time, and carrying a given chromo-electromagnetic charge.
- QCD is a *Quantum Field Theory*. This means that there is no deterministic time-evolution for the above fields. In fact, the only meaningful physical observables in any Quantum Field Theory are the *correlations* between the degrees of freedom. Lattice QCD provides prescription rules on how to measure physical observables (for example the mass of a proton) using correlations among field variables. These correlations are computed numerically by averaging the corresponding operator over multiple *field configurations*, also known as *paths* or *histories*. Each configuration represents a possible evolution in time of a small portion of space of about $(10^{-14} \text{ meters})^3$ for about 10^{-22} seconds.
- Field configurations are generated via a Markov Chain Monte Carlo (MCMC) algorithm using a transition probability that encodes the physical laws of QCD. The “Quantum” aspect of the theory is represented by the stochastic field fluctuations present in the gauge configurations and averaged over.
- For practical purposes any Lattice QCD computation is divided into three main steps: 1) gauge field configurations are generated using the MCMC; 2) for each gauge configuration one places the quarks in a certain state and let them evolve according to the Dirac equation in the background gauge field (the solution of the Dirac equation on a given gauge configuration is called a *quark propagator*); 3) the indices of a gauge configuration and its corresponding quark propagators are contracted together to compute the operator corresponding to a given physical observable, which is then averaged over all the gauge configurations.

- A typical gauge configuration U has a size of 96 points in time and 64^3 points in space, corresponding to 7 gigabytes of data. A typical quark propagator q for a single source on the above gauge configuration has a size of 2.5 gigabytes. Most Lattice QCD computations involve about 1000 gauge configurations and a minimum of 12 quark sources each, thus generating $10 \div 100$ terabytes of data. Usually gauge configurations and quark propagators are stored and are reused for multiple observables in a semi-industrial fashion. Typical computations require 1-10 million hours of computing time for a Pentium 4 @ 3GHz equivalent CPU.
- One complication consists in the fact that some of the degrees of freedom in the gauge field U are redundant but cannot be eliminated in the computation. In fact $U_{x,\mu,i,j}$ must be unitary matrices in the indices i, j and only operators invariant under the simultaneous transformations $U_{x,\mu,i,j} \rightarrow \sum_{m,n} \Lambda_{x,i,m} \Lambda_{x+\mu,j,n}^* U_{x,\mu,m,n}$ and $q_{x,\alpha,i} \rightarrow \sum_m \Lambda_{x,i,m} q_{x,\alpha,m}$ have a physical significance¹. The above transformation is referred to as *gauge invariance* and it puts a major constraint on what can be visualized.
- The only input of a Lattice QCD computation are parameters that loosely correspond to the masses of the quarks and to the lattice discretization scale. Physical observables have a dependence on the discretization scale that is known as *running*. For a sufficiently small discretization scale, the effect of the running can be corrected for and the results of the computation, in physical units, can be made independent on it. Physical observables also depend on the quark masses and, in fact, these are currently determined by a fine tuning the input parameters in Lattice QCD computations.

There are multiple reasons why extracting visual information from Lattice QCD data is important and here we list some of them:

- The gauge configurations have a non-trivial topological structure that can be isolated by removing short term fluctuations, a process called *cooling*. It is known that the total topological charge changes very slowly under MCMC steps, but it is not known how the local charge evolves.

¹Here $\Lambda_{x,i,j}$ is an arbitrary field of unitary matrices in the indices i, j

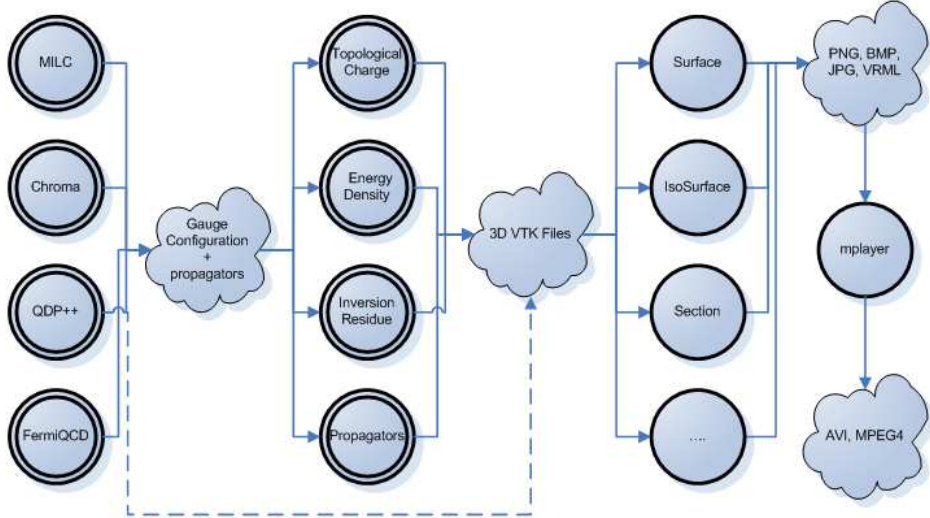


Figure 1: The figure shows the data flow in our visualization toolkit. The double circles represent parallel components including Lattice QCD algorithms and projection plug-ins. The single circle represent Mayavi visualization plug-ins.

- Some observables are themselves extended objects (for example the wave function of a quark inside a hadron or the energy density in presence of a quark-antiquark couple) but so far only 1D or 2D sections are usually visualized.
- The algorithms used for the MCMC and to invert the Dirac operator are both iterative. Therefore it is interesting to visualize how information propagates, step by step, across the lattice in order to understand the local convergence of these algorithms.
- Because of the size of the data structures involved, Lattice QCD algorithms are implemented as tightly-coupled parallel programs written in C/C++. Visualization can help monitor the communication patterns and identify bugs and network problems.
- Lattice QCD requires knowledge of multiple disciplines and therefore it has a very steep learning curve. The visualization of actual computations can serve a didactic purpose thus fostering a better intuitive understanding of QCD and pushing scientific progress.

3 Implementation

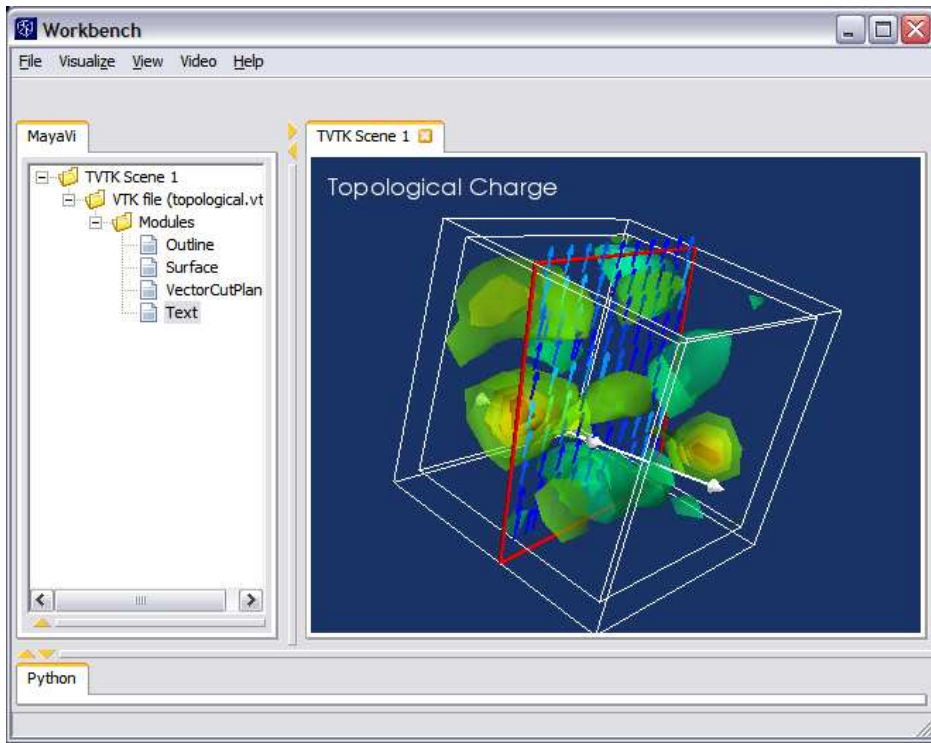


Figure 2: A screenshot of the Enthought Workbench showing the topological charge for a time-slice of a 4D gauge configuration.

The main architecture of our system, fig. 1, is comprised of two main parts: a set of projection operators implemented in C/C++ as parallel MPI programs and a graphical interface based on the Enthought Workbench [13] and Mayavi 2.0 [14] (a Python interface to VTK [15]). We will refer to the former as a projection plug-in as opposed to the visualization plug-ins provided by Mayavi.

An example of a projection plug-in is a parallel algorithm that reads gauge configurations, cools it, computes the topological charge in 4 dimensions, takes a time slice and saves it as 3D scalar field in the VTK file format.

An example of a visualization plug-in is an algorithm that reads the above VTK file and generates iso-surfaces.

The Workbench, fig. 2, provides a GUI for the entire system and allows

users to interactively manipulate the VTK files: display, rotate, edit, save them in some other standard graphical formats, including JPG, PNG, and VRML.

Mayavi is a Python interface to VTK and allows scripting of the above operations. A typical script would loop over a large set of fields, process each of them using the same plug-ins and produce the individual frames as an animation.

Independently on the set of plug-ins used we identified three general recurrent patterns:

- Given one configuration, project and visualize the different time-slices.
- Given one set of configurations and one time-slice t , project and visualize the same time slice for each configuration.
- Given a set of configurations, for each time-slice, project the time-slice on each configuration, average over all configurations and visualize the average time-slice.

In order to remove visual unpleasant effects of high-frequency quantum fluctuations, when necessary, we adopted the following gauge-invariant smoothing algorithm for the gauge configuration:

$$U_{x,\mu,i,j} = \mathcal{P}[\xi U_{x,\mu,i,j} + (1 - \xi) \sum_{n,m} U_{x,\nu,i,m} U_{x+\nu,\mu,m,n} U_{x+\mu,\nu,j,n}^*] \quad (1)$$

$$+ U_{x-\nu,\mu,m,i}^* U_{x-\nu,\mu,m,n} U_{x+\mu-\nu,\nu,n,j}] \quad (2)$$

Here $x \pm \mu$ are the coordinates of a lattice point shifted from x in direction $\pm \mu$, ξ is an arbitrary smoothing parameter, and \mathcal{P} is a projection operator into the $SU(3)$ group.

4 Examples and Conclusions

This project started about six months ago. We have successfully produced a set of prototype projection plug-ins that compute topological charge, wave functions, energy density, and density of heatbath hits. Examples of images are shown in figs. 3 and 4.

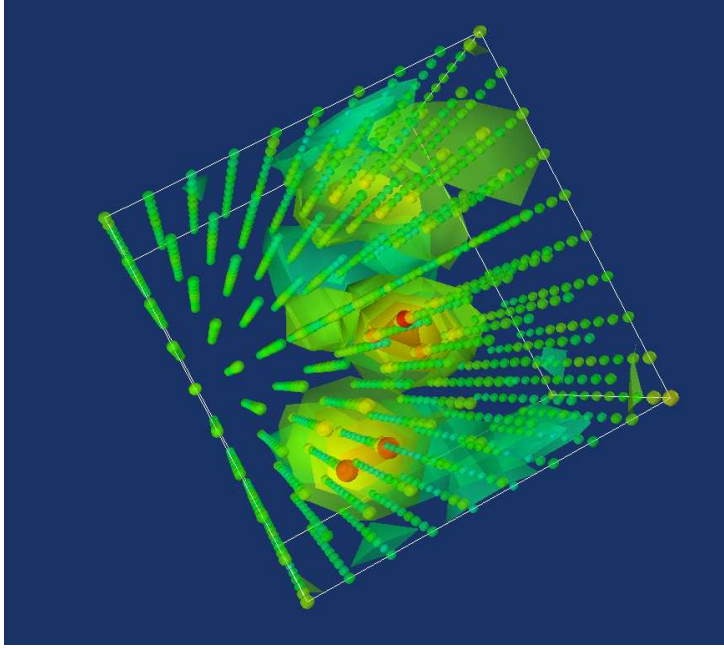


Figure 3: The figure shows iso-surfaces for the topological charge for a time-slice of small test gauge configuration. The spheres show the lattice geometry.

The field of visualization of Lattice QCD data is still in its infancy, but has a large potential impact for the physics community. It will help us better understand local properties of the algorithms and the spatial characteristics of extended physical objects such as mesons, hadrons and glue-balls. We also strongly believe that visualization is important to better explain what Lattice QCD is and to attract more students to this exciting area of research.

5 Acknowledgments

This project is supported by the Department of Energy under the Scientific Discovery Through Advanced Computing grant DE-FC02-06ER41441. We wish to thank the Fermilab theory group for continuing to share their data and their computing resources with the author. We also thank Dr. P. Ramachandran for developing Mayavi and his email support to this project. We finally thank the DePaul students involved in the project: Joel McGraw, Tony Garcia, and Martin Hulth.

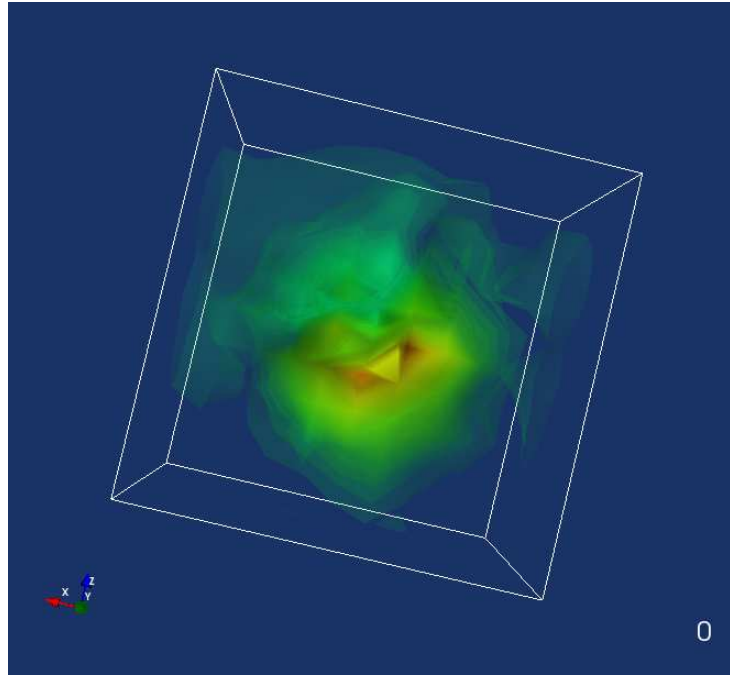


Figure 4: Wave function of a heavy-light meson computed on a single gauge configuration.

References

- [1] W. Marciano and H. Pagels, *Physics Reports* **36** (1978) pp. 135
- [2] M. Di Pierro, *International Journal of Modern Physics A* **21,3** (2006)
- [3] FERMILAB-Pub-01/197
- [4] A. Kronfeld, *Journal of Physics* **46** (2006) pp. 147-151
- [5] G. Bhanot et al., *Nuclear Physics B - Proc. Suppl.* **140** (2005) pp.823-825
- [6] S. Aoki *et al.*, *Nuclear Physics B - Proc. Suppl.* **129-130** (2004) pp.859-861
- [7] D. J. Holmgren, *Nuclear Physics B - Proc. Suppl.* **140** (2005) pp.183-189

- [8] apeNEXT Collaboration, *Nuclear Physics B - Proc. Suppl.* **119** (2003) pp.1038-1040
- [9] S. Gottlieb, *IEEE: Computing in Science and Engineering* **8** (2006) pp.15
- [10] S. Gottlieb, *Nuclear Physics B - Proc. Suppl.* **106-107** (2002) pp.1031-1033
- [11] M. Di Pierro, *Nuclear Physics B - Proc. Suppl.* **106-107** (2002) pp.1034-1036
- [12] R. Brower, *Journal of Physics - Conf. Series* pp.142
- [13] <http://www.enthought.com>
- [14] P. Ramachandran, 4th Annual Symposium, Aeronautical Society of India, 2001.
- [15] W.J. Schroeder *et al.*, *IEEE - Computer Graphics and Applications* **20** (2000) pp. 20-27

Visualization workflow for Lattice QCD

Brian Schinazi, Yaoqian Zhong, Massimo Di Pierro

School of Computing, College of Computing and Digital Media, DePaul University
243 S Wabash Avenue, Chicago, IL, USA

Abstract

The Vis application provides an easy-to-use interface for the processing and visualization of certain high-energy physics datasets.

1 Introduction

Lattice QCD [?] is a numerical approach to the study of quarks, the elementary constituents of protons, neutrons and other forms of matter. In 1968, the study of physics reached a turning point when the structure and interactions of all known particles were described by a single mathematical expression, known as the Standard Model Lagrangian [?]. Since that time, predictions based on the Standard Model have been extremely accurate, and have been able to account for the results of every high energy physics experiment. Still, physicists continue to explore nature at smaller and smaller scales and to look for a breakdown of the model, manifested as a discrepancy between predictions and experiments. This would be a major discovery.

The part of the Standard Model that describes quarks specifically is called Quantum Chromodynamics [?]. This constitutes perhaps the most fascinating part of the Standard Model, as quarks are the only elementary particles subject to the strong nuclear force – a highly non-linear interaction that allow quarks to bind together in complex structures. Practically all of the composite particles we see in experiments are made up of quarks.

The goal of Lattice QCD is twofold: to compute from first principles the properties (such as masses and lifetimes) of these composite particles, and to extract fundamental parameters of QCD (such as particles' masses) from a comparison of theory with experiment.

Typical computations consist of taking a small portion of space ($10^{-15}m$ of side) and its evolution over a short period of time ($10^{-23}s$), and then performing a Markov Chain Monte Carlo (MCMC) simulation of all of its possible evolutions (1000 histories). We call the data saved at each MCMC step a gauge configuration. Next, correlation functions are measured over all simulated evolutions of the system. It can be proven that such an algorithm is equivalent to simulating a quantum-mechanical system. Finally, observable quantities are extracted from the correlation functions.

Until recently, visualization techniques have not been used in the study of QCD. The main reason is that the objects being computed have no obvious correspondence with physical 3D objects. The content of the portion of space which is simulated contains purely random data, since each data set is just a step of a MCMC. The physics is encoded in the probability distribution used to generate the MCMC, and not in the data itself.

We believe that there are some useful applications of visualization techniques to Lattice QCD: they can be used for didactic purposes, they can be used to better understand the behavior of the MCMC algorithms, and they can be used to detect certain types of error in the computation.

One type of error we are interested in is a systematic one: the possible long auto-correlation of topological charge distribution. The portion of space-time that is simulated contains a field that can be thought of as the chromo-electromagnetic field of gluons, the particles that mediate interactions between quarks (analogous to the electro-magnetic field being represented by photons, but in this case having three types of charges). One can also associate a local topological charge density to the field. It should be noted that these fields all live in 4D and therefore must be projected on to 3D in order to be visualized.

The elementary steps of Lattice QCD algorithms are local and, for typical production computations, they do not significantly change the total topological charge. The question, therefore, is whether or not they change the local topological charge density. If they do not, then the computation is biased because the MCMC must get stuck in a topological sector and is not sampling properly. Visualization techniques can be applied in this case, because we have, for example, been able to use them to show that the answer is yes – typical production computations are in fact not stuck in a topological sector.

Our goal is to automate the workflow of physicists working with this data and allow them to:

- store and share gauge configuration for multiple MCMC streams.
- schedule computing jobs for each stream, in particular the computation of the topological charge density.
- visualize the topological charge density (and other derived fields) using iso-surfaces and/or volume plots.
- interact with the data using a web interface (rotate the topological charge and change visualization parameters).

2 Implementation

Vis, at its core, is a web application for storing collections of datasets and scheduling computations on the files in the sets. A set here is a MCMC stream, and the files in the set are the gauge configurations. Computations can be numerical algorithms and/or visualizations. The computations are submitted via an available Portable Batch System installation and can be parallel jobs.

Users can create an account in the system, login, and perform operations such as creating a new stream, uploading files into the stream, scheduling computations, searching and downloading streams submitted by other users, and viewing the results of computations performed on streams already in the system.

Some computations are scheduled automatically when data is uploaded, because new files need to be explored in order to detect their structure, they must be converted to a standard format, and then analyzed to extract some basic physical parameters that are important for cataloging the file and detecting possible errors.

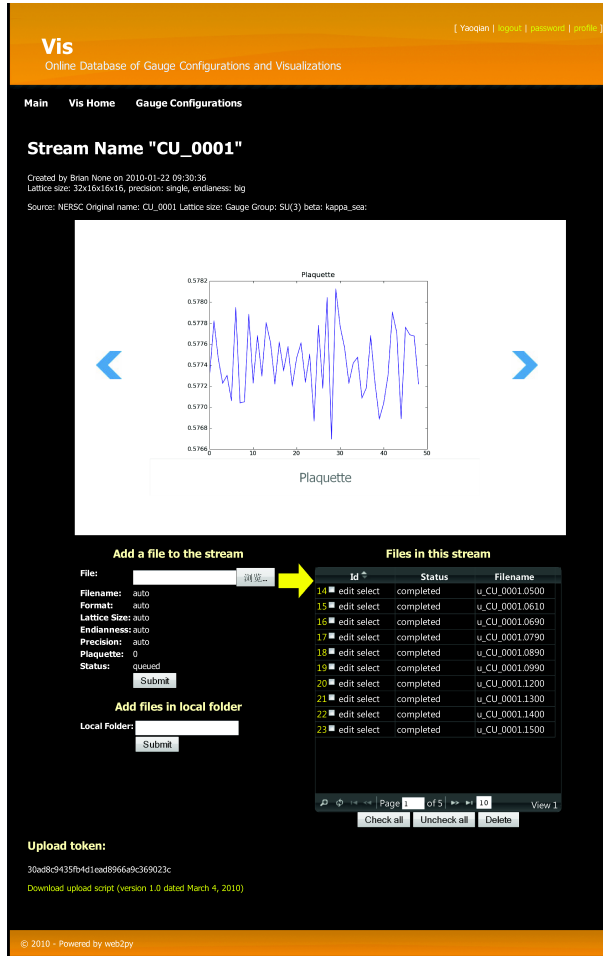


Figure 1: Screenshot of the stream view, including the MC history for the average plaquette and a list of files in the stream.

Individual files can be very large (100M-1GB each) and therefore it may

not be practical to upload them via the web interface, which does not support pausing and resuming. To avoid this problem, the system provides an alternate upload mechanism. When a new stream is created, a security token is issued to the user. The user can utilize a provided program to automatically upload every file from a local folder, authenticating via the downloaded token.

New processing		Completed and In-Progree Processing		
Status:	queued	Id	Status	Algorithm
Algorithm:	topological_charge	30	edit select	completed
	<input type="button" value="Submit"/>	219	edit select	queued

Figure 2: Screenshot of the processing view, showing information about the processing of files in a stream, including the status of the computations and the algorithm that was used.

The algorithm that computes the topological charge density generates output in VTK format. These files can, to a limited extent, be manipulated via the browser using a JavaScript widget that displays isosurfaces at 60% of the dataset’s minimum and maximum values.

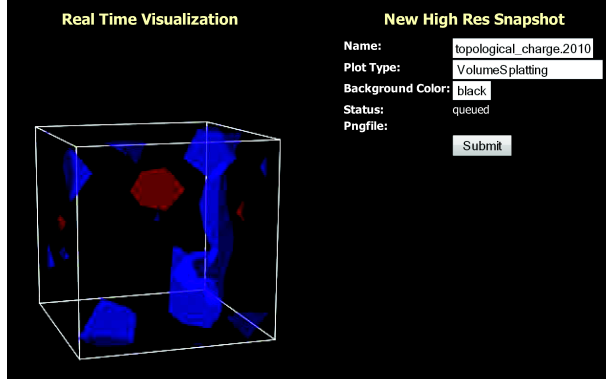


Figure 3: Screenshot showing widget that allows limited manipulation of visualized datasets.

The user can choose a visualization angle, specify additional parameters, and then schedule a full visualization job to generate a high-res image.

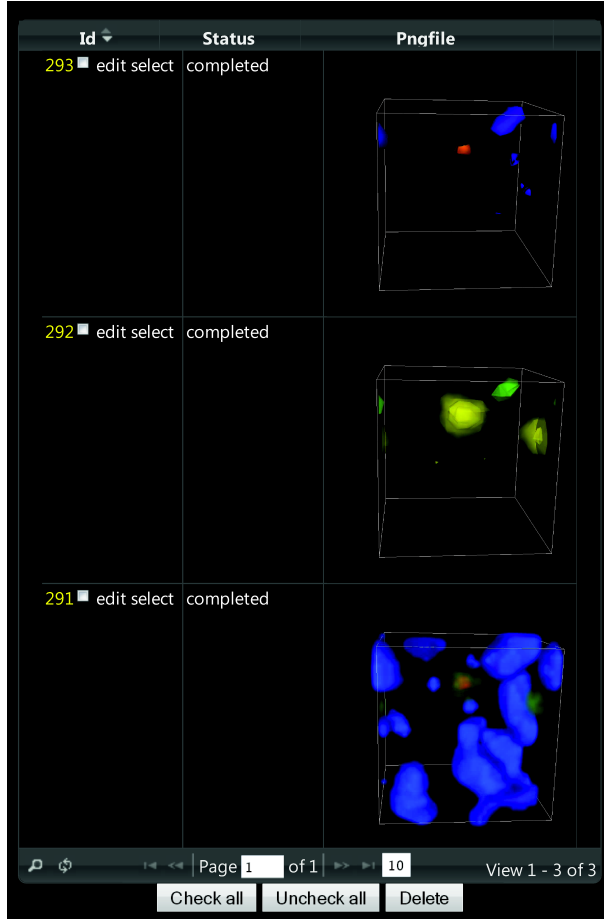


Figure 4: Using the browser-based interface, the user can set parameters for the visualization and then submit the job for processing.

The web interface was built using web2py [?]. We utilize matplotlib [?] for 2D plotting and VisIt [?] for 3D visualization, although we are exploring the possibility of moving to VISH [?] for the latter.

3 Summary

At this point Vis is primarily in the prototype stage, because it is hosted on a small PC and lacks the computing resources and bandwidth to transfer and store very large files. However, the program is fully functional and has been used to process some streams of gauge configurations that are made freely available by various groups via the NERSC archive [?].

Visualization algorithms can help physicists gain new insights into the physics

of QCD, and Lattice QCD computations in particular. Our hope is that Vis can lower the barrier of entry, and enable physicists to look more deeply into their data.

Vis can be downloaded from:

<https://launchpad.net/qcdvis>

4 Acknowledgements

Project funded by the Department of Energy grant DEFC02-06ER41441.

Visualization for Lattice QCD

Massimo Di Pierro

*School of Computer Science, Telecommunications and Information Systems
DePaul University, 243 S Wabash Ave, Chicago, IL 60604, USA
E-mail: mdipierro@cs.depaul.edu*

We present a prototype visualization toolkit for Lattice Quantum Chromodynamics. The toolkit consists of a set of parallel algorithms for the computation of the topological charge, energy density, density of heat-bath hits, two and three point correlation functions, that are interfaced with a Graphical User Interface for an interactive visualization of the fields. The toolkit allows both real-time and off-line visualization, scripting for automation, and the ability to combine individual frames into animations (to produce, for example, an animation of the topological charge as function of the MCMC step). The toolkit also includes analysis and plotting tools to automate the typical workflow of Lattice QCD computations.

PoS(LATTICE 2007)031

*The XXV International Symposium on Lattice Field Theory
July 30-4 August 2007
Regensburg, Germany*

1. Introduction

Typical Lattice QCD simulations generate Tera-bytes of data in the intermediate steps of the computation but the results of each simulation consist of few numbers with a couple of digits of precision. We believe that the ability to visualize the data produced in the intermediate steps of the computations can provide additional value to current and future simulations. On the one hand, data visualization can facilitate the communication of physical concepts and strengthen the outreach effort of the lattice community. On the other hand, it will improve our ability to identify bugs in the algorithms and potential sources of bias in the computations, it will help find pathologies in the convergence properties of the inverters and, perhaps, improve our understanding of Lattice QCD.

Other authors in the past have generated excellent visualizations from Lattice QCD computations [1, 2]. Our project differs from those since it aims to build a comprehensive set of user friendly tools, as opposed to making specific visualizations.

Our toolkit consists mainly of a set of parallel algorithms for Lattice QCD that read typical data files, such as gauge configurations and propagators, and produce various types of projections into 4D gauge invariant scalar fields, for example the topological charge density. The 4D scalar fields are partitioned by time slice and stored together and in parallel in binary VTK files which can be read by most visualization applications including MayaVi, Paraview, VisIt and OpenDX. We have modified the MayaVi2 interface to allow real-time image update and animations. Visualizations and animations can be scripted in Python.

The toolkit also includes an analysis and plotting tool to extract information form log files and to study, both off-line and in real-time, the results of the computation (plot partial averages, sample distributions, moving averages, bootstrap errors, etc.).

Our toolkit is a work in progress and the long term goal is that of developing a comprehensive set of components for automating the workflow of Lattice QCD computations and extract visual information from them.

Many of the images shown in this paper, although they are the result of real Lattice QCD computations, should be considered qualitative in nature because their purpose is to explain the capabilities of the toolkit and not present new physics results. For this reason they have been computed on small lattices, relatively to modern state of the art computations; moreover the parameters (quark masses and gauge coupling) have not been tuned to match the physical ones.

The current version of the toolkit, additional images and some movies can be downloaded from <http://mdp.cti.depaul.edu/vqcd>.

2. Visualization Tools

The main component of our visuation toolkit is a library of parallel lattice QCD algorithms. Programs using the library are generated using meta-programming techniques and they do not require programming by the user. These programs can read gauge configurations generated by FermiQCD, UKQCD, MILC, Chroma and QDP++ code and apply algorithms in the desired order. For example 1) perform cooling, 2) compute the topological charge; 3) slice and save as VTK file.

VTK, or Visualization Tool Kit, is a standard format for storing large 3D data sets. It supports both structured and unstructured meshes, scalar, vectors and tensor fields. We designed a VTK

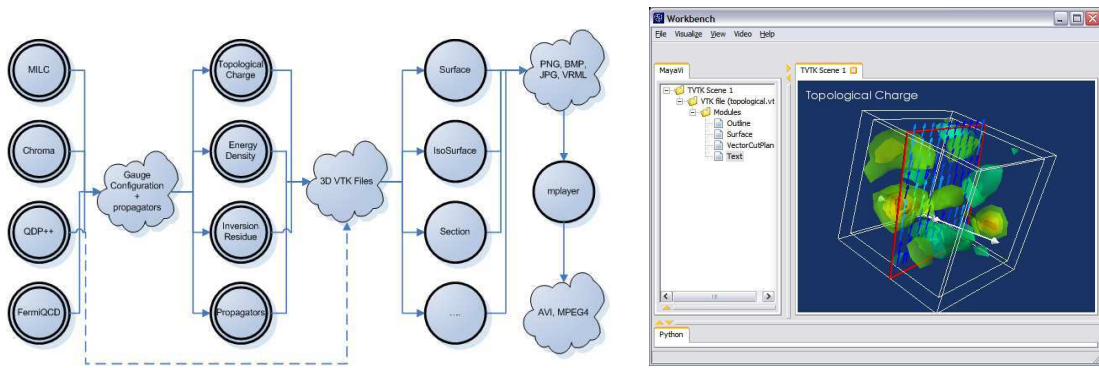


Figure 1: The figure represents the workflow diagram for our toolkit. The figure on the right is a screenshot of the modified MayaVi2 workbench. Via the workbench it is possible to interact with the visualization in real-time.

based file format to store the most general type of 4-dimensional field. All local field components are stored together and different time-slices are separated but stored in the same file.

In this way it is possible to use any standard visualization application to read the field and use the GUI to browse through the time-slices and the field components interactively. Most visualization applications have a pipeline design that allows to send the data through various filters, smoothing and rendering algorithms. The most common ways to render a 3d scalar field is by means of volume density plots or by iso-surfaces (fig. 1-left).

Different fields and algorithms can then be overlapped, rotated, scaled, projected and sliced interactively. For our toolkit we choose to use the MayaVi2 Workbench (fig. 1-right). This is an open source application written in Python that interacts with VTK via the MayaVi2 API. We modified the workbench and included the ability to loop over multiple LQCD files in order to handle large numbers of files at once (for example loop over all files in a folder, produce one image for each file and then encode the frames into an MPEG animation) and to monitor files for changes (for example to see how a field evolves while a LQCD computation is in progress).

In this paper we reproduce, as examples, screenshots of animations generated by our toolkit.

Fig. 2 shows isosurfaces for the topological charge (instantons) at different steps of the heat-bath Markov Chain. The initial gauge configuration is characterized by half of the lattice in a cold state and half in a hot state. A qualitative but interesting result of this visualization is that instantons do not appear to diffuse from the hot to the cold part of the lattice, instead their density(size) decreases(increases) in the hot half of the lattice and increases(decreases) in the cold half. We adopted the following definition of local topological charge in accord with ref. [3]

$$Q(x) = \text{Re} \langle F_{\mu\nu}(x) \tilde{F}_{\mu\nu}(x) \rangle \quad (2.1)$$

$F_{\mu\nu}$ is the smeared chromo-electro-magnetic field.

Fig. 3 shows the energy density for a $SU(2)$ gauge field in presence of a static quark and a static anti-quark as more gauge configurations are averaged. The initial noise (in the first image) dissipates and coherence causes the emergence of the flux tube connecting the quark and the anti-quark (in the third image). Our computation is performed without abelian projection using 1000

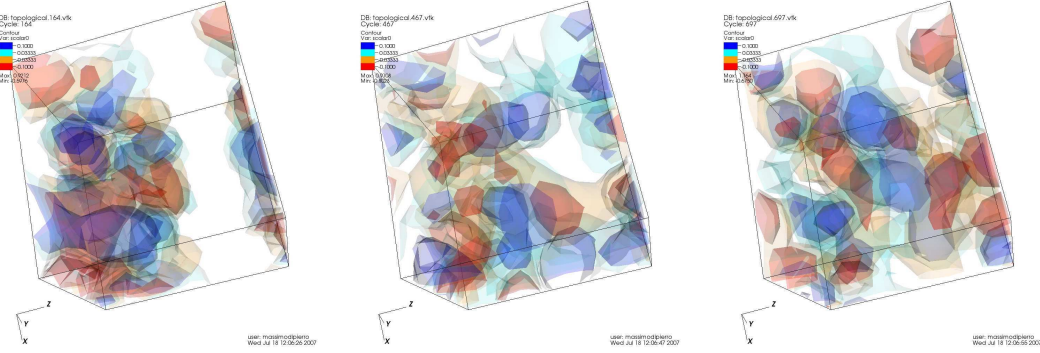


Figure 2: The figures show isosurfaces for the topological charge (instantons) at different steps of the heathbath Markov Chain. The initial gauge configuration is characterized by half of the lattice in a cold state and half in a hot state. A qualitative but interesting result of this visualization is that instantons do not diffuse from the hot to the cold part of the lattice, instead their denity(size) decreases(increases) in the hot half of the lattice and increases(decreases) in the cold half.

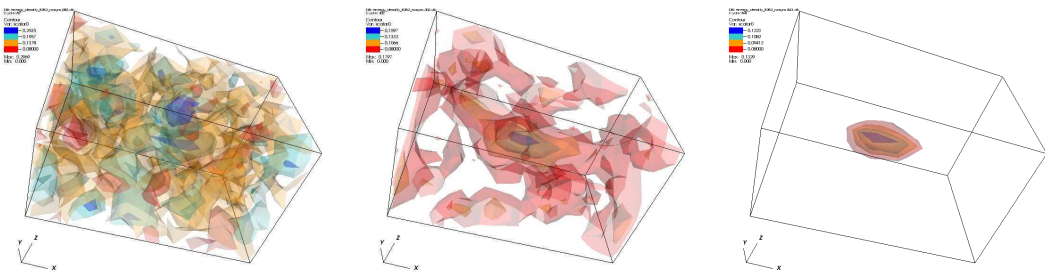


Figure 3: The figures show the energy density for a $SU(2)$ gauge field in presence of a static quark and a static anti-quark as more gauge configurations are averaged. The initial noise (in the first image) dissipates and coherence causes the appearance of the a flux tube connecting the quark and the anti-quark (in the third image).

gauge configurations and the result is qualitatively different from those computations with abelian projection. In fact, our case the peak in the energy density is at the center of the flux tube, while in the abelian projected case there are two peaks where the quarks are localized. We adopted the following definition of energy density, in accord with ref. [4]

$$V_{\mu\nu}(\vec{x}) = \frac{\langle WP_{\mu\nu}(T/2, \vec{x}) \rangle}{\langle W \rangle} - \langle P_{\mu\nu}(T/2, \vec{x}) \rangle \quad (2.2)$$

$V_{0i} \equiv E_i^2$, $V_{ij} \equiv \epsilon_{ijk} B_k^2$ and $x = (T/2, \vec{x})$. P is a $SU(2)$ plaquette. W is the Wilson loop corresponding the static quark and anti-quark.

Fig. 4 shows the only non-zero components of a cold Wilson propagator, respectively ψ_{00} , ψ_{20} and ψ_{30} , i.e. solution of the Dirac equation $(\not{D} - m)\psi = \delta$ in absence of background field. δ is a delta function localized at the center of the lattice where only spin component 0 and color component 0 are different from zero.

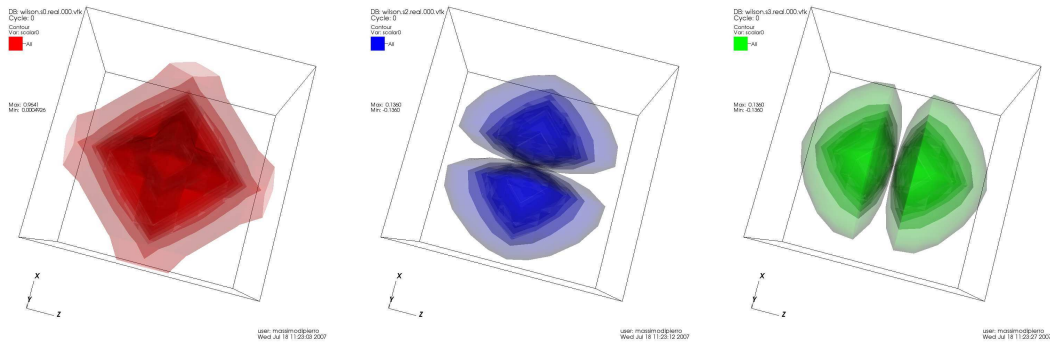


Figure 4: The only non-zero components of a cold Wilson propagator, respectively the real parts of ψ_{00} , ψ_{20} and ψ_{30} , i.e. solution of the Dirac equation $(\not{D} - m)\psi = \delta$ in absence of background field.

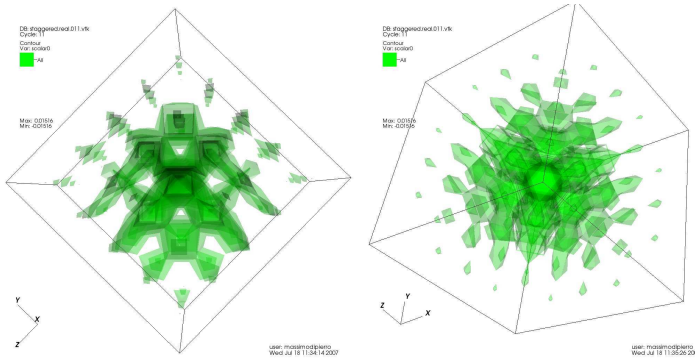


Figure 5: A cold staggered propagator, viewed from a face and viewed from corner of the lattice respectively..

Fig. 5 shows a cold staggered propagator, viewed from a face and viewed from corner of the lattice respectively. Because of symmetries of the action, the view is identical from and face and any corner.

Fig. 6 shows symmetric and anti-symmetric components of the light (valence) quark in a heavy-light meson. The resulting wave function is the QCD analogous of the chemical orbital for the hydrogen atom. They are computed by inserting a $\bar{q}q$ operator, at different locations in space, in between creation and annihilation operators for a B meson

$$f_\alpha(\vec{x}) = \langle B(+t)| \bar{q}_\alpha(\vec{x}) q_\alpha(\vec{x}) |B(-t) \rangle \quad (2.3)$$

Here $B(t) = \bar{h}(t, \vec{0}) \gamma^5 h(t, \vec{0})$. h is a static quark.

3. Analysis Tools

Some of the critical components of many Lattice QCD computations are the Monte Carlo average, the study of convergence of the average, the estimation of the bootstrap error and analysis of the distribution of bootstrap samples. This process is repeated for many quantities, then final

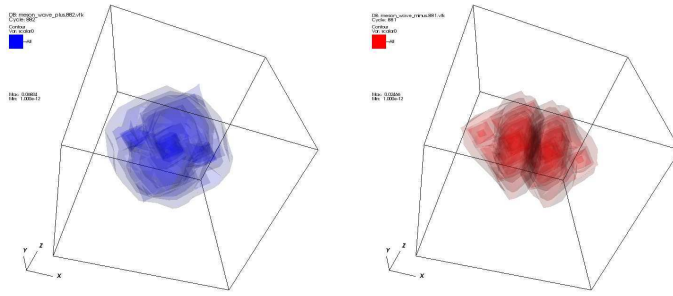


Figure 6: Symmetric and anti-symmetric components of the light quark in a B meson.

results are aggregated, fitted, and various types of plots are produced. Our analysis tool automates this workflow.

First, our system is provided with log (output) files containing various quantities measured on the individual gauge configurations. As an example, we consider log files that look like this:

```
2pt[0]=1.01232634
2pt[1]=0.33123125
...
3pt[0][0]=4.23452345
3pt[0][1]=5.52348454
...
```

for various combinations of the indices and for each gauge configurations. (The log files can also contain additional text, such as comments, that are of no interest here.)

Second, our system is provided with an expression like¹

```
"3pt[<t1>][<t2>]" / ("2pt[<t1>]" * "2pt[<t2>]" )
```

The sub-expressions in quotes are the patterns to look for in the log files, the variables between $<\dots>$ are defined by the expression itself and are matched with the patterns. The rest is just a mathematical formula, function of the sub-expressions in quotes.)

Third, by clicking one button, the system does everything else:

- Matches all occurrences of “2pt[...]” and “3pt[...]” in the logfiles as function of t_1 and t_2 .
- For each occurrence of “2pt[...]” and “3pt[...]” it computes autocorrelations, distributions, moving averages, and generates the corresponding plots.
- It builds all possible instances of the above expression, for example $3pt[3][4]/(2pt[3] * 2pt[4])$. For each of them it computes moving average, mean, bootstrap error, distribution of bootstrap samples, and generates the corresponding plots (including bar plots as function of t_1 and t_2).

¹this is a typical operator that appears, for example, when computing the expectation value of an operator sandwiched between two creation/annihilation operators, as in eq.2.3.

-
- All plots (typically hundreds or thousands of them for each expression) and numerical results can be browsed via a Graphical User Interface
 - Plots are interactive. They can be zoomed over and customized for printing.
 - All bar plots allow fitting and extrapolations, including correlated, constrained, non-linear and bayesian fits using an easy to understand and natural syntax.

4. Conlcusions and Outlook

In this paper we have presented the general design and the current capability of a visualization toolkit for Lattice QCD. It comprises of two parts: a set of parallel algorithms for computing quantities of physical interest and generating corresponding VTK files, and an analysis and plotting tool to automate the workflow of typical computations.

Although all the components shown here are fully functional, this project is still in its infancy. Our aim is to extend its functionality by adding components that may be of interest to physicists. Moreover the toolkit is in the process of being integrated with the broader USQCD software effort.

Acknowledgements

This project is supported by a Scientific Discovery through Advanced Computing (SciDAC) grant DE-FC02-06ER41441 from the Department of Energy.

We wish to acknowledge the Fermilab Theory Group for collaborating on this and other related projects. We also wish to thank Vincent Harvey for his substantial and indenspensible contribution in developing this toolkit.

References

- [1] D. Leinweber, Proceedings of "Workshop on Light-Cone QCD and Nonperturbative Hadron Physics", Adelaide, Australia, 13-22 Dec 1999. [hep-lat/0004025]
- [2] M. Feurstein *et al.* Nucl. Phys. B (Proc. Supp.) Vol. 53, 1-3 (1997) pp.553-556
- [3] F. Bonnet *et al.* Phys. Rev. D 62, 094509 (2000)
- [4] D. G. Caldi and T. Sterling, Phys. Rev. Lett. 60, 24 (1988) pp.2454

Analysis and Visualization Tools for Lattice QCD

Massimo Di Pierro*

School of Computing - DePaul University - Chicago, IL - USA

E-mail: mdipierro@cs.depaul.edu

Yaoqian Zhong

School of Computing - DePaul University - Chicago, IL - USA

E-mail: ati_zhong@hotmail.com

We developed a toolkit for analysis and visualization of QCD data. The analysis tools include a web based application for extracting data in real time from log files, computing autocorrelation, moving averages, bootstrap samples and bootstrap errors from user provided functions, non-linear Bayesian correlated fits, make the relative plots, and facilitate collaborative work. The visualization tools include standard QCD algorithms with the additional ability to save intermediate steps of the computation in parallel in the VTK file format for real time visualization of on-going computations. To demonstrate, we made visualizations showing the convergence of the MinRes inverter for different sources, evolution of the topological charge under different algorithms for dynamical fermions, energy density in space in the presence of static quark-antiquark, and heavy-light wave functions. Our toolkit is self contained and works in cooperation with many existing QCD code.

The XXVII International Symposium on Lattice Field Theory - LAT2009
July 26-31 2009
Peking University, Beijing, China

*Speaker.

1. Introduction

Our work consists of building computer programs to facilitate collaboration, analysis and presentation of data for Lattice QCD physicists. We mainly distinguish two classes of such tools:

- A web based application (also available as a self-standing GUI tool) for collaboration, Monte Carlo analysis and 2D visualization of analysis results.
- A collection of parallel algorithms for generating 3D images and animations from Lattice QCD gauge configurations.

We briefly describe each of these tools in the following two sections.

2. Analysis and 2D Visualization Tools

In a typical Monte Carlo computation [1] one can distinguish two main phases. In Phase I, a computationally intensive Markov Chain Monte Carlo (MCMC) program generates gauge configurations and, for each configuration, measures multiple correlation functions. In Phase II, the output of the above program is analyzed to produce averages and plots. While Phase II requires less computation than I, it is not less expensive in human time, and the one that requires the most collaboration among people. For this reason we have created a web based tool called *mc4qcd* that performs the following steps:

- It **acquires** data from the users, in the form of log files from phase I. The system does not dictate a file format for these log files. It just requires that they contain multiple measurements for the same quantity (once per gauge configuration) and that each quantity is labeled using a prefix. The prefix may contain an index. For example, the log file may contain lines similar to “ $2pt[4] = 0.121235$ ” or “2-point correlation function at 4: 0.121235”. The log file can contain additional text that will be ignored in the parsing.
- It **parses** the data using regular expressions to extract quantitative information. The regular expressions are provided by the user, can be different for each log file, and may be applied to multiple runs. An example could be: “Extract all 2pt and 3pt correlation functions.”
- It **filters** the data based on user preferences. For example “consider only 2pt correlation functions separated by less than 12 time-slices”.
- It **mines** the data for expressions of interest. For example “compute all possible ratios of $3pt[< t_1 >][< t_2 >]/(2pt[< t_1 >] \times 2pt[< t_2 >])$ ”.
- It **represents** the data in multiple formats such as text based, plots and histograms. For example “show an histogram of the bootstrap samples for $3pt/2pt^2$ ”. The various plot types include: raw data, autocorrelations, moving averages, bootstrap samples, averages with bootstrap errors.
- It allows one to further **refine** the data and **interact** with the data by fitting the bootstrap results using Bayesian correlated fits with arbitrary non-linear functions.

The entire process is executed via a browser, it requires login, and enforces access control on all data at every step. This facilitates collaboration between members of a group by allowing them to easily locate and search data and plots. Users can also comment on each other's data (if they have access to it) and the comments can include Latex expressions. In this way, the thought process of the physicist working on the data is stored together with the data in the web application. The underlying libraries can be used to batch script all the functions provided by the web application.

Figure 1 shows some screenshots from the *mc4qcd* program. The top-left screenshot lists the data sets available to a user, links possible analysis algorithms, and analysis results. The plots represent an example of autocorrelation functions for the $2pt$ at 3 different time slices, the histograms of the bootstrap samples, and a plot of $2pt[t]$ with an exponential fit as function of t.

Although this program was designed specifically for lattice QCD in mind, it can be used for the analysis and plotting of MCMC data in other areas of Physics.

The program is packaged together with a web server and a file based relational database into a single application that runs on Windows, Mac and Linux. Its only dependencies are the Python interpreter and the matplotlib library.

3. 3D Visualization Tools

Typical Lattice QCD computations generate a large quantity of data that is normally only looked at in aggregated form (numbers with a precision of a few digits and simple 2D plots). A lot of the information is discarded. While this is the nature of MCMC computations, we believe there may be a value in looking in more detail at the data being generated in order to identify patterns that may lead to better understanding of the algorithms and/or that may be symptomatic of errors in the computations. Moreover, it will better present scientific results and educate the public about Lattice QCD.

Our toolkit comprises of a set of Lattice QCD libraries for implementing actual computations. These libraries have been modified to be able to save their intermediate state, in parallel, into fields (gauge, fermions, scalars) which can be visualized in 3D interactively (volume plots, iso-surfaces, slices).

Our toolkit can read multiple gauge configurations formats including ILDG, Lime, Nersc (3x2 and 3x3), MILC and FermiQCD [2]. The file format is automatically detected and each file is converted into a FermiQCD format for further analysis.

The output fields (for example the energy density, the topological charge, the component of a propagator) are saved as scalars and VTK files. Each time-slice is saved as a separate scalar field within the same VTK file. The VTK files can be combined using an mpeg-encoder to make movies.

The Visualization Toolkit (VTK) is an open source, platform independent, graphics engine with libraries for parallel rendering of 3D visualizations. VTK is being developed by a large collaboration of universities, laboratories (Sandia, Los Alamos, and Lawrence Livermore), and private companies. VTK provides core functionality for many existing visualization packages such as VisIT (developed by LLNL), MayaVi and Paraview. All these packages are compatible and can interoperate with our software.

Here we present two case studies of usage of our toolkit.

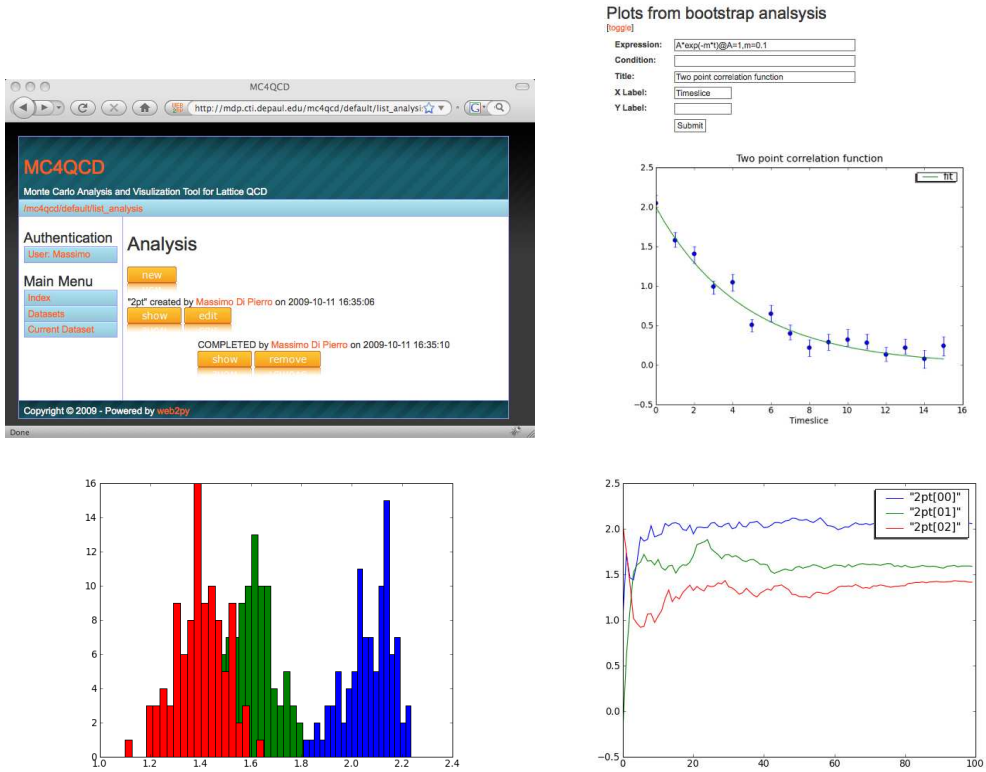


Figure 1: The top-left image shows a page of the mc4qcd program. This page allows a user to select a data-set and run one or more analysis algorithms on that data-set. The top-right image shows a typical plot generated by the system for a 2 point correlation function analysis on the database. The images at the bottom show, from left to right respectively, the distribution of bootstrap samples and moving averages for $2pt[t]$ at three different values of t . These plots and more are generated automatically by the web application upon upload of a data-set.

3.1 Autocorrelation length

In this case study [3] we visualize topological charge density and measure how fast or slow it evolves under the Markov Chain Monte Carlo (MCMC) for different algorithms and different simulation parameters (the dynamic quark mass in particular). This would give us strong confidence that current Lattice QCD computation are adequately sampling the space of all possible configurations as opposed to getting stuck in one topological sector, and provide an effective tool for developing algorithms that maximize equilibration of the topological charge. We analyzed ad hoc gauge configurations generated with small trajectories by Michael Clark and Chulwoo Jung respectively:

- Two ensembles of 32×24^3 dynamical Wilson gauge configurations with $\beta = 5.6$ and quark masses of 66MeV and 33MeV respectively. ($dt = 0.1$)
- One ensemble of 64×24^3 dynamical Domain Wall gauge configurations with beta=2.13, two degenerate light quarks of 14MeV, and one strange quark of 74MeV. ($dt = \frac{1}{6}$).

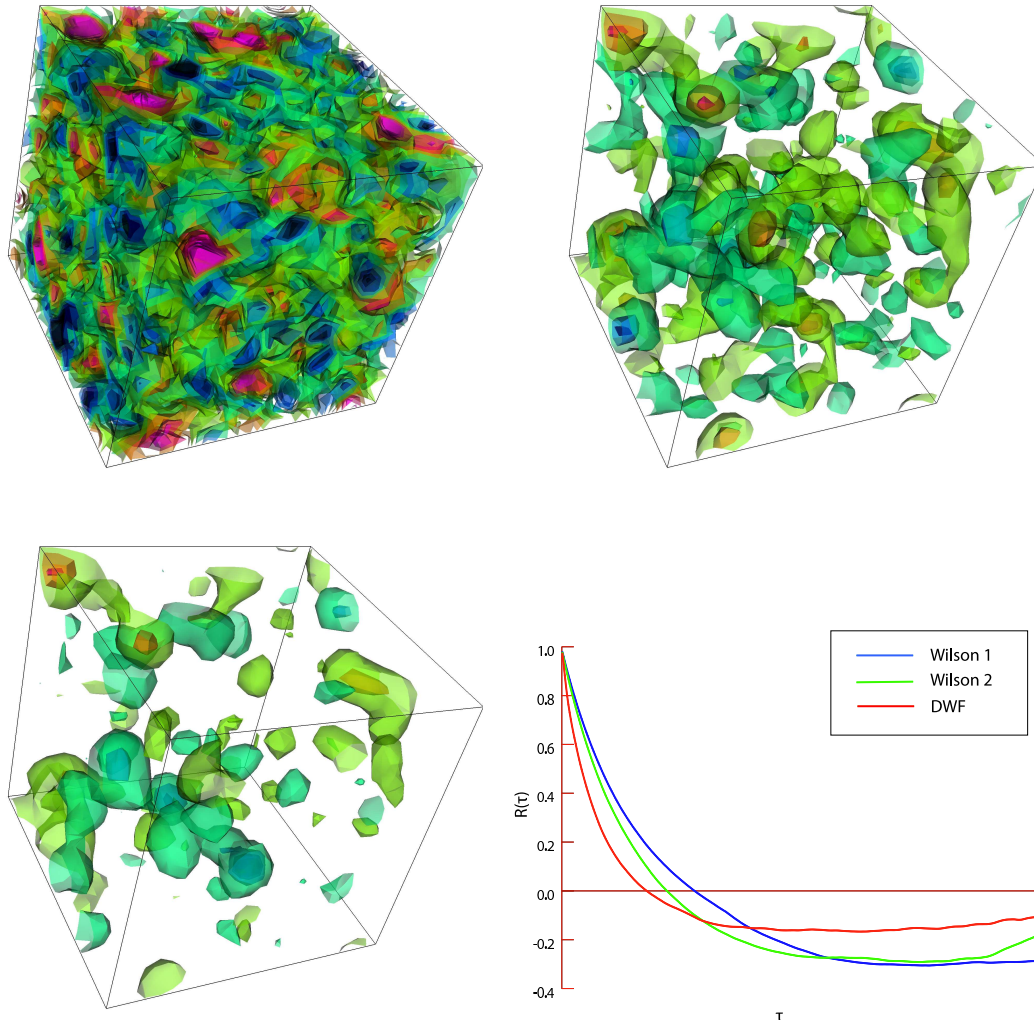


Figure 2: The images show topological charge density at different cooling steps for a sample gauge configuration. The plot at the bottom-right shows the autocorrelation length for the computed topological change density for the three ensembles of production quality gauge configurations discussed in the paper.

We performed 20 gauge invariant APE smearing steps for cooling, shown in figure 2, computed the topological change, and computed the average autocorrelation of the topological change density.

The result is shown in bottom-right plot. The autocorrelation crosses 0 after about 100 steps. This indicates that the local topological charge becomes de-correlated after about 10 MCMC steps at $dt = 1$ which is typical for production grade Lattice QCD computations.

3.1.1 Inversion Residue

Visualization can be used to represent various types of fields; for example, wave functions, form factors, and/or bare quark propagators. Visualizing the latter can be useful to understand the rate of convergence of the inverters at a local level as opposed to at a global level (as measured by

the total residue). In this example we show how we have modified the MinRes inverter to visualize a quark propagator on a typical production quality gauge configuration:

```
class MinResVtk {
public: static inversion_stats inverter(...) {
    ...
    psi_in.update();
    mul_Q(r,psi_in,U,coeff);
    r*=-1;
    r+=psi_in;
    psi_out=psi_in;
    do {
        r.update(); // sync parallel buffers
        mul_Q(q,r,U,coeff);
        alpha=q*r;
        alpha/=norm_square(q);
        mdp_add_scaled_field(psi_out, alpha, r);
        mdp_add_scaled_field(r, -alpha, q);
        residue=sqrt(norm_square(r)/r.global_size());
        forallsites(x) // project into a scalar
        for(int a=0, s(x)=0; a<4; a++)
            for(int k=0; k<psi_in.nc; k++)
                s(x)+=sqrt(real(psi_out(x,a,k)*conj(psi_out(x,a,k))));
        s.save_vtk(filename,...); // save as VTK file
    } while (...);
    return stats;
}
}
```

Figure 3 show the absolute value of a quark propagator for a planar source (top) and a solid source (bottom), after a few inversion steps (left) and after convergence (right), for the same gauge configuration. The visualization indicates that the inversion algorithm converges uniformly everywhere.

4. Conclusions

We believe visualization will prove to be an important tool for understanding Lattice QCD algorithms and the MCMC evolution. For example the exact nature of the topological objects responsible for confinement is yet to be understood satisfactorily. We also believe visualization can play an important role in education and outreach outside the core of the Lattice QCD community. Our tools are Open Source (GPL2) and can be downloaded from:

<https://launchpad.net/qcdmc>
<https://launchpad.net/qcd>

Acknowledgements

We thank Argonne National Laboratory for proving computing resources Michael Clark (BU) and Chulwoo Jung (BNL) for proving the USQCD gauge configurations used in some of our im-

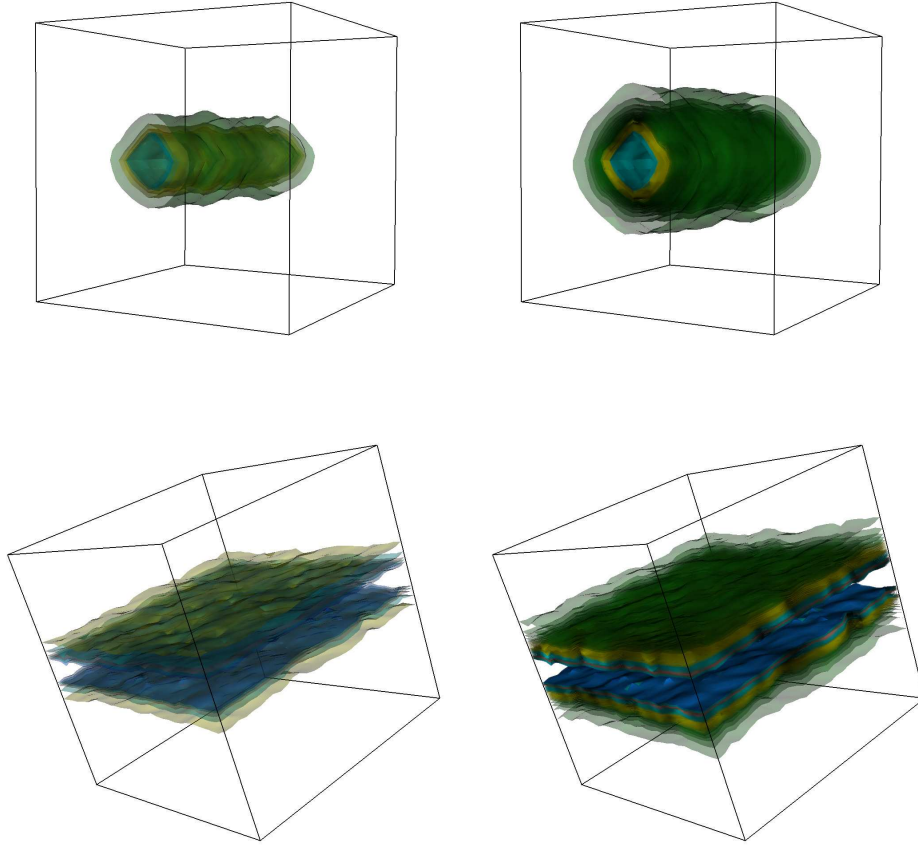


Figure 3: The first three images show the topological charge for a typical gauge configuration at different cooling steps. The plot at the bottom-right shows auto-correlation for the three different ensembles of gauge configurations discussed in the paper.

ages. We also thank James Osborn (ANL), John Negele (MIT), Richard Brower (BU), and Steven Gottlieb (Indiana) for various comments and advice.

This project is funded by the US Department of Energy under grant DEFC02-06ER41441.

References

- [1] M. Di Pierro, J. Mod. Physics A21 (2006)
- [2] M. Di Pierro *et al.*, Lattice 2003, Nucl. Phys. B Proc. Suppl. (2004)
- [3] M. Di Pierro *et al.*, J. Phys. Conf. Ser. 180 (2009) 012068

Vis: Online Analysis Tool for Lattice QCD

Massimo Di Pierro*

School of Computing - DePaul University - Chicago

E-mail: mdipierro@cs.depaul.edu

Yaoqian Zhong

School of Computing - DePaul University - Chicago

E-mail: ati_zhong@hotmail.com

Brian Schinazi

School of Computing - DePaul University - Chicago

E-mail: schinazi@gmail.com

Vis is a system that implements Software as a Service for Lattice QCD computations. At its core, it is a repository of gauge configurations accessed via either a web interface or programmatically via a web service. It gives users the ability to upload data and queue computing jobs for background execution. Jobs can be analysis algorithms and/or visualization algorithms (topological charge, polyakov lines, energy density, etc.). It exposes web services which are accessible from a command line script that allows, for example, to upload all gauge configurations in the current folder, request the server to make a plot of the average plaquette, and generate a movie of the topological charge. It interfaces with VisIt (also running server-side) for 3D visualizations and uses matplotlib for 2D plots. Data and results are automatically posted online with a role based access control mechanism. All major tasks can be executed directly from the web interface.

Lattice 2010

*Speaker.

1. Introduction

In this paper we present a tool for storing and organizing Lattice gauge configurations, for scheduling PBS jobs, including visualization jobs, and for viewing the results of those jobs.

The typical Lattice QCD workflow can be summarized in three steps:

- Lattice gauge configurations are generated, one after the other, in a Markov Chain Monte Carlo. Here we will refer to each chain as a stream.
- An algorithm runs on each gauge configuration in a stream and produces a numerical output (typically a correlation function) which is stored in a file.
- The numerical outputs generated in the previous steps are aggregated and averaged in order to compute a quantity of physical interest (for example masses, lifetimes, or wave functions).

This process is today performed by the larger community in an industrial fashion. Physicists have come together to standardize file formats for storing gauge configurations, for their remote storage and distribution, and for job management and submission. Yet today there are still multiple formats (NERSC [7] 2x3, NERSC 3x3, SciDAC [3], IDLG [6], MILC [2], FermiQCD [2]), with each format having the possibility to have big or small endianness or to contain single or double precision values, there are multiple systems for distribution (scp, gridftp, ILDG), and there are multiple hardware architectures to submit jobs to, which can have different configurations.

This multitude of options creates an entry barrier for young scientists who want to be involved in Lattice QCD research and also constitutes a major expense (in terms of time) for the more senior physicists already in this field. This is particularly true when visualization algorithms are involved. These involve additional file formats, third party dependencies, and domain-specific knowledge.

Vis is prototype software that provides an abstraction layer on top of existing systems that perform the tasks described above. It provides a simple to use web interface to store data that is independent of the file format. It supports importing all of the most common file formats for gauge configurations. Streams can be searched and individual files can be uploaded and downloaded via the web interface. Files can also be uploaded and downloaded using batch scripts that provide file integrity, pause and resume functionality, and security. All users are authenticated and all uploads are signed with the user credentials. Streams can be private to the owner or made publicly available.

Once files are uploaded into a stream, they are automatically converted into a common file format and some standard initial computations are performed on the data: endianness and precision are detected and the average (aggregate and moving) of the plaquette is computed. Metadata about stream is then stored, based on the credentials of the user and the computed parameters, and is available for use for search. These steps require no actions from the user's side.

Once a stream has been uploaded and cataloged, it is made available based on the permissions above. Users can then select a stream and run additional algorithms on it, such as an algorithm that computes the topological charge density. This is one of the major applications of Vis, for which it incorporates some domain specific logic to handle VTK files (for visualization purposes) and interoperates with VisIt [5] for 3D volume plots, iso-surfaces and rendering, and with matplotlib [4] for 2D plots.

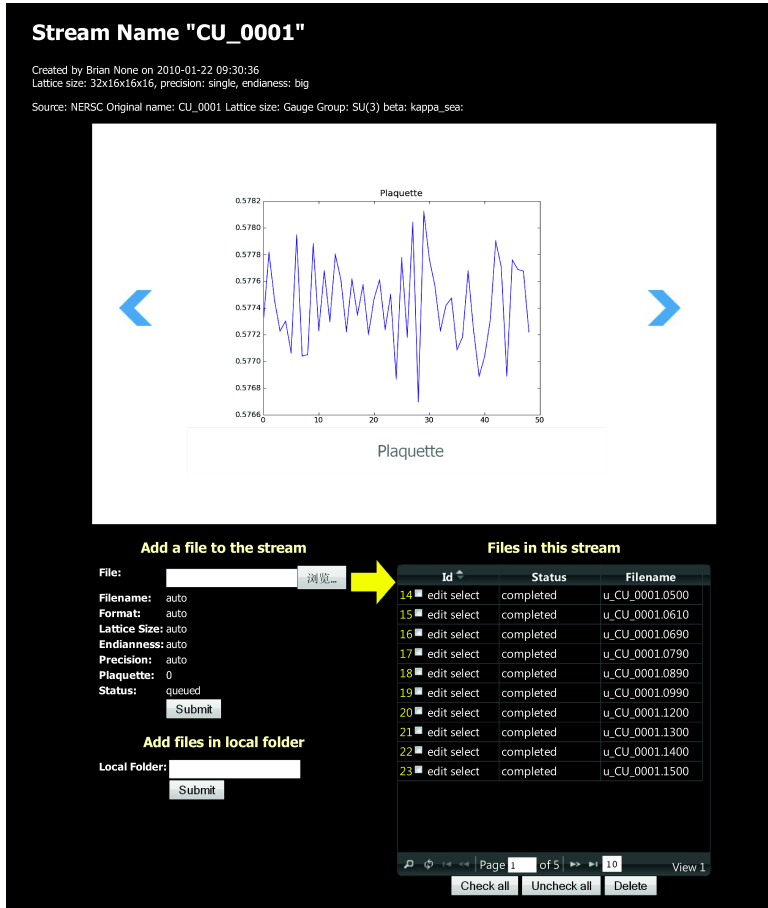


Figure 1: As an example we downloaded a stream of gauge configurations from NERSC [7] into Vis (CU_0001). Vis detects the endianness, precision, computes and plots the average plaquette, as represented in the figure (the plot is generated using matplotlib [4]).

With Vis, users can interact with data and schedule jobs without domain specific knowledge and with minimal previous training. This frees the physicist from some of the most pedantic and repetitive tasks. It also allows tracking of data, tracking of progress, and avoids duplication of effort.

2. Implementation

Vis is implemented in the Python programming language using the web2py [1] web framework. It uses a Database Abstraction Layer to interface with the database. It includes a collection of algorithms written in C++ using FermiQCD, but it is not limited to FermiQCD. Other binary programs can be registered with the system.

In its simplest installation it comes with its own web server and a file based transaction-safe relational database based on SQL. In a more complex installation, it can use other web servers (for example Apache) and other databases (MySQL, PostgreSQL, Oracle, MSSQL, FireBird, DB2, Informix, and Ingres). All data but the gauge configurations themselves are stored in the database.



Figure 2: The figure shows the screen that allows the user to select an algorithm and schedule a job. The right hand side lists submitted jobs and completed ones.

The gauge configurations are stored in binary files which are organized into a structure of nested sub-directories, to avoid having too many files under the same folder. This folder structure can and should be hosted on a different filesystem than the primary database. These files are then referenced by individual configfile records, which are referenced by the table containing the record of the files' stream (fig. 1).

Since configfiles are uploaded by users, even though the system requires authentication, the system must account for exposure to directory traversal attacks. One such attack is performed via filenames that contain special characters not allowed by the file system. Vis implements many security features to prevent this vulnerability, as well as others classified by the Open Web Application Security Project (OWASP), including SQL Injection and Cross Site Scripting.

Although streams are created by the web interface, and the files can be uploaded in the same manner, this is not a practical approach and Vis provides an alternative mechanism. Upon creation, each stream is associated with a security token that is a random universally unique identifier (UUID). The owner of the stream can use a provided shell script to easily discover all gauge configuration file from a given local folder and upload them to the server into the stream identified by the UUID. Files have their hashes computed, and are then uploaded one at the time, while showing a progress bar. In case of network error or other upload failure, the script will resume and will use the hash values of the files to determine whether each file has already been successfully uploaded into the stream or whether it has changed locally and needs to be re-uploaded. The script communicates with the server using XML-RPC. An option can be set to have the script also submits jobs to be subsequently run against the data being uploaded.

Progress can be monitored both locally and via the web interface.

Algorithms are submitted via the Portable Batch System (PBS). Vis implements two queues, one that lists algorithms to be submitted per stream and a queue that maps the PBS queue. Vis does not immediately submit all jobs to PBS but monitors the PBS jobs to keep the workload limited and constant (fig. 2).

At the time of writing, only a few algorithms are supported and adding new algorithms requires editing of the Vis source code. Planned improvements include the ability for the user to register any third party program with Vis by providing a startup and configuration script.

Visualization algorithms are somewhat special because they consist of three steps. In the first step, data is analyzed and projected into one or more 3D scalar fields, which are then saved in VTK files. In the second step, the user interacts with the VTK file (this requires a crude but fast visual representation of the data). In the third step the data is visualized at high resolution, for purposes such as printing or high-quality display.

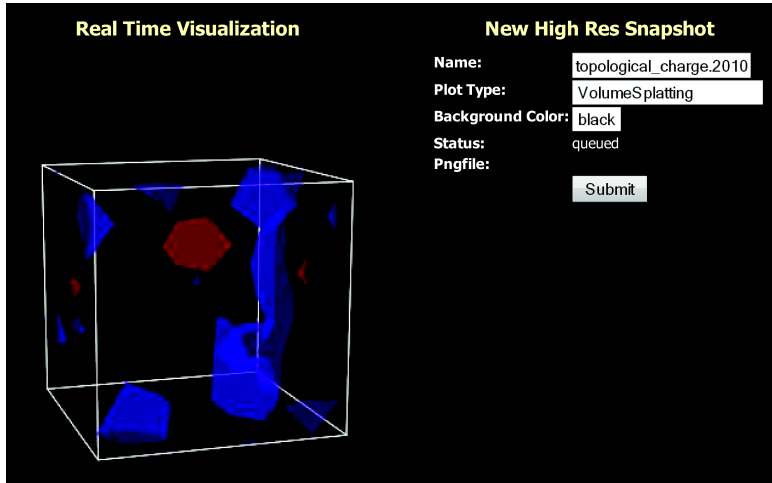


Figure 3: When a job is completed, the user can interact with the output (the VTK files) using the 3D JavaScript Widget shown in the figure. The user can submit a request for high resolution rendering of the data (for example using the volumetric splatting algorithm on black background).

Vis includes workflow and tools that distinguish these steps. Step one consists of a regular Lattice QCD algorithm and it is treated as any other algorithm. Step two is the most complex one to handle via a web interface. For this purpose, we created a 3D JavaScript widget that computes iso-surfaces and allows real time rotation (fig. 3) with the need to install a visualization program on the client-side. Once the user has identified an optimal point of view for visualization of the data, step three can be performed by selecting a high resolution volume or iso-surfaces plot and clicking a button.

Following submission, a VisIt job runs in the background and produces the specified image. A multiple choice menu allows users to pick settings for VisIt (such as colors, axes formatting, etc). There is no need to interact with the visualization engine directly (fig.4).

It is also possible to schedule visualizations of every gauge configuration in a stream and have Vis assemble the resulting images into a video using the ffmpeg open source multimedia tool.

3. Conclusions

Although Vis is still a work in progress, it constitutes one more step toward the ideal goal of the authors to provide a complete QCD Software as a Service platform. Today only the step of generating gauge configurations is performed efficiently in a semi-industrial way. This is primarily because this step is the most computationally expensive and there are few reliably-tested programs available to generate gauge configurations. Yet many other tasks performed by lattice QCD physicists can be automated. This presents many benefits: it reduces the margin of error, provides better optimization of resources, allows better tracking of data and work progress, and, most importantly, it frees the time of scientists for more intellectual activities such as developing new models, new algorithms, and tackling new problems.

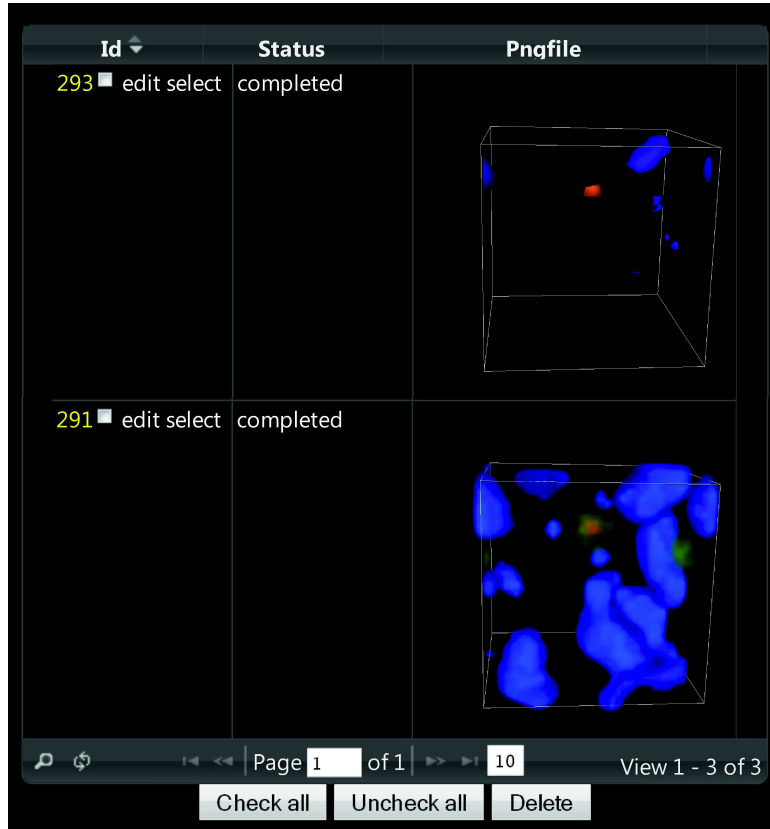


Figure 4: This screen shows a list of visualizations scheduled for the current VTK file. If a visualization is completed, a thumbnail of the image is displayed. The image can be downloaded by clicking on the thumbnail.

At this point Vis is a stand-alone web application but it can be integrated with existing ILDG tools to provide a unified interface to Lattice QCD computations.

In the near future we are planning a better integration with FermiQCD to provide a wider choice of algorithms; a better customization to allow support for algorithms written with different Lattice QCD libraries; a more sophisticated workflow management system to handle complex conditional dependencies; and integration with mc4qcd (a web based plotting and analysis tool also written by the authors).

The hardware currently dedicated to VIS is very limited both in terms of speed and space. Dedication of better hardware to this system will enable us to provide QCD as a service to interested users.

The current version of Vis can be downloaded from:

<https://launchpad.net/qcdvis>

Acknowledgements

This project was funded by the Department of Energy, grant DEFC02-06ER41441.

References

- [1] Massimo Di Pierro. web2py website, 2010.
- [2] Massimo Di Pierro and Jonthan M. Flynn. Lattice QFT with FermiQCD. *PoS*, LAT2005:104, 2006.
- [3] Robert G. Edwards. Nuclear physics using lattice QCD in the SciDAC era, 2009.
- [4] John Hunter, Darren Dale, and Michael Droettboom. matplotlib website, 2010.
- [5] Lawrence Livermore National Security, LLC. Visit website, 2010.
- [6] C. Maynard. International Lattice Data Grid: Turn on, plug in, and download. In *Symposium on Lattice Field Theory*, 2009.
- [7] U.S. DOE. Nersc website, 2010.

Making QCD Lattice Data Accessible and Organized through Advanced Web Interfaces

Massimo Di Pierro*

School of Computing - DePaul University - Chicago

E-mail: mdipierro@cs.depaul.edu

James Hetrick

University of the Pacific

E-mail: jhetrick@pacific.edu

Shreyas Cholia

Lawrence Berkely Laboratory

E-mail: scholia@lbl.gov

David Skinner

Lawrence Berkely Laboratory

E-mail: deskinner@lbl.gov

The Gauge Connection at qcd.nersc.gov is one of the most popular repositories of QCD lattice ensembles. It is used to access 16TB of archived QCD data from the High Performance Storage System (HPSS) at the National Energy Research Scientific Computing Center (NERSC). Here, we present a new web interface for qcd.nersc.gov which allows physicists to browse and search the data, as well as download individual files or entire ensembles in batch. Our system distinguishes itself from others because of its ease of use and web based workflow.

XXIX International Symposium on Lattice Field Theory
July 10-16 2011
Squaw Valley, Lake Tahoe, California

*Speaker.

1. Introduction

The Gauge Connection Lattice QCD data archive has been operated by the National Energy Research Scientific Computing [6] (NERSC) center since 1998. With over 16TBytes of data, the NERSC archive is one of the largest public repositories of lattice gauge ensembles. Its popularity has largely been due to the ease-of-use of its web interface compared to more complex grid based tools.

We are now updating the Gauge Connection to provide a number of modern features, while maintaining the simplicity and ease-of-use of the original. We are adding the ability to search data using tags. We are also providing capabilities to move data easily between the archive and the user's computer, or between two remote computers using both web and grid tools. The archive is now database driven and its pages are dynamically generated in order to facilitate access to the most recent local and remote data. It provides some visualization of the data. New data can easily be uploaded to the archive where it is automatically discovered and cataloged.

The archive can now deliver data in a variety of file formats (including ILDG [5], single and double precision, and FermiQCD [3]) by translating data on the fly after download. We have designed the new website to provide additional capabilities beyond data access, including wiki capabilities to annotate the data and link external work derived from archive data (derived data, software, tutorials, and publications).

Each gauge ensemble is also associated with a discussion forum allowing registered users to add their own comments. The archive has a more sophisticated access control mechanism and users can have four possible roles: administrators (can manage every aspect), editors (can edit the wiki pages linked to the data), registered users (can download data and comment) and anonymous visitors (can browse the wiki pages and query the data by tags). User management is greatly simplified through the use of a single-sign-on service that allows the user to log in with an existing identity from an external OpenID provider like Google or Yahoo.

2. Backend Architecture

The NERSC data is stored on the High Performance Storage System (HPSS), a hierarchical tape storage system designed to manage and access multiple petabytes of data at high speeds [?]. HPSS stores 16 terabytes of Lattice QCD data, mostly generated by the MILC [4] Collaboration. HPSS exposes different data access interfaces including a custom command line client (HSI), a C API, an FTP interface, a parallel FTP interface, as well as a GridFTP interface that can be used via Globus Online. We leverage the HPSS FTP interface to provide web access to the Lattice QCD data.

The system performs nightly introspection of the folder structure (through the HSI and FTP interfaces), reproduces this folder structure in the database, automatically tags data by parsing the file names, groups files with similar name patterns, and publishes the data online. For each folder in HPSS a corresponding web page is generated dynamically. The web structure has the same hierarchy as the folder structure on the HPSS backend.

The new web interface is designed to mimic the iPhone interface and works on both regular browsers and mobile devices.



Figure 1: The main web page for `qcd.nerc.gov` allows browsing and searching for gauge ensembles.

Volume Tag	Ensemble Name
volume/12^3x12	CU/0001/u_CU_0001.5400
volume/16^3x16	CU/0004/u_CU_0004.5000
volume/16^3x48	MILC/1241/u_MILC_1241.2250
volume/20^3x20	MILC/1242/u_MILC_1242.2450
volume/20^3x48	MILC/1243/u_MILC_1243.2400
volume/20^3x64	MILC/1244/u_MILC_1244.2450
volume/24^3x24	MILC/1245/u_MILC_1245.2345
	MILC/1246/u_MILC_1246.2265

Figure 2: The left image show statics by tags. The right image shows topoligical change images from representative elements of various selected ensembles.



Figure 3: The image shows the page corresponding to a folder. The name of the folder is on top, followed by a folder description (optional) and by the tags applied to the folder. Files in the folder are grouped by their prefix (pattern). Patterns are shown at the bottom, above users' comments.

Every page on the QCD site is editable using a wiki syntax similar to wikipedia and registered users can comment on the pages. Both the wiki and comments allow Latex syntax for formulas. Gauge ensembles can be searched by direct browsing of the folder structure or by tag (contributing collaboration, lattice size, beta value, dynamical quark masses, etc.). The system generates interactive charts with statistics by tags.

Some ensembles have been processed off-line to generate meta-data such as a topological charge densities and have been linked to images and movies of said topological charge density. The system is data agnostic and can, in principle, store other data besides gauge ensembles. For example, it can store quark propagators and eigenvalues, examples of which are already in the system. The system uses standard third party web analytics tools to track usage and to geo-tag visitors on a map.

Here is how a simple file access workflow works. The user logs in to the Gauge Connection website (fig. 1) and searches for a desired dataset (fig. 2). When the user finds the ensemble that he/she wants (fig. 3), the user click on the appropriate file to download it. The system checks that the user is logged in, and then pulls the data from tape through the HPSS FTP server. Once the data is available (the tape has been mounted in HPSS), it is streamed back directly to the client browser. Alternatively the user can copy the link to the page for the entire ensemble and pass it to a command line script (provided) that will download every file in the ensemble, one by one, in batch, converting on the fly to the desired format.

3. Frontend Architecture

The system is based on web2py [2], a framework for rapid development of secure database driven web applications. It is written in Python and supports many standard databases including Sqlite, MySQL, PostgreSQL, Oracle, MSSQL, Informix, DB2, Sybase, Firebird, and Google Bit Table using a Database Abstraction Layer (DAL). The DAL generates SQL dynamically and as needed.

The system uses jQuery Mobile for page layout and a custom JavaScript library for charting. It uses the Google Chart API for Latex rendering and the Janrain web service for Single Sign On.

The visualizations of topological charge density are produced offline using Visit (LLNL) and the FermiQCD Visualization Toolkit.

The system has a modular Model-View-Controller design which separates the data representation from the data presentation and from the application workflow. This makes the code compact and easy to maintain. It includes a web based IDE, a web based database management tool and internationalization capabilities.

The complete model for the system consists of just a few lines of code used to describe the data that is stored:

```

1 # represents a folder in HPSS
2 db.define_table('catalog_folder',
3     Field('root_id', 'reference catalog_folder'),
4     Field('path'),
5     Field('title'),
6     Field('header', 'text'),
7     Field('footer', 'text'),
8     Field('pattern_ignore'),
9     Field('pattern_group'),
10    Field('comments', 'boolean', default=True))
11
12 # a tag to be applied to a folder
13 db.define_table('tag',
14     Field('name'),
15     Field('root_id', 'reference catalog_folder'))
16
17 # a file contained in a folder
18 db.define_table('catalog_file',
19     Field('root_id', 'reference catalog_folder'),
20     Field('filename'),
21     Field('md5'),
22     Field('pattern'),
23     Field('extension'),
24     Field('size', 'decimal(20,0)'),
25     Field('mtime', 'datetime'))
```

Each Field has a name and a type.

A dispatcher function maps web pages into function calls. These functions are defined in the controller. For example, all web pages of the form

`http://.../root/<path>`

Correspond to a `<path>` in the file system and they are mapped into the following function:

```

1 @cache(request.env.path_info, 60)
2 def root():
3     path = '/'.join(request.args)
4     (d,t,f) = (db.catalog_folder, db.tag, db.catalog_file)
5     query = (d.path==path) if path else (d.root_id==0)
6     page = db(query).select().first() or redirect(URL('error'))
7     tags = db(t.root_id==page.id).select()
8     subfolders = db(d.root_id==page.id).select()
9     patterns = db(f.root_id==page.id).select(
10         f.pattern, f.id.count(), f.size.sum(),
11         f.mtime.year(), groupby=f.pattern, orderby=f.pattern)
12
13     return locals()
```

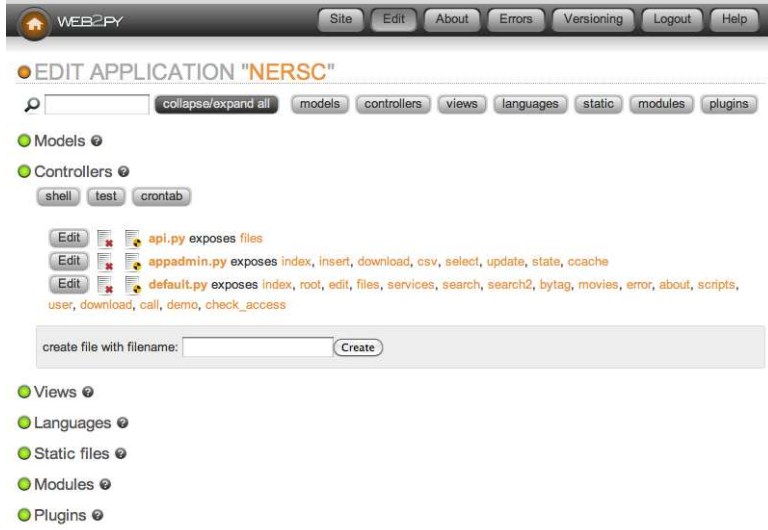


Figure 4: The system administrative interface.

This code parses the URL in the request for the path, defines some local variables (`d, t, f`) referencing the tables, builds a query to fetch the content of the folder: the path, the tags, the subfolders and the patterns (i.e. groups of files with the same prefix). At statements follow the DAL syntax:

```
1 variable = db(query).select(what, how)
```

The `@cache(...)` decorator instructs the framework to cache each page for 60 seconds. This means the if a page is requested more than once every 60 seconds, it will not hit the database more than one time. This results in better performance.

The system enforces different types of access control. It provides a web based administrative interface only accessible to managers (fig. 4. All downloads require user login).

The system itself is not domain specific and has no knowledge about QCD files and conventions. The domain specific knowledge is in a separate script that runs in background and populates the database from the file/folder structure. This means the system can be used to publish data of a different nature with minimal work. The system retains the original ability to download individual files using the web interface. Since these files can be big, the download requires login in order to prevent Denial of Service attacks.

The system exposes RESTful web services APIs based on the JSON protocol which can be used to access the data programmatically. Some gauge ensembles are comprised of thousands of files. To download them in batch we provide a script `qcdutils_get.py`, written in Python with no dependencies, available from [1].

In this example we use the script to download all files in the `demo` ensemble:

```
1 $ qcdutils_get.py http://qcd.nersc.gov/nersc/api/files/demo
2 http://qcd.nersc.org/nersc/api/files/demo
3 target folder: demo
4 total files to download: 1
5 downloading demo.nersc
```

```
6 demo.nersc 100% |#####
7 completed download: 1/1
```

We now ask the script to convert all data from NERSC to ILDG(32bits):

```
1 $ qcdutils_get.py --convert ildg --float demo/demo.nersc
2 converting: demo/demo.nersc -> demo/demo.nersc.ildg
3   (precision: f, size: 4x8x8x8)
4 100% |#####|#####|#####|#####|#####|#####|#####|#####|
```

`qcdutils` keeps an internal log of all the operations completed to avoid duplication of work. It remembers what was downloaded/converted and where things are. We can ask `qcdutils` for a log of the completed tasks:

```
1 $ qcdutils_get.py demo/qcdutils.catalog.db
2 demo.nersc created on 2011-06-17T13:42:30.876812
3   [14e7cf9106bfcc16388aeac285ccdad9]
4 demo.nersc.ildg created on 2011-06-17T13:42:34.424604
5   [5a1ae13ddd5cab7ddfe1b17454822ff5]
```

4. Conclusions and Outlook

The system allows the user to register any URL and dynamically generates buttons that, when pressed, pass a link to the data at the associated URL. This allows for the creation of third party web services that can feed data directly from the new NERSC web interface allowing for decentralization of services. We can provide tools to help create such services. For example, we can build workflows that interface the data archive with a batch queue on a large computational system.

We envision a future when the different research groups will provide their computing capabilities and their lattice QCD algorithms as web services for the consumption of other members in the collaboration. The NERSC site provides more than just data for these collaborations - it also offers an infrastructure to register those third party services in a transparent way.

Acknowledgements

This work was funded by Department of Energy grant DEFC02-06ER41441 and by National Science Foundation grant 0970137.

References

- [1] Massimo Di Pierro. `qcdutils`, 2010.
- [2] Massimo Di Pierro. `web2py` website, 2010.
- [3] Massimo Di Pierro and Jonthan M. Flynn. Lattice QFT with FermiQCD. *PoS*, LAT2005:104, 2006.
- [4] S. Gottlieb. Benchmarking and tuning the MILC code on clusters and supercomputers. *Nuclear Physics B Proceedings Supplements*, 106:1031–1033, 2001.
- [5] C. Maynard. International Lattice Data Grid: Turn on, plug in, and download. In *Symposium on Lattice Field Theory*, 2009.
- [6] U.S. DOE. Nersc website, 2010.

Improving Non-linear Fits

Massimo Di Pierro

School of Computing, DePaul University, 243 S Wabash Ave, Chicago IL 60604

February 8, 2012

Abstract

In this notes we describe an algorithm for non-linear fitting which incorporates some of the features of linear least squares into a general minimum χ^2 fit and provide a pure Python implementation of the algorithm. It consists of the variable projection method (varpro), combined with a Newton optimizer and stabilized using the steepest descent with an adaptative step. The algorithm includes a term to account for Bayesian priors. We performed tests of the algorithm using simulated data. This method is suitable, for example, for fitting with sums of exponentials as often needed in Lattice Quantum Chromodynamics.

1 Introduction

Fitting is one the most common recurrent tasks in scientific computing. Fitting involves minimizing the χ^2 , i.e. weighted sum of squares of the difference between observed data and expected data [1]. The expected data is computing using a function f which depends on some unknown parameters. The χ^2 is minimized by varying these unknown parameters in order to find a minimum.

Usually there are two common approaches to fitting:

- If the function f is linear in the unknown parameters, then the fitting problem has an exact solution which can be computed via the linear least squares.
- If the function f is nonlinear in its parameters, the minimization is carried out using a non-linear optimization algorithm based on the Newton method [3], the Steepest Descent [4], or more sophisticated techniques such as the Levenberg-Marquadt.

There is also a *non-linear least squares* algorithm. It is different from the one described in this paper and it is equivalent to performing a Newton optimization where the first order derivatives of the fitting functions are computed analytically.

When the fitting function depends of both some linear parameters and some non-linear ones, the two methods above can be combined. This approach, described here, is known as VARiable PROjection method [5]. An implemention of it which uses the Levenberg-Marquadt algorithm for the non-linear part can be found in Netlib [6]. The approach consists of defining a function g which takes as input the non-linear parameters of the original fitting function and returns the χ^2 . The function g , internally uses the least square algorithm to compute the linear coefficients exactly (as function of the non-linear coefficients and the input data) and uses this result to compute the χ^2 . In our implementaton the complete fit is performed by passing the function g to a non-linear Newton optimizer stabilized using an adaptative steepest-descent.

One application of this procedure is, for example, in lattice QCD, where typically one has to fit data points using a sum of exponentials of the form $a_i e^{-b_i t}$. a_i and b_i are the parameters to be determined.

Fits like the one described become unstable when two of the b coefficients are very close to each other. In order to avoid this situation we modified the algorithm to account for *a priori* constraints on the fitting parameters in the form of a Bayesian contribution to the χ^2 . This can be used to stabilize the fit [7].

2 Algorithm

We want to fit data points of the form $(x_i, y_i \pm \delta y_i)$. We will do it by minimizing the χ^2 defined as

$$\chi^2(\mathbf{a}, \mathbf{b}) = \sum_i \left| \frac{y_i - f(x_i, \mathbf{a}, \mathbf{b})}{\delta y_i} \right|^2 \quad (1)$$

The function f is known but depends on unknown parameters $\mathbf{a} = (a_0, a_1, \dots)$ and $\mathbf{b} = (b_0, b_1, \dots)$. In terms of these parameters the function f can be written as follows:

$$f(x, \mathbf{a}, \mathbf{b}) = \sum_j a_j f_j(x, \mathbf{b}) \quad (2)$$

An example is the following one:

$$f(x, \mathbf{a}, \mathbf{b}) = a_0 e^{-b_0 x} + a_1 e^{-b_1 x} + a_2 e^{-b_2 x} + \dots \quad (3)$$

The goal of our algorithm is to efficiently determine the parameters \mathbf{a} and \mathbf{b} which minimize the χ^2 .

We proceed by defining the following two quantities:

$$A(\mathbf{b}) = \begin{pmatrix} f_0(x_0, \mathbf{b})/\delta y_0 & f_1(x_0, \mathbf{b})/\delta y_0 & f_2(x_0, \mathbf{b})/\delta y_0 & \dots \\ f_0(x_1, \mathbf{b})/\delta y_1 & f_1(x_1, \mathbf{b})/\delta y_1 & f_2(x_1, \mathbf{b})/\delta y_1 & \dots \\ f_0(x_2, \mathbf{b})/\delta y_2 & f_1(x_2, \mathbf{b})/\delta y_2 & f_2(x_2, \mathbf{b})/\delta y_2 & \dots \\ \dots & \dots & \dots & \dots \end{pmatrix} \quad \mathbf{z} = \begin{pmatrix} y_0 / \delta y_0 \\ y_1 / \delta y_1 \\ y_2 / \delta y_2 \\ \dots \end{pmatrix} \quad (4)$$

In terms of A and \mathbf{z} the χ^2 can be rewritten as

$$\chi^2(\mathbf{a}, \mathbf{b}) = |A(\mathbf{b})\mathbf{a} - \mathbf{z}|^2 \quad (5)$$

We can minimize this function (in a) using the linear least squares algorithm, exactly:

$$\mathbf{a}(\mathbf{b}) = (A(\mathbf{b})^t A(\mathbf{b}))^{-1} (A(\mathbf{b})^t \mathbf{z}) \quad (6)$$

We define a function which returns the minimum χ^2 for a fixed input \mathbf{b} :

$$g(\mathbf{b}) = \min_{\mathbf{a}} \chi^2(\mathbf{a}, \mathbf{b}) = \chi^2(\mathbf{a}(\mathbf{b}), \mathbf{b}) = |A(\mathbf{b})\mathbf{a}(\mathbf{b}) - \mathbf{z}|^2 + \text{Bayesian}(\mathbf{b}) \quad (7)$$

Hence we have reduced the original problem to a simple problem by reducing the number of unknown parameters from $N_a + N_b$ to N_b .

We have arbitrarily added a term, **Bayesian** to the definition of χ^2 . This term can be set to zero, but also, according to Lepage *et al.* [7], we can choose it as follows:

$$\text{Bayesian}(\mathbf{b}) = \sum_i \left| \frac{b_i - \tilde{b}_i}{\delta b_i} \right|^2 \quad (8)$$

where $b_i \simeq \tilde{b}_i \pm \delta b_i$ is the *a priori* knowledge (or assumption) about the expected values for the b parameters, according to Bayesian statistics. The Bayesian term originates from the fact that ordinary statistics concerns the computation of probability that data is compatible with a given model while here we are concerned with the opposite problem, the probability that a certain model (defined by the unknown parameters a and b) is compatible with given data. In practice the effect of the **Bayesian** term is that of stabilizing the fit by constraining the values within a range specified by a point and its uncertainty by increasing the χ^2 quadratically when the fitting parameters depart from the priors.

The methodology described here (excluding the Bayesian contribution) is known as VARPRO [5] algorithm.

3 Code

The complete code is reported in the the Appendix. It contains the algorithm implemented in Python (use suggest version 2.7) and it uses the `numpy` library for linear algebra. The code defines partial derivatives, the gradient, the Hessian, and the 1-norm of a matrix. These functions are necessary for the inner workings of the Newton algorithm. The code also includes a modified multi-dimensional Newton optimization algorithm that reverts to the steepest descent when the Newton step fails to reduce the value of the function passed as input. The step of the minimum descent is adjusted automatically: it starts with a guess and reduces the step until the χ^2 is decreased by the move. This guarantees a decrease of the χ^2 at each iteration. Although it never explodes, it may still fail. This can happen because the target precision is not reached within the maximum number of allowed iterations or because the Hessian becomes singular, or because A matrix in the least squared fit becomes singular.

The main logic described in this notes is implemented in the function called `fit`.

The input of the function `fit` is:

- `data` is a list of $(x, y, \delta y)$ points to be fitted.
- `fs` is a list of functions f_i as described in the previous section. Each function must have the signature `lambda b, x: ...` where b is a list of b coefficients.
- `b` is a list of b values from which to start the optimization.
- `ap=1e-6` is the required target precision in the output.
- `rp=1e-4` is the required target relative precision.
- `ns=200` is the maximum number of steps performed by the Newton algorithm. If the Newton algorithm fails to converge within the required target absolute or relative precision within `ns` steps, the algorithm raises an exception.
- `bayesian=None` can be set to a function of `b` whose value is be added to the χ^2 in the intermediate steps.

The function `fit` returns a tuple containing a , b , the χ^2 and the Hessian. a and b are lists.

4 Examples

Here we report two examples of usage of the algorithm. In the first one we consider a fitting function of the form

$$f(x) = a_0x + a_1x^2 + \frac{a_2}{x + b_0} \quad (9)$$

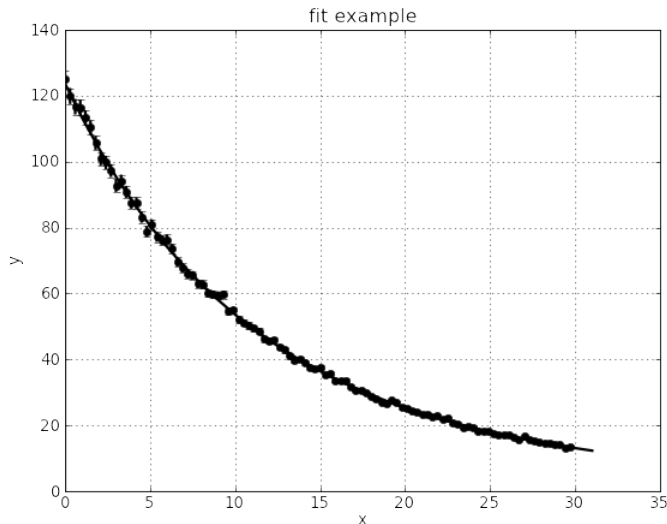


Figure 1: Example of simulated data (100 points) and their fit with three exponentials

We generated 100 points using the input values of $a_0 = 1$, $a_1 = 2$, $a_2 = 300$ and $b_0 = 10$ for $x = 0.1, 0.2, 0.3, \dots, 10$. For each point we computed y using the above formula and we added a random Gaussian noise with standard deviation equal to 1% of y . We set $\delta y = 1\%$ for each point. We then fitted the data using our method:

```

1 >>> import random
2 >>> def noise(i,x,r=0.05): return (float(i),x*(1.0+random.gauss(0,r)),abs(x)*r)
3 >>> def f(x): return x+x**2+300.0/(x+10)
4 >>> data = [noise(0.1*i,f(0.1*i),0.01) for i in range(1,101)]
5 >>> fs = [(lambda b,x: x),
6             (lambda b,x: x*x),
7             (lambda b,x: 1.0/(x+b[0]))]
8 >>> a , b, chi2, H = fit(data,fs,b=[5])
9 >>> print a, b
10 [1.053..., 0.995..., 299.065...] [9.990...]

```

The result shows that the fit converged within a few percent accuracy to the true values. Of course we do not expect the output to yield the exact same values which we used to generate the data, because we added the noise. The point here is that despite the noise, the fit is stable and consistent with expectation.

Notice that the notation `lambda b,x: ***` is nothing but the inline definition of an un-named function which takes `b,x` and input and produces `***` as output. Hence `fs` is a list containing three

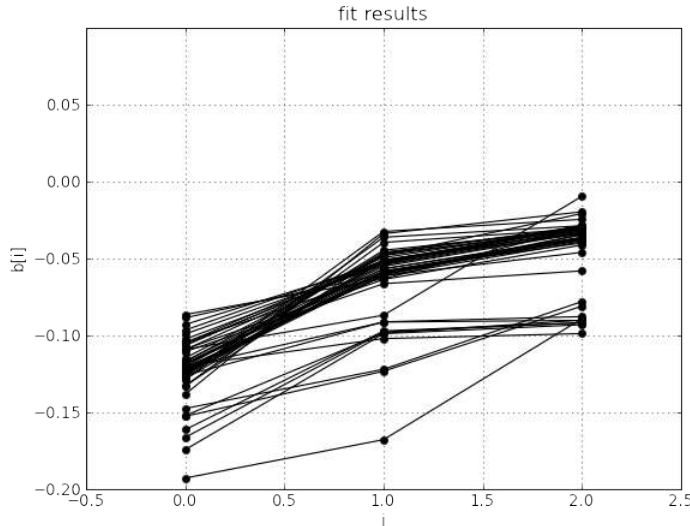


Figure 2: Parallel coordinates plot for 50 simulated experiments. The data from each simulated experiment is fitted and the resulting b_0 , b_1 , b_2 are shown in the plot, connected by a line. The density of lines indicates the most likely range of results and their correlation. The results are compatible with the input used to generate the simulated experiments: $b_0 = -0.10$, $b_1 = -0.04$, $b_2 = -0.02$.

functions.

In our second test we used a function which is the sum of three exponentials:

$$f(x) = a_0 e^{-b_0 x} + a_1 e^{-b_1 x} + a_2 e^{-b_2 x} \quad (10)$$

We performed a series of 50 simulated experiments. In each experiment we generated 100 data points x equally spaced between 0 and 32 and computed the corresponding y 's using the above formula with the input $a_0 = 100$, $a_1 = 10$, $a_2 = 1$ and $b_0 = -0.10$, $b_1 = -0.04$ and $b_2 = -0.02$ adding a 2% Gaussian noise and assuming a 2% error on each point. We then fit each simulated experiment. To improve the stability of the fit we added a Bayesian contribution to the χ^2 which corresponds to priors $b_0 \simeq -0.11 \pm 0.04$, $b_1 \simeq -0.05 \pm 0.04$, and $b_2 \simeq -0.03 \pm 0.04$.

Here is the code for each simulated experiment:

```

1 >>> from math import exp
2 >>> def f(x): return 100.0*exp(-0.10*x)+20.0*exp(-0.04*x)+4.0*exp(-0.02*x)
3 >>> xs = [0.3*i for i in range(100)]
4 >>> data = [noise(x,f(x),0.02) for x in xs]
5 >>> fs = [(lambda b,x: exp(b[0]*x)),

```

```

6      (lambda b,x: exp(b[1]*x)),
7      (lambda b,x: exp(b[2]*x)))
8 >>> def bayesian(b): return ((b[0]+0.11)**2+(b[1]+0.05)**2+(b[2]+0.03)**2)/0.04**2
9 >>> a, b, chi2, h = fit(data,fs,b=[-0.11,-0.05,-0.03],ns=100,bayesian=bayesian)
10 >>> print a, b
11 [98.041..., 10.795..., 16.281...] , [-0.103..., -0.052..., -0.029...]

```

The result of the fit is also shown in fig. 1.

In this example the contribution of the third exponential is too small to be determined from data. We have ignored results that are more than two standard deviations off from priors and we have displayed the resulting fitting values for b_0 , b_1 and b_2 in a parallel coordinates plot, fig. 2. The X-axis represent the i index of the b_i parameters and the Y-axis the corresponding values. The lines connect the b_0, b_1, b_2 values for each simulated experiment. Higher density of lines represents the most likely values and their correlation.

We found that in about 10% of our simulated experiments the algorithm failed to converge but this could be corrected by changing slightly the input starting point for the Newton optimizer.

5 Conclusions

In this notes we describe the varpro method for non-linear fitting which uses linear least squares fitting to reduce the space of the parameters to be explored. We provided an implementation in Python which uses a stabilized Newton method the non-linear part of the fit and includes contribution from Bayesian priors. In the case of fitting with a sum of exponentials it reduces the size of the parameter space by a factor of two. We have provided working code and examples of fitting simulated data.

Acknowledgements

We thank Carleton DeTar and Doug Toussaint for a useful discussion on this topic. We specially thank Martin Savage for pointing out to us that the method described here is known as the VARPRO algorithm, thus giving us the chance to properly acknowledge the original inventors [5].

References

- [1] E. B. Wilson, M. M. Hilderty, *The distribution of chi-squared*. Proceedings of the National Academy of Sciences, Washington, 17, 684–688 (1931)
- [2] C. L. Lawson and R. J. Hanson, *Solving Least Squares Problems*, Prentice-Hall (1974)

- [3] J. Nocedal, J. Stephen J., *Numerical Optimization*. Springer-Verlag (1999)
- [4] M. V. Fedoryuk, *Method of steepest descent*, in Hazewinkel, Michiel, Encyclopedia of Mathematics, Springer (2001)
- [5] G. H. Golub and V. Pereyra, *The differentiation of pseudo-inverses and non-linear least squares problems whose variables separate*, SIAM J. Numer. Anal. 10, 413-432 (1973)
- [6] <http://www.netlib.org/opt/varpro>
- [7] G. Lepage *et al.*, Nucl.Phys.Proc.Suppl.106:12-20,2002 [arXiv:hep-lat/0110175v1]

Appendix

```
1   ### Developed by Massimo Di Pierro <mdipierro@cs.depaul.edu>
2   ### License: BSD
3
4   from numpy import matrix
5   from numpy.linalg import *
6
7   def partial(f,i,h=1e-4):
8     """
9       definition of parital derivative, df/dx_i
10     """
11     def df(x,f=f,i=i,h=h):
12       x[i]+=h
13       u = f(x)
14       x[i]-=2*h
15       v = f(x)
16       x[i]+=h
17       return (u-v)/2/h
18     return df
19
20 def gradient(f, x, h=1e-4):
21     """
22       gradient of f in x
23     """
24     s = xrange(len(x))
25     return matrix([[partial(f,r,h)(x)] for r in s])
26
27 def hessian(f, x, h=1e-4):
28     """
29       hessian of f in x
30     """
31     s = xrange(len(x))
32     grad = [partial(f,r,h) for r in s]
33     return matrix([[partial(grad[r],r,h)(x) for c in s] for r in s])
34
35 def norm(A):
36     """
37       defines norm of a matrix to check convergence
38     """
39     rows, cols = A.shape
40     return max([sum(abs(A[r,c])) for r in xrange(rows)] \
41               for c in xrange(cols)])
42
43 def tolist(A):
44     rows, cols = A.shape
45     return [A[r,0] for r in xrange(rows)]
46
```

```

47 def optimize_newton_multi_imporved(f, x, ap=1e-6, rp=1e-4, ns=20):
48     """
49         Multidimensional Newton optimizer
50         on failure is performs a steepest descent
51     """
52     fx = f(x)
53     x = matrix([[element] for element in x])
54     h = 10.0
55     for k in xrange(ns):
56         grad = gradient(f,tolist(x))
57         (grad,H) = (gradient(f,tolist(x)), hessian(f,tolist(x)))
58         if norm(H) < ap:
59             raise ArithmeticError, 'unstable solution'
60         (fx_old, x_old, x) = (fx, x, x-(1.0/H)*grad)
61         fx = f(tolist(x))
62         while fx>fx_old: # revert to steepest descent
63             (fx, x) = (fx_old, x_old)
64             n = norm(grad)
65             (x_old, x) = (x, x - grad/n*h)
66             (fx_old, fx) = (fx, f(tolist(x)))
67             h = h/2
68             h = norm(x-x_old)*2
69             if k>2 and h/2<max(ap,norm(x)*rp):
70                 x = tolist(x)
71             return x, hessian(f,x)
72     raise ArithmeticError, 'no convergence'
73
74
75 def fit(data, fs, b, ap=1e-6, rp=1e-4, ns=200, bayesian=None):
76     na = len(fs)
77     def least_squares(b,data= data,fs=fs):
78         A = matrix([[fs[k](b,x)/dy for k in xrange(na)] for (x,y,dy) in data])
79         z = matrix([[y/dy] for (x,y,dy) in data])
80         a = inv(A.T*A)*(A.T*z)
81         chi2 = norm(A*a-z)**2
82         return a, chi2
83     def g(b,data= data,fs=fs,bayesian=bayesian):
84         a, chi2 = least_squares(b, data, fs)
85         if bayesian:
86             chi2 += bayesian(b)
87         return chi2
88     b, H = optimize_newton_multi_imporved(g,b,ap,rp,ns)
89     a, chi2 = least_squares(b,data,fs)
90     return tolist(a), b, chi2, H

```

The decay constants f_B and f_{D^+} from three-flavor lattice QCD

C. Bernard^a, C. DeTar^b, M. Di Pierro^c, A.X. El-Khadra^d, R.T. Evans^d, E. Freeland^{e,i}, E. Gamiz^d, Steven Gottlieb^f, U.M. Heller^g, J.E. Hetrick^h, R. Jain^d, A.S. Kronfeldⁱ, J. Laiho^{ia}, L. Levkova^b, P.B. Mackenzieⁱ, D. Renner^j, J.N. Simone^{*i}, R. Sugar^k, D. Toussaint^j, and R.S. Van de Waterⁱ

^a*Department of Physics, Washington University, St. Louis, Missouri, USA*

^b*Physics Department, University of Utah, Salt Lake City, Utah, USA*

^c*School of Computer Sci., Telecom. and Info. Systems, DePaul University, Chicago, Illinois, USA*

^d*Physics Department, University of Illinois, Urbana, Illinois, USA*

^e*Liberal Arts Department, The School of the Art Institute of Chicago, Chicago, Illinois, USA*

^f*Department of Physics, Indiana University, Bloomington, Indiana, USA*

^g*American Physical Society, One Research Road, Box 9000, Ridge, New York, USA*

^h*Physics Department, University of the Pacific, Stockton, California, USA*

ⁱ*Fermi National Accelerator Laboratory, Batavia, Illinois, USA*

^j*Department of Physics, University of Arizona, Tucson, Arizona, USA*

^k*Department of Physics, University of California, Santa Barbara, California, USA*

E-mail: simone@fnal.gov

Fermilab Lattice and MILC Collaborations

We present new preliminary results for the leptonic decay constants f_B and f_{D^+} determined in 2 + 1 flavor lattice QCD at lattice spacings $a = 0.09, 0.12$ and 0.15 fm. Results are obtained using the MILC Collaboration gauge configuration ensembles, clover heavy quarks in the Fermilab interpretation and improved staggered light quarks. Decay constants, computed at partially quenched combinations of the valence and sea light quark masses, are used to determine the low-energy parameters of staggered chiral perturbation theory. The physical decay constants are found in an extrapolation using the parameterized chiral formula.

*The XXV International Symposium on Lattice Field Theory
July 30-4 August 2007
Regensburg, Germany*

*Speaker.

1. Introduction

The D meson decay constants, when compared to precise experimental results, are a critical check of the lattice methods needed for f_B . In Ref. [1] we predicted $f_{D^+} = 201 \pm 3 \pm 17$ MeV in good agreement with the CLEO-c measurement $f_{D^+} = 223 \pm 17 \pm 3$ MeV revealed days later [2].

In this work we present new results for the D and B meson decay constants. Precise determinations of f_B , f_{B_s} and the ratio f_{B_s}/f_B are needed to study the Standard Model picture of B - \bar{B} and B_s - \bar{B}_s mixing. A progress report for the mixing matrix element study is presented in Ref. [3].

2. Simulation details

We use the MILC Collaboration three-flavor asqtad ensembles [4]. Details are tabulated in Table 1. For these ensembles, m_l denotes the mass of the two degenerate lighter sea quarks. A single heavier sea quark has a mass m_h near the strange quark mass. Upsilon spectroscopy tells us the heavy quark potential scale $r_1 = 0.318(7)$ fm [5]. The number of valence quark masses, $\#m_q$, used in this study is listed in the last column of the table.

The leptonic decay constant f_{H_q} for a meson H_q is defined by

$$\langle 0 | A_\mu | H_q(p) \rangle = i f_{H_q} p_\mu. \quad (2.1)$$

The combination $\phi_{H_q} = f_{H_q} \sqrt{m_{H_q}}$ emerges from a combined fit to lattice 2-pt functions:

$$C_O(t) = \langle O_{H_q}^\dagger(t) O_{H_q}(0) \rangle \quad (2.2)$$

$$C_{A4}(t) = \langle A_4(t) O_{H_q}(0) \rangle, \quad (2.3)$$

where O_{H_q} can be either a smeared or local operator.

The axial current renormalization is taken to be

$$Z_{A4}^{Qq} = \rho_{A4}^{Qq} \sqrt{Z_{V4}^{QQ} Z_{V4}^{qq}}. \quad (2.4)$$

a [fm]	am_h	am_l	β	r_1/a	configs	$\# m_q$
0.09	0.031	0.0031	7.08	3.69	435	11
		0.0062	7.09	3.70	557	10
		0.0124	7.11	3.72	518	8
0.12	0.05	0.005	6.76	2.64	529	12
		0.007	6.76	2.63	833	12
		0.01	6.76	2.62	592	12
		0.02	6.79	2.65	460	12
		0.03	6.81	2.66	549	12
0.15	0.0484	0.0097	6.572	2.13	631	9
		0.0194	6.586	2.13	631	9
		0.029	6.600	2.13	440	9

Table 1: MILC three-flavor lattice parameters. The last column lists the number of valence light quarks used in this study.

Factors $Z_{V_4}^{ff}$ are fixed nonperturbatively from scattering 3-pt functions and the known normalization of the vector current. Factors ρ_{A4}^{Qq} are known to one-loop order and are close to unity [6].

3. Staggered Chiral Perturbation Theory ($S\chi PT$)

With staggered quarks the (squared) taste-nonsinglet pseudoscalar meson masses are split:

$$M_{ab,\xi}^2 = (m_a + m_b)\mu + a^2 \Delta_\xi , \quad (3.1)$$

where m_a, m_b are quark masses and the (sixteen) mesons are labeled by their taste representation $\xi = P, A, T, V, I$ with $\Delta_P = 0$.

At next-to-leading order (NLO) in χ PT the expression for the decay constants is

$$\phi_{H_q} = \Phi_H [1 + \Delta f_H(m_q, m_l, m_h) + p_H(m_q, m_l, m_h)] \quad (3.2)$$

where Δf_H denotes the “chiral logs” and p_H denotes terms analytic in the meson masses.

With staggered quarks

$$\Delta f_H = -\frac{1+3g_{H^*H\pi}^2}{2(4\pi f_\pi)^2} [\bar{h}_q + h_q^I + a^2 (\delta'_A h_q^A + \delta'_V h_q^V)] . \quad (3.3)$$

Taste-breaking effects arise at finite a from the meson mass splittings and the δ'_A and δ'_V hair-pin terms [7]. Finite a effects reduce the chiral logarithm curvature, however, the expected QCD chiral logarithm is recovered in the continuum limit.

The NLO analytic terms are

$$p_H = \frac{1}{2(4\pi f_\pi)^2} [p_1(m_l, m_h) + p_2(m_q)] \quad (3.4)$$

$$p_1 = f_1(\Lambda_\chi) \left[\frac{11}{9}\mu(2m_l + m_h) + a^2 \left(\frac{3}{2}\bar{\Delta} + \frac{1}{3}\Delta_I \right) \right] \quad (3.5)$$

$$p_2 = f_2(\Lambda_\chi) \left[\frac{5}{3}\mu m_q + a^2 \left(\frac{3}{2}\bar{\Delta} - \frac{2}{3}\Delta_I \right) \right] , \quad (3.6)$$

where $\bar{\Delta}$ is the weighted average of taste splittings. The $O(a^2)$ terms ensure that dependence upon the chiral logarithm scale, Λ_χ , in f_1 and f_2 cancels that of Δf_q .

Equation (3.2) with the addition of four NNLO analytic terms parameterizes our chiral extrapolations. We fit ϕ_{H_q} to determine the parameters. Constraints (value and width) for μ , Δ_ξ , f_π , δ'_A and δ'_V come from χ PT for lattice pions and kaons [8]. The coupling $g_{D^*D\pi}^2 = 0.35 \pm 0.14$ is likewise constrained by the CLEO measurement [9]. From heavy quark symmetry we expect $g_{B^*B\pi}^2 \approx g_{D^*D\pi}^2$. The remaining parameters Φ_H , f_1 and f_2 and the NNLO analytic parameters are determined in the fit.

In order to extrapolate to the physical results we set $\Delta_\xi = \delta'_{A,V} = 0$, $m_h \rightarrow m_s$ and $m_l \rightarrow (m_u + m_d)/2$. Then ϕ_{H_d} (ϕ_{H_s}) is found in the limit $m_q \rightarrow m_d$ (m_s).

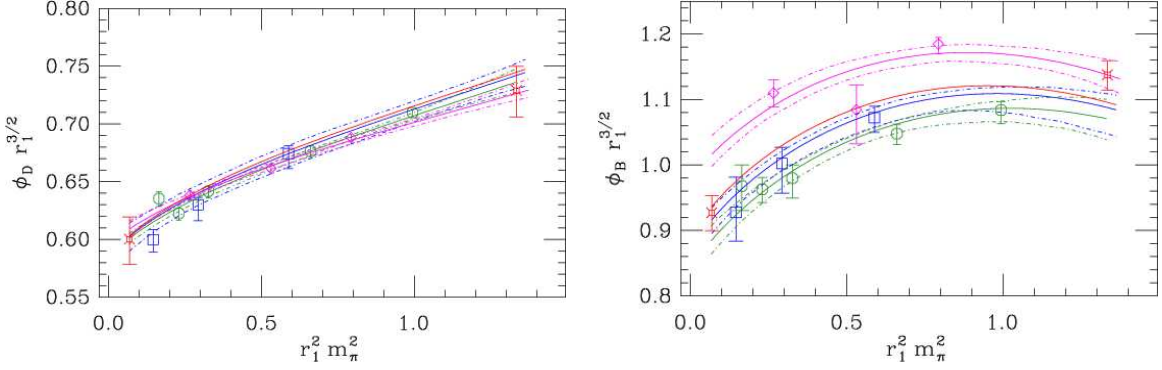


Figure 1: Chiral fits for the D (left) and B (right) mesons. Each fit is viewed along the direction in which $m_q = m_l$. Each fit is shown as a set of solid curves with the 68% confidence limits denoted by broken curves. Only statistical errors are shown. The $a = 0.09$ fm curve and data points are shown in blue, 0.12 fm in green and 0.15 fm in magenta. The $a^2 \rightarrow 0$ extrapolation curve and the $\phi_{H_{d,s}}$ points at physical values of m_u , m_d and m_s are shown in red. The statistical errors on the D and B physical points are of comparable size.

4. The Fit and Extrapolation for D and B

We determine both ϕ_{D+} and ϕ_{D_s} from a single fit of ϕ_{D_q} simulation results using the expression in Eqn. (3.2), adding the four NNLO analytic terms and allowing for an explicit $O(a^2)$ term. We combine simulation results from 11 gauge ensembles at lattice spacings of $a = 0.09$, 0.12 and 0.15 fm in the fit. A total of 116 points are included in the fit. A bootstrap procedure propagates errors and correlations among the simulated results through to the statistical errors on our results. An analogous fit procedure for the B meson simulation results yields ϕ_{B_d} and ϕ_{B_s} .

The D and B meson fits combining the three lattice spacings are shown in Figs. 1 and 2. Figure 1 shows each fit and the data points along the $m_q = m_l$ direction while Fig. 2 shows the valence mass dependence of the fit at fixed values of the sea quark mass. All of the fit points are visible in Fig. 2 while only the subset of points with $m_q = m_l$ is visible in Fig. 1.

Figure 1 shows the D system on the left and the B system on the right. In each plot, the solid blue, green and magenta curves are the fit to the lattice data for lattice spacings 0.09, 0.12 and 0.15 respectively. These curves include the a^2 effects described by the chiral fit function. The 68% confidence limits for each curve are indicated by dotted contours of the corresponding color.

In Fig. 2 we show the valence mass dependence the D and B systems. In each plot the D system (blue points and curves) is shown together with B system (green points and curves). Each plot in the figure corresponds to a single combination of lattice spacing and m_l from Table 1. Together, the points represent all of the simulation results for ϕ_{D_q} used in this study. The fit curves include the a^2 effects described by the chiral fit function. Each curve is shown with its 68% confidence contours. The expression in Eqn. (3.2) predicts a divergent logarithmic rise as $m_q \rightarrow 0$ with m_l fixed. Our fits detect these logarithms even though taste breaking effects obscure them, so they are not immediately obvious in the plots.

The extrapolation, $a \rightarrow 0$, $m_h \rightarrow m_s$ and $m_l = m_q$ is shown in Fig. 1 as a solid red curve for each of the D and B systems. Our result for ϕ_{D+} (ϕ_{B_d}) is found from the extrapolation by setting $m_l = \hat{m} = (m_u + m_d)/2$ and $m_q = m_d$. Likewise, ϕ_{D_s} (ϕ_{B_s}) is found by setting $m_q = m_s$. The physical

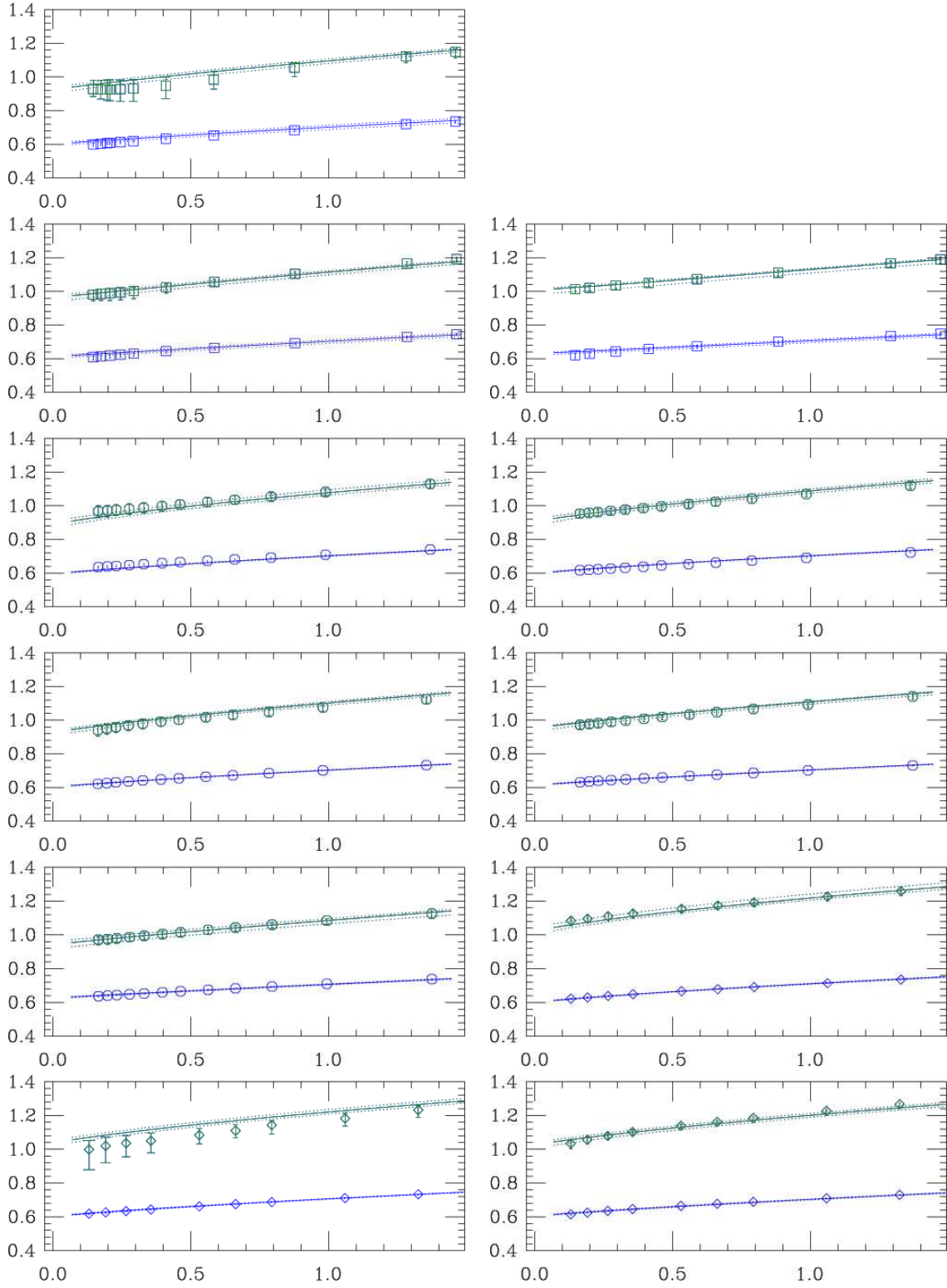


Figure 2: The m_q dependence of the single D fit (in blue) and the single B fit (in green) at fixed m_l . The figures ordered from left-to-right and top-to-bottom, have am_l equal to 0.0031, 0.0062, 0.0124 ($a = 0.09$ fm), 0.005, 0.007, 0.01, 0.02, 0.03 (0.12 fm), 0.0097, 0.0194 and 0.029 (0.15 fm) respectively. On the y-axis is $r_1^{3/2} \phi_{H_q}$ and on the x-axis is $r_1^2 m_\pi^2$. All 116 points in each fit are shown. The $\chi^2 = 98.6$ for the D fit and 48.5 for the B fit.

quantity	value	
ϕ_{D_s}	0.356(11)	GeV ^{3/2}
ϕ_{D_d}	0.293(11)	GeV ^{3/2}
$R_{D_{d/s}}$	0.824(8)	
ϕ_{B_s}	0.556(12)	GeV ^{3/2}
ϕ_{B_d}	0.453(13)	GeV ^{3/2}
$R_{B_{d/s}}$	0.815(15)	

Table 2: The main results of this preliminary study.

results are indicated with the red burst symbols. Since these points are projected into the $m_q = m_l$ plane of each figure, the central values do not lie on the red curve. The statistical errors for the physical ϕ_{H_q} values are shown in each figure. We find statistical errors comparable in magnitude for the physical ϕ_{D_q} and ϕ_{B_q} results.

5. Results and Outlook

Our preliminary results for the physical ϕ_{H_q} values and ratios with their statistical errors are in Table 2. We tabulate the major sources of uncertainty in Table 3. We omit listing uncertainties arising from terms of order $1/m_H$ in the chiral extrapolations since adding such terms changes the final results by less than the statistical errors. Such effects are still under investigation. Uncertainties from the input parameters r_1 and the light quark masses are found by propagating the uncertainties found in the MILC f_π and f_K determinations [5]. We estimate a 3.8% uncertainty in the bare charm mass and a 6.8% uncertainty in the bare bottom mass from variations in tuning procedures for the 0.09 fm lattice. Using simulation results for two heavy-quark masses near both charm and bottom, we estimate the uncertainties in ϕ_{H_q} . The uncertainties in Z_V^{ff} are statistical. Errors from unknown higher orders in ρ_{A_4} are estimated by considering higher orders effects to be as large as the 1-loop terms. Heavy quark discretization effects are estimated by power counting arguments. The dominant uncertainty in ϕ_{H_q} comes from effects of order $\alpha_s \Lambda a \times h(am)$ and $a^2 \Lambda^2$, where $h(am)$ is some mild function of the heavy quark mass. The uncertainties in the ratios are smaller by a factor of m_s/Λ . Light quark discretization effects are estimated by varying the extrapolation procedure. Finite volume effects are estimated by comparing theories at finite volume to the continuum.

From Table 2 and the experimental D^+ , D_s , B^0 and B_s masses we compute the decay constants:

$$f_{D_s} = 254 \pm 8 \pm 11 \text{ MeV} \quad (5.1)$$

$$f_{D^+} = 215 \pm 8 \pm 11 \text{ MeV} \quad (5.2)$$

$$f_{B_s} = 240 \pm 5 \pm 11 \text{ MeV} \quad (5.3)$$

$$f_{B_d} = 197 \pm 6 \pm 12 \text{ MeV} \quad (5.4)$$

where each of the first errors is statistical. The second error is the systematic error combined in quadrature from Table 3.

We also consider ratios of B to D decay constants where statistical and systematic errors are expected to be reduced due to cancellations. Statistical errors in the ratios are from a bootstrap

source	ϕ_{D_s}	ϕ_{D_d}	$R_{d/s}$	ϕ_{B_s}	ϕ_{B_d}	$R_{d/s}$
statistics	3.1	3.8	1.0	2.1	3.1	1.8
inputs r_1 , m_s , m_d and m_u	1.4	2.0	0.5	3.1	3.8	0.6
input m_c or m_b	2.7	2.7	<0.1	1.1	1.1	<0.1
Z_V^{QQ} and Z_V^{qq}	1.4	1.4	0	1.4	1.4	0
higher-order ρ_{A_4}	0.3	0.3	<0.2	1.3	1.1	<0.2
heavy quark discretization	2.7	2.7	0.3	1.9	1.9	0.2
light quark discretization	1.0	2.7	1.8	2.0	3.8	1.8
finite volume	0.2	0.6	0.6	0.2	0.6	0.6
total systematic	4.4	5.3	2.0	4.7	6.1	2.0

Table 3: The error budget for the decay constants and their ratios. Uncertainties are quoted as a percentage. The total combines systematic errors in quadrature.

procedure in order to preserve statistical correlations.

$$f_{D^+}/f_{D_s} = 0.845 \pm 0.008 \pm 0.017 \quad (5.5)$$

$$f_{B_d}/f_{B_s} = 0.821 \pm 0.015 \pm 0.017 \quad (5.6)$$

$$f_{B_d}/f_{D^+} = 0.919 \pm 0.051 \pm 0.056 \quad (5.7)$$

$$f_{B_s}/f_{D_s} = 0.945 \pm 0.043 \pm 0.043 \quad (5.8)$$

The overall systematic errors for the first two ratios come from Table 3. Systematic errors for the last two ratios also come from combining errors in quadrature. These errors may be overestimates since we have not studied possible correlations at present.

We will extend this study to include a lattice spacing of $a = 0.06$ fm. We will improve statistics at $a = 0.09$ and 0.12 fm and add another ensemble (sea quark mass combination) at 0.09 fm. A finer lattice spacing, more sea quark combinations and better statistics will help control light- and heavy-quark discretization effects and improve statistical errors. The new gauge configurations will be used by MILC to refine r_1 and the light quark masses inputs used in this study.

References

- [1] C. Aubin *et al.*, Phys. Rev. Lett. **95**, 122002 (2005) [arXiv:hep-lat/0506030].
- [2] M. Artuso *et al.* [CLEO Collaboration], Phys. Rev. Lett. **95**, 251801 (2005) [arXiv:hep-ex/0508057].
- [3] R. T. Evans, E. Gamiz, A. X. El-Khadra and M. Di Pierro, arXiv:0710.2880 [hep-lat].
- [4] C. Aubin *et al.*, Phys. Rev. D **70**, 094505 (2004) [arXiv:hep-lat/0402030].
- [5] C. Bernard *et al.* [MILC Collaboration], PoS **LAT2005**, 025 (2006) [arXiv:hep-lat/0509137].
- [6] A. X. El-Khadra, E. Gamiz, A. S. Kronfeld and M. A. Nobes, arXiv:0710.1437 [hep-lat].
- [7] C. Aubin and C. Bernard, Phys. Rev. D **73**, 014515 (2006) [arXiv:hep-lat/0510088].
- [8] C. Aubin *et al.* [MILC Collaboration], Phys. Rev. D **70**, 114501 (2004) [arXiv:hep-lat/0407028].
- [9] A. Anastassov *et al.* [CLEO Collaboration], Phys. Rev. D **65**, 032003 (2002) [arXiv:hep-ex/0108043].

A determination of the B_s^0 and B_d^0 mixing parameters in 2+1 lattice QCD

R. Todd Evans, Elvira Gámiz* and Aida X. El-Khadra

Department of Physics, University of Illinois, Urbana, IL 61801, USA

E-mail: rtevans@uiuc.edu, megamiz@uiuc.edu, axk@uiuc.edu

Massimo Di Pierro

School of Computer Sci., Telecom. and Info. Systems, DePaul University, Chicago, IL, USA

MDiPierro@cti.depaul.edu

Fermilab Lattice and MILC Collaborations

We report on the advances in our unquenched calculation of the matrix elements relevant for the analysis of $B^0 - \bar{B}^0$ mixing using the Asqtad (light quark) and Fermilab (heavy quark) actions. We have calculated the hadronic parameters for the mass and width differences in the neutral B meson system. Preliminary results are presented for $f_{B_q}^2 B_q$ as well as for the ratio $\xi^2 = f_{B_s}^2 B_{B_s} / f_{B_d}^2 B_{B_d}$.

*The XXV International Symposium on Lattice Field Theory
July 30-4 August 2007
Regensburg, Germany*

*Speaker.

1. Introduction

The very accurate experimental measurements of the mass differences between the heavy and light B_s^0 and B_d^0 mass eigenstates, ΔM_s [1] and ΔM_d [2], that describe the $B_s^0 - \bar{B}_s^0$ and $B_d^0 - \bar{B}_d^0$ mixings respectively, make improving the theoretical study of these quantities crucial. In the standard model (SM), the mass difference is given by [3]

$$\Delta M_{s(d)}|_{theor.} = \frac{G_F^2 M_W^2}{6\pi^2} |V_{ts(d)}^* V_{tb}|^2 \eta_2^B S_0(x_t) M_{B_{s(d)}} f_{B_{s(d)}}^2 \hat{B}_{B_{s(d)}}, \quad (1.1)$$

where $x_t = m_t^2/M_W^2$, η_2^B is a perturbative QCD correction factor, $S_0(x_t)$ is the Inami-Lim function and the products $f_{B_{s(d)}}^2 \hat{B}_{B_{s(d)}}$ parametrize the hadronic matrix elements in the effective theory with $f_{B_{s(d)}}$ the $B_{s(d)}^0$ decay constants and $\hat{B}_{B_{s(d)}}$ the (renormalization group invariant) bag parameters. The hadronic matrix elements can be calculated in lattice QCD. Our current knowledge of them limits the accuracy with which the CKM matrix elements appearing in Eqn. (1.1) can be determined from the experimental measurements of $\Delta M_{s(d)}$. The goal of our project is to calculate all the hadronic matrix elements which are relevant for the mass and width differences in the $B_{s(d)}^0$ systems in unquenched lattice QCD at the few percent level.

Many of the uncertainties that affect the theoretical calculation of the decay constants and bag parameters cancel totally or partially if one takes the ratio $\xi^2 = f_{B_s}^2 B_{B_s}/f_{B_d}^2 B_{B_d}$. Hence, this ratio and therefore the combination of CKM matrix elements related to it by Eqn. (1.1) can be determined with a significantly smaller error than the individual matrix elements. This is a crucial ingredient in the unitarity triangle analysis. In these proceedings we report our preliminary results for the determination of ξ , as well as for the quantities $f_{B_q}^2 B_{B_q}$.

Other work on this subject using 2 + 1 lattice QCD methods can be found in [4].

2. Operators, actions and matching calculation

The whole set of operators whose matrix elements are needed to determine the $B_{s(d)}^0$ mixing parameters are

$$\begin{aligned} Q^{s(d)} &= [\bar{b}^i \gamma_\mu (1 - \gamma_5) s^i(d^i)] [\bar{b}^j \gamma^\mu (1 - \gamma_5) s^j(d^j)], \\ Q_S^{s(d)} &= [\bar{b}^i (1 - \gamma_5) s^i(d^i)] [\bar{b}^j (1 - \gamma_5) s^j(d^j)], \\ Q_3^{s(d)} &= [\bar{b}^i (1 - \gamma_5) s^j(d^j)] [\bar{b}^j (1 - \gamma_5) s^i(d^i)], \end{aligned} \quad (2.1)$$

where i, j are color indices. In these proceedings we focus on the results for the first two pairs of operators, enough to determine $\Delta M_{s(d)}$, and leave the study of the third pair, needed for an improved determination of $\Delta \Gamma_{s(d)}$, for a forthcoming publication [5].

We use the Fermilab action [6] for the b valence quarks and the Asqtad action [7], for the light sea and valence quarks, u, d and s . The Fermilab action has errors starting at $O(\alpha_s \Lambda_{QCD}/M)$ and $O((\Lambda_{QCD}/M)^2)$, while the errors of the Asqtad action are $O(\alpha_s a^2, a^4)$.

The products $f_{B_{s(d)}}^2 B_{B_{s(d)}}^{\overline{MS}}$ in Eqn. (1.1) parametrize the matrix elements by

$$\langle \bar{B}_s^0 | Q^{s(d)} | B_s^0 \rangle^{\overline{MS}}(\mu) = \frac{8}{3} M_{B_{s(d)}}^2 f_{B_{s(d)}}^2 B_{B_{s(d)}}^{\overline{MS}}(\mu). \quad (2.2)$$

The lattice matrix elements $\langle \bar{B}_{s(d)}^0 | Q^{s(d)} | B_{s(d)}^0 \rangle^{\text{lat}}$ determine $f_{B_{s(d)}}^2 B_{B_{s(d)}}$ at tree level. Beyond tree-level, the operators $Q^{s(d)}$, mix with $Q_S^{s(d)}$ both on the lattice and in the continuum. Including one-loop corrections, the renormalized matrix element is given by

$$\frac{a^3}{2M_{B_{s(d)}}} \langle Q^{s(d)} \rangle^{\overline{MS}}(\mu) = [1 + \alpha_s \cdot \rho_{LL}(\mu, m_b)] \langle Q^{s(d)} \rangle^{\text{lat}}(a) + \alpha_s \cdot \rho_{LS}(\mu, m_b) \langle Q_S^{s(d)} \rangle^{\text{lat}}(a). \quad (2.3)$$

The $O\left(\frac{\Lambda_{QCD}}{M}\right)$ improvement is implemented by a rotation of the b quark as explained in [6], so the perturbative matching errors start at $O(\alpha_s^2, \alpha_s \Lambda/aM)$. The matching coefficients ρ_{LL} and ρ_{LS} are the differences between the continuum \overline{MS} and lattice renormalization coefficients calculated at one-loop order. We have calculated these coefficients for the same choice of lattice actions as used in the numerical simulations. We have checked that our results have the correct infrared behavior, that they are correct in the massless limit, and that they are gauge invariant. However, our results for the matching coefficients are still preliminary, because not all diagrams have been independently checked.

The optimal value of the strong coupling constant to be used in Eqn. (2.3) is the V-scheme coupling $\alpha_V(q^*)$ [8] where q^* is defined in [8, 9]. In the absence of a calculation of q^* for the specific processes we are studying, we choose $q^* = 2/a$, very close to the q^* calculated for heavy-light currents. The specific values for α_s we use are given in Table 1.

3. Simulation details

The matrix elements needed to determine both $f_{B_q}^2 B_{B_q}$ and B_{B_q} , are extracted from the following three-point and two-point functions

$$C_O(t_1, t_2) = \sum_{\vec{x}, \vec{y}} \langle \bar{b}(\vec{x}, t_1) \gamma_5 q(\vec{x}, t_1) | O(0) | \bar{b}(\vec{y}, t_2) \gamma_5 q(\vec{y}, t_2) \rangle, \\ C_Z(t) = \sum_{\vec{x}} \langle \bar{b}(\vec{x}, t) \gamma_5 q(\vec{x}, t) \bar{q}(0) \gamma_5 b(0) \rangle, \quad C_{A_4}(t) = \sum_{\vec{x}} \langle \bar{b}(\vec{x}, t) \gamma_0 \gamma_5 q(\vec{x}, t) \bar{q}(0) \gamma_5 b(0) \rangle, \quad (3.1)$$

where the operator O is any $Q^{s(d)}$ or $Q_S^{s(d)}$ defined in Eqn. (2.1). The B meson operators are smeared at the sink with a 1S onium wavefunction. All the correlation functions in Eqn. (3.1) are calculated using the open meson propagator method described in [10].

We have performed these calculations on the MILC coarse lattices ($a = 0.12 \text{ fm}$) with 2+1 sea quarks and for three different sea light quark masses. The strange sea quark mass is always set to 0.050. The light sea masses, $m_l \equiv m_{light}^{sea}$, number of configurations and other simulation details are collected in Table 1. The mass of the bottom quark is fixed to its physical value, while for each sea quark mass we determine the different matrix elements for six different values of the light valence quark mass in a generic meson B_q^0 , $m_q = 0.0415, 0.03, 0.020, 0.010, 0.007, 0.005$. We use $m_q = 0.0415$ for the valence strange mass in our simulations. It is close to the physical strange quark mass, $m_s^{phys.} = 0.036$ [11]. The matrix elements of the operators are extracted from simultaneous fits of three-point and two-point functions using Bayesian statistics.

m_l/m_s^{sea}	Volume	N_{conf}	$a^{-1}(\text{GeV})$	$\alpha_s = \alpha_V(2/a)$	$N_{sources}$
0.020/0.050	$20^3 \times 64$	460	1.605(29)	0.31	4
0.010/0.050	$20^3 \times 64$	590	1.596(30)	0.31	4
0.007/0.050	$20^3 \times 64$	890	1.622(32)	0.31	4

Table 1: Simulation parameters and α_s used in the matching with the continuum. m_l is the light sea quark mass.

4. Results

The results in Fig. 1 show $f_{B_q} \sqrt{B_{B_q}^{\overline{MS}}(m_b)}$ in lattice units as a function of the light valence mass am_q . The errors shown are statistical errors only; the analysis of the systematic errors is not yet complete.

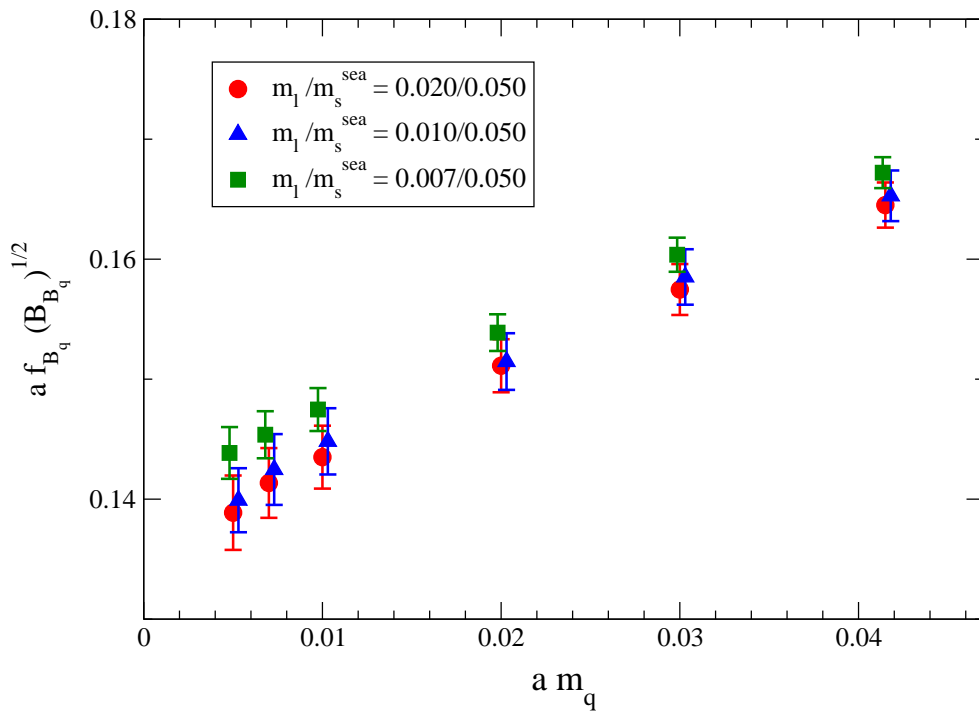


Figure 1: $f_{B_q} \sqrt{B_{B_q}^{\overline{MS}}(m_b)}$ in lattice units. The different symbols and colors correspond to different values of the sea light quark masses, m_l .

The statistical errors range between 1 – 3%. Some conclusions can be already extracted from this plot. The light sea quark mass dependence of $f_{B_q} \sqrt{B_{B_q}}$ is small compared to the statistical errors. The dependence on the light valence quark mass, however, is noticeable within statistics. In order to get a value for $f_{B_s} \sqrt{B_{B_s}^{\overline{MS}}(m_b)}$, since the s valence quark mass we are using is slightly larger than the physical one, we need an interpolation in the s valence quark mass together with a chiral

extrapolation to the physical sea quark masses. To determine $f_{B_d} \sqrt{B_{B_d}^{\overline{MS}}(m_b)}$ we need extrapolations in both the d valence quark mass and the sea quark masses. This is in progress.

In Fig. 2 we plot the ratio $\xi = f_{B_s} \sqrt{B_{B_s}} / f_{B_d} \sqrt{B_{B_d}}$ as a function of the d valence quark mass in the denominator. Again, our results are preliminary for the same reasons as mentioned before and the errors are only statistical. Most of the systematic errors cancel in the ratio, but not those associated with the chiral extrapolation in the light valence quark mass.

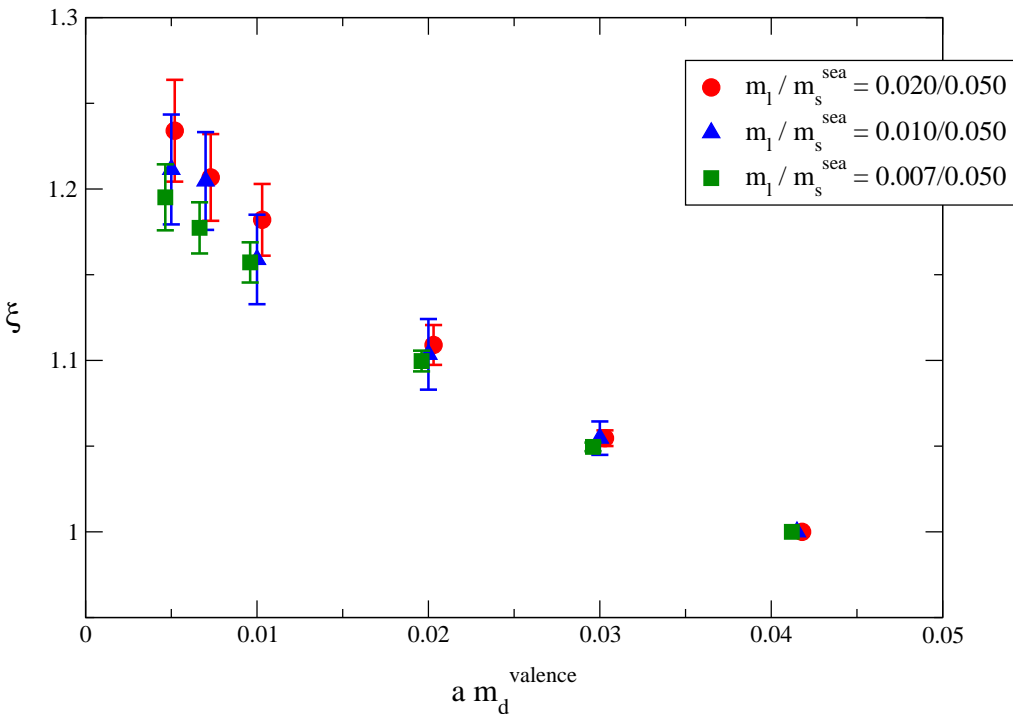


Figure 2: ξ as a function of the valence d mass for three different values of the light sea quark masses.

4.1 Chiral extrapolation

The continuum chiral expansion of the hadronic matrix element $\langle \bar{B}_q | Q | B_q \rangle$ at NLO in (partially quenched) heavy meson chiral perturbation theory (HMChPT) is given by [12]

$$\langle \bar{B}_q | Q | B_q \rangle = \beta(1 + w(T_q + W_q + S_q)) + c_0 m_q + c_1(m_U + m_D + m_S) \quad (4.1)$$

where m_U, m_D, m_S are the sea quark masses and m_q the light valence quark mass. β , w , c_0 and c_1 are low energy constants (LECs) to be determined from the fits. The functions T_q , W_q , and S_q contain the chiral logs and correspond to tadpole-, wave-function, and sunset-type contributions, respectively.

The effects of $O(a^2)$ taste changing interactions can be included in Eqn. (4.1) using staggered chiral perturbation theory (SChPT). In that case, the chiral log functions are modified to depend

	$f_{B_q} \sqrt{B_{B_q}}$	ξ
statistics	1 – 3	1 – 2
scale(a^{-1})	0.9	0
Higher order matching	~ 4.5	cancel to a large extent
Heavy quark discret.	2 – 3	< 0.5
Light quark discret. + χ PT fits	Work in progress	

Table 2: Error budget for $f_{B_q} \sqrt{B_{B_q}}$ and ξ in percent.

on the masses of the different taste multiplets. Explicit expressions from SChPT for heavy-light bilinear quantities can be found in [13, 14]. Similar terms are expected to contribute to our four-quark operators. The modified chiral logs contain other fixed LEC's, most of which are already determined to a high degree of certainty [14]. The logs also contain constants from heavy quark effective theory, in particular the mass splitting between the vector and pseudoscalar heavy mesons, $\Delta* = M_B* - M_B$, and the mass splittings between the pseudoscalar heavy mesons containing different valence and sea light quarks, $\delta_{qr} = M_{B_r} - M_{B_q}$. These HQET constants can be determined directly from the two-point function fits and used as input into the chiral fits, with the experimental values then used in the extrapolation.

We are still in the process of determining the exact SChPT form of Eqn. (4.1). Once the functional SChPT form of Eqn. (4.1) is completely determined, we plan to use it to simultaneously fit it to our lattice data points for all sea and valence quark masses, and to determine the unknown LEC's in the process. For the systematic error analysis, we plan to study the effects of changing the SChPT form, for example by adding NNLO analytic terms, and the effects of allowing the more poorly known fixed parameters to vary. Our physical results will then be obtained by turning the taste-violations off, and extrapolating (interpolating) to the physical light (strange) sea and valence quark masses.

We will quote results for ξ , $f_{B_s} \sqrt{B_{B_s}}$, $f_{B_d} \sqrt{B_{B_d}}$, B_{B_s} , and B_{B_d} when this step is completed. We expect light quark discretization effects to be an important source of uncertainty until we calculate the three-point correlators at several lattice spacings and use these in the chiral fits.

5. Summary and future work

We have presented preliminary results for $f_{B_q} \sqrt{B_{B_q}}$ for six different values of m_q as well as for the ratio ξ with five different values of $m_d^{valence}$. Our analysis on three ensembles with different sea light quark masses gives statistical errors between 1 – 3% for $f_{B_q} \sqrt{B_{B_q}}$ and 1 – 2% for the ratio ξ . The systematic error analysis is in progress, see Table 2.

Two important sources of error in the calculation of $f_{B_q} \sqrt{B_{B_q}}$, the matching uncertainties and heavy quark discretization errors, are expected to cancel to a large extent when taking the ratio. We have already checked that the difference between the tree level and the one-loop results for ξ with our preliminary results for the renormalization constants is less than 0.5%. The higher order matching errors in Table 2 have been naively estimated as being $O(1 \times \alpha_s^2)$ for the coarse lattice. Heavy quark discretization effects in the table are estimated by power counting [15].

We are in the process of generating lattice data on the coarse lattice with a smaller light sea quark mass, $m_l = 0.005$, which will further constrain the chiral extrapolations. Better fitting approaches and different smearings that could reduce statistical errors further are also being investigated. Results from these improvements will be presented in a future publication [5]. We also plan to present results for the decay width differences $\Delta\Gamma_s$ and $\Delta\Gamma_d$, for which we have already calculated all the hadronic matrix elements needed. Finally, we plan to improve this analysis by repeating this calculation at other lattice spacings to study the discretization errors in detail. Simulations on finer lattices will reduce both discretization and perturbative matching errors.

Acknowledgments

The numerical simulations for this work were carried out on the Fermilab lattice QCD clusters, which are a computing resource of the USQCD collaboration and are funded by the DOE. We are grateful to the Fermilab Computing Divisions for operating and maintaining the clusters. This work was supported in part by the DOE under grant no. DE-FG02-91ER40677 and by the Junta de Andalucía [P05-FQM-437 and P06-TIC-02302].

References

- [1] A. Abulencia *et al.* [CDF Collaboration], Phys. Rev. Lett. **97** (2006) 242003 [arXiv:hep-ex/0609040]; V. M. Abazov *et al.* [D0 Collaboration], Phys. Rev. Lett. **97** (2006) 021802 [arXiv:hep-ex/0603029].
- [2] A world average can be found in W. M. Yao *et al.* [Particle Data Group], J. Phys. G **33** (2006) 1.
- [3] A. J. Buras, M. Jamin and P. H. Weisz, Nucl. Phys. B **347** (1990) 491.
- [4] E. Dalgic *et al.*, Phys. Rev. D **76** (2007) 011501 [arXiv:hep-lat/0610104]; E. Gamiz *et al.*, PoS **LAT2007** (2007) 349; J. Wennekers, these proceedings.
- [5] R.T. Evans, *et al.* (Fermilab Lattice and MILC collaborations), in preparation.
- [6] A. X. El-Khadra, A. S. Kronfeld and P. B. Mackenzie, Phys. Rev. D **55** (1997) 3933 [arXiv:hep-lat/9604004].
- [7] S. Naik, Nucl. Phys. B **316** (1989) 238; G. P. Lepage, Phys. Rev. D **59** (1999) 074502 [hep-lat/9809157]; K. Orginos, D. Toussaint and R. L. Sugar [MILC Collaboration], Phys. Rev. D **60** (1999) 054503 [hep-lat/9903032].
- [8] G. P. Lepage and P. B. Mackenzie, Phys. Rev. D **48**, 2250 (1993) [hep-lat/9209022].
- [9] S. J. Brodsky, G. P. Lepage and P. B. Mackenzie, Phys. Rev. D **28**, 228 (1983).
- [10] R.T. Evans, A.X. El-Khadra and M. Di Pierro, PoS **LAT2006** (2006) 081.
- [11] C. Bernard, private communication.
- [12] W. Detmold and C. J. Lin, Phys. Rev. D **76**, 014501 (2007) [arXiv:hep-lat/0612028].
- [13] C. Aubin and C. Bernard, Phys. Rev. D **73**, 014515 (2006) [arXiv:hep-lat/0510088].
- [14] C. Aubin *et al.* [MILC Collaboration], Phys. Rev. D **70**, 114501 (2004) [arXiv:hep-lat/0407028].
- [15] C. Aubin *et al.*, Phys. Rev. Lett. **95**, 122002 (2005) [arXiv:hep-lat/0506030].

The $\overline{B} \rightarrow D^* \ell \bar{\nu}$ form factor at zero recoil from three-flavor lattice QCD: A model independent determination of $|V_{cb}|$

C. Bernard,¹ C. DeTar,² M. Di Pierro,³ A. X. El-Khadra,⁴ R. T. Evans,⁴
 E. D. Freeland,⁵ E. Gamiz,⁴ Steven Gottlieb,⁶ U. M. Heller,⁷ J. E. Hetrick,⁸
 A. S. Kronfeld,⁹ J. Laiho,^{1,9} L. Levkova,² P. B. Mackenzie,⁹ M. Okamoto,⁹
 J. Simone,⁹ R. Sugar,¹⁰ D. Toussaint,¹¹ and R. S. Van de Water⁹

(Fermilab Lattice and MILC Collaborations)

¹*Department of Physics, Washington University, St. Louis, Missouri, USA*

²*Physics Department, University of Utah, Salt Lake City, Utah, USA*

³*School of Computer Science, Telecommunications and Information Systems,
DePaul University, Chicago, Illinois, USA*

⁴*Physics Department, University of Illinois, Urbana, Illinois, USA*

⁵*Liberal Arts Department, The School of the Art Institute of Chicago, Chicago, Illinois, USA*

⁶*Department of Physics, Indiana University, Bloomington, Indiana, USA*

⁷*American Physical Society, Ridge, New York, USA*

⁸*Physics Department, University of the Pacific, Stockton, California, USA*

⁹*Fermi National Accelerator Laboratory, Batavia, Illinois, USA*

¹⁰*Department of Physics, University of California, Santa Barbara, California, USA*

¹¹*Department of Physics, University of Arizona, Tucson, Arizona, USA*

(Dated: January 26, 2009)

Abstract

We present the first lattice QCD calculation of the form factor for $\overline{B} \rightarrow D^* \ell \bar{\nu}$ with three flavors of sea quarks. We use an improved staggered action for the light valence and sea quarks (the MILC configurations), and the Fermilab action for the heavy quarks. The form factor is computed at zero recoil using a new double ratio method that yields the form factor more directly than the previous Fermilab method. Other improvements over the previous calculation include the use of much lighter light quark masses, and the use of lattice (staggered) chiral perturbation theory in order to control the light quark discretization errors and chiral extrapolation. We obtain for the form factor, $\mathcal{F}_{B \rightarrow D^*}(1) = 0.921(13)(20)$, where the first error is statistical and the second is the sum of all systematic errors in quadrature. Applying a 0.7% electromagnetic correction and taking the latest PDG average for $\mathcal{F}_{B \rightarrow D^*}(1)|V_{cb}|$ leads to $|V_{cb}| = (38.7 \pm 0.9_{exp} \pm 1.0_{theo}) \times 10^{-3}$.

PACS numbers: 12.38.Gc, 13.25.Hw, 12.15.Hh

I. INTRODUCTION

The Cabibbo-Kobayashi-Maskawa matrix element V_{cb} plays an important role in the study of flavor physics [1]. Since $|V_{cb}|$ is one of the fundamental parameters of the Standard Model, its value must be known precisely in order to search for new physics by looking for inconsistencies between Standard Model predictions and experimental measurements. For example, the Standard Model contribution to the kaon mixing parameter ϵ_K depends sensitively on $|V_{cb}|$ (as the fourth power), and the present errors on this quantity contribute errors to the theoretical prediction of ϵ_K that are around the same size as the errors due to B_K , the kaon bag parameter, which has been the focus of much recent work [2, 3, 4, 5]. It is possible to obtain $|V_{cb}|$ from both inclusive and exclusive semileptonic B decays, and both determinations are limited by theoretical uncertainties. The inclusive method [6, 7, 8, 9, 10] makes use of the heavy-quark expansion and perturbation theory. The method also requires non-perturbative input from experiment, which is obtained from the measured moments of the inclusive form factor $\overline{B} \rightarrow X_c \ell \bar{\nu}_\ell$ as a function of the minimum electron momentum. The dominant uncertainties in this method are the truncation of the heavy quark expansion and perturbation theory [11, 12]. In order to be competitive with the inclusive determination of $|V_{cb}|$ and thus serve as a cross-check, the exclusive method requires a reduction in the uncertainty of the $B \rightarrow D^*$ semileptonic form factor $\mathcal{F}_{B \rightarrow D^*}$, which has been calculated previously using lattice QCD in the quenched approximation [13].

Given the phenomenological importance of $|V_{cb}|$, we have revisited the calculation of $\mathcal{F}_{B \rightarrow D^*}$ at zero recoil using the 2+1 flavor MILC ensembles with improved light staggered quarks [14, 15]. The systematic error due to quenching is thus eliminated. The systematic error associated with the chiral extrapolation to physical light quark masses is also reduced significantly. Since staggered quarks are computationally less expensive than many other formulations, we are able to simulate at quite small quark masses; our lightest corresponds to a pion mass of roughly 240 MeV. Given the previous experience of the MILC Collaboration with chiral fits to light meson masses and decay constants [16], we are in a regime where we expect rooted staggered chiral perturbation theory (rS χ PT) [17, 18, 19, 20, 21] to apply. We therefore use the rS χ PT result for the $B \rightarrow D^*$ form factor [22] to perform the chiral extrapolation and to remove discretization effects particular to staggered quarks. In addition,

we introduce a set of ratios that allows us to disentangle light- and heavy-quark discretization effects, and we suggest a strategy for future improvement. Finally, we extract the $B \rightarrow D^*$ form factor using a different method from that originally proposed in Ref. [13]. This new method requires many fewer three-point correlation functions, and has allowed for a savings of roughly a factor of ten in computing resources, while at the same time simplifying the analysis.

The differential rate for the semileptonic decay $\overline{B} \rightarrow D^* \ell \bar{\nu}_\ell$ is

$$\frac{d\Gamma}{dw} = \frac{G_F^2}{4\pi^3} m_{D^*}^3 (m_B - m_{D^*})^2 \sqrt{w^2 - 1} \mathcal{G}(w) |V_{cb}|^2 |\mathcal{F}_{B \rightarrow D^*}(w)|^2, \quad (1)$$

where $w = v' \cdot v$ is the velocity transfer from the initial state to the final state, and $\mathcal{G}(w) |\mathcal{F}_{B \rightarrow D^*}(w)|^2$ contains a combination of four form factors that must be calculated non-perturbatively. At zero recoil $\mathcal{G}(1) = 1$, and $\mathcal{F}_{B \rightarrow D^*}(1)$ reduces to a single form factor, $h_{A_1}(1)$. Given $h_{A_1}(1)$, the measured decay rate determines $|V_{cb}|$.

The quantity h_{A_1} is a form factor of the axial vector current,

$$\langle D^*(v, \epsilon') | \mathcal{A}^\mu | \overline{B}(v) \rangle = i \sqrt{2m_B 2m_{D^*}} \overline{\epsilon}'^\mu h_{A_1}(1), \quad (2)$$

where \mathcal{A}^μ is the continuum axial-vector current and ϵ' is the polarization vector of the D^* . Heavy-quark symmetry plays a useful role in constraining $h_{A_1}(1)$, leading to the heavy-quark expansion [23, 24]

$$h_{A_1}(1) = \eta_A \left[1 - \frac{\ell_V}{(2m_c)^2} + \frac{2\ell_A}{2m_c 2m_b} - \frac{\ell_P}{(2m_b)^2} \right], \quad (3)$$

up to order $1/m_Q^2$, and where η_A is a factor that matches heavy-quark effective theory (HQET) to QCD [25, 26]. The ℓ 's are long distance matrix elements of the HQET. Heavy-quark symmetry forbids terms of order $1/m_Q$ at zero recoil [27], and various methods have been used to compute the size of the $1/m_Q^2$ coefficients, including quenched lattice QCD [13].

The earlier work by Hashimoto *et al.* [13] used three double ratios in order to obtain separately each of the three $1/m_Q^2$ coefficients in Eq. (3). These three double ratios also determine three out of the four coefficients appearing at $1/m_Q^3$ in the heavy-quark expansion. It was shown in Ref. [28] that, for the Fermilab method matched to tree level in α_s and to next-to-leading order in HQET, the leading discretization errors for the double ratios for this quantity are of order $\alpha_s(\overline{\Lambda}/2m_Q)^2 f_B(am_Q)$ and $(\overline{\Lambda}/2m_Q)^3 f_i(am_Q)$, where $\overline{\Lambda}$ is a QCD scale

stemming from the light degrees of freedom, such as that appearing in the HQET expansion for the heavy-light meson mass, $m_M = m_Q + \bar{\Lambda} + \dots$. The functions $f_i(am_Q)$ are coefficients depending on am_Q and α_s , but not on $\bar{\Lambda}$. When $am_Q \sim 1$, the $f_i(am_Q)$ are of order one; when $am_Q \ll 1$, they go like a power of am_Q , such that the continuum limit is obtained. The powers of 2 are combinatoric factors.

As discussed in Ref. [13], all uncertainties in the double ratios \mathcal{R} used in that work scale as $\mathcal{R} - 1$ rather than as \mathcal{R} . Statistical errors in the numerator and denominator are highly correlated and largely cancel in these double ratios. Also, most of the normalization uncertainty in the lattice currents cancels, leaving a normalization factor close to one which can be computed reliably in perturbation theory. Finally, the quenching error, relevant to Ref. [13] but not to the present unquenched calculation, scales as $\mathcal{R} - 1$ rather than as \mathcal{R} . This scaling of the error occurs because the double ratios constructed in Ref. [13] become the identity in the limit of equal bottom and charm quark masses.

In the calculation reported here, the form factor $h_{A_1}(1)$ is computed more directly using only one double ratio,

$$\mathcal{R}_{A_1} = \frac{\langle D^* | \bar{c} \gamma_j \gamma_5 b | \bar{B} \rangle \langle \bar{B} | \bar{b} \gamma_j \gamma_5 c | D^* \rangle}{\langle D^* | \bar{c} \gamma_4 c | D^* \rangle \langle \bar{B} | \bar{b} \gamma_4 b | \bar{B} \rangle} = |h_{A_1}(1)|^2, \quad (4)$$

which is exact to all orders in the heavy-quark expansion in the continuum.¹ The lattice approximation to this ratio still has discretization errors that are suppressed by inverse powers of heavy-quark masses [$\alpha_s(\bar{\Lambda}/2m_Q)^2$ and $(\bar{\Lambda}/2m_Q)^3$], but which again vanish in the continuum limit. The errors in the ratio introduced in Eq. (4) do not scale rigorously as $\mathcal{R}_{A_1} - 1$ because \mathcal{R}_{A_1} is not one in the limit of equal bottom and charm quark masses. Nevertheless, this double ratio still retains the desirable features of the previous double ratios, i.e., large statistical error cancellations and the cancellation of most of the lattice current renormalization. Because the quenching error has been eliminated, the rigorous scaling of all the errors as $\mathcal{R} - 1$, including the quenching error, is no longer crucial. The more direct method introduced here has the significant advantage that extracting coefficients from fits to HQET expressions as a function of heavy-quark masses is not necessary, and no error is introduced from truncating the heavy-quark expansion to a fixed order in $1/m_Q^n$. In

¹ Note that the notation \mathcal{R}_{A_1} stands for a different double ratio in Ref. [13].

short, for an unquenched QCD calculation, the method using Eq. (4) gives a smaller total error than the method used in Ref. [13] for a fixed amount of computer time .

The currents of lattice gauge theory must be matched to the normalization of the continuum to obtain \mathcal{R}_{A_1} . The matching factors mostly cancel in the double ratio [29, 30], leaving $h_{A_1}(1) = \sqrt{\mathcal{R}_{A_1}} = \rho\sqrt{R_{A_1}}$, where R_{A_1} is the lattice double ratio and ρ , the ratio of matching factors, is very close to 1. (For the remainder of this paper we shall use the convention that a script letter corresponds to a continuum quantity, while a non-script letter corresponds to a lattice quantity.) This ρ factor has been calculated to one-loop order in perturbative QCD, and is found to contribute less than a 0.5% correction. We have exploited the ρ factors to implement a blind analysis. Two of us involved in the perturbative calculation applied a common multiplicative offset to the ρ factors needed to obtain $h_{A_1}(1)$ at different lattice spacings. This offset was not disclosed to the rest of us until the procedure for determining the systematic error budget for the rest of the analysis had been finalized.

The unquenched MILC configurations generated with 2+1 flavors of improved staggered fermions make use of the fourth-root procedure for eliminating the unwanted four-fold degeneracy of staggered quarks. At non-zero lattice spacing, this procedure has small violations of unitarity [31, 32, 33, 34, 35] and locality [36]. Nevertheless, a careful treatment of the continuum limit, in which all assumptions are made explicit, argues that lattice QCD with rooted staggered quarks reproduces the desired local theory of QCD as $a \rightarrow 0$ [37, 38]. When coupled with other analytical and numerical evidence (see Refs. [39, 40, 41] for reviews), this gives us confidence that the rooting procedure is indeed correct in the continuum limit.

The outline of the rest of this paper is as follows: Section II describes the details of the lattice simulation. Section III discusses the fits to the double ratios accounting for oscillating opposite-parity states. Section IV summarizes the lattice perturbation theory calculation of the ρ factor. Section V introduces the rooted staggered chiral perturbation theory formalism and expressions used in the chiral extrapolations. Section VI then discusses our treatment of the chiral extrapolation and introduces our approach for disentangling heavy and light-quark discretization effects. Section VII provides a detailed discussion of our systematic errors, and we conclude in Section VIII.

II. LATTICE CALCULATION

The lattice calculation was done on the MILC ensembles at three lattice spacings with $a \approx 0.15$, 0.125 , and 0.09 fm; these ensembles have an $O(a^2)$ Symanzik improved gauge action and 2+1 flavors of “AsqTad” improved staggered sea quarks [42, 43, 44, 45, 46, 47]. The parameters for the MILC lattices used in this calculation are shown in Table I. We have several light masses at both full QCD and partially-quenched points ($m_{\text{val}} \neq m_{\text{sea}}$), and our light quark masses range between $m_s/10$ and $m_s/2$. Table II shows the valence masses computed on each ensemble. In this work we follow the notation [16] where m_s is the physical strange quark mass, \hat{m} is the average u - d quark mass, and \hat{m}' , m'_s indicate the nominal values used in simulations. In practice, the MILC ensembles choose m'_s within 10–30% of m_s and a range of \hat{m}' to enable a chiral extrapolation.

The heavy quarks are computed using the Sheikholeslami-Wohlert (SW) “clover” action [48] with the Fermilab interpretation via HQET [49]. The SW action includes a dimension-five interaction with a coupling c_{SW} that has been adjusted to the value u_0^{-3} suggested by tadpole-improved, tree-level perturbation theory [50]. The value of u_0 is calculated either from the plaquette ($a \approx 0.15$ fm and $a \approx 0.09$ fm), or from the Landau link ($a \approx 0.12$ fm). The adjustment of c_{SW} is needed to normalize the heavy quark’s chromomagnetic moment correctly [49].

The tadpole-improved bare quark mass for SW quarks is given by

$$am_0 = \frac{1}{u_0} \left(\frac{1}{2\kappa} - \frac{1}{2\kappa_{\text{crit}}} \right), \quad (5)$$

where tuning the parameter κ to the critical quark hopping parameter κ_{crit} would lead to a massless pion. The spin averaged B_s and D_s kinetic masses are computed on a subset of the ensembles in order to tune the bare κ values for bottom and charm (and hence the corresponding bare quark masses) to their physical values. These tuned values were then used in the $B \rightarrow D^* \ell \nu$ form-factor production run.

The relative lattice scale is determined by calculating r_1/a on each ensemble, where r_1 is related to the force between static quarks by $r_1^2 F(r_1) = 1.0$ [51, 52]. To avoid introducing implicit dependence on \hat{m}' , m'_s via $r_1(\hat{m}', m'_s, g^2)$ (where, as above, primes denote simulation masses), we interpolate in m'_s and extrapolate in \hat{m}' to obtain $r_1(\hat{m}, m_s, g^2)/a$ at the physical masses. We then convert from lattice units to r_1 units with $r_1(\hat{m}, m_s, g^2)/a$. Below we shall

TABLE I: Parameters of the simulations. The columns from left to right are the approximate lattice spacing in fm, the sea quark masses $a\hat{m}'/am'_s$, the linear spatial dimension of the lattice ensemble in fm, the dimensionless factor $m_\pi L$ (m_π corresponds to the taste-pseudoscalar pion composed of light sea quarks), the gauge coupling, the dimensions of the lattice in lattice units, the number of configurations used for this analysis, the bare hopping parameter used for the bottom quark, the bare hopping parameter used for the charm quark, and the clover term c_{SW} used for both bottom and charm quarks.

a (fm)	$a\hat{m}'/am'_s$	L (fm)	$m_\pi L$	$10/g^2$	Volume	# Configs	κ_b	κ_c	c_{SW}
0.15	0.0194/0.0484	2.4	5.5	6.586	$16^3 \times 48$	628	0.076	0.122	1.5673
0.15	0.0097/0.0484	2.4	3.9	6.572	$16^3 \times 48$	628	0.076	0.122	1.5673
0.12	0.02/0.05	2.4	6.2	6.79	$20^3 \times 64$	460	0.086	0.122	1.72
0.12	0.01/0.05	2.4	4.5	6.76	$20^3 \times 64$	592	0.086	0.122	1.72
0.12	0.007/0.05	2.4	3.8	6.76	$20^3 \times 64$	836	0.086	0.122	1.72
0.12	0.005/0.05	2.9	3.8	6.76	$24^3 \times 64$	528	0.086	0.122	1.72
0.09	0.0124/0.031	2.4	5.8	7.11	$28^3 \times 96$	516	0.0923	0.127	1.476
0.09	0.0062/0.031	2.4	4.1	7.09	$28^3 \times 96$	556	0.0923	0.127	1.476
0.09	0.0031/0.031	3.4	4.2	7.08	$40^3 \times 96$	504	0.0923	0.127	1.476

call this procedure the mass-independent determination of r_1 .

In order to fix the absolute lattice scale, one must compute a physical quantity that can be compared directly to experiment; we use the Υ 2S–1S splitting [53] and the most recent MILC determination of f_π [54]. The difference between these determinations results in a systematic error that turns out to be much smaller than our other systematics. When the Υ scale determination is combined with the continuum extrapolated r_1 value at physical quark masses, a value $r_1^{\text{phys}} = 0.318(7)$ fm [55] is obtained. The f_π determination is $r_1^{\text{phys}} = 0.3108(15)(^{+26}_{-79})$ fm [54]. Given r_1^{phys} , it is then straightforward to convert quantities measured in r_1 units to physical units.

The dependence on the lattice spacing a is mild in this analysis. Since a only enters the calculation through the adjustment of the heavy and light quark masses, the dependence of

TABLE II: Valence masses used in the simulations. The columns from left to right are the approximate lattice spacing in fm, the sea quark masses $a\hat{m}'/am'_s$ identifying the gauge ensemble, and the valence masses computed on that ensemble.

a (fm)	$a\hat{m}'/am'_s$	am_x
≈ 0.15	0.0194/0.0484	0.0194
≈ 0.15	0.0097/0.0484	0.0097, 0.0194
≈ 0.12	0.02/0.05	0.02
≈ 0.12	0.01/0.05	0.01, 0.02
≈ 0.12	0.007/0.05	0.007, 0.02
≈ 0.12	0.005/0.05	0.005, 0.02
≈ 0.09	0.0124/0.031	0.0124
≈ 0.09	0.0062/0.031	0.0062, 0.0124
≈ 0.09	0.0031/0.031	0.0031, 0.0124

$h_{A_1}(1)$ on a is small. Staggered chiral perturbation theory indicates that the a dependence coming from staggered quark discretization effects is small [22], and this is consistent with the simulation data.

In this work, we construct lattice currents as in Ref. [49],

$$J_\mu^{hh'} = \sqrt{Z_{V_4}^{hh} Z_{V_4}^{h'h'}} \bar{\Psi}_h \Gamma_\mu \Psi_{h'}, \quad (6)$$

where Γ_μ is either the vector ($i\gamma^\mu$) or axial-vector ($i\gamma^\mu\gamma_5$) current. The rotated field Ψ_h is defined by

$$\Psi_h = (1 + ad_1 \boldsymbol{\gamma} \cdot \mathbf{D}_{\text{lat}}) \psi_h, \quad (7)$$

where ψ_h is the (heavy) lattice quark field in the SW action. \mathbf{D}_{lat} is the symmetric, nearest-neighbor, covariant difference operator; the tree-level improvement coefficient is

$$d_1 = \frac{1}{u_0} \left(\frac{1}{2 + m_0 a} - \frac{1}{2(1 + m_0 a)} \right). \quad (8)$$

In Eq. (6) we choose to normalize the current by the factors of $Z_{V_4}^{hh}$ ($h = c, b$) since even for massive quarks they are easy to compute non-perturbatively. The continuum current is

related to the lattice current by

$$\mathcal{J}_\mu^{hh'} = \rho_{J_\Gamma} J_\mu^{hh'} \quad (9)$$

up to discretization effects, where

$$\rho_{J_\Gamma}^2 = \frac{Z_{J_\Gamma}^{bc} Z_{J_\Gamma}^{cb}}{Z_{V_4}^{cc} Z_{V_4}^{bb}}, \quad (10)$$

and the matching factors $Z_{J_\Gamma}^{hh'}$'s are defined in Ref. [30]. Note that the factor $\sqrt{Z_{V_4}^{bb} Z_{V_4}^{cc}}$ multiplying the lattice current in Eq. (6) cancels in the double ratio by design, leaving only the ρ factor, which is close to one and can be computed reliably using perturbation theory. The perturbative calculation of ρ_{J_Γ} is described in more detail in Section IV.

Interpolating operators are constructed from four-component heavy quarks and staggered quarks as follows. Let

$$\mathcal{O}_{D_j^*}(x) = \bar{\chi}(x)\Omega^\dagger(x)i\gamma_j\psi_c(x), \quad (11)$$

$$\mathcal{O}_B^\dagger(x) = \bar{\psi}_b(x)\gamma_5\Omega(x)\chi(x), \quad (12)$$

where χ is the one-component field in the staggered-quark action, and

$$\Omega(x) = \gamma_1^{x_1/a}\gamma_2^{x_2/a}\gamma_3^{x_3/a}\gamma_4^{x_4/a}. \quad (13)$$

The left (right) index of Ω^\dagger (Ω) can be left as a free taste index [41] or χ can be promoted to a four-component naive-quark field to contract all indices [56]. The resulting correlation functions are the same if the initial and final taste indices are set equal and then summed. The same kinds of operators have been used in previous calculations [57, 58, 59].

Lattice matrix elements are obtained from three-point correlation functions. The three-point correlation functions needed for the $B \rightarrow D^*$ transition at zero-recoil are

$$C^{B \rightarrow D^*}(t_i, t_s, t_f) = \sum_{\mathbf{x}, \mathbf{y}} \langle 0 | \mathcal{O}_{D^*}(\mathbf{x}, t_f) \bar{\Psi}_c \gamma_j \gamma_5 \Psi_b(\mathbf{y}, t_s) \mathcal{O}_B^\dagger(\mathbf{0}, t_i) | 0 \rangle, \quad (14)$$

$$C^{B \rightarrow B}(t_i, t_s, t_f) = \sum_{\mathbf{x}, \mathbf{y}} \langle 0 | \mathcal{O}_B(\mathbf{x}, t_f) \bar{\Psi}_b \gamma_4 \Psi_b(\mathbf{y}, t_s) \mathcal{O}_B^\dagger(\mathbf{0}, t_i) | 0 \rangle, \quad (15)$$

$$C^{D^* \rightarrow D^*}(t_i, t_s, t_f) = \sum_{\mathbf{x}, \mathbf{y}} \langle 0 | \mathcal{O}_{D^*}(\mathbf{x}, t_f) \bar{\Psi}_c \gamma_4 \Psi_c(\mathbf{y}, t_s) \mathcal{O}_{D^*}^\dagger(\mathbf{0}, t_i) | 0 \rangle. \quad (16)$$

In $C^{B \rightarrow D^*}$ the polarization of the D^* lies along spatial direction j . If the source-sink separation is large enough then we can arrange for both $t_s - t_i$ and $t_f - t_s$ to be large so that the lowest-lying state dominates. Then

$$C^{B \rightarrow D^*}(t_i, t_s, t_f) = \mathcal{Z}_{D^*}^{\frac{1}{2}} \mathcal{Z}_B^{\frac{1}{2}} \frac{\langle D^* | \bar{\Psi}_c \gamma_j \gamma_5 \Psi_b | B \rangle}{\sqrt{2m_{D^*}} \sqrt{2m_B}} e^{-m_B(t_s-t_i)} e^{-m_{D^*}(t_f-t_s)} + \dots, \quad (17)$$

where m_B and m_{D^*} are the masses of the B and D^* mesons and $\mathcal{Z}_H = |\langle 0 | \mathcal{O}_H | H \rangle|^2$.

In practice, the meson source and sink are held at fixed $t_i = 0$ and $t_f = T$, while the operator time $t_s = t$ is varied over all times in between. Using the correlators defined in Eqs. (14-16) we form the double ratio

$$R_{A_1}(t) = \frac{C^{B \rightarrow D^*}(0, t, T) C^{D^* \rightarrow B}(0, t, T)}{C^{D^* \rightarrow D^*}(0, t, T) C^{B \rightarrow B}(0, t, T)}. \quad (18)$$

All convention-dependent normalization factors, including the factors of $\sqrt{\mathcal{Z}_H/2m_H}$, cancel in the double ratio. In the window of time separations where the ground state dominates, a plateau should be visible, and the lattice ratio is simply related to the continuum ratio \mathcal{R}_{A_1} by a renormalization factor

$$\rho_{A_1} \sqrt{R_{A_1}} = \sqrt{\mathcal{R}_{A_1}} = h_{A_1}(1), \quad (19)$$

with ρ_{A_1} as in Eq. (10). The right-hand side of Eq. (17) is the first term in a series, with additional terms for each radial excitation, including opposite-parity states that arise with staggered quarks. Eliminating the opposite-parity states requires some care, and this is discussed in detail in the next section. In order to isolate the lowest-lying states we have chosen creation and annihilation operators, \mathcal{O}_B^\dagger and \mathcal{O}_{D^*} , that have a large overlap with the desired state. This was done by smearing the heavy quark and anti-quark propagator sources with 1S Coulomb-gauge wave-functions.

III. FITTING AND OPPOSITE-PARITY STATES

Extracting correlation functions of operators with staggered quarks presents an extra complication because the contributions of opposite-parity states introduce oscillations in time into the correlator fits [56]. Three-point functions obey the functional form

$$C^{X \rightarrow Y}(0, t, T) = \sum_{k=0} \sum_{\ell=0} (-1)^{kt} (-1)^{\ell(T-t)} A_{\ell k} e^{-m_X^{(k)} t} e^{-m_Y^{(\ell)} (T-t)}. \quad (20)$$

For odd k and ℓ the excited state contributions change sign as the position of the operator varies by one time slice. Although they are exponentially suppressed, the parity partners of the heavy-light mesons are not that much heavier than the ground states in which we are interested, so the oscillations can be significant at the source-sink separations typical of our calculations. These separations cannot be too large because of the rapid decrease of the signal due to the presence of the heavy quark.

Although one can fit a given three-point correlator to Eq. (20), in the calculation of $h_{A_1}(1)$ we use double ratios in which numerator and denominator are so similar that most of the fitting systematics cancel, and it is convenient to preserve this simplifying feature. We do this by forming a suitable average over correlator ratios with different (even and odd) source-sink separations. It turns out that the amplitudes of the oscillating states in $B \rightarrow D^*$ correlation functions are much smaller than they are in many other heavy-light transitions [60, 61], and that the oscillating states in $B \rightarrow D^*$ are barely visible at the present level of statistics. Even so, we introduce an average that reduces them still further, to the point where they are negligible.

Although we shall take the average of the double ratio, let us first examine the average of an individual three-point function. Expanding Eq. (20) so that it includes the ground state and the first oscillating state, we have

$$\begin{aligned} C^{X \rightarrow Y}(0, t, T) &= A_{00}^{X \rightarrow Y} e^{-m_X t - m_Y(T-t)} + (-1)^{T-t} A_{01}^{X \rightarrow Y} e^{-m_X t - m'_Y(T-t)} \\ &\quad + (-1)^t A_{10}^{X \rightarrow Y} e^{-m'_X t - m_Y(T-t)} + (-1)^T A_{11}^{X \rightarrow Y} e^{-m'_X t - m'_Y(T-t)} + \dots \\ &= A_{00}^{X \rightarrow Y} e^{-m_X t - m_Y(T-t)} [1 + c^{X \rightarrow Y}(0, t, T) + \dots], \end{aligned} \quad (21)$$

where in the last line we have pulled out the ground state amplitude and exponential dependence. The function $c^{X \rightarrow Y}(0, t, T)$ is defined

$$\begin{aligned} c^{X \rightarrow Y}(0, t, T) &\equiv \frac{A_{01}^{X \rightarrow Y}}{A_{00}^{X \rightarrow Y}} (-1)^{T-t} e^{-\Delta m_Y(T-t)} + \frac{A_{10}^{X \rightarrow Y}}{A_{00}^{X \rightarrow Y}} (-1)^t e^{-\Delta m_X t} \\ &\quad + \frac{A_{11}^{X \rightarrow Y}}{A_{00}^{X \rightarrow Y}} (-1)^T e^{-\Delta m_X t - \Delta m_Y(T-t)}, \end{aligned} \quad (22)$$

where $\Delta m_{X,Y} = m'_{X,Y} - m_{X,Y}$ is the splitting between the lowest-lying desired-parity state and the lowest-lying wrong-parity state. Note that the first two terms produce oscillations as the position of the operator is varied over the time extent of the lattice. The third term, however, changes sign only when the total source-sink separation is varied. It is this

term that our average is designed to suppress, since it will not be as clearly visible in the t dependence of the lattice data as those that oscillate in t .

We define the average to be

$$\begin{aligned}\overline{C}^{X \rightarrow Y}(0, t, T) &\equiv \frac{1}{2}C^{X \rightarrow Y}(0, t, T) + \frac{1}{4}C^{X \rightarrow Y}(0, t, T+1) \\ &+ \frac{1}{4}C^{X \rightarrow Y}(0, t+1, T+1).\end{aligned}\quad (23)$$

Substituting the expression for $C^{X \rightarrow Y}(0, t, T)$ from Eq. (21) into this definition gives

$$\overline{C}^{X \rightarrow Y}(0, t, T) = A_{00}^{X \rightarrow Y} e^{-m_X t - m_Y (T-t)} [1 + \bar{c}^{X \rightarrow Y}(0, t, T) + \dots], \quad (24)$$

where the function $\bar{c}^{X \rightarrow Y}$ is

$$\begin{aligned}\bar{c}^{X \rightarrow Y}(0, t, T) &\equiv \frac{A_{01}^{X \rightarrow Y}}{A_{00}^{X \rightarrow Y}} (-1)^{T-t} e^{-\Delta m_Y (T-t)} \left[\frac{1}{2} + \frac{1}{4}(1 - e^{-\Delta m_Y}) \right] \\ &+ \frac{A_{10}^{X \rightarrow Y}}{A_{00}^{X \rightarrow Y}} (-1)^t e^{-\Delta m_X t} \left[\frac{1}{2} + \frac{1}{4}(1 - e^{-\Delta m_X}) \right] \\ &+ \frac{A_{11}^{X \rightarrow Y}}{A_{00}^{X \rightarrow Y}} (-1)^T e^{-\Delta m_X t - \Delta m_Y (T-t)} \left[\frac{1}{2} - \frac{1}{4}(e^{-\Delta m_Y} + e^{-\Delta m_X}) \right].\end{aligned}\quad (25)$$

Note that Eq. (25) has the same exponential time dependence as Eq. (22), but with the size of the amplitudes reduced by the factors in square brackets. Thus, the average is equivalent to a smearing that reduces the oscillating state amplitudes. It is possible to compute the Δm_X precisely from fits to two-point correlators. We find values between about 0.2 and 0.4 in lattice units. Given these values, the first two factors in brackets reduce their respective amplitudes by approximately a factor of 2, and the targeted, non-oscillating term is reduced by a factor of $\sim 6\text{--}10$.

Specializing to the $B \rightarrow D^*$ case, consider the double ratio

$$\begin{aligned}R_{A_1}(0, t, T) &= \frac{A_{00}^{B \rightarrow D^*} A_{00}^{D^* \rightarrow B}}{A_{00}^{D^* \rightarrow D^*} A_{00}^{B \rightarrow B}} [1 + c^{B \rightarrow D^*}(0, t, T) + c^{D^* \rightarrow B}(0, t, T) \\ &- c^{D^* \rightarrow D^*}(0, t, T) - c^{B \rightarrow B}(0, t, T) + \dots],\end{aligned}\quad (26)$$

where we have again factored out the ground state contribution. Equation (26) follows from Eq. (18) treating the c 's as small. Note that the c 's are expected to be similar in numerator and denominator, and to the extent that they are the same they will cancel in this expression. Applying the average in Eq. (23) directly to the double ratio,

$$\begin{aligned}\overline{R}(0, t, T) &\equiv \frac{1}{2}R(0, t, T) + \frac{1}{4}R(0, t, T+1) \\ &+ \frac{1}{4}R(0, t+1, T+1),\end{aligned}\quad (27)$$

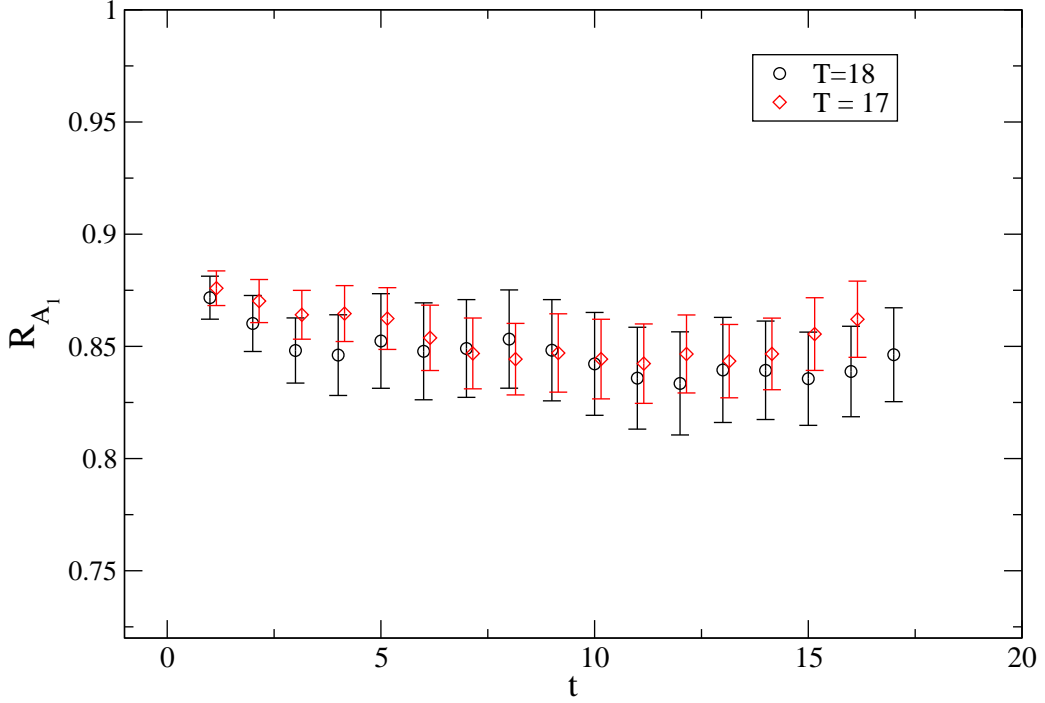


FIG. 1: Double ratio R_{A_1} on the $a\hat{m}' = 0.0124$ fine ($a = 0.09$ fm) ensemble. The source was fixed to time slice 0, and the operator position was varied as a function of time. Two different sink points were used with even and odd time separations between source and sink in order to study the effect of non-oscillating contributions from wrong parity states.

we get

$$\overline{R}_{A_1}(0, t, T) = \frac{A_{00}^{B \rightarrow D^*} A_{00}^{D \rightarrow B^*}}{A_{00}^{D \rightarrow D^*} A_{00}^{B \rightarrow B^*}} [1 + \bar{c}^{B \rightarrow D^*}(0, t, T) + \bar{c}^{D \rightarrow B^*}(0, t, T) - \bar{c}^{D \rightarrow D^*}(0, t, T) - \bar{c}^{B \rightarrow B^*}(0, t, T) + \dots], \quad (28)$$

where each of the oscillating state terms in the individual three-point functions is suppressed according to Eq. (25).

Although Δm_B and Δm_{D^*} can be obtained from fits to the two point correlators, the oscillating state amplitudes appearing in the three-point correlators must be determined directly from the three-point correlator data. Figure 1 shows the double ratio R_{A_1} used to obtain $h_{A_1}(1)$. The source is at time slice 0, the sink is at T , and the operator position is varied along t . Two different source-sink separations were generated that differed by a single time unit at the sink ($T = 17, 18$). The average of these two correlators was taken according

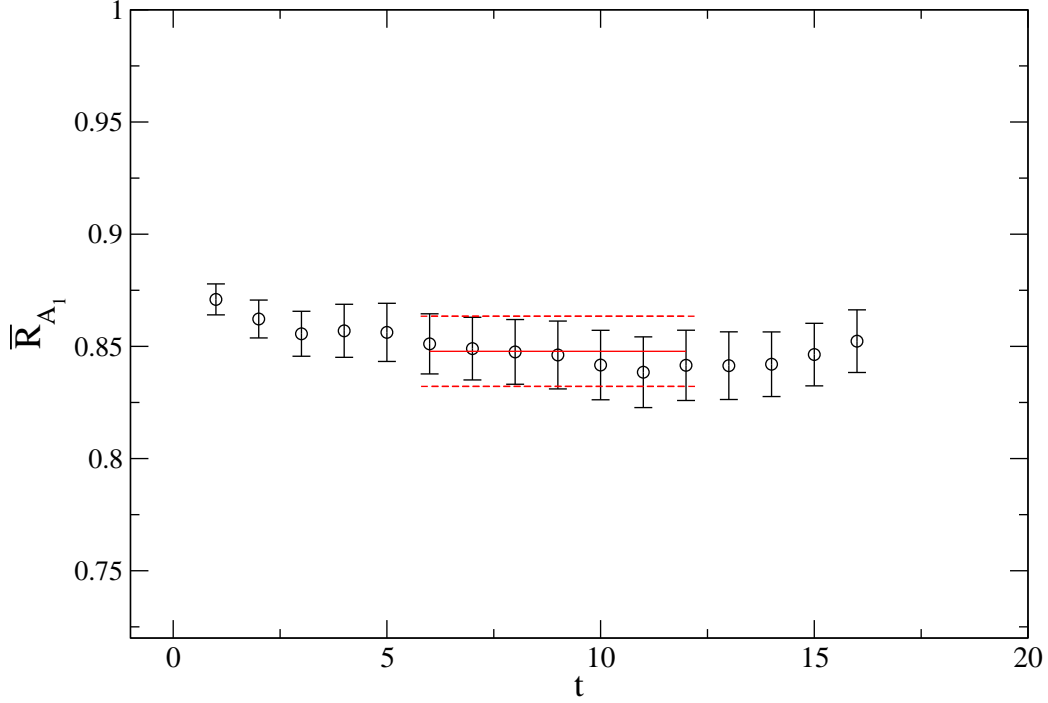


FIG. 2: Averaged double ratio, \overline{R}_{A_1} , of Eq. (27) on the $a\hat{m}' = 0.0124$ fine ($a = 0.09$ fm) ensemble. The plateau fit is shown with 1σ error band.

to Eq. (27), and this average was fit (including the full covariance matrix) to a constant, as shown in Fig. 2. There is no detectable oscillation even before the average is taken, as can be seen in Fig. 1; according to Eq. (25) the oscillating contributions are reduced even further in the average so that their systematic errors can be safely neglected.

IV. PERTURBATION THEORY

Lattice perturbation theory is needed in order to calculate the short-distance coefficient ρ_{A_1} defined in Eq. (10). Although naive lattice perturbation theory appears to converge slowly, the two main causes have been identified [50]: the bare gauge coupling is a poor expansion parameter, and coefficients are large when tadpole diagrams occur. If a renormalized coupling is used as an expansion parameter, and one computes only those quantities for which the tadpole diagrams largely cancel, then lattice perturbation theory seems to converge as well as perturbation theory in continuum QCD.

Only the vertex correction contributes to the ρ factor, as the wave-function renormalization (including all tadpoles) cancels by construction. Even the vertex correction partially cancels, and the one-loop coefficient is found to be small. The perturbative corrections to the ρ factor can be written as

$$\rho_{J_\Gamma}^{hh'} \equiv \frac{Z_{J_\Gamma}^{hh'}}{\sqrt{Z_{V_4}^{hh} Z_{V_4}^{h'h}}} = 1 + \alpha_V(q^*) 4\pi \rho_{J_\Gamma}^{hh'[1]} + \dots \quad (29)$$

where $\rho_{J_\Gamma}^{hh'[1]}$ is the coefficient of the one-loop correction, and the coupling α_V is the renormalized strong coupling constant in the V-scheme [50, 62], which is based on the static-quark potential. The coupling is determined following the procedure of Ref. [63]. The scale q^* of the running coupling $\alpha_V(q^*)$ should be chosen to be the typical momentum of a gluon in the loop. A prescription for calculating this scale was introduced by Brodsky, Lepage, and Mackenzie (BLM) [50, 62]. They define q^* by

$$\ln(q^{*2}) = \frac{\int d^4q f(q) \ln(q^2)}{\int d^4q f(q)}, \quad (30)$$

where $f(q)$ is the one-loop integrand and the numerator is the first log moment. This prescription was extended by Hornbostel, Lepage, and Morningstar (HLM) [64] to cases where the one-loop contribution is anomalously small leading to a break down of Eq. (30). The HLM prescription for q^* takes into account two-loop contributions to the gluon propagator via the inclusion of second log moments. Since we do encounter anomalously small one-loop corrections in ρ_{A_1} , the HLM prescription was used to determine q^* . Results for q_{HLM}^* and ρ_{A_1} needed for this calculation are given in Table III. The ρ factor varies somewhat as a function of lattice spacing, and is even slightly different from ensemble to ensemble at the same nominal lattice spacing, due to the slightly different β values used to generate the gauge fields.

The calculation of ρ_{A_1} is described in Refs. [65, 66]. It uses automated perturbation theory techniques to generate the Feynman rules and VEGAS [67] for the numerical integration of the loop integrals. As a check, it was verified that this calculation reproduces known results for the heavy-heavy currents with the Wilson plaquette action [29] and for the V_4 current in the massless limit with the Symanzik improved gauge action.

As mentioned in the introduction, we have exploited the ρ factor to implement a blind analysis. Two of us applied a multiplicative offset close to 1 to the ρ factor, generated with a

TABLE III: Computed values of ρ_{A_1} in the HLM prescription [64]. The first three columns label each ensemble with the approximate lattice spacing in fm, the light sea quark mass $a\hat{m}'$, and the strange quark mass am'_s . The fourth column is aq_{HLM}^* , where the error is calculated using the statistical error from VEGAS for the 0th, 1st, and 2nd moments of the one-loop integrals. The fifth column is ρ_{A_1} on that ensemble, and the errors are the statistical errors from the VEGAS evaluation, including the one-loop coefficients and q_{HLM}^* .

a (fm)	$a\hat{m}'$	am'_s	aq_{HLM}^*	ρ_{A_1}
0.15	0.0194	0.0484	2.03(10)	0.9966(2)
0.15	0.0097	0.0484	2.03(10)	0.9966(2)
0.12	0.02	0.05	1.96(10)	0.9964(2)
0.12	0.01	0.05	1.96(10)	0.9964(2)
0.12	0.007	0.05	1.96(10)	0.9964(2)
0.12	0.005	0.05	1.96(10)	0.9964(2)
0.09	0.0124	0.031	2.98(14)	1.00298(9)
0.09	0.0062	0.031	2.98(14)	1.00300(9)
0.09	0.0031	0.031	2.98(14)	1.00301(9)

random key. The offset was not unlocked until the procedure for determining the systematic errors in the rest of the analysis had been finalized.

V. STAGGERED CHIRAL PERTURBATION THEORY

The simulation masses \hat{m}'_{val} and \hat{m}'_{sea} (for valence and sea) are all larger than the physical \hat{m} . A controlled chiral extrapolation can be guided by an appropriate chiral effective theory that includes the effect of staggered-quark discretization errors. Rooted staggered chiral perturbation theory (rS χ PT), which has been formulated for heavy-light quantities in Ref. [68], is such a theory. In rS χ PT, a replica method is used to take into account the effect of rooting; this procedure has been justified in Refs. [33, 69].

Because of taste-symmetry breaking, the staggered theory has 16 light pseudoscalar mesons instead of 1. The tree-level relation for the masses of light staggered mesons in

the chiral theory is [17, 18]

$$m_{xy,\Xi}^2 = \mu_0(m_x + m_y) + a^2\Delta_\Xi , \quad (31)$$

where m_x and m_y are staggered quark masses, μ_0 is the continuum low-energy constant, and $a^2\Delta_\Xi$ are the splittings of the 16 pions of taste Ξ . For staggered quarks there exists a residual $SO(4)$ taste symmetry broken at $\mathcal{O}(a^2)$, such that there is some degeneracy among the 16 pions [17], and the taste index Ξ runs over the multiplets P, A, T, V, I with degeneracies 1, 4, 6, 4, 1. The splitting $a^2\Delta_P$ vanishes because there is an exact (non-singlet) lattice axial symmetry.

Schematically, the next-to-leading order (NLO) result for the relevant form factor is

$$h_{A_1}^{\text{NLO}}(1)/\eta_A = 1 + X_A(\Lambda_\chi) + \frac{g_{DD^*\pi}^2}{48\pi^2 f^2} \times \log s_{1-\text{loop}}(\Lambda_\chi) \quad (32)$$

where $X_A(\Lambda_\chi)$ is a low energy constant of the chiral effective theory, and is therefore independent of light quark mass and cancels the chiral scale dependence Λ_χ of the chiral logarithms. By heavy-quark symmetry, $X_A(\Lambda_\chi)$ is proportional to $1/m_c^2$ in the heavy-quark expansion. The term η_A is a factor which matches heavy-quark effective theory to QCD, and contains perturbative-QCD logarithmic dependence on the heavy-quark masses; it is independent of light quark mass. The term proportional to $g_{DD^*\pi}^2$ is short-hand for the one-loop staggered chiral logarithms, and is given in the appendix for ease of reference. The rooted staggered expression was derived in Ref. [22]. The one-loop staggered logarithms depend on both valence and sea quark masses, and include taste-breaking effects coming from the light quark sector. This expression also contains explicit dependence on the lattice spacing a , and requires as inputs the parameters of the staggered chiral lagrangian δ'_V, δ'_A , in addition to the staggered taste splittings $\Delta_{P,A,T,V,I}$ [16]. These parameters can be obtained from chiral fits to the light pseudoscalar meson sector and are held fixed in the chiral extrapolation of $h_{A_1}(1)$. The continuum low energy constant $g_{DD^*\pi}$ appears, and below we take a generous range inspired by a combined fit to many different experimental inputs, including a leading-order analysis of the D^* width. The D^*-D splitting $\Delta^{(c)}$ is well determined from experiment. The only other parameter that appears at NLO is the constant $X_A(\Lambda)$, and this is determined by our lattice data for $h_{A_1}(1)$.

Although the lattice data are well described by the NLO formula, it is useful to go beyond NLO and to include the next-to-next-to-leading-order (NNLO) analytic terms as a

way to estimate systematic errors. We do not include the NNLO logarithms because they are unknown and would require a two-loop calculation. The expression including analytic terms through NNLO is

$$h_{A_1}^{\text{NNLO}}(1)/\eta_A = 1 + \text{NLO} + c_1 m_{X_P}^2 + c_2 (2m_{U_P}^2 + m_{S_P}^2) + c_3 a^2, \quad (33)$$

where the subscript P on the meson masses indicates the taste pseudo-scalar mass. We use the notation from the rS χ PT literature that m_{X_Ξ} is a taste Ξ meson made of two valence x quarks, m_{U_Ξ} is a taste Ξ meson made of two light sea quarks, and m_{S_Ξ} is a taste Ξ meson made of two strange sea quarks. By heavy-quark symmetry, the c_i are suppressed by a factor of $1/m_c^2$. Since the only free parameter through NLO is an overall constant, we include the NNLO analytic terms in the fit used for our central value. This leads to a larger statistical error and is more conservative.

VI. TREATMENT OF CHIRAL EXTRAPOLATION

In this section, we discuss the approach we have developed to disentangle the heavy- and light-quark discretization effects and to perform the chiral and continuum extrapolations. In the Fermilab method, heavy-quark discretization errors can be estimated by comparing the heavy-quark expansions for lattice gauge theory and continuum QCD [28, 29, 30, 70]. The dependence on a is not simply a power series (unless $ma \ll 1$), so power-counting estimates in HQET are used. On the other hand, some of the light quark discretization effects are constrained by rS χ PT. The heavy-quark errors are asymptotically constrained by the Symanzik low-energy Lagrangian when $m_h a \ll 1$ and by heavy-quark symmetry even when $m_h a$ is close to 1. In the region in between, the errors smoothly interpolate the asymptotic behavior [49, 70]. The errors in the SW action used for the heavy quarks decrease with lattice spacing as $\alpha_s a$ in the $m_h a \ll 1$ region, as compared to the light quark (improved staggered) discretization errors, which decrease much faster, as $\alpha_s a^2$.

The first step of the method is to normalize the numerical data for $h_{A_1}(1)$ to a fiducial point by forming the ratio

$$\mathcal{R}_{\text{fid}}(m_x, \hat{m}', m'_s, a) \equiv \frac{h_{A_1}(m_x, \hat{m}', m'_s, a)}{h_{A_1}(m_x^{\text{fid}}, \hat{m}^{\text{fid}}, m_s^{\text{fid}}, a)}, \quad (34)$$

where m^{fid} is a fiducial mass, m_x is the light (spectator) valence quark, \hat{m}' is the isospin averaged light sea quark on a particular ensemble, and m'_s is the strange sea quark on that ensemble. (Note that the factor of η_A in Eqs. (32) and (33) cancels in the ratio.) The principle advantage of this ratio is that heavy quark discretization effects largely cancel, since the heavy quarks are the same in numerator and denominator. This allows us to disentangle the heavy-quark discretization effects from those of the light quark sector coming from staggered chiral logarithms, thus isolating the (taste-violating) discretization effects specific to the staggered light quarks. These light quark discretization effects can appear in non-analytic terms in rS χ PT and are due to violations of taste-symmetry. They can be removed to a given order in rS χ PT (we work to NLO) in fits to the numerical data at multiple lattice spacings using the explicit rS χ PT formula of Eq. (33), since this formula includes the staggered lattice artifacts. The continuum limit of the ratio \mathcal{R}_{fid} can be obtained using our fitted values for parameters in rS χ PT and taking $a \rightarrow 0$ in the rS χ PT expression for \mathcal{R}_{fid} . We do not need a more explicit ansatz for the functional form of the heavy-quark discretization effects, since they largely cancel in the ratio.

Normalizing the continuum extrapolated ratio \mathcal{R}_{fid} by h_{A_1} at the fiducial point on a very fine fiducial lattice where the heavy-quark discretization effects are small gives a value close to the physical continuum result,

$$h_{A_1}(\hat{m}, \hat{m}, m_s, 0) \approx h_{A_1}(m_x^{\text{fid}}, \hat{m}^{\text{fid}}, m_s^{\text{fid}}, a^{\text{fid}}) \times \mathcal{R}_{\text{fid}}(\hat{m}, \hat{m}, m_s, 0), \quad (35)$$

where the relation becomes exact as $a^{\text{fid}} \rightarrow 0$. Note that the requirement that the heavy-quark discretization effects must be small enforces the condition that the improved staggered light-quark discretization effects be even smaller (and likely negligible) because the staggered discretization effects decrease much faster with lattice spacing. The fiducial masses m_x^{fid} , \hat{m}^{fid} , and m_s^{fid} should be chosen large enough that it would be feasible to simulate this mass point on a very fine lattice (since the cost rises significantly as the mass of the light sea quarks is decreased), thus normalizing the lattice data to a point where the heavy-quark discretization effects are small. The fiducial masses should not be chosen so large, however, that rS χ PT would not be a reliable guide in performing the continuum and chiral extrapolation of \mathcal{R}_{fid} . This method can be considered the crudest form of step-scaling, but it does illustrate that one does not need lattices which are simultaneously fine enough for b quarks and large enough for light quarks in order to simulate, with high precision, quantities that involve both. In

practice, we find $m_x^{\text{fid}} = \hat{m}^{\text{fid}} \approx 0.4m_s$ and $m_s^{\text{fid}} \approx m_s$ are reasonable values for the fiducial masses. The fiducial lattice spacing should be chosen as fine as is practical; a succession of progressively finer fiducial lattices would be desirable for verifying that the a dependence is of the expected size. In this work we take our finest lattice (0.09 fm) as the fiducial lattice, but we apply Eq. (35) with the coarser lattices taken as fiducial lattices in order to estimate discretization errors. We note that the method presented above can be applied to all calculations involving the Fermilab treatment of heavy-quarks and staggered light quarks, not only the $B \rightarrow D^* \ell \nu$ form factor h_{A_1} . It may also be desirable to compute quantities at the fiducial point (or a succession of such points) using an even further improved action for the heavy quarks. Once the fiducial lattice spacing is of the order 0.03-0.01 fm, even the bottom quark may be treated as a “light” quark with the highly improved staggered action (HISQ) [71] or with chiral fermions, for which mass dependent discretization effects are small. Conserved currents could then be used for many simple heavy-light quantities, removing the need for a perturbative renormalization.

For the chiral extrapolation of h_{A_1} we find it useful to form two additional ratios,

$$\mathcal{R}_{\text{sea}}(\hat{m}', m'_s, a) \equiv \frac{h_{A_1}(m_x^{\text{fid}}, \hat{m}', m'_s, a)}{h_{A_1}(m_x^{\text{fid}}, \hat{m}^{\text{fid}}, m_s^{\text{fid}}, a)}, \quad (36)$$

$$\mathcal{R}_{\text{val}}(m_x, \hat{m}', m'_s, a) \equiv \frac{h_{A_1}(m_x, \hat{m}', m'_s, a)}{h_{A_1}(m_x^{\text{fid}}, \hat{m}', m'_s, a)}, \quad (37)$$

whose product is clearly \mathcal{R}_{fid} , Eq. (34). \mathcal{R}_{sea} and \mathcal{R}_{val} separate the sea and valence quark mass dependence, which makes it easier to assess systematic errors. The values of h_{A_1} that enter Eqs. (36) and (37) are obtained from

$$h_{A_1} = \rho \sqrt{\bar{R}_{A_1}}, \quad (38)$$

where \bar{R}_{A_1} is the average of double ratios defined in Eqs. (28). The ratios in Eqs. (36) and (37) are now quadruple ratios, where the excited state contamination is further suppressed over that of the double ratio. Performing the chiral extrapolation, taking the continuum limit of the two ratios, and multiplying them together we recover $\mathcal{R}_{\text{fid}}(\hat{m}, \hat{m}, m_s, 0)$ by construction. Thus, we can rewrite Eq. (35) as

$$h_{A_1}^{\text{phys}} \approx h_{A_1}(m_x^{\text{fid}}, \hat{m}^{\text{fid}}, m_s^{\text{fid}}, a^{\text{fid}}) \times [\mathcal{R}_{\text{sea}}(\hat{m}, m_s, 0) \times \mathcal{R}_{\text{val}}(\hat{m}, \hat{m}, m_s, 0)], \quad (39)$$

where, again, the relation becomes exact as $a^{\text{fid}} \rightarrow 0$.

TABLE IV: Fiducial masses used at the three different lattice spacings. The first four columns are the approximate lattice spacing in fm, the fiducial valence quark mass, the fiducial light sea quark mass, and the fiducial strange quark mass. The fifth and sixth columns are the values of $\sqrt{\bar{R}_{A_1}}$ and $h_{A_1}^{\text{fid}}$, respectively, computed at that fiducial point.

lattice spacing (fm)	am_x^{fid}	$a\hat{m}^{\text{fid}}$	am_s^{fid}	$\sqrt{\bar{R}_{A_1}}$	$h_{A_1}^{\text{fid}}$
0.15	0.0194	0.0194	0.0484	0.9211(73)	0.9180(73)
0.12	0.02	0.02	0.05	0.9112(73)	0.9079(73)
0.09	0.0124	0.0124	0.031	0.9210(85)	0.9237(85)

To the extent that the extrapolation in sea quark masses is mild, the ratio \mathcal{R}_{sea} should be close to one, since the valence light mass is the same in both numerator and denominator. \mathcal{R}_{val} contains less trivial chiral behavior. However, since the numerator and denominator are computed on the same ensemble (with different valence masses), they are correlated, and statistical errors tend to cancel in \mathcal{R}_{val} . The ratio \mathcal{R}_{sea} has small statistical errors because the valence mass m_x^{fid} in that ratio is relatively heavy. Of course, the heavy-quark discretization errors are significantly suppressed in both ratios, isolating the light quark mass dependence and staggered discretization effects. A direct chiral fit to the numerical data (not involving the ratios introduced here) would require a more explicit ansatz for the treatment of the heavy quark discretization effects than is needed in the ratio fits². Note that in the ratios the fiducial point need not be tuned to the same mass at every lattice spacing; differences can be accounted for in the fit itself. The fiducial points used at different lattice spacings are $m_x^{\text{fid}} = \hat{m}^{\text{fid}} = 0.4m'_s$ and $m_s^{\text{fid}} = m'_s$. The explicit values are given in Table IV, along with the calculated values of $\sqrt{\bar{R}_{A_1}}$ and $h_{A_1}^{\text{fid}}$ at that fiducial point.

The constant term $X_A(\Lambda_\chi)$ in Eq. (32) cancels in the ratios \mathcal{R}_{sea} and \mathcal{R}_{val} , so the behavior of these ratios is completely predicted through NLO in the chiral expansion. We find good agreement between the predicted form and the numerical data. However, given that our fiducial spectator quark mass is rather large (around $0.4m_s$), we include the NNLO analytic

² A direct (correlated) chiral fit would still, however, reflect the correlations which cause cancellations in the statistical errors in the ratios.

terms in the ratio fits in order to estimate systematic errors associated with the chiral expansion. There are only two new continuum low energy constants introduced at this higher order, and the ratios \mathcal{R}_{sea} and \mathcal{R}_{val} determine one each. There is also an analytic term proportional to a^2 appearing at this order, but it cancels in each of the \mathcal{R}_{sea} and \mathcal{R}_{val} ratios.

In future calculations, it would be feasible to use a much finer lattice spacing for the fiducial point, thereby further reducing heavy-quark discretization errors. For now, however, we use $h_{A_1}(m_x^{\text{fid}}, \hat{m}^{\text{fid}}, m_s^{\text{fid}}, 0.09 \text{ fm})$, with the fiducial masses in Table IV, in Eq. (39). As a way to estimate discretization errors we use our results for $h_{A_1}^{\text{fid}}$ at the two coarser lattice spacings in Eq. (39) also.

At the lattice spacings used in this work the light-quark discretization effects may still be non-negligible compared to heavy-quark discretization effects. With rS χ PT it is possible to remove from $h_{A_1}^{\text{fid}}$ the discretization effects associated with staggered chiral logarithms, although purely analytic discretization errors remain. Removing this subset of staggered effects leads to a value for the fiducial form-factor which we call the “taste-violations-out” value. Not removing them leads to the “taste-violations-in” value. The difference turns out to be negligible, less than 0.1% on our coarsest ensemble and less than 0.01% on the fine ensemble. Thus, the discretization effects in our lattice data coming from taste-violations in the staggered chiral logarithms are extremely small at the fiducial point mass, and we neglect this difference in the analysis.

Figure 3 shows the plateau fit to the ratio \mathcal{R}_{val} on the fine ensemble with $(a\hat{m}', am'_s) = (0.0062, 0.031)$. The valence mass in the numerator is the full QCD value of $am'_x = 0.0062$, while the fiducial valence mass in the denominator is $am_x^{\text{fid}} = 0.0124$. Both numerator and denominator are computed on the same ensemble, so they have the same sea quark masses, and correlated statistical errors largely cancel in the ratio, as expected. Excited-state contamination is also reduced. Computed values for \mathcal{R}_{sea} on all of our ensembles are given in Table V, and the computed values for \mathcal{R}_{val} are given in Table VI.

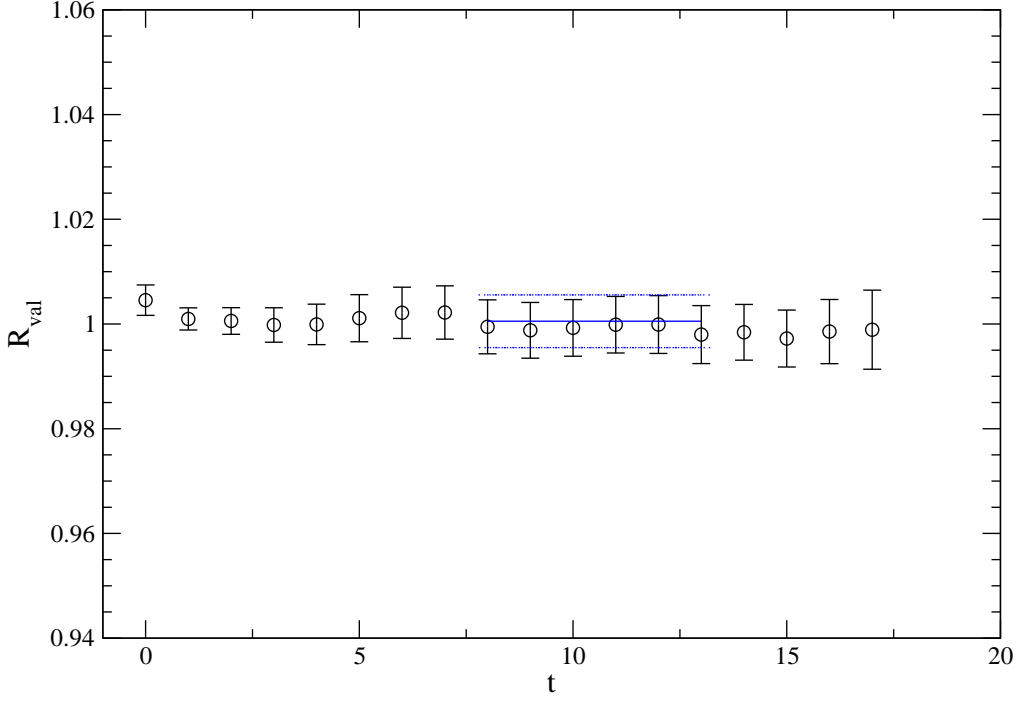


FIG. 3: \mathcal{R}_{val} on the $a\hat{m}' = 0.0062$ fine ensemble. The valence mass in the numerator is the full QCD value of $am'_x = 0.0062$ while the fiducial valence mass in the denominator is $am_x^{\text{fid}} = 0.0124$. The fit to a constant has a $\chi^2/\text{d.o.f} = 0.20$.

TABLE V: Computed values of \mathcal{R}_{sea} . The first three columns are the arguments of \mathcal{R}_{sea} as defined in Eq. (36); they are the light sea quark mass \hat{m}' , the strange quark mass m'_s , and the approximate lattice spacing in fm. The fourth column is \mathcal{R}_{sea} .

$a\hat{m}'$	am'_s	$a(\text{fm})$	\mathcal{R}_{sea}
0.0097	0.0484	0.15	1.009(12)
0.01	0.05	0.12	1.0070(98)
0.007	0.05	0.12	1.0027(91)
0.005	0.05	0.12	1.014(10)
0.0062	0.031	0.09	1.000(12)
0.0031	0.031	0.09	0.996(10)

TABLE VI: Computed values of \mathcal{R}_{val} . The first four columns are the arguments of \mathcal{R}_{val} as defined in Eq. (37); they are the light valence quark mass m_x , the light sea quark mass \hat{m}' , the strange quark mass m'_s , and the approximate lattice spacing in fm. The fifth column is \mathcal{R}_{val} .

am_x	$a\hat{m}'$	am'_s	$a(\text{fm})$	\mathcal{R}_{val}
0.0097	0.0097	0.0484	0.15	1.0056(65)
0.01	0.01	0.05	0.12	0.9994(41)
0.007	0.007	0.05	0.12	0.9900(57)
0.005	0.005	0.05	0.12	1.0081(90)
0.0062	0.0062	0.031	0.09	1.0005(50)
0.0031	0.0031	0.031	0.09	1.0043(62)

VII. SYSTEMATIC ERRORS

In the following subsections, we examine the uncertainties in our calculation due to fitting and excited states, the heavy-quark mass dependence, the chiral extrapolation of the light spectator quark mass, discretization errors, and perturbation theory. As mentioned in Section II, statistical uncertainties are computed with a single elimination jackknife and the full covariance matrix.

A. Fitting and excited states

We have examined plateau fits to the time dependence of the double and quadruple ratios introduced in Sections I and V. The χ^2 in our fits is defined with the full covariance matrix. The fits to the ratios were done under a single elimination jackknife, after blocking the numerical data by 8 on the fine lattices and by 4 on the coarse and coarser lattices. The blocking procedure averages 4 (or 8) successive configurations before performing the single elimination jackknife. These values for the block size were chosen such that the statistical error on the double ratio fit did not increase when a larger block size was used. Statistical errors were determined in fits that included the full correlation matrix, which was remade for each jackknife fit. The jackknife data sets on different ensembles were then combined

TABLE VII: Errors in the $\kappa_{b,c}$ parameters. The first column labels the heavy quark, the second gives the statistical and fitting error for the κ parameter, the third gives the discretization error, and the fourth combines these in quadrature.

κ	statistics + fitting	discretization	total
κ_c	1.2%	0.3%	1.2%
κ_b	5.6%	1.3%	5.7%

into a larger block-diagonal jackknife data set in order to perform the chiral fits. In this way, the fully correlated statistical errors were propagated through to the final result.

With our high statistics (several hundred lattice gauge field configurations for each ensemble), we are able to resolve the full covariance matrix well enough that we do not need to apply a singular value decomposition cut on the eigenvalues of the covariance matrix. The double ratio fit is needed to establish $h_{A_1}(1)$ at the fiducial point (which was computed on the 0.0124/0.031 fine ensemble), while the quadruple ratios, \mathcal{R}_{val} and \mathcal{R}_{sea} are computed on the other ensembles in order to perform the chiral extrapolation and to remove taste breaking non-analytic terms. We find that the fit to the double ratio at the fiducial point on the 0.0124/0.031 ensemble is well described by a constant over a range of seven time slices. The excited state contamination in the quadruple ratios is even further suppressed, and we find that the correlated χ^2 values allow for a constant fit region of six to ten time slices, depending upon the lattice spacing. We take the good correlated $\chi^2/\text{d.o.f.}$, ranging from 0.15 to 1.00, in our constant plateau fits as evidence that the excited state contamination in these fits is negligible as compared to other errors.

As an additional check of the jackknife fitting procedure, bootstrap fits were done to all of the double and quadruple ratios needed for this work. Close agreement was found for both central values and statistical errors. The statistical errors were typically the same size within 10%, and central values were well within 1σ . The jackknife procedure had slightly larger errors than that of the bootstrap.

B. Heavy-quark mass dependence

The value for $h_{A_1}(1)$ depends on the heavy-quark masses, which are set by tuning the hopping parameters κ_b and κ_c . The principal method starts by fitting the lattice pole energy to $E(\mathbf{p})$ to the dispersion relation,

$$E(\mathbf{p}) = M_1 + \frac{\mathbf{p}^2}{2M_2} + b_1 \mathbf{p}^4 + b_2 \sum_{j=1}^3 |p_j|^4 + \dots, \quad (40)$$

in order to obtain the kinetic mass M_2 (as well as b_1 and b_2 , which are unimportant here). In the Fermilab method [28, 30, 49], κ is adjusted so that the kinetic mass agrees with experiment. Here we take the spin-average of kinetic masses of pseudoscalar and vector heavy-strange mesons and obtain our central values for κ_b or κ_c , respectively, from the (spin-averaged) $B_s^{(*)}$ and $D_s^{(*)}$ masses. Applying this procedure we find statistical and fitting errors of 5.6% for κ_b and 1.2% for κ_c on the fine ($a = 0.09$ fm) ensembles. There is an additional error in κ due to discretization effects. We determine this error by estimating the size of discretization effects for the Fermilab action (at $a = 0.09$ fm) as in Ref. [72]. This error is 1.3% for κ_b and 0.3% for κ_c . Adding in quadrature the statistical and fitting error together with the discretization error leads to a total relative uncertainty of 5.7% for κ_b and 1.2% for κ_c . This error budget is summarized in Table VII. Note that these errors are conservative and are likely to decrease substantially with more sophisticated fitting methods and the higher statistics data set currently being generated.

We have computed $h_{A_1}(1)$ at several different values of the bare charm and bottom quark masses, and these simulated points can be used to estimate the error in $h_{A_1}(1)$ from the above uncertainties in the tuning of the heavy-quark κ values. Figure 4 illustrates the dependence of $h_{A_1}(1)$ as a function of bottom and charm quark κ values on one of the coarse ($a = 0.12$ fm) ensembles. The points labelled κ_b show $h_{A_1}(1)$ where we have fixed κ_c to the tuned charm value, but vary the bare κ_b along the x -axis. The points labelled κ_c are similar, where the value of κ_b is fixed at its tuned value, and the bare κ_c is varied. The above uncertainties in the κ 's, combined with the variation of $h_{A_1}(1)$ with κ , lead to a systematic error of 0.7% in $h_{A_1}(1)$, labelled “kappa tuning” in Table X.

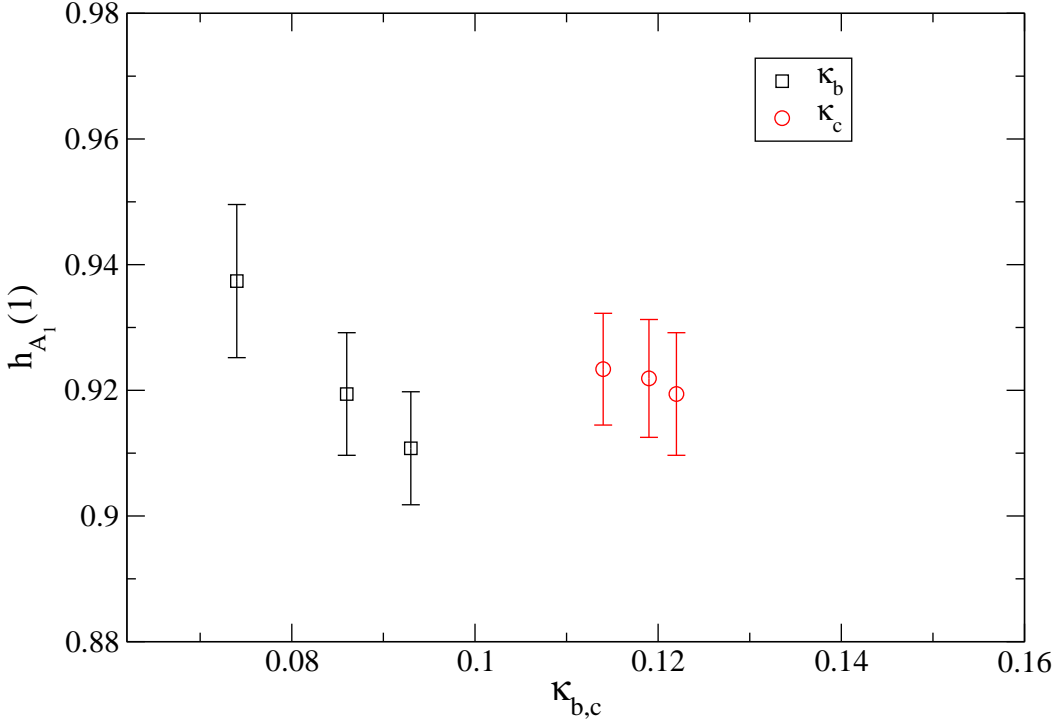


FIG. 4: $h_{A_1}(1)$ for different κ_h values on the coarse $\hat{m}' = 0.02$ ensemble (full QCD point). The points labelled κ_b show how $h_{A_1}(1)$ depends on κ_b when κ_c is fixed to its tuned value. For the points labelled κ_c the roles of κ_b and κ_c are reversed.

C. Perturbation theory

The perturbative calculation of ρ_{A_1} is needed to match the heavy-quark lattice current, and the calculation has been carried out to one-loop order [$O(\alpha_s)$]. As discussed in Section IV, much of the renormalization cancels when forming the ratios of Z factors that define ρ [Eq. (29)], and the coefficients of the perturbation series are small, by construction. The one-loop correction is quite small, only 0.3–0.4% on the different lattice spacings. We take the entire one-loop correction of 0.3% on the fine lattices as an estimate of the error introduced by neglecting higher orders in the perturbative expansion.

D. Chiral extrapolation

We estimate our systematic error due to the chiral extrapolation by comparing fits with and without the additional terms with coefficients c_i in Eq. (33), i.e. analytic terms of higher order than NLO in r χ PT, since the two-loop NNLO logarithms are unknown. We also compare with continuum χ PT, both NLO and (partial) NNLO. There are additional errors due to the uncertainties in the parameters that enter the NLO r χ PT formulas. By far the largest uncertainty of this kind is that due to the uncertainty in $g_{DD^*\pi}$. Finally, there is an error due to a mistuning of the parameter u_0 on the coarse lattices. All of these errors are discussed below in more detail. In the discussion of chiral extrapolation errors, it is important to keep in mind that the chiral logarithms (either r χ PT or continuum) are tiny ($\sim 3 \times 10^{-3}$) in the region where we have data. Non-analytic behavior is important only near the physical pion mass where the χ PT should be a very good description in the continuum. The main feature of the chiral extrapolation is a cusp that appears close to the physical pion mass (in the valence sector), due to the $D\pi$ threshold and the fact that the $D-D^*$ splitting is very close to the physical pion mass. This cusp represents real physics, and must be included in any version of the chiral extrapolation used to estimate systematic errors.

We extrapolate the light sea and light valence quark masses from the values used in the simulations, between $m_s/2$ and $m_s/10$, to the average physical light quark mass, around $m_s/27$. We use staggered chiral perturbation theory and the prescription introduced in Section VI to remove the non-analytic taste-breaking discretization effects coming from the staggered light quark sector. Separate fits are performed for the two ratios introduced in Eqs. (36) and (37), \mathcal{R}_{sea} and \mathcal{R}_{val} . The chiral extrapolation is performed on these ratios, and the staggered discretization errors appearing in the NLO chiral logarithms are removed by taking $a \rightarrow 0$ in the r χ PT expression. With the NNLO analytic terms given in Eq. (33) the chiral extrapolation formulas for the ratios are

$$\mathcal{R}_{\text{val}} = 1 + \text{NLO}_{\text{logs}} + c_1 m_{X_P}^2, \quad (41)$$

$$\mathcal{R}_{\text{sea}} = 1 + \text{NLO}_{\text{logs}} + c_2(2m_{U_P}^2 + m_{S_P}^2), \quad (42)$$

where NLO_{logs} is a schematic notation representing the chiral logarithms coming from numerator and denominator. These terms are different for the two ratios, and can be obtained straightforwardly from the definitions of the ratios Eqs. (36) and (37), and the formula for

$$\chi^2/\text{d.o.f.} = 0.91, \text{CL} = 0.51$$

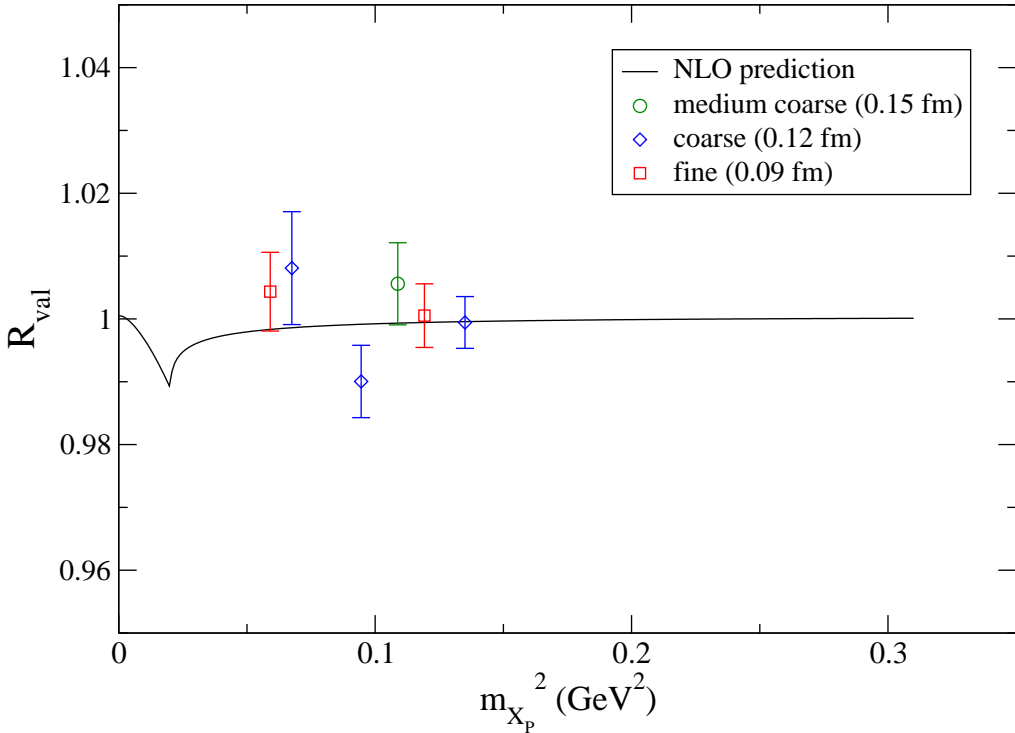


FIG. 5: \mathcal{R}_{val} ratio versus valence pion mass squared on all ensembles for the three different lattice spacings. The curve is the continuum prediction through NLO in continuum χ PT for this quantity. (See Appendix.)

the non-analytic terms in Eq (A1). The formula for \mathcal{R}_{val} in the continuum is given explicitly in Eq. (A6), for the purposes of illustration. The NNLO term $c_3 a^2$ in Eq. (33) cancels in the ratios, and \mathcal{R}_{sea} and \mathcal{R}_{val} each determine one of the remaining two NNLO coefficients. Note that the factor of η_A in Eqs. (32) and (33) cancels in the chiral formulas for the two ratios. The only free parameters in our chiral fits are c_1 and c_2 ; the rest are determined from phenomenology or from rS χ PT fits to the pseudoscalar sector.

The ratios in Eqs. (36) and (37) are completely predicted through NLO in the continuum once f_π , $g_{DD^*\pi}$, and the $D-D^*$ splitting $\Delta^{(c)}$ are taken from experiment. The constants f_π and $g_{DD^*\pi}$ appear in an overall multiplicative factor $\frac{g_{DD^*\pi}^2}{48\pi^2 f_\pi^2}$ in front of the logarithmic term, as can be seen in Eq. (A1) and Eq. (A6). We take a fairly conservative range for the constant $g_{DD^*\pi}$ determined from phenomenology, as discussed below, and the errors in this

quantity are accounted for in our final error budget. In the mass region where we have data, the NLO continuum chiral logarithms contribute to $h_{A_1}(1)$ at the $\sim 3 \times 10^{-3}$ level or less. Figure 5 illustrates this, where the NLO continuum χ PT prediction Eq. (A6) is plotted over our data points for \mathcal{R}_{val} . We find that the NLO continuum χ PT describes the data quite well, giving a $\chi^2/\text{d.o.f.} = 0.91$ and a corresponding $\text{CL}=0.51$. This result is unchanged in the rS χ PT fits; the effects of staggering are negligible in the region where we have data. We include the term proportional to c_1 in Eq. (41) in our fits used to obtain the central value for this quantity, as explained in Section V. (Since including a linear term proportional to c_1 increases the statistical error in h_{A_1} , we take our central value and statistical error from this fit to be conservative.) This ‘‘partial NNLO’’ fit also has a good $\chi^2/\text{d.o.f.} = 1.05$, with a corresponding $\text{CL}=0.39$. The constant linear term is small and consistent with zero [$c_1 = -0.006(15)$]. Figure 6 shows the fit to \mathcal{R}_{val} versus $m_{X_P}^2$ for all three lattice spacings using the rS χ PT formula, Eq. (41).

Although the data for \mathcal{R}_{val} is consistent with a constant, the cusp appearing close to the physical pion mass is a prediction of NLO χ PT and has a physical origin, namely the D - π threshold, as we have remarked. Thus, any fits used to estimate systematic errors, even those that are somewhat ad hoc, such as those including higher order polynomial terms, must include this cusp. Note that the cusp appears at the physical pion mass (in either SU(3) or SU(2) χ PT), and is therefore in a region where χ PT is expected to be a reliable expansion. The cusp is a property of the function $F(m, \Delta^{(c)}/m)$ given in Eq. (A2), and the position of the cusp as a function of $m_{X_P}^2$ is determined by the D - D^* splitting $\Delta^{(c)}$ and the physical pion mass. We take these two quantities from experiment rather than from the lattice, since the experimental uncertainties are much smaller.

We find that with or without the NNLO analytic terms, the χ PT (continuum or rooted staggered) describes the lattice data with $\chi^2/\text{d.o.f.}$ close to 1 and correspondingly good confidence levels. We find a confidence level for the fit to \mathcal{R}_{sea} of 0.76 for the fit that includes NNLO analytic terms. The strictly NLO expression for the lattice ratio \mathcal{R}_{sea} has no free parameters, but it describes the data with a confidence level of 0.73. Similar fits to \mathcal{R}_{val} are described above and yield reasonable confidence levels for both types of fits. Since the lattice data do not distinguish between these model fit functions, and the fit using only the NNLO analytic terms is not systematic in the chiral expansion, we assign the difference

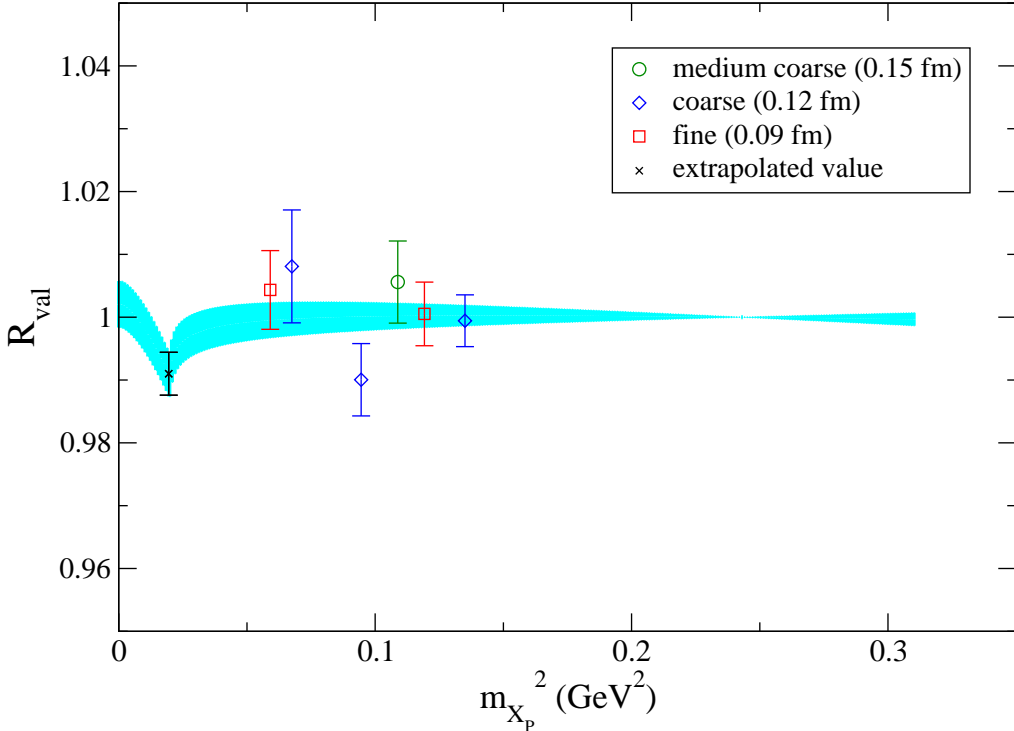


FIG. 6: \mathcal{R}_{val} ratio versus valence pion mass squared on all ensembles for the three different lattice spacings. The curve is the fit with 1 sigma error band to the ratio for all three lattice spacings using rS χ PT, extrapolated to the continuum by taking $a \rightarrow 0$ in the NLO staggered chiral logarithms.

between the two determinations, which is 0.9%, as the systematic error of leaving out higher order terms when performing the chiral extrapolation. The final results for \mathcal{R}_{sea} , \mathcal{R}_{val} , and \mathcal{R}_{fid} are given in Table VIII. The errors are statistical only; note that the strictly NLO values have no free parameters, and therefore no statistical errors. The final value of h_{A_1} still has statistical errors coming from the statistical errors in $h_{A_1}^{\text{fid}}$. The extrapolated results for \mathcal{R}_{fid} are consistent within the statistical errors of the NNLO fit. Again, we choose for our central value the result from the NNLO extrapolation with its larger errors to be conservative.

The cyan (gray) band in Figure 6 is the continuum extrapolation with $a \rightarrow 0$ in the rS χ PT formula. For this quantity, the staggered lattice artifacts affecting the chiral logarithms in h_{A_1} are negligible in the region where we have lattice data, which is due mainly to the small size of the chiral logarithms themselves. This is confirmed by the close agreement between the data points at each lattice spacing and the continuum curve. In fact, if we use continuum χ PT to perform the chiral extrapolation, the result is unchanged. The primary difference

TABLE VIII: Continuum extrapolated values of \mathcal{R}_{sea} , \mathcal{R}_{val} , \mathcal{R}_{fid} , and $h_{A_1}(1)$ evaluated at the physical quark masses. The first column labels the quantity. The second is the computed value including NNLO analytic terms in the chiral fit. The third is the quantity evaluated in purely NLO χ PT, and has no free parameters (once $g_{DD^*\pi}$, f_π and $\Delta^{(c)}$ are taken from phenomenology) in the chiral fit. The final row shows $h_{A_1}(1)$, which includes a statistical error coming from $h_{A_1}^{\text{fid}}$. The numbers are the same to the quoted precision using rS χ PT or continuum χ PT.

	w/ NNLO	strictly NLO
\mathcal{R}_{sea}	1.0059(90)	0.9983
\mathcal{R}_{val}	0.9910(34)	0.9895
\mathcal{R}_{fid}	0.997(10)	0.9878
$h_{A_1}(1)$	0.921(13)	0.9124(84)

between the rS χ PT expression and the continuum χ PT expression is the reduction of the cusp near the physical pion mass in rS χ PT, though our lattice data are not near enough to the physical pion mass to demonstrate this effect.

Figure 7 shows the fit to \mathcal{R}_{sea} , extrapolated to the continuum and to the physical strange sea quark mass. Note that this ratio does not produce a cancellation of correlations between numerator and denominator and so has larger statistical errors than \mathcal{R}_{val} . Here again the discretization effects due to staggered logarithms are negligibly small. Since the effects of including staggered discretization effects in the chiral logarithms are negligible in the region where we have numerical data, and since the only nontrivial feature in the chiral extrapolation is the cusp near the physical pion mass, which we describe by continuum χ PT (our extrapolated curve has $a \rightarrow 0$ in the rS χ PT formula and thus reduces to the continuum form), we conclude that staggered taste-violating effects appearing in chiral logarithms are essentially removed in our ratio extrapolations.

Figure 8 shows all of the full QCD points on the three lattice spacings. The curve is the quantity,

$$h_{A_1}^{\text{phys}}(\hat{m}') \approx h_{A_1}^{\text{fid}}(m_x^{\text{fid}}, \hat{m}^{\text{fid}}, m_s^{\text{fid}}, a^{\text{fid}}) \times [\mathcal{R}_{\text{sea}}(\hat{m}', m_s, 0) \times \mathcal{R}_{\text{val}}(\hat{m}', \hat{m}', m_s, 0)], \quad (43)$$

which again becomes an exact relation for the physical form factor when $a^{\text{fid}} \rightarrow 0$. The curve

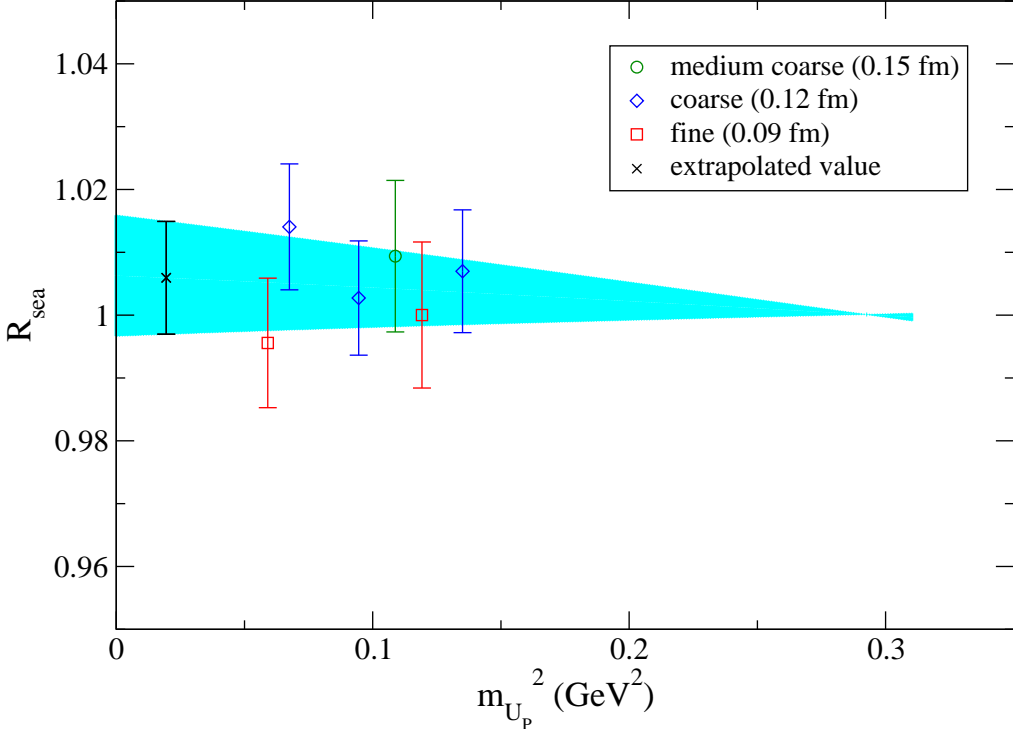


FIG. 7: \mathcal{R}_{sea} ratio versus $m_{U_P}^2$ for all ensembles and lattice spacings. The curve is the fit to all of the lattice data, extrapolated to the continuum. The curve is also extrapolated to the physical strange sea quark mass.

is thus the product of the two continuum extrapolated ratio fits shown in Figures 6 and 7, times the fiducial point, which we take to be $a\hat{m}^{\text{fid}} = 0.0124$ at the fine lattice spacing (the solid square in Figure 8). Because this is a full QCD curve, the valence mass m_x equals the light sea mass \hat{m}' . The other full QCD points are shown as open symbols in Figure 8 for comparison, though the fits were performed on the ratios and normalized by the fiducial point at $a\hat{m}^{\text{fid}} = 0.0124$. Note that the curve is already extrapolated in the strange sea quark mass, and so does not perfectly overlap with the $a\hat{m}^{\text{fid}} = 0.0124$ point. As discussed above, when this quantity is evaluated at $\hat{m}' = \hat{m}$ it yields the value of h_{A_1} at physical quark masses. The cross is the extrapolated value, where the solid line is the statistical error, and the dashed line is the total systematic error added to the statistical error in quadrature.

The low energy constant $g_{DD^*\pi}$ enters the chiral extrapolation formula and determines the size of the cusp near the physical pion mass. Our data do not constrain this constant, so we take a wide range for $g_{DD^*\pi}$ that encompasses the range of values coming from phe-

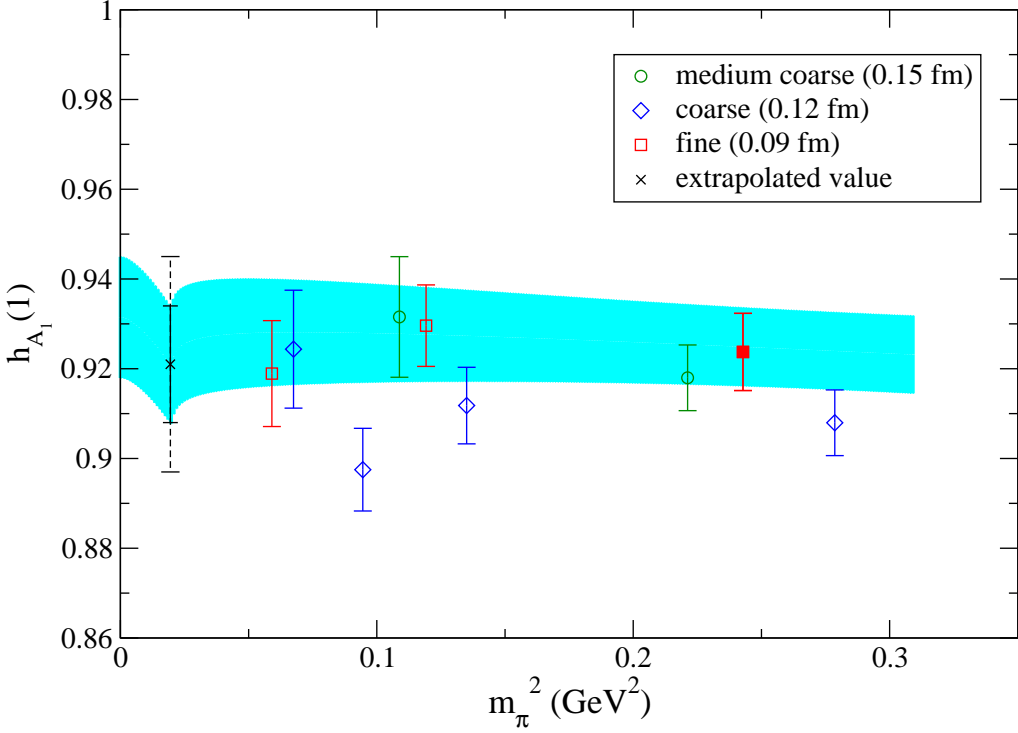


FIG. 8: The full QCD points versus m_π^2 on the three lattice spacings are shown in comparison to the continuum curve. The curve is the product of the two continuum extrapolated ratio fits shown in Figs. (6) and (7), times the fiducial point, which we have chosen to be the $\hat{m}' = 0.0124$ fine lattice point (the filled square). The curve is already extrapolated to the physical strange sea quark mass, and so does not perfectly overlap with the lattice data point at the fiducial value. The cross is the extrapolated value, where the solid line is the statistical error, and the dashed line is the total systematic error added to the statistical error in quadrature.

nomenclature and lattice calculations: fits to a wide range of experimental data prior to the measurement of the D^* width by Stewart ($g_{DD^*\pi} = 0.27^{+0.06}_{-0.03}$ [73]), an update of the Stewart analysis including the D^* width ($g_{DD^*\pi} = 0.51$; no error quoted [74]), quark models ($g_{DD^*\pi} \approx 0.38$ [75]), quenched lattice QCD ($g_{DD^*\pi}^{N_f=0} = 0.67 \pm 0.08^{+0.04}_{-0.06}$ [76]), two flavor lattice QCD in the static limit ($g_{\text{static}}^{N_f=2} = 0.516 \pm 0.051$ [77]), and the measurement of the D^* width ($g_{DD^*\pi} = 0.59 \pm 0.07$ [78]). There are as of yet no 2+1 flavor lattice calculations of $g_{DD^*\pi}$. For this work we take $g_{DD^*\pi} = 0.51 \pm 0.2$, leading to a parametric uncertainty of 0.9% in $h_{A_1}(1)$ that is included as a systematic error.

The additional low energy constants that enter the chiral formulas are the tree-level continuum coefficients μ_0 and f , and the taste-violating parameters that vanish in the continuum. These are the taste splittings, $a^2\Delta_\Xi$ with $\Xi = P, A, T, V, I$, and the taste-violating hairpin-coefficients, $a^2\delta'_A$ and $a^2\delta'_V$. We set f to the experimental value of the pion decay constant, $f_\pi = 0.1307$ GeV, in the coefficient of the NLO logarithms. The pion masses used as inputs in the rS χ PT formulas are computed from the bare quark masses and converted into physical units using

$$m_{xy}^2 = (r_1/r_1^{\text{phys}})^2 \mu_{\text{tree}}(m_x + m_y), \quad (44)$$

where μ_{tree} is obtained from fits to the light pseudo-scalar mass squared to the tree-level form (in r_1 units), $r_1^2 \mu_{\text{tree}}(m_x + m_y)$. This accounts for higher-order chiral corrections and is more accurate than using μ obtained in the chiral limit, giving a better approximation to the pion mass squared at a given light quark mass. Since the parameters in our lattice simulations at different lattice spacings are expressed in r_1 units, we require the physical value of r_1 to convert to physical units and take the physical pion mass and $\Delta^{(c)}$ from experiment. Thus, the $\approx 2.5\%$ uncertainty in r_1^{phys} gives a parametric error in the chiral extrapolation. Because the chiral extrapolation is so mild, however, this error turns out to be negligible compared to other systematic errors. Since we are taking the pion mass from experiment there is a negligible error due to the light quark mass uncertainty in the chiral extrapolation. The strange sea quark mass enters the chiral extrapolation formulas, but the dependence is weak, and the error in the bare strange quark mass leads to a negligible parametric error in h_{A_1} . The taste-splittings Δ_Ξ have been determined in Ref. [16], and their approximately 10% uncertainty also leads to a negligible error in $h_{A_1}(1)$. The taste-violating hairpin coefficients have much larger fractional uncertainties, but these too lead to a negligible uncertainty in $h_{A_1}(1)$. Even setting the rS χ PT parameters to zero does not change our result for $h_{A_1}(1)$ significantly. As mentioned above, our result does not change if we use the continuum χ PT formula in our chiral fits.

In the calculation of the form factor, the tadpole improved coefficient $c_{SW} = 1/u_0^3$ is obtained with u_0 from the Landau link on the coarse lattices, but from the plaquette for u_0 on the fine and coarser lattices. Though unintentional, there is nothing wrong with this, since it is not known *a priori* which provides the best estimate of the tadpole improvement factor. However, the u_0 term for the spectator light (staggered) quark, which appears in the

tadpole improvement of the Asqtad action, was taken from the Landau link on the coarse lattices, even though the sea quark sector used u_0 from the plaquette. On the fine and coarser lattices, u_0 was taken to be the same in the light valence and sea quark sectors. The estimates of u_0 from plaquette versus Landau link differ only by 4% on the coarse lattices.

Although the effect of this mistuning is expected to be small (correcting u_0 would lead to a slightly different valence propagator and different tuned κ values, thus leading to a small modification of the staggered chiral parameters in the valence sector for the coarse lattices used as inputs to the chiral fit), it is possible to study how much difference it makes using the h_{A_1} lattice data. Including all three lattice spacings and using our preferred chiral fit, we find $h_{A_1}(1) = 0.921(13)$ where the error here is statistical only. If we neglect the coarse data points, we find $h_{A_1}(1) = 0.920(17)$, almost unchanged except for a somewhat larger statistical error. We can also examine the ratios \mathcal{R}_{val} and \mathcal{R}_{sea} . In our preferred fit to all the lattice data these are 0.9910(34) and 1.0059(90) respectively, where the errors are again only statistical. If we drop the coarse lattice data, these become 0.9960(56) and 0.999(13) respectively. Since the ratio \mathcal{R}_{sea} has very little valence quark mass dependence, we can combine \mathcal{R}_{sea} from the fit to all of the lattice data with \mathcal{R}_{val} from the fit neglecting the coarse lattice data. This is useful, because \mathcal{R}_{sea} has the larger statistical error, so we would like to use the full lattice data set to determine this ratio, thus isolating the mistuning in the valence sector on the coarse lattices. When this is done we find that the central value of the final $h_{A_1}(1)$ is shifted upward by 0.4%, well within statistical errors and smaller than our other systematic errors. We assign a systematic error of 0.4% due to the u_0 mistuning.

E. Finite volume effects

The finite volume corrections to the integrals which appear in heavy-light χ PT formulas, including those for $B \rightarrow D^*$ were given by Arndt and Lin [79]. There are no new integrals appearing in the staggered case, and it is straightforward to use the results of Arndt and Lin in the rS χ PT for $h_{A_1}(1)$, as shown in Ref. [22]. We find that although the finite volume corrections in $h_{A_1}(1)$ would be large near the cusp at the physical pion mass on the current MILC ensembles (ranging in size from 2.5-3.5 fm), for the less chiral data points at which we have actually simulated, the finite volume effects are negligible. For all data points in our

TABLE IX: $h_{A_1}(1)$ at physical quark masses at different lattice spacings, where taste-violating effects have been removed, or shown to be negligible. Discretization effects due to analytic terms associated with the light quark sector and heavy-quark discretization effects remain in the lattice data.

a (fm)	$h_{A_1}(1)$
0.15	0.914(11)
0.12	0.907(14)
0.09	0.921(13)

simulations the finite volume corrections are less than 1 part in 10^4 . We therefore assign no error due to finite volume effects.

F. Discretization errors

As shown in Ref. [28, 29, 30, 49], the matching of lattice gauge theory to QCD is accomplished by normalizing the first few terms in the heavy-quark expansion. This is done by tuning the kinetic masses of the D_s and B_s mesons computed using the SW action (for the heavy quarks) to the experimental meson masses. Tree-level tadpole-improved perturbation theory is used to tune the coupling c_{SW} and the rotation coefficient d_1 for the bottom and charm quarks. Once this matching is done, the discretization errors in $h_{A_1}(1)$ are of order $\alpha_s(\overline{\Lambda}/2m_Q)^2$ and $(\overline{\Lambda}/2m_Q)^3$ [28], where the powers of two are combinatoric factors. The leading matching uncertainty is of the order $\alpha_s(\overline{\Lambda}/2m_c)^2$. We estimate the size of this error setting $\alpha_s = 0.3$, $\overline{\Lambda} = 500$ MeV, and $m_c = 1.2$ GeV, which gives $\alpha_s(\overline{\Lambda}/2m_c)^2 = 0.013$.

Since we have numerical data at three lattice spacings we are able to study how well the power counting estimate accounts for observed discretization effects. Making use of Eq. (43), but varying the fiducial lattice spacing from our lightest to coarsest lattices, we are able to obtain $h_{A_1}(1)$ at physical quark masses, with discretization effects associated with the staggered chiral logarithms removed in the ratios appearing in Eq. (43). The discretization effects that remain are: taste-violations in $h_{A_1}^{\text{fid}}$, taste violations at higher order than NLO

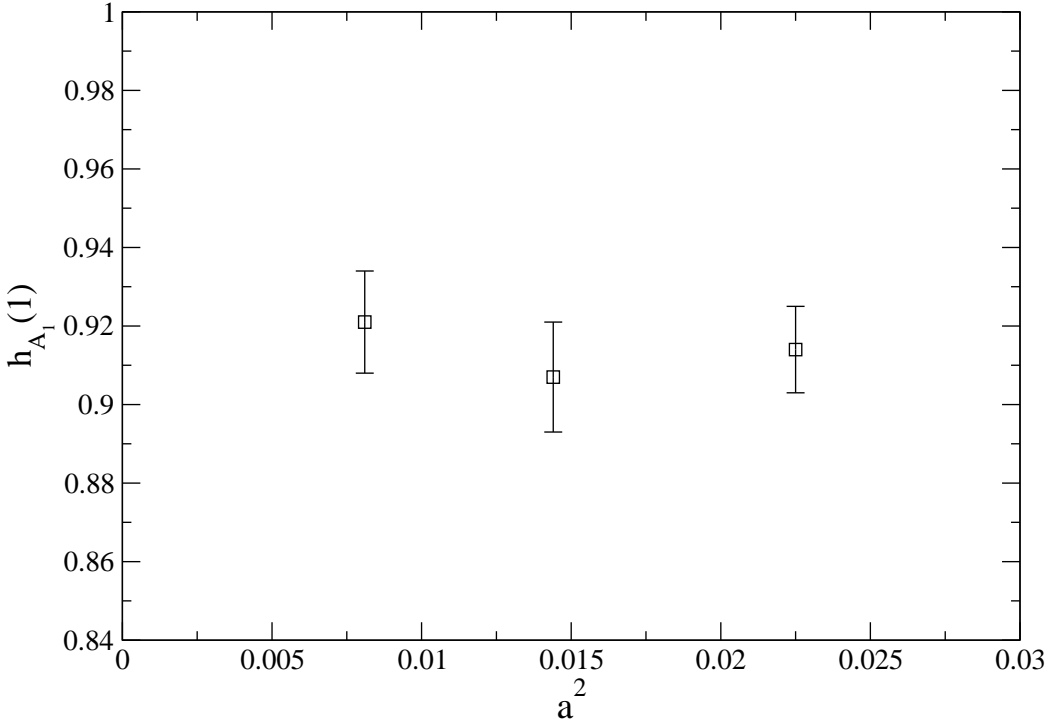


FIG. 9: $h_{A_1}(1)$ at physical quark masses versus a^2 (fm 2) where taste-violating effects have been removed, or shown to be negligible. Discretization effects due to analytic terms associated with the light quark sector and heavy-quark discretization effects remain in the lattice data.

in the ratios, the effect of the analytic term coming from light quark discretization effects (proportional to $\alpha_s a^2$), and the heavy-quark discretization effects. The taste-violations in $h_{A_1}^{\text{fid}}$ and the taste-violations in the ratios appearing at higher order than NLO have been shown to be negligible. We now consider the remaining discretization errors coming from the light quark analytic term and the heavy-quark discretization effects. Table IX presents the results for $h_{A_1}(1)$ as obtained from Eq. (43) and Figure 9 shows them plotted as a function of lattice spacing squared. Although the Fermilab action and currents possess a smooth continuum limit, the MILC ensembles are not yet at small enough a to obtain simply $O(a)$ or $O(a^2)$ behavior. The spread of the lattice data points gives some indication of the size of the remaining discretization effects, however, and we find that the fine (0.09 fm) lattice data point and the coarse (0.12 fm) lattice data point differ by 1.5%. This is similar to our power counting estimate, and we assign the larger of the two, 1.5%, as the systematic error due to residual discretization effects.

G. Summary

Our final result, given the error budget in Table X, is

$$h_{A_1} = 0.921(13)(8)(8)(14)(6)(3)(4), \quad (45)$$

where the errors are statistical, parametric uncertainty in $g_{DD^*\pi}$, chiral extrapolation errors, discretization errors, parametric uncertainty in heavy-quark masses (kappa tuning), perturbative matching, and the u_0 (mis)tuning on the coarse lattices. Adding all systematic errors in quadrature, we obtain

$$h_{A_1}(1) = 0.921(13)(20). \quad (46)$$

This final result differs slightly from that presented at Lattice 2007 [80], where a preliminary $h_{A_1}(1) = 0.924(12)(19)$ was quoted. There are three main changes in the analysis from the preliminary result: our earlier result used a value of α_s in the perturbative matching evaluated at the scale $2/a$, while the present result uses the HLM [64] prescription to fix the scale. This causes a change of 0.1%, well within the estimated systematic error due to the perturbative matching. In the previous result, the fine lattice data was blocked by 4 in the jackknife procedure; we now block by 8 to fully account for autocorrelation errors. This does not change the central value, but increases the statistical error slightly. Finally, we have chosen a value for $g_{DD^*\pi} = 0.51 \pm 0.2$ instead of $g_{DD^*\pi} = 0.45 \pm 0.15$ to be more consistent with the range of values quoted in the literature. This causes a decrease in $h_{A_1}(1)$ of 0.2%.

VIII. CONCLUSIONS

We have introduced a new method to calculate the zero-recoil form factor for the $B \rightarrow D^* \ell \nu$ decay. We include 2+1 flavors of sea quarks in the generation of the gauge ensembles, so the calculation is completely unquenched. We have introduced a new double ratio, which gives the form factor directly, and leads to a large savings in the computational cost. The simulation is performed in a regime where we expect rooted staggered chiral perturbation theory to apply; we therefore use the rS χ PT result for the $B \rightarrow D^*$ form factor [22] to perform the chiral extrapolation and to remove taste-breaking effects. To aid the chiral and continuum extrapolations, we introduced a set of ratios that has allowed us to largely disentangle light

TABLE X: Final error budget for $h_{A_1}(1)$ where each error is discussed in the text. Systematic errors are added in quadrature and combined in quadrature with the statistical error to obtain the total error.

Uncertainty	$h_{A_1}(1)$
Statistics	1.4%
$g_{DD^*\pi}$	0.9%
NLO vs NNLO χ PT fits	0.9%
Discretization errors	1.5%
Kappa tuning	0.7%
Perturbation theory	0.3%
u_0 tuning	0.4%
Total	2.6%

and heavy-quark discretization effects. Our new result, $\mathcal{F}(1) = h_{A_1}(1) = 0.921(13)(20)$ is consistent with the previous quenched result, $\mathcal{F}(1) = 0.913^{+0.029}_{-0.034}$ [13], but our errors are both smaller and under better theoretical control. This result allows us to extract $|V_{cb}|$ from the experimental measurement of the $B \rightarrow D^* \ell \nu$ form factor, which determines $\mathcal{F}(1)|V_{cb}|$. After applying a 0.7% electromagnetic correction to our value for $\mathcal{F}(1)$ [81], and taking the most recent PDG average for $|V_{cb}|\mathcal{F}(1) = (35.9 \pm 0.8) \times 10^{-3}$ [82], we find

$$|V_{cb}| = (38.7 \pm 0.9_{\text{exp}} \pm 1.0_{\text{theo}}) \times 10^{-3}. \quad (47)$$

This differs by about 2σ from the inclusive determination $|V_{cb}| = (41.6 \pm 0.6) \times 10^{-3}$ [82]. Our new value supersedes the previous Fermilab quenched number [13], as it should other quenched numbers such as that in Ref. [83]³.

Our largest error in $\mathcal{F}(1)$ is the systematic error due to heavy-quark discretization effects, which we have estimated using HQET power counting and inspection of the numerical data at three lattice spacings. This error can be reduced by going to finer lattice spacings, or by using an improved Fermilab action [70]. When using this improved action, it would be

³ Ref. [83] calculates the $B \rightarrow D^* \ell \nu$ form factor in the quenched approximation at zero and non-zero recoil momentum and uses a step-scaling method [84] to control the heavy-quark discretization errors.

necessary to improve the currents to the same order. We have introduced a method for separating the heavy and light-quark discretization errors, where the physical h_{A_1} can be factorized into two factors, $h_{A_1}^{\text{fid}} \times \mathcal{R}_{\text{fid}}$, such that the heavy quark discretization errors are largely isolated in $h_{A_1}^{\text{fid}}$. Combining our value of $\mathcal{R}_{\text{fid}} = 0.997(10)(13)$ (where the first error is statistical, and the second is due to systematics that do not cancel in the ratio) with a determination of $h_{A_1}^{\text{fid}}$ at finer lattice spacings and/or with an improved action would be a cost-effective way of reducing the heavy-quark discretization errors. The next largest error in our calculation of $\mathcal{F}(1)$ is statistical, and this error drives many of the systematic errors. This is mostly a matter of computing. It would also be desirable to perform the matching of the heavy-quark current to higher order in perturbation theory, or by using non-perturbative matching. With these improvements, it would be possible to bring the error in $\mathcal{F}(1)$ to or below 1%, allowing a very precise determination of $|V_{cb}|$ from exclusive semi-leptonic decays.

Acknowledgments

We thank Jon Bailey for a careful reading of the manuscript. Computations for this work were carried out in part on facilities of the USQCD Collaboration, which are funded by the Office of Science of the U.S. Department of Energy; and on facilities of the NSF Teragrid under allocation TG-MCA93S002. This work was supported in part by the United States Department of Energy under Grant Nos. DE-FC02-06ER41446 (C.D., L.L.), DE-FG02-91ER40661(S.G.), DE-FG02-91ER40677 (A.X.K.), DE-FG02-91ER40628 (C.B., J.L.), DE-FG02-04ER41298 (D.T.) and by the National Science Foundation under Grant Nos. PHY-0555243, PHY-0757333, PHY-0703296 (C.D., L.L.), PHY-0555235 (J.L.), PHY-0456556 (R.S.). R.T.E. and E.G. thank Fermilab and URA for their hospitality. Fermilab is operated by Fermi Research Alliance, LLC, under Contract No. DE-AC02-07CH11359 with the United States Department of Energy.

APPENDIX A: CHIRAL PERTURBATION THEORY

Eq. (34) of Ref. [22] gives the expression needed for $h_{A_1}(1)$ in partially-quenched χ PT with degenerate up and down quark masses (the 2+1 case) in the rooted staggered theory:

$$\begin{aligned}
h_{A_1}^{(B_x)PQ,2+1}(1)/\eta_A = & 1 + X_A(\Lambda_\chi) + \frac{g_{DD^*\pi}^2}{48\pi^2 f^2} \left\{ \frac{1}{16} \sum_{\substack{j=xu,xu,xs \\ \Xi=I,P,4V,4A,6T}} \overline{F}_{j\Xi} \right. \\
& + \frac{1}{3} \left[R_{X_I}^{[2,2]}(\{M_{X_I}^{(5)}\}; \{\mu_I\}) \left(\frac{d\overline{F}_{X_I}}{dm_{X_I}^2} \right) - \sum_{j \in \{M_I^{(5)}\}} D_{j,X_I}^{[2,2]}(\{M_{X_I}^{(5)}\}; \{\mu_I\}) \overline{F}_j \right] \\
& + a^2 \delta'_V \left[R_{X_V}^{[3,2]}(\{M_{X_V}^{(7)}\}; \{\mu_V\}) \left(\frac{d\overline{F}_{X_V}}{dm_{X_V}^2} \right) - \sum_{j \in \{M_V^{(7)}\}} D_{j,X_V}^{[3,2]}(\{M_{X_V}^{(7)}\}; \{\mu_V\}) \overline{F}_j \right] \\
& \left. + (V \rightarrow A) \right\}, \tag{A1}
\end{aligned}$$

where

$$\begin{aligned}
F(m_j, z_j) = & \frac{m_j^2}{z_j} \left\{ z_j^3 \ln \frac{m_j^2}{\Lambda_\chi^2} + \frac{1}{3} z_j^3 - 4z_j + 2\pi \right. \\
& - \sqrt{z_j^2 - 1} (z_j^2 + 2) \left(\ln \left[1 - 2z_j(z_j - \sqrt{z_j^2 - 1}) \right] - i\pi \right) \Big\} \\
\longrightarrow & (\Delta^{(c)})^2 \ln \left(\frac{m_j^2}{\Lambda_\chi^2} \right) + \mathcal{O}[(\Delta^{(c)})^3], \tag{A2}
\end{aligned}$$

with $\overline{F}(m_j, z_j) = F(m_j, -z_j)$, and $z_j = \Delta^{(c)}/m_j$, where $\Delta^{(c)}$ is the D - D^* mass splitting. The residues $R_j^{[n,k]}$ and $D_{j,i}^{[n,k]}$ are defined in Refs. [18, 19], and for completeness we quote them here:

$$\begin{aligned}
R_j^{[n,k]}(\{M\}, \{\mu\}) & \equiv \frac{\prod_{a=1}^k (\mu_a^2 - m_j^2)}{\prod_{i \neq j} (m_i^2 - m_j^2)}, \\
D_{j,l}^{[n,k]}(\{M\}, \{\mu\}) & \equiv -\frac{d}{dm_l^2} R_j^{[n,k]}(\{M\}, \{\mu\}). \tag{A3}
\end{aligned}$$

These residues are a function of two sets of masses, the numerator masses, $\{M\} = \{m_1, m_2, \dots, m_n\}$ and the denominator masses, $\{\mu\} = \{\mu_1, \mu_2, \dots, \mu_k\}$. In our 2+1 flavor case, we have

$$\begin{aligned}
\{M_X^{(5)}\} & \equiv \{m_\eta, m_X\}, \\
\{M_X^{(7)}\} & \equiv \{m_\eta, m_{\eta'}, m_X\}, \\
\{\mu\} & \equiv \{m_U, m_S\}. \tag{A4}
\end{aligned}$$

The masses m_{η_I} , m_{η_V} , $m_{\eta'_V}$ are given by [18]

$$\begin{aligned} m_{\eta_I}^2 &= \frac{m_{U_I}^2}{3} + \frac{2m_{S_I}^2}{3}, \\ m_{\eta_V}^2 &= \frac{1}{2} \left(m_{U_V}^2 + m_{S_V}^2 + \frac{3}{4}a^2\delta'_V - Z \right), \\ m_{\eta'_V}^2 &= \frac{1}{2} \left(m_{U_V}^2 + m_{S_V}^2 + \frac{3}{4}a^2\delta'_V + Z \right), \\ Z &\equiv \sqrt{(m_{S_V}^2 - m_{U_V}^2)^2 - \frac{a^2\delta'_V}{2}(m_{S_V}^2 - m_{U_V}^2) + \frac{9(a^2\delta'_V)^2}{16}}. \end{aligned} \quad (\text{A5})$$

The ratio $R_{\text{val}}^{\text{NLO}}$ in the continuum through NLO in χ PT is

$$\begin{aligned} \mathcal{R}_{\text{val}}^{\text{NLO}} &= 1 + \frac{g_{DD^*\pi}^2}{48\pi^2 f^2} \left\{ \sum_{j=u,d,s} \overline{F}_{xj} + \frac{1}{3} \left[R_X^{[2,2]}(\{M_X^{(5)}\}; \{\mu\}) \left(\frac{d\overline{F}_X}{dm_X^2} \right) \right. \right. \\ &\quad \left. \left. - \sum_{j \in \{M_X^{(5)}\}} D_{j,X}^{[2,2]}(\{M_X^{(5)}\}; \{\mu\}) \overline{F}_j \right] - \sum_{j=u,d,s} \overline{F}_{x'j} \right. \\ &\quad \left. - \frac{1}{3} \left[R_{X'}^{[2,2]}(\{M_{X'}^{(5)}\}; \{\mu\}) \left(\frac{d\overline{F}_{X'}}{dm_{X'}^2} \right) - \sum_{j \in \{M_{X'}^{(5)}\}} D_{j,X'}^{[2,2]}(\{M_{X'}^{(5)}\}; \{\mu\}) \overline{F}_j \right] \right\}, \end{aligned} \quad (\text{A6})$$

where

$$\{M_{X'}^{(5)}\} \equiv \{m_\eta, m_{X'}\}, \quad (\text{A7})$$

and where $m_{X'}$ is a valence pion made of two quarks set to the fiducial valence quark mass, and the subscript x' refers to a valence quark at the fiducial mass. This ratio is one by construction when the valence quark mass equals the fiducial valence quark mass.

- [1] E. Barberio *et al.* (Heavy Flavor Averaging Group (HFAG)) (2007), arXiv:0704.3575 [hep-ex].
- [2] E. Gamiz *et al.* (HPQCD) (2006), hep-lat/0603023.
- [3] T. Bae, J. Kim, and W. Lee, PoS **LAT2005**, 335 (2006), hep-lat/0510008.
- [4] D. J. Antonio *et al.* (RBC) (0200), hep-ph/0702042.
- [5] C. Aubin, J. Laiho, and R. S. Van de Water, PoS **LAT2007**, 375 (2007), arXiv:0710.1121.
- [6] J. Chay, H. Georgi, and B. Grinstein, Phys. Lett. **B247**, 399 (1990).
- [7] I. I. Y. Bigi, N. G. Uraltsev, and A. I. Vainshtein, Phys. Lett. **B293**, 430 (1992), hep-ph/9207214.

- [8] I. I. Y. Bigi, B. Blok, M. A. Shifman, N. G. Uraltsev, and A. I. Vainshtein (1992), hep-ph/9212227.
- [9] I. I. Y. Bigi, M. A. Shifman, N. G. Uraltsev, and A. I. Vainshtein, Phys. Rev. Lett. **71**, 496 (1993), hep-ph/9304225.
- [10] I. I. Y. Bigi, M. A. Shifman, and N. Uraltsev, Ann. Rev. Nucl. Part. Sci. **47**, 591 (1997), hep-ph/9703290.
- [11] O. Büchmuller and H. Flächer, Phys. Rev. **D73**, 073008 (2006), hep-ph/0507253.
- [12] C. W. Bauer, Z. Ligeti, M. Luke, A. V. Manohar, and M. Trott, Phys. Rev. **D70**, 094017 (2004), hep-ph/0408002.
- [13] S. Hashimoto, A. S. Kronfeld, P. B. Mackenzie, S. M. Ryan, and J. N. Simone, Phys. Rev. **D66**, 014503 (2002), hep-ph/0110253.
- [14] C. W. Bernard *et al.*, Phys. Rev. **D64**, 054506 (2001), hep-lat/0104002.
- [15] C. Aubin *et al.*, Phys. Rev. **D70**, 094505 (2004), hep-lat/0402030.
- [16] C. Aubin *et al.* (MILC), Phys. Rev. **D70**, 114501 (2004), hep-lat/0407028.
- [17] W.-J. Lee and S. R. Sharpe, Phys. Rev. **D60**, 114503 (1999), hep-lat/9905023.
- [18] C. Aubin and C. Bernard, Phys. Rev. **D68**, 034014 (2003), hep-lat/0304014.
- [19] C. Aubin and C. Bernard, Phys. Rev. **D68**, 074011 (2003), hep-lat/0306026.
- [20] S. R. Sharpe and R. S. Van de Water, Phys. Rev. **D71**, 114505 (2005), hep-lat/0409018.
- [21] C. Aubin and C. Bernard, Nucl. Phys. Proc. Suppl. **140**, 491 (2005), hep-lat/0409027.
- [22] J. Laiho and R. S. Van de Water, Phys. Rev. **D73**, 054501 (2006), hep-lat/0512007.
- [23] A. F. Falk and M. Neubert, Phys. Rev. **D47**, 2965 (1993), hep-ph/9209268.
- [24] T. Mannel, Phys. Rev. **D50**, 428 (1994), hep-ph/9403249.
- [25] A. Czarnecki, Phys. Rev. Lett. **76**, 4124 (1996), hep-ph/9603261.
- [26] A. Czarnecki and K. Melnikov, Nucl. Phys. **B505**, 65 (1997), hep-ph/9703277.
- [27] M. E. Luke, Phys. Lett. **B252**, 447 (1990).
- [28] A. S. Kronfeld, Phys. Rev. **D62**, 014505 (2000), hep-lat/0002008.
- [29] J. Harada *et al.*, Phys. Rev. **D65**, 094513 (2002), hep-lat/0112044.
- [30] J. Harada, S. Hashimoto, A. S. Kronfeld, and T. Onogi, Phys. Rev. **D65**, 094514 (2002), hep-lat/0112045.
- [31] S. Prelovsek, Phys. Rev. **D73**, 014506 (2006), hep-lat/0510080.

- [32] C. W. Bernard, C. E. DeTar, Z. Fu, and S. Prelovsek, PoS **LAT2006**, 173 (2006), hep-lat/0610031.
- [33] C. Bernard, Phys. Rev. **D73**, 114503 (2006), hep-lat/0603011.
- [34] C. Bernard, C. E. Detar, Z. Fu, and S. Prelovsek, Phys. Rev. **D76**, 094504 (2007), arXiv:0707.2402.
- [35] C. Aubin, J. Laiho, and R. S. Van de Water, Phys. Rev. **D77**, 114501 (2008), arXiv:0803.0129.
- [36] C. Bernard, M. Golterman, and Y. Shamir, Phys. Rev. **D73**, 114511 (2006), hep-lat/0604017.
- [37] Y. Shamir, Phys. Rev. **D75**, 054503 (2007), hep-lat/0607007.
- [38] Y. Shamir, Phys. Rev. **D71**, 034509 (2005), hep-lat/0412014.
- [39] S. Dürr, PoS **LAT2005**, 021 (2005), hep-lat/0509026.
- [40] S. R. Sharpe, PoS **LAT2006**, 022 (2006), hep-lat/0610094.
- [41] A. S. Kronfeld, PoS **LAT2007**, 016 (2007), arXiv:0711.0699.
- [42] T. Blum *et al.*, Phys. Rev. **D55**, 1133 (1997), hep-lat/9609036.
- [43] K. Orginos and D. Toussaint (MILC), Phys. Rev. **D59**, 014501 (1999), hep-lat/9805009.
- [44] J. F. Lagae and D. K. Sinclair, Phys. Rev. **D59**, 014511 (1999), hep-lat/9806014.
- [45] G. P. Lepage, Phys. Rev. **D59**, 074502 (1999), hep-lat/9809157.
- [46] K. Orginos, D. Toussaint, and R. L. Sugar (MILC), Phys. Rev. **D60**, 054503 (1999), hep-lat/9903032.
- [47] C. W. Bernard *et al.* (MILC), Phys. Rev. **D61**, 111502 (2000), hep-lat/9912018.
- [48] B. Sheikholeslami and R. Wohlert, Nucl. Phys. **B259**, 572 (1985).
- [49] A. X. El-Khadra, A. S. Kronfeld, and P. B. Mackenzie, Phys. Rev. **D55**, 3933 (1997), hep-lat/9604004.
- [50] G. P. Lepage and P. B. Mackenzie, Phys. Rev. **D48**, 2250 (1993), hep-lat/9209022.
- [51] R. Sommer, Nucl. Phys. **B411**, 839 (1994), hep-lat/9310022.
- [52] C. W. Bernard *et al.* (MILC), Phys. Rev. **D62**, 034503 (2000), hep-lat/0002028.
- [53] A. Gray *et al.* (HPQCD), Phys. Rev. Lett. **95**, 212001 (2005), hep-lat/0507015.
- [54] C. Bernard (MILC), PoS **LAT2007**, 090 (2007), arXiv:0710.1118 [hep-lat].
- [55] C. Bernard *et al.* (MILC), PoS **LAT2005**, 025 (2006), hep-lat/0509137.
- [56] M. Wingate, J. Shigemitsu, C. T. Davies, G. P. Lepage, and H. D. Trottier, Phys. Rev. **D67**, 054505 (2003), hep-lat/0211014.

- [57] M. Okamoto *et al.*, Nucl. Phys. Proc. Suppl. **140**, 461 (2005), hep-lat/0409116.
- [58] C. Aubin *et al.* (Fermilab Lattice), Phys. Rev. Lett. **94**, 011601 (2005), hep-ph/0408306.
- [59] C. Aubin *et al.*, Phys. Rev. Lett. **95**, 122002 (2005), hep-lat/0506030.
- [60] E. Dalgic *et al.*, Phys. Rev. **D73**, 074502 (2006), hep-lat/0601021.
- [61] R. T. Evans, A. X. El-Khadra, and M. Di Pierro (Fermilab Lattice and MILC), PoS **LAT2006**, 081 (2006).
- [62] S. J. Brodsky, G. P. Lepage, and P. B. Mackenzie, Phys. Rev. **D28**, 228 (1983).
- [63] Q. Mason *et al.* (HPQCD), Phys. Rev. Lett. **95**, 052002 (2005), hep-lat/0503005.
- [64] K. Hornbostel, G. P. Lepage, and C. Morningstar, Phys. Rev. **D67**, 034023 (2003), hep-ph/0208224.
- [65] A. X. El-Khadra, E. Gamiz, A. S. Kronfeld, and M. A. Nobes, PoS **LAT2007**, 242 (2007), 0710.1437.
- [66] A. X. El-Khadra, E. Gamiz, A. S. Kronfeld, and M. A. Nobes (2008), in preparation.
- [67] G. P. Lepage, J. Comput. Phys. **27**, 192 (1978).
- [68] C. Aubin and C. Bernard, Phys. Rev. **D73**, 014515 (2006), hep-lat/0510088.
- [69] C. Bernard, M. Golterman, and Y. Shamir, Phys. Rev. **D77**, 074505 (2008), arXiv:0712.2560.
- [70] M. B. Oktay and A. S. Kronfeld (2008), arXiv:0803.0523.
- [71] E. Follana *et al.* (HPQCD), Phys. Rev. **D75**, 054502 (2007), hep-lat/0610092.
- [72] A. S. Kronfeld, Nucl. Phys. Proc. Suppl. **53**, 401 (1997), hep-lat/9608139.
- [73] I. W. Stewart, Nucl. Phys. **B529**, 62 (1998), hep-ph/9803227.
- [74] M. C. Arnesen, B. Grinstein, I. Z. Rothstein, and I. W. Stewart, Phys. Rev. Lett. **95**, 071802 (2005), hep-ph/0504209.
- [75] R. Casalbuoni *et al.*, Phys. Rept. **281**, 145 (1997), hep-ph/9605342.
- [76] A. Abada *et al.*, Nucl. Phys. Proc. Suppl. **119**, 641 (2003), hep-lat/0209092.
- [77] H. Ohki, H. Matsufuru, and T. Onogi (2008), arXiv:0802.1563 [hep-lat].
- [78] A. Anastassov *et al.* (CLEO), Phys. Rev. **D65**, 032003 (2002), hep-ex/0108043.
- [79] D. Arndt and C. J. D. Lin, Phys. Rev. **D70**, 014503 (2004), hep-lat/0403012.
- [80] J. Laiho (Fermilab Lattice and MILC), PoS **LAT2007**, 358 (2007), arXiv:0710.1111.
- [81] A. Sirlin, Nucl. Phys. **B196**, 83 (1982).
- [82] C. Amsler *et al.* (Particle Data Group), Phys. Lett. **B667**, 1 (2008).

- [83] G. M. de Divitiis, R. Petronzio, and N. Tantalo (2008), 0807.2944.
- [84] M. Guagnelli, F. Palombi, R. Petronzio, and N. Tantalo, Phys. Lett. **B546**, 237 (2002), hep-lat/0206023.

The $B \rightarrow \pi \ell \nu$ semileptonic form factor from three-flavor lattice QCD: A model-independent determination of $|V_{ub}|$

Jon A. Bailey,¹ C. Bernard,² C. DeTar,³ M. Di Pierro,⁴ A.X. El-Khadra,⁵
 R.T. Evans,⁵ E. D. Freeland,⁶ E. Gamiz,⁵ Steven Gottlieb,⁷ U.M. Heller,⁸
 J.E. Hetrick,⁹ A.S. Kronfeld,¹ J. Laiho,² L. Levkova,³ P.B. Mackenzie,¹
 M. Okamoto,¹ J. N. Simone,¹ R. Sugar,¹⁰ D. Toussaint,¹¹ and R.S. Van de Water^{1,*}

(Fermilab Lattice and MILC Collaborations)

¹*Fermi National Accelerator Laboratory, Batavia, Illinois, USA*

²*Department of Physics, Washington University, St. Louis, Missouri, USA*

³*Physics Department, University of Utah, Salt Lake City, Utah, USA*

⁴*School of Computer Sci., Telecom. and Info. Systems,
DePaul University, Chicago, Illinois, USA*

⁵*Physics Department, University of Illinois, Urbana, Illinois, USA*

⁶*Liberal Arts Department, The School of the Art Institute of Chicago, Chicago, Illinois, USA*

⁷*Department of Physics, Indiana University, Bloomington, Indiana, USA*

⁸*American Physical Society, One Research Road, Ridge, New York, USA*

⁹*Physics Department, University of the Pacific, Stockton, California, USA*

¹⁰*Department of Physics, University of California, Santa Barbara, California, USA*

¹¹*Department of Physics, University of Arizona, Tucson, Arizona, USA*

(Dated: February 24, 2009)

Abstract

We calculate the form factor $f_+(q^2)$ for B -meson semileptonic decay in unquenched lattice QCD with 2+1 flavors of light sea quarks. We use Asqtad-improved staggered light quarks and a Fermilab bottom quark on gauge configurations generated by the MILC Collaboration. We simulate with several light quark masses and at two lattice spacings, and extrapolate to the physical quark mass and continuum limit using heavy-light meson staggered chiral perturbation theory. We then fit the lattice result for $f_+(q^2)$ simultaneously with that measured by the BABAR experiment using a parameterization of the form factor shape in q^2 which relies only on analyticity and unitarity in order to determine the CKM matrix element $|V_{ub}|$. This approach reduces the total uncertainty in $|V_{ub}|$ by combining the lattice and experimental information in an optimal, model-independent manner. We find a value of $|V_{ub}| \times 10^3 = 3.38 \pm 0.36$.

PACS numbers: 12.15.Hh, 12.38.Gc, 13.20.He

*ruthv@bnl.gov

I. INTRODUCTION

The semileptonic decay $B \rightarrow \pi \ell \nu$ is a sensitive probe of the heavy-to-light quark-flavor changing $b \rightarrow u$ transition. When combined with an experimental measurement of the differential decay rate, a precise QCD determination of the $B \rightarrow \pi \ell \nu$ form factor allows a clean determination of the Cabibbo-Kobayashi-Maskawa (CKM) matrix element $|V_{ub}|$ with all sources of systematic uncertainty under control. In the Standard Model, the differential decay rate for this process is

$$\frac{d\Gamma(B \rightarrow \pi \ell \nu)}{dq^2} = \frac{G_F^2 |V_{ub}|^2}{192\pi^3 m_B^3} \left[(m_B^2 + m_\pi^2 - q^2)^2 - 4m_B^2 m_\pi^2 \right]^{3/2} |f_+(q^2)|^2, \quad (1)$$

where $q \equiv p_B - p_\pi$ is the momentum transferred from the B -meson to the outgoing leptons. The form factor, $f_+(q^2)$, parameterizes the hadronic contribution to the weak decay, and must be calculated nonperturbatively from first principles using lattice QCD.

A precise knowledge of CKM matrix elements such as $|V_{ub}|$ is important not only because they are fundamental parameters of the Standard Model, but because inconsistencies between independent determinations of the CKM matrix elements and CP -violating phase would provide evidence for new physics. Although the Standard Model has been amazingly successful in describing the outcome of most particle physics experiments to date, it cannot account for gravity, dark matter and dark energy, or the large matter-antimatter asymmetry of the universe. Thus we know that it is incomplete, and expect new physics to affect the quark-flavor sector to some degree, although we do not know *a priori* what experimental and theoretical precision will be needed to observe it.

The determination of $|V_{ub}|$ from $B \rightarrow \pi \ell \nu$ semileptonic decay relies upon the assumption that, because the leading Standard Model decay amplitude is mediated by tree-level W -boson exchange, it will not be significantly affected by new physics at the current level of achievable precision. Recently, however, hints of new physics have appeared in various regions of the heavy-quark flavor sector such as CP -asymmetries in $B \rightarrow K\pi$ [1], constraints on $\sin(2\beta)$ from $\Delta F = 2$ neutral meson mixing and 1-loop penguin-induced decays [2], and the phase of the B_s -mixing amplitude [3–5]. The unexpected inconsistency most relevant to our new lattice QCD calculation of the $B \rightarrow \pi \ell \nu$ form factor and $|V_{ub}|$ is the current “ f_{D_s} puzzle” [6]. The HPQCD Collaboration’s lattice QCD calculation of the D_s -meson leptonic decay constant f_{D_s} [7] disagrees with the latest results from the Belle, BABAR, and CLEO experiments [8–12] at the 3σ level, although HPQCD’s determinations of the

masses m_{D^+} and m_{D_s} and the decay constants f_π , f_K , and f_{D^+} all agree quite well with experimental measurements [13, 14]. Furthermore, because the significance of the discrepancy is dominated by the statistical experimental uncertainties, it cannot easily be explained by an underestimate of the theoretical uncertainties. Additional lattice QCD calculations of f_{D_s} are needed to either confirm or reduce the inconsistency. If the disagreement holds up, however, it is evidence for a large new physics contribution to a tree-level Standard Model process at the few percent-level. Therefore, although $B \rightarrow \pi\ell\nu$ semileptonic decay provides a theoretically clean method for determining $|V_{ub}|$ within the framework of the Standard Model, we should keep in mind that new physics could appear in $b \rightarrow u$ transitions.

Understanding and controlling all sources of systematic uncertainty in lattice QCD calculations of hadronic weak matrix elements is essential in order to allow accurate determinations of Standard Model parameters and reliable searches for new physics. The hadronic amplitudes for $B \rightarrow \pi\ell\nu$, in particular, can be calculated accurately using current lattice QCD methods because the decay process is “gold plated”, i.e., there is only a single stable hadron in both the initial and final states. Lattice calculations with staggered quarks allow for realistic QCD simulations with dynamical quarks as light as $m_s/10$, multiple lattice spacings, large physical volumes, and high statistics. The resulting simulations of many light-light and heavy-light meson quantities with dynamical staggered quarks are in excellent numerical agreement with experimental results [15]. This includes both postdictions, such as the pion decay constant [16], and predictions, as in the case of the B_c meson mass [17]. Such successes show that the systematic uncertainties in these lattice QCD calculations are under control, and give confidence that additional calculations using the same methods are reliable.

The publicly available MILC gauge configurations with three flavors of improved staggered quarks [18] that have enabled these precise lattice calculations make use of the “fourth-root” procedure for removing the undesired four-fold degeneracy of staggered lattice fermions. Although this procedure has not been rigorously proven correct, Shamir uses plausible assumptions to argue that the continuum limit of the rooted theory is in the same universality class as QCD [19, 20]. The rooting procedure leads to violations of unitarity that vanish in the continuum limit; both theoretical arguments [21, 22] and numerical simulations [23–25], however, show that the unitarity-violating lattice artifacts in the pseudo-

Goldstone boson sector can be described and hence removed using rooted Staggered Chiral Perturbation Theory (rS χ PT), the low-energy effective description of the rooted staggered lattice theory [26–28]. Given the wealth of numerical and analytical evidence supporting the validity of the rooting procedure, most of which is reviewed in Refs. [29–31], we work under the plausible assumption that the continuum limit of the rooted staggered theory is QCD. We note, however, that it is important to have crosschecks of lattice calculations of phenomenologically-important quantities using a variety of fermion formulations, since they all have different sources of systematic uncertainty.

Both existing unquenched lattice calculations of the $B \rightarrow \pi\ell\nu$ form factor use the MILC configurations. When combined with the Heavy Flavor Averaging Group’s latest determination of the experimental decay rate from ICHEP 2008 [32], they yield the following values for $|V_{ub}|$:

$$|V_{ub}| \times 10^3 = 3.40 \pm 0.20^{+0.59}_{-0.39} \quad \text{HPQCD [33]}, \quad (2)$$

$$|V_{ub}| \times 10^3 = 3.62 \pm 0.22^{+0.63}_{-0.41} \quad \text{Fermilab-MILC [34]}, \quad (3)$$

where the errors are experimental and theoretical, respectively. Both analyses primarily rely upon data generated at a “coarse” lattice spacing of $a \approx 0.12$ fm, and use a smaller amount of “fine” data at $a \approx 0.09$ fm to check the estimate of discretization errors. Neither is therefore able to extrapolate the $B \rightarrow \pi\ell\nu$ form factor to the continuum ($a \rightarrow 0$). The most significant difference in the two calculations is their use of different lattice formulations for the bottom quarks. The HPQCD Collaboration [33] uses nonrelativistic (NRQCD) heavy quarks [35], whereas we use relativistic clover quarks with the Fermilab interpretation [36] via heavy quark effective theory (HQET) [37–39]. Both methods work quite well for heavy bottom quarks. The Fermilab treatment, however, has the advantage that it can also be applied to charm quarks; we can therefore use the same method for other semileptonic form factors such as $D \rightarrow \pi\ell\nu$, $D \rightarrow K\ell\nu$, and $B \rightarrow D^*\ell\nu$ [40, 41]. The two unquenched lattice calculations of the $B \rightarrow \pi\ell\nu$ form factor, which have largely independent sources of systematic uncertainty, nevertheless lead to consistent values of $|V_{ub}|$ with similar total errors of $\sim 15\%$.

In this paper we present a new *model-independent* unquenched lattice QCD calculation of the $B \rightarrow \pi\ell\nu$ semileptonic form factor and $|V_{ub}|$. Our work builds upon the previous

Fermilab-MILC calculation and improves upon it in several ways. We now include data on both the coarse and fine MILC lattices, and can therefore take the $a \rightarrow 0$ limit of our data which is generated at nonzero lattice spacing. We also have additional statistics on a subset of the coarse ensembles. The most important improvements, however, are in the analysis procedures.

We have removed all model-dependent assumptions about the shape in q^2 of the form factor from the current analysis. Our result is therefore theoretically cleaner and more reliable than those of previous lattice QCD calculations. The first refinement over previous unquenched lattice $B \rightarrow \pi\ell\nu$ form factor calculations is in the treatment of the chiral and continuum extrapolations. We simultaneously extrapolate to physical quark masses and zero lattice spacing and interpolate in the momentum transfer q^2 by performing a single fit to our entire data set (all values of m_q , a , and q^2) guided by functional forms derived in heavy-light meson staggered chiral perturbation theory (HMS χ PT) [42]. We thereby extract the physical form factor $f_+(q^2)$ in a controlled manner without introducing a particular ansatz for the form factor's q^2 dependence. The second refinement over previous unquenched $B \rightarrow \pi\ell\nu$ lattice form factor calculations is in the combination of the lattice form factor result and experimental data for the decay rate to determine the CKM matrix element $|V_{ub}|$. We fit our lattice numerical Monte Carlo data and the 12-bin BABAR experimental data [43] together to the model-independent “z-expansion” of the form factor given in Ref. [44], in which the form factor is described by a power series in a small quantity z with the sum of the squares of the series coefficients bounded by unitarity constraints. We leave the relative normalization factor, $|V_{ub}|$, as a free parameter to be determined by the fit, thereby extracting $|V_{ub}|$ in an optimal, model-independent way. Others have also fit lattice and experimental results together using different, equally-valid, parameterizations [45, 46]. This work, however, is the first to use the full correlation matrices, derived directly from the data, for both the lattice calculation and experimental measurement.

This paper is organized as follows. In Sec. II we describe the details of our numerical simulations. We discuss the gluon, light-quark, and heavy-quark lattice actions, and present the parameters used, such as the quark masses and lattice spacings. We then define the matrix elements needed to calculate the semileptonic form factors and discuss the method for matching the lattice heavy-light current to the continuum. Next we describe our analysis for

determining the form factors in Sec. III. This is a three-step procedure. We first fit pion and B -meson 2-point correlation functions to extract the meson masses. We then fit the $B \rightarrow \pi$ 3-point function, using the masses and amplitudes from the 2-point fits as input, to extract the lattice form factors at each value of the light quark mass and lattice spacing. Finally, we extrapolate the results at unphysical quark masses and nonzero lattice spacing to the physical light quark masses and zero lattice spacing using $\text{HMS}\chi\text{PT}$. In Sec. IV we estimate the contributions of the various systematic uncertainties to the form factors, discussing each item in the error budget separately. We then present the final result for $f_+(q^2)$ with a detailed breakdown of the error by source in each q^2 bin. We combine our result for the form factor with experimental data from the BABAR Collaboration to determine the CKM matrix element $|V_{ub}|$ in Sec. V. We also define the model-independent description of the form factor shape that we use in the fit and discuss alternative parameterizations of the form factor. Finally, in Sec. VI we compare our results with those of previous unquenched lattice calculations. We also compare our determination of $|V_{ub}|$ with inclusive determinations and to the preferred values from the global CKM unitarity triangle analysis. We conclude by discussing the prospects for improvements in our calculation and its impact on searches for new physics in the quark flavor sector.

II. LATTICE CALCULATION

In this section we describe the details of our numerical lattice simulations. We first present the actions and parameters used for the light (up, down, strange) and heavy (bottom) quarks in Sec. II A. We then define the procedure for constructing lattice correlation functions with both staggered light and Wilson heavy quarks in Sec. II B. Finally, in Sec. II C, we show how to match the lattice heavy-light vector currents to the continuum with a mostly nonperturbative method, so that lattice perturbation theory is only needed to estimate a small correction.

A. Actions and Parameters

We use the ensembles of lattice gauge fields generated by the MILC Collaboration and described in Ref. [18] at two lattice spacings, $a \approx 0.12$ and 0.09 fm, in our numerical lattice

TABLE I: Lattice simulation parameters. The columns from left to right are the approximate lattice spacing in fm, the bare light quark masses am_l/am_s , the linear spatial dimension of the lattice in fm, the dimensionless factor $m_\pi L$ (corresponding to the taste-pseudoscalar pion composed of light sea quarks), the dimensions of the lattice in lattice units, the number of configurations used for this analysis, the clover term c_{SW} and bare κ value used to generate the bottom quark, and the improvement coefficient used to rotate the bottom quark field in the $b \rightarrow u$ vector current.

a (fm)	am_l/am_s	L (fm)	$m_\pi L$	Volume	# Configs.	c_{SW}	κ_b	d_1
0.09	0.0062/0.031	2.4	4.1	$28^3 \times 96$	557	1.476	0.0923	0.09474
0.09	0.0124/0.031	2.4	5.8	$28^3 \times 96$	518	1.476	0.0923	0.09469
0.12	0.005/0.05	2.9	3.8	$24^3 \times 64$	529	1.72	0.086	0.09372
0.12	0.007/0.05	2.4	3.8	$20^3 \times 64$	836	1.72	0.086	0.09372
0.12	0.01/0.05	2.4	4.5	$20^3 \times 64$	592	1.72	0.086	0.09384
0.12	0.02/0.05	2.4	6.2	$20^3 \times 64$	460	1.72	0.086	0.09368

simulations of the $B \rightarrow \pi \ell \nu$ semileptonic form factor. The ensembles include the effects of three dynamical staggered quarks — two degenerate light quarks with masses ranging from $m_s/8 - m_s/2$ and one heavier quark tuned to within 10–30% of the physical strange quark mass. This allows us to perform a controlled extrapolation to both the continuum and the physical average u - d quark mass. The physical lattice volumes are all sufficiently large ($m_\pi L \gtrsim 4$) to ensure that effects due to the finite spatial extent remain small.

For each independent ensemble we compute the light valence quark in the 2-point and 3-point correlation functions only at the same mass, m_l , as the light quark in the sea sector. Thus all of our simulations are at the “full QCD” point. Note, however, that we still have many correlated data points on each ensemble because of the multiple pion energies. Table I shows the combinations of lattice spacings, lattice volumes, and quark masses used in our calculation.

For bottom quarks in 2-point and 3-point correlation functions we use the Sheikholeslami-Wohlert (SW) “clover” action [47] with the Fermilab interpretation via HQET [36, 37], which is well-suited for heavy quarks, even when $am_Q \gtrsim 1$. Because the spin-flavor symmetry of heavy quark systems is respected by the lattice regulator, the expansion in $1/m_Q$ of the heavy-quark lattice action has the same form as the $1/m_Q$ expansion of the heavy-

quark part of the QCD action. Discretization effects in the lattice heavy-quark action are therefore parameterized order-by-order in the heavy-quark expansion by deviations of effective operator coefficients from their values in continuum QCD. Thus, in principle, the lattice heavy-quark action can be improved to arbitrarily high orders in HQET by tuning a sufficiently large number of parameters in the lattice action. In practice, we tune the hopping parameter, κ , and the clover coefficient, c_{SW} , of the SW action, to remove discretization effects through next-to-leading order, $\mathcal{O}(1/m_Q)$, in the heavy-quark expansion.

The SW action includes a dimension-five interaction with a coupling c_{SW} that must be adjusted to normalize the heavy quark's chromomagnetic moment correctly [36]. In our calculation we set the value of $c_{\text{SW}} = u_0^{-3}$, as suggested by tadpole-improved, tree-level perturbation theory [48]. We determine the value of u_0 either from the plaquette ($a \approx 0.09$ fm) or from the Landau link ($a \approx 0.12$ fm). The tadpole-improved bare quark mass for SW quarks is given by

$$am_0 = \frac{1}{u_0} \left(\frac{1}{2\kappa} - \frac{1}{2\kappa_{\text{crit}}} \right), \quad (4)$$

such that tuning the parameter κ to the critical quark hopping parameter κ_{crit} leads to a massless pion. Before generating the correlation functions needed for the $B \rightarrow \pi\ell\nu$ form factor, we compute the spin-averaged B_s kinetic mass on a subset of the available ensembles in order to tune the bare κ value for bottom (and hence the corresponding bare quark mass) to its physical value [36]. We then use the tuned value of κ_b for the $B \rightarrow \pi\ell\nu$ form-factor production runs. Table I shows the values of the clover coefficient and tuned κ_b used in our calculation.

In order to take advantage of the improved action in the calculation of the $B \rightarrow \pi\ell\nu$ form factor, we must also improve the flavor-changing vector current to the same order in the heavy-quark expansion. We remove errors of $\mathcal{O}(1/m_Q)$ in the vector current by rotating the heavy-quark field used in the matrix element calculation as

$$\psi_b \longrightarrow \Psi_b = \left(1 + a d_1 \vec{\gamma} \cdot \vec{D}_{\text{lat}} \right) \psi_b, \quad (5)$$

where \vec{D}_{lat} is the symmetric, nearest-neighbor, covariant difference operator. We set d_1 to its tadpole-improved tree-level value of [36]

$$d_1 = \frac{1}{u_0} \left(\frac{1}{2 + m_0 a} - \frac{1}{2(1 + m_0 a)} \right). \quad (6)$$

The values of the rotation parameter used in our calculation are given in Table I.

In order to convert dimensionful quantities determined in our lattice simulations into physical units, we need to know the value of the lattice spacing, a , which we find by computing a physical quantity that can be compared directly with experiment. We first determine the relative lattice scale by calculating the ratio r_1/a on each ensemble, where r_1 is related to the force between static quarks, $r_1^2 F(r_1) = 1.0$ [49]. These r_1/a estimates are then smoothed by fitting to a smooth function of the gauge coupling and quark masses. This scale-setting method has the advantage that the ratio r_1/a can be determined precisely from a fit to the static quark potential [50, 51]. We convert all of our data from lattice spacing units into r_1 units before performing any chiral fits in order to account for slight differences in the value of the lattice spacing between ensembles. In this work we use the value of $r_1^{\text{phys}} = 0.3108(15)(^{+26}_{-79})$ obtained by combining a recent lattice determination of $r_1 f_\pi$ [52] with the PDG value of $f_\pi = 130.7 \pm 0.1 \pm 0.36$ MeV [53] to convert lattice results from r_1 units to physical units.

B. Heavy-light meson correlation functions

The $B \rightarrow \pi l\nu$ semileptonic form factors parameterize the hadronic matrix element of the $b \rightarrow u$ quark flavor-changing vector current $\mathcal{V}^\mu \equiv i\bar{u}\gamma^\mu b$:

$$\langle \pi | \mathcal{V}^\mu | B \rangle = f_+(q^2) \left(p_B^\mu + p_\pi^\mu - \frac{m_B^2 - m_\pi^2}{q^2} q^\mu \right) + f_0(q^2) \frac{m_B^2 - m_\pi^2}{q^2} q^\mu, \quad (7)$$

where q^2 is the momentum transferred to the outgoing lepton pair. For calculations on the lattice and in HQET, it is more convenient to write the matrix element as [54]

$$\langle \pi | \mathcal{V}^\mu | B \rangle = \sqrt{2m_B} [v^\mu f_{\parallel}(E_\pi) + p_\perp^\mu f_{\perp}(E_\pi)], \quad (8)$$

where $v^\mu = p_B^\mu/m_B$ is the four-velocity of the B -meson, $p_\perp^\mu = p_\pi^\mu - (p_\pi \cdot v)v^\mu$ is the component of the pion momentum orthogonal to v , and $E_\pi = p_\pi \cdot v = (m_B^2 + m_\pi^2 - q^2)/(2m_B)$ is the energy of the pion in the B -meson rest frame ($\vec{p}_B = \vec{0}$). In this frame the form factors $f_{\parallel}(E_\pi)$ and $f_{\perp}(E_\pi)$ are directly proportional to the hadronic matrix elements:

$$f_{\parallel}(E_\pi) = \frac{\langle \pi | \mathcal{V}^0 | B \rangle}{\sqrt{2m_B}}, \quad (9)$$

$$f_{\perp}(E_\pi) = \frac{\langle \pi | \mathcal{V}^i | B \rangle}{\sqrt{2m_B}} \frac{1}{p_\pi^i}. \quad (10)$$

We therefore first calculate the hadronic matrix elements in Eqs. (9) and (10) in the rest frame of the B -meson to obtain $f_{\parallel}(E_\pi)$ and $f_{\perp}(E_\pi)$, and then extract the standard form factors $f_0(q^2)$ and $f_+(q^2)$ using the following relations:

$$f_0(q^2) = \frac{\sqrt{2m_B}}{m_B^2 - m_\pi^2} [(m_B - E_\pi)f_{\parallel}(E_\pi) + (E_\pi^2 - m_\pi^2)f_{\perp}(E_\pi)], \quad (11)$$

$$f_+(q^2) = \frac{1}{\sqrt{2m_B}} [f_{\parallel}(E_\pi) + (m_B - E_\pi)f_{\perp}(E_\pi)]. \quad (12)$$

These relations automatically satisfy the kinematic constraint $f_+(0) = f_0(0)$.

The 2-point and 3-point correlation functions needed to extract the lattice matrix element for $B \rightarrow \pi \ell \nu$ decay are

$$C_2^\pi(t; \vec{p}_\pi) = \sum_{\vec{x}} e^{i\vec{p}_\pi \cdot \vec{x}} \langle \mathcal{O}_\pi(0, \vec{0}) \mathcal{O}_\pi^\dagger(t, \vec{x}) \rangle, \quad (13)$$

$$C_2^B(t) = \sum_{\vec{x}} \langle \mathcal{O}_B(0, \vec{0}) \mathcal{O}_B^\dagger(t, \vec{x}) \rangle, \quad (14)$$

$$C_{3,\mu}^{B \rightarrow \pi}(t, T; \vec{p}_\pi) = \sum_{\vec{x}, \vec{y}} e^{i\vec{p}_\pi \cdot \vec{y}} \langle \mathcal{O}_\pi(0, \vec{0}) V_\mu(t, \vec{y}) \mathcal{O}_B^\dagger(T, \vec{x}) \rangle, \quad (15)$$

where \mathcal{O}_B and \mathcal{O}_π are interpolating operators for the B -meson and pion, respectively, and V_μ is the heavy-light vector current on the lattice.

In practice, to construct the heavy-light bilinears we must combine a staggered light quark, which is a 1-component spinor, with a 4-component Wilson-type bottom quark; we do so using the method established by Wingate *et al.* in Ref. [55]. For the B meson we use a mixed-action interpolating operator:

$$\mathcal{O}_{B,\Xi}(x) = \bar{\psi}_\alpha(x) \gamma_5^5 \Omega_{\beta\Xi}(x) \chi(x), \quad (16)$$

where α, β are spin indices and $\Omega(x) \equiv \gamma_0^{x_0} \gamma_1^{x_1} \gamma_2^{x_2} \gamma_3^{x_3}$. The fields ψ and χ are the 4-component clover quark field and 1-component staggered field, respectively. Based on the transformation properties of $\mathcal{O}_{B,\Xi}(x)$ under shifts by one lattice spacing, Ξ plays the role of a (fermionic) taste index [31, 55]. Once $\mathcal{O}_{B,\Xi}(x)$ is summed over 2^4 hypercubes in the correlation functions that we compute, Ξ also takes on the role of a taste degree of freedom, in the sense of Refs. [56, 57]. Because the heavy quark field $\bar{\psi}_\alpha(x)$ is slowly varying over a hypercube, it does not affect the construction of Refs. [56, 57].

For the pion we use the local pseudoscalar interpolating operator,

$$\mathcal{O}_\pi(x) = \varepsilon(x) \bar{\chi}(x) \chi(x), \quad (17)$$

where $\varepsilon(x) \equiv (-1)^{(x_1+x_2+x_3+x_4)}$. We take the vector current to be

$$V_{\Xi}^{\mu}(x) = \bar{\Psi}_{\alpha}(x)\gamma_{\alpha\beta}^{\mu}\Omega_{\beta\Xi}(x)\chi(x), \quad (18)$$

where Ψ is the rotated heavy-quark field given in Eq. (5). When forming $C_2^B(t)$ and $C_{3,\mu}^{B\rightarrow\pi}(t, T; \vec{p}_{\pi})$, we sum over the taste index. This yields the same correlation functions, with respect to taste, as in Ref. [55]. Our principal difference with Ref. [55] is to use 4-component heavy quarks instead of 2-component non-relativistic quarks, and to derive the correlators in the staggered formalism, without the introduction of naive fermions.

We work in the rest frame of the B -meson, so only the pions carry momentum. We compute both the 2-point function $C_2^{\pi}(t; \vec{p}_{\pi})$ and the 3-point function $C_{3,\mu}^{B\rightarrow\pi}(t, T; \vec{p}_{\pi})$ at discrete values of the momenta $\vec{p}_{\pi} = 2\pi(0, 0, 0)/L, 2\pi(1, 0, 0)/L, 2\pi(1, 1, 0)/L, 2\pi(1, 1, 1)/L$, and $2\pi(2, 0, 0)/L$ allowed by the finite spatial lattice volume. We use only data through momentum $\vec{p}_{\pi} = 2\pi(1, 1, 1)/L$, however, because the statistical errors in the correlators increase significantly with momentum.

We use a local source for the pions throughout the calculation, while we smear the B -meson wavefunction in both the 2-point function $C_2^B(t)$ and the 3-point function $C_{3,\mu}^{B\rightarrow\pi}(t, T; \vec{p}_{\pi})$:

$$\tilde{\mathcal{O}}_{B,\Xi}(t, \vec{x}) = \sum_{\vec{y}} S(\vec{y}) \bar{\psi}_{\alpha}(t, \vec{x} + \vec{y}) \gamma_{\alpha\beta}^5 \Omega_{\beta\Xi}(t, \vec{x}) \chi(t, \vec{x}), \quad (19)$$

where $S(\vec{y})$ is the spatial smearing function. This reduces contamination from heavier excited states and allows a better determination of the desired ground state amplitude. In our study of choices for how to smear the B -meson, we found that a wall source, $S(\vec{y}) = 1$, worked extremely well for suppressing excited state contamination, but at the cost of large statistical errors in the 2-point and 3-point correlation functions. In contrast, use of a 1S wavefunction, $S(\vec{y}) = \exp(-\mu|\vec{y}|)$, optimized to have good overlap with the charmonium ground state led to smaller statistical errors at the cost of undesirably large excited state contributions to the 3-point function that would make it difficult to extract the ground state amplitude. In order to achieve a balance between small statistical errors and minimal excited state contamination, we tune the coefficient of the exponential in the 1S wavefunction to the smallest value (*i.e.*, the widest smearing) for which the B -meson 2-point effective mass is still well-behaved; we find a value of $a\mu = 0.20$ for the coarse ensembles. We note that our determination of the

optimal B -meson smearing function is consistent with the theoretical expectation that the B -meson wavefunction should be wider than the charmonium wavefunction.

For the calculation of the 3-point function, we fix the location of the pion source at $t_i = 0$ and the location of the B -meson sink at $t_f = T$, and vary the position of the operator over all times t in between. If the source-sink separation is too small then the entire time range $0 < t < T$ is contaminated by excited states, but if the source-sink separation is too large then the correlation function becomes extremely noisy. In practice, we set the sink time to $T = 16$ on the coarse lattices; we have checked, however, that our results using this choice are consistent with those determined from using $T = 12$ and $T = 20$. On the fine lattices we scale the source sink separation by the approximate ratio of the lattice spacings, $a_{\text{fine}}/a_{\text{coarse}}$, and use $T = 24$.

In order to minimize the statistical errors given the available number of configurations in each ensemble, we compute the necessary 2-point and 3-point correlations not only with a source time of $t_i = 0$, but also with source times of $t_i = n_t/4, n_t/2$, and $3n_t/4$ (n_t is the temporal extent of the lattice) and the sink time T shifted accordingly. We then average the results from the four source times; this effectively increases our statistics by a factor of four.

C. Heavy-light current renormalization

In order to recover the desired continuum matrix element, the lattice amplitude must be multiplied by the appropriate renormalization factor $Z_{V_\mu}^{bl}$:

$$\langle \pi | \mathcal{V}_\mu | B \rangle = Z_{V_\mu}^{bl} \times \langle \pi | V_\mu | B \rangle, \quad (20)$$

where V_μ and \mathcal{V}_μ are the lattice and continuum $b \rightarrow u$ vector currents, respectively. This removes the dominant discretization errors from the lattice current operator. In terms of the form factors, Eq. (20) can be rewritten as

$$f_{\parallel} = Z_{V_0}^{bl} \times f_{\parallel}^{\text{lat}} \quad (21)$$

$$f_{\perp} = Z_{V_i}^{bl} \times f_{\perp}^{\text{lat}}, \quad (22)$$

where explicit expressions relating $f_{\parallel}^{\text{lat}}$ and f_{\perp}^{lat} to correlation functions are given in Eqs. (40) and (41).

In this work, we calculate $Z_{V_\mu}^{bl}$ via the mostly nonperturbative method used in the earlier quenched Fermilab calculation [54]. We first rewrite $Z_{V_\mu}^{bl}$ as

$$Z_{V_\mu}^{bl} = \rho_{V_\mu}^{hl} \sqrt{Z_V^{bb} Z_V^{ll}}. \quad (23)$$

The flavor-conserving renormalization factors Z_V^{bb} and Z_V^{ll} account for most of the value of Z_V^{bl} [38]. They can be determined from standard heavy-light meson charge normalization conditions:

$$Z_V^{ll} \times \langle D|V^{ll,0}|D\rangle = 1, \quad (24)$$

$$Z_V^{bb} \times \langle B|V^{bb,0}|B\rangle = 1, \quad (25)$$

where the light-light and heavy-heavy lattice vector currents are given by

$$V_{\Xi\Xi'}^{ll,\mu}(x) = \chi^\dagger(x)\Omega(x)_{\Xi\alpha}^\dagger \gamma_\alpha^\mu \Omega(x)_{\beta\Xi'} \chi(x), \quad (26)$$

$$V^{bb,\mu}(x) = \bar{\Psi}_{b\alpha}(x)\gamma_\alpha^\mu \Psi_{b\beta}(x), \quad (27)$$

respectively. In order to reduce the statistical errors in Z_V^{ll} , we compute the lattice matrix element $\langle D|V^{ll,0}|D\rangle$ using a clover charm quark as the spectator in the 3-point correlation function. We eliminate contamination from staggered oscillating states in the determination of Z_V^{bb} by using a clover strange quark for the spectator in the 3-point correlation function $\langle B|V^{bb,0}|B\rangle$. Once Z_V^{ll} and Z_V^{bb} have been determined nonperturbatively, the remaining correction factor in Eq. (23), $\rho_{V_\mu}^{hl}$, is expected to be close to unity because most of the radiative corrections, including contributions from tadpole graphs, cancel in the ratio [38]. We therefore estimate $\rho_{V_\mu}^{hl}$ from 1-loop lattice perturbation theory [48].

The matching factor $\rho_{V_\mu}^{hl}$ has been calculated by a subset of the present authors, and a separate publication describing the details is in preparation [58]. The corrections to $\rho_{V_\mu}^{hl}$ can be expressed as a perturbative series expansion in powers of the strong coupling:

$$\rho_{V_\mu}^{hl} = 1 + 4\pi\alpha_V(q^*)\rho_{V_\mu}^{hl[1]} + \mathcal{O}(\alpha_V^2), \quad (28)$$

where $\alpha_V(q^*)$ is the renormalized coupling constant in the V -scheme and is determined from the static quark potential with the same procedure as is used in Ref. [59]. The scale q^* , which should be the size of a typical gluon loop momentum, is computed via an extension of the methods outlined by Brodsky, Lepage, and Mackenzie [48, 60] and Hornbostel, Lepage, and Morningstar [61]. The value of q^* ranges from 2.0–4.5 GeV for the parameters used

in our simulations. The 1-loop coefficient, $\rho_{V_\mu}^{hl[1]}$, and higher moments are calculated using automated perturbation theory and numerical integration as described in Refs. [62, 63]. We find that the perturbative corrections to matrix elements of the temporal vector current, V_0 , are less than a percent, while the corrections to matrix elements of the spatial vector current, V_i , are 3–4%.

III. ANALYSIS

In this section, we describe the three-step analysis procedure used to calculate the $B \rightarrow \pi\ell\nu$ semileptonic form factor, $f_+(q^2)$. In the first subsection, Sec. III A, we describe how we fit the pion and B -meson 2-point correlation functions in order to determine the pion energies and B -meson mass. We use both of these quantities in the later determination of the lattice form factors $f_{\parallel}(E_\pi)$ and $f_{\perp}(E_\pi)$. Next, in Sec. III B, we construct a useful ratio of the 3-point correlation function $\langle \pi|V|B \rangle$ to the 2-point functions. We then fit this ratio to a simple plateau ansatz to extract the desired form factors. Finally, in Sec. III C, we extrapolate the form factors calculated at unphysically heavy quark masses and finite lattice spacing to the physical light quark masses and zero lattice spacing using next-to-leading order (NLO) HMS χ PT expressions extended with next-to-next-to-leading order (NNLO) analytic terms. (We perform a simultaneous extrapolation in m_q and a and interpolation in E_π .) We then take the appropriate linear combination of $f_{\parallel}(E_\pi)$ and $f_{\perp}(E_\pi)$ to determine the desired form factor, $f_+(q^2)$, with statistical errors.

A. Two-point correlator fits

The pion and B -meson 2-point correlators obey the following functional forms:

$$C_2^\pi(t; \vec{p}_\pi) = \sum_m (-1)^{mt} |\langle 0 | \mathcal{O}_\pi | \pi^{(m)} \rangle|^2 \frac{e^{-E_\pi^{(m)} t}}{2E_\pi^{(m)}}, \quad (29)$$

$$C_2^B(t) = \sum_m (-1)^{mt} |\langle 0 | \mathcal{O}_B | B^{(m)} \rangle|^2 \frac{e^{-m_B^{(m)} t}}{2m_B^{(m)}}. \quad (30)$$

In the above expressions, terms with odd m contain the prefactor $(-1)^t$. This leads to visible oscillations in time in the meson propagators; such behavior arises with staggered quarks because the parity operator is a composition of spatial inversion and translation through

one timeslice [64, 65]. The contributions of the opposite-parity oscillating states are found to be significant throughout the entire time range and must therefore be included in fits to extract the desired ground state energy.

Because the statistical errors in the pion energies and B -meson mass contribute very little to the total statistical error in the $B \rightarrow \pi\ell\nu$ form factor, we use a simple procedure to fit the 2-point functions. Although this does not optimize the determinations of E_π and m_B , it is sufficient for the purpose of this analysis. We first select a fit range, $t_{\min}\text{--}t_{\max}$, that allows a good correlated, unconstrained fit including only contributions from the ground state and its opposite-parity partner. We then reduce t_{\min} by one timeslice and redo the fit. If the correlated confidence level is too low ($\lesssim 10\%$), we increase the number of states and try the fit again with the same time range. Otherwise, if the fit is good, we reduce t_{\min} by one more timeslice and repeat the fit. We repeat this procedure until we can no longer get a good fit without using a large number (greater than 4) of states. We note that, by including only as many states as the data can determine, we minimize the possibility of spurious solutions in which the fitter exchanges the ground state with one of the same-parity excited states. We have, however, checked that this method yields the same results within statistical errors as a constrained fit that includes up to three or four pairs of states.

Figure 1 shows examples of both m_π vs. t_{\min} (left plot) and m_B vs. t_{\min} (right plot) on the $am_l/am_s = 0.02/0.05$ coarse ensemble, which has the largest light quark mass of the coarse ensembles. The masses are stable as t_{\min} is reduced, and the statistical errors in m_B become smaller as additional timeslices are added to the fit. The statistical errors are determined by performing a separate fit to 500 bootstrap ensembles; each fit uses the full single elimination jackknife correlation matrix which is remade before every fit. The size of the statistical errors does not change when the number of bootstrap ensembles is increased by factors of two or four. We select the time range to use in the $B \rightarrow \pi\ell\nu$ analysis based on several criteria: a good correlated confidence level, relatively symmetric upper and lower bootstrap error bars, no 5σ or greater outliers in the bootstrap distribution, and no sign of excited state contamination. The red (filled) data points in Fig. 1 mark the chosen fit ranges for the ensemble in the example plots. Figures 2 and 3 show the corresponding pion and B -meson correlator fits, respectively, which go through the data points (shown with jackknife errors) quite well.

The gauge configurations have been recorded every six trajectories, and the remaining

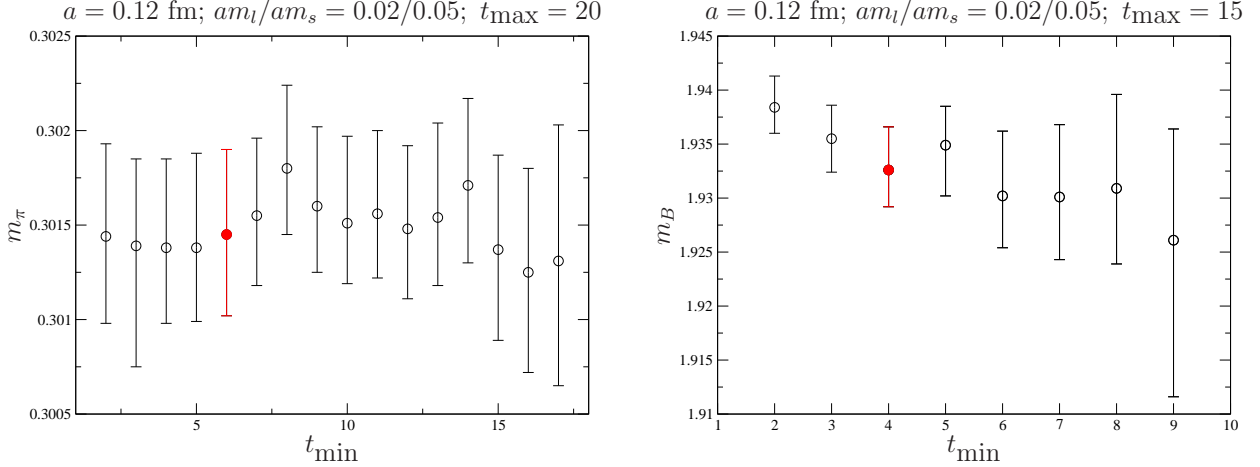


FIG. 1: Pion mass (left plot) and B -meson mass (right plot) versus minimum timeslice in 2-point correlator fit. The red (filled) data points show the fit ranges selected for use in the $B \rightarrow \pi \ell \nu$ form factor analysis.

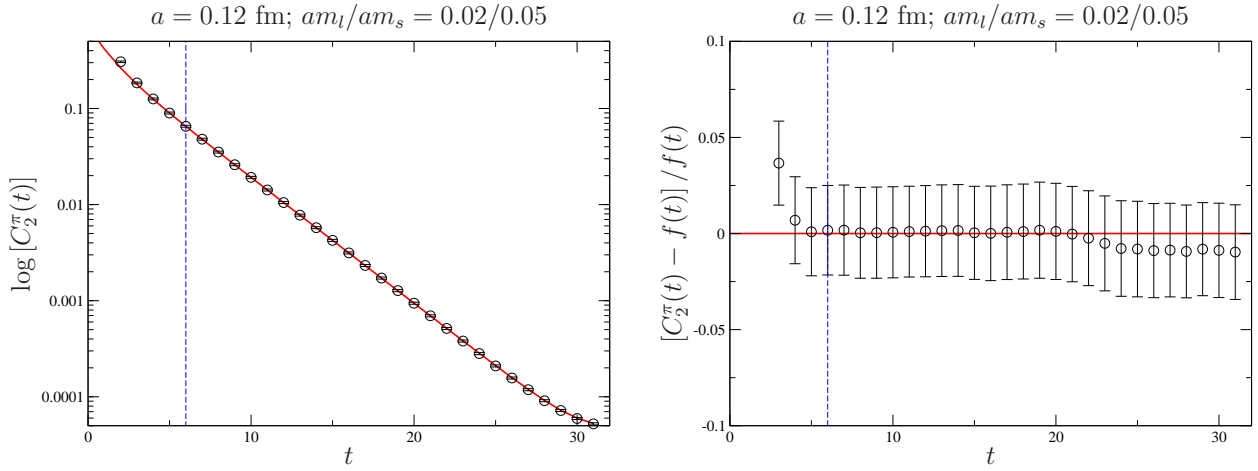


FIG. 2: Pion correlator fit corresponding to the red data point in the left-hand graph of Fig. 1. The left plot shows the fit (red line) to the zero-momentum pion propagator on a log scale, while the right plot shows the deviation of the fit from the data point for each timeslice. On both plots the dashed vertical line indicates t_{\min} . Single elimination jackknife statistical errors are shown.

autocorrelations between consecutive configurations cannot be neglected. We address this by averaging a block of successive configurations together before calculating the correlation matrix and performing the fit. We determine the optimal block size by increasing the number of configurations in a block until the single elimination jackknife statistical error in the correlator data remains constant within errors. This is shown for a representative timeslice of the pion propagator on a coarse ensemble in Fig. 4. We find that it is necessary

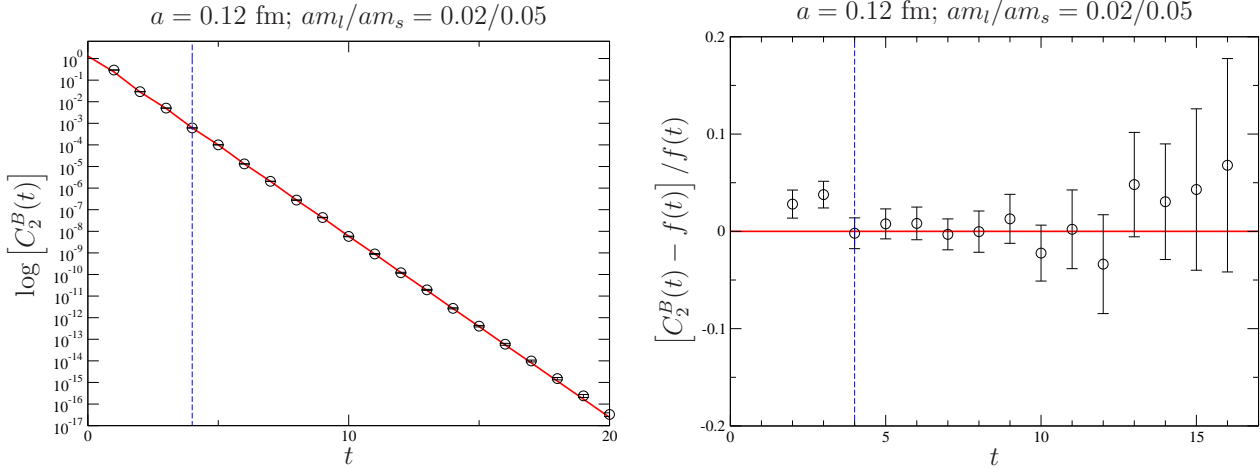


FIG. 3: B -meson correlator fit corresponding to the red data point in the right-hand graph of Fig. 1. The left plot shows the fit (red line) to the B -meson propagator on a log scale, while the right plot shows the deviation of the fit from the data point for each timeslice. On both plots the dashed vertical line indicates t_{\min} . Single elimination jackknife statistical errors are shown.

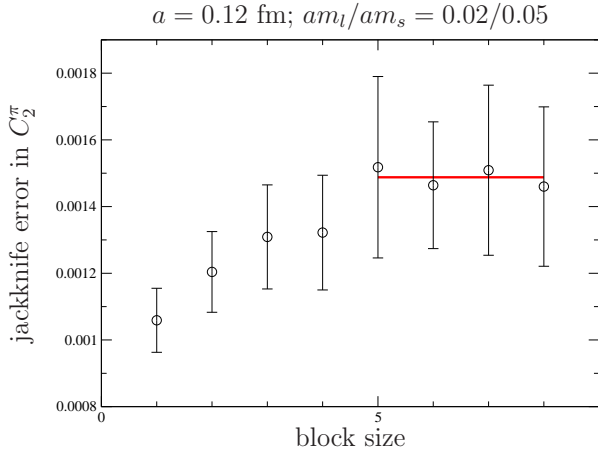


FIG. 4: Single-elimination jackknife error versus block size in the zero-momentum pion propagator at $t = 6$. The statistical errors in the errors are calculated with an additional single elimination jackknife loop. The red line is an average of the errors for block sizes 5–8 and is only to make it easier to see that the statistical error plateaus after a block size of 5; it is not used in the form factor analysis.

to use a block size of 5 on the coarse ensembles and 8 on the fine ensembles, and we use these values for the rest of the form factor analysis. We note that the size of the statistical errors that arises from blocking by 5 on the coarse ensemble is consistent with that estimated based on a calculation of the integrated autocorrelation time.

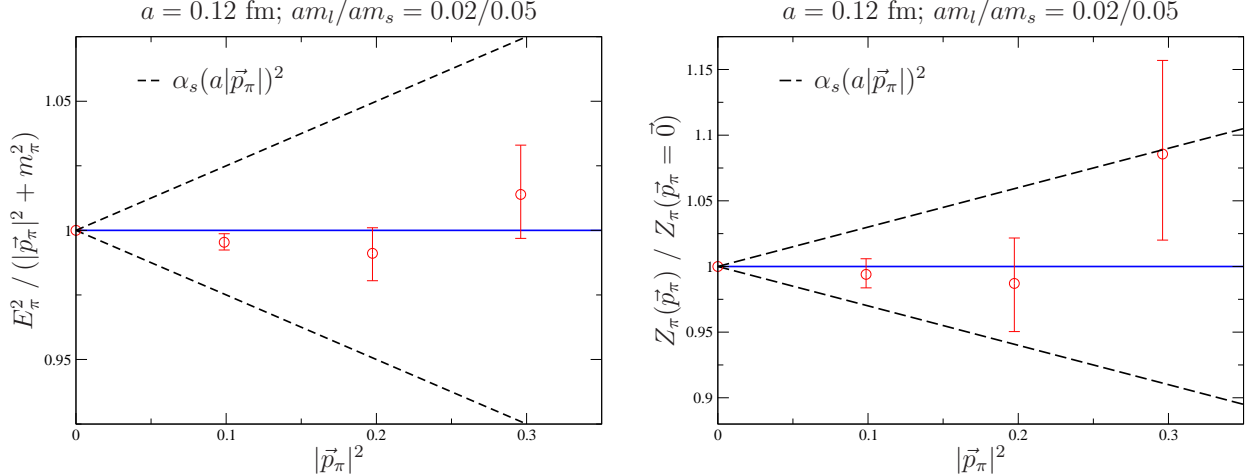


FIG. 5: Comparison of pion energy E_π (left plot) and amplitude Z_π (right plot) with the prediction of the continuum dispersion relation. We also show a power-counting estimate for the size of momentum-dependent discretization errors, which are of $\mathcal{O}(\alpha_s(a|\vec{p}_\pi|)^2)$, as dashed black lines.

The pion energy E_π that is extracted from fitting the 2-point function, $C_2^\pi(t; \vec{p}_\pi)$, should satisfy the dispersion relation $E_\pi^2 = |\vec{p}_\pi|^2 + m_\pi^2$ in the continuum limit due to the restoration of rotational symmetry. Similarly, the pion amplitude, $Z_\pi \equiv |\langle 0 | \mathcal{O}_\pi | \pi \rangle|$, should be independent of \vec{p}_π as $a \rightarrow 0$. As shown in Fig. 5, our results are consistent with these continuum relations within statistical errors.¹ We therefore replace the pion energy E_π by $\sqrt{|\vec{p}_\pi|^2 + m_\pi^2}$ when calculating the lattice form factors $f_\parallel(E_\pi)$ and $f_\perp(E_\pi)$ in order to reduce the total statistical uncertainty. The pion amplitude drops out of the form factor calculation, however, because we take suitable ratios of 3-point to 2-point correlators.

B. Three-point correlator fits

The $B \rightarrow \pi$ 3-point correlator obeys the following functional form:

$$C_{3,\mu}^{B \rightarrow \pi}(t, T) = \sum_{m,n} (-1)^{mt} (-1)^{n(T-t)} A_\mu^{mn} e^{-E_\pi^{(m)} t} e^{-m_B^{(n)}(T-t)}, \quad (31)$$

where

$$A_\mu^{mn} \equiv \frac{\langle 0 | \mathcal{O}_\pi | \pi^{(m)} \rangle}{2E_\pi^{(m)}} \langle \pi^{(m)} | V_\mu | B^{(n)} \rangle \frac{\langle B^{(n)} | \mathcal{O}_B | 0 \rangle}{2m_B^{(n)}}. \quad (32)$$

¹ As this analysis was being completed we generated data with four times the statistics on the $am_l/am_s = 0.02/0.05$ coarse ensemble. In order to make the comparison to the continuum expectation clearer, we use the higher statistics data in Fig. 5.

Writing out the first four terms of $C_{3,\mu}^{B \rightarrow \pi}(t, T)$ makes the behavior of the 3-point correlator as a function of both t and T more transparent:

$$\begin{aligned} C_{3,\mu}^{B \rightarrow \pi}(t, T) &= A_\mu^{00} e^{-E_\pi^{(0)} t} e^{-m_B^{(0)}(T-t)} + (-1)^{(T-t)} A_\mu^{01} e^{-E_\pi^{(0)} t} e^{-m_B^{(1)}(T-t)} \\ &\quad + (-1)^t A_\mu^{10} e^{-E_\pi^{(1)} t} e^{-m_B^{(0)}(T-t)} + (-1)^T A_\mu^{11} e^{-E_\pi^{(1)} t} e^{-m_B^{(1)}(T-t)} + \dots \end{aligned} \quad (33)$$

As in the case of the pion and B -meson propagators, the leading contributions from the opposite-parity excited states (the A_μ^{10} and A_μ^{01} terms) change sign when $t \rightarrow t + 1$; these produce visible oscillations in the correlation function along the time direction. The sub-leading contribution from the opposite-parity excited states (the A_μ^{11} term), however, only changes sign when the source-sink separation is varied, *e.g.*, $T \rightarrow T + 1$; this contribution is not as clearly visible in the data as those that oscillate with the time slice t .

The lattice form factors are related to the ground-state amplitude of the 3-point function $C_{3,\mu}^{B \rightarrow \pi}(t, T)$ as follows:

$$f_{\parallel}^{\text{lat}} = A_0^{00} \left(\frac{2E_\pi \sqrt{2m_B}}{Z_\pi Z_B} \right) \quad (34)$$

$$f_{\perp}^{\text{lat}} = A_i^{00} \left(\frac{2E_\pi \sqrt{2m_B}}{Z_\pi Z_B} \right) \frac{1}{p_\pi^i}, \quad (35)$$

where, as before, $Z_\pi \equiv |\langle 0 | \mathcal{O}_\pi | \pi \rangle|$ and $Z_B \equiv |\langle 0 | \mathcal{O}_B | B \rangle|$. The pion and B -meson energies and amplitudes are known from the 2-point fits described in the previous subsection. Thus, the goal is to determine the 3-point amplitude A_μ^{00} for μ along both the spatial and temporal directions.

In principle, the easiest way to determine the coefficient A_μ^{00} is to divide the 3-point function $C_{3,\mu}^{B \rightarrow \pi}(t, T)$ by the appropriate 2-point functions and fit to a constant (plateau) ansatz in a region of time slices $0 \ll t \ll T$ that are sufficiently far from both the pion and B -meson sources, such that excited state contamination can be neglected. In practice, however, oscillating excited-state contributions are significant throughout the interval between the pion and B -meson, so our raw correlator data cannot be fit to such a simple function. Therefore we construct an average correlator in which the oscillations are reduced before performing any fits. This method for determining the form factors requires knowledge of E_π and m_B ; we use the values determined in the 2-point fits described in the previous subsection and propagate the bootstrap uncertainties in order to properly account for correlations.

The final ratio of correlators used to determine A_μ^{00} entails several pieces. To begin consider the carefully constructed average of the value of the B -meson propagator at time

slice t with that at $t+1$:

$$\begin{aligned} C_2^B(t) \longrightarrow C_2'^B(t) &= \frac{e^{-m_B^{(0)}t}}{2} \left[\frac{C_2^B(t)}{e^{-m_B^{(0)}t}} + \frac{C_2^B(t+1)}{e^{-m_B^{(0)}(t+1)}} \right] \\ &= \frac{Z_B^2}{2m_B^{(0)}} e^{-m_B^{(0)}t} + (-1)^t \frac{Z_B'^2}{2m_B^{(1)}} e^{-m_B^{(1)}t} \left(\frac{1 - e^{-\Delta m_B}}{2} \right) + \dots, \end{aligned} \quad (36)$$

where $\Delta m_B \equiv m_B^{(1)} - m_B^{(0)}$. By removing the leading exponential behavior from the correlator *before* taking the average we suppress the leading oscillating contribution by a factor of the mass-splitting $\Delta m_B/2$ while leaving the desired ground state amplitude unaffected. Note also that, while this procedure affects the size of the excited state amplitudes, it does not alter the functional form of the correlator, nor does it alter the energies in the exponentials. Therefore the average in Eq. (36) is equivalent to using a smeared source that has a smaller coupling to the opposite-parity excited states. This averaging procedure can be iterated in order to make the oscillating terms arbitrarily small. Empirically, we find that two iterations are sufficient for all of our numerical data:

$$\begin{aligned} \bar{C}_2^B(t) &\equiv \frac{e^{-m_B^{(0)}t}}{4} \left[\frac{C_2^B(t)}{e^{-m_B^{(0)}t}} + \frac{2C_2^B(t+1)}{e^{-m_B^{(0)}(t+1)}} + \frac{C_2^B(t+2)}{e^{-m_B^{(0)}(t+2)}} \right] \\ &\approx \frac{Z_B^2}{2m_B^{(0)}} e^{-m_B^{(0)}t} + (-1)^t \frac{Z_B'^2}{2m_B^{(1)}} e^{-m_B^{(1)}t} \left(\frac{\Delta m_B^2}{4} \right) + \mathcal{O}(\Delta m_B^3). \end{aligned} \quad (37)$$

At our various light quark masses and lattice spacings the mass-splittings lie in the range $0.1 \lesssim \Delta m_B \lesssim 0.3$ in lattice units; thus use of the iterated average in Eq. (37) reduces the leading oscillating state amplitude by a factor of ~ 50 –400 such that it can be safely neglected.

In the case of the $B \rightarrow \pi$ 3-point correlation function, we wish to reduce both the oscillating contributions and the less visible non-oscillating contributions that arise from the cross-term between the lowest-lying pion and B -meson opposite-parity states. If these contributions are reduced sufficiently, we can safely neglect all of them when extracting the ground-state amplitude A_μ^{00} . We therefore construct a slightly more sophisticated average which combines the correlator both at consecutive time slices (t and $t+1$) and at consecutive

source-sink separations (T and $T+1$):

$$\begin{aligned}
\overline{C}_{3,\mu}^{B \rightarrow \pi}(t, T) &= \frac{e^{-E_\pi^{(0)} t} e^{-m_B^{(0)}(T-t)}}{8} \\
&\times \left[\frac{C_{3,\mu}^{B \rightarrow \pi}(t, T)}{e^{-E_\pi^{(0)} t} e^{-m_B^{(0)}(T-t)}} + \frac{C_{3,\mu}^{B \rightarrow \pi}(t, T+1)}{e^{-E_\pi^{(0)}(t)} e^{-m_B^{(0)}(T+1-t)}} + \frac{2 C_{3,\mu}^{B \rightarrow \pi}(t+1, T)}{e^{-E_\pi^{(0)}(t+1)} e^{-m_B^{(0)}(T-t-1)}} \right. \\
&+ \frac{2 C_{3,\mu}^{B \rightarrow \pi}(t+1, T+1)}{e^{-E_\pi^{(0)}(t+1)} e^{-m_B^{(0)}(T-t)}} + \frac{C_{3,\mu}^{B \rightarrow \pi}(t+2, T)}{e^{-E_\pi^{(0)}(t+2)} e^{-m_B^{(0)}(T-t-2)}} + \left. \frac{C_{3,\mu}^{B \rightarrow \pi}(t+2, T+1)}{e^{-E_\pi^{(0)}(t+2)} e^{-m_B^{(0)}(T-t-1)}} \right] \\
&\approx A_\mu^{00} e^{-E_\pi^{(0)} t} e^{-m_B^{(0)}(T-t)} + (-1)^T A_\mu^{11} e^{-E_\pi^{(1)} t} e^{-m_B^{(1)}(T-t)} \left(\frac{\Delta m_B}{2} \right) \\
&+ \mathcal{O}(\Delta E_\pi^2, \Delta E_\pi \Delta m_B, \Delta m_B^2).
\end{aligned} \tag{38}$$

This average reduces the unwanted parity states' contamination significantly. It eliminates both the leading $\mathcal{O}(1)$ and subleading $\mathcal{O}(\Delta E_\pi)$ contributions to the oscillating A^{10} term, the two lowest-order $\mathcal{O}(1, \Delta m_B)$ contributions to the oscillating A^{01} term, and the $\mathcal{O}(1, \Delta E_\pi)$ contributions to the non-oscillating A^{11} term. The size of the remaining A^{11} term is a factor of $\sim 7\text{--}20$ times smaller than in the unsmeared 3-point correlator.

We can now safely ignore contamination from opposite-parity states and determine the lattice form factors in a simple manner. We construct the following ratio of the smeared correlators:

$$\overline{R}_{3,\mu}^{B \rightarrow \pi}(t, T) \equiv \frac{\overline{C}_{3,\mu}^{B \rightarrow \pi}(t, T)}{\sqrt{\overline{C}_2^\pi(t) \overline{C}_2^B(T-t)}} \sqrt{\frac{2E_\pi}{e^{-E_\pi^{(0)} t} e^{-m_B^{(0)}(T-t)}}}. \tag{39}$$

The lattice form factors are then:

$$f_{\parallel}^{\text{lat}} = \overline{R}_{3,0}^{B \rightarrow \pi}(t, T) \tag{40}$$

$$f_{\perp}^{\text{lat}} = \frac{1}{p_\pi^i} \overline{R}_{3,i}^{B \rightarrow \pi}(t, T). \tag{41}$$

We fit $f_{\parallel}^{\text{lat}}$ and f_{\perp}^{lat} as defined in Eqs. (40)–(41) to a plateau in the region $0 \ll t \ll T$ where ordinary excited state contributions can be neglected. Figure 6 shows the determinations of $f_{\parallel}^{\text{lat}}$ (left plot) and f_{\perp}^{lat} (right plot) for all of the momenta that we use in the chiral extrapolation on the coarse ensemble with $am_l/am_s = 0.02/0.05$. In practice, we fit a range of four time slices, choosing the interval that results in the best correlated confidence level. We have cross-checked the determination of the form factors via Eqs. (40)–(41) against determinations of the form factor that explicitly include excited state dependence in the fit ansatz and find that the results agree within errors. Our preferred method, however, yields the smaller statistical uncertainty in the form factors.

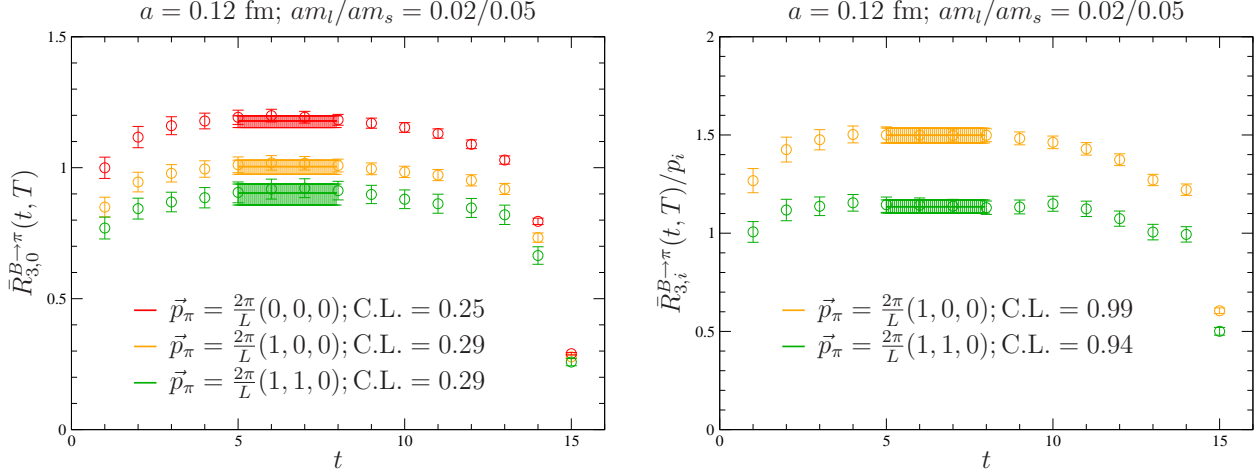


FIG. 6: Determination of the form factors f_{\parallel} (left plot) and f_{\perp} (right plot) from plateau fits to the ratios defined in Eqs. (40) and (41). The statistical errors on the data points are from a single-elimination jackknife. The statistical errors in the plateau determination are from separate fits of 500 bootstrap ensembles.

C. Continuum and chiral extrapolation

The quark masses in our numerical lattice simulations are heavier than the physical up and down quark masses. The effects of non-zero lattice spacings in Asqtad simulations are also too large to be neglected. In order to account for these facts, we calculate the desired hadronic matrix elements for multiple values of the light quark masses and lattice spacing, and then extrapolate to the physical quark masses and continuum using functional forms from heavy-light meson staggered chiral perturbation theory (HMS χ PT) [42]. The HMS χ PT expressions are derived using the symmetries of the staggered lattice theory, and therefore contain the correct dependence of the form factors on the quark mass and lattice spacing. In the case of the $B \rightarrow \pi \ell \nu$ form factors, the HMS χ PT expressions are also functions of the pion energy (recall that we work in the frame where the B -meson is at rest).

HMS χ PT is a systematic expansion in inverse powers of the heavy quark mass. In the chiral and soft pion limits ($m_l \rightarrow 0$ and $E_\pi \rightarrow 0$), the leading-order continuum HM χ PT expressions for f_{\parallel} and f_{\perp} take the following simple forms:

$$f_{\parallel}(E_\pi) = \frac{\phi_B}{f_\pi} \quad (42)$$

$$f_{\perp}(E_\pi) = \frac{\phi_{B^*}}{f_\pi} \frac{g_{B^* B \pi}}{E_\pi + \Delta_B^*}, \quad (43)$$

where $\phi_B \equiv f_B \sqrt{m_B}$, f_B is the B -meson decay constant, and f_π is the pion decay constant. The coefficient $g_{B^*B\pi}$ parameterizes the size of the $B^*-B-\pi$ coupling. In the static heavy quark limit, heavy quark spin symmetry does not distinguish between the pseudoscalar B -meson and the vector B^* -meson, which implies that the decay constant $\phi_{B^*} = \phi_B$ and the mass difference $\Delta_B^* \equiv m_{B^*} - m_B \rightarrow 0$. Inclusion of the parameter Δ_B^* , however, ensures the proper location of the pole at $m_{B^*}^2$ in the physical form factor $f_+(q^2)$. At the next order in the heavy quark expansion, $\mathcal{O}(1/m_b)$ corrections split the degeneracy between the B - and B^* -meson masses and decay constants. Furthermore, in the chiral and soft pion limits, all $1/m_b$ corrections can be absorbed into the values of the parameters ϕ_B , ϕ_{B^*} , $g_{B^*B\pi}$, and Δ_B^* [66]; thus f_\parallel and f_\perp retain the functional forms in Eqs. (42) and (43) even at NLO in $\text{HM}\chi\text{PT}$.

At lowest-order in $S\chi\text{PT}$, discretization effects split the degeneracies among the 16 tastes of pseudo-Goldstone mesons:

$$m_{xy,\Xi}^2 = \mu(m_x + m_y) + a^2 \Delta_\Xi, \quad (44)$$

where x and y indicate the quark flavors, μ is a continuum low-energy constant, and Δ_Ξ is the mass-splitting of a meson with taste Ξ . An exact $U(1)_A$ symmetry protects the taste pseudoscalar meson from receiving a mass-shift to all orders in $S\chi\text{PT}$, implying that $\Delta_P = 0$. In addition, at $\mathcal{O}(a^2)$, a residual $SO(4)$ taste-symmetry preserves the degeneracies among mesons that are in the same irreducible representation: P, V, A, T, I [26]. Numerically, the size of the taste-splittings turn out to be comparable to those of the pion masses for the $a = 0.09$ fm and $a = 0.12$ fm Asqtad staggered lattices used in this work [16].

We extrapolate our numerical form factor data using $\text{HMS}\chi\text{PT}$ expressions derived to zeroth order in $1/m_b$. The fit functions therefore depend upon the three remaining expansion parameters: m_l , a , and E_π . The $\text{HMS}\chi\text{PT}$ expressions for the form factors to $\mathcal{O}(m_l, a^2, E_\pi^2)$ are given explicitly in Eqs.(65)–(67) of Ref. [42]. Schematically, they read

$$f_\parallel(m_l, E_\pi, a) = \frac{c_\parallel^{(0)}}{f_\pi} \left[1 + \log s + c_\parallel^{(1)} m_l + c_\parallel^{(2)} (2m_l + m_s) + c_\parallel^{(3)} E_\pi + c_\parallel^{(4)} E_\pi^2 + c_\parallel^{(5)} a^2 \right] \quad (45)$$

$$\begin{aligned} f_\perp(m_l, E_\pi, a) &= \frac{c_\perp^{(0)}}{f_\pi} \left[\frac{1}{E_\pi + \Delta_B^* + \log s} + \frac{1}{E_\pi + \Delta_B^*} \times \log s \right] \\ &+ \frac{c_\perp^{(0)}/f_\pi}{E_\pi + \Delta_B^*} \left[c_\perp^{(1)} m_l + c_\perp^{(2)} (2m_l + m_s) + c_\perp^{(3)} E_\pi + c_\perp^{(4)} E_\pi^2 + c_\perp^{(5)} a^2 \right], \end{aligned} \quad (46)$$

where “logs” indicate non-analytic functions of the pseudo-Goldstone meson masses, *e.g.*, $m_\pi^2 \ln(m_\pi^2/\Lambda_\chi^2)$. The continuum low-energy constant $g_{B^*B\pi}$ enters these expressions in the coefficients of the chiral logarithms, which are completely fixed at this order. We use the phenomenological value of $g_{B^*B\pi} = 0.51$ [44] for the central value and vary $g_{B^*B\pi}$ by a reasonable amount (see Sec. IV B) to estimate its contribution to the systematic uncertainty. Because the size of the mass-splitting Δ_B^* is poorly determined from the lattice data and is consistent with the physical value within statistical errors, we fix Δ_B^* to the PDG value, 45.78 MeV [13], in our fits. The chiral logarithms also depend upon six extra constants that parameterize discretization effects due to the light staggered quarks: the four taste splittings $a^2 \Delta_V, a^2 \Delta_A, a^2 \Delta_T, a^2 \Delta_I$ and the two flavor-neutral “hairpin” coefficients $a^2 \delta'_V$ and $a^2 \delta'_A$ [27]. These parameters can be determined separately from fits to light pseudoscalar meson masses and decay constants; we therefore hold them fixed to the values determined in Ref. [67] while performing the continuum-chiral extrapolation. The variation of these parameters within their statistical errors results in a negligible change to the extrapolated form factors. The five terms analytic in m_l , a^2 , and E_π absorb the dependence upon the scale in the chiral logarithms, Λ_χ , such that the form factor is scale-independent. We leave the tree-level coefficients $c_{\parallel,\perp}^{(0)}$ and the NLO analytic term coefficients $c_{\parallel,\perp}^{(1)} - c_{\parallel,\perp}^{(5)}$ as free parameters to be determined via the fit to the lattice form factor data. In practice, we omit the analytic term proportional to $(2m_l + m_s)$ from our fits because the strange sea quark mass is tuned to approximately the same value on each of our ensembles and we have simulated only full QCD points. This term is therefore largely indistinguishable from the analytic term proportional to m_l . We have checked that omission of the sea quark mass analytic term has a negligible impact on the form factors in the chiral and continuum limits.

In both earlier unquenched analyses of the $B \rightarrow \pi \ell \nu$ semileptonic form factor [33, 34], the chiral extrapolation is performed as a two-step procedure: first interpolate the lattice data to fiducial values of E_π and then extrapolate the results to the physical quark masses and continuum independently at each value of E_π . The function used for the interpolation (which is different in the two analyses) introduces a systematic uncertainty that is difficult to estimate. In both cases, the chiral-continuum extrapolation makes use of the correct functional forms derived in HMS χ PT, but, by extrapolating the results for each value of E_π separately, the constraint that the low-energy constants of the chiral effective Lagrangian

are independent of the pion energy is lost. This omission of valuable information about the form factor shape introduces a further error that is unnecessary. The new analysis presented here instead employs a simultaneous fit using $\text{HMS}\chi\text{PT}$ to our entire data set (all values of m_l , a , and E_π) to extrapolate to physical quark masses and the continuum and interpolate in the pion energy [68]. This improved method eliminates the systematic uncertainties introduced in the two-step interpolate-then-extrapolate procedure, and exploits the available information in an optimal way.

We perform our combined chiral and continuum extrapolation using the method of constrained curve fitting [69]. Although we know that lattice data generated with sufficiently small quark masses and fine lattice spacings, and, in the case of the $B \rightarrow \pi\ell\nu$ form factor, sufficiently low pion energies, must be described by lattice χPT , we do not know precisely the range of validity of the effective theory. Furthermore, the order in χPT to which we must work and the allowed parameter values depend upon both the quantity of interest and the size of the statistical errors. We therefore need a fitting procedure that both incorporates our general theoretical understanding of the suitable chiral effective theory and accounts for our limited knowledge of the values of the low-energy constants and sizes of the higher-order terms. Constrained curve fitting provides just such a method.

Next-to-leading order χPT breaks down for pion energies around and above the kaon mass. Less than half of our numerical form factor data, however, is below this cutoff. Therefore, although we do not expect NLO $\text{HMS}\chi\text{PT}$ to describe our data through momentum $p = 2\pi(1, 1, 0)/L$, we cannot remove those points without losing the majority of our data. Nor can we abandon the NLO $\text{HMS}\chi\text{PT}$ expressions for f_{\parallel} and f_{\perp} , Eqs. (45) and (46), which are the only effective field theory guides that we have for extrapolating the numerical lattice form factor data to the continuum and physical quark masses. We therefore perform the continuum-chiral extrapolation using the full NLO $\text{HMS}\chi\text{PT}$ expressions for f_{\parallel} and f_{\perp} , including the 1-loop chiral logarithms, *plus* additional NNLO analytic terms to allow a good fit to the data through $p = 2\pi(1, 1, 0)/L$. The NNLO terms smoothly interpolate between the region in which χPT is valid and the region in which the pion energies are too large and the higher-order chiral logarithms in E_π can be approximated as polynomials.

We express the analytic terms in the formulae for f_{\parallel} and f_{\perp} , Eqs. (45) and (46), as

products of dimensionless expansion parameters:

$$\chi_{m_l} = \frac{2\mu m_l}{8\pi^2 f_\pi^2} \sim 0.05\text{--}0.19 \quad (47)$$

$$\chi_{a^2} = \frac{a^2 \overline{\Delta}}{8\pi^2 f_\pi^2} \sim 0.03\text{--}0.09 \quad (48)$$

$$\chi_{E_\pi} = \frac{\sqrt{2} E_\pi}{4\pi f_\pi} \sim 0.22\text{--}0.78, \quad (49)$$

where $\overline{\Delta}$ is the average staggered taste-splitting and we show the range of values for each of these parameters corresponding to our numerical lattice data. (Note that we omit the $\vec{p} = 2\pi(1, 1, 1)/L$ data points from our chiral fits because these would lead to $\chi_{E_\pi} \gtrsim 1$.) Because each of the above expressions is normalized by the chiral scale, $\Lambda_\chi \approx 4\pi f_\pi$, the undetermined coefficients $c_{\parallel, \perp}^{(1)} - c_{\parallel, \perp}^{(5)}$ should be of $\mathcal{O}(1)$ in these units. We therefore constrain the values of the low-energy constants $c_{\parallel, \perp}^{(0)} - c_{\parallel, \perp}^{(5)}$ in our fits with Gaussian priors of width 2 centered about 0.

The statistical errors in the numerical lattice data come from the 3-point fits described in the previous subsection. In order to account for the correlations among the various pion energies on the same sea quark ensemble in the chiral-continuum extrapolation, we preserve the bootstrap distributions. We perform a separate correlated fit to each of the 500 bootstrap ensembles in which we remake the full bootstrap covariance matrix for each fit. We average the 68% upper and lower bounds on the form factor distributions to determine the statistical and systematic errors in f_\parallel and f_\perp that are plotted in Fig. 7 and presented in Table II below.

Because we do not know *a priori* how many terms are necessary to describe the available lattice data, we begin with strictly NLO fits using the formulae for f_\parallel and f_\perp in Eqs. (45) and (46). We fit the lattice data for f_\parallel and f_\perp separately even though the ratio of leading-order coefficients, $c_\perp^{(0)}/c_\parallel^{(0)}$, is predicted to equal $g_{B^* B\pi}$ to NLO in χ PT; this is because the value of $g_{B^* B\pi}$ is known to only $\sim 50\%$ from phenomenology. We obtain a good fit of the f_\perp lattice data to the NLO expression without the inclusion of higher-order NNLO terms. This is probably because the shape of f_\perp is dominated by the $1/(E_\pi + \Delta^*)$ behavior and therefore largely insensitive to the other terms. We cannot, however, obtain a good fit of f_\parallel to the strictly NLO expression, and must add higher-order terms in order to obtain a successful fit. Specifically, NNLO analytic terms proportional to $m_l E_\pi$ and E_π^3 are both necessary to achieve a confidence level better than 10%.

Although we could, at this point, choose to truncate the HMS χ PT extrapolation formulae

to include only those terms necessary for a good confidence level, we instead include “extra” NNLO analytic terms to both the f_{\parallel} and f_{\perp} fits, constraining the values of their coefficients with Gaussian priors of 0 ± 2 . The introduction of more free parameters increases the statistical errors in the extrapolated values of the form factors; these larger errors reflect the uncertainty in the size of the newly-included higher-order contributions. We continue to add higher-order analytic terms until the central values of the extrapolated form factors stabilize and the statistical errors in the form factors reach a maximum. This indicates that any further terms are of sufficiently high order that they do not affect the fit and can safely be neglected. We find that this occurs once the extrapolation formulae for f_{\parallel} and f_{\perp} contain all eight sea-quark mass-independent NNLO analytic terms. The inclusion of NNNLO analytic terms does not further increase the size of the error bars.

Figure 7 shows the preferred constrained fits of f_{\parallel} (upper plot) and f_{\perp} (lower plot) versus E_{π}^2 , where both the x - and y -axes are in r_1 units.² Each fit is to the NLO $\text{HMS}\chi\text{PT}$ expression, Eqs. (45) and (46), plus all sea-quark mass-independent NNLO analytic terms. The square symbols indicate fine lattice data, while the circles denote coarse data. The six colored curves show the fit result projected onto the masses and lattice spacings of the six sea quark ensembles; the red line should go through the red circles, and so forth. The thick black curve shows the form factor in the continuum at physical quark masses with symmetrized bootstrap statistical errors.

We use functions and constraints based on $\text{HMS}\chi\text{PT}$ to perform the chiral-continuum extrapolation because we know that $\text{HMS}\chi\text{PT}$ is the correct low-energy effective description of the lattice theory. Nevertheless, we must compare various properties with theoretical expectations in order to check for overall consistency. An essential first test is that we can successfully fit the data with good confidence levels and obtain low-energy coefficients that are of the predicted size. We can also verify the convergence of the series expansion by calculating the ratios of the higher-order contributions to the leading-order form factor

² As a cross-check of the constrained fits, we also perform unconstrained fits of f_{\parallel} and f_{\perp} with only the minimal number of analytic terms needed for a good fit. The results are consistent, but the unconstrained fit results have smaller statistical errors because they include 6–8 fewer fit parameters.

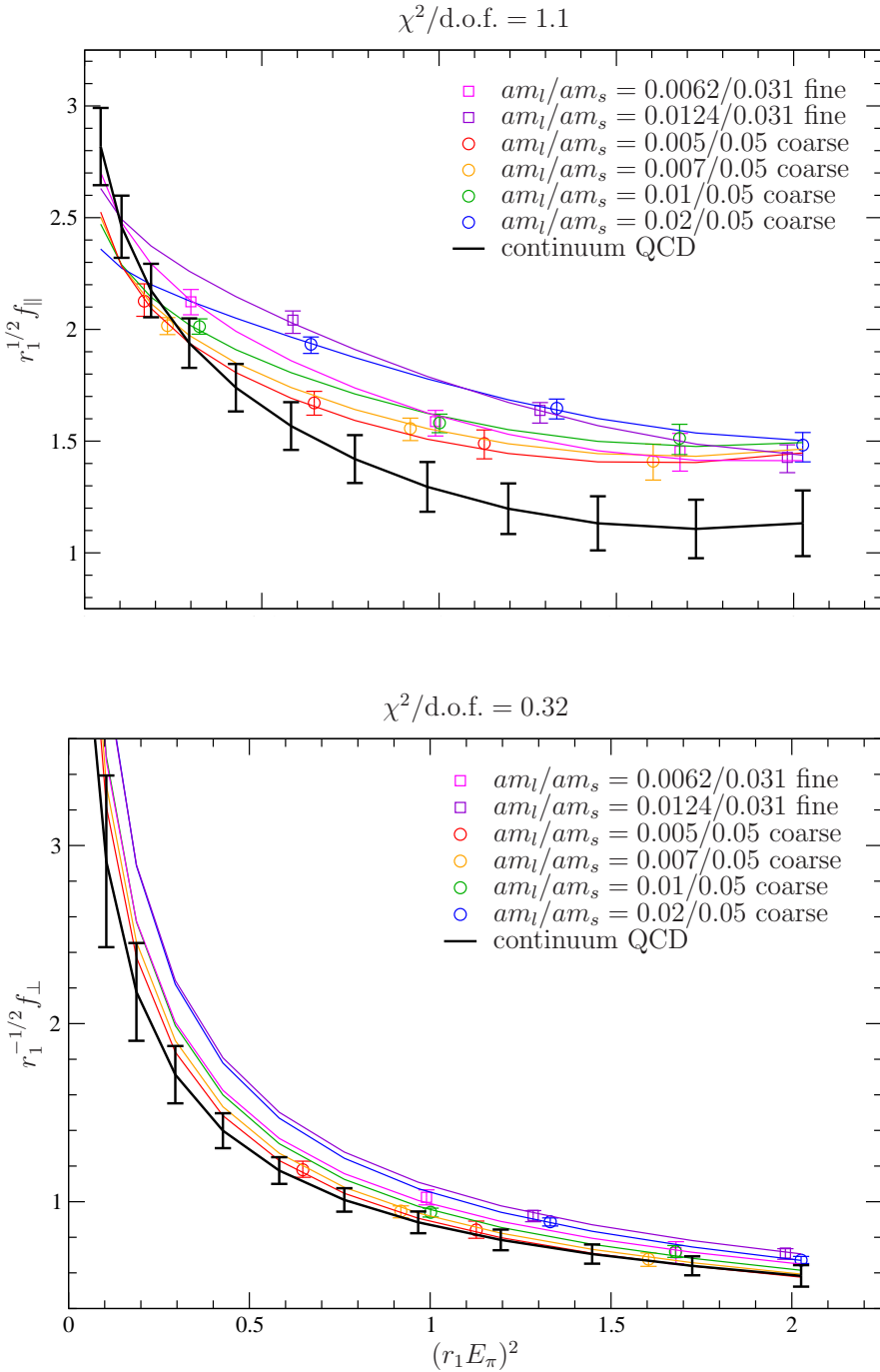


FIG. 7: Chiral-continuum extrapolation of f_{\parallel} (upper) and f_{\perp} (lower) using constrained NLO HMS χ PT plus all NNLO analytic terms with $g_{B^*B\pi} = 0.51$ and $r_1 = 0.311$ fm. The square symbols indicate $a \approx 0.09$ fm lattice data points while the circular symbols indicate $a \approx 0.12$ fm coarse data points. The black curve is the chiral-continuum extrapolated form factor symmetrized bootstrap statistical errors only.

contributions:

$$\left. \frac{f_{\parallel}^{\text{NLO}}}{f_{\parallel}^{\text{LO}}} \right|_{E_{\pi}=500 \text{ MeV}} \approx 47\%, \quad \left. \frac{f_{\perp}^{\text{NLO}}}{f_{\perp}^{\text{LO}}} \right|_{E_{\pi}=500 \text{ MeV}} \approx 48\%, \quad (50)$$

$$\left. \frac{f_{\parallel}^{\text{NNLO}}}{f_{\parallel}^{\text{LO}}} \right|_{E_{\pi}=500 \text{ MeV}} \approx 3\%, \quad \left. \frac{f_{\perp}^{\text{NNLO}}}{f_{\perp}^{\text{LO}}} \right|_{E_{\pi}=500 \text{ MeV}} \approx 4\%, \quad (51)$$

where we choose a nominal value of $E_{\pi} = 500$ MeV for illustration because it is on the high end of the expected range of validity of χ PT. Finally, because the leading-order coefficient, $c_{\parallel}^{(0)}$, is expected to be equal to $\phi_B \equiv f_B \sqrt{m_B}$ in HM χ PT, we can compare its value with that of ϕ_B determined from our preliminary decay constant analysis. Although the B -meson decay constant calculation uses the same staggered gauge configurations, it employs different heavy-light meson 2-point correlation functions with the axial current, a different HMS χ PT fit function, and different perturbative renormalization factors, and is therefore largely independent of the $B \rightarrow \pi \ell \nu$ semileptonic form factor calculation. For the preferred f_{\parallel} fit shown in Fig. 7, we find $c_{\parallel}^{(0)} = 0.81 \pm 0.07$, where the errors are statistical only. This is quite close to our current preliminary result, $r_1^{3/2} \phi_B = 0.92 \pm 0.03$ (statistical error only) [70, 71], especially considering that the HMS χ PT extrapolation formula for f_{\parallel} neglects some of the $\mathcal{O}(1/m_b)$ contributions.

An interesting use of our numerical $B \rightarrow \pi \ell \nu$ form factor data is to determine the approximate value of the $B^*-B-\pi$ coupling, $g_{B^*B\pi}$, from lattice QCD. For the preferred fits shown in Fig. 7, we find that the ratio of leading-order coefficients is

$$g_{B^*B\pi} \approx \frac{c_{\perp}^{(0)}}{c_{\parallel}^{(0)}} = 0.22 \pm 0.07, \quad (52)$$

and is independent of the choice for $g_{B^*B\pi}$ in the chiral logarithms within statistical errors. This determination omits the $\mathcal{O}(1/m_b)$ corrections to the chiral logarithms in the HMS χ PT extrapolation formulae for f_{\parallel} and f_{\perp} , Eqs. (45) and (46), and neglects the difference between ϕ_B and ϕ_{B^*} ; we do not attempt to estimate the systematic uncertainty introduced by these or other effects. The value is lower than the determination of Stewart, $g_{B^*B\pi} = 0.51$, which comes from a combined analysis of several experimental quantities, including the D^* -meson decay width, through $\mathcal{O}(1/m_c)$ in HM χ PT [44]. It is consistent, however, with the range of values determined by the HPQCD Collaboration, who allowed $g_{B^*B\pi}$ to be a free parameter in their chiral-continuum extrapolation and found $0 < g_{B^*B\pi} \lesssim 0.45$ [33].

IV. ESTIMATION OF SYSTEMATIC ERRORS

In this section, we discuss all of the sources of systematic uncertainty in our calculation of the $B \rightarrow \pi \ell \nu$ form factor $f_+(q^2)$. We present each error in a separate subsection for clarity. The value of the form factor $f_+(q^2)$, along with the total error budget, is given in Table II.

A. Chiral-continuum extrapolation fit ansatz

We use the method of constrained curve fitting to estimate the effect of neglected higher-order terms in the $\text{HMS}\chi\text{PT}$ chiral-continuum extrapolation formulae. Our fit procedure is described in detail in Sec. III C. Therefore, the errors in f_{\parallel} and f_{\perp} extrapolated to physical quark masses and zero lattice spacing shown in Fig. 7 reflect *both* the statistical errors in the Monte Carlo data and the systematic errors due to our limited knowledge of the higher-order terms, which we specified with priors. We do not need to include a separate systematic uncertainty due to the choice of fit function, as would be the case had we used an unconstrained fit with fewer terms.

B. $g_{B^* B\pi}$ uncertainty

We fix the size of the B^* - B - π coupling to $g_{B^* B\pi} = 0.51$ in the coefficients of the chiral logarithms while extrapolating to the physical light quark masses and continuum. Our choice is based upon the following considerations. Because the coupling $g_{B^* B\pi}$ is expected to be approximately equal to $g_{D^* D\pi}$ due to heavy-quark symmetry, we use the phenomenological value of the D^* - D - π coupling determined by Stewart in Ref. [44], which comes from a combined analysis of several experimental quantities that includes the D^* -meson decay width [72]. This value is presented without errors, and is an update of Stewart's earlier analysis in Ref. [73] which incorporates additional experimental results. His earlier calculation finds a significantly lower value of $g_{D^* D\pi} = 0.27^{+0.04+0.05}_{-0.02-0.02}$, where the first errors are experimental and the second errors come from an estimate of the sizes of the 1-loop counterterms [73]. A more recent phenomenological determination of the D^* - D - π coupling by Kamenik and Fajfer, which also includes up-to-date experimental data, improves upon the analysis method of Stewart by including contributions from both positive and negative parity heavy mesons in the loops [74]. They find an even higher value of $g_{D^* D\pi} = 0.66^{+0.08}_{-0.06}$, where

the uncertainty only reflects the error due to counterterms. We therefore conclude that, although recent experimental measurements of the D^* width may constrain the coupling [72] at tree-level, the size of $g_{B^*B\pi}$ is not well-determined in the literature.

In order to determine the error in the form factor from the uncertainty $g_{B^*B\pi}$ we vary the parameter over a generous range. The smallest value of $g_{B^*B\pi}$ that we have seen in the literature is $g_{D^*D\pi} = 0.27$ [73]. The largest is $g_{D^*D\pi} = 0.67$, which comes from a quenched lattice calculation [75]. (There has not yet been an unquenched “2+1” flavor determination of $g_{B^*B\pi}$.) We therefore vary $g_{B^*B\pi}$ over the entire range from 0.27–0.67 and take the largest difference from the preferred determination of $f_+(q^2)$ using $g_{B^*B\pi} = 0.51$ as the systematic error due to the uncertainty in the B^* - B - π coupling. The lattice data is largely insensitive to the value of $g_{B^*B\pi}$ in the coefficient of the chiral logarithms; all values of the parameter yield similar fit confidence levels. The resulting systematic uncertainty in $f_+(q^2)$ is less than 3% for all q^2 bins despite varying $g_{B^*B\pi}$ by almost 50%.

C. Scale (r_1) uncertainty

We use the MILC Collaboration’s determination of the scale from their calculation of f_π , $r_1 = 0.311$ fm, to convert between lattice and physical units [52]. The parameter r_1 enters the form factor calculation in a number of places: we use the PDG values of f_π and Δ_B^* in the chiral-continuum extrapolation formulae [13], we set m_π to the PDG value in the resulting fit functions to determine the form factors at the physical point, and we convert f_{\parallel} and f_{\perp} to physical units via r_1 before combining them to extract $f_+(q^2)$. An alternative determination using the HPQCD Collaboration’s lattice data for the Υ 2S-1S [76] splitting yields a result that is $\sim 2\%$ larger, $r_1 = 0.317$ fm. We therefore repeat the chiral-continuum extrapolation of f_{\parallel} and f_{\perp} using this higher value of r_1 , combine them into the dimensionless form factor $f_+(q^2)$ using this higher value of r_1 , and take the difference from the preferred form factor result as the systematic error due to uncertainty in the overall lattice scale. The difference ranges from 1–1.5% for most q^2 values. This is consistent with our naive expectation that a $\sim 2\%$ difference in r_1 will result in a $\sim 1\%$ difference in $f_+(q^2)$ because f_{\parallel} has dimensions of $\text{GeV}^{1/2}$ and f_{\perp} has dimensions of $\text{GeV}^{-1/2}$.

D. Light quark mass (\widehat{m} , m_s) determinations

We obtain the form factors f_{\parallel} and f_{\perp} in continuum QCD by setting the lattice spacing to zero and the light quark masses to their physical values in the $\text{HMS}\chi\text{PT}$ expressions, once the coefficients have been determined from fits to the numerical lattice data. We use the most recent calculations of the bare quark masses by the MILC Collaboration from fits to light pseudoscalar meson masses:

$$r_1 \widehat{m} \times 10^3 = 3.78(16) \quad (53)$$

$$r_1 m_s \times 10^3 = 102(4), \quad (54)$$

where \widehat{m} is the average of the up and down quark masses and the quoted errors include both statistics and systematics [52]. We vary the bare light quark mass, $r_1 \widehat{m}$, within its stated uncertainty and take the maximal difference from the preferred form factor result to be the systematic error; we find that the error is 0.3% or less for all values of q^2 . We perform the same procedure for the bare strange quark mass, and find that the resulting error ranges from $\sim 0.5\text{--}1.5\%$ over the various q^2 bins.

E. Bottom quark mass (m_b) determination

The value of the form factor $f_+(q^2)$ depends upon the b -quark mass, which we fix to its physical value throughout the calculation. Specifically, we first determine the value of the hopping parameter, κ , in the SW action for which the lattice kinetic mass agrees with the experimentally-measured B_s -meson mass. We then use this tuned κ_b when calculating all of the 2- and 3-point heavy-light correlators needed for the $B \rightarrow \pi \ell \nu$ form factor. With our current tuning procedure we are able to determine κ_b to $\sim 6\%$ accuracy. This uncertainty in κ_b is conservative; it is primarily due to poor statistics, and will decrease considerably after the analysis of the larger data set that is currently being generated.

The uncertainty in κ_b produces an uncertainty in the form factor. We estimate this by calculating the form factor f_+ at two additional values of κ (one above and one below the tuned value) on the $am_l/am_s = 0.02/0.05$ coarse ensemble. This is sufficient because the heavy-quark mass-dependence of the form factor is largely independent of the sea quark masses and lattice spacing. We find the largest dependence upon κ_b at momentum $\vec{p} =$

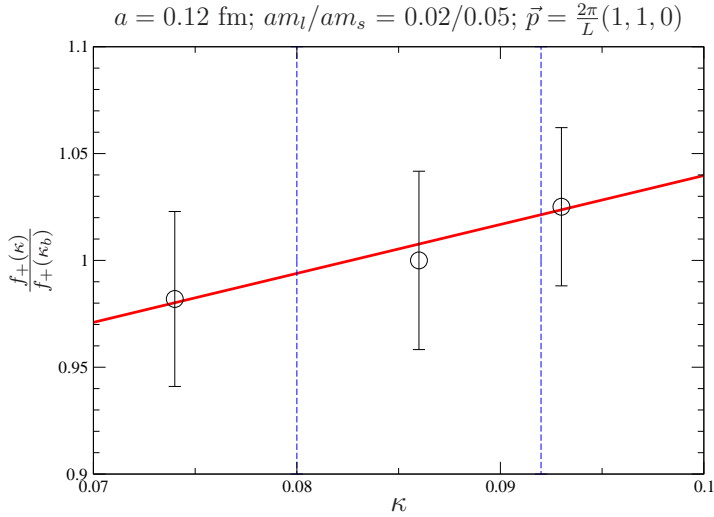


FIG. 8: Normalized form factor f_+ at momentum $\vec{p} = 2\pi(1, 1, 0)/L$ as a function of κ on the $am_l/am_s = 0.02/0.05$ coarse ensemble. The central data point corresponds to the tuned κ_b , and the thick red line shows a linear fit to the three data points. The two dashed vertical lines indicate the upper and lower bounds on κ_b .

$2\pi(1, 1, 0)/L$, shown in Fig. 8, for which a 6% uncertainty in κ_b produces a 1.2% uncertainty in the form factor. We therefore take 1.2% to be the systematic error in $f_+(q^2)$ due to uncertainty in the determination of the b -quark mass.

F. Gluon and light-quark discretization errors

We estimate the size of discretization errors in the form factor $f_+(q^2)$ with power-counting. We choose conservative values for the parameters that enter the estimates: $\Lambda = 700$ MeV and $\alpha_V(q^*) = 1/3$, which is a typical value on the fine lattice spacing [58, 63].

We calculate the $B \rightarrow \pi \ell \nu$ semileptonic form factor using a one-loop Symanzik-improved gauge action for the gluons [77–80] and the Asqtad-improved staggered action for the light up, down, and strange quarks [81, 82]. Because both the gluon and light quark actions are $\mathcal{O}(a^2)$ -improved, the leading discretization effects are of $\mathcal{O}(\alpha_s(a\Lambda)^2)$. We parameterize these errors in the fit to numerical lattice form factor data by including analytic terms proportional to a^2 in the HMS χ PT extrapolation formulae for f_{\parallel} and f_{\perp} . Because we only have data at two lattice spacings, however, we do not include a separate term proportional to $\alpha_s(a\Lambda)^2$ to account for the fact that α_s differs by a few percent between the lattice spacings. We then

remove the majority of light quark and gluon discretization effects from the final result by taking $a \rightarrow 0$. Similarly, we identify and remove higher-order discretization effects in the chiral-continuum extrapolation through the NNLO analytic terms in the fit functions. The remaining gluon and light quark discretization errors are negligible.

The calculation of the $B \rightarrow \pi\ell\nu$ form factor requires 2-point and 3-point functions with nonzero momenta, which introduces momentum-dependent discretization errors. The leading p -dependent discretization error is of $\mathcal{O}(\alpha_s(ap)^2)$. We parameterize these errors, up to variations in α_s at the two lattice spacings, with the two NNLO analytic terms proportional to $a^2 E_\pi^2$ and $a^2 m_l$ in the extrapolation formulae for f_{\parallel} and f_{\perp} and remove them by taking the continuum limit of the resulting fit functions. This also largely removes errors of $\mathcal{O}(\alpha_s^2(ap)^2)$. The remaining momentum-dependent discretization effects are of $\mathcal{O}(\alpha_s(ap)^4)$. On the 28^3 fine lattices, $\alpha_s(ap)^4 = 0.003$ for our highest-momentum data points with $a\vec{p} = 2\pi(1, 1, 0)/28$. Therefore the uncertainty in $f_+(q^2)$ due to momentum-dependent discretization effects is negligible compared with our other systematic errors.

G. Heavy-quark discretization errors

We use HQET as a theory of cutoff effects to estimate the size of discretization errors due to use of the Fermilab action for the heavy bottom quark. Because both the lattice and continuum theories can be described by HQET, heavy-quark discretization effects can be classified as a short-distance mismatch of higher-dimension operators [37–39]. Each contribution to the error is given by [83]

$$\text{error}_i = |[\mathcal{C}_i^{\text{lat}}(m_Q, m_0 a) - \mathcal{C}_i^{\text{cont}}(m_Q)] \langle \mathcal{O}_i \rangle|, \quad (55)$$

where \mathcal{O}_i is an effective operator, and $\mathcal{C}_i^{\text{lat}}(m_Q, m_0 a)$ and $\mathcal{C}_i^{\text{cont}}(m_Q)$ are the corresponding short-distance coefficients when HQET is used to describe lattice gauge theory or continuum QCD, respectively. The coefficient mismatch can be written as

$$\mathcal{C}_i^{\text{lat}}(m_Q, m_0 a) - \mathcal{C}_i^{\text{cont}}(m_Q) = a^{\dim \mathcal{O}_i - 4} f_i(m_0 a), \quad (56)$$

and the relative error in our matrix elements can be estimated by setting $\langle \mathcal{O}_i \rangle \sim \Lambda_{\text{QCD}}^{\dim \mathcal{O}_i - 4}$. Then each contribution to the error is

$$\text{error}_i = f_i(m_0 a) (a \Lambda_{\text{QCD}})^{\dim \mathcal{O}_i - 4}, \quad (57)$$

recovering the counting in powers of a familiar from Symanzik, while maintaining the full $m_0 a$ dependence. The functions f_i can be deduced from Refs. [36, 84] and are compiled in Appendix A. Adding all contributions of $\mathcal{O}(\alpha_s a)$ and $\mathcal{O}(a^2)$ from the action and the current, we obtain a relative error of 2.84% (4.16%) for f_{\parallel} and 3.40% (4.98%) for f_{\perp} on the fine (coarse) lattices. We therefore take 3.4% to be the error in $f_+(q^2)$ due to heavy-quark discretization effects.

H. Heavy-light current renormalization

We determine the majority of the heavy-light current renormalization nonperturbatively. The dependence of Z_V^{bb} on the sea quark masses and on the mass of the light spectator quark in the 3-point correlator are both negligible; the statistical error in Z_V^{bb} is $\sim 1\%$. The dependence of Z_V^{ll} on the sea quark masses is also negligible, and the statistical error in Z_V^{ll} is $\sim 1\%$. We therefore include $\sqrt{(1\%^2 + 1\%^2)} \approx 1.4\%$ as the systematic uncertainty in the form factor $f_+(q^2)$ due to the uncertainty in the nonperturbative renormalization factors Z_V^{bb} and Z_V^{ll} for all values of q^2 .

We determine the remaining renormalization of the heavy-light current using lattice perturbation theory. The 1-loop correction to f_{\perp} is $\sim 3\%$ on the fine ensembles and $\sim 4\%$ on the coarse ensembles. Because we calculate $\rho_{V_\mu}^{hl}$ to $\mathcal{O}(\alpha_s)$, the leading corrections are of $\mathcal{O}(\alpha_s^2)$. We might therefore expect the 2-loop corrections to $\rho_{V_\mu}^{hl}$ to be a factor of α_s smaller, or $\sim 1\%$. In order to be conservative, however, we take the entire size of the 1-loop correction on the fine lattices, or 3%, as the systematic uncertainty in $f_+(q^2)$ due to higher-order perturbative contributions for all q^2 bins.

I. Tadpole parameter (u_0) tuning

In order to improve the convergence of lattice perturbation theory, we use tadpole-improved actions for the gluons, light quarks, and heavy quarks [48]. We take u_0 from the average plaquette for the gluon and sea quark action [18]. On the fine lattice, we make the same choice for the valence quarks. For historical reasons, however, we use u_0 determined from the average link in Landau gauge for the valence quarks on the coarse ensembles. The difference between u_0 from the two methods is 3–4% on the coarse ensembles. We must,

therefore, estimate the error in the form factor due to this poor choice of tuning.

The tadpole-improvement factor enters the calculation of $f_+(q^2)$ in several ways. The factor of u_0 that enters the normalization of the heavy Wilson and light staggered quark fields cancels exactly between the $\langle \pi | V^\mu | B \rangle$ lattice matrix element and the nonperturbative renormalization factor $\sqrt{Z_V^{bb} Z_V^{ll}}$. The most significant effect of the mixed u_0 values is in the chiral-continuum extrapolation of f_{\parallel} and f_{\perp} . The different choices for valence and sea quark actions imply that the coarse lattice data is partially quenched. We study this effect by performing the chiral extrapolation in two ways: one assuming that both valence and sea quarks have the mass of the sea quark and the other assuming that both have the mass of the valence quark. This leads to a 3% error in the highest q^2 bin, and a $\sim 1 - 1.5\%$ error in the bins that affect the determination of $|V_{ub}|$. Most of the other effects of changing u_0 in the lattice action and current can be absorbed into our estimate of the uncertainty from higher-order perturbative corrections to ρ_V^{hl} , to discretization errors, and to the normalization of the Naik term. All but the last are already budgeted in Table II. The Naik term in the Asqtad action ensures that the leading discretization errors in the pion dispersion relation are $\mathcal{O}(\alpha_s a^2 p^2)$. We therefore estimate the error in $f_+(q^2)$ due to different Naik terms in the valence and sea sectors to be equal to the largest value of $\alpha_s a^2 p^2$ on the coarse lattice times the ratio of the Landau link over plaquette u_0 cubed, or $\sim 0.2\%$.

We add the flat error from the Naik term to the bin-by-bin error due to the light quark mass used in the chiral extrapolation in quadrature to obtain the total uncertainty. Although our estimate is of necessity rather rough, we find that the errors due to u_0 tuning are much smaller than the dominant errors in $f_+(q^2)$. Our error estimate is therefore adequate for the determinations of the $B \rightarrow \pi \ell \nu$ form factor and $|V_{ub}|$ presented in this work.

J. Finite volume effects

We estimate the uncertainty in the form factor $f_+(q^2)$ due to finite-volume effects using 1-loop finite volume HMS χ PT. The finite volume corrections to the HMS χ PT expressions for f_{\parallel} and f_{\perp} are given in Ref. [42] in terms of integrals calculated in Ref. [85]. It is therefore straightforward to find the relevant corrections for our simulation parameters. We find that the 1-loop finite volume corrections are well below a percent for all of our lattice data points. Because finite volume errors increase as the light quark mass decreases, they are

largest on the $am_l/am_s = 0.007/0.05$ coarse ensemble. The biggest correction is to f_\perp at $\vec{p} = 2\pi(1, 1, 0)/L$, and is 0.5%. We therefore take this to be the uncertainty in $f_+(q^2)$ due to finite volume errors for all q^2 bins.

V. MODEL-INDEPENDENT DETERMINATION OF $|V_{ub}|$

It is well-established that analyticity, crossing symmetry, and unitarity largely constrain the possible shapes of semileptonic form factors [86–89]. In this section we apply constraints based on these general properties to our lattice result for the form factor $f_+(q^2)$ and thereby extract a model-independent value for the CKM matrix element $|V_{ub}|$.

Until now the standard procedure used to extract $|V_{ub}|$ from $B \rightarrow \pi\ell\nu$ semileptonic decays has been to integrate the form factor $|f_+(q^2)|^2$ over a region of q^2 , and then combine the result with the experimentally measured decay rate in this region:

$$\frac{\Gamma(q_{\min})}{|V_{ub}|^2} = \frac{G_F^2}{192\pi^3 m_B^3} \int_{q_{\min}^2}^{q_{\max}^2} dq^2 [(m_B^2 + m_\pi^2 - q^2)^2 - 4m_B^2 m_\pi^2]^{3/2} |f_+(q^2)|^2. \quad (58)$$

The integration, however, necessitates a continuous parameterization of the form factor over the full range from q_{\min}^2 to q_{\max}^2 .

In our earlier, preliminary unquenched analysis, we determine $f_+(q^2)$ by fitting the lattice data points to the Bećirević-Kaidalov (BK) parameterization [90],

$$f_+(q^2) = \frac{f_+(0)}{(1 - \tilde{q}^2)(1 - \alpha \tilde{q}^2)}, \quad (59)$$

$$f_0(q^2) = \frac{f_+(0)}{(1 - \tilde{q}^2/\beta)}, \quad (60)$$

where $\tilde{q}^2 \equiv q^2/m_{B^*}^2$. The BK ansatz contains three free parameters and incorporates many of the known properties of the form factor such as the kinematic constraint at $q^2 = 0$, heavy-quark scaling, and the location of the B^* pole. The HPQCD Collaboration instead uses the four-parameter Ball-Zwicky (BZ) parameterization [91], which is the same as the BK function in Eq. (59) plus an additional pole to capture the effects of multiparticle states. In both cases, however, the choice of fit function introduces a systematic uncertainty that is difficult to quantify.

It is likely the BK and BZ parameterizations can be safely used to interpolate between data points, whether they be at high q^2 from lattice QCD or at low q^2 from experiment.

TABLE II: Statistical and systematic error contributions to the $B \rightarrow \pi\ell\nu$ form factor. Each source of uncertainty is discussed in Sec. IV. For each of the 12 q^2 bins, the error is shown as a percentage of the total form factor, $f_+(q^2)$, which is given in the second row from the top. Because the bootstrap errors in the form factor are asymmetric, the errors shown are the average of the upper and lower bootstrap errors. In order to facilitate the use of our result, we also present the normalized statistical and systematic bootstrap correlation matrices in Table IV and the total bootstrap covariance matrix in Table V.

q^2 (GeV 2)	26.5	25.7	25.0	24.3	23.5	22.8	22.1	21.3	20.6	19.8	19.1	18.4
$f_+(q^2)$	9.04	6.32	4.75	3.75	3.06	2.56	2.19	1.91	1.69	1.51	1.37	1.27
statistics + χ PT (%)	24.4	18.5	13.5	9.6	7.1	6.3	6.5	6.9	7.2	7.5	8.2	9.8
$g_{B^*B\pi}$ uncertainty	1.1	0.3	0.8	1.8	2.4	2.8	2.9	2.8	2.6	2.5	2.6	2.9
r_1	0.4	0.7	0.9	1.1	1.2	1.3	1.4	1.4	1.5	1.5	1.4	1.4
\hat{m}	0.2	0.2	0.2	0.2	0.2	0.2	0.2	0.3	0.3	0.3	0.3	0.3
m_s	0.6	0.6	0.6	0.7	0.7	0.8	0.8	0.9	1.0	1.1	1.2	1.3
m_b	1.2	1.2	1.2	1.2	1.2	1.2	1.2	1.2	1.2	1.2	1.2	1.2
heavy quark discretization	3.4	3.4	3.4	3.4	3.4	3.4	3.4	3.4	3.4	3.4	3.4	3.4
nonperturbative Z_V	1.4	1.4	1.4	1.4	1.4	1.4	1.4	1.4	1.4	1.4	1.4	1.4
perturbative ρ	3.0	3.0	3.0	3.0	3.0	3.0	3.0	3.0	3.0	3.0	3.0	3.0
u_0	2.9	2.1	1.2	0.5	0.3	0.8	1.1	1.3	1.4	1.3	1.3	1.3
finite volume	0.5	0.5	0.5	0.5	0.5	0.5	0.5	0.5	0.5	0.5	0.5	0.5
total systematics (%)	5.9	5.4	5.3	5.4	5.7	5.9	6.0	6.1	6.0	6.0	6.0	6.2

It is less clear, however, how well these ansatze can be trusted to extrapolate the form factor shape beyond the reach of the data points. Furthermore, comparisons of lattice and experimental determinations of BK or BZ fit parameters are not necessarily meaningful. For example, if the slope parameters α from experiment and lattice QCD were found to be inconsistent, we would not know whether theory and experiment disagree, or whether the parameterization is simply inadequate. A parameterization that circumvents this issue is therefore desirable. In this work we pursue an analysis based on the model-independent z -parameterization, which is pedagogically reviewed in Ref. [87].

A. Analyticity, unitarity, and heavy-quark constraints on heavy-light form factors

All form factors are analytic functions of q^2 except at physical poles and threshold branch points. In the case of the $B \rightarrow \pi l\nu$ form factors, $f(q^2)$ is analytic below the $B\pi$ production region except at the location of the B^* pole. The fact that analytic functions can always be expressed as convergent power series allows the form factors to be written in a particularly useful manner.

Consider mapping the variable q^2 onto a new variable, z , in the following way:

$$z(q^2, t_0) = \frac{\sqrt{1 - q^2/t_+} - \sqrt{1 - t_0/t_+}}{\sqrt{1 - q^2/t_+} + \sqrt{1 - t_0/t_+}}, \quad (61)$$

where $t_+ \equiv (m_B + m_\pi)^2$, $t_- \equiv (m_B - m_\pi)^2$, and t_0 is a free parameter. Although this mapping appears complicated, it actually has a simple interpretation in terms of q^2 ; this transformation maps $q^2 > t_+$ (the production region) onto $|z| = 1$ and maps $q^2 < t_+$ (which includes the semileptonic region) onto real $z \in [-1, 1]$. In terms of z , the form factors have a simple form:

$$f(q^2) = \frac{1}{P(q^2)\phi(q^2, t_0)} \sum_{k=0}^{\infty} a_k(t_0) z(q^2, t_0)^k, \quad (62)$$

where the Blaschke factor $P(q^2)$ is a function that contains subthreshold poles and the outer function $\phi(q^2, t_0)$ is an arbitrary analytic function (outside the cut from $t_+ < q^2 < \infty$) whose choice only affects the particular values of the series coefficients a_k .

For the case of the $B \rightarrow \pi l\nu$ form factor $f_+(q^2)$, the Blaschke factor $P_+(q^2) = z(q^2, m_{B^*}^2)$

accounts for the B^* pole. In this work we use the same outer function as in Ref. [44]:

$$\begin{aligned}\phi_+(q^2, t_0) &= \sqrt{\frac{3}{96\pi\chi_J^{(0)}}} \left(\sqrt{t_+ - q^2} + \sqrt{t_+ - t_0} \right) \left(\sqrt{t_+ - q^2} + \sqrt{t_+ - t_-} \right)^{3/2} \\ &\times \left(\sqrt{t_+ - q^2} + \sqrt{t_+} \right)^{-5} \frac{(t_+ - q^2)}{(t_+ - t_0)^{1/4}},\end{aligned}\quad (63)$$

where $\chi_J^{(0)}$ is a numerical factor that can be calculated via the operator product expansion (OPE) [88, 92]. This choice of $\phi_+(q^2, t_0)$, when combined with unitarity and crossing-symmetry, leads to a particularly simple constraint on the series coefficients in Eq. (62). Although the t -dependence of Eq. (63) appears complicated, it is designed so that the sum over the squares of the series coefficients is t -independent:

$$\sum_{k=0}^{\infty} a_k^2 = \frac{1}{2\pi i} \oint \frac{dz}{z} |P(z)\phi(z)f(z)|^2 \equiv A, \quad (64)$$

where the value of the constant A depends upon the choice of $\chi_J^{(0)}$ in Eq. (63). Because the decay process $B \rightarrow \pi\ell\nu$ is related to the scattering process $\ell\nu \rightarrow B\pi$ by crossing symmetry, the sum of the series coefficients is bounded by unitarity, *i.e.*, the fact that the production rate of $B\pi$ states is less than or equal to the production of all final states that couple to the $b \rightarrow u$ vector current. In particular, if one chooses the numerical factor $\chi_J^{(0)}$ to be equal to the appropriate integral of the inclusive rate $\ell\nu \rightarrow X_b$, the sum of the coefficients is bounded by unity:

$$\sum_{k=0}^N a_k^2 \lesssim 1, \quad (65)$$

where this constraint holds for any value of N and the “ \lesssim ” symbol indicates higher-order corrections to $\chi_J^{(0)}$ in α_s and the OPE.

Such higher-order corrections turn out to be negligible for the $B \rightarrow \pi\ell\nu$ form factor because the bound in Eq. (65) is far from saturated, *i.e.*, the sizes of the coefficients turn out to be much less than one. Becher and Hill [93] have pointed out that this is due to the fact that the b -quark mass is so large. In the heavy-quark limit, the leading contributions to the integral in Eq. (64) are of $\mathcal{O}(\Lambda^3/m_b^3)$, where Λ is a typical hadronic scale. Assuming that the ratio $\Lambda/m_b \sim 0.1$, the heavy-quark bound on the a_k 's is approximately thirty times more constraining than the bound from unitarity alone:

$$\sum_{k=0}^N a_k^2 \sim \left(\frac{\Lambda}{m_B} \right)^3 \approx 0.001. \quad (66)$$

We point out that the authors of Ref. [46] have recently proposed a slightly different parameterization of the $B \rightarrow \pi\ell\nu$ form factor with a simpler choice of outer function, $\phi = 1$:

$$f_+(q^2) = \frac{1}{1 - q^2/m_{B^*}^2} \sum_{k=0}^{\infty} b_k(t_0) z(q^2, t_0)^k. \quad (67)$$

This choice enforces the correct scaling behavior, $f_+(q^2) \sim 1/q^2$ as $q^2 \rightarrow \infty$. It leads, however, to a more complicated constraint on the series coefficients:

$$\sum_{j,k=0}^N B_{jk} b_j b_k \lesssim 1, \quad (68)$$

where the elements of the symmetric matrix B_{jk} are calculable functions of t_0 . Because $B \rightarrow \pi\ell\nu$ semileptonic decay is far from $q^2 \rightarrow \infty$, and because the unitary bound is so far from being saturated, the choice of outer function should make a negligible impact on the resulting determination of $|V_{ub}|$. We therefore use the more standard outer function given in Eq. (63) because the constraint in Eq. (65) is independent of the number of terms in the power series, and is therefore simpler to implement.

The free parameter t_0 can be chosen to make the maximum value of $|z|$ as small as possible in the semileptonic region; we choose $t_0 = 0.65t_-$ as in Ref. [44]. For $B \rightarrow \pi l\nu$ semileptonic decays this maps the physical region onto:

$$0 < t < t_- \mapsto -0.34 < z < 0.22. \quad (69)$$

The bound on the coefficients in the z -expansion combined with the small numerical values of $|z|$ in the physical region ensures that one needs only the first few terms in the z -expansion to accurately describe the form factor shape. Moreover, as the precision of both the lattice calculations and experimental measurements improve, one may easily include higher-order terms as needed.

B. Determination of $|V_{ub}|$ using z -parameterization

In 2007 the BABAR Collaboration published a measurement of the shape of the $B \rightarrow \pi\ell\nu$ semileptonic form factor with results for 12 separate q^2 bins between $q_{\min}^2 \approx 1 \text{ GeV}^2$ and $q_{\max}^2 \approx 24 \text{ GeV}^2$ [43]. This suggests that lattice QCD calculations are now needed primarily to provide a precise form factor normalization at one value of q^2 in order to determine $|V_{ub}|$.

The minimal error in $|V_{ub}|$ can, of course, still be attained by using all of the available information on the form factor shape and normalization, provided that one analyzes the data in a model-independent way.

Because as many terms can be added as are needed to describe the $B \rightarrow \pi\ell\nu$ form factor to the desired accuracy, use of the convergent series expansion allows for a systematically improvable determination of $|V_{ub}|$. We fit our lattice numerical Monte Carlo data and the 12-bin BABAR experimental data together to the z -expansion, leaving the relative normalization factor, $|V_{ub}|$, as a free parameter to be determined by the fit. In this way we determine $|V_{ub}|$ in an optimal, model-independent way.

We first fit the lattice numerical Monte Carlo data and the 12-bin BABAR experimental data *separately* to the z -expansion in order to check for consistency. We use Gaussian priors with central value 0 and width 1 on each coefficient in the z -expansion to impose the unitarity constraint. Although this manner of constraining the coefficients is less stringent than the strict bound given in Eq. (65), the choice does not matter because the unitary bound is far from saturated and the individual coefficients all turn out to be much less than 1. We obtain identical fit results even when the coefficients are completely unconstrained.

The left-hand plot in Fig. 9 shows the BABAR measurement of the $B \rightarrow \pi\ell\nu$ semileptonic form factor, $f_+(q^2)$ [43]. The right-hand plot shows the same data multiplied by the functions $P_+(q^2)$ and $\phi_+(q^2, t_0)$ and plotted versus the variable z . After remapping from q^2 to z there is almost no curvature in the experimental data. This indicates that most of the curvature in the data is due to well-understood QCD effects that are parameterized by the functions $P_+(q^2)$ and $\phi_+(q^2, t_0)$. Consequently the experimental data is well-described by a normalization (a_0) and slope (a_1/a_0), as shown in Fig. 9. The slope of the BABAR experimental $B \rightarrow \pi\ell\nu$ form factor data is

$$\frac{a_1}{a_0} = -1.60 \pm 0.26. \quad (70)$$

If one includes a curvature term in the z -fit, the coefficient a_2 is poorly determined, but is found to be negative at $\sim 1.5\sigma$. The value of a_1 is consistent with the result of the linear fit.

Figure 10 shows the lattice determination of the $B \rightarrow \pi\ell\nu$ semileptonic form factor, f_+ vs. q^2 (left plot) and the remapped form factor, $P_+\phi_+f_+$ vs. z (right plot). As is the case for the experimental data, the shape of the lattice form factor is less striking after taking

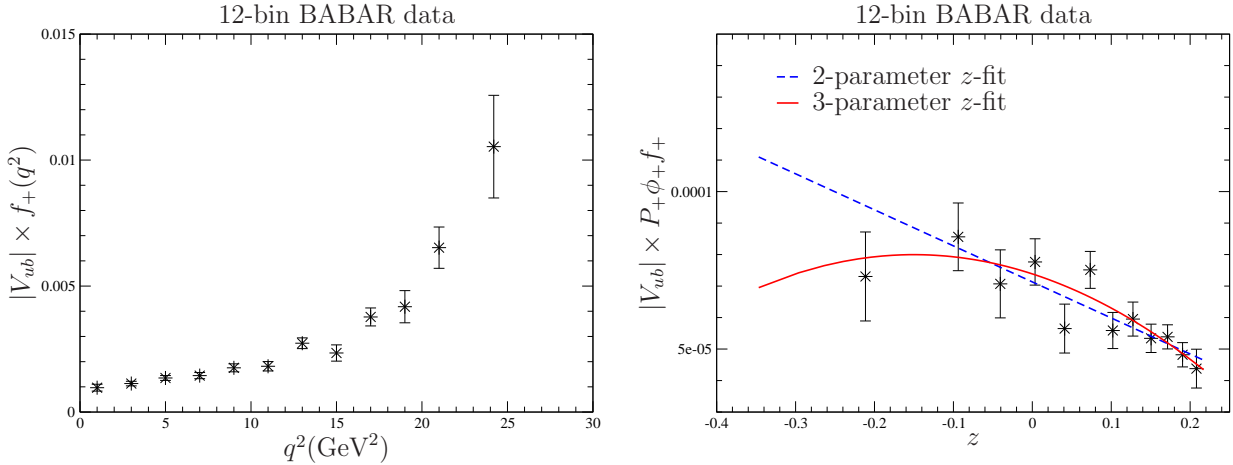


FIG. 9: Experimental data for the $B \rightarrow \pi l \nu$ form factor times the CKM element $|V_{ub}|$ from the BABAR collaboration [43]. The left plot shows $|V_{ub}| \times f_+$ versus q^2 while the right plot shows $|V_{ub}| \times f_+$ multiplied by the functions $P_+ \phi_+$ and plotted against the new variable z . Both the 2-parameter fit (dashed blue line) and 3-parameter fit (solid red curve) have good $\chi^2/\text{d.o.f.}'s.$

out the B^* pole and other known QCD effects. When the lattice calculation of the form factor is fit to the z -parameterization, however, it determines both a slope and a curvature. One cannot, in fact, successfully fit the lattice data without including a curvature term. The slope and curvature of the lattice determination of the $B \rightarrow \pi \ell \nu$ form factor are

$$\frac{a_1}{a_0} = -1.75 \pm 0.91, \quad (71)$$

$$\frac{a_2}{a_0} = -5.22 \pm 1.39. \quad (72)$$

The above uncertainties are the standard errors computed from the inverse of the parameter Hessian matrix that result from a fit using the full covariance matrix determined from the bootstrap distributions of chiral-continuum extrapolated values of f_{\parallel} and f_{\perp} , including systematics.

Because the shapes of the lattice calculation and experimental measurement of the form factor are consistent, we now proceed to fit them simultaneously to the z -expansion and determine $|V_{ub}|$. The numerical lattice and measured experimental data are independent, so we construct a block-diagonal covariance matrix where one block is the total lattice error matrix and the other is the total experimental error matrix. The combined fit function includes the series coefficients (a_k 's) plus an additional parameter for the relative normalization between the lattice and experimental results ($|V_{ub}|$). In order to account for the systematic uncertainty in $|V_{ub}|$ due to poorly-constrained higher-order terms in z , we con-

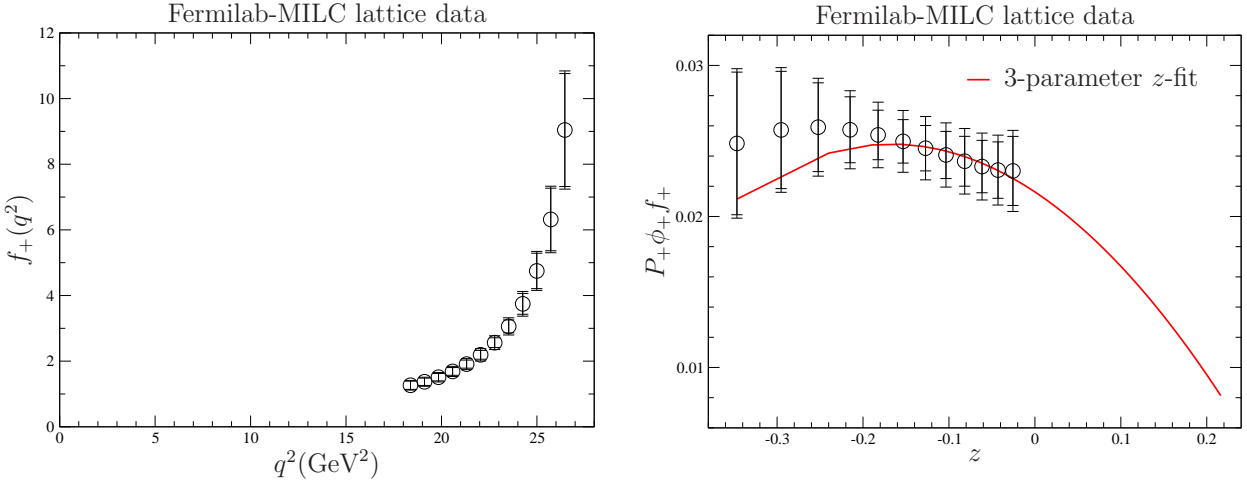


FIG. 10: Lattice calculation of the $B \rightarrow \pi \ell \nu$ form factor. The left plot shows f_+ vs. q^2 while the right plot shows $P_+ \phi_+ f_+$ vs. z . The inner error bars indicate the statistical error, while the outer error bars indicate the sum of the statistical and systematic added in quadrature. A 3-parameter z -fit is needed to describe the lattice data with a good $\chi^2/\text{d.o.f.}$

tinue to add terms in the series until the error in $|V_{ub}|$ reaches a maximum. This occurs once we include the term proportional to z^3 . The resulting combined z -fit is shown in Fig. 11, and the corresponding fit parameters are

$$|V_{ub}| \times 10^3 = 3.38 \pm 0.36, \quad (73)$$

$$a_0 = 0.0218 \pm 0.0021, \quad (74)$$

$$a_1 = -0.0301 \pm 0.0063, \quad (75)$$

$$a_2 = -0.059 \pm 0.032, \quad (76)$$

$$a_3 = 0.079 \pm 0.068. \quad (77)$$

The values of the coefficients are all much smaller than one, as expected from heavy-quark power-counting. The sum of the squares of the coefficients is $\sum a_k^2 = 0.011 \pm 0.012$, and is consistent with the prediction of Becher and Hill within uncertainties in the series coefficients and in the choice of the hadronic scale in Eq. (66) [93].

By combining all of the available numerical lattice Monte Carlo data and 12-bin BABAR experimental data for the $B \rightarrow \pi \ell \nu$ form factor in a simultaneous fit we are able to determine $|V_{ub}|$ to $\sim 11\%$ accuracy. This error is independent (within $\lesssim 0.5\%$) of the choice of the parameter t_0 used in the change of variables from q^2 to $z(q^2, t_0)$ and in the outer function $\phi_+(q^2, t_0)$. In order to demonstrate the advantage of the combined fit method, we compare

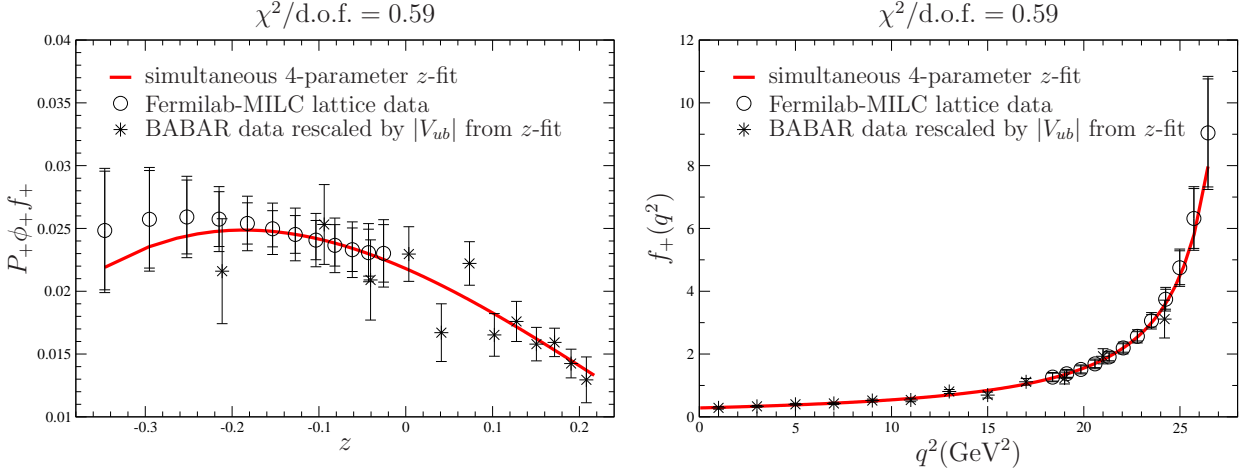


FIG. 11: Model-independent determination of $|V_{ub}|$ from a simultaneous fit of lattice and experimental $B \rightarrow \pi \ell \nu$ semileptonic form factor data to the z -parameterizaton. The left plot shows $P_+ \phi_+ f_+$ vs. z while the right plot shows f_+ vs. q^2 . Inclusion of terms in the power-series through z^3 yields the maximum uncertainty in $|V_{ub}|$; the corresponding 4-parameter z -fit is given by the red curve in both plots. The circles denote the Fermilab-MILC lattice data, while the stars indicate the 12-bin BABAR experimental data, rescaled by the value of $|V_{ub}|$ determined in the simultaneous z -fit.

the error in $|V_{ub}|$ given in Eq. (73) with that obtained from separate z -fits of the lattice and experimental data. A z -fit to the 12-bin BABAR experimental data alone determines the normalization a_0^{exp} to $\sim 8\%$, while a z -fit to our numerical lattice data determines a_0^{lat} to $\sim 14\%$. Thus separate fits lead to a determination of $|V_{ub}| \equiv a_0^{\text{exp}}/a_0^{\text{lat}}$ with an approximately 16% total uncertainty.³ The combined fit yields a significantly smaller error and is thus preferred.

When the numerical lattice data and experimental data are fit simultaneously, utilizing all of the available data points is of secondary importance for reducing the total uncertainty

³ Because the values of the coefficients of the power-series in z depend upon the choice of the parameter t_0 in Eqs. (61)–(63), we could, in principle, choose a different value of t_0 in order to minimize the error in either a_0^{exp} or a_0^{lat} . For example, use of $t_0 = 22.8 \text{ GeV}^2$ reduces the uncertainty in the lattice normalization because the error in the lattice form factor is smallest at this q^2 -value. Use of $t_0 = 22.8 \text{ GeV}^2$ greatly increases the uncertainty in the experimental normalization, however, because the experimental data is poorly-determined at large values of q^2 . Ultimately, this choice of t_0 leads to an even worse determination of $|V_{ub}|$ than from our standard choice of $t_0 = 0.65t_-$. Although we did not attempt to determine the value of t_0 that minimizes the total error in $|V_{ub}|$, the errors resulting from separate fits were greater than that obtained with the simultaneous fit for all values of t_0 that we tried.

in $|V_{ub}|$. For example, we can evaluate the importance of the low q^2 experimental points to the extraction of $|V_{ub}|$ by removing them from the combined z -fit. Including only the three experimental data points with $q^2 > 18 \text{ GeV}^2$, we find a consistent value of $|V_{ub}|$ with only a $\sim 1\%$ larger uncertainty. Similarly, we can evaluate the importance of having many lattice data points, rather than only a single point, by using only the most precise lattice point with a total error of $\sim 9\%$. This allows the form factor shape to be completely determined by the experimental data. We find a consistent value of $|V_{ub}|$ but with an even larger error of $\sim 13\%$. We therefore conclude that combining all of the numerical lattice data with all of the experimentally-measured BABAR data minimizes the total uncertainty in $|V_{ub}|$. Because the small error in our final determination of $|V_{ub}|$ is primarily due to the power of the combined z -fit method, one could easily use the procedure outlined in this section to improve the exclusive determination of $|V_{ub}|$ from existing lattice QCD calculations of the $B \rightarrow \pi \ell \nu$ form factor such as that by the HPQCD Collaboration [33].

VI. RESULTS AND CONCLUSIONS

Combining our latest unquenched lattice calculation of the $B \rightarrow \pi \ell \nu$ form factor with the 12-bin BABAR experimental data, we find the following model-independent value for $|V_{ub}|$:⁴

$$|V_{ub}| \times 10^3 = 3.38 \pm 0.36. \quad (78)$$

The total error is $\sim 11\%$, and it is nontrivial to separate the error precisely into contributions from statistical, systematic, and experimental uncertainty because of the combined z -fit procedure used. If we assume, however, that the error in $|V_{ub}|$ is dominated by the most precisely determined lattice point (which is not quite true, as shown in the previous section), we can estimate that the contributions are roughly equally divided as $\sim 6\%$ lattice statistical, $\sim 6\%$ lattice systematic, and $\sim 6\%$ experimental.

Our result is consistent with, although slightly lower than, our earlier, preliminary de-

⁴ At three conferences during Summer 2008 we presented a version of this model-independent analysis with a numerical value for $|V_{ub}|$ that is $1-\sigma$ lower than that given here in Eq. (79). We have since improved several aspects of the lattice calculation, most notably reducing the statistical errors that enter the chiral and continuum extrapolations of f_\perp and f_\parallel and, hence, f_+ . Equation (78) is our final result for $|V_{ub}|$ based on the lattice data from the ensembles in Table I and the methodology of Secs. III and V.

termination of $|V_{ub}|$. The reduction in central value is primarily due to a change in the lattice determination of the form factor, not the procedure used to determine $|V_{ub}|$. Because our new analysis uses a second lattice spacing, we are able to take the continuum limit of the form factor. We find that the continuum extrapolation increases the overall normalization of $f_+(q^2)$, and hence decreases the value of $|V_{ub}|$. Our errors are smaller than those of previous exclusive determinations primarily because we have reduced the size of the discretization errors, which are significantly smaller than in the previous Fermilab-MILC calculation ($\sim 7\% \rightarrow 3\%$) because of the additional finer lattice spacing.

Our new result is $\sim 1\text{--}2\sigma$ lower than most inclusive determinations of $|V_{ub}|$, which typically range from $4.0 - 4.5 \times 10^{-3}$ [32]. Much of the variation among the inclusive values is due to the choice of input parameters — in particular that of the b -quark mass [94]. The recent determination of m_b by Kühn, Steinhauser, and Sturm using experimental data for the cross section for $e^+e^- \rightarrow \text{hadrons}$ in the bottom threshold region yields the value of m_b to percent-level accuracy [95], and is consistent with the PDG average [13]. Neubert has shown, however, that an updated extraction of m_b from fits to $B \rightarrow X_c \ell \nu$ moments using only the theoretically cleanest channels (excluding $b \rightarrow X_s \gamma$) results in a larger b -quark mass and hence smaller inclusive value of $|V_{ub}|$, thereby reducing the tension between inclusive and exclusive determinations [96].

Our result is consistent with the currently preferred values for $|V_{ub}|$ determined by the global CKM unitarity triangle analyses of the CKMfitter Collaboration, $|V_{ub}| \times 10^3 = 3.44^{+0.22}_{-0.17}$ [97], and UTfit Collaboration, $|V_{ub}| \times 10^3 = 3.48 \pm 0.16$, [98]. Further reduction in the errors is therefore essential for a more stringent test of the CKM framework and a more sensitive probe of physics beyond the Standard Model.

The dominant uncertainty in our lattice calculation of the $B \rightarrow \pi \ell \nu$ form factor comes from the statistical errors in the 2-point and 3-point correlations. This error can be reduced in a straightforward manner with use of an improved source for the pion and/or additional gauge configurations. The statistical errors in the nonperturbative renormalization factors Z_V^{bb} and Z_V^{ll} can be brought to below a percent in the same way. The chiral-continuum extrapolation error, which is inextricably linked to the statistical errors in the correlation functions, can also be improved by simulating at more light quark masses and an additional finer lattice spacing of $a \sim 0.06$ fm. Presumably a better constrained chiral and continuum extrapolation will reduce the size of other q^2 -dependent errors such as those from $g_{B^* B \pi}$, r_1 ,

and the light quark masses by some unknown amount as well. Use of a finer lattice with $a \sim 0.06$ fm will further decrease the momentum-dependent and heavy-quark discretization errors, which we now estimate with power-counting. The extraction of $|V_{ub}|$ can also be improved by including more experimental measurements of the $B \rightarrow \pi\ell\nu$ branching fraction. This, however, will require understanding the correlations among the various systematic uncertainties. Given these refinements of the current calculation, an even more precise, model-independent value of $|V_{ub}|$ can be obtained in the near future.

Acknowledgments

We thank Richard Hill and Enrico Lunghi for helpful discussions, and Thomas Becher for valuable comments on the manuscript. Computations for this work were carried out in part on facilities of the USQCD Collaboration, which are funded by the Office of Science of the U.S. Department of Energy, and on facilities of the NSF Teragrid under allocation TG-MCA93S002. This work was supported in part by the United States Department of Energy under Grant Nos. DE-FC02-06ER41446 (C.D., L.L.), DE-FG02-91ER40661(S.G.), DE-FG02-91ER40677 (A.X.K., R.T.E., E.G.), DE-FG02-91ER40628 (C.B., J.L.), DE-FG02-04ER41298 (D.T.) and by the National Science Foundation under Grant Nos. PHY-0555243, PHY-0757333, PHY-0703296 (C.D., L.L.), PHY-0555235 (J.L.), PHY-0456556 (R.S.). R.T.E. and E.G. were supported in part by URA visiting scholar awards. Fermilab is operated by Fermi Research Alliance, LLC, under Contract No. DE-AC02-07CH11359 with the United States Department of Energy.

APPENDIX A: ESTIMATE OF HEAVY QUARK DISCRETIZATION ERRORS

In this Appendix we collect the short-distance functions f_i used to estimate the heavy-quark discretization effects. For more background, see Refs. [36–39, 83, 84].

1. $\mathcal{O}(a^2)$ errors

We start with these because explicit expressions for the functions $f_i(m_0a)$ are available.

a. $\mathcal{O}(a^2)$ errors from the Lagrangian

There are two bilinears, $\bar{h}\vec{D} \cdot \vec{E}h$ and $\bar{h}i\vec{\Sigma} \cdot [\vec{D} \times \vec{E}]h$, and many four-quark operators. At tree level the coefficients of all four-quark operators vanish and the coefficients of the two bilinears are the same. The mismatch function is given by

$$f_E(m_0a) = \frac{1}{8m_E^2 a^2} - \frac{1}{2(2m_2a)^2}. \quad (\text{A1})$$

Using explicit expressions for $1/m_2$ [36] and $1/m_E^2$ [84], one finds

$$f_E(m_0a) = \frac{1}{2} \left[\frac{c_E(1 + m_0a) - 1}{m_0a(2 + m_0a)(1 + m_0a)} - \frac{1}{4(1 + m_0a)^2} \right]. \quad (\text{A2})$$

We use $c_E = 1$ in our numerical simulations.

b. $\mathcal{O}(a^2)$ errors from the current

There are three terms with non-zero coefficients, $\bar{q}\Gamma\vec{D}^2h$, $\bar{q}\Gamma i\vec{\Sigma} \cdot \vec{B}h$, and $\bar{q}\Gamma\vec{\alpha} \cdot \vec{E}h$, which can be deduced from Eq. (A17) of Ref. [36]. Their coefficients can be read off from Eqs. (A19) [36]. When $c_B = r_s$ the first two share the same coefficient:

$$\begin{aligned} f_X(m_0a) &= \frac{1}{8m_X^2 a^2} - \frac{\zeta d_1(1 + m_0a)}{m_0a(2 + m_0a)} - \frac{1}{2(2m_2a)^2}, \\ &= \frac{1}{2} \left[\frac{1}{(2 + m_0a)(1 + m_0a)} + \frac{1}{2(1 + m_0a)} - \frac{1}{4(1 + m_0a)^2} - \frac{1}{(2 + m_0a)^2} \right], \\ &= \frac{1}{2} \left[\frac{1}{2(1 + m_0a)} - \left(\frac{m_0a}{2(2 + m_0a)(1 + m_0a)} \right)^2 \right], \end{aligned} \quad (\text{A3})$$

where the last term on the second line comes from using the tree-level d_1 . For the third operator, $\bar{q}\Gamma\vec{\alpha} \cdot \vec{E}h$,

$$\begin{aligned} f_Y(m_0a) &= \frac{1}{2} \left[\frac{d_1}{m_2a} - \frac{\zeta(1 - c_E)(1 + m_0a)}{m_0a(2 + m_0a)} \right], \\ &= \frac{2 + 4m_0a + (m_0a)^2}{4(1 + m_0a)^2(2 + m_0a)^2}, \end{aligned} \quad (\text{A4})$$

where the last line reflects the choices made for c_E and d_1 .

2. $\mathcal{O}(\alpha_s a)$ errors

Because we improve both the action and current, the mismatch functions $f_i(m_0a)$ start at order α_s , and we do not have explicit expressions for them. (The calculation of these

functions would be needed to match at the one-loop level.) So we shall take unimproved tree-level coefficients as a guide to the combinatoric factors and consider asymptotic behavior in the limits $m_0a \rightarrow 0, \infty$.

a. $\mathcal{O}(\alpha_s a)$ errors from the Lagrangian

There are two bilinears, the kinetic energy $\bar{h}\vec{D}^2 h$ and the chromomagnetic moment $\bar{h}i\vec{\Sigma} \cdot \vec{B}h$. There is no mismatch in the coefficient of the kinetic energy, by assumption, since we identify the kinetic mass with the heavy-quark mass. This tuning is imperfect, but the associated error is budgeted in Sec. IV E.

At the tree level the chromomagnetic mismatch is

$$f_B^{[0]}(m_0a) = \frac{c_B - 1}{2(1 + m_0a)}. \quad (\text{A5})$$

This has the right asymptotic behavior in both limits, so our ansatz for the one-loop mismatch function is simply

$$f_B^{[0]}(m_0a) = \frac{\alpha_s}{2(1 + m_0a)}, \quad (\text{A6})$$

and error_B is this function multiplied by $a\Lambda$.

b. $\mathcal{O}(\alpha_s a)$ errors from the current

There is only one correction at tree level, but more generally there are two for the temporal current and four for the spatial current. (See Eqs. (2.27)–(2.32) of Ref. [38].)

The tree-level mismatch function ends up being the same as d_1 :

$$f_3^{[0]}(m_0a) = \frac{m_0a}{2(2 + m_0a)(1 + m_0a)}. \quad (\text{A7})$$

It is, however, an accident that it vanishes as $m_0a \rightarrow 0$. Therefore, we instead take

$$f_3(m_0a) = \frac{\alpha_s}{2(2 + m_0a)}, \quad (\text{A8})$$

which has the right asymptotic behavior.

TABLE III: Relative error from mismatches in the heavy quark Lagrangian and current for the bottom quark with $\Lambda = 700$ MeV. To obtain the totals given in the text E and X are counted twice, and 3 is counted twice for f_{\parallel} and four times for f_{\perp} . Entries are in per cent.

a (fm)	$\alpha_V(q^*)$	$m_0 a$	B	3	E	X	Y
0.09	0.33	2.018	1.76	1.32	0.28	0.80	0.24
0.12	0.41	2.617	2.48	1.94	0.39	1.26	0.33

3. Numerical estimates

The relative errors due to mismatches in the heavy quark Lagrangian and current on the MILC coarse and fine ensembles are tabulated in Table III. At the fine lattice spacing we take the typical $\alpha_V(q^*)$ to be $\frac{1}{3}$, and we use one-loop running to obtain $\alpha_V(q^*)$ at the coarse lattice spacing. The contribution error_Y from the $\vec{\alpha} \cdot \vec{E}$ error in the current is so small both because $c_E = 1$ in our simulation and because d_1 is small. Adding the individual errors given in Table III in quadrature, and taking into account multiple contributions of the same size, we find the total error to be 2.84% (4.16%) for f_{\parallel} and 3.40% (4.98%) for f_{\perp} on the fine (coarse) lattices.

APPENDIX B: STATISTICAL AND SYSTEMATIC ERROR MATRICES

In this Appendix we present the normalized statistical and systematic bootstrap correlation matrices for the $B \rightarrow \pi\ell\nu$ form factor, $f_+(q^2)$, that were used in our model-independent determination of $|V_{ub}|$. In order to facilitate the use of our result, we also show the resulting total covariance matrix.

TABLE IV: Normalized statistical (upper) and systematic (lower) bootstrap correlation matrices for the $B \rightarrow \pi\ell\nu$ form factor, $f_+(q^2)$. These should be combined with the values of $f_+(q^2)$ presented in Table II to reconstruct the full correlation matrices.

q^2 (GeV 2)	26.5	25.7	25.0	24.3	23.5	22.8	22.1	21.3	20.6	19.8	19.1	18.4
26.5	1.00	0.99	0.97	0.88	0.66	0.29	-0.01	-0.16	-0.19	-0.14	-0.04	0.05
25.7	0.99	1.00	0.99	0.92	0.73	0.38	0.07	-0.09	-0.13	-0.09	0.00	0.08
25.0	0.97	0.99	1.00	0.97	0.82	0.51	0.21	0.04	-0.02	0.01	0.07	0.13
24.3	0.88	0.92	0.97	1.00	0.93	0.69	0.42	0.25	0.18	0.17	0.20	0.21
23.5	0.66	0.73	0.82	0.93	1.00	0.91	0.72	0.56	0.48	0.43	0.39	0.32
22.8	0.29	0.38	0.51	0.69	0.91	1.00	0.94	0.85	0.77	0.69	0.58	0.42
22.1	-0.01	0.07	0.21	0.42	0.72	0.94	1.00	0.98	0.92	0.84	0.69	0.48
21.3	-0.16	-0.09	0.04	0.25	0.56	0.85	0.98	1.00	0.98	0.92	0.78	0.55
20.6	-0.19	-0.13	-0.02	0.18	0.48	0.77	0.92	0.98	1.00	0.97	0.86	0.66
19.8	-0.14	-0.09	0.01	0.17	0.43	0.69	0.84	0.92	0.97	1.00	0.95	0.80
19.1	-0.04	0.00	0.07	0.20	0.39	0.58	0.69	0.78	0.86	0.95	1.00	0.94
18.4	0.05	0.08	0.13	0.21	0.32	0.42	0.48	0.55	0.66	0.80	0.94	1.00

q^2 (GeV 2)	26.5	25.7	25.0	24.3	23.5	22.8	22.1	21.3	20.6	19.8	19.1	18.4
26.5	1.00	0.98	0.95	0.89	0.85	0.88	0.9	0.91	0.91	0.92	0.91	0.90
25.7	0.98	1.00	0.98	0.92	0.87	0.87	0.88	0.89	0.90	0.91	0.9	0.88
25.0	0.95	0.98	1.00	0.97	0.94	0.94	0.94	0.94	0.95	0.95	0.95	0.94
24.3	0.89	0.92	0.97	1.00	0.99	0.99	0.98	0.98	0.98	0.98	0.97	
23.5	0.85	0.87	0.94	0.99	1.00	0.99	0.99	0.98	0.98	0.98	0.98	0.98
22.8	0.88	0.87	0.94	0.99	0.99	1.00	1.0	1.00	0.99	0.99	0.99	0.99
22.1	0.90	0.88	0.94	0.98	0.99	1.00	1.00	1.00	1.00	1.00	1.00	1.00
21.3	0.91	0.89	0.94	0.98	0.98	1.00	1.00	1.00	1.00	1.00	1.00	1.00
20.6	0.91	0.90	0.95	0.98	0.98	0.99	1.00	1.00	1.00	1.00	1.00	1.00
19.8	0.92	0.91	0.95	0.98	0.98	0.99	1.00	1.00	1.00	1.00	1.00	1.00
19.1	0.91	0.9	0.95	0.98	0.98	0.99	1.00	1.00	1.00	1.00	1.00	1.00
18.4	0.90	0.88	0.94	0.97	0.98	0.99	1.00	1.00	1.00	1.00	1.00	1.00

TABLE V: Total bootstrap covariance matrix for the $B \rightarrow \pi\ell\nu$ form factor, $f_+(q^2)$, derived by adding the statistical and systematic errors in quadrature. The elements of the matrix are given by $M_{ij} = \sigma_{f_+(q_i^2)} \times \sigma_{f_+(q_j^2)}$, where $\sigma_{f_+(q_i^2)}$ is the total uncertainty in $f_+(q^2)$ in the i 'th q^2 bin.

q^2 (GeV 2)	26.5	25.7	25.0	24.3	23.5	22.8	22.1	21.3	20.6	19.8	19.1	18.4
26.5	5.13	2.74	1.49	0.79	0.39	0.18	0.06	0.01	-0.0	0.01	0.03	0.05
25.7	2.74	1.48	0.82	0.45	0.24	0.12	0.05	0.02	0.01	0.02	0.03	0.04
25.0	1.49	0.82	0.47	0.27	0.15	0.09	0.05	0.03	0.02	0.02	0.02	0.03
24.3	0.79	0.45	0.27	0.17	0.11	0.07	0.05	0.03	0.03	0.02	0.02	0.02
23.5	0.39	0.24	0.15	0.11	0.08	0.06	0.04	0.04	0.03	0.03	0.02	0.02
22.8	0.18	0.12	0.09	0.07	0.06	0.05	0.04	0.04	0.03	0.03	0.02	0.02
22.1	0.06	0.05	0.05	0.05	0.04	0.04	0.04	0.03	0.03	0.03	0.02	0.02
21.3	0.01	0.02	0.03	0.03	0.04	0.04	0.03	0.03	0.03	0.02	0.02	0.02
20.6	0.00	0.01	0.02	0.03	0.03	0.03	0.03	0.03	0.02	0.02	0.02	0.02
19.8	0.01	0.02	0.02	0.02	0.03	0.03	0.03	0.02	0.02	0.02	0.02	0.02
19.1	0.03	0.03	0.02	0.02	0.02	0.02	0.02	0.02	0.02	0.02	0.02	0.02
18.4	0.05	0.04	0.03	0.02	0.02	0.02	0.02	0.02	0.02	0.02	0.02	0.02

-
- [1] S.-W. Lin et al. (Belle), Nature **452**, 332 (2008).
- [2] E. Lunghi and A. Soni (2008), 0803.4340.
- [3] T. Aaltonen et al. (CDF), Phys. Rev. Lett. **100**, 161802 (2008), 0712.2397.
- [4] V. M. Abazov et al. (D0) (2008), 0802.2255.
- [5] M. Bona et al. (UTfit) (2008), 0803.0659.
- [6] B. A. Dobrescu and A. S. Kronfeld, Phys. Rev. Lett. **100**, 241802 (2008), 0803.0512.
- [7] E. Follana, C. T. H. Davies, G. P. Lepage, and J. Shigemitsu (HPQCD), Phys. Rev. Lett. **100**, 062002 (2008), 0706.1726.
- [8] K. Abe et al. (Belle) (2007), 0709.1340.
- [9] B. Aubert et al. (BABAR), Phys. Rev. Lett. **98**, 141801 (2007), hep-ex/0607094.
- [10] T. K. Pedlar et al. (CLEO), Phys. Rev. **D76**, 072002 (2007), 0704.0437.

- [11] K. M. Ecklund et al. (CLEO), Phys. Rev. Lett. **100**, 161801 (2008), 0712.1175.
- [12] S. Stone (2008), 0806.3921.
- [13] C. Amsler et al. (Particle Data Group), Phys. Lett. **B667**, 1 (2008).
- [14] B. I. Eisenstein et al. (CLEO) (2008), 0806.2112.
- [15] C. T. H. Davies et al. (HPQCD, MILC, and Fermilab Lattice), Phys. Rev. Lett. **92**, 022001 (2004), hep-lat/0304004.
- [16] C. Aubin et al. (MILC), Phys. Rev. **D70**, 114501 (2004), hep-lat/0407028.
- [17] I. F. Allison et al. (HPQCD, MILC, and Fermilab Lattice), Phys. Rev. Lett. **94**, 172001 (2005), hep-lat/0411027.
- [18] C. W. Bernard et al. (MILC), Phys. Rev. **D64**, 054506 (2001), hep-lat/0104002.
- [19] Y. Shamir, Phys. Rev. **D71**, 034509 (2005), hep-lat/0412014.
- [20] Y. Shamir, Phys. Rev. **D75**, 054503 (2007), hep-lat/0607007.
- [21] C. Bernard, Phys. Rev. **D73**, 114503 (2006), hep-lat/0603011.
- [22] C. Bernard, M. Golterman, and Y. Shamir, Phys. Rev. **D77**, 074505 (2008), 0712.2560.
- [23] S. Prelovsek, Phys. Rev. **D73**, 014506 (2006), hep-lat/0510080.
- [24] C. Bernard, C. E. Detar, Z. Fu, and S. Prelovsek, Phys. Rev. **D76**, 094504 (2007), 0707.2402.
- [25] C. Aubin, J. Laiho, and R. S. Van de Water, Phys. Rev. **D77**, 114501 (2008), 0803.0129.
- [26] W.-J. Lee and S. R. Sharpe, Phys. Rev. **D60**, 114503 (1999), hep-lat/9905023.
- [27] C. Aubin and C. Bernard, Phys. Rev. **D68**, 034014 (2003), hep-lat/0304014.
- [28] S. R. Sharpe and R. S. Van de Water, Phys. Rev. **D71**, 114505 (2005), hep-lat/0409018.
- [29] S. Dürr, PoS **LAT2005**, 021 (2006), hep-lat/0509026.
- [30] S. R. Sharpe, PoS. **LAT2006**, 022 (2006), hep-lat/0610094.
- [31] A. S. Kronfeld, PoS **LAT2007**, 016 (2007), 0711.0699.
- [32] F. Di Lodovico (HFAG), update presented at ICHEP 2008, <http://www.slac.stanford.edu/xorg/hfag/semi/ichep08/home.shtml>.
- [33] E. Dalgic et al. (HPQCD), Phys. Rev. **D73**, 074502 (2006), [Erratum-ibid. **D75**, 119906 (2007)], hep-lat/0601021.
- [34] M. Okamoto et al. (Fermilab Lattice, MILC, and HPQCD), Nucl. Phys. Proc. Suppl. **140**, 461 (2005), hep-lat/0409116.
- [35] G. P. Lepage, L. Magnea, C. Nakhleh, U. Magnea, and K. Hornbostel, Phys. Rev. **D46**, 4052 (1992), hep-lat/9205007.

- [36] A. X. El-Khadra, A. S. Kronfeld, and P. B. Mackenzie, Phys. Rev. **D55**, 3933 (1997), hep-lat/9604004.
- [37] A. S. Kronfeld, Phys. Rev. **D62**, 014505 (2000), hep-lat/0002008.
- [38] J. Harada et al., Phys. Rev. **D65**, 094513 (2002), hep-lat/0112044.
- [39] J. Harada, S. Hashimoto, A. S. Kronfeld, and T. Onogi, Phys. Rev. **D65**, 094514 (2002), hep-lat/0112045.
- [40] C. Aubin et al. (Fermilab Lattice and MILC), Phys. Rev. Lett. **95**, 122002 (2005), hep-lat/0506030.
- [41] C. Bernard et al. (2008), 0808.2519.
- [42] C. Aubin and C. Bernard, Phys. Rev. **D76**, 014002 (2007), 0704.0795.
- [43] B. Aubert et al. (BABAR), Phys. Rev. Lett. **98**, 091801 (2007), hep-ex/0612020.
- [44] M. C. Arnesen, B. Grinstein, I. Z. Rothstein, and I. W. Stewart, Phys. Rev. Lett. **95**, 071802 (2005), hep-ph/0504209.
- [45] J. M. Flynn and J. Nieves, Phys. Rev. **D76**, 031302 (2007), 0705.3553.
- [46] C. Bourrely, I. Caprini, and L. Lellouch (2008), 0807.2722.
- [47] B. Sheikholeslami and R. Wohlert, Nucl. Phys. **B259**, 572 (1985).
- [48] G. P. Lepage and P. B. Mackenzie, Phys. Rev. **D48**, 2250 (1993), hep-lat/9209022.
- [49] R. Sommer, Nucl. Phys. **B411**, 839 (1994), hep-lat/9310022.
- [50] C. W. Bernard et al. (MILC), Phys. Rev. **D62**, 034503 (2000), hep-lat/0002028.
- [51] C. Aubin et al. (MILC), Phys. Rev. **D70**, 094505 (2004), hep-lat/0402030.
- [52] C. Bernard et al. (MILC), PoS **LAT2007**, 090 (2007), 0710.1118.
- [53] W. M. Yao et al. (Particle Data Group), J. Phys. **G33**, 1 (2006).
- [54] A. X. El-Khadra, A. S. Kronfeld, P. B. Mackenzie, S. M. Ryan, and J. N. Simone, Phys. Rev. **D64**, 014502 (2001), hep-ph/0101023.
- [55] M. Wingate, J. Shigemitsu, C. T. H. Davies, G. P. Lepage, and H. D. Trottier (HPQCD), Phys. Rev. **D67**, 054505 (2003), hep-lat/0211014.
- [56] F. Gliozzi, Nucl. Phys. **B204**, 419 (1982).
- [57] H. Kluberg-Stern, A. Morel, O. Napoly, and B. Petersson, Nucl. Phys. **B220**, 447 (1983).
- [58] A. X. El-Khadra, E. Gamiz, A. S. Kronfeld, and M. A. Nobes, in preparation.
- [59] Q. Mason et al. (HPQCD), Phys. Rev. Lett. **95**, 052002 (2005), hep-lat/0503005.
- [60] S. J. Brodsky, G. P. Lepage, and P. B. Mackenzie, Phys. Rev. **D28**, 228 (1983).

- [61] K. Hornbostel, G. P. Lepage, and C. Morningstar, Phys. Rev. **D67**, 034023 (2003), hep-ph/0208224.
- [62] M. Lüscher and P. Weisz, Nucl. Phys. **B266**, 309 (1986).
- [63] A. X. El-Khadra, E. Gamiz, A. S. Kronfeld, and M. A. Nobes, PoS **LAT2007**, 242 (2007), 0710.1437.
- [64] M. F. L. Golterman and J. Smit, Nucl. Phys. **B245**, 61 (1984).
- [65] G. W. Kilcup and S. R. Sharpe, Nucl. Phys. **B283**, 493 (1987).
- [66] G. Burdman, Z. Ligeti, M. Neubert, and Y. Nir, Phys. Rev. **D49**, 2331 (1994), hep-ph/9309272.
- [67] C. Bernard et al. (MILC), update of Ref. [52], private communication.
- [68] S. Aoki et al. (JLQCD), Phys. Rev. **D64**, 114505 (2001), hep-lat/0106024.
- [69] G. P. Lepage et al., Nucl. Phys. Proc. Suppl. **106**, 12 (2002), hep-lat/0110175.
- [70] C. Bernard et al. (Fermilab Lattice and MILC), PoS **LAT2007**, 370 (2007).
- [71] C. Bernard et al. (Fermilab Lattice and MILC), update of Ref. [70], to be published in PoS **LAT2008** (278) (2008).
- [72] A. Anastassov et al. (CLEO), Phys. Rev. **D65**, 032003 (2002), hep-ex/0108043.
- [73] I. W. Stewart, Nucl. Phys. **B529**, 62 (1998), hep-ph/9803227.
- [74] S. Fajfer and J. F. Kamenik, Phys. Rev. **D74**, 074023 (2006), hep-ph/0606278.
- [75] A. Abada et al., Nucl. Phys. Proc. Suppl. **119**, 641 (2003), hep-lat/0209092.
- [76] A. Gray et al. (HPQCD), Phys. Rev. **D72**, 094507 (2005), hep-lat/0507013.
- [77] M. G. Alford, W. Domm, G. P. Lepage, G. Hockney, and P. B. Mackenzie, Phys. Lett. **B361**, 87 (1995), hep-lat/9507010.
- [78] C. W. Bernard et al. (MILC), Phys. Rev. **D58**, 014503 (1998), hep-lat/9712010.
- [79] M. Lüscher and P. Weisz, Commun. Math. Phys. **97**, 59 (1985).
- [80] M. Lüscher and P. Weisz, Phys. Lett. **B158**, 250 (1985).
- [81] G. P. Lepage, Phys. Rev. **D59**, 074502 (1999), hep-lat/9809157.
- [82] K. Orginos, D. Toussaint, and R. L. Sugar (MILC), Phys. Rev. **D60**, 054503 (1999), hep-lat/9903032.
- [83] A. S. Kronfeld, Nucl. Phys. Proc. Suppl. **129**, 46 (2004), hep-lat/0310063.
- [84] M. B. Oktay and A. S. Kronfeld, Phys. Rev. **D78**, 014504 (2008), 0803.0523.
- [85] D. Arndt and C. J. D. Lin, Phys. Rev. **D70**, 014503 (2004), hep-lat/0403012.

- [86] C. Bourrely, B. Machet, and E. de Rafael, Nucl. Phys. **B189**, 157 (1981).
- [87] C. G. Boyd, B. Grinstein, and R. F. Lebed, Phys. Rev. Lett. **74**, 4603 (1995), hep-ph/9412324.
- [88] L. Lellouch, Nucl. Phys. **B479**, 353 (1996), hep-ph/9509358.
- [89] C. G. Boyd and M. J. Savage, Phys. Rev. **D56**, 303 (1997), hep-ph/9702300.
- [90] D. Bećirević and A. B. Kaidalov, Phys. Lett. **B478**, 417 (2000), hep-ph/9904490.
- [91] P. Ball and R. Zwicky, Phys. Rev. **D71**, 014015 (2005), hep-ph/0406232.
- [92] S. C. Generalis, J. Phys. **G16**, 785 (1990).
- [93] T. Becher and R. J. Hill, Phys. Lett. **B633**, 61 (2006), hep-ph/0509090.
- [94] P. Gambino, talk presented at CKM 2008.
- [95] J. H. Kühn, M. Steinhauser, and C. Sturm, Nucl. Phys. **B778**, 192 (2007), hep-ph/0702103.
- [96] M. Neubert (2008), 0801.0675.
- [97] J. Charles et al. (CKMfitter), preliminary results for Summer 2008, http://ckmfitter.in2p3.fr/plots_Summer2008/ckmEval_results.html.
- [98] L. Silvestrini (UTFit), preliminary result presented at Lattice 2008, <http://www.utfit.org/>.

B and D Meson Decay Constants

C. Bernard,¹ C. DeTar,² M. Di Pierro,³ A. X. El-Khadra,⁴ R. T. Evans,⁴ E. D. Freeland,⁵ E. Gamiz,⁴ S. A. Gottlieb,⁶ U. M. Heller,⁷ J. E. Hetrick,⁸ A. S. Kronfeld,⁹ J. Laiho,^{1, 9} L. Levkova,² P. B. Mackenzie*,⁹ J. Simone,⁹ R. Sugar,¹⁰ D. Toussaint,¹¹ and R. S. Van de Water⁹

¹*Washington University*, ²*University of Utah*, ³*DePaul University*, ⁴*University of Illinois*, ⁵*The School of the Art Institute of Chicago*, ⁶*Indiana University*, ⁷*American Physical Society*,

⁸*University of the Pacific*, ⁹*Fermi National Accelerator Laboratory*, ¹⁰*University of California, Santa Barbara*, ¹¹*University of Arizona*

E-mail: mackenzie@fnal.gov

Fermilab Lattice and MILC Collaborations

We present an update of our calculations of the decay constants of the D , D_s , B , and B_s mesons in unquenched $2+1$ flavor QCD. We use the MILC library of improved staggered gauge ensembles at lattice spacings 0.09, 0.12, and 0.15 fm, clover heavy quarks with the Fermilab normalizations, and improved staggered light valence quarks.

*The XXVI International Symposium on Lattice Field Theory
July 14-19 2008
Williamsburg, Virginia, USA*

*Speaker.

1. Introduction

In 2005, combined work by the Fermilab Lattice and MILC Collaborations [1] determined the value of the D_s decay constant f_{D_s} to around 10% before it had been determined to that accuracy by experiment. When the subsequent experimental determination agreed to within one sigma, we claimed that as a successful prediction. As lattice calculations become increasingly accurate, of course, at some point we do not expect perfect agreement between the Standard Model and experiment. With sufficient precision, the effects of Beyond-the-Standard-Model physics will start to show up in low energy measurements. We do not know what that precision will be, so we must be cautious in interpreting deviations between theory and experiment.

Since then, we have increased the precision of our calculations. Our result for f_{D_s} remains about 10% below the experimental result, and with the increased precision of theory and experiment, no longer agrees to within one sigma with experiment, as we describe in this paper. Further, earlier this year new results on the π , K , D , and D_s decay constants appeared from the HPQCD Collaboration [2]. They used a new lattice fermion method, Highly Improved Staggered Quarks, or “HISQ” fermions, which allowed them to calculate all four decay constants with nearly identical methods. They found very good agreement with experiment for the π and K decay constants. Their value for the D decay constant was subsequently confirmed by CLEO [3]. For f_{D_s} , they also found a result around 10% below experiment, but with improved precision. Instead of agreement between theory and experiment, there is now a greater than three sigma discrepancy. This is the only quantity in lattice QCD phenomenology with staggered fermions in which such a clear disagreement has arisen between theory and experiment, so a puzzle has developed. Precise calculations with other lattice methods are of great interest.

2. Calculations

We are finishing a reanalysis of the existing data for our calculations of f_D , f_{D_s} , f_B , and f_{B_s} that is reducing some of our largest uncertainties. We are also preparing for new runs this year with four times the statistics. Our calculations are done with improved staggered (“asqtad”) light quarks [4, 5], and clover/Fermilab [6] $\mathcal{O}(a)$ improved heavy quarks. We use the MILC 2 + 1 flavor library of unquenched gauge configurations [7], with lattice spacings of around 0.15, 0.12, and 0.09 fm (the so-called coarser, coarse, and fine ensembles). The masses of light sea-quarks range between $0.6m_s$ and $0.1m_s$. On each of the eleven ensembles, we use from eight to twelve partially quenched valence quark masses, ranging from around m_s to $0.1m_s$.

The decay constants are defined by

$$\langle 0 | A_\mu | H_q(p) \rangle = i f_{H_q} p_\mu. \quad (2.1)$$

The combination decay amplitude

$$\phi_{H_q} = f_{H_q} \sqrt{M_{H_q}} \quad (2.2)$$

can be obtained from the correlators

$$C_0(t) = \left\langle O_{H_q}^\dagger(t) O_{H_q}(0) \right\rangle, \quad (2.3)$$

$$C_{A_4}(t) = \left\langle A_4(t) O_{H_q}(0) \right\rangle. \quad (2.4)$$

The current normalizations are obtained from

$$Z_{A_4}^{Qq} = \rho_{A_4}^{Qq} \sqrt{Z_{V_4}^{QQ} Z_{V_4}^{qq}}, \quad (2.5)$$

where $Z_{V_4}^{QQ}$ and $Z_{V_4}^{qq}$ are determined nonperturbatively and the remaining (perturbatively calculated) short distance corrections in the deviation of $\rho_{A_4}^{Qq}$ from 1 are no more than 0.6%.

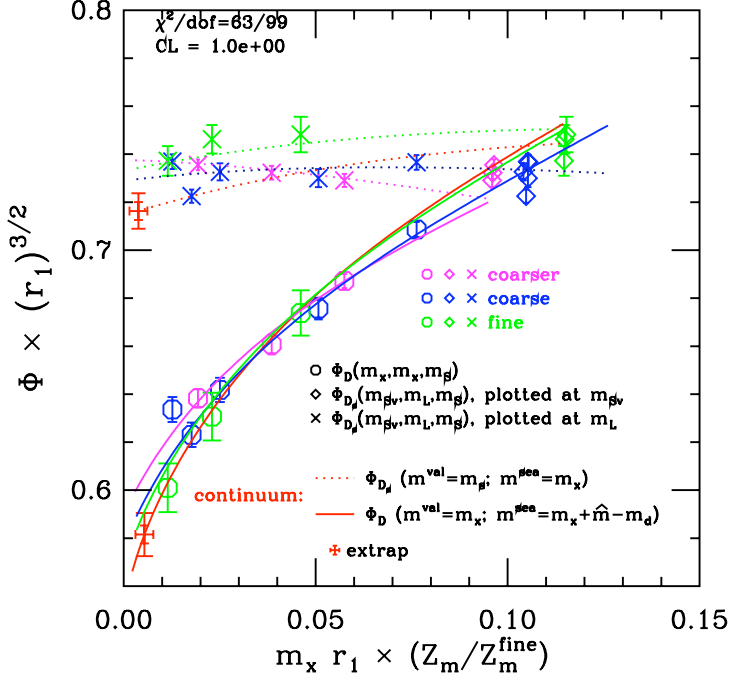


Figure 1: The leptonic decay amplitudes f/\sqrt{M} for the D and D_s mesons, extrapolated to the chiral limit. Units are in terms of the heavy-quark potential parameter, r_1 .

Figure 1 shows the extrapolation of the D and D_s leptonic decay amplitudes to the physics light quark limit. (Units are in terms of the heavy-quark potential parameter r_1 .) For ϕ_D (octagons), we show only those (fully unquenched) points for which the light valence and sea masses are equal to m_x , the mass on the abscissa. For ϕ_{D_s} , we keep both the strange sea mass (m_S) and the strange valence mass (m_{Sv}) fixed to their simulated values, and plot either as a function of the up/down sea mass m_L (crosses), or at m_{Sv} (diamonds). The chiral extrapolations make use of all the partially quenched data in addition to the points shown.

The m_q dependence is much stronger for the D than the D_s , as expected, since in the D_s it affects only the sea quarks and not the valence quarks. The slope is larger in the continuum limit, because taste breaking effects tend to suppress the dependence on the quark mass at finite a . Figure 2 shows the same thing for the B and B_s decay amplitudes, with a qualitatively similar picture.

Figure 3 shows the extrapolation of the ratio ϕ_D/ϕ_{D_s} to the chiral limit. The slope is strongest in the continuum limit (red line and cross), as expected.

3. Results

Table 1 shows the uncertainty budgets for the D_s , D , B_s , and B meson decay amplitudes ϕ_M , and for the ratios $R_D \equiv \phi_D/\phi_{D_s}$ and $R_B \equiv \phi_B/\phi_{B_s}$. The three largest uncertainties in our previous

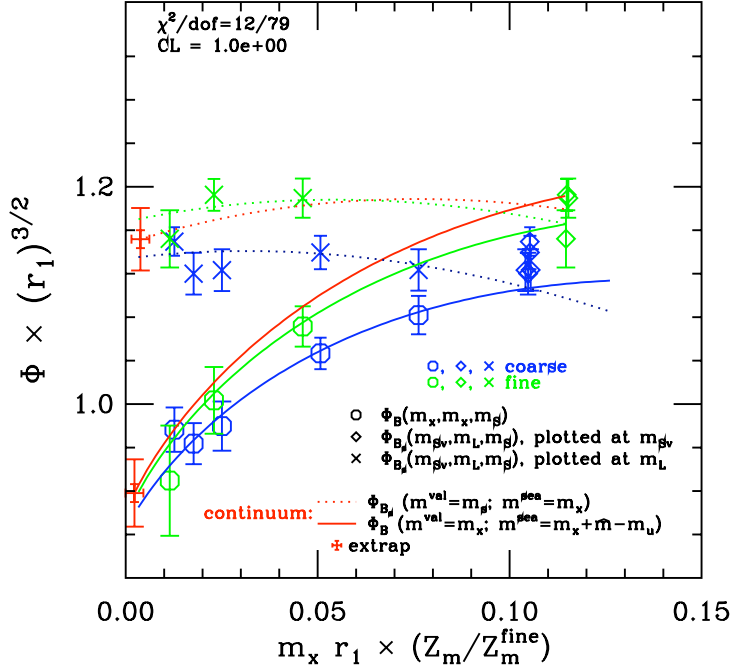


Figure 2: The same as for Fig. 1, but for the B and B_s mesons.

results were statistics, heavy quark discretization, and the heavy quark mass. The statistical error in the D and D_s decay amplitudes has been reduced this year through an improvement in analysis method, and without additional data. We are currently incorporating into the chiral and continuum extrapolation fits a term for the heavy quark discretization which we expect to substantially reduce the uncertainty from this source. The last uncertainty that is large is due to the input heavy quark mass, and will be removed with a more careful determination of this quantity.

We obtain for the decay constants

$$f_D = 207(11) \text{ MeV}, \quad (3.1)$$

Table 1: Uncertainty budgets in per cent for the leptonic decay amplitudes ϕ_{D_s} , ϕ_D , ϕ_{B_s} , and ϕ_B , and for the ratios $R_D \equiv \phi_D/\phi_{D_s}$ and $R_B \equiv \phi_B/\phi_{B_s}$.

	ϕ_{D_s}	ϕ_{D_d}	R_D	ϕ_{B_s}	ϕ_{B_d}	R_B
Statistics	1.0	1.5	1.0	2.5	3.4	2.2
Inputs r_1, m_s, m_l	1.4	2.1	0.6	1.8	2.5	0.6
Inputs m_b or m_c	2.7	2.7	0.1	1.1	1.1	0.1
Z	1.4	1.4	<0.1	1.4	1.4	<0.1
Higher order ρ_{A_4}	0.1	0.1	<0.1	0.4	0.4	<0.1
Heavy q disc.	2.7	2.7	0.3	1.9	1.9	0.2
Light q disc. & χ extr.	1.2	2.6	1.6	2.0	2.4	2.4
V	0.2	0.6	0.6	0.2	0.6	0.6
Total systematic	4.5	5.3	1.8	3.8	4.4	2.6

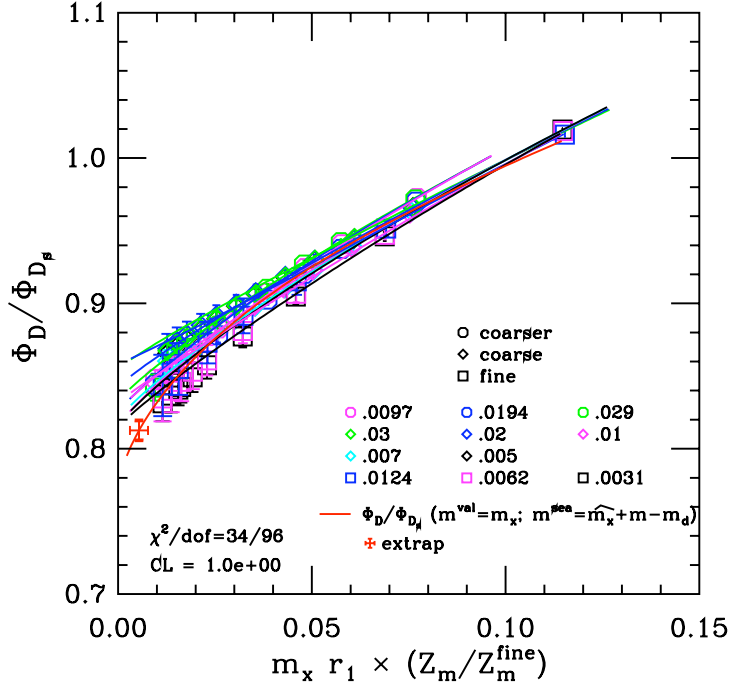


Figure 3: The ratio of the D and D_s meson leptonic decay amplitudes, extrapolated to the chiral limit.

$$f_{D_s} = 249(11) \text{ MeV}, \quad (3.2)$$

$$f_B = 195(11) \text{ MeV}, \quad (3.3)$$

$$f_{B_s} = 243(11) \text{ MeV}, \quad (3.4)$$

and for the ratios

$$f_D/f_{D_s} = 0.833(19), \quad (3.5)$$

$$f_B/f_{B_s} = 0.803(28). \quad (3.6)$$

In Figure 4, we compare our results for f_D and f_{D_s} with the calculations of HPQCD [2] and with experiment [3, 8]. For f_D , there is very good agreement between experiment, HPQCD, and the Fermilab/MILC result. For f_{D_s} , there is

- agreement between HPQCD and Fermilab/MILC,
- 1.6σ disagreement between Fermilab/MILC and experiment, and
- 3.5σ disagreement between HPQCD and experiment.

Many uncertainties cancel in the ratio f_D/f_{D_s} , so we examined this quantity to see if it could enhance the significance of the discrepancy between our results and experiment. For now, looking at f_D/f_{D_s} doesn't sharpen the picture. In Figure 5, we show our results for f_D/f_{D_s} compared with the calculations of HPQCD and with experiment. There is a slight disagreement between HPQCD and FNAL/MILC in the ratio, even though f_D and f_{D_s} agree within one sigma. Further, the experimental uncertainties are independent. They add in quadrature, increasing the size of the experimental uncertainty and decreasing the significance of any discrepancy.

New results for f_D and f_{D_s} recently appeared from ETMC using twisted-mass fermions [9]. They obtained $f_D = 205 \pm 10$ MeV and $f_{D_s} = 248 \pm 9$ MeV, which is in accord with the staggered determinations. They present a thorough uncertainty analysis, although we would quibble with their use of two rather than three light sea quarks without the inclusion of an uncertainty estimate for that approximation. Based on the difference between our unquenched and quenched calculations of f_{D_s} (249 MeV vs. 213 MeV) [10], we might have guessed a possible uncertainty of 5% from leaving out one of the three light sea quarks. (We see charm sea quarks as a different story, since $m_c \sim 1/a$ at our lattice spacings, and the dynamical effects of c quarks are for the most part above the cut-off.)

Three sigma discrepancies between experiment and the Standard Model have occasionally appeared and then disappeared before, but the discrepancy in f_{D_s} is hard to understand. The uncertainty is dominated by experimental statistical error, and three sigma statistical fluctuations are very rare. One can double the theory error, and still have a three sigma discrepancy. To explain the discrepancy as a theory error, one would have to find a mistake in the theory analysis of f_{D_s} whose correction would not affect the correct prediction of f_D . It is hard to imagine such a mistake. The calculations of f_D and f_{D_s} are almost identical. The only difference is that f_{D_s} should be somewhat easier, in that it doesn't require an extrapolation to the physical light quark masses. It may be premature to draw ultimate conclusions about the discrepancy, but the result is puzzling enough that Kronfeld and Dobrescu have investigated possible new-physics explanations for the discrepancy [11].

4. Outlook

We are in the process of reanalyzing our existing data, in which we hope to bring down several of our largest uncertainties. New runs are starting with quadruple the current statistics and at smaller lattice spacings, which we expect to help with several of the uncertainties. Comparison of f_{D_s} in theory and experiment remains a puzzle. This is the only known instance in which lattice

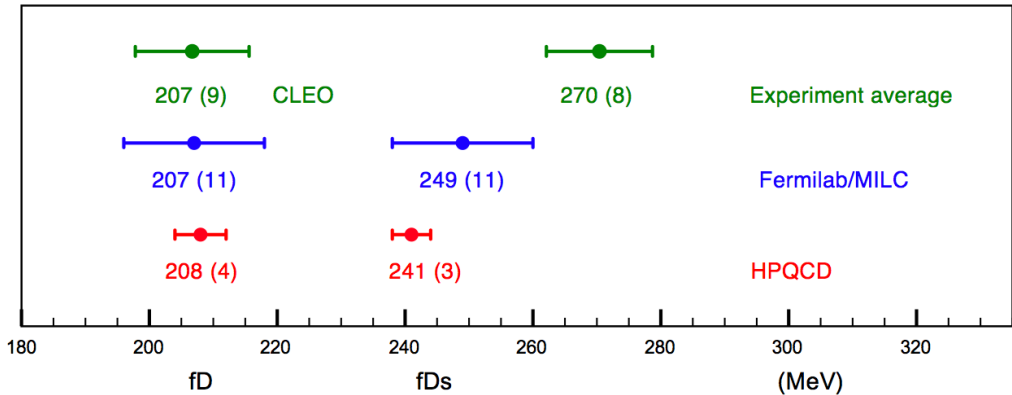


Figure 4: Comparison of f_D and f_{D_s} with the calculations of HPQCD and with experiment.

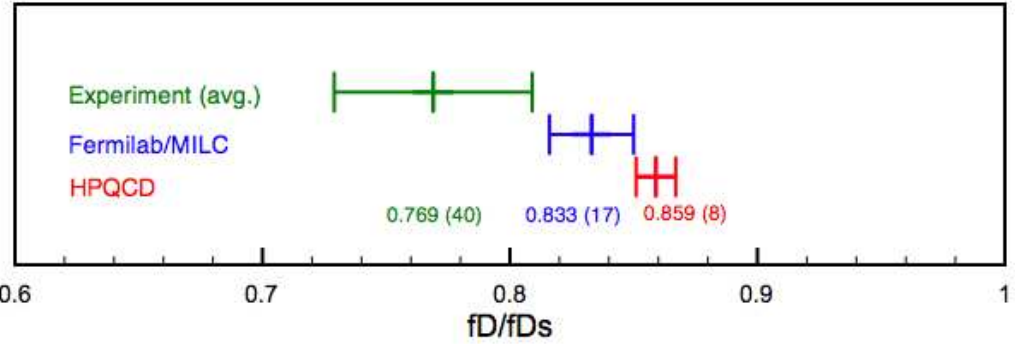


Figure 5: Results for f_D/f_{D_s} compared with the calculations of HPQCD and with experiment.

QCD with staggered fermions seems to clearly fail to reproduce the Standard Model. This provides a good target of opportunity for calculations with other lattice fermion methods.

References

- [1] C. Aubin *et al.*, “Charmed meson decay constants in three-flavor lattice QCD,” Phys. Rev. Lett. **95**, 122002 (2005) [arXiv:hep-lat/0506030].
- [2] E. Follana, C. T. H. Davies, G. P. Lepage and J. Shigemitsu [HPQCD Collaboration and UKQCD Collaboration], “High Precision determination of the pi, K, D and Ds decay constants from lattice QCD,” Phys. Rev. Lett. **100**, 062002 (2008) [arXiv:0706.1726 [hep-lat]].
- [3] B. I. Eisenstein *et al.* [CLEO Collaboration], “Precision Measurement of $B(D^+ \rightarrow \mu^+ \nu)$ and the Pseudoscalar Decay Constant f_{D^+} ,” arXiv:0806.2112 [hep-ex].
- [4] G. P. Lepage, “Flavor-symmetry restoration and Symanzik improvement for staggered quarks,” Phys. Rev. D **59**, 074502 (1999) [arXiv:hep-lat/9809157].
- [5] K. Orginos and D. Toussaint [MILC collaboration], “Testing improved actions for dynamical Kogut-Susskind quarks,” Phys. Rev. D **59**, 014501 (1999) [arXiv:hep-lat/9805009].
- [6] A. X. El-Khadra, A. S. Kronfeld and P. B. Mackenzie, “Massive Fermions in Lattice Gauge Theory,” Phys. Rev. D **55**, 3933 (1997) [arXiv:hep-lat/9604004].
- [7] C. Aubin *et al.* [MILC Collaboration], “Light pseudoscalar decay constants, quark masses, and low energy constants from three-flavor lattice QCD,” Phys. Rev. D **70** (2004) 114501 [arXiv:hep-lat/0407028].
- [8] J. Rosner and S. Stone, “Decay constants of charged pseudoscalar mesons”, arXiv:0802.1043 [hep-ex], in C. Amsler *et al.* [Particle Data Group], Phys. Lett. B **667**, 1 (2008).
- [9] B. Blossier, V. Lubicz, S. Simula and C. Tarantino, “Pseudoscalar meson decay constants f_K , f_D and f_{D_s} , from Nf=2 twisted mass Lattice QCD,” arXiv:0810.3145 [hep-lat].
- [10] A. X. El-Khadra, A. S. Kronfeld, P. B. Mackenzie, S. M. Ryan and J. N. Simone, “B and D meson decay constants in lattice QCD,” Phys. Rev. D **58**, 014506 (1998) [arXiv:hep-ph/9711426].
- [11] B. A. Dobrescu and A. S. Kronfeld, “Accumulating evidence for nonstandard leptonic decays of D_s mesons,” Phys. Rev. Lett. **100**, 241802 (2008) [arXiv:0803.0512 [hep-ph]]; A. S. Kronfeld, talk at *Lattice 2008*, PoS(LATTICE 2008) 282.

Visualization of semileptonic form factors from lattice QCD

C. Bernard,¹ C. DeTar,² M. Di Pierro,³ A.X. El-Khadra,⁴ R.T. Evans,⁴ E.D. Freeland,⁵ E. Gamiz,⁴ Steven Gottlieb,⁶ U.M. Heller,⁷ J.E. Hetrick,⁸ A.S. Kronfeld,⁹ J. Laiho,¹ L. Levkova,² P.B. Mackenzie,⁹ M. Okamoto,⁹ M.B. Oktay,² J.N. Simone,⁹ R. Sugar,¹⁰ D. Toussaint,¹¹ and R.S. Van de Water¹²
 (Fermilab Lattice and MILC Collaborations)

¹Department of Physics, Washington University, St. Louis, Missouri, USA

²Physics Department, University of Utah, Salt Lake City, Utah, USA

³School of Computer Science, Telecommunications and Information Systems, DePaul University, Chicago, Illinois, USA

⁴Physics Department, University of Illinois, Urbana, Illinois, USA

⁵Liberal Arts Department, The School of the Art Institute of Chicago, Chicago, Illinois, USA

⁶Department of Physics, Indiana University, Bloomington, Indiana, USA

⁷American Physical Society, Ridge, New York, USA

⁸Physics Department, University of the Pacific, Stockton, California, USA

⁹Fermi National Accelerator Laboratory, Batavia, Illinois, USA

¹⁰Department of Physics, University of California, Santa Barbara, California, USA

¹¹Department of Physics, University of Arizona, Tucson, Arizona, USA

¹²Physics Department, Brookhaven National Laboratory, Upton, New York, USA

(Dated: August 26, 2009)

Comparisons of lattice-QCD calculations of semileptonic form factors with experimental measurements often display two sets of points, one each for lattice QCD and experiment. Here we propose to display the output of a lattice-QCD analysis as a curve and error band. This is justified, because lattice-QCD results rely in part on fitting, both for the chiral extrapolation and to extend lattice-QCD data over the full physically allowed kinematic domain. To display an error band, correlations in the fit parameters must be taken into account. For the statistical error, the correlation comes from the fit. To illustrate how to address correlations in the systematic errors, we use the Bećirević-Kaidalov parametrization of the $D \rightarrow \pi l\nu$ and $D \rightarrow K l\nu$ form factors, and an analyticity-based fit for the $B \rightarrow \pi l\nu$ form factor f_+ .

PACS numbers: 13.20.Fc, 13.20.He, 12.38.Gc

The past several years have witnessed considerable improvement in our understanding of semileptonic decays of D and B mesons. Measurements have advanced in accuracy from 6–20% on the normalization [1, 2, 3] and $\sim 10\%$ on the shape [4] to $\sim 1\%$ on both [5]. Meanwhile, *ab initio* calculations in QCD with lattice gauge theory have become realistic [6, 7, 8, 9], now incorporating the effects of sea quarks that were omitted in earlier work [10, 11, 12, 13, 14]. In this article, we discuss how to present both together, so that the agreement (or, in principle, lack thereof) is easy to assess.

We focus on reactions mediated by electroweak vector currents, leading to pseudoscalar mesons, π or K , in the final state. At the quark level, a heavy quark h decays into a daughter quark d (not necessarily the down quark), with a spectator antiquark \bar{q} . Writing the decay $H \rightarrow Pl\nu$, the form factors are defined by

$$\langle P|V^\mu|H\rangle = f_+(q^2)(p_H + p_P - \Delta)^\mu + f_0(q^2)\Delta^\mu \quad (1)$$

where $q = p_H - p_P$ is the 4-momentum of the lepton system, and $\Delta^\mu = (p_H + p_P) \cdot q q^\mu / q^2 = (m_H^2 - m_P^2)q^\mu / q^2$. Equation (1) is general, applying to $K \rightarrow \pi l\nu$ as well as to D and B decays. For lattice QCD, it is more convenient to express the transition matrix element as

$$\langle P|V^\mu|H\rangle = \sqrt{2m_H} [v^\mu f_{||}(E) + p_\perp^\mu f_\perp(E)], \quad (2)$$

where $v = p_H/m_H$, and $p_\perp = p_P - Ev$ and $E = v \cdot p_P$

denote the 3-momentum and energy of the final-state meson in the rest frame of the initial state. The energy E is related to q^2 via

$$q^2 = m_H^2 + m_P^2 - 2m_H E. \quad (3)$$

Neglecting the lepton mass, $0 \leq q^2 \leq q_{\max}^2 = (m_H - m_P)^2$ is kinematically allowed in the semileptonic decay.

The form factors $f_+(q^2)$ and $f_0(q^2)$ are related to $f_{||}(E)$ and $f_\perp(E)$ by

$$f_+(q^2) = (2m_H)^{-1/2} [f_{||}(E) + (m_H - E)f_\perp(E)], \quad (4)$$

$$f_0(q^2) = \frac{\sqrt{2m_H}}{m_H^2 - m_P^2} [(m_H - E)f_{||}(E) - p_\perp^2 f_\perp(E)], \quad (5)$$

with Eq. (3) understood. Equations (4) and (5) imply $f_+(0) = f_0(0)$, as required in Eq. (1).

Two aspects of lattice-QCD calculations are important here. First (as in all lattice-QCD calculations), it is computationally demanding to have a spectator quark with mass as small as those of the up and down quarks; for $P = \pi$ the same applies to the daughter quark. In recent unquenched calculations, the mass of the $\bar{q}q$ pseudoscalar $P_{\bar{q}q}$ lies in the range $0.1m_K^2 \lesssim m_{P_{\bar{q}q}}^2 \lesssim m_K^2$. Second (of special importance in semileptonic decays), the calculations take place in a finite spatial volume, so the 3-momentum takes discrete values. In typical cases the

box-size $L \approx 2.5$ fm, so the smallest nonzero momentum $\mathbf{p}_{(1,0,0)} = 2\pi(1,0,0)/L$ satisfies $|\mathbf{p}_{(1,0,0)}| \approx 500$ MeV.

After generating numerical data at several values of $(E, m_{P_{qq}}^2)$, the next step for lattice-QCD calculations is to carry out a chiral extrapolation, $m_{P_{qq}}^2 \rightarrow m_\pi^2$, of the data for f_\perp and f_\parallel [15, 16]. The chiral extrapolation must reflect the fact that the form factors are analytic in $E = \sqrt{\mathbf{p}^2 + m_P^2}$, not \mathbf{p} [17]. Note also that f_\perp and f_+ can be computed only with $\mathbf{p} \neq \mathbf{0}$, hence $E > m_P$ or, equivalently, $q^2 < q_{\max}^2$. The statistical and discretization uncertainties in $f_+(q^2, m_{P_{qq}}^2)$ start out smallest at $q_{(1,0,0)}^2$, corresponding to $\mathbf{p}_{(1,0,0)}$. A sensible chiral extrapolation will propagate this feature to $f_+(q^2, m_\pi^2)$. Similarly, the statistical and discretization uncertainties in $f_0(q^2, m_\pi^2)$ are smallest near q_{\max}^2 .

When $|\mathbf{p}|a$ becomes too large, discretization effects grow out of control. Therefore, the kinematic domain of lattice-QCD calculations is limited to, these days, $|\mathbf{p}| \lesssim 1$ GeV, with a corresponding upper limit on E and lower limit on q^2 . To extend the form factor over the full physical kinematic domain, a parametrization of the q^2 dependence is needed.

One choice is the Bećirević-Kaidalov (BK) ansatz [18]

$$f_+(q^2) = \frac{F}{(1 - \tilde{q}^2)(1 - \alpha\tilde{q}^2)}, \quad (6)$$

$$f_0(q^2) = \frac{F}{1 - \tilde{q}^2/\beta}, \quad (7)$$

where $\tilde{q}^2 = q^2/m_{H^*}^2$ (H^* is the vector meson of flavor $h\bar{d}$), and F , α , and β are free parameters to be fitted. A key feature of Eq. (6) is the built-in pole at $q^2 = m_{H^*}^2$, or $E = -(m_{H^*}^2 - m_H^2 - m_P^2)/2m_H < 0$, an indisputable feature of the physical f_+ . Further singularities at higher negative energy are modeled by the BK parameters α and β . A similar possibility is the Ball-Zwicky (BZ) ansatz [8, 19], which has one more parameter for f_+ than BK. A shortcoming of these parametrizations is that comparisons of lattice-QCD and experimental slope parameters can be misleading [20, 21], because lattice-QCD slopes are determined near $q^2 = q_{\max}^2$, whereas experimental slopes are determined near $q^2 = 0$.

Another approach based on analyticity and unitarity is to write the form factors as

$$f_+(q^2) = \frac{1}{(1 - \tilde{q}^2)\phi_+(q^2)} \sum_{k=0}^N a_k z^k, \quad (8)$$

$$f_0(q^2) = \frac{1}{\phi_0(q^2)} \sum_{k=0}^N b_k z^k, \quad (9)$$

where $\phi_{+,0}$ are arbitrary, but suitable, functions, and the series coefficients are fit parameters. The variable

$$z = \frac{\sqrt{1 - q^2/t_+} - \sqrt{1 - t_0/t_+}}{\sqrt{1 - q^2/t_+} + \sqrt{1 - t_0/t_+}}, \quad (10)$$

where $t_+ = (m_H + m_P)^2$ and t_0 can be chosen to make $|z|$ small for all kinematically allowed q^2 . Like BK and

BZ, Eq. (8) builds the H^* pole into f_+ , but this approach is model independent because unitarity [17, 22, 23] and heavy-quark physics [21] impose bounds on $\sum_k |a_k|^2$, $\sum_k |b_k|^2$, and because kinematics set $|z| < 1$. Consequently, the series can be truncated safely, once additional terms are negligible compared to other uncertainties in the analysis.

In all approaches the output of an analysis of lattice-QCD form factors is a fit, usually a two-stage fit of chiral extrapolation followed by q^2 parametrization. Clearly, the final fit describes a curve, and the error matrix of the fit parameters describes an error band. Nevertheless, lattice-QCD results usually have been plotted as a set of points with error bars at fiducial values of q^2 (or E). These points evoke the underlying discrete nature of the 3-momentum \mathbf{p} but, in general, the chosen values of q^2 (or E) have nothing to do with the original discrete values of \mathbf{p} . A plot with a curve plus error band exhibits the same information, while giving a visually superior sense of the correlations between points on the curve.

The experimental measurements of $f_+(q^2)$ come from counting events in bins of q^2 and removing coupling and kinematic factors. The analysis inevitably entails some fitting, to correct for acceptance, etc., but the postfit bins of q^2 faithfully mirror the input to such fits.

If one would like to compare the calculations with the measurements, it is appealing to represent one as a curve with error band, and the other as points with error bars. Bearing the foregoing remarks in mind, it seems natural to draw the curve for lattice-QCD calculations. A few years ago, we prepared illustrative plots for $D \rightarrow Kl\nu$ with the Fermilab-MILC [6, 7] lattice-QCD calculations and FOCUS [4] and Belle [24] measurements. The intent was pedagogical, and we showed the plots at seminars and conferences [25].

Unfortunately, the error band in that effort was impressionistic, not rigorous. With the prospect of yet-more-precise results based on CLEO-c's full accumulation of 818 pb^{-1} [5], we now present a version that treats the error band as rigorously as possible. We also prepare plots for $D \rightarrow \pi l\nu$ and $B \rightarrow \pi l\nu$.

As before we shall base the plots for D decays on Ref. [6]. The final result of this analysis consists of the BK parameters (F, α, β) and the 3×3 error matrix. The full statistical error matrix is contained in a detailed, unpublished description of a BK-based analysis of $B \rightarrow \pi l\nu$ form factors [26]. The best fit, statistical errors, and systematic errors are tabulated in Table I. The statistical correlation matrices $\rho_{ij} = \sigma_{ij}^2 / (\sigma_{ii}^2 \sigma_{jj}^2)^{1/2}$ are tabulated in Table II. The correlations among systematic errors are discussed below.

Propagating (correlated) fluctuations in F , α , and β to the form factors, one finds relative squared-errors

$$\frac{\sigma_{++}^2}{f_+^2} = \frac{\sigma_{FF}^2}{F^2} + 2\frac{\sigma_{F\alpha}^2}{F} \frac{\tilde{q}^2}{1 - \alpha\tilde{q}^2} + \sigma_{\alpha\alpha}^2 \left(\frac{\tilde{q}^2}{1 - \alpha\tilde{q}^2} \right)^2, \quad (11)$$

$$\frac{\sigma_{00}^2}{f_0^2} = \frac{\sigma_{FF}^2}{F^2} - 2\frac{\sigma_{F\beta}^2}{F\beta} \frac{\tilde{q}^2}{\beta - \tilde{q}^2} + \sigma_{\beta\beta}^2 \left(\frac{\tilde{q}^2}{\beta - \tilde{q}^2} \right)^2. \quad (12)$$

These errors are plotted as a function of q^2 in Fig. 1 as solid curves. The relative statistical errors are smallest for q^2 such that

$$\sigma_{F\alpha}^2 = -F\sigma_{\alpha\alpha}^2\tilde{q}^2/(1-\alpha\tilde{q}^2), \quad (13)$$

$$\sigma_{F\beta}^2 = F\sigma_{\beta\beta}^2\tilde{q}^2/\beta(\beta-\tilde{q}^2). \quad (14)$$

It is illustrative to take $\sigma_{F\alpha}^2$ and $\sigma_{F\beta}^2$ from Tables I and II and solve Eqs. (13) and (14) for \tilde{q}^2 . We call these values \tilde{q}_α^2 and \tilde{q}_β^2 and tabulate them, as well as $\tilde{q}_{(1,0,0)}^2$ and \tilde{q}_{\max}^2 , in Table III. As one can see from Fig. 1 and Table III, the statistical error is smallest between $\tilde{q}_{(1,0,0)}^2$ and \tilde{q}_{\max}^2 , as expected. One may view this outcome as a check on the fitting procedures.

One can reverse this strategy to determine the correlation between the systematic errors of F and the slope parameters. In the error budget of Ref. [6] the largest systematic effect comes from discretization errors. These should be smallest around $\tilde{q}_{(1,0,0)}^2$ and \tilde{q}_{\max}^2 for f_+ and f_0 , respectively, because those correspond to the smallest $|\mathbf{p}|$ yielding the respective matrix elements. This yields

$$\rho_{F\alpha}^{\text{syst}} = -0.198 \quad (D \rightarrow K), \quad -0.329 \quad (D \rightarrow \pi), \quad (15)$$

$$\rho_{F\beta}^{\text{syst}} = +0.471 \quad (D \rightarrow K), \quad +0.533 \quad (D \rightarrow \pi), \quad (16)$$

and the dashed curves in Fig. 1.

It is customary to combine statistical and systematic uncertainties by adding the two σ^2 (matrices). Carrying out this procedure leads to the curves and bands in Fig. 2. The error bands seem to contradict the conventional wisdom that the lattice-QCD uncertainties are smallest near q_{\max}^2 . This is not entirely the case for the *relative* error, as seen in Fig. 1. As q^2 increases, the relative errors decrease until hitting a minimum somewhere between $\tilde{q}_{(1,0,0)}^2$ and \tilde{q}_{\max}^2 , as is reasonable. The form factors rise faster than the relative errors drop, leading to the increasing absolute error seen in Fig. 2. These features are not an artifact of the BK parametrization, as we shall see below with the $B \rightarrow \pi l\nu$ form factor f_+ .

Figure 2 is the first main result of this article. It shows the form factors f_+ and f_0 for $D \rightarrow Kl\nu$ and $D \rightarrow \pi l\nu$. The lattice-QCD results are shown as curves (red for f_+ , blue for f_0) with two error bands, one statistical (orange for f_+ , gray for f_0), the other systematic and statistical combined (yellow for f_+ , light blue for f_0). Experimental measurements for f_+ [24, 27, 28, 29] are overlaid as points with error bars. It may require careful scrutiny to see which experiment is which, but a glance reveals how well the points and curves agree. The agreement is good for $D \rightarrow \pi l\nu$ and very good for $D \rightarrow Kl\nu$.

For the z expansion the propagation of errors is even simpler. Focusing on f_+ , one has from Eq. (8)

$$\frac{\sigma_{++}^2}{f_+^2} = \frac{\sum_{k,l=0}^N \sigma_{kl}^2 z^{k+l}}{\left[\sum_{k=0}^N a_k z^k\right]^2}, \quad (17)$$

where the indices on σ^2 correspond to those on the series coefficients. The coefficients and error matrix for the

TABLE I: Best-fit values of BK parameters with statistical and systematic errors, successively, in parentheses [6, 7, 26].

Decay	F	α	β
$D \rightarrow Kl\nu$	0.73(3)(7)	0.50(4)(7)	1.31(7)(13)
$D \rightarrow \pi l\nu$	0.64(3)(6)	0.44(4)(7)	1.41(6)(7)

TABLE II: Statistical error correlation matrices $\rho_{ij} = \sigma_{ij}^2/(\sigma_{ii}^2\sigma_{jj}^2)^{1/2}$ of the BK parameters [26].

$D \rightarrow K$	F	α	β
F	1.000	-0.597	0.530
α	-0.597	1.000	-0.316
β	0.530	-0.316	1.000
$D \rightarrow \pi$	F	α	β
F	1.000	-0.583	0.535
α	-0.583	1.000	-0.312
β	0.535	-0.312	1.000

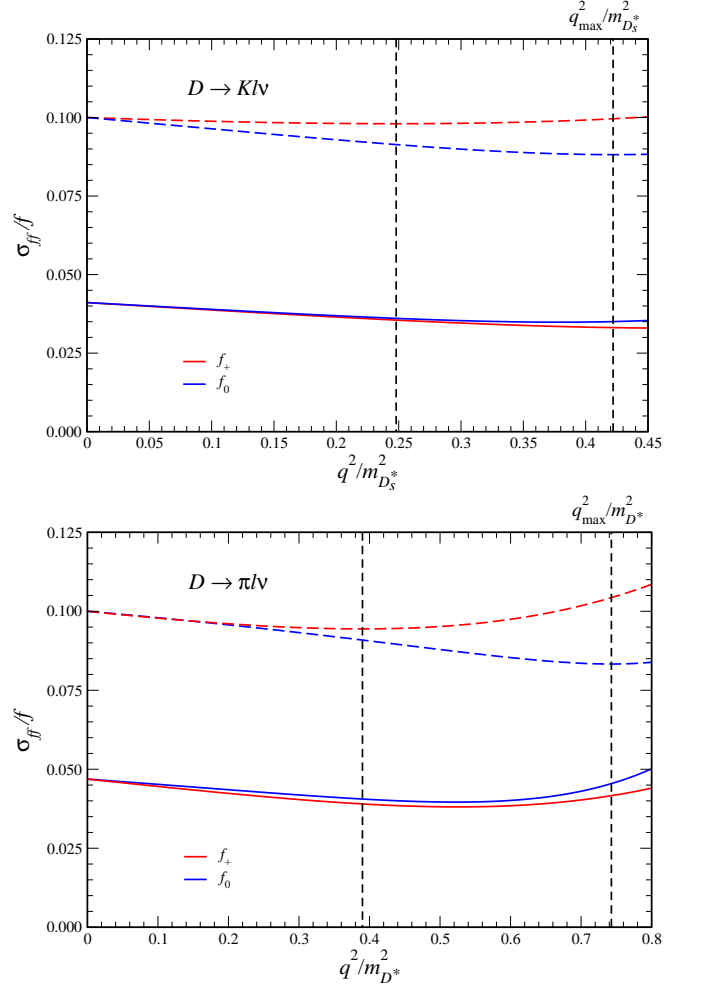


FIG. 1: Relative errors vs q^2 . Solid (dashed) curves show the fitted statistical (estimated systematic) error for f_+ (red curves) and f_0 (blue curves). Vertical lines show $q_{(1,0,0)}^2$ and q_{\max}^2 .

TABLE III: Useful quantities for generating and assessing Figs. 1, 2, and 3.

Decay	H^*	m_{H^*} (MeV)	$E_{(1,0,0)}$ (MeV)	$q_{(1,0,0)}^2$ (GeV 2)	q_{\max}^2 (GeV 2)	$\tilde{q}_{(1,0,0)}^2$	\tilde{q}_{\max}^2	\tilde{q}_α^2	\tilde{q}_β^2
$D \rightarrow K l \nu$	D_s^*	2112	704	1.10	1.88	0.25	0.42	0.47	0.38
$D \rightarrow \pi l \nu$	D^*	2008	518	1.57	3.00	0.39	0.74	0.53	0.52
$B \rightarrow \pi l \nu$	B^*	5325	518	22.4	26.4	0.79	0.93	—	—

$N = 3$ fit ($t_0 = 0.65q_{\max}^2$) are tabulated in Table IV. The z -series fit was carried out after assigning q^2 -dependent systematic uncertainties, so Table IV refers to the combined statistical and systematic errors of this analysis.

This information, combined with the outer function ϕ_+ [9], is used to produce Fig. 3, the second main result

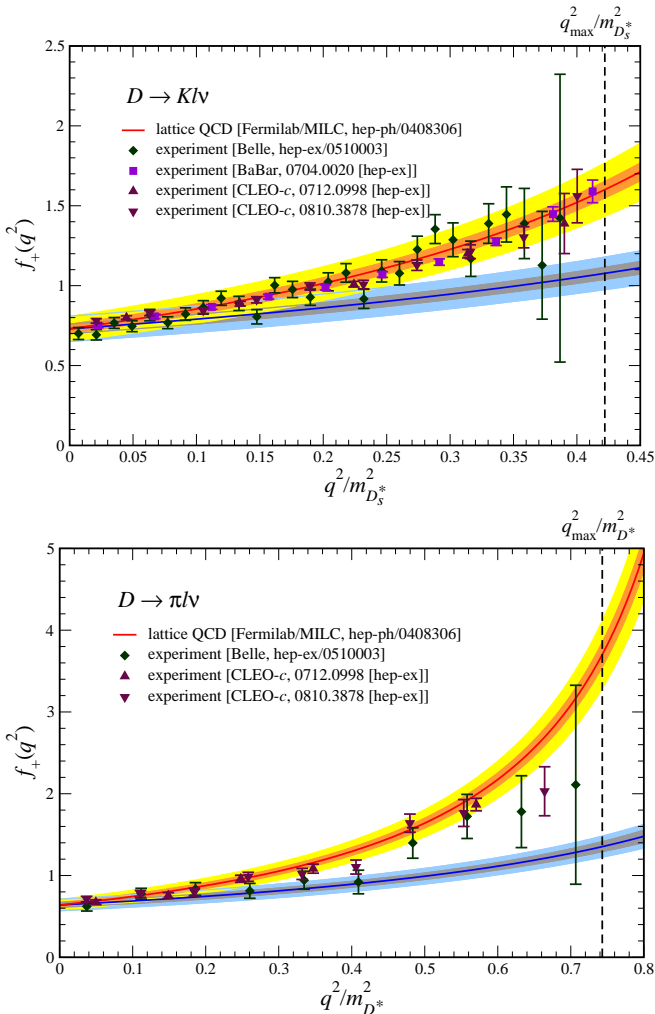


FIG. 2: Form factors f_+ (and f_0) for semileptonic D decays, from lattice QCD [6, 26], expressed as a red (blue) curve with an orange (gray) statistical error band and a yellow (light blue) combined error band. Error bands take correlations into account. Measurements of f_+ are from Belle (green diamonds) [24], BaBar (magenta squares) [27], and CLEO-c (maroon triangles) [28, 29]. The vertical line shows q_{\max}^2 .

TABLE IV: Best-fit values a_k and correlation matrix ρ_{kl} of the 3-term z expansion of f_+ for $B \rightarrow \pi l \nu$, with statistical and systematic errors combined [9].

Fit: 0.0216(27) -0.0378(191) -0.113(27)			
ρ	a_0	a_1	a_2
a_0	1.000	0.640	0.475
a_1	0.640	1.000	0.964
a_2	0.474	0.964	1.000

of this paper. Now the curve and error band conform with preconceptions, for several reasons. First, $q_{(1,0,0)}^2$ is close to q_{\max}^2 , rather than in the middle of the kinematic range. Second, the chiral extrapolation in Ref. [9] is less aggressive than that in Ref. [6], leading to a larger but more realistic error at $q^2 = 0$. The most striking aspect is that even though the absolute error in f_+ is increasing for $\tilde{q}^2 \geq 0.8$, the band remains narrow. The band simply conveys the point-to-point correlations better.

This paper shows in detail how to compare semileptonic form factors from lattice-QCD and from experiments. For illustration we use the BK parametrization

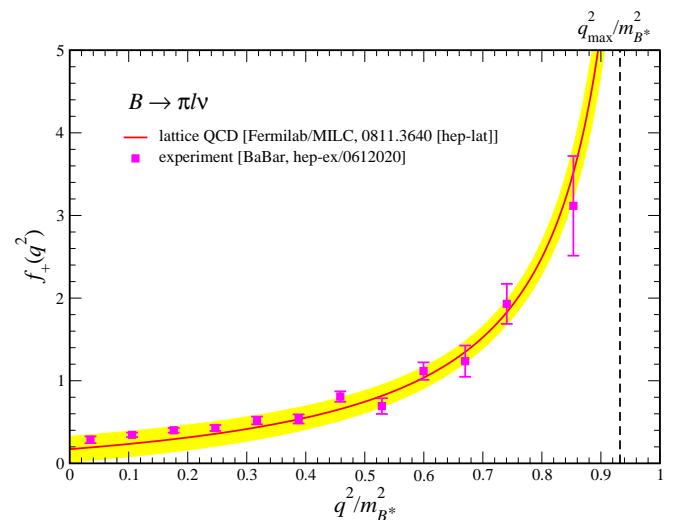


FIG. 3: Form factor f_+ for $B \rightarrow \pi l \nu$ expressed as a curve (red) from the best fit with a total error band (yellow) from taking correlations in the fit parameters into account [9], overlaid with measurements of $|V_{ub}|f_+/(3.38 \times 10^{-3})$ from BaBar (magenta squares) [30]. The vertical line shows q_{\max}^2 .

for $D \rightarrow K\ell\nu$ and $D \rightarrow \pi\ell\nu$, and the z expansion for $B \rightarrow \pi\ell\nu$. Clearly, the idea is more general. For example, an interesting prospect relevant to semileptonic form factors is to inject 3-momenta smaller than $\mathbf{p}_{(1,0,0)}$ using “twisted” boundary conditions [31, 32, 33]. That strategy should improve the accuracy of parameters in the chiral extrapolation and, hence, the BK, BZ, or z fits. The output of any fit could still be exhibited as outlined here, although one should bear in mind that superior visualization of a fitting procedure does not repair any shortcomings of the fit itself.

Acknowledgments

We would like to thank Ian Shipsey for encouraging us to think carefully about the correlations in the systematic errors. We would like to thank Laurenz Widhalm for providing the Belle data in numerical form [24], and Shipsey for the BaBar and CLEO D -decay data [27, 28, 29].

Computations for this work were carried out in part on facilities of the USQCD Collaboration, which are funded by the Office of Science of the United States Department of Energy. This work was supported in part by the U.S. Department of Energy under Grants No. DE-FC02-06ER41446 (C.D., L.L., M.B.O.), No. DE-FG02-91ER40661 (S.G.), No. DE-FG02-91ER40677 (A.X.K., R.T.E., E.G.), No. DE-FG02-91ER40628 (C.B., J.L.), and No. DE-FG02-04ER41298 (D.T.); by the National Science Foundation under Grants No. PHY-0555243, No. PHY-0757333, No. PHY-0703296 (C.D., L.L., M.B.O.), No. PHY-0555235 (J.L.), and No. PHY-0757035 (R.S.); and by Universities Research Associates (R.T.E., E.G.). This manuscript has been coauthored by an employee of Brookhaven Science Associates, LLC, under Contract No. DE-AC02-98CH10886 with the U.S. Department of Energy. Fermilab is operated by Fermi Research Alliance, LLC, under Contract No. DE-AC02-07CH11359 with the U.S. Department of Energy.

-
- [1] M. Ablikim *et al.* [BES Collaboration], Phys. Lett. B **597**, 39 (2004) [arXiv:hep-ex/0406028].
 - [2] G. S. Huang *et al.* [CLEO Collaboration], Phys. Rev. Lett. **94**, 011802 (2005) [arXiv:hep-ex/0407035].
 - [3] J. M. Link *et al.* [FOCUS Collaboration], Phys. Lett. B **607**, 51 (2005) [arXiv:hep-ex/0410068].
 - [4] J. M. Link *et al.* [FOCUS Collaboration], Phys. Lett. B **607**, 233 (2005) [arXiv:hep-ex/0410037].
 - [5] D. Besson *et al.* [CLEO Collaboration], Phys. Rev. D **80**, 032005 (2009) [arXiv:0906.2983 [hep-ex]].
 - [6] C. Aubin *et al.* [Fermilab Lattice, MILC, and HPQCD Collaborations], Phys. Rev. Lett. **94**, 011601 (2005) [arXiv:hep-ph/0408306].
 - [7] M. Okamoto *et al.* [Fermilab Lattice, MILC, and HPQCD Collaborations], Nucl. Phys. Proc. Suppl. **140**, 461 (2005) [arXiv:hep-lat/0409116].
 - [8] E. Dalgic néé Gulez *et al.* [HPQCD Collaboration], Phys. Rev. D **73**, 074502 (2006) [arXiv:hep-lat/0601021]; **75**, 119906(E) (2007).
 - [9] J. A. Bailey *et al.*, Phys. Rev. D **79**, 054507 (2009) [arXiv:0811.3640 [hep-lat]].
 - [10] K. C. Bowler *et al.* [UKQCD Collaboration], Phys. Lett. B **486** (2000) 111 [arXiv:hep-lat/9911011].
 - [11] A. Abada *et al.*, Nucl. Phys. B **619** (2001) 565 [arXiv:hep-lat/0011065].
 - [12] A. X. El-Khadra *et al.*, Phys. Rev. D **64**, 014502 (2001). [arXiv:hep-ph/0101023].
 - [13] S. Aoki *et al.* [JLQCD Collaboration], Phys. Rev. D **64** (2001) 114505 [arXiv:hep-lat/0106024].
 - [14] J. Shigemitsu *et al.*, Phys. Rev. D **66**, 074506 (2002) [arXiv:hep-lat/0207011].
 - [15] D. Bećirević, S. Prelovšek, and J. Zupan, Phys. Rev. D **67**, 054010 (2003) [arXiv:hep-lat/0210048].
 - [16] C. Aubin and C. Bernard, Phys. Rev. D **76**, 014002 (2007) [arXiv:0704.0795 [hep-lat]].
 - [17] L. Lellouch, Nucl. Phys. B **479**, 353 (1996) [arXiv:hep-ph/9509358].
 - [18] D. Bećirević and A. B. Kaidalov, Phys. Lett. B **478**, 417 (2000) [arXiv:hep-ph/9904490].
 - [19] P. Ball and R. Zwicky, Phys. Rev. D **71**, 014015 (2005) [arXiv:hep-ph/0406232].
 - [20] R. J. Hill, Phys. Rev. D **73**, 014012 (2006) [arXiv:hep-ph/0505129].
 - [21] T. Becher and R. J. Hill, Phys. Lett. B **633**, 61 (2006) [arXiv:hep-ph/0509090].
 - [22] C. Bourrely, B. Machet, and E. de Rafael, Nucl. Phys. B **189**, 157 (1981).
 - [23] C. G. Boyd, B. Grinstein, and R. F. Lebed, Phys. Rev. Lett. **74**, 4603 (1995) [arXiv:hep-ph/9412324]; C. G. Boyd and M. J. Savage, Phys. Rev. D **56**, 303 (1997) [arXiv:hep-ph/9702300].
 - [24] L. Widhalm *et al.* [Belle Collaboration], Phys. Rev. Lett. **97**, 061804 (2006) [arXiv:hep-ex/0604049]; K. Abe *et al.* [Belle Collaboration], arXiv:hep-ex/0510003.
 - [25] A. S. Kronfeld *et al.* [Fermilab Lattice, MILC, and HPQCD Collaborations], PoS **LAT2005**, 206 (2006) [Int. J. Mod. Phys. A **21**, 713 (2006)] [arXiv:hep-lat/0509169]; A. S. Kronfeld [Fermilab Lattice, MILC, and HPQCD Collaborations], J. Phys. Conf. Ser. **46**, 147 (2006) [arXiv:hep-lat/0607011].
 - [26] M. Okamoto [for the Fermilab Lattice and MILC Collaborations], unpublished (2005). A public report of this work is contained in Ref. [7]. This line of analysis was superseded by Ref. [9].
 - [27] B. Aubert *et al.* [BaBar Collaboration], Phys. Rev. D **76**, 052005 (2007) [arXiv:0704.0020 [hep-ex]].
 - [28] D. Cronin-Hennessy *et al.* [CLEO Collaboration], Phys. Rev. Lett. **100**, 251802 (2008) [arXiv:0712.0998 [hep-ex]]; S. Dobbs *et al.* [CLEO Collaboration], Phys. Rev. D **77**, 112005 (2008) [arXiv:0712.1020 [hep-ex]].
 - [29] J. Y. Ge *et al.* [CLEO Collaboration], Phys. Rev. D **79**, 052010 (2009) [arXiv:0810.3878 [hep-ex]].
 - [30] B. Aubert *et al.* [BaBar Collaboration], Phys. Rev. Lett. **98**, 091801 (2007) [arXiv:hep-ex/0612020].

- [31] P. F. Bedaque, Phys. Lett. B **593**, 82 (2004) [arXiv:nucl-th/0402051].
- [32] C. T. Sachrajda and G. Villadoro, Phys. Lett. B **609**, 73 (2005) [arXiv:hep-lat/0411033].
- [33] J. M. Flynn, A. Jüttner, and C. T. Sachrajda [UKQCD Collaboration], Phys. Lett. B **632**, 313 (2006) [arXiv:hep-lat/0506016].

Quarkonium mass splittings with Fermilab heavy quarks and 2+1 flavors of improved staggered sea quarks

T. Burch^{*}, C.E. DeTar and L. Levkova[†]

Physics Department, University of Utah, Salt Lake City, UT 84112, USA

E-mail: ludmila@physics.utah.edu

M. Di Pierro

School of Computer Sci., Telecom. and Info. Systems, DePaul University, Chicago, Illinois, USA

A.X. El-Khadra

Physics Department, University of Illinois, Urbana, Illinois, USA

Steven Gottlieb

Department of Physics, Indiana University, Bloomington, IN 47405, USA

A.S. Kronfeld, P.B. Mackenzie, and J.N. Simone

Fermi National Accelerator Laboratory, Batavia, IL 60510, USA

We present results from an ongoing lattice study of the lowest lying charmonium and bottomonium level splittings using the Fermilab heavy quark formalism. Our objective is to test the performance of this action on MILC-collaboration ensembles of (2 + 1) flavors of light improved staggered (asqtad) quarks. Measurements are done on 16 ensembles with degenerate up and down quarks of various masses, thus permitting a chiral extrapolation, and over lattice spacings ranging from 0.09 fm to 0.18 fm, thus permitting study of lattice-spacing dependence. We examine combinations of the mass splittings that are sensitive to components of the effective quarkonium potential.

The XXVII International Symposium on Lattice Field Theory - LAT2009

July 26-31 2009

Peking University, Beijing, China

^{*}Present address: Institut für Theoretische Physik, Universität Regensburg, 93040 Regensburg, Germany.

[†]Speaker.

ensemble	a (approx) (fm)	sea quark ratio m_{ud}/m_s
Extra coarse	0.18	0.6, 0.4, 0.2, 0.1
Medium coarse	0.15	0.6, 0.4, 0.2, 0.1
Coarse	0.12	0.6, 0.4, 0.2, 0.15, 0.1
Fine	0.09	0.4, 0.2, 0.1

Table 1: Light quark mass ratios and lattice spacings for the ensembles used in this study. The strange quark mass is set to approximately its physical value.

1. Introduction

The well-studied charmonium and bottomonium systems have long been used as a test bed for phenomenological models and lattice methods. It is well known that including light sea quarks is essential for obtaining good agreement with experiment. Few studies have carried out a systematic treatment that includes both the chiral (sea quark) and continuum limit. The present study describes progress to date in such an ongoing study [1]. It is based on charm and bottom masses that were determined in previous studies [2]. We limit our attention to lattices with spacing $a \geq 0.09$ fm. Table 1 lists the 16 ensembles used in this study [3–5].

We simulate the heavy charm and bottom quarks with the Fermilab action [6],

$$\begin{aligned} S = & \sum_n \bar{\psi}_n \psi_n - \kappa \sum_n \left[\bar{\psi}_n (1 - \gamma_4) U_{n,4} \psi_{n+\hat{4}} + \bar{\psi}_{n+\hat{4}} (1 + \gamma_4) U_{n,4}^\dagger \psi_n \right] \\ & - \kappa \zeta \sum_{n,i} \left[\bar{\psi}_n (r_s - \gamma_i) U_{n,i} \psi_{n+\hat{i}} + \bar{\psi}_{n+\hat{i}} (r_s + \gamma_i) U_{n,i}^\dagger \psi_n \right] \\ & - c_B \kappa \zeta \sum_n \bar{\psi}_n i \boldsymbol{\Sigma} \cdot \mathbf{B}_n \psi_n - c_E \kappa \zeta \sum_{n;i} \bar{\psi}_n \boldsymbol{\alpha} \cdot \mathbf{E}_n \psi_n . \end{aligned}$$

The energy of a single quark of spatial momentum \mathbf{p} in nonrelativistic approximation is

$$E(\mathbf{p}) = m_1 + \frac{\mathbf{p}^2}{2m_2} + O(p^4),$$

where m_1 is the rest mass and m_2 is the “kinetic” mass. They can be made equal if we tune the temporal anisotropy ζ . Instead, we set $\zeta = 1$ and limit our attention to mass splittings for which the additive mass renormalization cancels. We also take $c_B = c_E = 1/u_0^3$, where u_0 is the tadpole factor. These choices are explained in greater detail in [7]. The resulting action is just the standard clover action with the clover coefficient set according to the Fermilab interpretation.

2. Tuning the heavy quark masses

There are a variety of possible ways to determine the masses (κ 's) of the charm and bottom quarks. Since we know the lattice scale from other measurements, determining the heavy quark mass involves matching a lattice mass with an experimentally observed mass. Tuning to the rest mass M_1 of quarkonium is clearly inaccurate, since it inherits the large additive renormalization

ensemble	a	κ_c	κ_b
Extra coarse	0.18 fm	0.120	—
Medium coarse	0.15 fm	0.122	0.076
Coarse	0.12 fm	0.122	0.086
Fine	0.09 fm	0.127	0.0923

Table 2: Tuned charm and bottom κ 's.

of the quark mass m_1 . Tuning the kinetic mass M_2 of quarkonium is a possibility, but that mass includes a strong binding energy that we would like to study independently of the tuning [8]. So a cleaner approach tunes to the spin-averaged kinetic masses of the $\bar{D}_s = \frac{1}{4}m_{D_s} + \frac{3}{4}m_{D_s^*}$ and the corresponding \bar{B}_s multiplet [2, 7]. The heavy-light system has only a mild binding contribution. In this way our study of quarkonium binding is more predictive. Results of tuning are shown in Table 2. Tuning errors are discussed in detail in Ref. [7].

All tuning methods should agree in the continuum limit. Discrepancies at nonzero lattice spacing come from discretization artifacts that grow with ma , *i.e.*, the quark mass in lattice units. So, for example, at $a = 0.15$ fm we find that the tuned charm mass is approximately the same whether obtained from the kinetic mass of the D_s multiplet or the kinetic charmonium mass, but the tuned bottom mass differs significantly: $\kappa_b = 0.94$ from tuning the kinetic bottomonium mass and 0.76 from tuning the B_s multiplet.

Nonetheless, there are situations that require tuning the quarkonium rest mass. For our companion study of charmonium annihilation effects, mixing between quarkonium states and glueball states could be important [9]. In this case it is important to arrange for a correct placement of the unmixed charmonium and glueball eigenenergies of the lattice hamiltonian, *i.e.*, the unmixed rest masses [10]. However, in that study we hope for at best 15% accuracy in computing the tiny mass shifts coming from annihilation, so we tolerate a mistuning of the kinetic quark mass.

3. Results

We measure quarkonium correlators with smeared relativistic and nonrelativistic S-wave and P-wave sources and sinks. To extract masses, we use a multistate fit model with loose Bayesian priors, and we determine statistical errors in mass splittings from a bootstrap analysis. We present a sampling of results. More are given in [7]. We examine them in terms of a traditional nonrelativistic decomposition of the effective heavy quark potential, namely, central, spin-spin, spin-orbit, and tensor contributions.

3.1 Charmonium hyperfine splitting

Hyperfine splitting provides a direct measure of the strength of the spin-spin chromomagnetic interaction. In Fig. 1 we show our results for charmonium hyperfine splitting. Here only the quark line “connected” diagrams are included. The dependence on sea quark mass is evidently quite weak. The continuum extrapolation, shown with kappa tuning errors included, gives 116(5) MeV compared with 117(1) MeV from experiment. It would clearly be good to reduce κ -tuning errors.

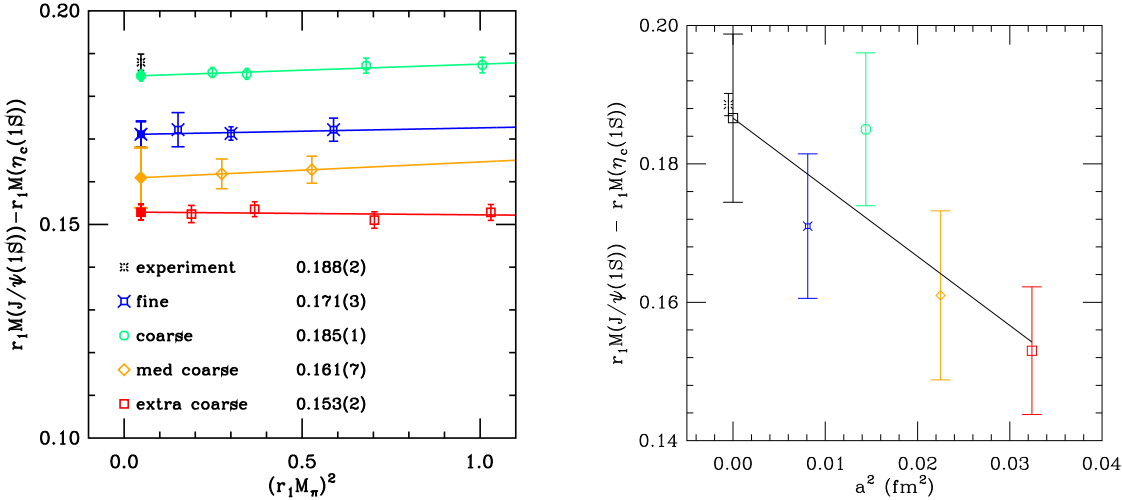


Figure 1: Results for charmonium hyperfine splitting. Splittings are in $r_1 = 0.318$ fm units. ($1/r_1 = 620$ MeV). The left panel shows the chiral extrapolation with only statistical errors shown. The right panel shows the continuum extrapolation in a^2 with kappa tuning errors of 6% included.

superfine	0.06 fm	$-3.4(3)$ MeV
fine	0.09 fm	$-5.5(8)$ MeV

Table 3: Contribution from charm annihilation to the charmonium hyperfine splitting

The contribution to the charmonium correlator and mass from quark line disconnected diagrams is expected to be small, so they are usually ignored. Because it is so small, it is a challenge to calculate it [9]. Our most recent results are given in Table 3.1. We find that annihilation processes actually decrease the magnitude of the splitting. The effect is smaller than or comparable to our current errors in the connected contribution.

3.2 Bottomonium hyperfine splitting

In Fig. 2 we show results for hyperfine splitting of the bottomonium ground state. The continuum extrapolation gives 53(8) MeV. The η_b was recently found [11, 12] with a splitting of 71(4) MeV from the $\Upsilon(1S)$. The HPQCD collaboration reports 61(4)(13) [13] using an NRQCD method with a chromomagnetic interaction of a quality comparable to ours.

3.3 2S – 1S level splitting

In Fig. 3 we show results for the splitting of the spin-averaged $\bar{2}\bar{S}$ and $\bar{1}\bar{S}$ levels. This quantity tests the “central” part of the quarkonium effective potential. We see that agreement with experiment in the charmonium case is not good. It is better in the bottomonium case. Our fit model does not include open charm states. So the $2S$ charmonium state could be confused with the nearby open charm threshold that comes closer as the light sea quark mass decreases. The dashed line locates

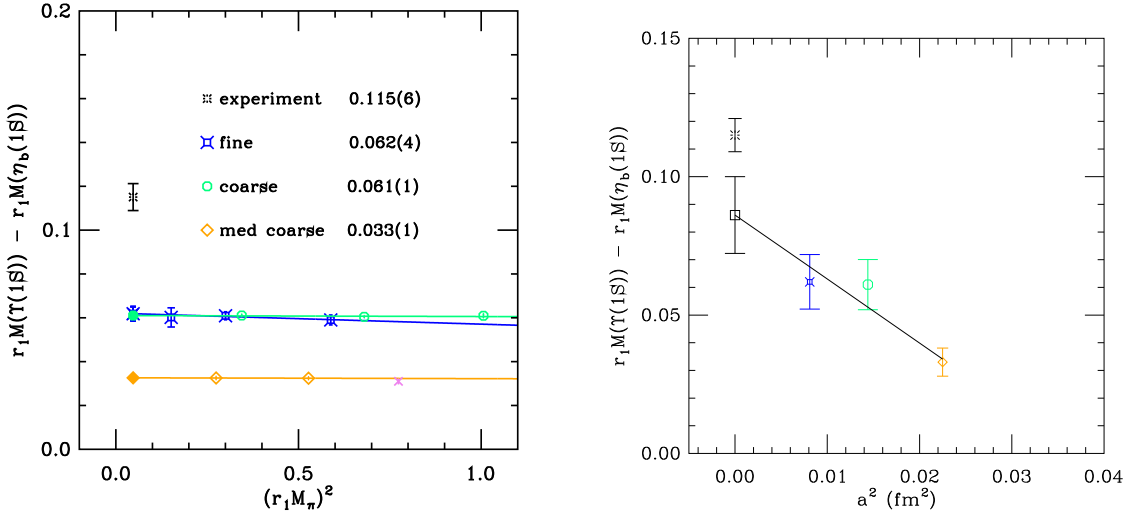


Figure 2: The left panel shows the chiral extrapolation with only statistical errors shown. The right panel shows the continuum extrapolation in a^2 with kappa tuning errors of 15% included, resulting in 53(9) MeV.

the physical open charm threshold. For the bottomonium case the open bottom threshold is safely off scale.

3.4 1P – 1S splitting

The spin-averaged $\overline{1P} - \overline{1S}$ splitting, shown in Fig. 4, also tests the central part of the potential. Within errors, our results seem to approach the experimental value.

3.5 Spin-orbit and tensor components

The contribution to the $J = 0, 1$, and 2 P-wave masses from the spin-orbit term in the quarkonium effective potential can be isolated with the combination

$$m_{1P_{\text{spin-orbit}}} = \frac{1}{9} (5m_{c2} - 2m_{c0} - 3m_{c1})$$

Our result is shown in Fig. 5. This term tests the strength of the chromoelectric interaction. In both cases the results seem to approach the experimental value in the chiral and continuum limits.

Similarly, the contribution to the P-wave levels from the tensor component is proportional to the combination

$$m_{1P_{\text{tensor}}} = \frac{1}{9} (3m_{c1} - m_{c2} - 2m_{c0}),$$

shown in Fig. 6. Since the tensor and spin-spin components both measure the strength of the chromomagnetic interaction, here we divide by the 1S hyperfine splitting to see whether they are proportional. It appears that they are not. Still the results seem to approach the experimental values in the chiral and continuum limits.

3.6 Full spectrum

In Fig. 7 we reconstruct the low-lying quarkonium spectrum from splittings, starting from the experimental value for the spin-averaged 1S level.

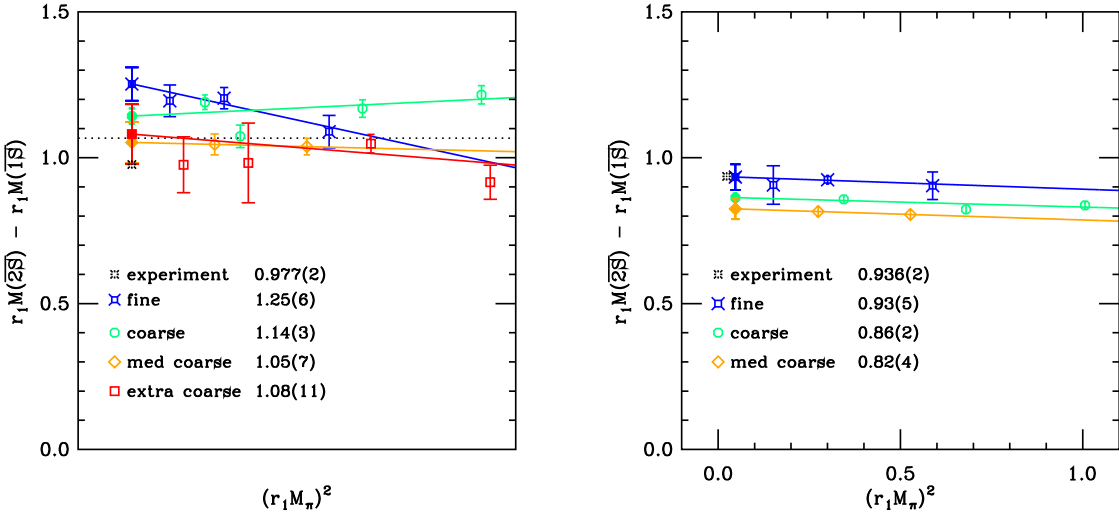


Figure 3: Splitting of the spin-averaged $2S$ and $1S$ levels in charmonium (left) and bottomonium (right). The dashed line indicates the physical open charm threshold. Since the η'_b has not been observed the “experimental” point uses only the $\Upsilon(2S)$ in the splitting.

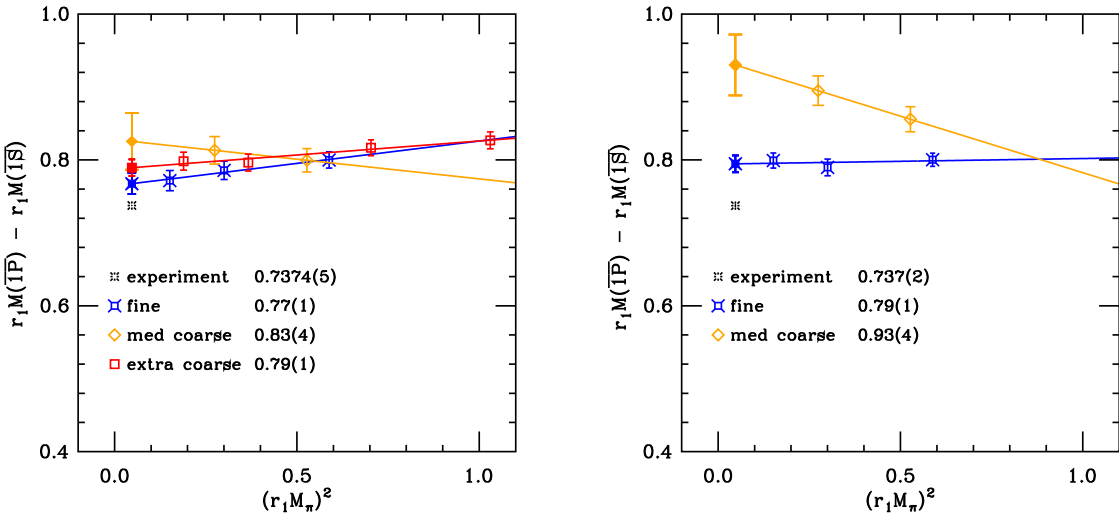


Figure 4: Splitting of the spin-averaged $1P$ and $1S$ levels in charmonium (left) and bottomonium (right).

4. Conclusion and Outlook

We have seen that in most cases quarkonium level splittings are quite insensitive to the light sea quark masses. Systematic uncertainties in tuning the quark masses are much larger than our statistical errors. With the present set of lattice spacings and the present level of precision, the Fermilab action seems to perform well in the charmonium system, but there are indications that lattice discretization artifacts affect some of our bottomonium splittings. Work currently underway

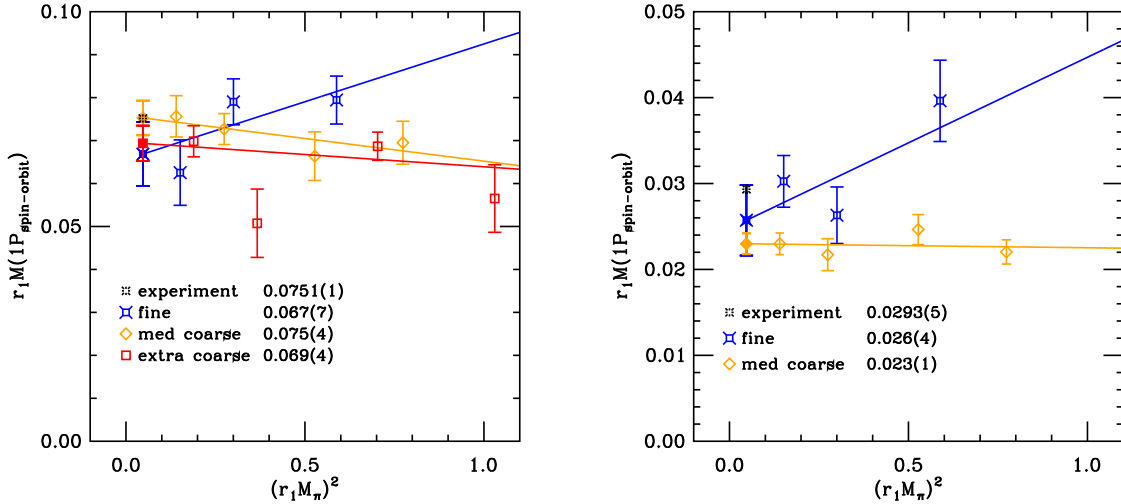


Figure 5: Spin-orbit combination from the $1P$ levels for charmonium (left) and bottomonium (right).

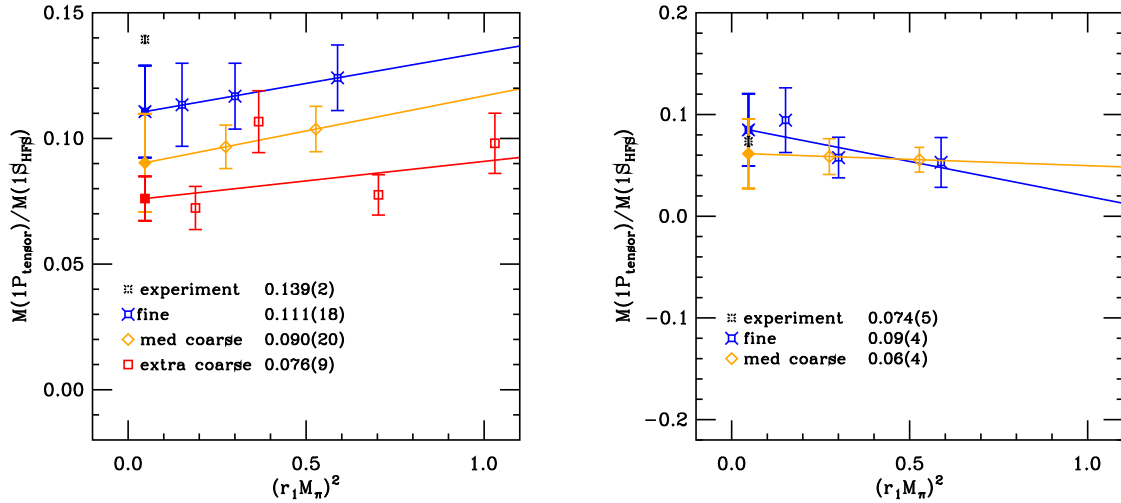


Figure 6: The $1P$ tensor combination, divided by the $1S$ hyperfine splitting for charmonium (left) and bottomonium (right).

seeks a more precise determination of the charm and bottom masses and will use the still finer MILC-collaboration 0.06 fm lattices.

Acknowledgments

Work is supported by grants from the US Department of Energy and US National Science Foundation. The lattice ensembles used in this study were generated by the MILC collaboration. Computations for this work were carried out on facilities of the USQCD Collaboration, which are

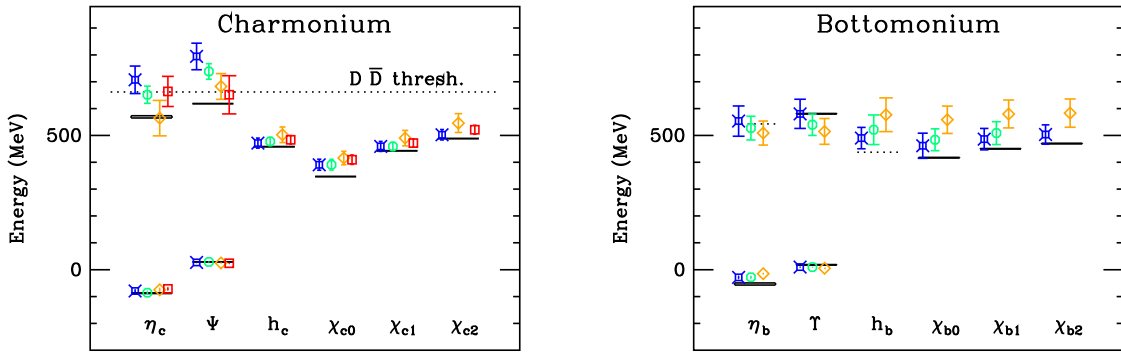


Figure 7: All quarkonium levels in this study, constructed from splittings from the physical $\bar{D}S$ level for charmonium (left) and bottomonium (right). Error bars include kappa tuning errors. Symbol colors distinguish the lattice spacings: 0.18 fm (red), 0.15 fm (orange), 0.12 fm (green), 0.09 fm (blue)

funded by the Office of Science of the U.S. Department of Energy. T.B. acknowledges current support by the DFG (SFB/TR55).

References

- [1] M. Di Pierro *et al.*, *Nucl. Phys. Proc. Suppl.* **119**, 586 (2003) [[arXiv:hep-lat/0210051](#)]; *Nucl. Phys. Proc. Suppl.* **129**, 340 (2004) [[arXiv:hep-lat/0310042](#)]; S. Gottlieb *et al.*, PoS(LAT2005)203 (2006) [[arXiv:hep-lat/0510072](#)]; PoS(LAT2006)175 (2006) [[arXiv:0910.0048 \[hep-lat\]](#)].
- [2] C. Bernard *et al.* [Fermilab Lattice and MILC Collaborations], in preparation (2009).
- [3] C. W. Bernard *et al.*, *Phys. Rev. D* **64**, 054506 (2001) [[arXiv:hep-lat/0104002](#)].
- [4] C. Aubin *et al.*, *Phys. Rev. D* **70**, 094505 (2004) [[arXiv:hep-lat/0402030](#)].
- [5] A. Bazavov *et al.* [MILC collaboration], *Rev. Mod. Phys.* (to be published) [[arXiv:0903.3598](#)].
- [6] A. X. El-Khadra, A. S. Kronfeld and P. B. Mackenzie, *Phys. Rev. D* **55**, 3933 (1997) [[arXiv:hep-lat/9604004](#)].
- [7] T. Burch *et al.* [Fermilab Lattice and MILC Collaborations], in preparation (2009).
- [8] A. S. Kronfeld, *Nucl. Phys. Proc. Suppl.* **53**, 401 (1997) [[arXiv:hep-lat/9608139](#)].
- [9] L. Levkova and C. E. DeTar, PoS(LATTICE 2008)133 [[arXiv:0809.5086](#)] and work in preparation (2009).
- [10] Y. Chen *et al.*, *Phys. Rev. D* **73**, 014516 (2006) [[arXiv:hep-lat/0510074](#)].
- [11] B. Aubert *et al.* [BaBar Collaboration], *Phys. Rev. Lett.* **101**, 071801 (2008), [[arXiv:0807.1086](#)].
- [12] B. Aubert *et al.* [BaBar Collaboration], [[arXiv:0903.1124](#)].
- [13] A. Gray *et al.* [HPQCD Collaboration], *Phys. Rev. D* **72**, 094507 (2005) [[arXiv:hep-lat/0507013](#)].

Progress on charm semileptonic form factors from 2+1 flavor lattice QCD

Jon A. Bailey^{*a†}, **A. Bazavov**^b, **C. Bernard**^c, **C. Bouchard**^e, **C. DeTar**^d, **A.X. El-Khadra**^e,
E.D. Freeland^c, **W. Freeman**^b, **E. Gamiz**^{a,e}, **Steven Gottlieb**^{e,f,g}, **U.M. Heller**^h,
J.E. Hetrickⁱ, **A.S. Kronfeld**^a, **J. Laiho**^c, **L. Levkova**^d, **P.B. Mackenzie**^a, **M.B. Oktay**^d,
M. Di Pierro^j, **J.N. Simone**^a, **R. Sugar**^k, **D. Toussaint**^b, and **R.S. Van de Water**^l

^a*Theoretical Physics Department, Fermilab, Batavia, IL 60510, USA*

^b*Department of Physics, University of Arizona, Tucson, AZ 85721, USA*

^c*Department of Physics, Washington University, St. Louis, MO 63130, USA*

^d*Physics Department, University of Utah, Salt Lake City, UT 84112, USA*

^e*Physics Department, University of Illinois, Urbana, IL 61801, USA*

^f*Department of Physics, Indiana University, Bloomington, IN 47405, USA*

^g*National Center for Supercomputing Applications, University of Illinois, Urbana, IL 61801, USA*

^h*American Physical Society, One Research Road, Ridge, NY 11961, USA*

ⁱ*Physics Department, University of the Pacific, Stockton, CA 95211, USA*

^j*School of Computing, DePaul University, Chicago, IL 60604, USA*

^k*Department of Physics, University of California, Santa Barbara, CA 93106, USA*

^l*Department of Physics, Brookhaven National Laboratory, Upton, NY 11973, USA*

The Fermilab Lattice and MILC Collaborations

Lattice calculations of the form factors for the charm semileptonic decays $D \rightarrow Kl\nu$ and $D \rightarrow \pi l\nu$ provide inputs to direct determinations of the CKM matrix elements $|V_{cs}|$ and $|V_{cd}|$ and can be designed to validate calculations of the form factors for the bottom semileptonic decays $B \rightarrow \pi l\nu$ and $B \rightarrow Kl\bar{l}$. We are using Fermilab charm (bottom) quarks and asqtad staggered light quarks on the 2+1 flavor asqtad MILC ensembles to calculate the charm (bottom) form factors. We outline improvements to the previous calculation of the charm form factors and detail our progress. We expect our current round of data production to allow us to reduce the theoretical uncertainties in $|V_{cs}|$ and $|V_{cd}|$ from 10.5% and 11%, respectively, to about 7%.

*The XXVII International Symposium on Lattice Field Theory
July 26-31, 2009
Peking University, Beijing, China*

^{*}Speaker.

[†]jabaley@fnal.gov

1. Introduction

The CKM matrix elements $|V_{cs}|$ and $|V_{cd}|$ can be extracted to greatest precision (currently to 0.02% and 0.4%, respectively) by assuming CKM unitarity and performing a fit to all data [1]. However, the simplest tests of unitarity require direct determinations of the CKM matrix elements.

The decay rate for $D \rightarrow K(\pi)l\nu$ is proportional to a form factor and $|V_{cs}|$ ($|V_{cd}|$). Experiments can measure the decay rates and the form factor shapes, but nonperturbative calculations of the strong force are required to fix the form factor normalizations and extract $|V_{cs(d)}|$. Therefore these decays allow direct determinations of $|V_{cs(d)}|$ and consistency checks between lattice QCD and unitarity. Such consistency increases our confidence in both.

In June CLEO-c published the results of an analysis of 818 pb^{-1} collected at charm threshold [2]. Combining the CLEO-c results with the first 2+1 flavor lattice calculations of the $D \rightarrow K(\pi)l\nu$ form factors [3, 4] yields $|V_{cs(d)}|$ [2]:

$$|V_{cs}| = 0.985(1 \pm 0.9\% \pm 0.6\% \pm 10.5\%), \quad (1.1)$$

$$|V_{cd}| = 0.234(1 \pm 3\% \pm 0.9\% \pm 11\%). \quad (1.2)$$

The first errors are experimental statistical errors, and the second are experimental systematics. The third errors are due to uncertainties in the lattice QCD calculations. The theory errors dominate the uncertainties.

Discretization effects are the dominant source of the theory errors [3]. Other uncertainties enter because of incomplete suppression of oscillations due to opposite-parity states, truncation effects in fits to staggered chiral perturbation theory ($S\chi PT$), and model-dependence implicit in the Becirevic-Kaidalov (BK) parameterization [3, 5].

These sources of uncertainty were addressed in work on $B \rightarrow \pi l\nu$ decays [6]. By calculating the $D \rightarrow K(\pi)l\nu$ form factors using the same methods, we may be able to validate their application to calculations of the form factors for $B \rightarrow \pi l\nu$ and $B \rightarrow Kl\bar{l}$. The former decay allows a precise determination of $|V_{ub}|$ and a stringent test of unitarity. The latter is a rare decay and a prime candidate for new physics. Below we describe our progress in reducing the uncertainties in the charm form factors and anticipate the reduction of the uncertainties in $|V_{cs(d)}|$.

2. Ensembles and quark masses

To decrease discretization effects and improve our control of the chiral extrapolation, we are generating full QCD and partially quenched data on each of the ensembles shown in Table 1. These ensembles include the four most chiral coarse ensembles used in the calculations of Ref. [3], the two fine ($a \approx 0.09 \text{ fm}$) ensembles included in our recent calculation of the form factor for $B \rightarrow \pi l\nu$ [6], two additional fine ensembles, three superfine ($a \approx 0.06 \text{ fm}$) ensembles, and one ultrafine ($a \approx 0.045 \text{ fm}$) ensemble [7]. The MILC Collaboration has increased the number of configurations in each of the previously used coarse and fine ensembles by a factor of four, and we expect a corresponding decrease in all statistics-dominated uncertainties by a factor of two.

We have found that randomizing the spatial location of the sources significantly decreases autocorrelations in 2-point functions, which suggests that we may be able to increase our statistics further by increasing the number of source times on each configuration. We have nearly completed

	$\approx a$ (fm)	am_l/am_s	Volume	N_{conf}	am_{valence}
coarse	0.12	0.02/0.05	$20^3 \times 64$	2052	0.005, 0.007, 0.01,
		0.01/0.05	$20^3 \times 64$	2259	0.02, 0.03, 0.0415,
		0.007/0.05	$20^3 \times 64$	2110	0.05; 0.0349
		0.005/0.05	$24^3 \times 64$	2099	
fine	0.09	0.0124/0.031	$28^3 \times 96$	1996	0.0031, 0.0047, 0.0062,
		0.0062/0.031	$28^3 \times 96$	1946	0.0093, 0.0124, 0.031;
		0.00465/0.031	$32^3 \times 96$	983	0.0261
		0.0031/0.031	$40^3 \times 96$	1015	
superfine	0.06	0.0036/0.018	$48^3 \times 144$	668	0.0036, 0.0072, 0.0018,
		0.0025/0.018	$56^3 \times 144$	800	0.0025, 0.0054, 0.0160;
		0.0018/0.018	$64^3 \times 144$	826	0.0188
ultrafine	0.045	0.0028/0.014	$64^3 \times 192$	861	TBD

Table 1: Asqtad staggered quark ensembles generated by the MILC Collaboration [7, 8, 9] and slated for upcoming heavy-light analyses, together with the valence quark masses being used at each lattice spacing. The last valence mass listed at each lattice spacing (after the semicolon) is the tuned strange quark mass. We are presently generating correlators at four source times on each ensemble and investigating the possibility of adding more source times to further increase the total number of source-configurations.

data generation at four source times on the coarse ensembles, the fine ensembles with $m_l = 0.4m_s$, $0.2m_s$, and $0.1m_s$, and the superfine ensemble with $m_l = 0.2m_s$.

Power counting arguments [3, 6] indicate that including these ensembles will effectively eliminate discretization effects due to light quarks and gluons, while heavy-quark discretization effects will be reduced but remain significant. To improve our estimates of heavy-quark discretization effects, we are investigating including them in chiral-continuum expansions [10]. This approach incorporates the information from power counting while more systematically fixing the appropriate hadronic scales.

3. Correlators and correlator ratios

The form factors parameterize the hadronic matrix elements of the flavor-changing vector currents,

$$\langle K(\pi)|V_\mu|D\rangle = \sqrt{2m_D} \left[v_\mu f_{||}^{D \rightarrow K(\pi)}(q^2) + p_{\perp\mu} f_{\perp}^{D \rightarrow K(\pi)}(q^2) \right], \quad (3.1)$$

where V_μ is the lattice current corresponding to $i\bar{s}\gamma_\mu c$ ($i\bar{d}\gamma_\mu c$), $v = p_D/m_D$ is the four-velocity of the D meson, $p_\perp = p_{K(\pi)} - (p_{K(\pi)} \cdot v)v$ is the component of kaon (pion) momentum perpendicular to v , and $q^2 \equiv (p_D - p_{K(\pi)})^2$ is the invariant mass of the leptons. We work in the D -meson rest frame, in which the form factors are proportional to the temporal and spatial components of the hadronic matrix elements, and $q^2 = m_D^2 + m_{K(\pi)}^2 - 2m_D E_{K(\pi)}$.

One way to extract the hadronic matrix elements is by considering simple ratios of 3-point to 2-point correlators [3],

$$\frac{C_{3,\mu}^{D \rightarrow K(\pi)}(t, T; \mathbf{p}_{K(\pi)})}{C_2^{K(\pi)}(t; \mathbf{p}_{K(\pi)}) C_2^D(T-t)}, \quad (3.2)$$

where T is the separation between source and sink in the 3-point functions, and

$$C_{3,\mu}^{D \rightarrow K(\pi)}(t, T; \mathbf{p}_{K(\pi)}) = \sum_{\mathbf{x}, \mathbf{y}} e^{i\mathbf{p}_{K(\pi)} \cdot \mathbf{y}} \langle \mathcal{O}_{K(\pi)}(t_i, \mathbf{0}) V_\mu(t, \mathbf{y}) \mathcal{O}_D^\dagger(t_f, \mathbf{x}) \rangle, \\ t \in [t_i, t_f = (t_i + T) \bmod n_t], \quad (3.3)$$

$$C_2^{K(\pi)}(t; \mathbf{p}_{K(\pi)}) = \sum_{\mathbf{x}} e^{i\mathbf{p}_{K(\pi)} \cdot \mathbf{x}} \langle \mathcal{O}_{K(\pi)}(t_i, \mathbf{0}) \mathcal{O}_{K(\pi)}^\dagger(t, \mathbf{x}) \rangle, \\ t \in [t_i, t_f = (t_i + n_t) \bmod n_t], \quad (3.4)$$

$$C_2^D(t) = \sum_{\mathbf{x}} \langle \mathcal{O}_D(t_i, \mathbf{0}) \mathcal{O}_D^\dagger(t, \mathbf{x}) \rangle, \quad t \in [t_i, t_f = (t_i + n_t) \bmod n_t]. \quad (3.5)$$

where n_t is the temporal extent of the lattice, and $\mathbf{p}_{K(\pi)}$ is the momentum of the outgoing kaon (pion). We calculate the correlators for momenta $\mathbf{p}_{K(\pi)} = (0, 0, 0), (1, 0, 0), (1, 1, 0), (1, 1, 1)$, and $(2, 0, 0)$ (in units of $2\pi/L$, where L is the spatial extent of the lattice) and all times t in the ranges shown. We increase statistics by averaging correlators with source times $t_i = 0, n_t/4, n_t/2, 3n_t/4$. The D -meson interpolating operators \mathcal{O} are smeared with a charmonium wavefunction to suppress coupling to excited states.

C_3 is calculated with insertions of the current operator at all times t between the source and sink. At sufficiently large source-sink separations T and times t sufficiently far from both source and sink ($0 \ll t \ll T$), a plateau emerges in the ratio (3.2). This plateau is directly proportional to the desired hadronic matrix element.

In practice we find that oscillations from opposite-parity excited states contaminate the entire plateau region [3, 6]. We therefore consider the more carefully constructed correlator ratios introduced in Ref. [6]:

$$\bar{R}_{3,\mu}^{D \rightarrow K(\pi)}(t, T; q^2) \equiv \frac{1}{\phi_{K(\pi)\mu}} \frac{\bar{C}_{3,\mu}^{D \rightarrow K(\pi)}(t, T; \mathbf{p}_{K(\pi)})}{\sqrt{\bar{C}_2^{K(\pi)}(t; \mathbf{p}_{K(\pi)}) \bar{C}_2^D(T-t)}} \sqrt{\frac{2E_{K(\pi)}}{e^{-E_{K(\pi)}t} e^{-m_D(T-t)}}}, \quad (3.6)$$

where $\phi_{K(\pi)\mu} \equiv (1, \mathbf{p}_{K(\pi)})$ and the correlators \bar{C}_3, \bar{C}_2 are constructed from the correlators C_3, C_2 to eliminate oscillations from opposite-parity states:

$$\bar{C}_3(t, T) \equiv \frac{1}{8} \left[C_3(t, T) + C_3(t, T+1) e^{m_D} + 2C_3(t+1, T) e^{E_{K(\pi)} - m_D} + 2C_3(t+1, T+1) e^{E_{K(\pi)}} \right. \\ \left. + C_3(t+2, T) e^{2(E_{K(\pi)} - m_D)} + C_3(t+2, T+1) e^{2E_{K(\pi)} - m_D} \right], \quad (3.7)$$

$$\bar{C}_2(t) \equiv \frac{1}{4} [C_2(t) + 2C_2(t+1) e^{m_D} + C_2(t+2) e^{2m_D}]. \quad (3.8)$$

Experience suggests that the errors in direct fits to the oscillating states can be larger than errors in simpler fits. The construction of (3.6) and (3.7, 3.8) allows us to fit the ratios to constants without introducing systematic errors. In the plateau region ($0 \ll t \ll T$), the ratios $\bar{R}_{3,\mu}^{D \rightarrow K(\pi)}$ for $\mu = 0$ ($\mu = i$) approach the form factors $f_{\parallel}^{D \rightarrow K(\pi)}$ ($f_{\perp}^{D \rightarrow K(\pi)}$).

For source-sink separations $T = 16$ and $T = 20$, examples of the plateaus are shown in Figs. 1 and 2, where the features leading to the choice of these T -values can also be seen. As the source-sink separation increases, signal-to-noise decreases. As the source-sink separation decreases, the

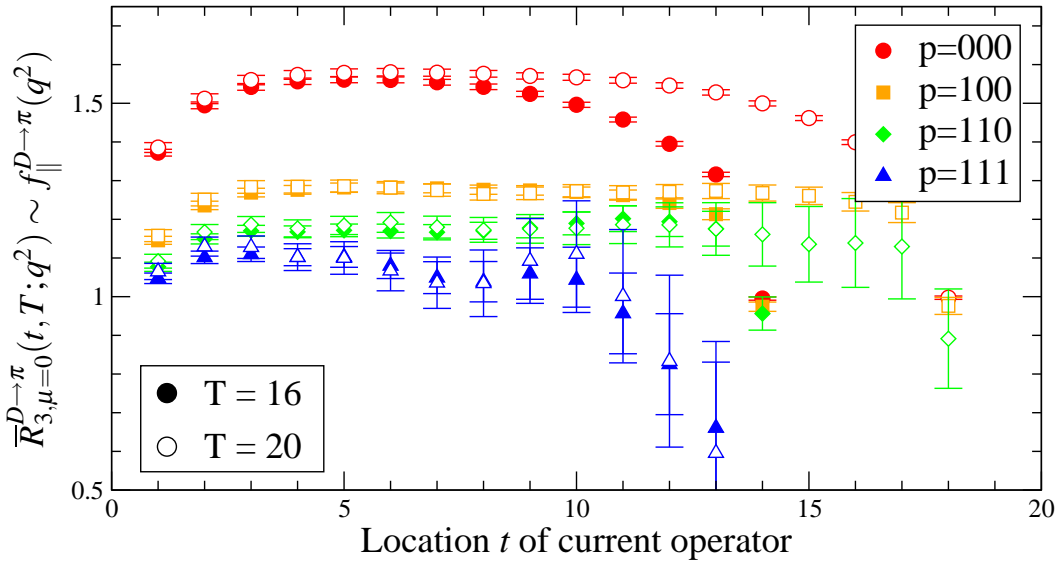


Figure 1: Ratios of correlators for extracting the form factor $f_{||}^{D\rightarrow\pi}(q^2)$. The correlators were calculated on 2110 configurations of the coarse ensemble with $m_l = 0.14m_s$. $T = 16, 20$ are the source-sink separations, and the three-momenta p of the pions are given in units of $2\pi/L$, where L is the spatial extent of the lattice. Note the excited state contamination in the zero momentum data with $T = 16$.

plateau region shrinks and eventually disappears. The optimal T -value is the smallest for which a plateau exists. For this T , signal-to-noise is maximized without sacrificing the plateau to excited state contamination. The statistical errors increase with momentum, so the optimal T is momentum dependent.

To optimize T we generated data with $T = 16, 18$, and 20 on the coarse $m_l = 0.14m_s$ ensemble. As shown in Figs. 1 and 2, for $T = 20$ plateaus exist for all momenta. At zero momentum, comparing the $T = 16$ data with the $T = 20$ data reveals the effects of excited state contamination in the $T = 16$ data for all t ; the plateau has essentially vanished. At nonzero momentum, comparing the $T = 16$ data with the $T = 20$ data reveals smaller statistical errors in the $T = 16$ data with intact plateau regions. The larger T allows checks for excited state contamination at smaller momenta, and the smaller T allows us to minimize statistical errors at larger momenta. On the remaining ensembles, we expect the optimal T -value in physical units to be similar. We are therefore generating data on each ensemble with two aT -values of approximately $0.12 \text{ fm} \times 16$ and $0.12 \text{ fm} \times 20$.

4. Renormalization and chiral-continuum-energy extrapolation-interpolation

Lattice form factors obtained from the plateaus in Figs. 1 and 2 must be renormalized and extrapolated to zero lattice spacing and the physical light quark masses. The renormalization factors can be written as products of non-perturbatively calculable factors Z_V and perturbatively calculable factors ρ . The uncertainties in these renormalization factors contribute to the uncertainties in the form factors and CKM matrix elements.

To perform simultaneous chiral-continuum extrapolations and the kaon (pion) energy interpolation, we can use staggered heavy meson partially quenched chiral perturbation theory (χ PT)

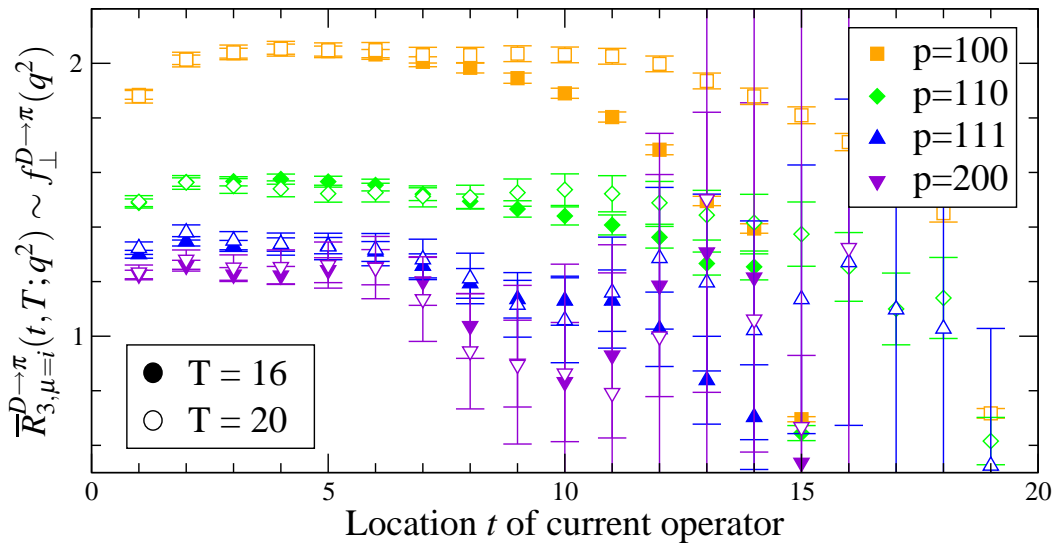


Figure 2: Ratios of correlators for extracting the form factor $f_\perp^{D \rightarrow \pi}(q^2)$. The correlators were calculated on 2110 configurations of the coarse ensemble with $m_l = 0.14m_s$. $T = 16, 20$ are the source-sink separations, and the three-momenta p of the pions are given in units of $2\pi/L$, where L is the spatial extent of the lattice. The consistency of the results for $T = 16$ and $T = 20$ indicates that the smaller source-sink separation can be used to minimize statistical errors without introducing significant excited state contamination.

with constrained curve fitting [6, 11, 12]. This approach incorporates the energy-dependence of the form factors and yields a model-independent result while accounting for the systematic error due to truncating the expansion.

To extract $|V_{cs(d)}|$, one can divide the experimental results [2] by the lattice form factors evaluated at $q^2 = 0$. However, minimizing the uncertainty in $|V_{cs(d)}|$ requires a simultaneous fit to all (experimental and lattice) data. The analyticity-based parameterization described in Ref. [13] captures the energy-dependence of the form factors throughout the kinematic domains, so using it to fit the data and extract CKM matrix elements does not introduce model-dependent systematic errors.

For $D \rightarrow K(\pi)l\nu$, the energy-domains of the lattice and experimental data overlap significantly, allowing a stringent test of the consistency of the shapes of the form factors as determined independently by the lattice and experiment. This test provides important validation for applying the analyticity-based parameterization to the extraction of $|V_{ub}|$ from $B \rightarrow \pi l\nu$, in which the overlap of the lattice data and experimental data is smaller and this self-consistency check, less powerful.

5. Expected uncertainties

A projected error budget for the form factors at $q^2 = 0$ is shown in Table 2. The expected uncertainties reflect previous experience with $B \rightarrow \pi l\nu$ [6], including the use of improved correlator ratios, χ PT with constrained curve fitting, and the analyticity-based parameterization to eliminate systematic errors due to incomplete cancellation of oscillating state contributions, truncation of the chiral expansion, and model-dependence in the BK parameterization. The projections also reflect the four-fold increase in statistics on the coarse ensembles and the addition of the two largest

Stat. + χ PT	$g_{D^*D\pi}$	r_1	\hat{m}	m_s	κ_c	p_π	HQ	Z_V	ρ	$L^3 < \infty$	Sys.	Total
4.9	2.9	1.4	0.3	1.3	0.2	0.1	3.9	0.7	0.7	0.5	5.4	7.3

Table 2: Contributions to the relative uncertainties in the form factors at $q^2 = 0$ assuming data with four source times on the four extended coarse ensembles, two largest fine ensembles, and the superfine $m_l = 0.2m_s$ ensemble. The errors are due to limited statistics and the truncation of chiral perturbation theory; uncertainties in the $D^*D\pi$ coupling, scale, average up-down quark mass, strange quark mass, and charm hopping parameter; momentum-dependent discretization effects from the light quarks and gluons; heavy-quark discretization effects; uncertainties in the renormalization factors Z_V and ρ ; and finite volume effects. The last two entries are the total systematics and the total error, both added in quadrature.

fine ensembles and the superfine $m_l = 0.2m_s$ ensemble. The increase in statistics decreases our statistical uncertainties by a factor of two, while the addition of the superfine ensemble reduces systematic errors due to heavy-quark discretization effects.

Heavy-quark discretization effects and the uncertainty in the $D^*D\pi$ coupling dominate the systematic uncertainties, while statistics and χ PT truncation error are alone comparable to the entire remaining systematic error. Heavy-quark discretization effects are sensitive to the smallest lattice spacings included, so they will decrease further with the addition of the ultrafine ensemble in Table 1. The error due to the $D^*D\pi$ coupling may respond to the increased statistics. From Table 2 and Eqs. (1.1) and (1.2), we expect to reduce the theoretical uncertainties in the CKM matrix elements from about 11% to about 7%.

Fermilab is operated by Fermi Research Alliance, LLC, under Contract No. DE-AC02-07CH11359 with the United States Department of Energy.

References

- [1] C. Amsler *et al.* [Particle Data Group], Phys. Lett. B **667**, 1 (2008).
- [2] D. Besson *et al.* [CLEO Collaboration], Phys. Rev. D **80**, 032005 (2009) [arXiv:0906.2983 [hep-ex]].
- [3] C. Aubin *et al.* [Fermilab Lattice and MILC Collaborations], Phys. Rev. Lett. **94**, 011601 (2005) [arXiv:hep-ph/0408306].
- [4] C. Bernard *et al.* [Fermilab Lattice and MILC Collaborations], Phys. Rev. D **80**, 034026 (2009) [arXiv:0906.2498 [hep-lat]].
- [5] D. Becirevic and A. B. Kaidalov, Phys. Lett. B **478**, 417 (2000) [arXiv:hep-ph/9904490].
- [6] J. A. Bailey *et al.* [Fermilab Lattice and MILC Collaborations], Phys. Rev. D **79**, 054507 (2009) [arXiv:0811.3640 [hep-lat]].
- [7] A. Bazavov *et al.*, arXiv:0903.3598 [hep-lat].
- [8] C. W. Bernard *et al.* [MILC Collaboration], Phys. Rev. D **64**, 054506 (2001) [arXiv:hep-lat/0104002].
- [9] C. Aubin *et al.* [MILC Collaboration], Phys. Rev. D **70**, 094505 (2004) [arXiv:hep-lat/0402030].
- [10] A. Bazavov *et al.* [Fermilab Lattice and MILC Collaborations], PoS(LAT2009)249.
- [11] C. Aubin and C. Bernard, Phys. Rev. D **73**, 014515 (2006) [arXiv:hep-lat/0510088].
- [12] C. Aubin and C. Bernard, Phys. Rev. D **76**, 014002 (2007) [arXiv:0704.0795 [hep-lat]].
- [13] T. Becher and R. J. Hill, Phys. Lett. B **633**, 61 (2006) [arXiv:hep-ph/0509090].

Quarkonium mass splittings in three-flavor lattice QCD

T. Burch,¹ C. DeTar,¹ M. Di Pierro,² A. X. El-Khadra,³ E. D. Freeland,⁴
Steven Gottlieb,^{5,6} A. S. Kronfeld,⁷ L. Levkova,¹ P. B. Mackenzie,⁷ and J. N. Simone⁷

(Fermilab Lattice and MILC Collaborations)

¹*Department of Physics, University of Utah, Salt Lake City, Utah, USA*

²*School of Computing, DePaul University, Chicago, Illinois, USA*

³*Physics Department, University of Illinois, Urbana, Illinois, USA*

⁴*Department of Physics, Washington University, St. Louis, Missouri, USA*

⁵*Department of Physics, Indiana University, Bloomington, Indiana, USA*

⁶*National Center for Supercomputing Applications, University of Illinois, Urbana, Illinois, USA*

⁷*Fermi National Accelerator Laboratory, Batavia, Illinois, USA*

(Dated: December 14, 2009)

We report on calculations of the charmonium and bottomonium spectrum in lattice QCD. We use ensembles of gauge fields with three flavors of sea quarks, simulated with the asqtad improved action for staggered fermions. For the heavy quarks we employ the Fermilab interpretation of the clover action for Wilson fermions. These calculations provide a test of lattice QCD, including the theory of discretization errors for heavy quarks. We provide, therefore, a careful discussion of the results in light of the heavy-quark effective Lagrangian. By and large, we find that the computed results are in agreement with experiment, once parametric and discretization errors are taken into account.

PACS numbers: 12.38.Gc, 14.40.Gx

I. INTRODUCTION

Quarkonium plays an important role in the application of QCD to hadronic physics. Early calculations of charmonium based on potential models gave strong support to the interpretation of these states as bound states of a new heavy quark [1, 2]. Although physically the charmonium state is analogous to positronium, its historical role as a model system of QCD proved to be analogous to that of the hydrogen atom in quantum mechanics. The charmonium spectrum provided a simple example of how QCD works, made even more compelling with the subsequent observation of the bottomonium states.

Although the analysis of the quarkonium spectrum based on potential models is a significant triumph of QCD, an *ab initio* calculation based on lattice QCD, an approach that can simultaneously deal with light quarks would be even more satisfying. However, in lattice QCD, the continuum limit requires that am approaches zero, where a is the lattice spacing and m is the mass of the state. Quarkonium states and their constituent quarks are so heavy, that it is often impractical to use so small a lattice spacing that am is small. Both lattice NRQCD [3, 4] and the Fermilab action [5] have been developed to treat heavy quarks in lattice gauge theory. Thus, the successful calculation of the spectrum of charmonium and bottomonium becomes a significant test of these techniques.

This paper describes the current state of the quarkonium spectrum based on the Fermilab approach to heavy quarks, using gauge configurations provided by the MILC Collaboration [6] that incorporate the effects of three light quarks: up, down, and strange. We have been studying the quarkonium spectrum using this formal-

ism for some time [7], starting on ensembles with two flavors of sea quark [8], and new ensembles of configurations have become available during the course of the project. In this paper, we report on results with four lattice spacings from $a \approx 0.18$ fm to ≈ 0.09 fm. We do not yet consider this work a definitive calculation using our approach. Results from two finer lattice spacings should become available in the future. As we detail below, the tuning of the bare valence heavy-quark masses, via the heavy-light meson spectrum [9], is not yet precise enough to give satisfactory answers to all the questions that have arisen. In the future, we expect to have better control of the heavy-quark masses. Nevertheless, already we can successfully reproduce important features of the quarkonium spectrum, and we consider this another important testbed in which to assess the errors that arise from our treatment of the heavy quarks. Knowledge of these errors is also important for calculations of properties of heavy-light mesons, for example those pertaining to semileptonic decays [10], leptonic decays [11], and B - B mixing [12], as well as the heavy-light spectrum [9].

Prior lattice QCD work on quarkonium with different sea-quark content has been reviewed by Bali [13]. More recently, Dudek and collaborators have used the quenched approximation to explore decays [14], radiative transitions [15], and the excited-state spectrum [16] of charmonium. Meinel has used lattice NRQCD to compute the bottomonium spectrum at one lattice spacing on four ensembles with 2+1 domain-wall sea quarks [17]. The HPQCD Collaboration has calculated the quarkonium spectrum on many of the same MILC ensembles used in our work, using lattice NRQCD for bottomonium [18, 19], and using highly improved staggered quarks (HISQ) for charmonium [20]. Lattice NRQCD is

not very accurate for charmonium, and HISQ requires very small lattice spacings for b quarks [21]. An advantage of the Fermilab method is that it allows the same treatment for both the charmed and bottom quarks. Predictions of the $c\bar{b}$ spectrum have also been made, for the pseudoscalar B_c using NRQCD b quarks and the charmed quark propagators from this project [22], and also for the vector B_c^* using NRQCD b quarks and HISQ charmed quarks [23].

The plan of this paper is as follows. In Sec. II, we describe our methodology, explaining the actions used for gluons, light sea quarks, and the heavy valence quarks. We describe, in detail, how to use the heavy-quark effective Lagrangian to understand heavy-quark discretization errors in quarkonium masses. We also discuss the construction of the hadronic correlators and how they are fit to determine meson masses. Several broad issues inform the uncertainties (statistical and systematic), and they are discussed in Sec. III. In Sec. IV, we show our results for the splittings between various states or combinations of states. Where possible, we have organized the presentation of the mass splittings around individual terms in the heavy-quark effective action, which clarifies the approach to the continuum limit at available lattice spacings. Section V contains our conclusions and suggestions on ways to improve on this calculation.

II. METHODOLOGY

In this section, we collect several sets of information needed to understand the results that follow. Section II A defines the notation for different quarkonium states and splittings. Then we provide details of the lattice gauge configurations that we have used in Sec. II B. Next, in Sec. II C, we review the Fermilab method, discussing in detail how it can be understood via an effective Lagrangian. This discussion provides a link between the lattice fermion action and the computed mass splittings; an important theme in this paper is to scrutinize our numerical results according to these theoretical expectations. Last, we explain how we form correlation functions in Sec. II D, and how we fit them to obtain masses in Sec. II E.

A. Notation

In this paper, we use two notations for hadrons and their masses, both the standard names from the Particle Data Group [24] and the spectroscopic notation $n^{2S+1}L_J$, where S , L , and J are the spin, orbital, and total angular momentum, respectively, of the n th radial excitation. As usual, $L = 0, 1, 2, \dots$ are denoted S, P, D, \dots

It is often convenient to discuss spin-averaged masses (and mass splittings), which we indicate with a horizontal

line, such as $\overline{1S}$ or $\overline{1^3P}$. In particular,

$$M(\overline{1S}) = \frac{1}{4}(M_{\eta_c} + 3M_{J/\psi}), \quad (2.1)$$

$$M(\overline{1^3P}) = \frac{1}{9}(M_{\chi_{c0}} + 3M_{\chi_{c1}} + 5M_{\chi_{c2}}), \quad (2.2)$$

using charmonium for illustration. For brevity we usually write $\overline{1P}$ for $\overline{1^3P}$. These spin-averages are sensitive to the leading term in a nonrelativistic expansion. Note that the $\overline{1P}$ and 1^1P_1 (also denoted h_c and h_b) levels are nearly the same in nature, which can be explained by the spin-spin interaction's short range— $\delta(\mathbf{r})$ in the context of potential models [2].

Complementary to the spin-averaged masses are spin-splittings that hone in on spin-dependent corrections [25, 26]. Below, we examine the hyperfine splittings

$$M(nS_{\text{HFS}}) = M_{J/\psi} - M_{\eta_c}, \quad (2.3)$$

using charmonium $1S$ notation on the right-hand side. For the P states two combinations are of interest

$$M(nP_{\text{spin-orbit}}) = \frac{1}{9}(5M_{\chi_{c2}} - 2M_{\chi_{c0}} - 3M_{\chi_{c1}}), \quad (2.4)$$

$$M(nP_{\text{tensor}}) = \frac{1}{9}(3M_{\chi_{c1}} - M_{\chi_{c2}} - 2M_{\chi_{c0}}), \quad (2.5)$$

again using charmonium $1S$ notation on the right-hand side. $M(nS_{\text{HFS}})$ and $M(nP_{\text{tensor}})$ are sensitive to spin-spin interactions, and $M(nP_{\text{spin-orbit}})$ to spin-orbit interactions.

B. Configuration details

These calculations have been carried out on lattice gauge configurations provided by the MILC Collaboration [6], listed in Table I. They were generated via the R algorithm [27] with the one-loop Symanzik-improved Lüscher-Weisz gluon action [28] combined with $2+1$ flavors of sea quarks simulated with the asqtad action [29]. The n_f -dependent part of the one-loop couplings [30] became available only after the ensembles were generated. We have used ensembles at four lattice spacings: $a \approx 0.18, 0.15, 0.12$, and 0.09 fm (also called in the text “extra-coarse”, “medium-coarse”, “coarse” and “fine” ensembles, respectively). The first four columns of Table I list the parameters of these ensembles, including the masses of the sea quarks, denoting the pair as am_l/am_s . The lattice scale of each ensemble with different sea quark masses was kept approximately fixed using the length r_1 [31, 32] from the static quark potential. The absolute scale from the 1^3S-1^3P splitting was determined on most of our ensembles by the HPQCD Collaboration [18, 19]. Details on the r_1 determinations can be found in review of other work on the MILC ensembles [33]. Combining this determination with more recent work [34, 35], leads us to take the range $r_1 = 0.318^{+0.000}_{-0.007}$ fm in this paper.

TABLE I: Run parameters and configuration numbers for the ensembles used to study charmonium and bottomonium η , J/ψ , Υ , h , χ_0 , and χ_1 states with relativistic operators, and h and all χ_J states with nonrelativistic operators. The labels a and b are used to distinguish between the two runs with the same $\beta = 6.76$ but different am_l/am_s .

a (fm)	β	am_l/am_s	$N_s^3 \times N_t$	relativistic				nonrelativistic			
				κ_c	N_{conf}^c	κ_b	N_{conf}^b	κ_c	N_{conf}^c	κ_b	N_{conf}^b
≈ 0.18	6.503	0.0492/0.082	$16^3 \times 48$	0.120	401	—	—	0.120	400	—	—
	6.485	0.0328/0.082	"	"	331	—	—	"	501	—	—
	6.467	0.0164/0.082	"	"	645	—	—	"	647	—	—
	6.458	0.0082/0.082	"	"	400	—	—	"	601	—	—
≈ 0.15	6.600	0.0290/0.0484	$16^3 \times 48$	—	—	—	—	0.122	580	0.076	595
	6.586	0.0194/0.0484	"	0.122	631	0.076	631	"	580	"	595
	6.572	0.0097/0.0484	"	"	631	"	631	"	629	"	631
	6.566	0.00484/0.0484	$20^3 \times 48$	—	—	—	—	"	601	"	600
≈ 0.12	6.81	0.03/0.05	$20^3 \times 64$	0.122	549	0.086	549	—	—	—	—
	6.79	0.02/0.05	"	"	460	"	460	—	—	—	—
	6.76, a	0.01/0.05	"	"	593	"	539	—	—	—	—
	6.76, b	0.007/0.05	"	"	403	—	—	—	—	—	—
≈ 0.09	7.11	0.0124/0.031	$28^3 \times 96$	0.127	517	0.0923	517	0.127	518	0.0923	510
	7.09	0.0062/0.031	"	"	557	"	557	"	557	"	557
	7.08	0.0031/0.031	$40^3 \times 96$	"	504	"	504	"	504	"	504

C. Heavy quark formulation

In this work, the charmed and bottom quarks are simulated with the Fermilab action [5]

$$\begin{aligned}
 S = & \sum_n \bar{\psi}_n \psi_n - \kappa \sum_n \left[\bar{\psi}_n (1 - \gamma_4) U_{n,4} \psi_{n+\hat{4}} + \bar{\psi}_{n+\hat{4}} (1 + \gamma_4) U_{n,4}^\dagger \psi_n \right] \\
 & - \kappa \zeta \sum_{n,i} \left[\bar{\psi}_n (r_s - \gamma_i) U_{n,i} \psi_{n+i} + \bar{\psi}_{n+i} (r_s + \gamma_i) U_{n,i}^\dagger \psi_n \right] \\
 & - c_B \kappa \zeta \sum_n \bar{\psi}_n i \boldsymbol{\Sigma} \cdot \mathbf{B}_n \psi_n - c_E \kappa \zeta \sum_{n;i} \bar{\psi}_n \boldsymbol{\alpha} \cdot \mathbf{E}_n \psi_n,
 \end{aligned} \tag{2.6}$$

where U denotes the gluon field, and ψ and $\bar{\psi}$ denote the quark and antiquark fields. The clover definitions of the chromomagnetic and chromoelectric fields \mathbf{B} and \mathbf{E} are standard and given, for example, in Ref. [5]. When $\zeta = r_s = 1$ and $c_B = c_E = 0$, S reduces to the Wilson action [36]; when $\zeta = r_s = 1$ and $c_B = c_E = c_{SW}$, it reduces to the Sheikholeslami-Wohlert action [37]. The relation between the hopping parameter κ and the bare mass is

$$m_0 a = \frac{1}{2\kappa} - 1 - 3r_s \zeta \tag{2.7}$$

in four space-time dimensions.

To motivate our choices of the input parameters κ , ζ , r_s , c_B , and c_E , let us review the nonrelativistic interpretation of Wilson fermions [5]. The pole energy of a single

quark of spatial momentum \mathbf{p} is

$$E(\mathbf{p}) = m_1 + \frac{\mathbf{p}^2}{2m_2} + O(p^4), \tag{2.8}$$

where the quark rest mass m_1 and the kinetic mass m_2 are defined at all orders of perturbation theory via the self energy [38]. At the tree level,

$$m_1 = a^{-1} \ln(1 + m_0 a), \tag{2.9}$$

$$\frac{1}{m_2} = \frac{2\zeta^2}{m_0(2 + m_0 a)} + \frac{ars\zeta}{1 + m_0 a}. \tag{2.10}$$

In general, $m_1 \neq m_2$ unless $m_0 a \ll 1$; for charmed and bottom quarks on the ensembles listed in Table I one has $m_0 a \lesssim 1$, $m_0 b a \gtrsim 1$. One could tune ζ so that $m_2 = m_1$, and we shall revisit that strategy below.

Equation (2.8) is the simplest example of a nonrelativistic interpretation of physical quantities computed

with the action in Eq. (2.6). This is justified, because in quarkonium the relative momentum of the heavy quarks is small compared with the heavy-quark mass. This is the basis of the phenomenological success of potential models, which yield estimates of the relative velocity and, equivalently, internal momentum. For charmonium

$$v \approx 0.55, \quad p \approx 840 \text{ MeV}, \quad (2.11)$$

and for bottomonium

$$v \approx 0.31, \quad p \approx 1475 \text{ MeV}. \quad (2.12)$$

For both systems the typical kinetic energy is 450 MeV, as seen, for example, in the $\overline{1P}\text{-}\overline{1S}$ splitting. The kinetic energies $\frac{1}{2}m_2v^2$ are small on our lattices, and the momenta m_2v are marginally small (especially for bottomonium).

The nonrelativistic interpretation can be extended beyond the tree level and to higher order in the nonrelativis-

tic expansion using effective field theories. This has been pursued in detail emphasizing heavy-light hadrons [39, 40, 41], and here we explain the ideas in the context of quarkonium. As in the Symanzik effective theory, one introduces a continuum effective Lagrangian, but here it is an effective Lagrangian valid for heavy quarks. With quarkonium, the appropriate power-counting rule for the effective Lagrangian is that of nonrelativistic QED [42] and nonrelativistic QCD (NRQCD) [3, 4, 43]. So one has

$$S \doteq - \sum_s \int d^4x \mathcal{L}_{\text{HQ}}^{(s)}, \quad (2.13)$$

where s counts the powers of velocity. Here \doteq means that the lattice gauge theory on the left-hand side, defined in our case by Eq. (2.6), is given an effective description by the right-hand side. The first several terms of the effective Lagrangian are

$$\mathcal{L}_{\text{HQ}}^{(2)} = -\bar{h}^{(+)}(D_4 + m_1)h^{(+)} + \frac{\bar{h}^{(+)}\mathbf{D}^2h^{(+)}}{2m_2} - \bar{h}^{(-)}(D_4 + m_1)h^{(-)} + \frac{\bar{h}^{(-)}\mathbf{D}^2h^{(-)}}{2m_2}, \quad (2.14)$$

$$\begin{aligned} \mathcal{L}_{\text{HQ}}^{(4)} &= \frac{\bar{h}^{(+)}i\boldsymbol{\sigma} \cdot \mathbf{B}h^{(+)}}{2m_B} + \frac{\bar{h}^{(+)}i\boldsymbol{\sigma} \cdot (\mathbf{D} \times \mathbf{E})h^{(+)}}{8m_E^2} + \frac{\bar{h}^{(+)}(\mathbf{D} \cdot \mathbf{E})h^{(+)}}{8m_{E'}^2} + \frac{\bar{h}^{(+)}(\mathbf{D}^2)^2h^{(+)}}{8m_4^3} + \frac{1}{6}a^3w_4\bar{h}^{(+)}D_i^4h^{(+)} \\ &+ \frac{\bar{h}^{(-)}i\boldsymbol{\sigma} \cdot \mathbf{B}h^{(-)}}{2m_B} - \frac{\bar{h}^{(-)}i\boldsymbol{\sigma} \cdot (\mathbf{D} \times \mathbf{E})h^{(-)}}{8m_E^2} - \frac{\bar{h}^{(-)}(\mathbf{D} \cdot \mathbf{E})h^{(-)}}{8m_{E'}^2} + \frac{\bar{h}^{(-)}(\mathbf{D}^2)^2h^{(-)}}{8m_4^3} + \frac{1}{6}a^3w_4\bar{h}^{(-)}D_i^4h^{(-)}, \end{aligned} \quad (2.15)$$

where $h^{(+)}$ is a two-component field describing the quark, and $h^{(-)}$ is a two-component field describing the anti-quark. The short-distance coefficients m_1 , m_2^{-1} , m_B^{-1} , m_E^{-2} , $m_{E'}^{-2}$, m_4^{-3} , and w_4 depend on the bare quark masses, the bare gauge coupling, and all other couplings of the (improved) lattice action. The terms in $\mathcal{L}_{\text{HQ}}^{(s)}$ scale with the heavy quark's velocity as v^s , with the rules [4] $\mathbf{D} \sim m_2v$, $\mathbf{E} \sim m_2^2v^3$, and $\mathbf{B} \sim m_2^2v^4$. In particular, the nonrelativistic kinetic energy, $\mathbf{D}^2/2m_2 \sim \frac{1}{2}m_2v^2$, is an essential part of quarkonium dynamics, which is why m_2 appears with v in the power counting. The short-distance coefficients m_B^{-1} , m_E^{-2} , etc., can be expanded in perturbation theory, with $\alpha_s \sim v$ [4]. We have put the rest mass $m_1\bar{h}^{(\pm)}h^{(\pm)}$ and temporal kinetic energy $\bar{h}^{(\pm)}D_4h^{(\pm)}$ into $\mathcal{L}_{\text{HQ}}^{(2)}$, because by the equation of motion $D_4 + m_1 \sim \mathbf{D}^2/2m_2 \sim \frac{1}{2}m_2v^2$. The next set of terms, $\mathcal{L}_{\text{HQ}}^{(6)}$, are not written out, because they are numerous yet merely describe subleading contributions to the splittings examined below.

One would like to adjust κ , ζ , r_s , c_B , and c_E so that the lattice gauge theory matches continuum QCD with controllable uncertainty. One would also like to reduce the number of input parameters as much as possible, to make the simulation easier to carry out. The coupling r_s

is redundant: any choice is allowed as long as the doubling problem is solved. We take

$$r_s = 1. \quad (2.16)$$

To derive tuning criteria for the others, one refers to the NRQCD description of continuum QCD, which takes the same form as Eqs. (2.14) and (2.15), but with the following substitutions:

$$m_1 \mapsto m, \quad (2.17)$$

$$m_2 \mapsto m, \quad (2.18)$$

$$\frac{1}{m_B} \mapsto \frac{Z_B}{m}, \quad (2.19)$$

$$\frac{1}{m_E^2} \mapsto \frac{Z_E}{m^2}, \quad (2.20)$$

$$\frac{1}{m_{E'}^2} \mapsto \frac{Z_{E'}}{m^2}, \quad (2.21)$$

$$\frac{1}{m_4^3} \mapsto \frac{Z_4}{m^3}, \quad (2.22)$$

$$w_4 \mapsto 0, \quad (2.23)$$

where the last is a consequence of Lorentz invariance, as is the exact equality of the rest and kinetic masses. The

matching factors Z_i are unity at the tree level and have a perturbative expansion. To bring the lattice field theory in line with continuum QCD, one must then simply adjust the lattice couplings so that the lattice quantities on the left in (2.17)–(2.23) become, to some accuracy, the continuum quantities on the right. In principle, this matching could be carried out nonperturbatively [44], although we do not pursue that strategy here.

If one restricts one's attention to mass splittings and matrix elements, it is not necessary to adjust a coupling to tune m_1 . The operators $\bar{h}^{(\pm)}h^{(\pm)}$ are number operators, commuting with everything else in the Hamiltonian [39]. It is therefore acceptable to tolerate a large discretization error in the rest mass, and, consequently, one does not need to adjust ζ . We take

$$\zeta = 1. \quad (2.24)$$

To obtain the correct dynamics, one must adjust κ so that the rest of $\mathcal{L}_{\text{HQ}}^{(2)}$ is correctly tuned. In other words, one must identify the kinetic quark mass m_2 with the physical quark mass.

The adjustment of c_B stems from a concrete realization of (2.19). At the tree level

$$\frac{1}{m_B} = \frac{2\zeta^2}{m_0(2+m_0a)} + \frac{ac_B\zeta}{1+m_0a}, \quad (2.25)$$

so to ensure $m_B = m_2$ (as desired at the tree level where $Z_B = 1$), one needs $c_B = r_s$. In practice, we take [recalling Eq. (2.16)]

$$c_B = u_0^{-3} \quad (2.26)$$

to account for tadpole diagrams at higher orders in perturbation theory [45]. On the coarse ensembles, we set u_0 from the Landau link; on the other ensembles, we set it from the plaquette.

In principle, the adjustment of c_E should stem from (2.20). These simulations have been carried out, however, in concert with calculations of heavy-light masses [9], for which the adjustment of c_E is a subleading effect [39, 46]. Thus, we have taken

$$c_E = c_B. \quad (2.27)$$

Using formulae in Ref. [51], we can estimate the error stemming from $1/m_E^2$, finding a tree-level mismatch of

$$\frac{1}{4m_E^2} - \frac{1}{4m_2^2} = \frac{a^2}{(2+m_0a)(1+m_0a)} - \frac{a^2}{4(1+m_0a)^2}, \quad (2.28)$$

where the right-hand side holds for $\zeta = r_s = c_B = c_E = 1$. At the tree level $m_E = m_{E'}$, so the same error is made in the Darwin terms $\bar{h}^{(\pm)}\mathbf{D} \cdot \mathbf{E} h^{(\pm)}$.

An advantage of using Eqs. (2.13), (2.14) and (2.15) to describe our lattice calculation is that it clarifies which parameters in S play a key role in various splittings defined in Sec. II A. The spin-averaged masses receive energy (beyond $2m_1$) from the balance between the kinetic energies $\bar{h}^{(\pm)}\mathbf{D}^2h^{(\pm)}$ and the exchange of temporal gluons between $\bar{h}^{(+)}A_4h^{(+)}$ and $\bar{h}^{(-)}A_4h^{(-)}$. As discussed above, they are sensitive to m_2 , motivating the tuning of κ (and the fixed choice for ζ). The hyperfine splittings $M(nS_{\text{HFS}})$ arise from exchange of spatial gluons between $\bar{h}^{(+)}i\sigma \cdot \mathbf{B} h^{(+)}$ and $\bar{h}^{(-)}i\sigma \cdot \mathbf{B} h^{(-)}$. Hence they are proportional to $1/m_B^2$ and, drilling further back to S , sensitive to the coupling c_B . The same line of dependency holds for the tensor splittings $M(nP_{\text{tensor}})$. Similarly, the spin-orbit part of the χ_{cJ} and χ_{bJ} levels arise from exchange of a temporal gluon between $\bar{h}^{(\pm)}i\sigma \cdot (\mathbf{D} \times \mathbf{E})h^{(\pm)}$ and $\bar{h}^{(\mp)}A_4h^{(\mp)}$. Hence they are proportional to $1/m_E^2$ and, referring back to S , sensitive to c_E .

With the tree-level adjustment of c_B , the hyperfine splittings should be expected to have errors of order $\alpha_s m v^4$ from radiative corrections to m_B^{-1} [relative error: $O(\alpha_s) \sim O(v)$], and of order v^6 from the terms $\bar{h}^{(\pm)}\{\mathbf{D}^2, i\sigma \cdot \mathbf{B}\}h^{(\pm)}$ in $\mathcal{L}_{\text{HQ}}^{(6)}$ [relative error: $O(v^2)$]. Similarly, with $c_E = c_B$, we expect leading errors of order $a^2 m^3 v^4$ in the spin-orbit part of the χ splittings [relative error: $O(m^2 a^2)$], as well as radiative corrections to m_E^{-2} [relative error: again $O(\alpha_s) \sim O(v)$]. On the MILC ensembles both relative errors are expected to be a few to several percent [51], and, perhaps counterintuitively, smaller for bottomonium than charmonium [51].

The lattice action in Eq. (2.6) does not contain parameters to tune the two terms proportional to p^4 in Eq. (2.15). The mismatches

$$\frac{1}{8m_4^3} - \frac{1}{8m_2^3} = \frac{a^2}{2m_0(2+m_0a)^2(1+m_0a)} + \frac{a^2(1+4m_0a)}{4m_0(2+m_0a)(1+m_0a)^2} + \frac{m_0a^4}{8(1+m_0a)^3} \quad (2.29)$$

and

$$a^3 w_4 = \frac{2a^2}{m_0(2+m_0a)} + \frac{a^3}{4(1+m_0a)} \quad (2.30)$$

(given again for $\zeta = r_s = c_B = c_E = 1$) cause errors of order $a^2 m^3 v^4$ in the spin-averaged splittings. The rel-

ative errors, $O(m^2 a^2)$, are again expected to be a few to several percent, but in this case larger for bottomonium than for charmonium [51]. For plots of the a dependence of discretization effects caused by Eqs. (2.28),

(2.29), and (2.30), see Figs. 2 and 3 of Ref. [51].

To tune κ nonperturbatively, one adjusts it so that a hadron mass agrees with the experimentally measured value. Let us define M_1 and M_2 for a hadron analogously to Eq. (2.8).¹ From the effective Lagrangian description for quarkonium, Eqs. (2.13)–(2.15), it follows that

$$M_1 = 2m_1 + B_1, \quad (2.31)$$

$$M_2 = 2m_2 + B_2, \quad (2.32)$$

where the binding energy B_1 is determined by terms of order v^2 and higher, but B_2 by terms of order v^4 and higher [52]. In the splittings of rest masses, m_1 drops out, so we can obtain well-tuned results for B_1 (and their differences) by adjusting κ so that m_2 corresponds to a physical quark. That suggests tuning κ so that, say, $M_2(\bar{1}S)$ agrees with experiment. The spin average is useful, because it eliminates the leading effect of a mistuned chromomagnetic coupling c_B .

A better approach, still using a hadron's kinetic mass, is as follows. Reference [52] analyzes the Breit equation to show how higher-order potentials and the p^4 terms generate B_2 , tracing how the mismatches noted in Eqs. (2.29) and (2.30) propagate to B_2 . This analysis reveals that the discretization error in B_2 is smaller for heavy-light hadrons than for quarkonium states. For heavy-light hadrons, the largest part of the kinetic binding energy comes from the light quarks and gluons, and, since the light quark has mass $ma \ll 1$, its contribution to the kinetic binding energy of the meson has only a small discretization error. To tune κ for charmed and bottom quarks, it is therefore better to use heavy-light states, such as $D_s^{(*)}$ and $B_s^{(*)}$, whose kinetic masses have the smallest statistical, discretization, and chiral extrapolation errors. In fact, the leading discretization error, from the chromomagnetic energy, can again be removed by taking the spin-averaged mass of the pseudoscalar and vector mesons.

It is sometimes thought that the tuning inaccuracy of the kinetic binding energy B_2 can be circumvented by adjusting ζ so that (a hadron's) $M_1 = M_2$, and then fixing M_1 to experiment. But any discretization error in B_2 is then propagated to ζ and, hence, throughout the rest of the simulation. It is, therefore, just as clean to leave $\zeta = 1$ and tune M_2 to a target meson mass, as we have done here.

At this stage, it may be helpful to compare and contrast the Fermilab approach [5, 51] with lattice NRQCD [3, 4]. The construction of lattice NRQCD starts with the (dimensionally regulated and $\overline{\text{MS}}$ -renormalized) NRQCD effective Lagrangian for continuum QCD [42, 43], and then discretizes it. This process can be repeated order-by-order in perturbation theory.

In the Fermilab method, a version of the Wilson-Sheikholeslami-Wohlert lattice action is used, but the results are interpreted with (dimensionally regulated and $\overline{\text{MS}}$ -renormalized) NRQCD with modified short-distance coefficients. This is possible because Wilson fermions possess heavy-quark symmetry, and the proposed improvements preserve this feature. Then the parallel structure of the NRQCD descriptions of QCD and lattice gauge theory are used to match the latter to the former. In both frameworks, the lattice action can be systematically improved via the nonrelativistic expansion [4, 51].

At a practical level, early spectrum calculations [47] use a lattice-NRQCD action [4] that adjusts, at the tree level, the full v^4 Lagrangian and the spin-dependent v^6 Lagrangian.² The p^4 terms are, thus, correctly normalized at the tree level, so the quarkonium and heavy-light kinetic mass tunings are comparably accurate. On the other hand, the Fermilab action has tree-level errors in the v^6 and even some of the v^4 terms. The errors diminish monotonically as a is reduced, however. This is especially important for charmonium: here the nonrelativistic expansion is not especially good, but it is needed only to organize the matching of the most important couplings in S , knowing that further errors, such as those described by $\mathcal{L}_{\text{HQ}}^{(6)}$, are of the form $(mv^2a)^2$ and smaller.

In summary, the pattern of discretization effects leads us to tune κ via kinetic masses corresponding to the $\bar{1}S$ D_s and B_s mesons. The main spectroscopic results, presented in Sec. IV, are for mass splittings, in which case the uncertainties are minimized by quoting differences of our computed rest masses.

D. Correlator construction

The meson correlator at a given spatial momentum \mathbf{p} and time t is defined as

$$C_{ab}(\mathbf{p}, t) = \sum_{\mathbf{x}} e^{-i\mathbf{p}\cdot\mathbf{x}} \langle 0 | O_a(\mathbf{x}, t) O_b^\dagger(\mathbf{0}, 0) | 0 \rangle, \quad (2.33)$$

where \mathbf{x} is the spatial coordinate. The source and sink meson operators O_b and O_a have the form

$$O_c(\mathbf{x}, t) = \sum_{\mathbf{y}} \bar{\psi}(\mathbf{x}, t) \Gamma \phi_c(\mathbf{x} - \mathbf{y}) \psi(\mathbf{y}, t), \quad (2.34)$$

where Γ is a product of Dirac matrices appropriate for the meson spin structure, and $\phi_c(\mathbf{x} - \mathbf{y})$ is a smearing function. Neglecting the disconnected piece, the meson correlator can be re-written with the quark propagators

$$G(\mathbf{x}, t; \mathbf{0}, 0) = \int [d\psi][d\bar{\psi}] \psi(\mathbf{x}, t) \bar{\psi}(\mathbf{0}, 0) e^{-S}, \quad (2.35)$$

¹ In this paper, we use m_1, m_2, \dots for quark masses, and M_1, M_2, \dots for hadron masses.

² The HPQCD Collaboration's most recently published unquenched calculations [19] of the bottomonium spectrum with lattice NRQCD are obtained from an action without the spin-dependent v^6 corrections.

TABLE II: Nonrelativistic meson operators for the $1P$ states. The smearing operator in spatial direction i is denoted by p_i . The indices j and k are different from i and each other, and repeated indices on the last line are not summed over.

Meson	$^{2S+1}L_J$	Irrep.	Operator
h	1P_1	T_1	$p_i, i = 1, 2, 3$
χ_0	3P_0	A_1	$\sum_{i=1}^3 \sigma_i p_i$
χ_1	3P_1	T_1	$\sigma_j \times p_k, i = 1, 2, 3$
χ_2	3P_2	T_2	$\sigma_j p_k + \sigma_k p_j, i = 1, 2, 3$
χ_2	3P_2	E_2	$\sigma_j p_j - \sigma_k p_k, i = 1, 2$

with S from Eq. (2.6), yielding

$$C_{ab}(\mathbf{p}, t) = \sum_{\mathbf{x}} e^{-i\mathbf{p}\cdot\mathbf{x}} \times \text{Tr} [G(\mathbf{0}, 0; \mathbf{x}, t) \Gamma G_{ab}(\mathbf{x}, t; \mathbf{0}, 0) \Gamma^\dagger], \quad (2.36)$$

where

$$G_{ab}(\mathbf{x}, t; \mathbf{0}, 0) = \sum_{\mathbf{y}, \mathbf{z}} \phi_a(\mathbf{x} - \mathbf{y}) G(\mathbf{y}, t; \mathbf{z}, 0) \phi_b^\dagger(\mathbf{z}) \quad (2.37)$$

is the smeared quark propagator.

For the P states, we use two types of quarkonium correlators, which we call “relativistic” and “nonrelativistic.” In the relativistic case, all four spin components of the quark propagators were used to construct the two-point functions. We used point and smeared sources and sinks. The smearing functions $\phi_c(\mathbf{x})$ are $1S$ and $2S$ wavefunctions of the QCD-motivated Richardson potential [53]. At the sink, spatial momentum $\mathbf{p} = 2\pi(n_1, n_2, n_3)/L$ is given to the quarkonium state. We restrict the range of \mathbf{p} such that $\sum n_i^2 \leq 9$. Using this approach, we computed correlation functions for the $1S$ and $2S$ states for the pseudoscalar and the vector to study both the kinetic and rest masses. For the $1P$ states h , χ_0 and χ_1 we computed only the rest masses.

In the nonrelativistic approach to constructing the two-point functions, the meson operators project onto two of the Dirac components of the quark fields. Table II gives the explicit form of these operators. At the source and sink we smear the quark propagators with a P -type wavefunction $\phi_c(\mathbf{r}) = \phi_{1S}(|\mathbf{r}|)\hat{r}_i$ where $\phi_{1S}(|\mathbf{r}|)$ is a Richardson $1S$ wavefunction [53] and $i = 1, 2, 3$. At the origin we set $\phi_c(\mathbf{0}) = 0$. The relativistic interpolating operators include extra lower Dirac components that increase the overlap with excited states. Therefore, one should expect that the overlap of the nonrelativistic meson operators with the $1P$ ground states to be better than in the relativistic case. We used these nonrelativistic operators at $\mathbf{p} = \mathbf{0}$ for the h , χ_0 , χ_1 , and χ_2 states. In Sec. III A, we compare the results for the first three states with the corresponding results from relativistic operators.

For both correlator constructions, we use several time-slice positions for the source vectors. In the case of the coarse $\beta = 6.76$, $am_l/am_s = 0.005/0.05$ ensemble and

TABLE III: Prior central values for the ground-state masses. The priors’ widths are all fixed to 0.5.

a (fm)	κ	$M_{q\bar{q}}a$
≈ 0.18	0.120	1.932386
≈ 0.15	0.122	1.841549
	0.076	3.818718
≈ 0.12	0.122	1.539279
	0.086	3.187431
≈ 0.09	0.127	1.184840
	0.0923	2.818421

all medium-coarse ensembles, we use eight sources for the relativistic operators; in all other cases, we use four.

E. Fitting methods

To determine the mass spectrum, we fit our correlator data with a Bayesian procedure, taking priors guided by potential models [53, 54]. The priors, listed in Table III, are the same for both relativistic and nonrelativistic correlators. To find the quarkonium masses from relativistic correlators, we use a delta function and a $1S$ smearing wavefunction as the source and sink. We fit simultaneously two or three source-sink combinations for the zero-momentum states, including the ground state and up to two excited states. The minimum and maximum source-sink separation is varied, and the best fit is selected based on the confidence level and the size of the errors in the ground state and first excited state masses. After choosing the fit range, 250 bootstrap samples are generated to provide an error estimate.

The fitting method in the case of nonrelativistic operators is similar except we use the same P -type wavefunction, described above, for both source and sink. In this case, we use no more than a ground state plus one excited state in the fitting form. The quality of data in the nonrelativistic case is such that often a fit with just the ground state is enough, provided the fitting range is appropriately chosen.

III. GENERAL RESULTS

Before presenting results for mass splittings (in Sec. IV) we discuss three general issues: a comparison of the statistical quality of relativistic and nonrelativistic operators (Sec. III A); a numerical comparison of tuning κ via M_2 in heavy-light and quarkonium (Sec. III B); and a discussion of how uncertainties from tuning κ are propagated to the mass splitting (Sec. III C).

TABLE IV: Rest masses of the charmonium states η_c , J/ψ , h_c , χ_{c0} , and χ_{c1} calculated with relativistic operators. All masses in units of $r_1 = 0.318$ fm. The star denotes masses that differ from their counterparts in Table V by more than 1.5σ .

a (fm)	β	κ_c	$\eta_c(1^1S_0)$	$\eta_c(2^1S_0)$	$J/\psi(1^3S_1)$	$\psi(2^3S_1)$	$h_c(1^1P_1)$	$\chi_{c0}(1^3P_0)$	$\chi_{c1}(1^3P_1)$
≈ 0.18	6.503	0.120	3.2924(9)	4.24(6)	3.4452(16)	4.35(7)	4.185(17)	\star 4.079(12)	\star 4.052(89)
	6.485	"	3.3071(14)	4.42(4)	3.4581(18)	4.48(3)	4.214(26)	4.117(15)	\star 4.173(13)
	6.467	"	3.3327(7)	4.39(27)	3.4862(11)	4.45(11)	4.213(29)	4.109(12)	4.200(25)
	6.458	"	3.3481(13)	4.47(6)	3.5004(16)	4.43(10)	\star 4.217(18)	4.106(18)	\star 4.181(19)
≈ 0.15	6.586	0.122	3.5688(8)	4.66(3)	3.7317(13)	4.75(3)	\star 4.476(8)	4.341(6)	4.450(7)
	6.572	"	3.5883(9)	4.64(5)	3.7501(14)	4.79(2)	\star 4.495(8)	4.368(6)	4.471(17)
≈ 0.12	6.81	0.122	3.8721(11)	5.16(4)	4.0594(18)	5.25(3)	4.807(17)	4.626(10)	4.755(19)
	6.79	"	3.8876(12)	5.14(3)	4.0747(18)	5.22(4)	4.821(12)	4.657(10)	4.791(10)
	6.76, <i>a</i>	"	3.8824(9)	5.09(4)	4.0677(15)	5.10(5)	4.800(13)	4.658(8)	4.758(15)
	6.76, <i>b</i>	"	3.9009(8)	5.12(3)	4.0864(11)	5.27(3)	4.817(14)	4.650(30)	4.785(15)
≈ 0.09	7.11	0.127	4.2740(26)	5.33(13)	4.4460(22)	5.55(6)	5.159(29)	5.027(16)	5.185(10)
	7.09	"	4.2885(15)	5.52(4)	4.4596(15)	5.66(4)	\star 5.149(24)	\star 4.986(15)	\star 5.123(19)
	7.08	"	4.2889(26)	5.51(5)	4.4613(33)	5.65(7)	5.167(33)	\star 4.986(26)	5.133(48)

TABLE V: Rest masses of the charmonium states h_c , χ_{c0} , χ_{c1} , and χ_{c2} calculated with nonrelativistic operators. All masses in units of $r_1 = 0.318$ fm. The star denotes masses that differ from their counterparts in Table IV by more than 1.5σ .

a (fm)	β	κ_c	$h_c(1^1P_1)$	$\chi_{c0}(1^3P_0)$	$\chi_{c1}(1^3P_1)$	$\chi_{c2}(1^3P_2)$
≈ 0.18	6.503	0.120	4.213(1)	\star 4.111(9)	\star 4.210(9)	4.272(15)
	6.485	"	4.227(7)	4.105(8)	\star 4.200(7)	4.286(10)
	6.467	"	4.223(12)	4.127(7)	4.227(8)	4.278(15)
	6.458	"	\star 4.253(9)	4.128(9)	\star 4.222(9)	4.310(11)
≈ 0.15	6.600	0.122	4.492(7)	4.344(6)	4.458(7)	4.537(11)
	6.586	"	\star 4.493(7)	4.349(7)	4.462(7)	4.536(13)
	6.572	"	\star 4.516(9)	4.375(9)	4.488(9)	4.574(10)
	6.566	"	4.548(10)	4.405(6)	4.526(7)	4.614(10)
≈ 0.09	7.11	0.127	5.199(11)	5.030(8)	5.170(12)	5.257(12)
	7.09	"	\star 5.198(13)	\star 5.034(11)	\star 5.168(13)	5.257(14)
	7.08	"	5.178(15)	\star 5.047(8)	5.167(13)	5.232(18)

TABLE VI: Rest masses of the bottomonium states η_b , Υ , h_b , χ_{b0} , and χ_{b1} calculated with relativistic operators. All masses in units of $r_1 = 0.318$ fm. The star denotes masses that differ from their counterparts in Table VII by more than 1.5σ .

a (fm)	β	κ_b	$\eta_b(1^1S_0)$	$\eta_b(2^1S_0)$	$\Upsilon(1^3S_1)$	$\Upsilon(2^3S_1)$	$h_b(1^1P_1)$	$\chi_{b0}(1^3P_0)$	$\chi_{b1}(1^3P_1)$
≈ 0.15	6.586	0.076	7.3776(8)	8.202(5)	7.4100(9)	8.209(5)	8.269(120)	\star 8.162(35)	\star 8.147(40)
	6.572	"	7.4061(9)	8.241(63)	7.4386(9)	8.248(7)	8.321(13)	8.292(11)	8.318(11)
≈ 0.12	6.81	0.086	8.0690(10)	8.933(12)	8.1299(12)	8.957(12)	8.919(15)	8.855(13)	8.898(13)
	6.79	"	8.0563(17)	8.910(14)	8.1167(19)	8.929(14)	8.902(19)	8.850(21)	8.874(38)
	6.76, <i>a</i>	"	7.9815(9)	8.870(11)	8.0426(13)	8.890(10)	8.860(20)	8.796(13)	8.839(14)
≈ 0.09	7.11	0.0923	10.2040(15)	11.130(78)	10.2627(19)	11.160(32)	11.050(14)	\star 11.006(13)	\star 11.049(10)
	7.09	"	10.1861(11)	11.142(20)	10.2468(15)	11.161(18)	\star 11.056(19)	10.992(14)	11.034(13)
	7.08	"	10.1795(26)	11.112(30)	10.2397(33)	11.137(56)	\star 11.066(19)	\star 11.017(12)	\star 11.048(14)

TABLE VII: Rest masses of the charmonium states h_b , χ_{b0} , χ_{b1} , and χ_{b2} calculated with nonrelativistic operators. All masses in units of $r_1 = 0.318$ fm. The star denotes masses that differ from their counterparts in Table VI by more than 1.5σ .

a (fm)	β	κ_b	$h_b(1^1P_1)$	$\chi_{b0}(1^3P_0)$	$\chi_{b1}(1^3P_1)$	$\chi_{b2}(1^3P_2)$
≈ 0.15	6.600	0.076	8.254(8)	8.220(8)	8.243(8)	8.274(9)
	6.586	"	8.252(10)	\star 8.216(10)	\star 8.242(10)	8.276(10)
	6.572	"	8.321(11)	8.288(10)	8.312(11)	8.341(11)
	6.566	"	8.369(9)	8.335(9)	8.359(9)	8.391(10)
≈ 0.09	7.11	0.0923	11.046(9)	\star 10.981(10)	\star 11.022(11)	11.077(8)
	7.09	"	\star 11.020(10)	10.973(10)	11.006(12)	11.040(10)
	7.08	"	\star 11.014(10)	\star 10.964(11)	\star 11.008(10)	11.045(9)

A. Relativistic vs. nonrelativistic operators

The statistical quality of our data can be judged from Fig. 1, which shows examples of typical two-point functions for the $1S$ pseudoscalar and vector states and their corresponding effective masses, calculated with relativistic operators. The data are from the coarse ensemble with $am_l/am_s = 0.01/0.05$. We have a clear signal and the effective masses have well-established plateaus. As already mentioned, for the $1P$ states we used both relativistic and nonrelativistic types of operators. Figure 2 compares the effective masses of the $h_c(1P)$ and $h_b(1P)$ states, calculated with both types of operators. The data show that the effective masses obtained with nonrelativistic operators plateau at an earlier t_{\min} . Despite the fact that the statistics in the nonrelativistic case are, in this example, three times lower than in the relativistic case, the errors on the fitted h_c and h_b masses are smaller than the ones calculated with relativistic operators. This finding holds for all of the $1P$ states studied here. Our statistics with the nonrelativistic operators are 2–3 times lower than with the relativistic ones (except for the medium-coarse case where they are 6 times lower), yet the errors on the masses are up to 50% smaller, and in some cases

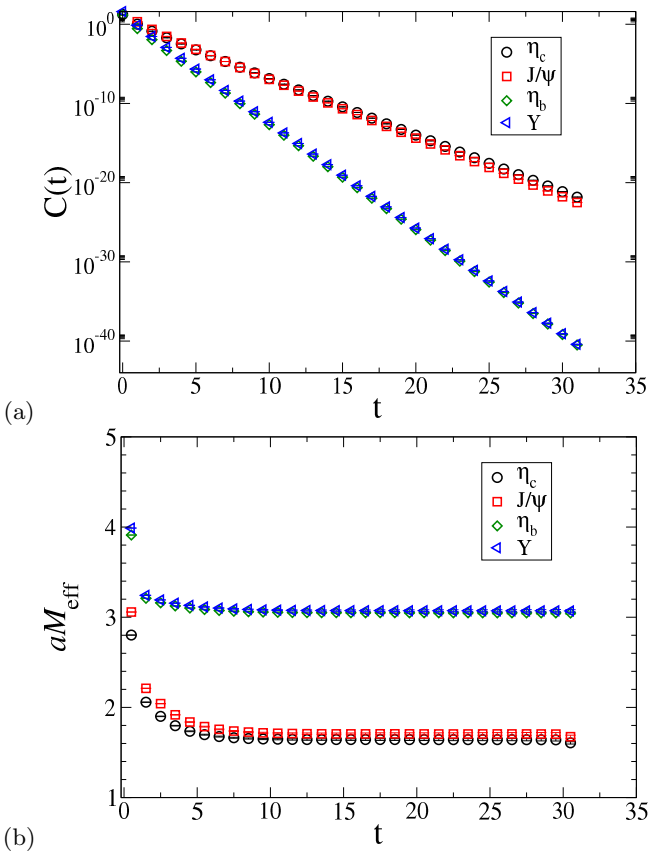


FIG. 1: Propagators (a) and effective masses (b) for the η_c , J/ψ , η_b , and Υ states, with delta-function sources and sinks, from the coarse ensemble with $am_l/am_s = 0.01/0.05$.

smaller still—see Tables IV–VII for numerical comparisons. The nonrelativistic operators couple much more weakly to the excited states and, thus, yield effective mass plateaus of better quality and fitted masses with smaller errors. All of our results for quarkonium masses are listed in Tables IV–VII with statistical errors calculated with the bootstrap method and symmetrized.

The central values of the $1P$ states calculated with relativistic and nonrelativistic operators occasionally differ by more than 1.5 uncorrelated σ . This difference arises more often than expected, especially once correlations are considered. In the tables, these cases are labeled with a star. To check whether this difference is due to statistics, in some cases we carried out simultaneous fits to both the relativistic and nonrelativistic correlators. The masses extracted this way turned out to be indistinguishable from the masses from nonrelativistic data alone. This was not surprising, because the data from relativistic sources had larger fluctuations than that from nonrelativistic sources. Thus, in our further analysis of the chiral extrapolation and a dependence, we use the nonrelativistic results for the $1P$ states wherever they are available.

B. κ tuning in quarkonium and heavy-strange mesons

In Sec. II C, we argued that the best way to tune the hopping parameter κ is to use the spin-averaged kinetic mass of heavy-strange hadrons. If instead one would tune to the kinetic mass of the (spin-averaged) quarkonium ground state, the resulting tuned κ could be different at nonzero lattice spacing. To study this discrepancy we have computed the quarkonium $\overline{1S}$ kinetic mass for a wide range of κ on the medium-coarse ensemble with $am_l/am_s = 0.0290/0.0484$. Figure 3 shows the results

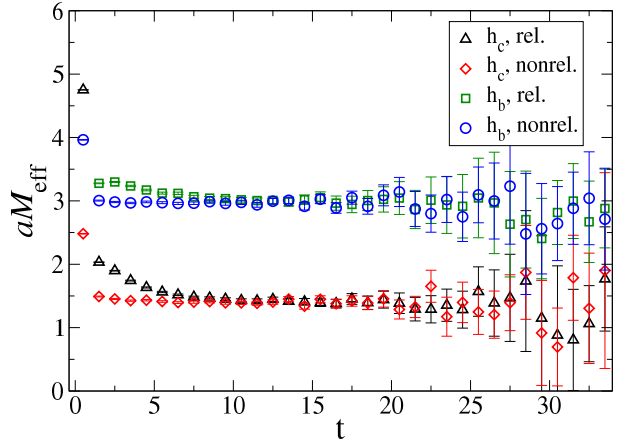


FIG. 2: Comparison between effective masses for h_c and h_b calculated with relativistic and nonrelativistic operators, on the fine ensemble with $am_l/am_s = 0.0124/0.031$.

and also shows the physical $aM(\overline{1S})$ and aM_{Υ} .³ From a polynomial fit to the data, we get $\kappa_c \approx 0.122$ for the charmed quark, which is the same value as the one we obtain from matching to D_s . However, because the relevant discretization effects are larger in bottomonium than in B mesons, the tuned values of the hopping parameter differ substantially: $\kappa_b \approx 0.094$ from Υ vs. $\kappa_b \approx 0.076$ from B_s .

When we tune to the D_s , some uncertainty in κ arises. We take the tuning error in κ_c to be 0.0015 and in κ_b to be 0.006. Reference [9] finds uncertainties (statistical and fitting) in this range on the medium-coarse, coarse, and fine ensembles, and here we assume the same for the extra-coarse ensembles. We discuss in the next subsection how to propagate these errors to our computed splittings.

Above we mentioned a small difference in tuning the clover coupling for the coarse ensembles. The value of the tadpole coefficient u_0 used in that analysis was determined from mean Landau gauge link whereas the coefficient used in the others was determined from the plaquette. This difference means that our bare quark mass, *i.e.*, κ , has a slightly different definition on the coarse ensembles. Discrepancies in mass splittings caused by this choice should be eliminated via the nonperturbative tuning.

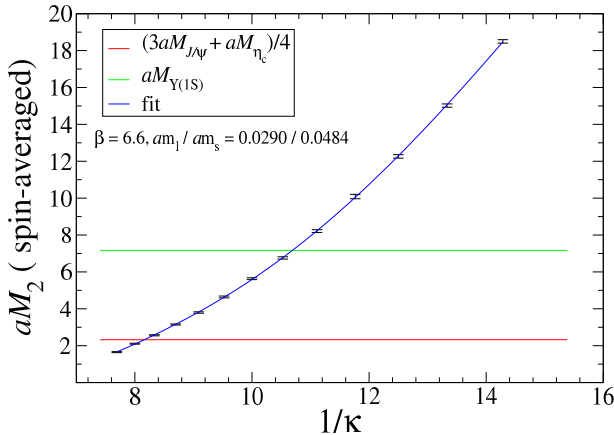


FIG. 3: Spin-averaged kinetic mass aM_2 as a function of κ , over a wide range, on the medium-coarse ensemble with $am_l/am_s = 0.0290/0.0484$. With a polynomial fit to the data, we can read off $\frac{1}{4}(aM_{\eta_c} + 3aM_{J/\psi})$ and aM_{Υ} , finding $\kappa_c \approx 0.122$ and $\kappa_b \approx 0.094$.

³ When this tuning was carried out, the η_b had not yet been observed by experiment.

TABLE VIII: 1^3S_1 - 1^1S_0 hyperfine splittings in r_1 units as a function of the valence κ calculated for the medium-coarse ensemble with $am_l/am_s = 0.0290/0.0484$.

κ	$r_1[M(1^3S_1) - M(1^1S_0)]$
0.070	0.0247(9)
0.075	0.0299(11)
0.080	0.0369(12)
0.085	0.0442(13)
0.090	0.0531(14)
0.095	0.0631(15)
0.100	0.0749(17)
0.105	0.0885(18)
0.110	0.1029(23)
0.115	0.1244(27)
0.120	0.1499(33)
0.125	0.1836(40)
0.130	0.2335(49)

C. κ -tuning uncertainties

Tables IV–VII and most of the plots in Sec. IV show statistical errors only, because the foremost aim of this paper is to understand the pattern of discretization errors. A systematic error also arises from inaccuracies in tuning κ_c and κ_b , and to study the continuum limit it is necessary to propagate this error to the mass splittings. We discuss here how we treat these uncertainties.

Several pieces of evidence show that the spin-averaged splittings depend very little on κ . These splittings vary little from charmonium to bottomonium [24], a feature understood to be a consequence of both systems lying between the confining and Coulombic part of the potential [1, 2]. This feature is, in fact, reproduced in our lattice-QCD data. Moreover, earlier work in the quenched approximation [55] and with $n_f = 2$ [8] show negligible κ dependence for spin-averaged splittings. Thus, we shall assume that the κ -tuning error for these splittings can be neglected.

For spin-dependent splittings, we compute the $1S$ hyperfine splitting as a function of κ , on the medium-coarse ensemble with $am_l/am_s = 0.0290/0.0484$, the same ensemble as in Fig. 3. The data are summarized in Table VIII. We fit the data to the form

$$\mu = 1/\kappa - 1/\kappa_{cr}, \quad (3.1)$$

$$HFS = b_0/\mu^2 + b_1/\mu^3 + b_2/\mu^4 + b_3/\mu^5 + b_4/\mu^6, \quad (3.2)$$

for $\kappa_{cr} = 0.145$, which enforces the requirement that, at large heavy quark mass $m_0 = \mu/2a$, the splitting goes as $1/m_0^2$. The fit gives $\chi^2/\text{dof} = 0.6/8$. From the fit result we estimate that an error of 0.0015 in the determination of κ_c results in a 6% error in the charmonium hyperfine splitting, and an error of 0.006 in the determination of κ_b , a 22% error in the bottomonium hyperfine splitting. We expect that these errors are characteristic of all splittings driven by the spin-spin and tensor terms in the quarkonium effective potential, since in the non-

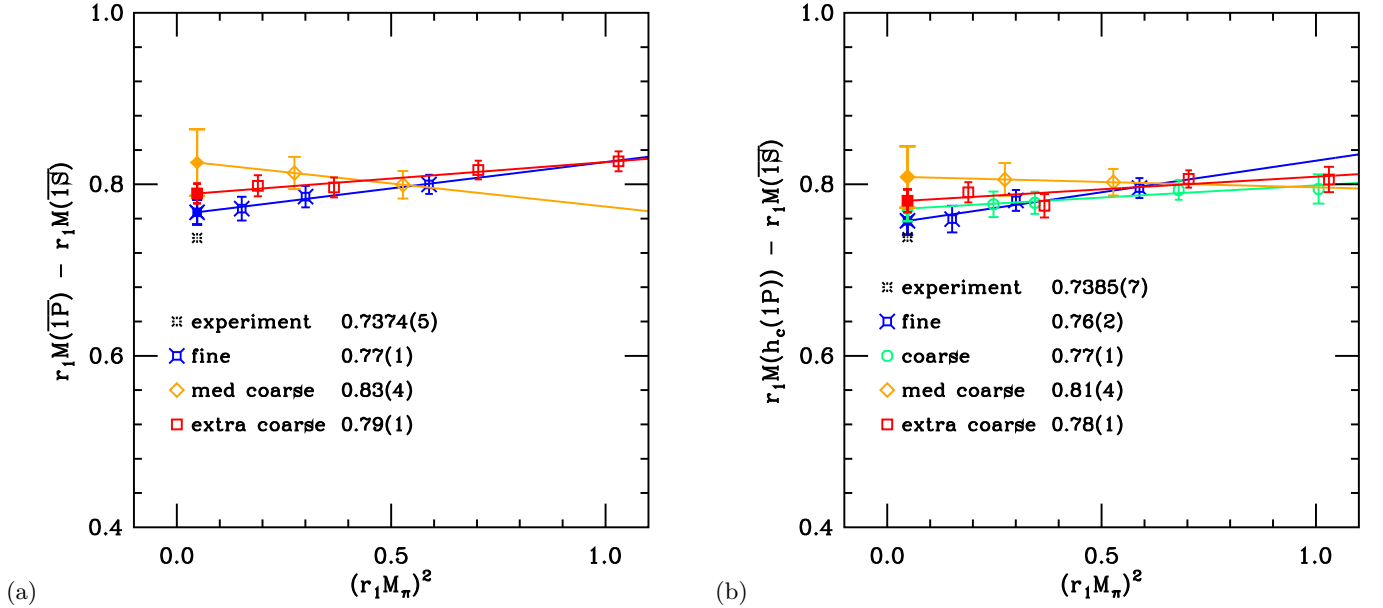


FIG. 4: The (a) $\overline{1P}-\overline{1S}$ and (b) $1^1P_1-\overline{1S}$ splittings in charmonium. The fine ensemble data are in blue fancy squares, the coarse in green circles, the medium-coarse in orange diamonds and the extra-coarse in red squares. The chirally extrapolated values are given in the legend and plotted with filled symbols.

relativistic treatment, they all stem from the same term in the heavy-quark effective Lagrangian.

The spin-orbit splitting remains to be considered. In our data and in experiment, it decreases from charmonium to bottomium similarly to the hyperfine and tensor splittings. Therefore, we shall assume the same relative error from the uncertainty in tuning κ .

Below we also present results for the splittings between twice the spin-averaged mass of D_s and D_s^* , and of B_s and B_s^* , and the corresponding $\overline{1S}$ quarkonium mass. To estimate their κ -tuning errors we have calculated these spin-averaged masses for several values of κ near κ_c and κ_b on the coarse ensemble with $am_l/am_s = 0.01/0.05$. These direct measurements allow us to propagate the κ -tuning errors from the masses to the mass splittings. We obtain an error of 1.3% for charm and 13% for bottom. We assume the same error for these splittings at other lattice spacings.

IV. SPECTRUM RESULTS

We now present plots of quarkonium mass splittings as a function of the square of the sea-quark pion mass. The splittings and their errors are calculated using the bootstrap method. In most cases, we expect the dependence on the sea-quark mass to be mild, so we perform on our results a chiral extrapolation linear in M_π^2 down to the physical pion. The extrapolated values are denoted in each plot with filled symbols. The error bars come from symmetrizing the 1σ (68%) interval of the bootstrap distribution.

Where possible, we compare our results to experi-

mental measurements. As a rule we take the average values from the compilation of the Particle Data Group [24]. The exception is the mass of the $\eta_b(1S)$ meson, which has only recently been observed. We take $M_{\eta_b} = 9390.9 \pm 2.8$ MeV, based on our average of two measurements by the BaBar Collaboration [48, 49] and one by the CLEO Collaboration [50].

In examining the results, we are interested in seeing how well we can understand discretization errors via the nonrelativistic description of Eqs. (2.13)–(2.15). We therefore carry out separate chiral extrapolations at each lattice spacing, and discuss whether the a dependence, and any deviations from experiment, make sense.

From the effective Lagrangian discussion, we expect different discretization errors to affect spin-averaged and spin-dependent splittings. Errors in the spin-averaged splittings stem from the Darwin ($\mathbf{D} \cdot \mathbf{E}$) term and the two p^4 terms. Errors in the spin-dependent splittings stem from the chromomagnetic ($i\boldsymbol{\sigma} \cdot \mathbf{B}$) and spin-orbit ($i\boldsymbol{\sigma} \cdot \mathbf{D} \times \mathbf{E}$) terms. Moreover, from the general structure of potentials arising from QCD [25, 26], we learn that $i\boldsymbol{\sigma} \cdot \mathbf{B}$ predominantly affects $M(nS_{\text{HFS}})$ and $M(nP_{\text{tensor}})$, while $i\boldsymbol{\sigma} \cdot \mathbf{D} \times \mathbf{E}$ affects $M(nP_{\text{spin-orbit}})$.

A. Spin-averaged splittings

Let us start with $\overline{1P}-\overline{1S}$ and $1^1P_1-\overline{1S}$ splittings, plotted in Figs. 4 and 5 vs. $(r_1 M_\pi)^2$. In the nonrelativistic picture, they arise predominantly at order v^2 via the kinetic energy, which our tuning of κ should normalize correctly. The spin-dependent terms in $\mathcal{L}_{\text{HQ}}^{(4)}$ [cf. Eq. (2.15)]

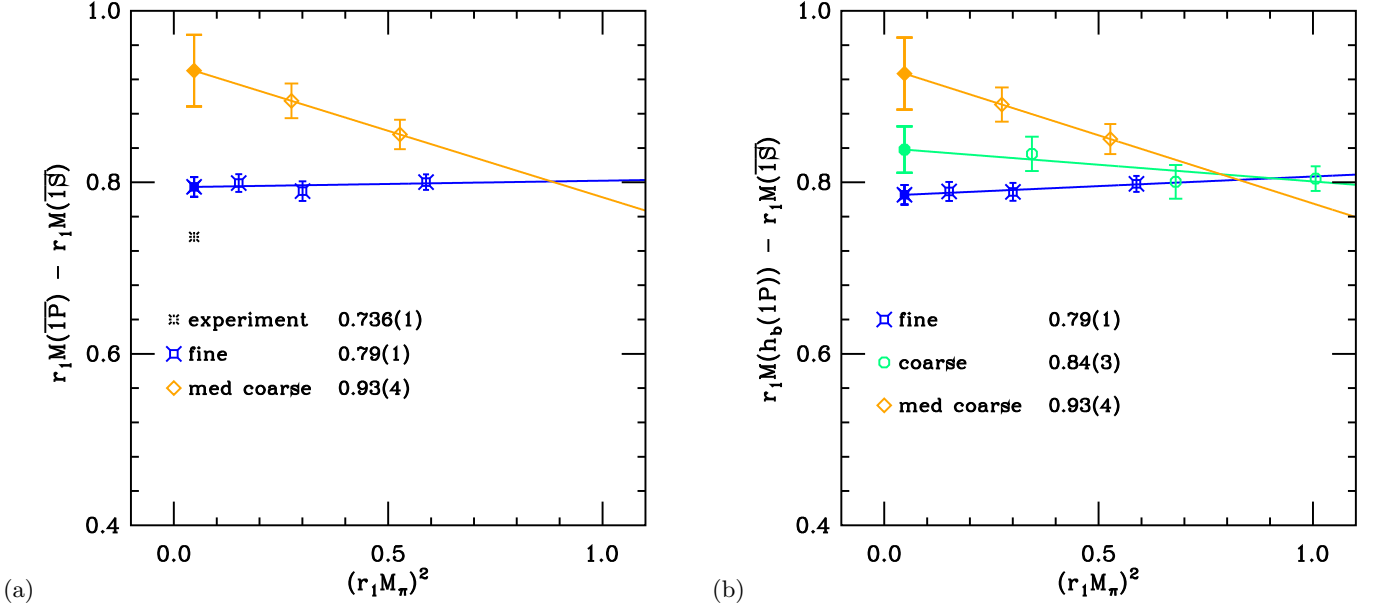


FIG. 5: The (a) $\bar{1}P\text{-}\bar{1}S$ and (b) $1^1P_1\text{-}\bar{1}S$ splittings in bottomonium. Color code as in Fig. 4.

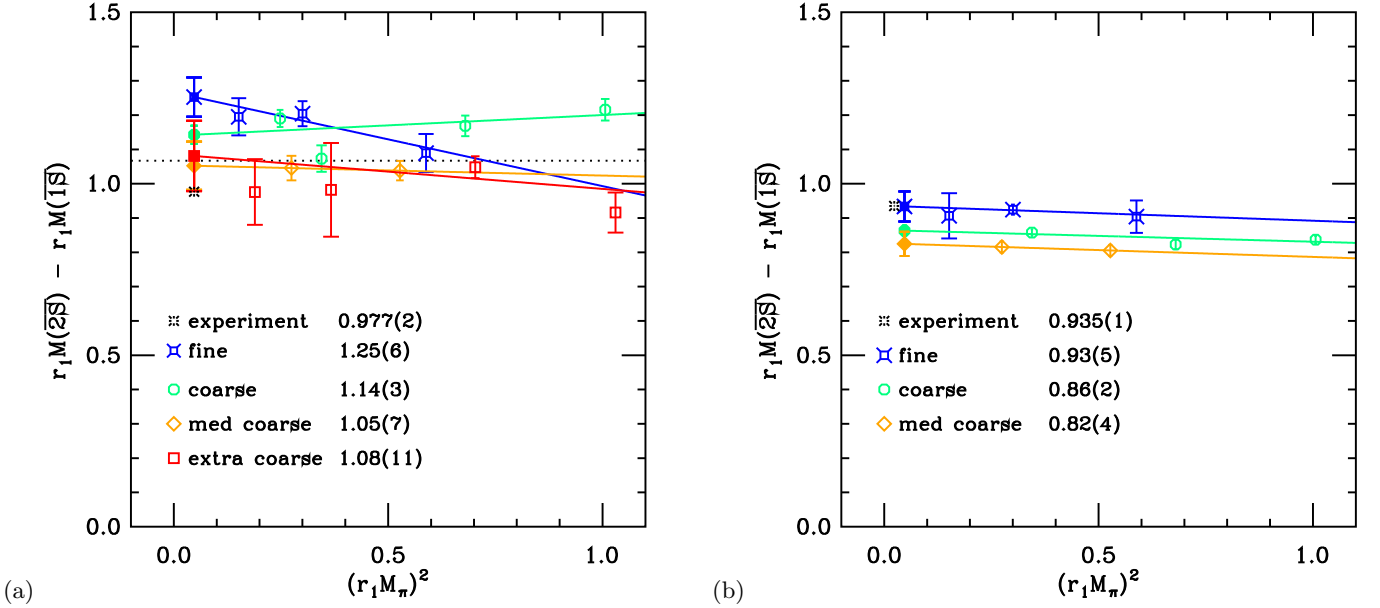


FIG. 6: Splitting between the $\bar{2}S$ and $\bar{1}S$ levels of (a) charmonium, (b) bottomonium. The dotted line in (a) indicates the open-charm threshold. The experimental point in (b) is *not* the spin-averaged splitting, but the $\Upsilon(2S)\text{-}\bar{1}S$ mass difference, since the η'_b has not been observed.

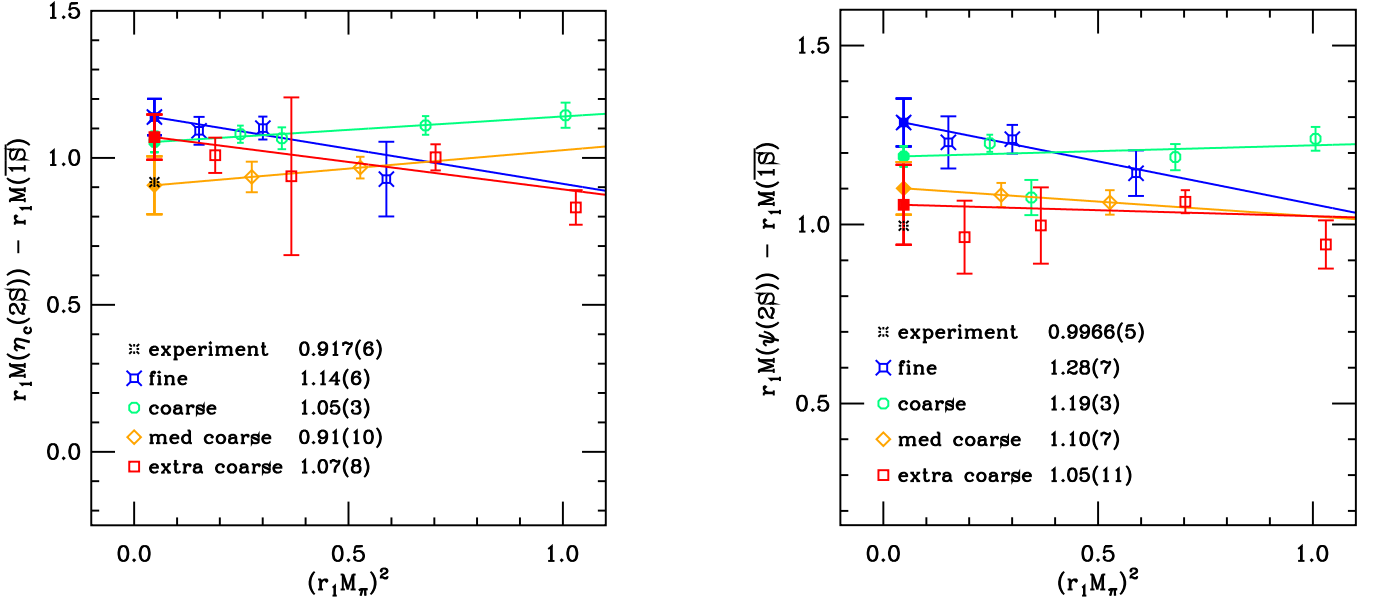
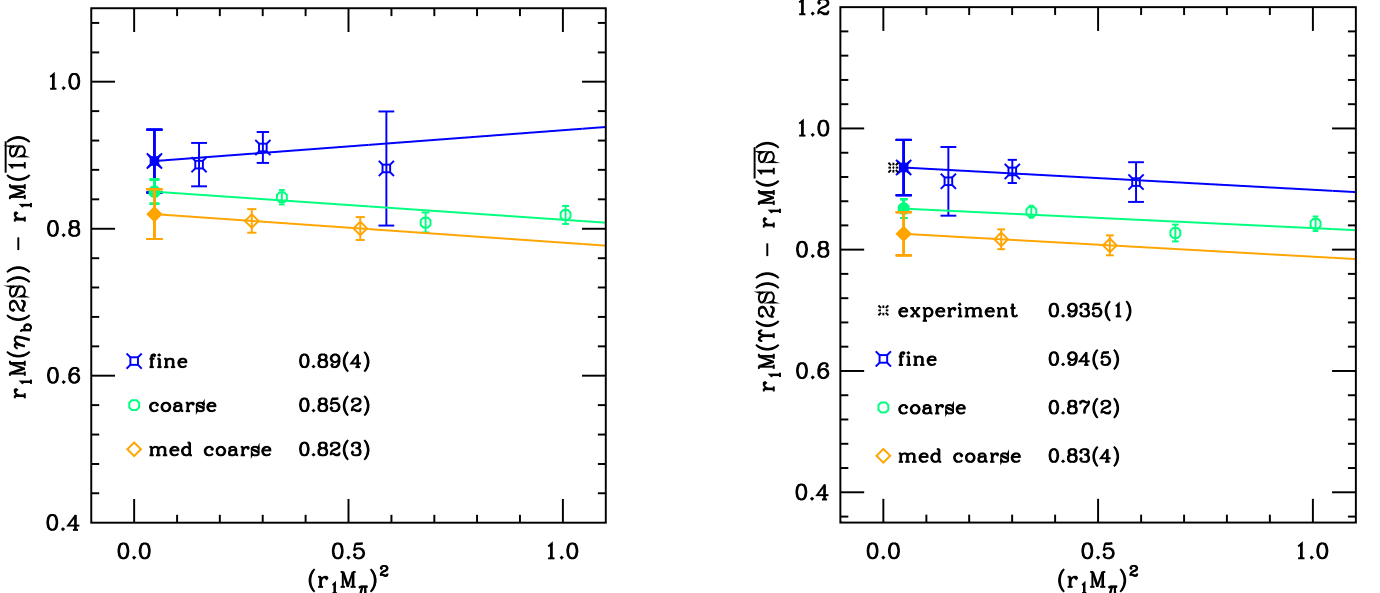
do not contribute to spin averages ($\bar{1}S$, $\bar{1}P$) or to a spin singlet (1^1P_1). Discretization errors remain, however, at order v^4 via the mismatches in Eqs. (2.28)–(2.30). We assess these results using the error estimates in Ref. [51], which account for both the a dependence and the relative v^2 suppression.

Our results for charmonium are shown in Fig. 4. Our results for both splittings approach the continuum physical point as the lattice spacing decreases, and the size of the discretization effects is about what one expects:

5–6% from $m_E \neq m_2$ and 3–6% from $m_4 \neq m_2$ [51].

The $\bar{1}P\text{-}\bar{1}S$ and $1^1P_1\text{-}\bar{1}S$ splittings in bottomonium are given in Fig. 5. These splittings agree acceptably with experiment, given the estimated discretization errors, 2–3% from $m_E \neq m_2$ and 2–5% from $m_4 \neq m_2$ [51]. We cannot compare the $h_b(1^1P_1)$ mass with experiment, because that state has not been observed [24], but our results for the 1^1P_1 level agree very well with the $\bar{1}3P_J$ average.

Next let us examine the $\bar{2}S\text{-}\bar{1}S$ splitting. We fit a correlator matrix constructed from two interpolating opera-

FIG. 7: Splittings in charmonium between the individual $2S$ states and the $1S$ level.FIG. 8: Splittings in bottomonium between the individual $2S$ states and the $1S$ level.

tors, local and smeared, to three or more states (*i.e.*, two or more excited states). The error we assign to the mass determination estimates the uncertainties in our method. The results for charmonium as a function of $(r_1 M_\pi)^2$ are shown in Fig. 6a. The lattice data appear to lie significantly above the experimental value at the smaller lattice spacings. The individual $2S$ levels show the same trends we observe in the spin-averaged level. In Fig. 7 we plot separately the $\eta_c(2S)$ - $1S$ and $\psi(2S)$ - $1S$. We see that both $\eta_c(2S)$ and $\psi(2S)$ are responsible for the behavior seen in Fig. 6a, the latter especially so. The results for bottomonium (Fig. 6b) are more satisfactory.

We suggest two possible reasons for the behavior of the charmonium $2S$ - $1S$ splitting results. First, the $2S$ are the only excited states in this study. Excited states are more difficult than ground states to determine accurately. With only two operators, our fits are less reliable, even though our fit model has at least three states. Second, the fit procedure does not take into account adequately the possible contribution of multiple open charm levels. For example, we have not used a two-body operator in the matrix correlator. With unphysically large quark masses, the open charm levels are unphysically high. As the sea quark mass is decreased, they come down. Moreover, the

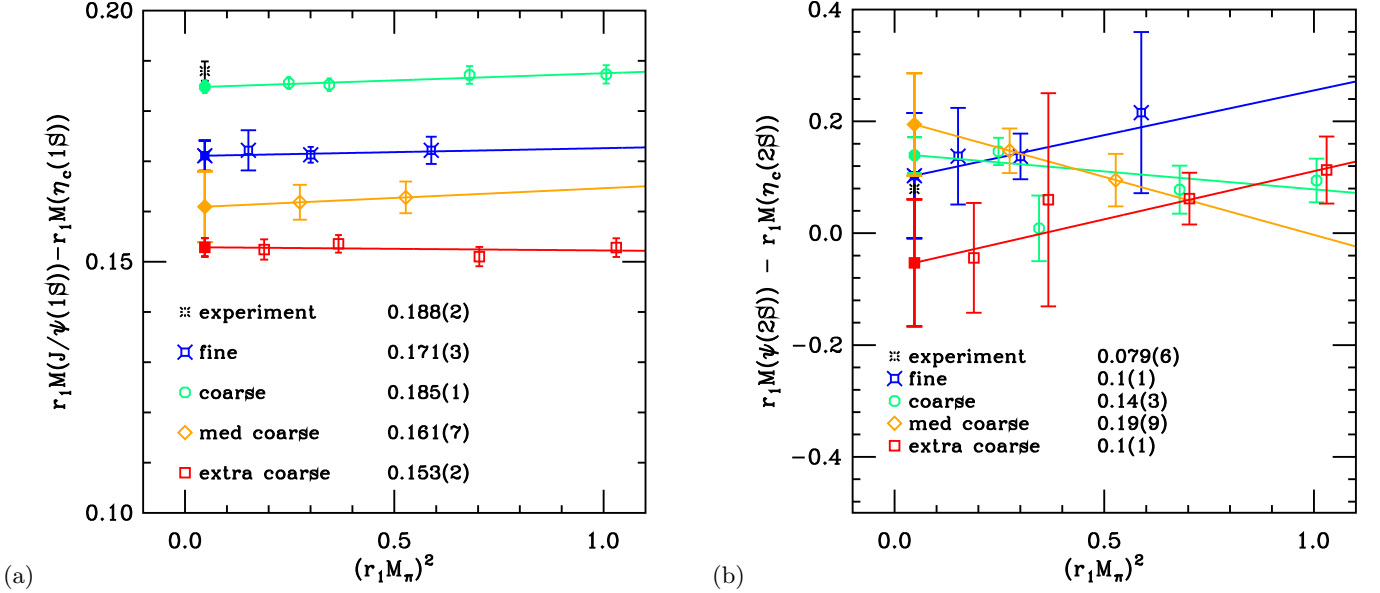


FIG. 9: Charmonium hyperfine splittings for (a) 1S, (b) 2S.

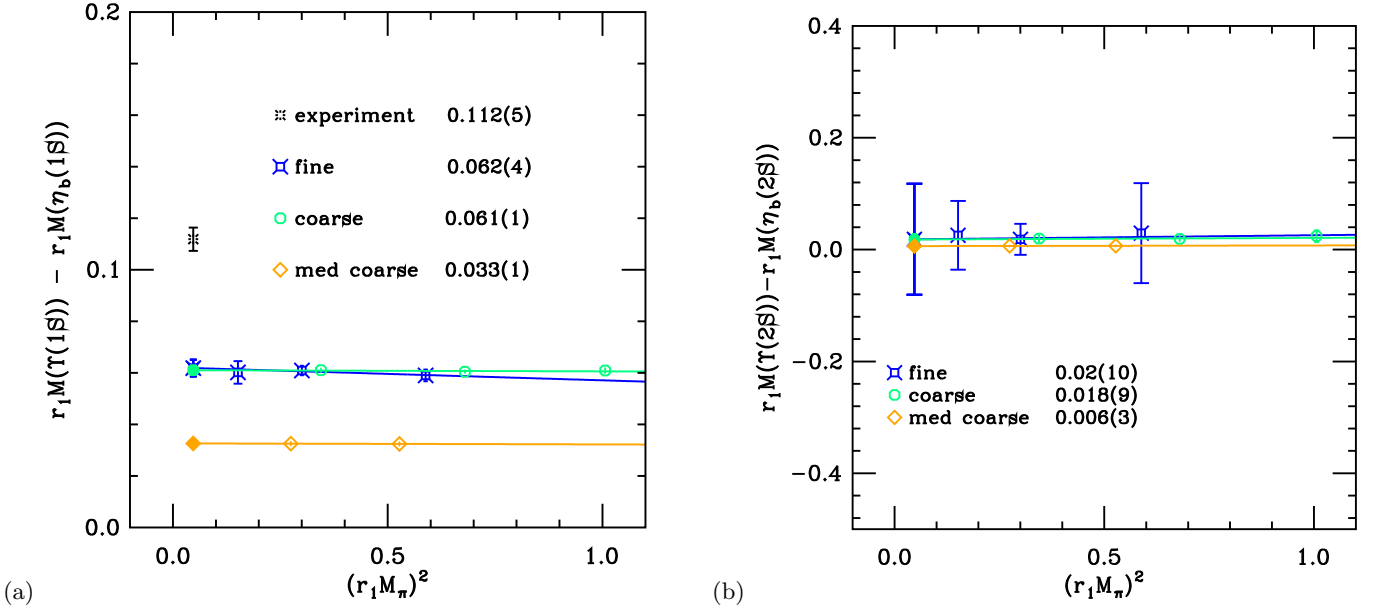


FIG. 10: Bottomonium hyperfine splittings for (a) 1S, (b) 2S.

box size of our lattices at the lightest sea quark mass is larger, which decreases the discrete level spacing of the would-be open-charm continuum. The dotted line in Fig. 6a shows the location of the physical open charm threshold. It is dangerously close to the physical 2S levels, especially the $\psi(2S)$. Thus it is conceivable that nearby multiple open charm levels are being confused with the 2S and artificially raise its fitted mass. This explanation is consistent with the observed gradual rise of this level in the fine ensembles with decreasing light quark mass but not with the trends seen in the coarse and medium-coarse ensembles.

For bottomonium in Fig. 6b, the open bottom threshold is safely distant (off scale in this plot), so we do not expect a similar confusion in this channel. Figure 8 shows the individual 2S bottomonium levels separately. There is no comparison for the first excited pseudoscalar state $\eta_b(2S)-\bar{1}S$, because the state has not yet been observed [24], although the extrapolated values appear to approach a consistent continuum limit. The first excited vector state splitting $T(2S)-\bar{1}S$ is given in Fig. 8b. The chirally extrapolated values monotonically approach the experimental value and for the fine ensembles our splitting agrees with the experiment.

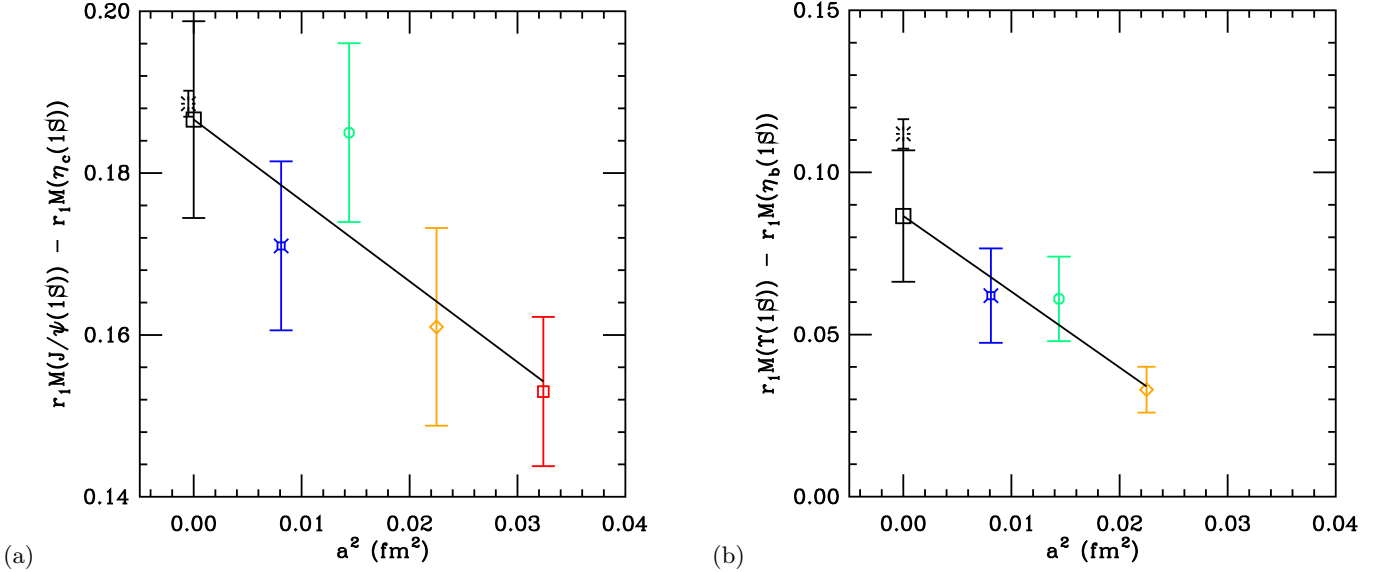


FIG. 11: Continuum extrapolations for the 1S hyperfine splittings for (a) charmonium, (b) bottomonium. The symbols and colors of the data points are the same as throughout the paper. Here the error bars on the data points include our estimates for the κ -tuning systematic error. The plotted experimental η_b mass comes from the average of recent measurements [48, 49, 50], as discussed in the text.

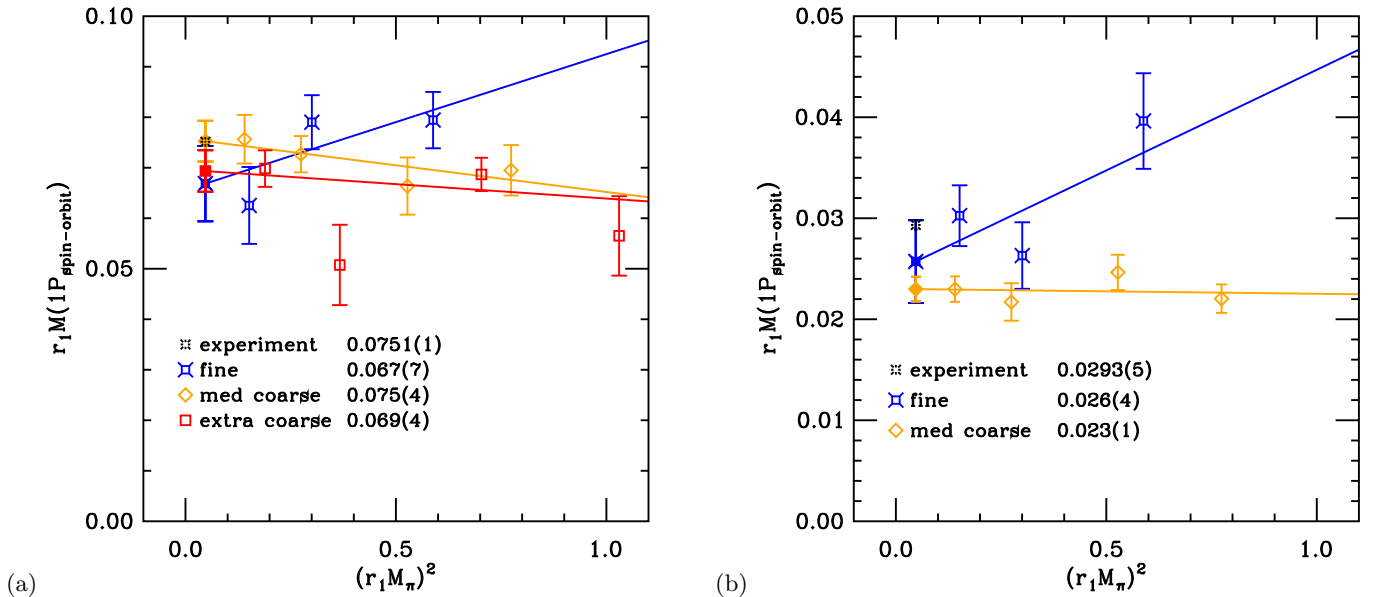


FIG. 12: Spin-orbit splittings in 1P levels, with $M(1P_{\text{spin-orbit}})$ defined in Eq. (2.4), for (a) charmonium and (b) bottomonium.

B. Hyperfine splittings

Now let us turn to the hyperfine structure. Our results for the hyperfine splitting in charmonium and bottomonium are presented in Figs. 9 and 10. For the 1S levels and for 2S bottomonium, there is little dependence on the sea quark mass. To assess the approach to the continuum limit one must bear in mind that the errors in Figs. 9 and 10 are statistical only, and the systematic error from κ -tuning must also be taken into account. We thus take the values at the physical pion mass, apply the

κ -tuning error and plot these data *vs.* a^2 , as shown in Fig. 11. Both data sets are consistently linear in a^2 , so we carry out such an extrapolation. The extrapolated values in units of r_1 are 0.187(12) for charmonium, with $\chi^2/\text{dof} = 1.9/2$, and 0.087(20) for bottomonium, with $\chi^2/\text{dof} = 0.55/1$. One can see, from comparing Fig. 11 with Fig. 9 and 10, that the κ -tuning uncertainties inherited from the heavy-strange kinetic mass are larger than the statistical uncertainties of the quarkonium rest-mass splittings.

In physical units these extrapolated results are

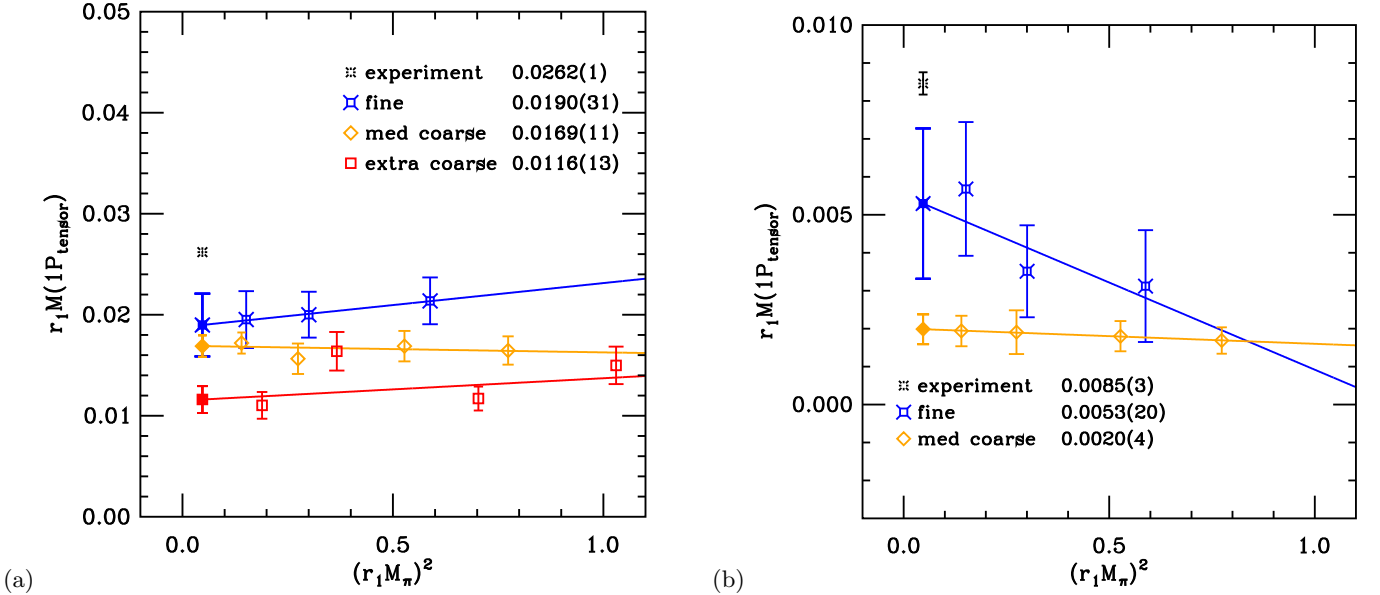
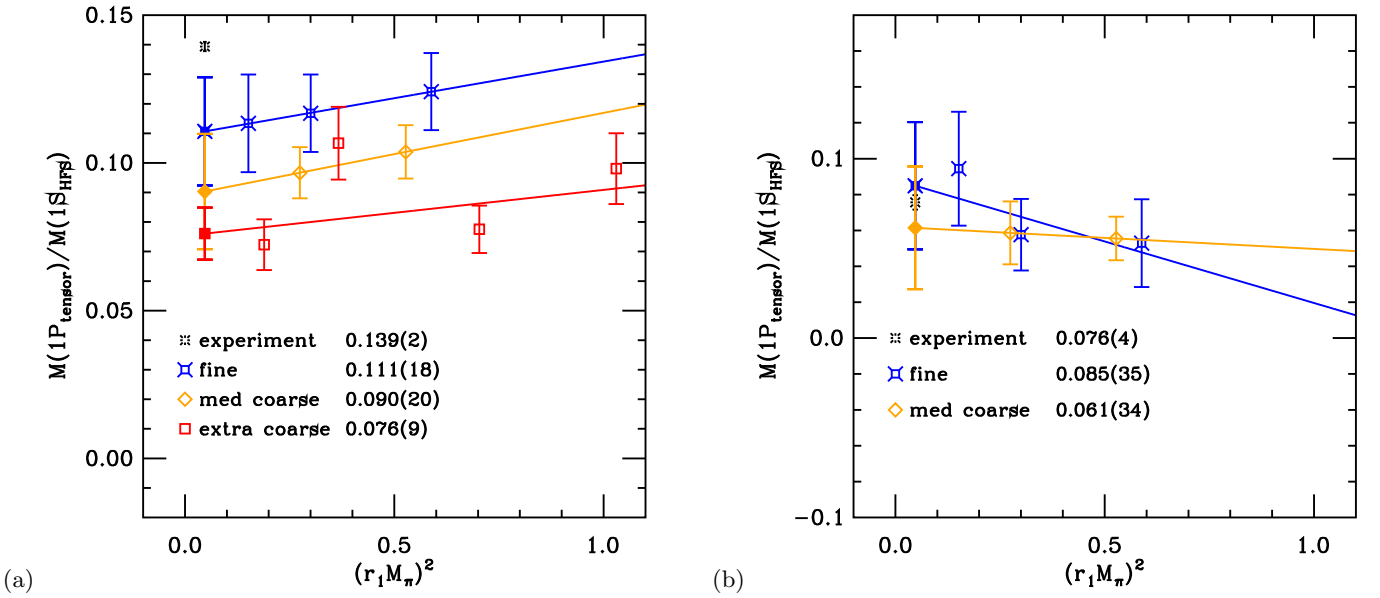
FIG. 13: Tensor splittings in 1P levels, with $M(1P_{\text{tensor}})$ defined in Eq. (2.5), for (a) charmonium and (b) bottomonium.

FIG. 14: Ratio of the 1P tensor and 1S hyperfine splittings, for (a) charmonium and (b) bottomonium.

$M_{J/\psi(1S)} - M_{\eta_c(1S)} = 116.0 \pm 7.4^{+2.6}_{-0.0}$ MeV and $M_{\Upsilon(1S)} - M_{\eta_b(1S)} = 54.0 \pm 12.4^{+1.2}_{-0.0}$ MeV, where the second error comes from converting from r_1 units to MeV. For charmonium the average of experimental measurements is 116.4 ± 1.2 MeV [24], so our result is perfectly consistent. For bottomonium, the experimental measurements are $71.4^{+2.3}_{-3.1} \pm 2.7$ MeV [48], $66.1^{+4.9}_{-4.8} \pm 2.0$ MeV [49], and $68.5 \pm 6.6 \pm 2.0$ MeV [50]; symmetrizing the error bars and taking a weighted average, we find $M_{\Upsilon(1S)} - M_{\eta_b(1S)} = 69.4 \pm 2.8$ MeV. Our hyperfine splitting thus falls 1.2σ short. Note that with lattice NRQCD, the HPQCD Collaboration finds $M_{\Upsilon(1S)} - M_{\eta_b(1S)} = 61 \pm 4 \pm 13$ MeV [19], which agrees with the recent experimental measure-

ments, yet also with our result.

The errors on the final 1S hyperfine splittings quoted here encompass statistics (as amplified by extrapolations), κ tuning, and r_1 . In addition, the coupling c_B has been adjusted only at the tree-level, introducing an error of $O(\alpha_s a)$ that our continuum extrapolation would not eliminate. A preliminary result for the one-loop correction to c_B is available [56], suggesting that a very small correction is needed beyond the tadpole improvement of Eq. (2.26), when u_0 is set from the Landau link.

The 2S hyperfine splittings for both charmonium and bottomonium are shown in Figs. 9b and 10b. Unfortunately, these results are not very useful. Although the

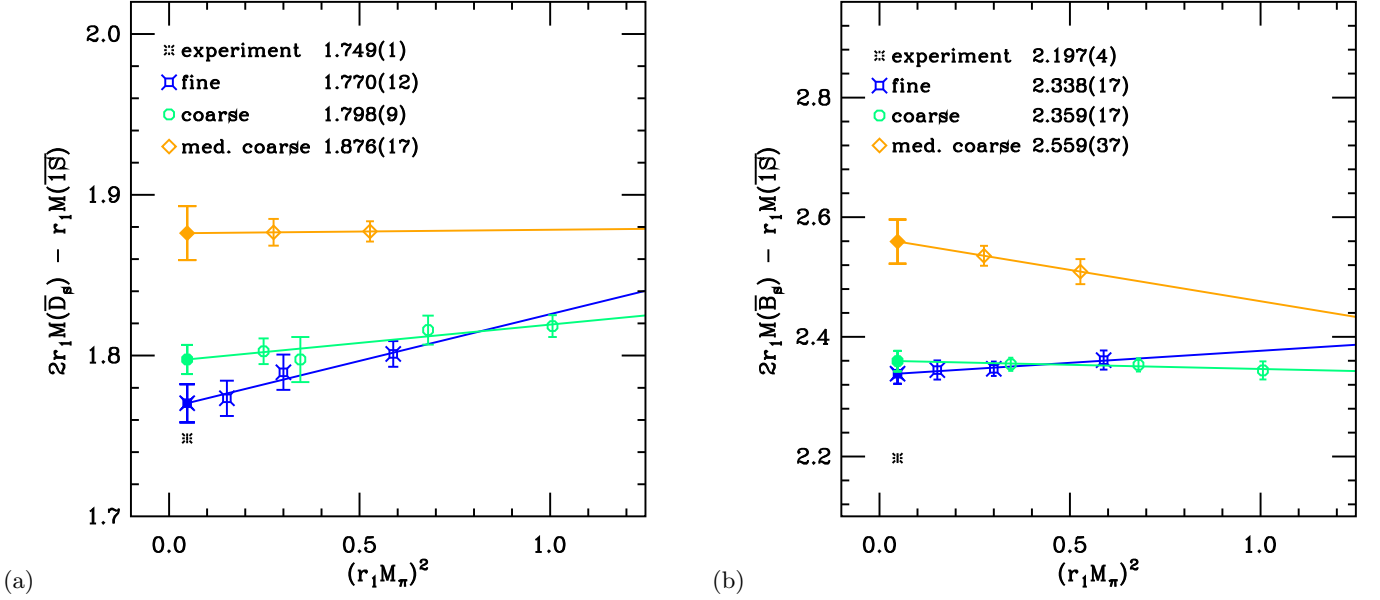


FIG. 15: Quarkonium–heavy-light splittings (a) $2M(\overline{D}_s) - M(\overline{1S})$ and (b) $2M(\overline{B}_s) - M(\overline{1S})$.

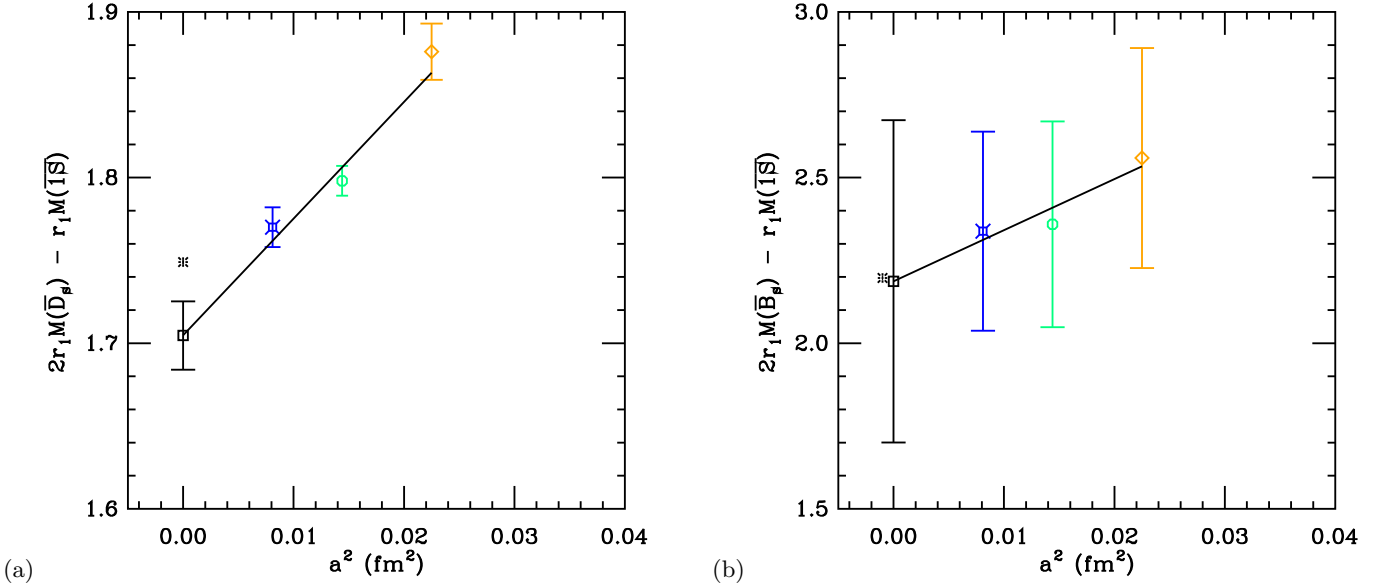


FIG. 16: Continuum extrapolations of (a) $2M(\overline{D}_s) - M(\overline{1S})$ and (b) $2M(\overline{B}_s) - M(\overline{1S})$.

charmonium splitting agrees, within large errors, with experiment, one should bear in mind the issue of threshold effects surrounding our determination of the $\psi(2S)$ mass, discussed above. The bottomonium splitting does not suffer from this problem, but the statistical and fitting errors are still too large to make a prediction of the as yet unobserved $\eta_b(2S)$ mass.

C. P -state splittings

We now turn to splittings between the 1^3P_J levels, which stem from two contributions [25]. As discussed

above, one comes from exchanging a Coulomb gluon between a spin-orbit term, $\bar{h}^{(\pm)}i\sigma \cdot (\mathbf{D} \times \mathbf{E})h^{(\pm)}$ in Eq. (2.15), and the static potential, $\bar{h}^{(\mp)}A_4h^{(\mp)}$. The other comes from exchanging a transverse gluon between the chromomagnetic terms, $\bar{h}^{(+)}i\sigma \cdot \mathbf{B}h^{(+)}$ and $\bar{h}^{(-)}i\sigma \cdot \mathbf{B}h^{(-)}$. These two contributions can be separated by forming the combinations in Eqs. (2.4) and (2.5) [26].

The spin-orbit splittings $M(1P_{\text{spin-orbit}})$ are shown in Fig. 12 for charmonium and bottomonium. They exhibit a small lattice-spacing dependence and agree well with experiment, indicating that the chromoelectric interactions and, hence, c_E are adjusted accurately enough. The tensor splittings $M(1P_{\text{tensor}})$ are shown in Fig. 13

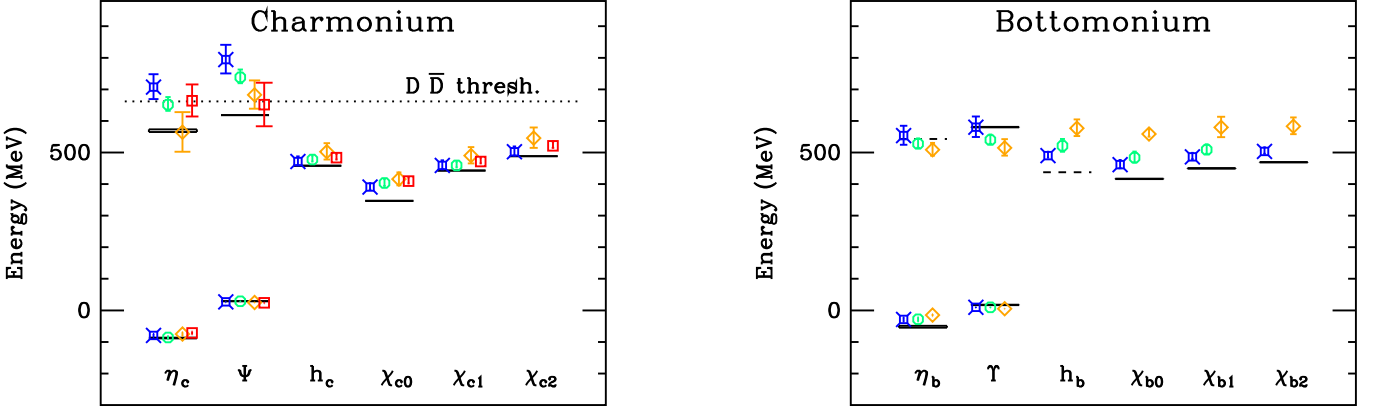


FIG. 17: Quarkonium spectrum as splittings from the $\overline{1S}$ level for $\bar{c}c$ (left) and $\bar{b}b$ (right). The fine-ensemble results are in blue fancy squares, the coarse in green circles, the medium-coarse in orange diamonds and the extra-coarse in red squares. Solid lines show the experimental values, and dashed lines estimates from potential models. The dotted line in the left panel indicates the physical open-charm threshold. The error on the data points combines statistical, κ -tuning, and r_1 uncertainties.

for charmonium and bottomonium. These chromomagnetic effects seem to approach the experimental value as a decreases. Since the tensor and the spin-spin potential components both measure the effects of the chromomagnetic interaction, we plot the ratio of the $1P$ tensor splitting to the $1S$ hyperfine splitting in Fig. 14. The coefficient m_B^{-1} should drop out from the ratio and if there are no effects from higher-dimension operators, the ratio should be a constant which agrees with the continuum limit. If a higher-dimension operator has a significant contribution, then the ratio need not agree any better than the splittings themselves. The charmonium case, Fig. 14a, seems to suggest that the higher-dimension operator matters, the bottomonium case, Fig. 14b, seems to suggest it does not. This outcome is plausible, because the v^2 suppression of the higher-dimension operator is 10% in bottomonium, but only 30% in charmonium [cf. Eqs. (2.11) and (2.12)].

D. Quarkonium vs. heavy-strange mesons

Unlike other approaches to heavy quarks, lattice QCD is supposed to treat heavy-light mesons and quarkonium on the same footing. If we form the splitting

$$2M(\overline{D}_s) - M(\overline{1S}) \quad (4.1)$$

the rest mass drops out, leaving a pure QCD quantity. Here $M(\overline{D}_s)$ denotes the spin average of D_s and D_s^* masses. This mass difference is interesting from the point of view of the discretization effects, which should contribute less to the \overline{D}_s and \overline{B}_s than to the charmonium and bottomonium $\overline{1S}$ states. We show this splitting (also for the bottom-quark sector) combining our quarkonium rest masses with the Fermilab-MILC heavy-strange rest masses [9] in Fig. 15. The correlation in the error is treated correctly with the bootstrap method, and, as

elsewhere in this paper, the bootstrap errors are symmetrized. Clearly, discretization effects are important at nonzero a .

In Fig. 16, we incorporate the κ -tuning errors and show the a dependence of the above splittings. Carrying out an extrapolation linear in a^2 , which is empirically suitable, we find $r_1[2M(\overline{D}_s) - M(\overline{1S})] = 1.705 \pm 0.021$ and $r_1[2M(\overline{B}_s) - M(\overline{1S})] = 2.19 \pm 0.49$; these correspond to $2M(\overline{D}_s) - M(\overline{1S}) = 1058 \pm 13^{+24}_{-0}$ MeV and $2M(\overline{B}_s) - M(\overline{1S}) = 1359 \pm 304^{+31}_{-0}$ MeV, with the uncertainty in r_1 yielding the second error bar. The bottomonium extrapolation agrees with the experimental value, but the combined statistical and κ -tuning errors are quite large. The charmonium extrapolation is 1σ shy of the experimental value. Given the empirical nature of our continuum extrapolation, this is completely satisfactory.

E. Summary of spectrum results

To summarize our results, Fig. 17 shows the charmonium and the bottomonium spectra as splittings from the $\overline{1S}$ level and compares them to the experimental results. We have plotted the chirally extrapolated values at each lattice spacing and included statistical, κ -tuning, and r_1 uncertainties. Solid lines show the experimental values, where they are known, and dashed lines show estimates from potential models [54] in other cases.

For the splittings discussed above, Table IX shows the continuum limit, taken via linear extrapolations in a^2 . One should bear in mind that the NRQCD-based theory of cutoff effects, explained in Sec. II C, anticipates a less trivial lattice-spacing dependence. The linear-in- a^2 extrapolations are consistent with the data, which are not yet sufficient to resolve more complicated functional forms. In Table IX the second (asymmetric) error bar comes from the conversion to MeV with $r_1 = 0.318^{+0}_{-0.007}$ fm = $1.611^{+0}_{-0.035}$ GeV $^{-1}$ [33, 34, 35].

TABLE IX: Continuum extrapolations of splittings in charmonium and bottomonium in MeV. The first error comes from statistics and accumulated extrapolation systematics; the second comes from the uncertainty in scale setting with $r_1 = 0.318^{+0.000}_{-0.007}$ fm.

Splitting	Charmonium		Bottomonium	
	This work	Experiment	This work	Experiment
$1P\text{-}1S$	$473 \pm 12^{+10}_{-0}$	457.5 ± 0.3	$446 \pm 18^{+10}_{-0}$	456.9 ± 0.8
$1P_1\text{-}1S$	$469 \pm 11^{+10}_{-0}$	457.9 ± 0.4	$440 \pm 17^{+10}_{-0}$	—
$2S\text{-}1S$	$792 \pm 42^{+17}_{-0}$	606 ± 1	$599 \pm 36^{+13}_{-0}$	$(580.3 \pm 0.8)^a$
$1^3S_1\text{-}1^1S_0$	$116.0 \pm 7.4^{+2.6}_{-0}$	116.4 ± 1.2	$54.0 \pm 12.4^{+1.2}_{-0}$	69.4 ± 2.8
$1P$ tensor	$15.0 \pm 2.3^{+0.3}_{-0}$	16.25 ± 0.07	$4.5 \pm 2.2^{+0.1}_{-0}$	5.25 ± 0.13
$1P$ spin-orbit	$43.3 \pm 6.6^{+1.0}_{-0}$	46.61 ± 0.09	$16.9 \pm 7.0^{+0.4}_{-0}$	18.2 ± 0.2
$1S\text{ } \bar{s}Q\text{-}\bar{Q}Q$	$1058 \pm 13^{+24}_{-0}$	1084.8 ± 0.8	$1359 \pm 304^{+31}_{-0}$	1363.3 ± 2.2

^a $\Upsilon(2S)\text{-}\overline{1S}$ instead of $\overline{2S}\text{-}\overline{1S}$.

The charmonium and bottomonium spectra by and large show good agreement with experiment. The charmonium hyperfine splitting agrees very well; the bottomonium splitting agrees at 1.2σ . The tensor and spin-orbit splittings also agree well, for both systems. The $1P_1\text{-}1S$ and $1P\text{-}1S$ spin-averaged splittings agree at $1.1\text{-}1.3\sigma$ for $\bar{c}c$; the $1P\text{-}1S$ at 0.6σ for $\bar{b}b$. As discussed above, the charmonium $2S$ states are too high, because our operator basis and statistics proved to be insufficient to disentangle the bound states from open-charm threshold effects. For bottomonium the $\overline{2S}\text{-}\overline{1S}$ splitting does not suffer from threshold effects and agrees well. When the r_1 uncertainty is included, the splitting of quarkonium relative to the heavy-strange spectrum, $2M(\overline{D}_s) - M(\overline{1S})$ and $2M(\overline{B}_s) - M(\overline{1S})$, also agrees well with experiment.

V. CONCLUSIONS

Quarkonium properties offer an excellent test of lattice QCD, because they are relatively well-understood hadrons, via potential models and effective field theories. This paper attempts a thorough study of the charmonium and bottomonium mass splittings, using lattice gauge fields with 2+1 flavors of sea quarks. By using the Fermilab method for heavy quarks, we are able to study both systems, as well as heavy-light hadrons, with the same basic theoretical tool. By using the MILC ensembles, we are able to study a wide range of lattice spacing, and a wide range of up and down sea-quark masses, down to $0.10m_s$.

Our aim here has been to develop methods and to compare discretization effects against expectations that are gleaned from an effective theory analysis. An important technical finding for ground P states is that nonrelativistic operators are superior to relativistic operators in overlap and, hence, statistics.

Our calculations reproduce most features of the mass splittings, to the extent expected. This optimistic conclusion is marred somewhat, because we find that the errors

from κ tuning are significant for spin-dependent splittings. Agreement with experiment is found only when these uncertainties, which stem from the heavy-strange kinetic mass, are taken into account. In some other cases, such as leptonic decay constants for heavy-light mesons [11], uncertainties in κ also influence significantly the final error budget.

In the continuation of this project, we hope to improve on the results presented here in several ways. First, the MILC ensembles now contain approximately four times as many configurations, and they extend to smaller lattice spacings, $a \approx 0.06$ fm and $a \approx 0.045$ fm. The finer lattice will bring charm into the region where Symanzik-motivated continuum extrapolations are justified and should bring bottomonium discretization effects under 1%. To this end it may also prove worthwhile to incorporate the p^4 corrections of the improved Fermilab action [51]. Higher statistics and twisted-boundary conditions [57] should improve the tuning of κ and, thus, reduce errors from this source as well.

Acknowledgments

Computations for this work were carried out on facilities of the USQCD Collaboration, which are funded by the Office of Science of the U.S. Department of Energy. This work was supported in part by the U.S. Department of Energy under Grants No. DE-FC02-06ER41446 (T.B., C.D., L.L.), No. DE-FG02-91ER40661 (S.G.), No. DE-FG02-91ER40677 (A.X.K.), No. DE-FG02-91ER40628 (E.D.F.); by the National Science Foundation under Grants No. PHY-0555243, No. PHY-0757333, No. PHY-0703296 (T.B., C.D., L.L.), and No. PHY-0555235 (E.D.F.); and by the M. Hildred Blewett Scholarship of the American Physical Society (E.D.F.). Fermilab is operated by Fermi Research Alliance, LLC, under Contract No. DE-AC02-07CH11359 with the U.S. Department of Energy.

[1] C. Quigg and J. L. Rosner, Phys. Rept. **56**, 167 (1979).

[2] W. Kwong, J. L. Rosner, and C. Quigg, Ann. Rev. Nucl.

- Part. Sci. **37**, 325 (1987).
- [3] G. P. Lepage and B. A. Thacker, Nucl. Phys. Proc. Suppl. **4**, 199 (1988); B. A. Thacker and G. P. Lepage, Phys. Rev. D **43**, 196 (1991).
- [4] G. P. Lepage, L. Magnea, C. Nakhleh, U. Magnea, and K. Hornbostel, Phys. Rev. D **46**, 4052 (1992) [arXiv:hep-lat/9205007].
- [5] A. X. El-Khadra, A. S. Kronfeld, and P. B. Mackenzie, Phys. Rev. D **55**, 3933 (1997) [arXiv:hep-lat/9604004].
- [6] C. Aubin *et al.* [MILC Collaboration], Phys. Rev. D **70**, 094505 (2004) [arXiv:hep-lat/0402030]; C. W. Bernard *et al.* [MILC Collaboration], Phys. Rev. D **64**, 054506 (2001) [arXiv:hep-lat/0104002].
- [7] M. Di Pierro *et al.*, Nucl. Phys. Proc. Suppl. **119**, 586 (2003) [arXiv:hep-lat/0210051]; Nucl. Phys. Proc. Suppl. **129**, 340 (2004) [arXiv:hep-lat/0310042]; S. Gottlieb *et al.*, PoS **LAT2005**, 203 (2006) [arXiv:hep-lat/0510072]; PoS **LAT2006**, 175 (2006) [arXiv:0910.0048 [hep-lat]].
- [8] A. X. El-Khadra, S. A. Gottlieb, A. S. Kronfeld, P. B. Mackenzie, and J. N. Simone, Nucl. Phys. Proc. Suppl. **83**, 283 (2000).
- [9] C. Bernard *et al.* [Fermilab Lattice and MILC Collaborations], in preparation.
- [10] C. Aubin *et al.* [Fermilab Lattice and MILC Collaborations], Phys. Rev. Lett. **94**, 011601 (2005) [arXiv:hep-ph/0408306]; C. Bernard *et al.* [Fermilab Lattice and MILC Collaborations], Phys. Rev. D **79**, 014506 (2009) [arXiv:0808.2519 [hep-lat]]; J. A. Bailey *et al.* [Fermilab Lattice and MILC Collaborations], Phys. Rev. D **79**, 054507 (2009) [arXiv:0811.3640 [hep-lat]]; C. Bernard *et al.* [Fermilab Lattice and MILC Collaborations], Phys. Rev. D **80**, 034026 (2009) [arXiv:0906.2498 [hep-lat]].
- [11] C. Aubin *et al.* [Fermilab Lattice and MILC Collaborations], Phys. Rev. Lett. **95**, 122002 (2005) [arXiv:hep-lat/0506030]; C. Bernard *et al.* [Fermilab Lattice and MILC Collaborations], PoS **LATTICE 2008**, 278 (2008) [arXiv:0904.1895 [hep-lat]]; A. Bazavov *et al.* [Fermilab Lattice and MILC Collaborations], PoS **LATTICE 2009**, 249 (2009).
- [12] R. T. Evans *et al.* [Fermilab Lattice and MILC Collaborations], PoS **LAT2006**, 081 (2006); PoS **LATTICE 2007**, 354 (2007); [arXiv:0710.2880 [hep-lat]]; PoS **LATTICE 2008**, 052 (2008).
- [13] G. S. Bali, Phys. Rept. **343**, 1 (2001) [arXiv:hep-ph/0001312].
- [14] J. J. Dudek and R. G. Edwards, Phys. Rev. Lett. **97**, 172001 (2006) [arXiv:hep-ph/0607140].
- [15] J. J. Dudek, R. G. Edwards, and D. G. Richards, Phys. Rev. D **73**, 074507 (2006) [arXiv:hep-ph/0601137]. J. J. Dudek, R. Edwards, and C. E. Thomas [Hadron Spectrum Collaboration], Phys. Rev. D **79**, 094504 (2009) [arXiv:0902.2241 [hep-ph]].
- [16] J. J. Dudek, R. G. Edwards, N. Mathur, and D. G. Richards, Phys. Rev. D **77**, 034501 (2008) [arXiv:0707.4162 [hep-lat]].
- [17] S. Meinel, Phys. Rev. D **79**, 094501 (2009) [arXiv:0903.3224 [hep-lat]].
- [18] C. T. H. Davies *et al.* [HPQCD, MILC and Fermilab Lattice Collaborations], Phys. Rev. Lett. **92**, 022001 (2004) [arXiv:hep-lat/0304004].
- [19] A. Gray *et al.* [HPQCD Collaboration], Phys. Rev. D **72**, 094507 (2005) [arXiv:hep-lat/0507013].
- [20] E. Follana *et al.* [HPQCD Collaboration and UKQCD Collaboration], Phys. Rev. D **75**, 054502 (2007) [arXiv:hep-lat/0610092].
- [21] C. McNeile, C. T. H. Davies, E. Follana, K. Hornbostel, G. P. Lepage, and J. Shigemitsu [HPQCD Collaboration], arXiv:0910.2921 [hep-lat].
- [22] I. F. Allison, C. T. H. Davies, A. Gray, A. S. Kronfeld, P. B. Mackenzie, and J. N. Simone [HPQCD and Fermilab Lattice Collaborations], Phys. Rev. Lett. **94**, 172001 (2005) [arXiv:hep-lat/0411027].
- [23] E. B. Gregory *et al.* [HPQCD Collaboration], arXiv:0909.4462 [hep-lat].
- [24] C. Amsler *et al.* [Particle Data Group], Phys. Lett. B **667**, 1 (2008) and 2009 update at <http://pdg.lbl.gov/>.
- [25] E. Eichten and F. Feinberg, Phys. Rev. D **23**, 2724 (1981).
- [26] M. E. Peskin, “Aspects of the dynamics of heavy quark systems,” SLAC-PUB-3273 (1983).
- [27] S. A. Gottlieb, W. Liu, D. Toussaint, R. L. Renken, and R. L. Sugar, Phys. Rev. D **35**, 2531 (1987).
- [28] M. Lüscher and P. Weisz, Phys. Lett. B **158**, 250 (1985); P. Weisz, Nucl. Phys. B **212**, 1 (1983). P. Weisz and R. Wohlert, Nucl. Phys. B **236**, 397 (1984); **247**, 544(E) (1984); G. Curci, P. Menotti and G. Paffuti, Phys. Lett. B **130**, 205 (1983); **135**, 516(E) (1984); M. Lüscher and P. Weisz, Commun. Math. Phys. **97**, 59 (1985); **98**, 433(E) (1985).
- [29] K. Orginos and D. Toussaint [MILC Collaboration], Phys. Rev. D **59**, 014501 (1999) [arXiv:hep-lat/9805009]; J. F. Lagaë and D. K. Sinclair, Phys. Rev. D **59**, 014511 (1999) [arXiv:hep-lat/9806014]; D. Toussaint and K. Orginos [MILC Collaboration], Nucl. Phys. Proc. Suppl. **73**, 909 (1999) [arXiv:hep-lat/9809148]; G. P. Lepage, Phys. Rev. D **59**, 074502 (1999) [arXiv:hep-lat/9809157]; K. Orginos, R. Sugar, and D. Toussaint, Nucl. Phys. Proc. Suppl. **83**, 878 (2000) [arXiv:hep-lat/9909087].
- [30] Z. Hao, G.M. von Hippel, R.R. Horgan, Q.J. Mason, and H.D. Trottier, Phys. Rev. D **76** (2007) 034507 [arXiv:0705.4660 [hep-lat]].
- [31] R. Sommer, Nucl. Phys. B **411**, 839 (1994) [arXiv:hep-lat/9310022].
- [32] C. W. Bernard *et al.*, Phys. Rev. D **62**, 034503 (2000) [arXiv:hep-lat/0002028].
- [33] A. Bazavov *et al.*, arXiv:0903.3598 [hep-lat].
- [34] A. Bazavov *et al.* [MILC Collaboration], PoS **CD09** (2009) 007 [arXiv:0910.2966 [hep-ph]]; PoS **LATTICE 2009** (2009) 079 [arXiv:0910.3618 [hep-lat]].
- [35] C. T. H. Davies, E. Follana, I. D. Kendall, G. P. Lepage, and C. McNeile [HPQCD Collaboration], arXiv:0910.1229 [hep-lat].
- [36] K. G. Wilson, in *New Phenomena in Subnuclear Physics*, edited by A. Zichichi (Plenum, New York, 1977).
- [37] B. Sheikholeslami and R. Wohlert, Nucl. Phys. B **259**, 572 (1985).
- [38] B. P. G. Mertens, A. S. Kronfeld, and A. X. El-Khadra, Phys. Rev. D **58**, 034505 (1998) [arXiv:hep-lat/9712024].
- [39] A. S. Kronfeld, Phys. Rev. D **62**, 014505 (2000) [arXiv:hep-lat/0002008].
- [40] J. Harada, S. Hashimoto, K.-I. Ishikawa, A. S. Kronfeld, T. Onogi, and N. Yamada, Phys. Rev. D **65**, 094513 (2002) [arXiv:hep-lat/0112044]; **71**, 019903(E) (2005).
- [41] J. Harada, S. Hashimoto, A. S. Kronfeld, and T. Onogi, Phys. Rev. D **65**, 094514 (2002) [arXiv:hep-lat/0112045].
- [42] W. E. Caswell and G. P. Lepage, Phys. Lett. B **167**, 437 (1986).

- [43] G. T. Bodwin, E. Braaten, and G. P. Lepage, Phys. Rev. D **46**, 1914 (1992) [hep-lat/9205006].
- [44] H. W. Lin and N. Christ, Phys. Rev. D **76**, 074506 (2007) [arXiv:hep-lat/0608005].
- [45] G. P. Lepage and P. B. Mackenzie, Phys. Rev. D **48**, 2250 (1993) [arXiv:hep-lat/9209022].
- [46] N. H. Christ, M. Li, and H. W. Lin, Phys. Rev. D **76**, 074505 (2007) [arXiv:hep-lat/0608006].
- [47] C. T. H. Davies, K. Hornbostel, A. Langnau, G. P. Lepage, A. Lidsey, J. Shigemitsu, and J. H. Sloan, Phys. Rev. D **50**, 6963 (1994) [arXiv:hep-lat/9406017].
- [48] B. Aubert *et al.* [BaBar Collaboration], Phys. Rev. Lett. **101**, 071801 (2008) [arXiv:0807.1086 [hep-ex]].
- [49] B. Aubert *et al.* [BaBar Collaboration], Phys. Rev. Lett. **103**, 161801 (2009) [arXiv:0903.1124 [hep-ex]].
- [50] G. Bonvicini *et al.* [CLEO Collaboration], arXiv:0909.5474 [hep-ex].
- [51] M. B. Oktay and A. S. Kronfeld, Phys. Rev. D **78**, 014504 (2008) [arXiv:0803.0523 [hep-lat]].
- [52] A. S. Kronfeld, Nucl. Phys. Proc. Suppl. **53**, 401 (1997) [arXiv:hep-lat/9608139].
- [53] J. L. Richardson, Phys. Lett. B **82**, 272 (1979).
- [54] W. Buchmüller and S.-H. H. Tye, Phys. Rev. D **24**, 132 (1981).
- [55] A. X. El-Khadra, Nucl. Phys. Proc. Suppl. **30**, 449 (1993) [arXiv:hep-lat/9211046].
- [56] M. Nobes and H. Trottier, PoS **LAT2005**, 209 (2006) [arXiv:hep-lat/0509128].
- [57] P. F. Bedaque, Phys. Lett. B **593**, 82 (2004) [arXiv:nucl-th/0402051]; C. T. Sachrajda and G. Villadoro, Phys. Lett. B **609**, 73 (2005) [arXiv:hep-lat/0411033].

The D_s and D^+ Leptonic Decay Constants from Lattice QCD

Fermilab Lattice and MILC Collaborations

A. Bazavov^a, C. Bernard^{b*}, C. DeTar^c, E.D. Freeland^b, E. Gamiz^{d,e}, Steven Gottlieb^{f,g}, U.M. Heller^h, J.E. Hetrickⁱ, A.X. El-Khadra^d, A.S. Kronfeld^e, J. Laiho^b, L. Levkova^c, P.B. Mackenzie^e, M.B. Oktay^c, M. Di Pierro^j, J.N. Simone^{†‡}, R. Sugar^k, D. Toussaint^a, and R.S. Van de Water^l

^aDepartment of Physics, University of Arizona, Tucson, Arizona, USA

^bDepartment of Physics, Washington University, St. Louis, Missouri, USA

^cPhysics Department, University of Utah, Salt Lake City, Utah, USA

^dPhysics Department, University of Illinois, Urbana, Illinois, USA

^eFermi National Accelerator Laboratory, Batavia, Illinois, USA

^fDepartment of Physics, Indiana University, Bloomington, Indiana, USA

^gNational Center for Supercomputing Applications, University of Illinois, Urbana, Illinois, USA

^hAmerican Physical Society, One Research Road, Box 9000, Ridge, New York, USA

ⁱPhysics Department, University of the Pacific, Stockton, California, USA

^jSchool of Computer Sci., Telecom. and Info. Systems, DePaul University, Chicago, Illinois, USA

^kDepartment of Physics, University of California, Santa Barbara, California, USA

^lPhysics Department, Brookhaven National Laboratory, Upton New York, USA

We present the leptonic decay constants f_{D_s} and f_{D^+} computed on the MILC collaboration's 2 + 1 flavor asqtad gauge ensembles. We use clover heavy quarks with the Fermilab interpretation and improved staggered light quarks. The simultaneous chiral and continuum extrapolation, which determines both decay constants, includes partially-quenched lattice results at lattice spacings $a \approx 0.09, 0.12$ and 0.15 fm. We have made several recent improvements in our analysis: a) we include terms in the fit describing leading order heavy-quark discretization effects, b) we have adopted a more precise input r_1 value consistent with our other D and B meson studies, c) we have retuned the input bare charm masses based upon the new r_1 . Our preliminary results are $f_{D_s} = 260 \pm 10$ MeV and $f_{D^+} = 217 \pm 10$ MeV.

The XXVII International Symposium on Lattice Field Theory - LAT2009

July 26-31 2009

Peking University, Beijing, China

*cb@lump.wustl.edu

†Speaker.

‡simone@fnal.gov

1. Introduction

We report on progress in the Fermilab Lattice and MILC Collaboration calculation of the D meson decay constants. This work is a continuation of the program that predicted the decay constants: $f_{D^+} = 201(3)(17)$ and $f_{D_s} = 249(3)(16)$ MeV [1], in good agreement with the CLEO-c value of $f_{D^+} = 205.8 \pm 8.5 \pm 2.5$ [2, 3]. We have since extended this calculation to two additional ensembles at our finest lattice spacing $a \approx 0.09$ fm and we have replaced a limited set of very coarse ($a \approx 0.18$ fm) ensembles with higher statistic ensembles at a somewhat finer spacing $a \approx 0.15$ fm. In our last update [4] we reported: $f_{D^+} = 207(11)$ and $f_{D_s} = 249(11)$, where f_{D_s} is about 0.6σ lower than the recent experimental average [5]. The value of f_{D_s} remains an pressing issue given that experimental average is about 2.1σ higher than the most precise lattice result from the HPQCD collaboration [6]. The apparent tension between experiment and lattice predictions has motivated suggestions of physics beyond the Standard Model [7].

Smaller statistical uncertainties and better control of systematic effects are key to resolving the f_{D_s} puzzle. In this report, we have doubled statistics on the most chiral of the $a \approx 0.09$ fm lattices; otherwise, statistics have not changed. A new generation of calculations, now underway, aims to increase statistics by a factor of four overall. Our progress includes: a) a better method of accounting for heavy-quark discretization effects b) a more precise input value for the scale parameter r_1 , consistent with our other heavy quark studies and c) more precisely tuned input charm kappa values.

2. Staggered chiral perturbation theory for heavy-light mesons

We use the asqtad improved staggered action for both sea and light valence quarks. Leading discretization effects split the light pseudoscalar meson masses,

$$M_{ab,\xi}^2 = (m_a + m_b)\mu + a^2 \Delta_\xi , \quad (2.1)$$

where there are sixteen tastes in representations $\xi = P, A, T, V, I$.

Staggered chiral perturbation theory for heavy-light mesons accounts for such taste breaking effects [8]. At NLO in the chiral expansion, for $2 + 1$ flavors, and at leading order in the heavy quark expansion,

$$\phi_{H_q} = \Phi_0 [1 + \Delta f_H(m_q, m_l, m_h) + p_H(m_q, m_l, m_h) + c_L \alpha_V^2 a^2] , \quad (2.2)$$

where $\phi_{H_q} = f_{H_q} \sqrt{m_{H_q}}$ and f_{H_q} is the decay constant of a heavy meson H_q consisting of a heavy quark and a light quark of mass m_q . The heavier sea quark has mass m_h and the two degenerate light sea quarks have mass m_l . The ϕ_{H_q} , in general, are partially quenched: $m_q \neq m_l$ and $m_q \neq m_h$. The chiral logarithm terms, Δf_H , are a dependent as a consequence of the mass splittings in Eq. (2.1) as well as from ‘‘hairpin’’ terms proportional to the low energy constants $a^2 \delta'_A$ and $a^2 \delta'_V$. The a dependence of the analytic terms, p_H , ensures that ϕ_{H_q} is unchanged by a change in the chiral scale, Λ_χ , of the logarithms. The expression in Eq. (2.2) is used in our combined chiral and continuum extrapolations. In practice, we add the NNLO analytic terms to the fit function in order to extend the fit up to $m_q \sim m_s$ and extract f_{D_s} . Priors for the parameters $a^2 \delta'_A$ and $a^2 \delta'_V$ as well as values of the physical light quark masses are obtained from the MILC analysis of f_π and f_K [9].

3. Discretization effects from clover heavy quarks

We use tadpole-improved clover charm quarks. At leading order, discretization errors are a combination of $\mathcal{O}(a^2\Lambda_{HQ}^2)$ and $\mathcal{O}(\alpha a\Lambda_{HQ})$ effects where α is the QCD coupling and Λ_{HQ} is the scale in the heavy quark expansion. Our past studies have estimated heavy quark discretization effects using such power counting arguments to bound the error at the smallest lattice spacing, taking $\Lambda_{HQ} \approx 700$ MeV. This rather crude method does not effectively use the data to guide the error estimate.

This study introduces a new procedure: the leading order heavy quark discretization errors are modeled to leading order as part of the combined chiral and continuum extrapolation. At tree-level, discretization effects arise from both the quark action and the (improved) current [10, 11, 12]. We add five extra terms to Equation 2.2:

$$\Phi_0 [a^2\Lambda_{HQ}^2 \{c_E f_E(am_Q) + c_X f_X(am_Q) + c_Y f_Y(am_Q)\} + \alpha_V a\Lambda_{HQ} \{c_B f_B(am_Q) + c_3 f_3(am_Q)\}] \quad (3.1)$$

The coefficients c_E , c_X , c_Y , c_B and c_3 are additional parameters determined in the fit while the f_i are (smooth) functions of the heavy quark mass, am_Q , known at tree level. We introduce priors for the coefficients constraining them to be $\mathcal{O}(1)$ while setting $\Lambda_{HQ} = 700$ MeV and $m_c \sim 1.2$ GeV. Currently the data are too noisy and the shapes of the functions f_i are too similar for the fit to prefer a particular Λ_{HQ} . Including the heavy-quark discretization terms increases the decay constants by a few MeV and increases the error from $\sim 1.8\%$ to $\sim 3.8\%$. The larger error now includes the residual heavy-quark discretization uncertainty in addition to residual light-quark discretization effects (encoded in Eq. (2.2)) as well as statistical errors. We quote a combined uncertainty from all the three sources of error.

4. Lattice spacing determination from r_1

The distance r_1 is a property of the QCD potential between heavy quarks. The ratio r_1/a , for lattice spacing a , has been computed for all of the MILC gauge ensembles. At intermediate stages of the decay constant analysis quantities are converted from lattice units to r_1 units using r_1/a . The value of r_1 must then be input in order to convert results to physical units. The r_1 value is also an input to the process of determining other quantities such as the bare charm quark masses as discussed in the next section.

Figure 1 depicts several r_1 determinations. The first two determinations historically (circa 2004–2005) are labeled “HPQCD $\Upsilon(2S-1S)$ ” [13] and “MILC $\Upsilon(2S-1S)$ ” [14]. They are both based on the same analysis of the Υ spectrum by the HPQCD Collaboration using a subset of the current MILC ensembles. The two determinations differ mainly in the details of the continuum extrapolation. The MILC Collaboration is also able to infer a value of r_1 based on the value of f_π they find in their analysis of the light mesons. Recent light-meson analyses include results from finer lattice spacings than the earlier Υ spectrum study and the resulting r_1 values are known to better precision. The figure shows the result of two recent analyses labeled ‘MILC f_π 2007’ [15] and ‘MILC f_π 2009’ [9]. The (preliminary) 2009 result agrees at the 0.9σ level with the MILC Υ value but differs from the HPQCD Υ value at the 1.8σ level. As these proceedings were being

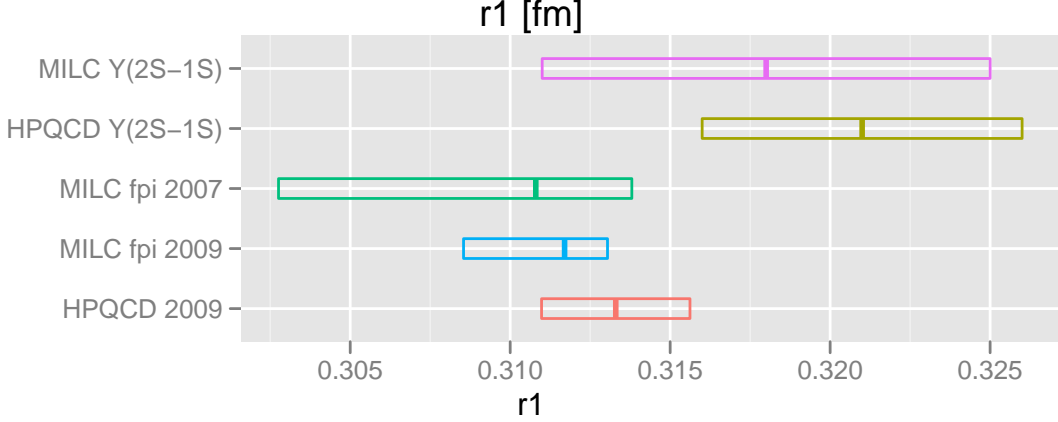


Figure 1: Values of scale parameter r_1 in fermi units. The “HPQCD $\Upsilon(2S-1S)$ ” value uses the HPQCD collaboration Υ spectrum results to set the physical value [13]. The “MILC $\Upsilon(2S-1S)$ ” value derives from essentially the same spectrum analysis [14]. MILC determines r_1 more precisely from their calculation of f_π : “MILC f_π 2007” [15] and “MILC f_π 2009” [9]. In a very recent update, “HPQCD 2009”, several physical quantities, including recent Υ results, are used as inputs [16].

r_1 [fm]:		0.3108			0.318		
a	κ run	κ tune	$\delta\phi_s$	% ϕ_s	κ tune	$\delta\phi_s$	% ϕ_s
0.09	0.127	0.1272	-0.0043	-0.56	0.1267	+0.0065	+0.84
0.12	0.122	0.1222	-0.0036	-0.50	0.1215	+0.0091	+1.26
0.15	0.122	0.1222	-0.0031	-0.42	0.1213	+0.0108	+1.47
δf_{D_s} [MeV]		-1.8			+1.3		

Table 1: Tuning of κ charm at the three lattice spacings for two choices of r_1 . The shift $\delta\phi_s$ is the change in ϕ at the strange quark mass when κ changes from the run value to tuned κ value. The corresponding change in extrapolated f_{D_s} is δf_{D_s} . In each case, all other extrapolation inputs are fixed to their appropriate (r_1 dependent) values.

prepared, HPQCD published a new value for r_1 [16], labeled “HPQCD 2009” in the figure, in much better agreement with MILC’s recent r_1 values.

In this study, we use the MILC r_1 determinations from f_π to set the physical scale. Our central value for r_1 (the 2007 value) was also used in our studies of the semileptonic decays on the same lattices [17, 18]. The range of the 2009 MILC r_1 determination is used to set a symmetric uncertainty around the central value. Hence, we take $r_1 = 0.3108 \pm 0.0022$. Our previous decay constant studies used the MILC Υ value: $r_1 = 0.318 \pm 0.007$ as an input which is about one σ higher.

5. Retuning kappa charm

We determine the value of κ for the charm quark by requiring that the spin-averaged kinetic masses of the lattice pseudoscalar and vector mesons made from a heavy clover quark and strange

source	ϕ_{D_s}	ϕ_{D^+}	R_{D^+/D_s}
statistics and discretization effects	2.6	3.4	1.3
chiral extrapolation	2.0	2.5	0.8
inputs r_1 , m_s , m_d and m_u	0.7	0.7	0.3
input m_c	1.0	1.2	0.2
Z_V^{cc} and Z_V^{qq}	1.4	1.4	0
higher-order ρ_{A_4}	0.3	0.3	0.2
finite volume	0.2	0.6	0.6
total	3.8	4.7	1.7

Table 2: Uncertainties as a percentage of ϕ and the ratio. The total combines all of the errors in quadrature.

asqtad valence quark equal the spin-averaged D_s meson mass. The tuning depends upon r_1 in the conversion between lattice and physical masses.

In the past year, we have conducted new kappa-tuning runs with at least four times the statistics of our older tunings. At each lattice spacing, we simulated mesons for three values of κ around charm and three light-quark masses around strange allowing us to retune κ for a given r_1 .

Table 1 shows preliminary tunings for κ charm based upon the two input values: $r_1 = 0.3108$ fm (present value) and $r_1 = 0.318$ fm (past studies). For each r_1 , the (preliminary) tuned kappa and the corresponding change $\delta\phi_s = \phi_s(\kappa \text{ tune}) - \phi_s(\kappa \text{ run})$ is listed by lattice spacing. The “run” kappa values are those used in the decay constant simulations. We adjust each ϕ_q point by $\delta\phi_s$ prior to the chiral extrapolation to correct for the mistuning of kappa. The bottom row of the table shows the resulting change in f_{D_s} . The opposite signs of the differences show that keeping kappa tuned partly compensates the change in r_1 . We find that changing r_1 from 0.318 fm to 0.3108 fm while keeping kappa charm tuned increases f_{D_s} by about 4.2 MeV.

6. The chiral and continuum extrapolation, results and uncertainty budget

We fit ϕ_{D_q} results from lattice simulations on eleven asqtad MILC ensembles [14] at the three lattice spacings: $a \approx 0.09, 0.12$ and 0.15 fm. Our valence quark masses are in the range $0.1m_s \leq m_q \lesssim m_s$. Since our last report, we have doubled the statistics at the most chiral of the $a \approx 0.09$ ensembles. The 3×4 panel of plots at the top in Fig. 2 shows the ϕ_{D_q} points and the fit where the fit function includes the lattice-spacing effects described in Sections 2 and 3. The plot at the bottom of Fig. 2 shows the extrapolations in the limit $a = 0$. The upper (D_s) curve shows $m_l \rightarrow \hat{m}$ setting $m_q = m_h = m_s$, while the lower (D^+) curve shows $m_q, m_l \rightarrow \hat{m}$ setting $m_h = m_s$. The physical quark mass inputs are from the MILC light meson analysis and $\hat{m} = (m_u + m_d)/2$. The points denoted by the red triangles correspond to physical f_{D_s} and f_{D^+} . Our preliminary results are:

$$f_{D^+} = 217 \pm 10 \text{ MeV}, \quad f_{D_s} = 260 \pm 10 \text{ MeV} \quad \text{and} \quad f_{D_s}/f_{D^+} = 1.20 \pm 0.02. \quad (6.1)$$

We have combined the statistical and the systematic uncertainties listed in Table 2 in quadrature. Our largest uncertainty is the combined uncertainty from statistical and residual discretization effects. The second largest uncertainty, chiral extrapolation, is an estimate of chiral expansion effects not included in the fit function and effects from variation in the extrapolation procedure. The

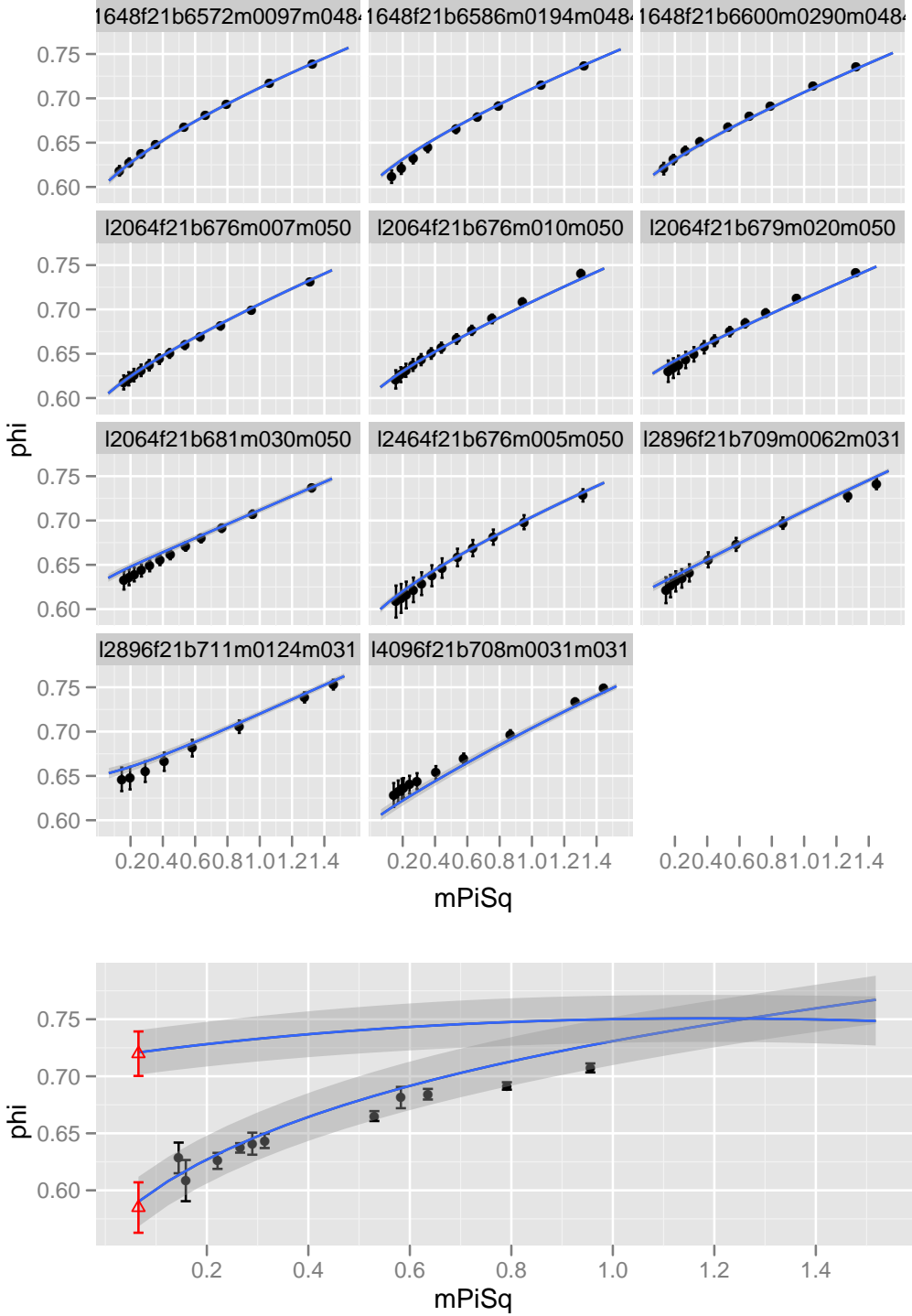


Figure 2: The preliminary D meson chiral extrapolation. The 3×4 matrix of plots (top) show the ϕ data and corresponding fit including a^2 effects. Reading from left to right and top to bottom, plots correspond to $(a, m_l/m_h)$ values of $(0.15, 0.2)$, $(0.15, 0.4)$, $(0.15, 0.6)$, $(0.12, 0.14)$, $(0.12, 0.2)$, $(0.12, 0.4)$, $(0.12, 0.6)$, $(0.12, 0.1)$, $(0.09, 0.2)$, $(0.09, 0.4)$ and $(0.09, 0.1)$. The larger plot (bottom) shows an overlay of the f_{D_s} and f_{D^+} extrapolations. The extrapolated curves are the fit (with error bands) taking $a^2 \rightarrow 0$ and fixing/extrapolating the light quarks to their physical masses. The extrapolations are not expected to go through any of the points which are computed at finite a . None of the data points having m_q near m_s seen the upper panel are visible in the D_s extrapolation.

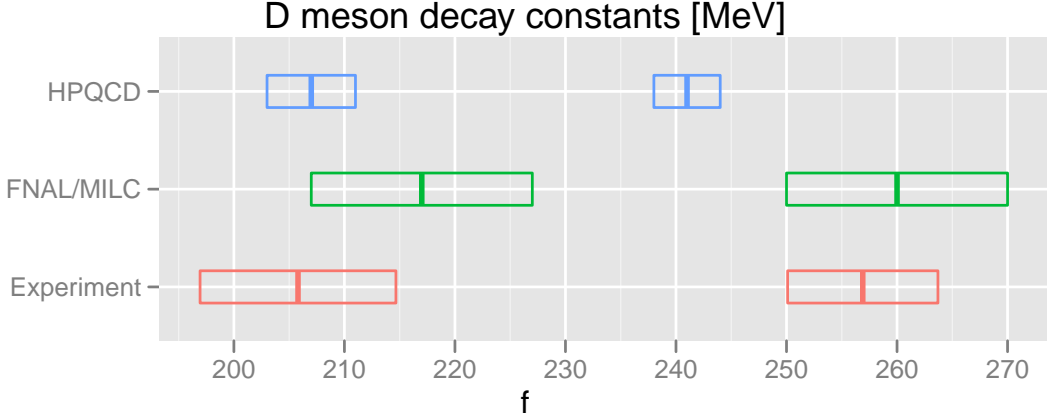


Figure 3: Comparisons of the Fermilab/MILC values of f_{D^+} and f_{D_s} to values from the HPQCD Collaboration [6] and recent experimental values [3][5].

third largest error is the statistical error in the nonperturbative calculation of the current renormalizations Z_V^{cc} and Z_V^{qq} . The value of f_{D_s} is about eleven MeV (one sigma) higher than our earlier value. Using nominal kappa values rather than tuned values at the previous r_1 value accounts for about 1.3 MeV of the difference. Changing to the new r_1 while keeping kappa tuned results in a 4.2 MeV increase. Incorporating heavy quark effects into the fit increases f_{D_s} by about 2 MeV. Higher statistics on the most chiral of the $a \approx 0.09$ fm lattice increases f_{D_s} by about 1 MeV. These changes combine nonlinearly in the fit to yield the net increase.

Figure 3 compares the Fermilab and MILC Collaboration values for the decay constants with the HPQCD Collaboration [6] values and with the experimental results. The experimental result for f_{D^+} is from CLEO [3] while the f_{D_s} value is the Heavy Flavor Averaging Group average [5] of determinations by CLEO, BaBar and Belle. The Fermilab / MILC results remain in agreement with experiment. The total error on the experimental average for f_{D_s} is now smaller than our error providing a challenge for future lattice determinations. The apparent discrepancy between the HPQCD value of f_{D_s} and the other two f_{D_s} values is most striking. The HPQCD value is lower by about $1.8\text{--}2.1\sigma$. The source of this difference may be clarified by further lattice simulations.

7. Summary and future plans

We have made several improvements in our analysis: a) discretization effects from both heavy and light quarks are modeled in our extrapolation function, b) we adopted a more precise r_1 value which derived from the MILC f_π analysis rather than the r_1 value related to early Υ spectrum results c) we have improved the tuning of kappa charm. These improvements to the analysis will be more crucial in our next generation of decay constant study. We will increase statistics by a factor of four and extend the analysis to the finer lattice spacings $a \approx 0.06$ and 0.045 fm which will reduce our combined statistical plus discretization error as well as help reduce uncertainties attributed to chiral extrapolation procedures. In addition, a new high-statistics computation of the nonperturbative part of the current renormalization aims for an error below the 0.5% level.

References

- [1] C. Aubin *et al.*, *Charmed meson decay constants in three-flavor lattice QCD*, *Phys. Rev. Lett.* **95** (2005) 122002, [[hep-lat/0506030](#)].
- [2] **CLEO** Collaboration, M. Artuso *et al.*, *Improved Measurement of $\mathcal{B}(D^+ \rightarrow \mu^+ \nu)$ and the Pseudoscalar Decay Constant f_{D^+}* , *Phys. Rev. Lett.* **95** (2005) 251801, [[hep-ex/0508057](#)].
- [3] **CLEO** Collaboration, B. I. Eisenstein *et al.*, *Precision Measurement of $\mathcal{B}(D^+ \rightarrow \mu^+ \nu)$ and the Pseudoscalar Decay Constant f_{D^+}* , *Phys. Rev.* **D78** (2008) 052003, [[0806.2112](#)].
- [4] C. Bernard *et al.*, *B and D Meson Decay Constants*, *PoS LATTICE2008* (2008) 278, [[0904.1895](#)].
- [5] H. F. A. G. C. Physics), “ f_{D_s} world average.” www.slac.stanford.edu/xorg/hfag/charm/PIC09/f_ds/results.html, 2009.
- [6] **HPQCD** Collaboration, E. Follana, C. T. H. Davies, G. P. Lepage, and J. Shigemitsu, *High Precision determination of the π , K , D and D_s decay constants from lattice QCD*, *Phys. Rev. Lett.* **100** (2008) 062002, [[0706.1726](#)].
- [7] B. A. Dobrescu and A. S. Kronfeld, *Accumulating evidence for nonstandard leptonic decays of D_s mesons*, *Phys. Rev. Lett.* **100** (2008) 241802, [[0803.0512](#)].
- [8] C. Aubin and C. Bernard, *Staggered chiral perturbation theory for heavy-light mesons*, *Phys. Rev.* **D73** (2006) 014515, [[hep-lat/0510088](#)].
- [9] **The MILC** Collaboration, A. Bazavov *et al.*, *Results from the MILC collaboration’s SU(3) chiral perturbation theory analysis*, *PoS LAT2009* (2009) 079, [[0910.3618](#)].
- [10] A. S. Kronfeld, *Application of heavy-quark effective theory to lattice QCD. I: Power corrections*, *Phys. Rev.* **D62** (2000) 014505, [[hep-lat/0002008](#)].
- [11] J. Harada *et al.*, *Application of heavy-quark effective theory to lattice QCD. II: Radiative corrections to heavy-light currents*, *Phys. Rev.* **D65** (2002) 094513, [[hep-lat/0112044](#)].
- [12] M. B. Oktay and A. S. Kronfeld, *New lattice action for heavy quarks*, *Phys. Rev.* **D78** (2008) 014504, [[0803.0523](#)].
- [13] A. Gray *et al.*, *The Upsilon spectrum and m_b from full lattice QCD*, *Phys. Rev.* **D72** (2005) 094507, [[hep-lat/0507013](#)].
- [14] C. Aubin *et al.*, *Light hadrons with improved staggered quarks: Approaching the continuum limit*, *Phys. Rev.* **D70** (2004) 094505, [[hep-lat/0402030](#)].
- [15] C. Bernard *et al.*, *Status of the MILC light pseudoscalar meson project*, *PoS LAT2007* (2007) 090, [[0710.1118](#)].
- [16] C. T. H. Davies, E. Follana, I. D. Kendall, G. P. Lepage, and C. McNeile, *Precise determination of the lattice spacing in full lattice QCD*, [`0910.1229`](#).
- [17] C. Bernard *et al.*, *The $\bar{B} \rightarrow D^* \ell \bar{\nu}$ form factor at zero recoil from three-flavor lattice QCD: A Model independent determination of $|V_{cb}|$* , *Phys. Rev.* **D79** (2009) 014506, [[0808.2519](#)].
- [18] J. A. Bailey *et al.*, *The $B \rightarrow \pi \ell \bar{\nu}$ semileptonic form factor from three-flavor lattice QCD: A Model-independent determination of $|V_{ub}|$* , *Phys. Rev.* **D79** (2009) 054507, [[0811.3640](#)].

Tuning Fermilab Heavy Quarks in 2+1 Flavor Lattice QCD with Application to Hyperfine Splittings

C. Bernard,¹ C. DeTar,² M. Di Pierro,³ A.X. El-Khadra,⁴ R.T. Evans,^{4,5} E.D. Freeland,^{1,*}
E. Gámiz,^{4,6} Steven Gottlieb,^{7,8} U.M. Heller,⁹ J.E. Hetrick,¹⁰ A.S. Kronfeld,⁶ J. Laiho,^{1,11}
L. Levkova,² P.B. Mackenzie,⁶ J.N. Simone,⁶ R. Sugar,¹² D. Toussaint,¹³ and R.S. Van de Water¹⁴
(Fermilab Lattice and MILC Collaborations)

¹*Department of Physics, Washington University, St. Louis, Missouri 63130, USA*

²*Physics Department, University of Utah, Salt Lake City, Utah 84112, USA*

³*School of Computing, DePaul University, Chicago, Illinois 60604, USA*

⁴*Physics Department, University of Illinois, Urbana, Illinois 61801, USA*

⁵*Institut für Theoretische Physik, Universität Regensburg, 93040 Regensburg, Germany*

⁶*Fermi National Accelerator Laboratory, Batavia, Illinois 60510, USA*

⁷*Department of Physics, Indiana University, Bloomington, Indiana 47405, USA*

⁸*National Center for Supercomputing Applications, University of Illinois, Urbana 61801, Illinois, USA*

⁹*American Physical Society, One Research Road, Ridge, New York 11961, USA*

¹⁰*Physics Department, University of the Pacific, Stockton, California 95211, USA*

¹¹*Department of Physics and Astronomy, University of Glasgow, Glasgow, Scotland, UK*

¹²*Department of Physics, University of California, Santa Barbara, California 93106, USA*

¹³*Department of Physics, University of Arizona, Tucson, Arizona 85721, USA*

¹⁴*Physics Department, Brookhaven National Laboratory, Upton, New York 11973, USA*

(Dated: February 23, 2011)

We report the non-perturbative tuning of parameters— κ_c , κ_b , and κ_{crit} —that are related to the bare heavy-quark mass in the Fermilab action. This requires the computation of the masses of $D_s^{(*)}$ and $B_s^{(*)}$ mesons comprised of a Fermilab heavy quark and a staggered light quark. Additionally, we report the hyperfine splittings for $D_s^{(*)}$ and $B_s^{(*)}$ mesons as a cross-check of our simulation and analysis methods. We find a splitting of 145 ± 15 MeV for the D_s system and 40 ± 9 MeV for the B_s system. These are in good agreement with the Particle Data Group average values of 143.9 ± 0.4 MeV and 46.1 ± 1.5 MeV, respectively. The calculations are carried out with the MILC 2+1 flavor gauge configurations at three lattice spacings $a \approx 0.15, 0.12$ and 0.09 fm.

I. INTRODUCTION

Lattice QCD calculations play a critical role in the study of standard model physics and the search for new physics. For a set of lattice QCD calculations to be viable, several basic tasks are necessary. The bare gauge coupling must be eliminated in favor of an observable allowing the conversion from lattice to physical units; the bare masses in the lattice action must be tuned to correspond to physical quarks; and experimentally established quantities must be calculated in order to substantiate the method’s accuracy and reliability. Once these tasks are complete, a variety of quantities inaccessible to or not yet determined by experiment may be calculated, such as decay constants, form factors, and mass spectra.

The Fermilab Lattice and MILC Collaborations have reported several calculations [1–8] based on ensembles of lattice gauge fields with 2+1 flavors of sea quarks, generated by the MILC Collaboration [9, 10]. Details of the scale setting can be found in Refs. [11, 12], and details of the light-quark mass tuning in Ref. [11]. In this paper, we report on the necessary tuning of the heavy-quark action for charmed and bottom quarks. In particular, we describe calculations of the heavy-light pseudoscalar and vector meson masses using, for light quarks, the asqtad staggered action [13] and, for heavy quarks, the Fermilab interpretation [14] of the Sheikholeslami-Wohlert (“clover”) action [15] for Wilson fermions [16]. We use the spin-average of these meson masses to nonperturbatively tune the hopping parameter κ , which is equivalent to the bare heavy-quark mass. We also describe the determination of κ_{crit} , the value of κ for which a degenerate Wilson pseudoscalar’s mass vanishes. The value of κ_{crit} plays a minor role in the calculation of heavy-light matrix elements [3–5], and a more important role when determining a renormalized quark mass [6]. Finally, as a by-product of these calculations, we report the spin-dependent hyperfine splittings for B_s and D_s mesons, which test how well we have improved the chromomagnetic interaction.

Two aspects of the Fermilab method are important here. First, the Fermilab interpretation makes no assumptions about the size of the quark mass. Therefore, we are able to treat both charm and bottom quarks within the same framework. Second, since the Sheikholeslami-Wohlert action maintains the spin and flavor symmetries of heavy quarks, heavy-quark effective theory (HQET) can be used to interpret and improve lattice discretization effects [17, 18]. HQET techniques can be used to show

*eliz@fnal.gov

how the improvement works for observables, such as meson masses, in a way simpler than, though equivalent to, the Symanzik improvement program [19].

This paper is organized as follows. Section II reviews the theoretical framework upon which these calculations are based. Section III contains specific descriptions of the gauge configurations, actions, and operators used for the meson masses. Section IV covers the components of the numerical analysis. Section V details the fitting procedures. Section VI presents the results for the non-perturbative tuning of the heavy-quark hopping parameters κ_c and κ_b , the hyperfine splitting, and the critical hopping parameter κ_{crit} . Section VII summarizes with a discussion of improvements to these calculations that are currently underway. Details of the meson-mass discretization error estimation are given in Appendix A. Appendices B and C tabulate intermediate numerical results. The partially quenched chiral perturbation theory expression for the hyperfine splitting is derived in Appendix D.

II. THEORETICAL BACKGROUND

The hopping-parameter form of the heavy-quark action is [14]

$$S = S_0 + S_B + S_E, \quad (2.1)$$

where

$$S_0 = \sum_n \bar{\psi}_n \psi_n - \kappa \sum_{n,\mu} [\bar{\psi}_n (1 - \gamma_\mu) U_{n,\mu} \psi_{n+\hat{\mu}} + \bar{\psi}_{n+\hat{\mu}} (1 + \gamma_\mu) U_{n,\mu}^\dagger \psi_n], \quad (2.2)$$

$$S_B = \frac{i}{2} c_B \kappa \sum_{n;i,j,k} \epsilon_{ijk} \bar{\psi}_n \sigma_{ij} B_{n;k} \psi_n, \quad (2.3)$$

$$S_E = i c_E \kappa \sum_{n;i} \bar{\psi}_n \sigma_{0i} E_{n;i} \psi_n, \quad (2.4)$$

where $\sigma_{\mu\nu} = \frac{i}{2} [\gamma_\mu, \gamma_\nu]$. The chromomagnetic and chromoelectric fields $B_{n;i}$ and $E_{n;i}$ are standard and given in Ref. [14]. The term S_0 includes dimension-five terms to alleviate the fermion doubling problem [16]. The couplings c_E and c_B of the dimension-five operators in S_B and S_E are chosen to reduce discretization effects [14, 15].

The hopping parameter κ is related to the tadpole-improved bare quark mass by

$$am_0 = \frac{1}{u_0} \left(\frac{1}{2\kappa} - \frac{1}{2\kappa_{\text{crit}}} \right), \quad (2.5)$$

where a is the lattice spacing, u_0 is the tadpole-improvement factor [20], and κ_{crit} is the value of κ for which the pseudoscalar meson mass (of two degenerate Wilson quarks) vanishes. Our nonperturbative determination of κ_{crit} is discussed in Sec. VIC. To motivate our method of tuning κ , we first discuss the meson dispersion relation. We then turn to the HQET description of our Lagrangian to understand how to best use the dispersion relation.

The meson dispersion relation can be written, for $|\mathbf{p}| \ll m_0, a^{-1}$, as [14]

$$E(\mathbf{p}) = M_1 + \frac{\mathbf{p}^2}{2M_2} + O(\mathbf{p}^4). \quad (2.6)$$

Here, and throughout this work, we use lower-case m for quark masses and upper-case M for meson masses. M_1 and M_2 are known as the rest mass and kinetic mass, respectively. Because the lattice breaks Lorentz invariance, $M_1 \neq M_2$, although $M_1 \rightarrow M_2$ as $a \rightarrow 0$ for the action in Eq. (2.1). By tuning κ , one could adjust the bare, heavy-quark mass such that either M_1 or M_2 is equal to the physical meson mass. (To set $M_1 = M_2$ requires the introduction, and tuning, of an additional parameter in the action. This is possible but, as discussed below, not necessary [14].)

To clarify the role of the different masses in Eq. (2.6), it is useful to introduce an effective Lagrangian. This also sets up a language for discussing discretization errors later. Because the action in Eq. (2.1) has the same heavy-quark spin and flavor symmetries as continuum QCD, HQET is an obvious candidate for its description [17, 18]. To employ HQET, one separates the short-distance physics at the scale of the inverse heavy-quark mass $1/m_Q$ from the long-distance physics at the characteristic scale of QCD, Λ_{QCD} . The fact that we have a lattice does not change the validity or utility of this separation. It simply means that the lattice spacing a must be included in the description of the short-distance physics. Thus, the short-distance coefficients of HQET applied to Eq. (2.1) differ from those arrived at by applying HQET to continuum QCD; these differences are the heavy-quark discretization errors. Parameters in the lattice action can be chosen to minimize them.

We introduce the heavy-quark effective Lagrangian for our lattice gauge theory by writing [17, 18]

$$\mathcal{L}_{\text{LGT}} \doteq \mathcal{L}_{\text{light}} + \mathcal{L}_{\text{HQET}}, \quad (2.7)$$

where $\mathcal{L}_{\text{light}}$ is the Symanzik local effective Lagrangian for the light degrees of freedom and \doteq means the Lagrangian on the right-hand side describes the on-shell matrix elements of the Lagrangian on the left-hand side. The HQET Lagrangian has a power-counting scheme, denoted by

$$\mathcal{L}_{\text{HQET}} = \sum_s \mathcal{L}_{\text{HQET}}^{(s)}, \quad (2.8)$$

where $\mathcal{L}_{\text{HQET}}^{(s)}$ includes all operators of dimension $4 + s$, with coefficients of dimension $-s$ consisting of powers of the short distances, $1/m_Q$ or a . The first few terms in $\mathcal{L}_{\text{HQET}}$ are [17]

$$\mathcal{L}_{\text{HQET}}^{(0)} = -\bar{h}^{(+)}(D_4 + m_1)h^{(+)}, \quad (2.9)$$

$$\mathcal{L}_{\text{HQET}}^{(1)} = \bar{h}^{(+)} \frac{\mathbf{D}^2}{2m_2} h^{(+)} + \bar{h}^{(+)} \frac{i\boldsymbol{\sigma} \cdot \mathbf{B}}{2m_B} h^{(+)}, \quad (2.10)$$

$$\mathcal{L}_{\text{HQET}}^{(2)} = \bar{h}^{(+)} \frac{i\boldsymbol{\sigma} \cdot (\mathbf{D} \times \mathbf{E})}{8m_E^2} h^{(+)} + \bar{h}^{(+)} \frac{\mathbf{D} \cdot \mathbf{E}}{8m_D^2} h^{(+)}, \quad (2.11)$$

where $h^{(+)}$ is a two-component heavy-quark field, $\boldsymbol{\sigma}$ are the Pauli matrices, and \mathbf{B} and \mathbf{E} are the continuum gauge fields. The masses m_1, m_2, m_B, m_E , and m_D are functions of the bare-quark mass m_0 and the gauge coupling. For example, the masses m_1 and m_2 are defined to all orders in perturbation theory by Eq. (2.6), applied now to the pole energy of a one-quark state [21]. The entries in Eqs. (2.9)–(2.11) are commonly referred to as follows. $\mathcal{L}_{\text{HQET}}^{(0)}$ gives the rest mass. The first term of $\mathcal{L}_{\text{HQET}}^{(1)}$ is the kinetic energy and the second is the chromomagnetic, or hyperfine, interaction. The first term of $\mathcal{L}_{\text{HQET}}^{(2)}$ is the spin-orbit interaction while the second is known as the Darwin term.

For the pseudoscalar and vector meson rest masses, the HQET formalism can be used to show that [17]

$$M_1^{(*)} = m_1 + \bar{\Lambda}_{\text{lat}} - \frac{\lambda_{1,\text{lat}}}{2m_2} - d_J \frac{\lambda_{2,\text{lat}}}{2m_B} + O(1/m^2), \quad (2.12)$$

where J is the total meson angular momentum with $d_0 = 3$ and $d_1 = -1$ for the pseudoscalar (M_1) and vector (M_1^*) mesons, respectively. The quantities $\bar{\Lambda}_{\text{lat}}$, $\lambda_{1,\text{lat}}$, and $\lambda_{2,\text{lat}}$ are HQET matrix elements. At non-zero lattice spacing they contain discretization effects from $\mathcal{L}_{\text{light}}$, hence the subscript “lat”. The continuum limit of these quantities yields their counterparts in HQET applied to continuum QCD [17], which provides a basis for computing the continuum-QCD quantities $\bar{\Lambda}$ and λ_1 [22].

Mass splittings and matrix elements such as decay constants and form factors are not affected by the value of m_1 [17]. Thus, Eqs. (2.9) and (2.10) show that the kinetic mass m_2 is the first mass in the expansion that does play a role in the dynamics. We therefore would like to associate m_2 , and hence M_2 , with the physical mass, tolerating $m_1 \neq m_2$ (and $M_1 \neq M_2$) for nonzero lattice spacings. The nonperturbative tuning of κ then entails adjusting κ until the meson kinetic mass—determined by fits of Monte Carlo lattice data to the dispersion relation, Eq. (2.6)—equals that of the physical meson mass. A relation similar to Eq. (2.12) holds for M_2

$$M_2^{(*)} = m_2 + \bar{\Lambda}_{\text{lat}} + O(1/m), \quad (2.13)$$

with the leading discretization errors appearing in the $1/m$ contribution. Final values for the nonperturbative tuning of κ are given in Sec. VI A.

To calculate the hyperfine splitting of the D_s or B_s meson, consider

$$\Delta_1 \equiv M_1^* - M_1. \quad (2.14)$$

From Eq. (2.12),

$$M_1^* - M_1 = 4 \frac{\lambda_{2,\text{lat}}}{2m_B} + \dots, \quad (2.15)$$

which differs from the continuum splitting only by discretization errors in the light quarks and gluons appearing in $\lambda_{2,\text{lat}}$, the mismatch of m_B and its continuum counterpart (or, equivalently, the choice of c_B), and similar contributions from higher-dimension operators [17, 23]. The splitting of kinetic masses, $\Delta_2 \equiv M_2^* - M_2$, does not depend on m_B ; rather, it depends on

other generalized masses which are not tuned in our simulations.¹ Thus, Δ_1 formally has smaller discretization errors than Δ_2 . Δ_1 is also statistically cleaner than Δ_2 . In Eq. (2.15), $1/m_B$ is sensitive to the clover coupling c_B in Eq. (2.3), so Δ_1 tests how well it has been chosen. The B_s and D_s hyperfine splittings are given in Sec. VI B.

III. SIMULATIONS

In this section, we describe the gauge configurations used and the details of the actions, operators, and correlation functions that describe the heavy-light mesons. In Section III A, we discuss the gauge configurations and the parameters that describe each ensemble. We also review how the lattice spacing is determined and the values of the conversion factors r_1 and r_1/a . In Section III B, we discuss parameter choices for the valence quarks and the smearing of the heavy-quark wave function and how correlators are built from heavy and light quark fields.

A. Gauge Configurations and Related Parameters

We use the MILC gauge configurations [9, 10] that have 2+1 flavors of asqtad-improved staggered sea quarks [13] and a Symanzik-improved gluon action [24, 25]. Discretization errors from the sea quarks and gluons start at $O(\alpha_s a^2, a^4)$. The four-fold degeneracy of staggered sea quarks is removed by taking the fourth root of the determinant. To support the legitimacy of this procedure, Shamir has developed a renormalization-group framework for lattice QCD with staggered fermions, which he uses to argue that non-local effects of the rooted staggered theory are absent in the continuum limit [26]. Additional support for this procedure comes from chiral perturbation theory arguments [27, 28]. Reviews of these papers and of other evidence that this procedure reproduces the correct continuum limit appear in [11, 29, 30].

Table I lists the parameters of the gauge configurations used in this work. All configurations have been gauge-fixed to Coulomb gauge. Ensembles of configurations are grouped by their approximate lattice spacing and are referred to as “fine” ($a \approx 0.09$ fm), “coarse” ($a \approx 0.12$ fm), and “medium-coarse” ($a \approx 0.15$ fm). The simulation bare masses of the light and strange sea quarks are denoted by am'_l and am'_s , respectively, where am'_l is the mass of the two lighter sea-quarks. The range of am'_l is light enough that the physical up- and down-quark masses can be reached by a chiral extrapolation, while am'_s is close to the physical strange-quark mass. For convenience below, we write (am'_l, am'_s) to identify ensembles, e.g., “the (0.0031, 0.031) fine ensemble”. Also in Table I are the tadpole factors u_0 [20, 31], determined from the mean plaquette and used to improve the gauge-configuration actions [9, 10]. The value of the physical strange-quark mass is denoted by the unprimed m_s [31].

To convert between lattice and physical units, the physical value of the lattice spacing must be determined. We define the distance r_1 [12] by

$$r_1^2 F(r_1) = 1, \quad (3.1)$$

where $F(r)$ is the force between static quarks, calculated on the lattice. For each ensemble, this yields a value of r_1 in lattice units, r_1/a . The values are then “smoothed” by fitting $\ln(r_1/a)$, from all ensembles, to a polynomial in β and $2am'_l + am'_s$ [31]. The physical value of r_1 is obtained via the lattice calculation of an experimentally measurable quantity. We consider two current determinations here. One uses a lattice calculation of the $\Upsilon(2S)$ - $\Upsilon(1S)$ splitting [33] to arrive at $r_1 = 0.318(7)$ fm [10, 34]. A more recent determination using $r_1 f_\pi$ gives $r_1 = 0.3108(15)^{(+26)}_{(-79)}$ fm [35]. These two determinations are consistent within errors. Because the determination of r_1 from f_π uses finer lattice spacings, we take that value,

$$r_1 = 0.3108(^{+30}_{-80}) \text{ fm} \quad (3.2)$$

with no additional error. While this work was being completed, a new determination of r_1 that uses two mass splittings and one decay constant became available; $r_1 = 0.3133(^{+23}_{-3})$ [36], which is consistent with the value used in this work. Quantities can now be converted from lattice to physical units by using r_1 and the appropriate value of r_1/a given in Table I [31].

B. Meson Correlation Functions

Table II lists the values of parameters used in the valence-quark actions. For the light valence quark, we again use the asqtad action [13] and masses am'_q close to the physical value of the strange-quark mass, cf. Table I. From Eqs. (2.9)–(2.11), one can

¹ Tree-level expressions for these masses, and hence their mismatch, can be found in Ref. [23].

TABLE I: Parameters describing the ensembles used. The dimensions of the lattice are given in terms of the spatial (N_L) and temporal (N_T) size in lattice units. The gauge coupling is given by $\beta = 10/g^2$. The bare masses of the light and strange sea quarks are given by am'_l and am'_s , respectively. $L = aN_L$ is the linear spatial dimension of the lattice in fm. The column labeled N_{cf} is the number of configurations used in this work. The plaquette-determined tadpole-improvement factor is u_0 [31]. The physical strange quark mass is am_s [31] with errors, statistical and systematic, of less than one percent. The ratio r_1/a is described in the text; errors are Hessian from the smoothing fit. The final column lists the value of the inverse lattice spacing a^{-1} using $r_1 = 0.3108^{(+30)}_{(-80)}$ fm to convert from r_1/a ; errors are from the error on r_1 and r_1/a .

	$N_L^3 \times N_T$	β	am'_l	am'_s	L (fm)	N_{cf}	u_0	am_s	r_1/a	a^{-1} GeV
“Fine” $a \approx 0.09$ fm	$40^3 \times 96$	7.08	0.0031	0.031	3.5	435	0.8779	0.0252	3.692(6)	2.344^{+60}_{-23}
	$28^3 \times 96$	7.09	0.0062	0.031	2.4	557	0.8782	0.0252	3.701(5)	2.349^{+61}_{-23}
	$28^3 \times 96$	7.11	0.0124	0.031	2.4	518	0.8788	0.0252	3.721(5)	2.362^{+61}_{-23}
“Coarse” $a \approx 0.12$ fm	$24^3 \times 64$	6.76	0.005	0.05	2.9	529	0.8678	0.0344	2.645(3)	1.679^{+43}_{-16}
	$20^3 \times 64$	6.76	0.007	0.05	2.4	836	0.8678	0.0344	2.635(3)	1.672^{+43}_{-16}
	$20^3 \times 64$	6.76	0.010	0.05	2.4	592	0.8677	0.0344	2.619(3)	1.663^{+43}_{-16}
	$20^3 \times 64$	6.79	0.020	0.05	2.4	460	0.8688	0.0344	2.651(3)	1.683^{+43}_{-16}
	$20^3 \times 64$	6.81	0.030	0.05	2.4	549	0.8696	0.0344	2.657(4)	1.687^{+43}_{-16}
	$16^3 \times 48$	6.572	0.0097	0.0484	2.4	631	0.8604	0.0426	2.140(4)	1.358^{+35}_{-13}
“Medium-coarse” $a \approx 0.15$ fm	$16^3 \times 48$	6.586	0.0194	0.0484	2.4	631	0.8609	0.0426	2.129(3)	1.352^{+35}_{-13}
	$16^3 \times 48$	6.600	0.0290	0.0484	2.4	440	0.8614	0.0426	2.126(3)	1.350^{+35}_{-13}

see that with m_2 tuned to the physical mass, the leading mismatch between lattice and continuum physics is in the hyperfine term in $\mathcal{L}_{\text{HQET}}^{(1)}$. In principle, one can tune m_B to its continuum counterpart yielding a match between lattice and continuum actions for both terms in Eq. (2.10). Here, we use the tree-level expression for m_B , which leaves the leading mismatch at $O(\alpha_s a \Lambda)$. By setting $c_E = c_B$ we obtain the Sheikholeslami-Wohlert, $O(a)$ -improvement of discretization errors in the action [15]. From the HQET perspective, this leaves $m_E \neq m_2$ in Eq. (2.11), but the effects of this mistuning are at $O(a^2 \Lambda^2)$ and $O(\alpha_s a \Lambda^2 / m_Q)$. Implementing the improvements above and using tree-level tadpole improvement in the perturbative expressions [20, 24], we use $c_E = c_B = u_0^{-3}$.

The values of u_0 used in the heavy-quark and light-valence actions are given in Table II. For the fine and medium-coarse ensembles, they are the plaquette values used to generate the MILC gauge configurations. For the coarse ensembles, the Landau-gauge link value was used. The use of different u_0 definitions results in a slight mismatch between the light valence- and sea-quark actions. In part because the meson mass is relatively insensitive to the strange sea-quark mass, we do not expect any significant systematic errors from this mismatch. Changes in u_0 result in changes to the bare mass of the heavy quark as well, but this effect is partly absorbed by the nonperturbative tuning of κ and κ_{crit} . Table II also lists the nominal values of the light valence-quark mass and sets of κ values for bottom and charm mesons. These sets of κ values, and mesons created from them, are referred to as charm-type or bottom-type.

With the parameters of the actions set, we now turn to the construction of the two-point correlators. Contributions from excited states can be significantly reduced by using a spatially smeared source, sink, or both, for the heavy-quark propagator. For the correlators in this work, we use two types of source-sink combinations for the heavy quarks. One is simply a delta function for both the source and sink; we refer to this as the local correlator. The other smears the field $\psi(t, \mathbf{x})$ with a discretized version [37] of the $1S$ charmonium wavefunction, $S(\mathbf{y})$, based on the Richardson potential [38]:

$$\phi(t, \mathbf{x}) = \sum_{\mathbf{y}} S(\mathbf{y}) \psi(t, \mathbf{x} + \mathbf{y}), \quad (3.3)$$

and the smearing wavefunction is applied after fixing to Coulomb gauge. Correlators using $\phi(t, \mathbf{x})$ are referred to as smeared correlators. All light valence quarks have a local source and sink. The meson correlator is

$$C_{i,j}(t, \mathbf{p}) = \sum_{\mathbf{x}} \langle \mathcal{O}_j^\dagger(t, \mathbf{x}) \mathcal{O}_i(0, \mathbf{0}) \rangle e^{i\mathbf{p} \cdot \mathbf{x}}, \quad (3.4)$$

where i, j denote the source, sink smearing of the heavy-quark field; for this work $i = j$. $\mathcal{O}_i(t, \mathbf{x})$ is a bilinear interpolating operator with a gamma-matrix structure that yields quantum numbers appropriate for either pseudoscalar or vector mesons. To construct this operator, we combine a one-component, staggered light-quark spinor with a four-component, Wilson-type heavy-quark spinor in a manner similar to Ref. [39],

$$\mathcal{O}_\Xi(t, \mathbf{x}) = \bar{\psi}_\alpha(t, \mathbf{x}) \Gamma_{\alpha\beta} \Omega_\beta \Xi(t, \mathbf{x}) \chi(t, \mathbf{x}), \quad (3.5)$$

where $\Gamma = \gamma_5$ or γ_μ ; α, β are spin indices; and $\Omega(x) \equiv \gamma_1^{x_1} \gamma_2^{x_2} \gamma_3^{x_3} \gamma_4^{x_4}$. The fields $\bar{\psi}$ and χ are the Wilson-type and staggered fields, respectively, and the smeared correlator is constructed in the same way, but with ϕ instead of ψ . The transformation

TABLE II: Parameters used in the valence-quark actions. The bare masses of the light and strange sea quarks (am'_l, am'_s) label the ensemble. The mass of the light (staggered) valence quark is given by am'_q . c_E and c_B are the coefficients of the chromoelectric and chromomagnetic contributions to the Lagrangian. With $c_E = c_B$, they are the usual Sheikholeslami-Wohlert coupling. u_0 is the tadpole-improvement factor from measurements of the average plaquette for the fine and medium-coarse ensembles and from the Landau-gauge link on the coarse ensembles. Hopping parameter values κ used for bottom-like and charm-like heavy quarks are given in the final two columns.

Lattice	(am'_l, am'_s)	am'_q	$c_E = c_B$	u_0	bottom-type κ	charm-type κ
Fine	(0.0031, 0.031)	0.0272, 0.031	1.478	0.8779	0.0923	0.127
	(0.0062, 0.031)	0.0272, 0.031	1.476	0.8782	0.090, 0.0923, 0.093	0.1256, 0.127
	(0.0124, 0.031)	0.0272, 0.031	1.473	0.8788	0.0923	0.127
Coarse	(0.005, 0.050)	0.030, 0.0415	1.72	0.836	0.086	0.122
	(0.007, 0.050)	0.030, 0.0415	1.72	0.836	0.074, 0.086, 0.093	0.119, 0.122, 0.124
	(0.010, 0.050)	0.030, 0.0415	1.72	0.8346	0.074, 0.086, 0.093	0.119, 0.122, 0.124
	(0.020, 0.050)	0.030, 0.0415	1.72	0.8369	0.074, 0.086, 0.093	0.122, 0.124
	(0.030, 0.050)	0.030, 0.0415	1.72	0.8378	0.086	0.122
Medium-coarse	(0.0097, 0.0484)	0.0387, 0.0484	1.570	0.8604	0.070, 0.080	0.115, 0.122 ^a , 0.125
	(0.0194, 0.0484)	0.0387, 0.0484	1.567	0.8609	0.070, 0.076, 0.080	0.115, 0.122, 0.125
	(0.0290, 0.0484)	0.0484	1.565	0.8614	0.070, 0.080	0.115, 0.125

^aUsed only with $am'_q = 0.484$.

properties of $\mathcal{O}_\Xi(x)$ under shifts by one lattice spacing are such that Ξ can be viewed as playing the role of the (fermionic) taste index [30, 40]. In our correlation functions, $\mathcal{O}_\Xi(x)$ is summed over 2^4 hypercubes, and so Ξ can be interpreted as a taste degree of freedom in the sense of Refs. [41, 42].

IV. ANALYSIS OVERVIEW

In this section, we describe the components of our analysis. Section IV A discusses the two-point correlator fits used to determine the meson energies $aE(\mathbf{p})$. Section IV B describes how we fit the meson dispersion relation to obtain M_2 . Finally, Sec. IV C explains how κ is tuned and how the hyperfine splitting is determined.

A. Two-point Correlator Fits: $E(\mathbf{p})$

To determine $E(\mathbf{p})$, we simultaneously fit the local and smeared heavy-light-meson two-point correlators to the function

$$C_{i,i}(t, \mathbf{p}) = \sum_{\eta=0}^{N-1} \left[Z_{i,\eta}^2 \left(e^{-E_\eta(\mathbf{p})t} + e^{-E_\eta(\mathbf{p})(N_T-t)} \right) + (-1)^{t+1} (Z_{i,\eta}^p)^2 \left(e^{-E_\eta^p(\mathbf{p})t} + e^{-E_\eta^p(\mathbf{p})(N_T-t)} \right) \right], \quad (4.1)$$

where N_T is the temporal extent of the lattice, and terms proportional to $e^{-E_\eta(\mathbf{p})(N_T-t)}$ are due to periodic boundary conditions. To simplify notation in this subsection, the lattice spacing a is not written out explicitly. Correlation functions containing staggered light quarks have contributions from both desired- and opposite-parity states with the opposite-parity states having the temporally-oscillating prefactor $(-1)^{t+1}$ [39]. We take each energy level η in Eq. (4.1) to include a pair of states consisting of one desired- and one opposite-parity state; the number of pairs of states in a fit is given by N . Quantities associated with the tower of opposite-parity states are denoted by the superscript “p.”

Equation (4.1) contains $2N$ exponentials, and the number of time slices in our data set is finite. Although it is straightforward to separate the two different parities—because of the $(-1)^{t+1}$ —it is difficult to separate states within each tower. Rather than relying solely on taking t large enough, we use the technique of constrained curve fitting [39, 43, 44]. We thus minimize an augmented χ^2 [43],

$$\chi_{\text{aug}}^2 \equiv \chi^2 + \sum_k \frac{(P_k - \tilde{P}_k)^2}{\sigma_{P_k}^2}, \quad (4.2)$$

which means each fit parameter P_k is provided a prior Gaussian probability distribution function with central value and width $(\tilde{P}_k, \sigma_{\tilde{P}_k})$. The central value for fitted quantities comes from minimizing χ_{aug}^2 on the whole ensemble. We take the parameters to be $E_0^{(p)}, \ln(Z_{i,\eta}^{(p)})$, and (for $\eta > 0$) $\ln(\Delta E_\eta^{(p)})$, where $\Delta E_\eta^{(p)} = E_\eta^{(p)} - E_{\eta-1}^{(p)}$, thereby enforcing a tower of states with increasing energy.

In general, one considers a quantity to be determined by the data only if the statistical error, discussed next, is smaller than the corresponding prior width. In this work, we are most concerned with the lowest-lying desired parity state, and the data—not the priors—always determine E_0 and $Z_{i,0}$. For parameters that are poorly constrained by the data, such as those describing excited states, these priors prevent the fitter from searching fruitlessly along flat directions in parameter space. Because of the freedom in choosing the prior, we test whether the ground-state results are prior-independent, and stable. When testing the stability of fit results, we use the Hessian error, defined as

$$\sigma_{P_i} = \sqrt{2 \left(\frac{\partial^2 \chi_{\text{aug}}^2}{\partial P_i \partial P_j} \right)^{-1}_{ii}}, \quad (4.3)$$

because its straightforward definition allows it to be quickly calculated for a single fit.

When using χ_{aug}^2 to measure the goodness of fit, we count the degrees of freedom as the number of data points; the number of fit parameters is not subtracted since there are an equal number of extra terms in χ_{aug}^2 . In some cases, this could result in misleadingly low values of $\chi_{\text{aug}}^2/\text{dof}$. For example, if the prior width $\sigma_{\tilde{P}_k}$ is much larger than $(P_k - \tilde{P}_k)$, the associated term in χ_{aug}^2 will be much smaller than the others. This could be adjusted *a posteriori* by reducing the degrees of freedom, but it would require devising a criterion for “large $\sigma_{\tilde{P}_k}$ ”. We do not make such adjustments in our analyses. Instead, to determine goodness of fit, we monitor the values of $\chi_{\text{aug}}^2/\text{dof}$ from constrained fits, but rely equally on the stability of fit results.

We estimate statistical uncertainties by generating pseudo-ensembles via the bootstrap method. When fitting a pseudo-ensemble, the central value of each prior is drawn randomly from its Gaussian probability distribution while the prior width is kept the same [39, 43]. To prevent large, simultaneous but uncorrelated fluctuations among prior central values, which could destabilize a fit, we restrict the randomized prior central values to $\pm 1.5\sigma_{\tilde{P}}$. Final errors quoted for meson energies and functions thereof, such as the spin-averaged mass, are obtained from their bootstrap distributions. We define the upper (lower) 68%-distribution point as the value at which 16% of the distribution has a higher (lower) value. We refer to half of the distance between these two points as the average 68% bootstrap error.

B. Dispersion Relation Fits: The Kinetic Mass

Having determined $E(\mathbf{p})$, we use the dispersion relation to determine the kinetic meson mass, which we then use to tune the hopping parameter κ . The low-momentum expansion for $E(\mathbf{p})$ is

$$E(\mathbf{p}) = M_1 + \frac{\mathbf{p}^2}{2M_2} - \frac{a^3 W_4}{6} \sum_i p_i^4 - \frac{(\mathbf{p}^2)^2}{8M_4^3} + \dots, \quad (4.4)$$

where W_4 and the deviation of M_4 from M_2 capture lattice artifacts. (In the continuum limit $a^3 W_4 = 0$ and $M_4 = M_2$.) The vector \mathbf{n} is defined by

$$a\mathbf{p} = (2\pi/N_L) \mathbf{n}, \quad (4.5)$$

where N_L is the spatial extent of the lattice, given in Table I; data are generated for $|\mathbf{n}| \leq 3$. Noise in $E(\mathbf{p})$ increases with increasing momentum, though, and is substantial by the time $O(\mathbf{p}^4)$ effects become significant. For charm-type mesons, squaring the energy yields a substantial cancellation in the $\mathcal{O}(\mathbf{p}^4)$ contribution because $aM_1 \approx aM_2 \approx aM_4$. While this is not true for bottom-type mesons, the mass of these mesons is large enough to cause suppression via the $1/M$ factors whether $E(\mathbf{p})$ or $E^2(\mathbf{p})$ is used. By fitting to $E^2(\mathbf{p})$ then, the contributions from $O(\mathbf{p}^4)$ effects are reduced, and we are able to do a linear fit to low-momentum data, $|\mathbf{n}| \leq 2$. Setting $M_1 = E(\mathbf{0})$ from the zero-momentum correlator, we square Eq. (4.4) and fit

$$E^2(\mathbf{p}) - M_1^2 = C\mathbf{p}^2 \quad (4.6)$$

to obtain C . Finally, we set $M_2 = M_1/C$. The largest \mathbf{p} is chosen so that the $O(\mathbf{p}^4)$ effects are expected to be negligible, based on tree-level values of the analogous quark quantities w_4 and $1/m_4^3$. We confirm the negligibility of these terms by inspecting plots of the data and monitoring χ^2/dof . (We do not use constrained curve fitting here and so we minimize the usual χ^2 .) This procedure is repeated for each bootstrap-generated pseudo-ensemble, yielding bootstrap distributions for aM_1 and aM_2 .

C. The Hopping Parameter κ and the Hyperfine Splitting Δ_1

For tuning κ , it is helpful to remove the leading discretization errors from spin-dependent terms. Let the spin-averaged kinetic meson mass be

$$\overline{M}_2 = \frac{1}{4}(M_2 + 3M_2^*), \quad (4.7)$$

where M_2 and M_2^* are determined as described in Sec. IV B. This leaves the second, spin-independent term in Eq. (2.11) as the leading source of discretization error at $O(a^2 \Lambda^2)$. Our goal then is to determine the value of κ that will result in a value of \bar{M}_2 that agrees with the experimental value taken from the Particle Data Group (PDG).

For each lattice spacing, we use the following procedure to tune κ . Using three or more ensembles, we study the light sea-quark mass dependence of $a\bar{M}_2$ for at least one combination of κ and m'_q . This gives us some insight into the behavior of $a\bar{M}_2$ in the physical-sea-quark-mass limit and allows us to assign an uncertainty to $a\bar{M}_2$ due to non-physical sea-quark masses. Next, on at least one ensemble, we determine $a\bar{M}_2$ at two staggered, valence-quark masses near the strange-quark mass. This allows us to determine the dependence of $a\bar{M}_2$ on the staggered, valence-quark mass and interpolate linearly to the physical value if no simulated mass is close enough to the tuned strange-quark mass. Having dealt with the staggered-valence and light sea-quark masses, we take $a\bar{M}_2$ at the physical, strange valence-quark mass at two values of κ and interpolate linearly in κ to the spin-averaged value of the meson masses, given by the Particle Data Group (PDG) [45], converted to lattice units with a from Table I. Finally, we combine the uncertainties in the tuned value of κ from statistical and discretization errors in the meson mass, staggered-valence mass mistuning, non-physical sea-quark masses, and errors from the lattice-spacing conversion of the PDG mass.

To determine the hyperfine splitting, we start with the results for $M_1 = E(\mathbf{0})$. For each lattice spacing, we use values of $a\Delta_1$ at, or linearly interpolated to, the tuned charm and bottom κ values. We then consider uncertainties from statistics, the tuning of κ and am_s , non-physical sea-quark masses, and discretization. The value of $a\Delta_1$ on the fine lattice is taken as our central value and results on the coarse and medium coarse lattices are used in the error analysis. In the final value, we also include an uncertainty due to the conversion to physical units.

V. FITTING DETAILS FOR $E(\mathbf{p}), M_1, M_2$

In this section, we describe the details of our fitting procedure for the meson energy $E(\mathbf{p})$ and the meson rest and kinetic masses, M_1 and M_2 . Our objective here is to document thoroughly our fitting procedures, including values for the priors, and tests. Readers who are more interested in a summary can skip to Sec. V C.

Section V A discusses the parameters used in our two-point correlator fits for $E(\mathbf{p})$ (Sec. V A 1) and the evaluation of goodness of fit via $\chi_{\text{aug}}^2/\text{dof}$ and tests of stability (Sec. V A 2). In most tests discussed here, Hessian errors were used, because they are fast and straightforward. Our complete data set, exhibited in Table II, contains several ensembles at each of the three lattice spacings. As explained in Sec. V A 1, one ensemble at each lattice spacing is chosen for the purpose of setting priors in Eq. (4.2). For tuning κ , we need data over a range of κ and am'_q on a fixed ensemble. At the fine lattice spacing, such data were generated on only one ensemble, (0.0062, 0.031), so we set priors and tune κ on that same ensemble. For the coarse and medium-coarse lattice spacings, we have data for a range of κ and am'_q on several ensembles. We take the coarse (0.010, 0.050), and medium-coarse (0.0194, 0.0484) ensembles to set priors and then the ensembles with the smallest am'_l (and a range of κ and am'_q) to tune κ . We compute the hyperfine splittings from the same ensembles on which κ was tuned. These choices are summarized in Table III. Data from other ensembles listed in Table II are used to estimate uncertainties.

Fits of the dispersion relation to determine M_2 from $E(\mathbf{p})$ are comparatively simple, and Sec. V B provides details that may be of interest.

A. Two-point fits: $E(\mathbf{p}), M_1$

The number of gauge configurations in each ensemble is given in Table I. To improve statistics, we generate data at four time sources on each of the fine and coarse gauge configurations and at eight time sources for medium-coarse configurations. We also average the correlator points $C(t)$ and $C(N_T - t)$. In order to reduce the effect of correlations between data points from sequential configurations, we bin the data by groups of N_{bin} configurations. Because fits for this project were done in concert with other projects, $N_{\text{bin}} = 4$ was adopted. Comparisons of results using $N_{\text{bin}} = 2, 4$, and 6 on the ensembles used here show no significant change in the fit-result error bars or the bootstrap distributions. To account for correlations in the two-point correlator

TABLE III: Specific ensembles used in steps of the analyses. Setting priors is discussed in Sec. V A 1. Stability and goodness-of-fit tests done for $E(\mathbf{p})$ results are described in Sec. V A 2. κ -tuning and hyperfine-splitting results are given in Secs. VI A and VI B, respectively.

Lattice	setting priors	$E(\mathbf{p})$ tests, tuning κ , and the hyperfine splitting Δ_1
Fine	(0.0062, 0.031)	(0.0062, 0.031)
Coarse	(0.010, 0.050)	(0.007, 0.050)
Medium-coarse	(0.0194, 0.0484)	(0.0097, 0.0484)

data, the fitter uses the normalized, data-sample covariance matrix as an estimate of the correlation matrix. This matrix is remade for each bootstrap sample.

1. Priors, time ranges, N

We consider the setting of priors for the ground state parameters, excited-state amplitudes, and energy splittings separately. Ground-state ($\eta = 0$) parameters are well-determined by the data; thus, the ground-state priors can, and should, be negligibly constraining. In contrast, energy splittings and excited state amplitudes are not well determined by the data, and the related priors are chosen such that they put reasonable bounds on the parameters. The next paragraphs describe how the priors are set. Note that the same set of priors is used for all ensembles at a given lattice spacing, for all momenta in the range $|n| = 0$ to 2, and for all κ and am'_q of a given meson type, e.g., charm pseudoscalars. The priors used are tabulated in Tables IV–VI.

We use information from a subset of our data, one ensemble per lattice spacing, to set the priors for the two-point-correlator fits. This is necessary because we do not have enough external knowledge to set them independently. The ensembles used to help set the priors are listed in Table III. Other ensembles are statistically independent of these ensembles and so the prior information can be viewed as external to fits on those ensembles. If possible, though, we do not want to exclude any data from our analysis, including the ensembles used in the setting of priors. For this reason, our procedure for setting priors keeps the amount of information we take from these ensembles to a minimum. Specifically, for a parameter P , we use averages over ranges of parameters, like the momentum, for the prior central value \tilde{P} and chose prior widths $\sigma_{\tilde{P}}$ that are broad enough to cover the expected results for an entire subset of fits; e.g., the same priors are used for fits with $|n| = 0$ to 2.

To set ground-state priors, we first fit to large-time data with $N = 1$ in order to get a general idea of the ground-state parameter values. We then set $N > 1$ and fit correlators at low and high momenta to ascertain the range of values the ground state parameters may take. We set prior central values for the ground-state energy of the desired- and opposite-parity states, $aE_0(\mathbf{p})$ and $aE_0^p(\mathbf{p})$, at about the midpoint of the range seen in these fits.

To understand our logic for setting the prior widths for $aE_0(\mathbf{p})$ and $aE_0^p(\mathbf{p})$, recall that we use a Gaussian distribution for the prior \tilde{P} with a width $\sigma_{\tilde{P}}$. We set σ_{aE_0} and $\sigma_{aE_0^p}$ large enough so that results across the entire momentum range used in the analysis should fall well within the $1-\sigma_{aE_0}$, or $1-\sigma_{aE_0^p}$, range of the distribution. After priors for the remaining parameters are set, we perform a complete set of fits and, for at least one ensemble at each lattice spacing, verify that, indeed, the final fit results for aE_0 and aE_0^p fit well within their respective prior distributions.

Priors for the ground-state amplitudes are loosely based on the preliminary $N > 1$ fits described above. In most cases, the central value is the nearest whole number to the average of these results. For the desired-parity state, the widths $\sigma_{\tilde{P}}$ are chosen such that they easily span the range of values seen in the fits. For the opposite parity states, which are substantially noisier, the widths span the distance between the prior central value and the observed range in the results by about $1-\sigma_{\tilde{P}}$.

Priors for all excited-state amplitudes were set to have a relatively small central value and a wide width. To set the prior for the energy splitting, we note that experimentally measured meson splittings are a few hundred MeV. We also bear in mind that the sum of a series of exponentials with a very small energy splitting is not a well-posed problem. Therefore, we chose the central value of the splitting to be several hundred MeV, slightly large, with a generous prior width. For example, on the fine lattice the prior for the splitting, $\ln(a\Delta E) = -1.45(1.0)$ is equivalent to $\Delta E \approx 550^{+950}_{-350}$ MeV.

In the charm sector, the opposite-parity partner of the $D_s(0^-)$, the $D_{s0}^*(0^+)$, is close to the *DK* threshold. In this case, the energy splitting should not be viewed as a meson mass splitting, and our choice of prior for the $D_{s0}^*(0^+)$ energy splitting may be inappropriate. The parity-partner signal is noisy, though, and in tests of the priors widths we see no change in the non-oscillating ground state energy $aE(\mathbf{p})$, which is our main interest. For details, see Sec. V A 2.

To choose the time ranges for the fits, (t_{\min}, t_{\max}) , we first look at the data to determine the time by which the error in the data, e.g. the relative error in the correlator, has increased substantially. This gives us a potential value for t_{\max} . From effective mass plots we can also see at what time slice the majority of the excited-state contamination has died off, giving us a potential value for t_{\min} . Constrained curve fitting is designed to reduce excited-state contamination of the lower-state fit parameters. Nevertheless, we do not see a significant reduction in the error from fitting to the smallest possible time slice, which requires including a larger number of states in the fit. For simplicity, we chose final time ranges that are the same for similar sets of data. These can be found in Table VII.

With the time range set, we do fits for increasing values of the number of (pairs of) states N and look for the ground-state energy to stabilize. We choose the final values of N to be the minimum value needed to be in the stable region; these are given in Table VII. Figure 1 shows representative plots of $aE(\mathbf{p})$ versus N from fits on the (0.0062, 0.031) fine ensemble. It is clear that for the minimum-value N , the central value of the fit result is always well within the stable region. In some cases, though, the (Hessian) error from the minimum- N fit is smaller than that in the stable region. One could remedy this by choosing to fit with more states. Unfortunately, an increase in the number of states leads to non-gaussian bootstrap distributions with a significant number of outliers — clearly non-physical fit results that contain ground states with low energies and very small amplitudes. Using the minimum possible number of states, no outliers have been seen in the distributions.

TABLE IV: Priors used for fine-ensemble two-point correlator fits for pseudoscalar and vector mesons. Priors for all higher amplitudes and splittings are the same as those for the first excited state. The fit-parameter numbers 15–20 label the second excited state and so on. A prior of $\ln(a\Delta E) = -1.45^{+1.0}_{-1.0}$ on the fine ensembles corresponds approximately to $\Delta E = 550^{+950}_{-350}$ MeV.

fit parameter	fit-parameter number	Charm Mesons		Bottom Mesons	
		pseudoscalar	vector	pseudoscalar	vector
E_0	1	0.90(40)	0.90(40)	1.75(60)	1.75(60)
E_0^P	2	1.0(40)	0.95(40)	1.85(60)	1.85(60)
$\ln(Z_{1S,0})$	3	1.0(2.0)	1.0(2.0)	1.0(3.0)	1.0(3.0)
$\ln(Z_{1S,0}^P)$	4	1.0(2.0)	1.0(2.0)	1.0(3.0)	1.0(3.0)
$\ln(Z_{d,0})$	5	-2.0(2.0)	-2.0(2.0)	-2.0(3.0)	-2.0(3.0)
$\ln(Z_{d,0}^P)$	6	-2.0(2.0)	-2.0(2.0)	-2.0(3.0)	-2.0(3.0)
$\ln(\Delta E)$	8	-1.45(1.0)	-1.45(1.0)	-1.45(1.0)	-1.45(1.0)
$\ln(\Delta E^P)$	9	-1.45(1.0)	-1.45(1.0)	-1.45(1.0)	-1.45(1.0)
$\ln(Z_{1S,1})$	10	-1.0(3.0)	-1.0(3.0)	-1.0(3.0)	-1.0(3.0)
$\ln(Z_{1S,1}^P)$	11	-1.0(3.0)	-1.0(3.0)	-1.0(3.0)	-1.0(3.0)
$\ln(Z_{d,1})$	12	-1.0(3.0)	-1.0(3.0)	-1.0(3.0)	-1.0(3.0)
$\ln(Z_{d,1}^P)$	13	-1.0(3.0)	-1.0(3.0)	-1.0(3.0)	-1.0(3.0)

TABLE V: Same as Table IV, but for the coarse ensembles. A prior of $\ln(a\Delta E) = -1.2^{+0.5}_{-0.5}$ on the coarse ensembles corresponds approximately to $\Delta E = 500^{+300}_{-200}$ MeV.

fit parameter	fit-parameter number	Charm Mesons		Bottom Mesons	
		pseudoscalar	vector	pseudoscalar	vector
E_0	1	1.10(40)	1.2(40)	2.00(40)	2.00(40)
E_0^P	2	1.30(40)	1.3(40)	2.10(40)	2.10(40)
$\ln(Z_{1S,0})$	3	1.0(2.0)	1.0(2.0)	1.0(2.0)	1.0(2.0)
$\ln(Z_{1S,0}^P)$	4	1.0(3.0)	0.1(3.0)	-1.0(2.0)	-0.1(2.0)
$\ln(Z_{d,0})$	5	-1.0(2.0)	-1.0(2.0)	-2.0(2.0)	-1.0(2.0)
$\ln(Z_{d,0}^P)$	6	-1.0(3.0)	-2.0(3.0)	-2.0(2.0)	-2.0(2.0)
$\ln(\Delta E)$	8	-1.2(0.5)	-1.2(0.5)	-1.2(0.5)	-1.2(0.5)
$\ln(\Delta E^P)$	9	-1.2(0.5)	-1.2(0.5)	-1.2(0.5)	-1.2(0.5)
$\ln(Z_{1S,1})$	10	-1.0(3.0)	-1.0(3.0)	-1.0(3.0)	-1.0(3.0)
$\ln(Z_{1S,1}^P)$	11	-1.0(3.0)	-1.0(3.0)	-1.0(3.0)	-1.0(3.0)
$\ln(Z_{d,1})$	12	-1.0(3.0)	-1.0(3.0)	-1.0(3.0)	-1.0(3.0)
$\ln(Z_{d,1}^P)$	13	-1.0(3.0)	-1.0(3.0)	-1.0(3.0)	-1.0(3.0)

TABLE VI: Same as Table IV, but for the medium coarse ensembles. A prior of $\ln(a\Delta E) = -1.0^{+0.5}_{-0.5}$ on the medium-coarse ensembles corresponds approximately to $\Delta E = 500^{+300}_{-200}$ MeV.

fit parameter	fit-parameter number	Charm Mesons		Bottom Mesons	
		pseudoscalar	vector	pseudoscalar	vector
E_0	1	1.38(50)	1.46(50)	2.35(40)	2.38(50)
E_0^P	2	1.50(60)	1.58(60)	2.48(50)	2.50(50)
$\ln(Z_{1S,0})$	3	0.48(1.0)	0.95(1.0)	0.12(1.4)	0.60(1.0)
$\ln(Z_{1S,0}^P)$	4	-0.65(1.0)	0.20(1.0)	-1.0(2.0)	0.1(2.0)
$\ln(Z_{d,0})$	5	-0.90(1.0)	-0.74(1.0)	-1.15(1.0)	-0.8(1.0)
$\ln(Z_{d,0}^P)$	6	-2.4(1.4)	-1.8(2.0)	-2.5(3.0)	-1.8(3.0)
$\ln(\Delta E)$	8	-1.0(0.5)	-1.0(0.5)	-1.0(0.5)	-1.0(0.5)
$\ln(\Delta E^P)$	9	-1.0(0.5)	-1.0(0.5)	-1.0(0.5)	-1.0(0.5)
$\ln(Z_{1S,1})$	10	-1.0(3.0)	-1.0(3.0)	-1.0(3.0)	-1.0(3.0)
$\ln(Z_{1S,1}^P)$	11	-1.0(3.0)	-1.0(3.0)	-1.0(3.0)	-1.0(3.0)
$\ln(Z_{d,1})$	12	-1.0(3.0)	-1.0(3.0)	-1.0(3.0)	-1.0(3.0)
$\ln(Z_{d,1}^P)$	13	-1.0(3.0)	-1.0(3.0)	-1.0(3.0)	-1.0(3.0)

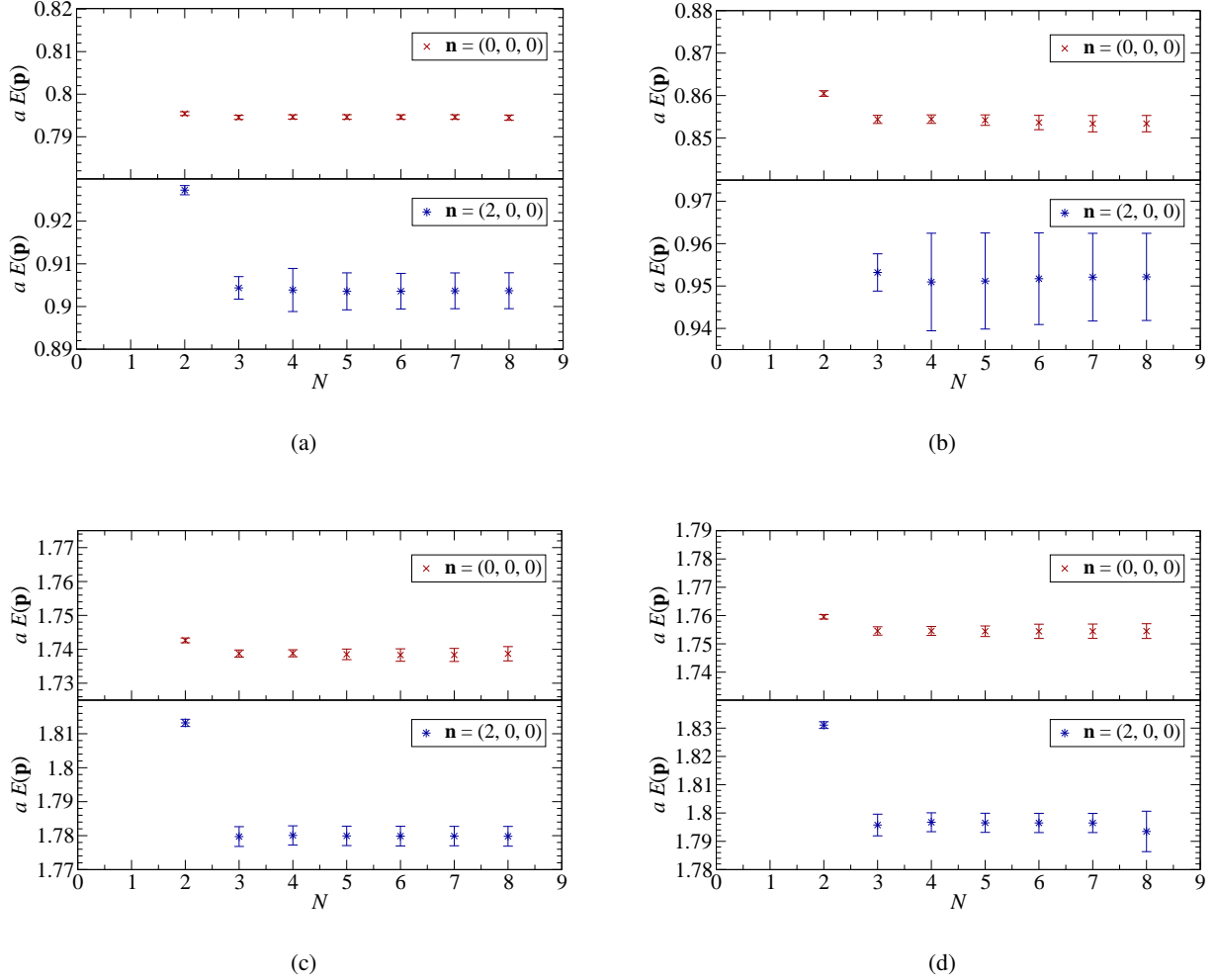


FIG. 1: Fitted values of $aE(\mathbf{p})$ vs. the number of (pairs of) states N for $\kappa = 0.127$, charm-type (a) pseudoscalar and (b) vector mesons and $\kappa = 0.090$, bottom-type (c) pseudoscalar and (d) vector mesons on the $(0.0062, 0.031)$ fine ensemble. Results shown are for mesons with momenta $\mathbf{n} = (0, 0, 0)$ and $(2, 0, 0)$. Errors are Hessian.

2. Tests of Stability and Goodness-of-fit

Having set the priors, time range, and number of states for the fits, we check the stability of the results and goodness of fit in several ways. For result stability, we check the effects of the time range used, the number of (pairs of) states N , and changes to the prior widths; we also compare the priors to the fit results. We look at a representative subset of fits for each lattice spacing: pseudoscalar and vector meson correlators at two different κ values (one for charm and one for bottom) for a given light-valence mass, on one ensemble per lattice spacing, and with momenta $\mathbf{n} = (0, 0, 0)$ and $(1, 1, 1)$ or $(2, 0, 0)$. The specific values of κ , am'_q , and (am'_l, am'_s) vary from test to test, and in some cases tests are extended to other values. A description of the data used in the tests discussed here can be found in Table VIII.

TABLE VII: Time range t_{\min} – t_{\max} and number of (pairs of) states N used in two-point correlator fits at each lattice spacing. For the time range, the first (second) number in parenthesis is t_{\min} for the 1S-smeared (local) correlator; t_{\max} is the same for both correlators.

Lattice spacing	Time range	N
Fine	$(2, 4)$ –25	3
Coarse	$(2, 8)$ –15	2
Medium-coarse	$(5, 6)$ –15	2

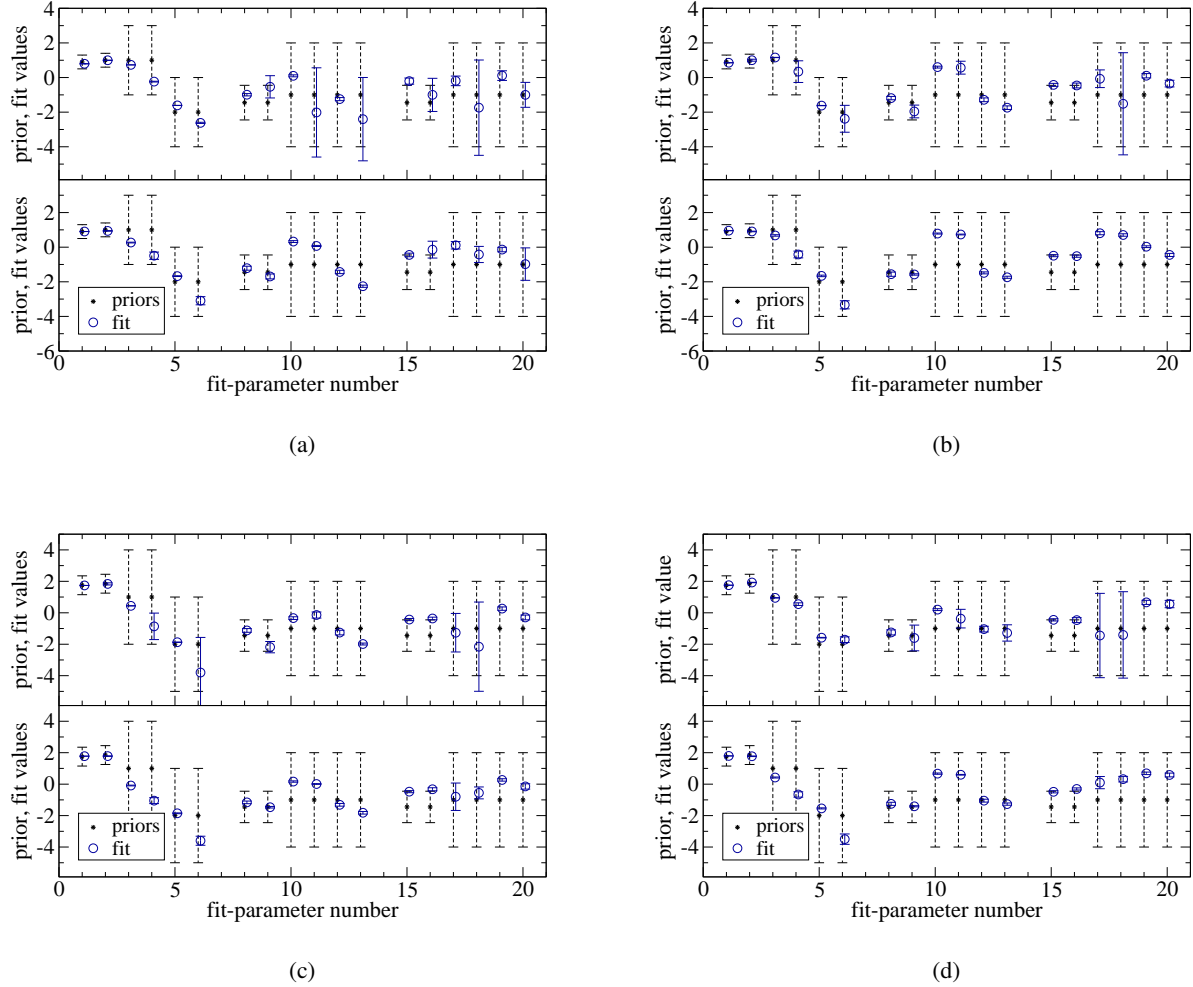


FIG. 2: Fit results shown as open (blue) circles are overlaid on the priors, black dots with dashed widths, for charm-type (a) pseudoscalar and (b) vector mesons and bottom-type (c) pseudoscalar and (d) vector mesons on the $(0.0062, 0.031)$ fine ensemble. $\kappa = 0.127$ and 0.090 for charm- and bottom-type mesons, respectively; $am'_q = 0.0272$. The upper [lower] plot is from a fit where the meson has momentum of $\mathbf{n} = (0, 0, 0)$ [$(2, 0, 0)$]. The fit-parameter numbers are defined in Table IV. In each panel, the leftmost cluster corresponds to quantities from the ground state; the middle cluster corresponds to the first excited state; and the right most cluster to the second excited state. Errors on the fit results are Hessian. For clarity, fit results are offset along the x -axis.

For the time-range tests, we vary t_{\min} over two to four time slices, increasing N if appropriate, and vary t_{\max} over five to ten time slices. We verify that there are no changes in the fit results beyond expected fluctuations.² For number-of-states tests, we

TABLE VIII: Data used in stability and goodness-of-fit tests.

Lattice	ensemble	κ	am'_q
Fine	$(0.0062, 0.031)$	$0.127; 0.090$ or 0.093	0.0272
Coarse	$(0.007, 0.050)$	$0.122; 0.086$	0.0415
Medium-coarse	$(0.0097, 0.0484)$	$0.125; 0.070$	0.0484

² In one case, $\kappa = 0.086$, coarse $(0.010, 0.005)$, although the ground-state energy is stable as t_{\max} is varied, the value of χ^2/dof becomes large as t_{\max} is increased beyond the final value ($t_{\max} = 15$). This ensemble is not used directly for κ tuning or hyperfine splitting determinations as explained in the

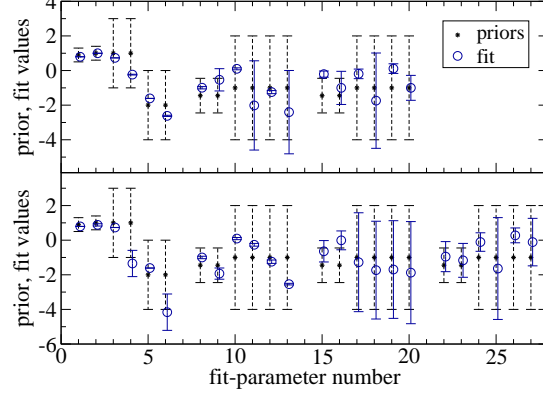


FIG. 3: Fit results shown as open (blue) circles are overlaid on the priors, black dots with dashed widths, for charm-type mesons on the (0.0062, 0.031) fine ensemble. $\kappa = 0.127$; $am'_q = 0.0272$; $\mathbf{n} = (0, 0, 0)$. The upper plot is the same as the upper left (pseudoscalar) panel of Fig. 2 (a). The lower plot is from a fit which only differs by the use of $N = 4$ pairs of states. The fit-parameter numbers are defined in Table IV. In each panel, the leftmost cluster corresponds to quantities from the ground state; the middle cluster corresponds to the first excited state; the next cluster corresponds to the second excited state and so on. The (desired-parity) ground-state quantities are stable to this change while other, excited-state, parameters are not. Errors on the fit results are Hessian. For clarity, fit results are offset along the x -axis.

verify that the result is stable as N is increased. Figure 1 shows example results for the (0.0062, 0.031) fine ensemble. Similar results are seen for the coarse and medium-coarse ensembles and for the ground-state amplitudes Z_{1S} and Z_d .

For prior-width tests, we reduce the widths by a factor of two for the non-oscillating ground state quantities and the energy splittings and repeat the fits. All changes observed are within statistical errors and, in most cases, the changes are substantially smaller than one σ . For charm, we also test for effects of the DK threshold near the $D_{s0}^*(0^+)$ state. This splitting is 50 to 100 MeV, which is a several- $\sigma_{\tilde{\Delta}_{aE_p}}$ deviation from our prior central value. We ran separate tests on each lattice spacing using a prior width of $\sigma_{\tilde{\Delta}_{aE_p}} = 2.5$ for the oscillating-state energy splitting. In units of MeV, this puts a 50-MeV splitting within $1\sigma_{\tilde{\Delta}_{aE_p}}$ of the prior central value. The ground and first-excited-state energies of the oscillating state are affected by this change but not in a systematic way. This indicates that the oscillating-state signal is not strong in our data. Our main interest, though, is the non-oscillating ground state energy $aE(\mathbf{p})$; this value is unaffected by the change in $\sigma_{\tilde{\Delta}_{aE_p}}$.

In addition, we compare fit results with their priors. Figure 2 gives examples of these comparisons for fits on the (0.0062, 0.031) fine ensemble for charm- and bottom-type mesons. The x -axis labels the fit-parameter number, defined in Table IV; the ground-state energy and amplitudes of the desired-parity state are at positions 1, 3, and 5. We find that fit results for ground-state quantities are well within the prior widths. For excited states, in some cases the fitter simply returns the prior value, indicating that the quantity is not constrained by the data. In other cases, the results appear to be constrained by the data, indicating that some excited-state signal is in the correlator and the fitter adjusts the amplitudes to absorb it. Although it may appear in Fig. 2 that a number of excited-state quantities are well-determined, this is an artifact of a minimum- N fit; unlike the ground-state parameters, the excited state results are not stable as N is increased. For example, Fig. 3 compares the fit results shown in the upper left (pseudoscalar) panel of Fig. 2 (a), which uses $N = 3$, with a fit which only differs by the use of $N = 4$. The comparison demonstrates that the (desired-parity) ground-state quantities are stable to the change in N while other, excited-state, parameters are not.

For goodness-of-fit we begin by looking at the augmented χ^2/dof for each fit and verify that it is ≈ 1 or smaller, where “ ≈ 1 ” is based on the 80% range of the χ^2/dof distribution for a given number of degrees of freedom. As a final check, we overlay the result on an effective-mass plot. We define the “effective energy”

$$2aE_{\text{eff}}(\mathbf{p}) = \ln [C(t)/C(t + 2a)] \quad (5.1)$$

using a step of two time units in order to accommodate the oscillating contribution from the opposite-parity state. Figure 4 shows plots comparing $aE_{\text{eff}}(\mathbf{p})$ to the fit result on the (0.0062, 0.031) fine ensemble. The ground-state-energy result from the

introduction to this section.

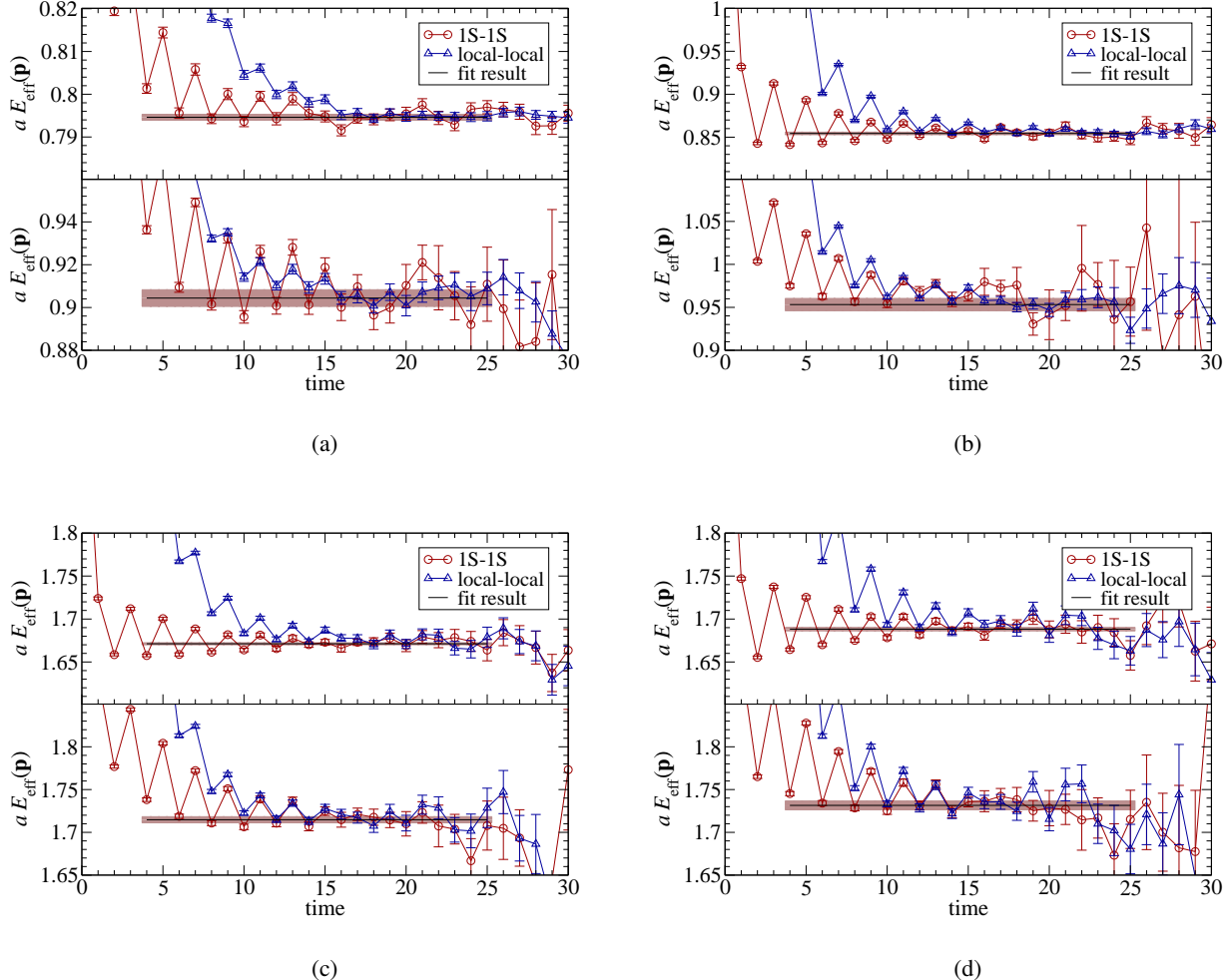


FIG. 4: Effective energy plots, $aE_{\text{eff}}(\mathbf{p})$, for charm-type (a) pseudoscalar and (b) vector mesons and bottom-type (c) pseudoscalar and (d) vector mesons on the $(0.0062, 0.031)$ fine ensemble. $\kappa = 0.127$ and 0.093 for charm- and bottom-type mesons, respectively; $am'_q = 0.0272$. The upper [lower] plot is from a fit where the meson has momentum of $\mathbf{n} = (0, 0, 0)$ [$\mathbf{n} = (2, 0, 0)$]. Open (blue) triangles mark the local correlator and open (red) circles mark the 1S-smeared correlator. Lines connecting the data points are simply to guide the eye; they are not a fit. The unadorned black line is the multi-correlator fit result and the shaded band marks the average 68% bootstrap error.

multiple-state fit is shown as a straight line segment over the time range fit. The band encompasses the average 68% bootstrap error. In each case, the fit result nicely matches the effective-energy plateau.

B. The kinetic mass M_2

Given results for $aE(\mathbf{p})$, we fit data where $|\mathbf{n}| \leq \sqrt{3}$ to Eq. (4.6) to determine the pseudoscalar and vector kinetic meson masses. Fits use a correlation matrix constructed from the bootstrap distributions. The tables in Appendix B give results for aM_2 , aM_2^* , and $a\bar{M}_2$ on the ensembles used for tuning, listed in Table III. Included in the tables are the χ^2/dof and the probability that χ^2 would exceed the value from the fit, known as the p value [45]. Typical dispersion relation fits are shown for the $(0.0062, 0.031)$ fine ensemble in Fig. 5.

In addition to statistical errors, we consider uncertainties from unphysical sea-quark masses, mistuning of the valence strange quark, and discretization. The noise in \bar{M}_2 makes it difficult to discern how \bar{M}_2 depends on the sea-quark masses. The \bar{M}_1 data is much cleaner, though, and we can use it to estimate the sea-quark error on \bar{M}_2 , and hence κ . To do this, we first note that, cf. Eq. (2.12),

$$aM_1 = am_1 + a\bar{\Lambda}_{\text{lat}} + O(1/m_Q) \quad (5.2)$$

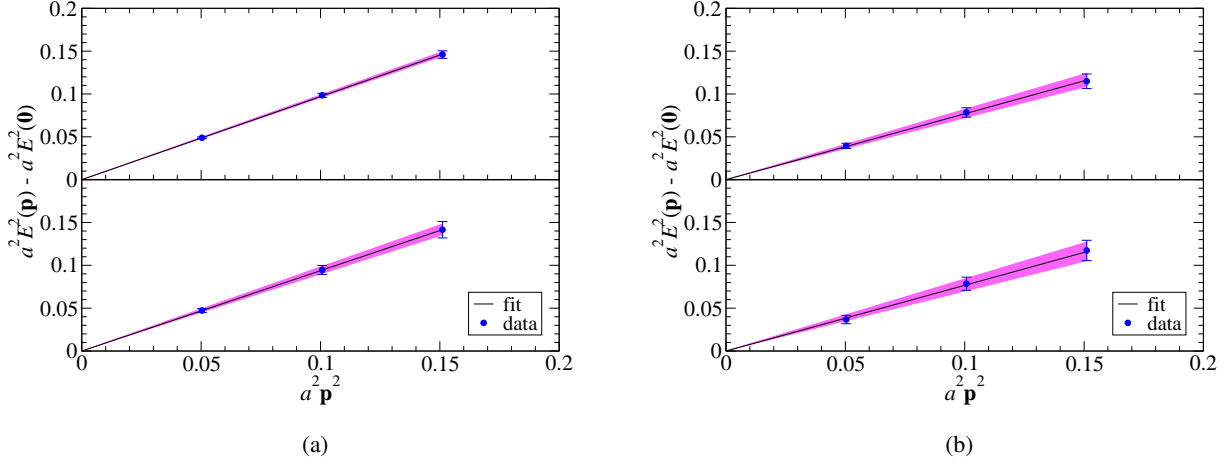


FIG. 5: Results of fits to the dispersion relation for (a) charm-type ($\kappa = 0.127$) and (b) bottom-type ($\kappa = 0.0923$) mesons on the (0.0062, 0.031) fine ensemble. (Blue) dots are the data. A black line shows the fit result with the (pink) shaded band showing the one-sigma error from the fit. Upper panels show results for pseudoscalars and lower for vectors.

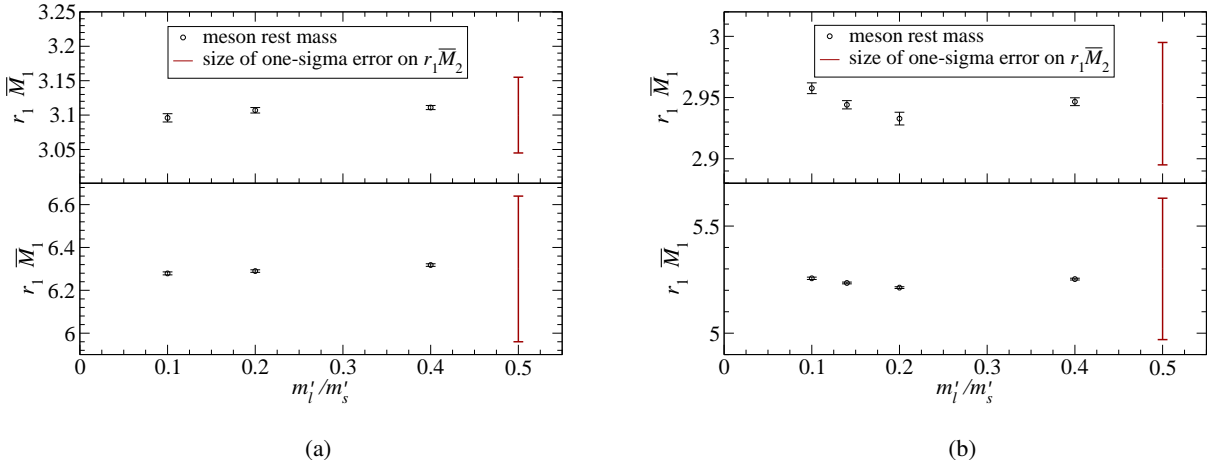


FIG. 6: The spin-averaged meson rest mass in physical units versus the ratio of the light to strange sea-quark masses m'_l/m'_s for the (a) fine and (b) coarse ensembles. Error bars are statistical only, from the average 68% bootstrap error. On the far right of the plot is a (red) bar indicating the size of the one-sigma statistical error on $r_1 \bar{M}_2$. The upper-panel plot is for charm-type mesons, lower is for bottom-type. Values of κ used are 0.127, 0.0923 on the fine ensembles with $am'_q = 0.0272$ and κ 0.122, 0.086 on the coarse ensembles with $am'_q = 0.0415$.

$$aM_2 = am_2 + a\bar{\Lambda}_{\text{lat}} + O(1/m_Q) \quad (5.3)$$

where am_1 and am_2 capture the leading heavy-quark dependence and $\bar{\Lambda}_{\text{lat}}$ depends only on the light degrees of freedom. Taking $a\bar{\Lambda}_{\text{lat}}$ to be the same for both $a\bar{M}_1$ and $a\bar{M}_2$ (see Appendix A and Ref. [46]) we can estimate the size of the effect of non-physical (light) sea quark masses on $a\bar{\Lambda}_{\text{lat}}$, and hence aM_2 , by studying the behavior of aM_1 as the light sea-quark masses are varied.

In Fig. 6, we plot the spin-averaged meson rest mass $r_1 \bar{M}_1$ versus the ratio of the light to strange sea-quark masses m'_l/m'_s for the coarse and fine ensembles used here. On the far right of each plot is a bar indicating the size of the 1- σ statistical error on $r_1 \bar{M}_2$; for fine this is from the (0.0062, 0.031) ensemble and for coarse the (0.007, 0.050) ensemble. The light sea-quark mass dependence is negligible compared to the statistical error on $r_1 \bar{M}_2$. We find similar behavior for the medium-coarse ensemble.

We must also consider how the non-physical value of the strange sea-quark mass affects \bar{M}_2 . The strange sea-quark mass is mistuned by an amount $0.19am'_s$, $0.31am'_s$ and $0.12am'_s$ on the fine, coarse, and medium-coarse ensembles, respectively. The continuum chiral perturbation theory expression for the heavy-light spin-averaged mass [47] shows that the leading sea-quark

dependence of \bar{M}_2 is proportional to the sum over the sea-quark masses, $2m'_l + m'_s$. Hence, varying am'_l tells us about the effect of varying am'_s . Figure 6 shows that a change of $0.3am'_s$ in am'_l has a negligible effect on \bar{M}_2 , so we conclude that the mistuning of am'_s has a negligible effect as well.

The tuned value of the strange-quark mass on each ensemble is given in Table I. On the fine lattice, the valence-quark mass used in the simulation, $am'_q = 0.0272$, differs from the physical value $am_s = 0.0252$ by 0.0020. A comparison of our results for $a\bar{M}_2$ in Table XVIII shows that even a deviation in am'_q of twice this size does not discernibly affect $a\bar{M}_2$. The situation is similar for the coarse and medium-coarse results. For the coarse ensembles, the simulation mass $am'_q = 0.03$ differs by 0.0044 from the tuned value of am_s . Table XIX shows that $a\bar{M}_2$ is barely affected at the $1-\sigma_{a\bar{M}_2}$ level as am'_q changes by over twice this size. For the medium-coarse ensembles, the simulation mass of 0.0484 differs from the tuned strange-quark mass by 0.0058. A comparison of the values of $a\bar{M}_2$ in Table XX shows that a deviation in am'_q just under twice this size yields, at most, a $1-\sigma_{a\bar{M}_2}$ variation in $a\bar{M}_2$. Therefore, we take our results of $a\bar{M}_2$ at $am'_q = 0.0272, 0.03$, and 0.0484 as the masses of the B_s and D_s on the fine, coarse and medium-coarse ensembles, respectively, with no additional error for valence-mass mistuning.

In Appendix A, we derive an expression for the discretization error in M_2 , $M_2 = M_{\text{continuum}} + \delta M_2$. The result, Eq. (A22), can be written

$$\delta M_2 = \frac{\bar{\Lambda}^2}{6m_2} \left[5 \left(\frac{m_2^3}{m_4^3} - 1 \right) + 4w_4(m_2a)^3 \right], \quad (5.4)$$

replacing $\langle p^2 \rangle$ of Eq. (A22) with $\bar{\Lambda}^2$. Expressions for the short-distance coefficients m_2 , m_4 , and w_4 are given in Appendix A [14, 23]. To estimate the discretization error, we use values of the physical (pole) quark mass (1.4 GeV for charm and 4.2 GeV for bottom) for m_2 in the prefactor of Eq. (5.4), and $\bar{\Lambda} = 0.7$ GeV. Using these values, u_0 from Table II, and κ_{crit} from Table XVII yields the values of δM_2 shown in Table IX. The error estimate in Eq. (5.4) pertains to the kinetic mass, but the main focus here is the tuning of κ . After tuning, we shall propagate this error from M_2 to κ_c and κ_b .

C. Fitting Summary

The preceding subsections contain many details intended for those engaged in similar analyses. In this section, we re-emphasize the main features of the analysis. Because, in this and related [3–8] work, we are interested in the ground state, we do not dwell on the excited states here.

Our priors are guided by the data, using one ensemble to set them and (generally) other ensembles for physical results. We choose a time range such that the fit results for the ground state are stable, listed in Table VII. We also test for stability as the number N of (pairs of) exponentials grows—as shown in one example in Fig. 1—and choose the minimum value of N for which the central value is stable within errors. The errors on the ground-state amplitudes and energies are always determined by the data, not the priors, as shown in Fig. 2 and 3. (In many cases, even excited-state information is data-determined, not prior-determined.) Figure 4 shows that the fits agree with the effective energies. (Note that the oscillations of aE_{eff} at small t are to be expected with staggered quarks.) In conclusion, the constrained curve fitting for $E(\mathbf{p})$ has worked as advertised, subsuming the subjectivity of fit ranges and different choices of N into robust results for both central value and error bar. Figures 5 and 6 show that, once $E(\mathbf{p})$ is well-determined, we can straightforwardly obtain the kinetic mass M_2 and the hyperfine splitting.

VI. RESULTS

In this section, we present the main results of these calculations, including our error analysis. Section VI A focuses on the tuned values of κ_c and κ_b , Sec. VI B on the D_s and B_s hyperfine splittings, and Sec. VI C on the critical value of the hopping

TABLE IX: The relative error in the tuned hopping parameter $\delta\kappa/\kappa$ due to discretization effects in the kinetic meson mass. The ensembles used are (0.0062, 0.031), (0.007, 0.050), and (0.0097, 00484) for the fine, coarse, and medium-coarse lattices, respectively. Values of κ are 0.127 and 0.0923 on fine; 0.122 and 0.086 on coarse; and, 0.122 and 0.076 on medium-coarse. The $[\dots]$ denotes the quantity in brackets in Eq. (5.4). We use $(\bar{\Lambda}^2/6m_{\text{ch}}) = 0.058\bar{3}$ and $(\bar{\Lambda}^2/6m_{\text{bot}}) = 0.019\bar{4}$ to convert the $[\dots]$ to δM_2 . Values of $\delta\kappa/\kappa$ are given as fractions not a percentage.

lattice spacing	charm				bottom					
	m_0a	$[\dots]$	δM_2	$\frac{dm_2a}{dm_0a}$	$\frac{\delta\kappa}{\kappa}$	m_0a	$[\dots]$	δM_2	$\frac{dm_2a}{dm_0a}$	$\frac{\delta\kappa}{\kappa}$
fine	0.391	1.31	0.0763	0.843	-0.0086	2.08	16.8	0.327	0.880	-0.0256
coarse	0.565	2.37	0.1384	0.831	-0.0203	2.62	23.6	0.459	0.899	-0.0440
medium-coarse	0.682	3.18	0.1857	0.830	-0.0346	3.56	37.2	0.724	0.922	-0.0756

parameter κ_{crit} .

A. The tuning of κ_c and κ_b

As discussed in Sec. V B, effects from non-physical sea-quark masses and the mistuning of the valence strange-quark mass are negligible compared to the statistical error on $a\bar{M}_2$. In that section, we explain why taking $a\bar{M}_2$ at certain values of am'_q is an acceptable approximation to $a\bar{M}_2$ at the tuned physical strange-quark mass. We choose to tune κ at those same am'_q , which are $am'_q = 0.0272$ on the (0.0062, 0.031) fine ensemble, $am'_q = 0.03$ on the (0.007, 0.050) coarse ensemble, and $am'_q = 0.0484$ on the (0.0097, 0.0484) medium-coarse ensemble.

To obtain the tuned κ for the charm (bottom) quark, κ_c (κ_b), we want to interpolate \bar{M}_2 to the PDG value of the spin-averaged D_s (B_s) mass [45]. In practice, it is simpler to do the interpolation with the meson mass in lattice units. Hence, we linearly interpolate $a\bar{M}_2$ to $a\bar{M}_{\text{PDG}}$, the PDG value for the meson mass converted to lattice units with a from Table I. This interpolation is repeated for the entire bootstrap distribution of $a\bar{M}_2$. We then estimate the statistical error on κ as the average 68% bootstrap error described in Sec. IV A. The discretization error in M_2 , δM_2 , is given by Eq. (5.4), and is always positive. This results in a single-sided, negative error bar on κ . We convert δM_2 to the error, $\delta\kappa$, using $dM_2/d\kappa \approx dm_2/d\kappa$ and expressions for m_0a and m_2a given in Appendix A. The $\delta\kappa$ are given in Table IX. The experimental errors on the PDG values are negligible. The remaining errors to consider are those which appear in the conversion between lattice and physical units. The error in the determination of r_1/a is negligible, so we only need to consider the error in r_1 , given in Eq. (3.2).

The error on r_1 is propagated to an error on a^{-1} and then to an error on $a\bar{M}_{\text{PDG}}$, denoted σ_{PDG} . Table X gives the values of the PDG meson masses used in this work and tabulates their spin-averaged mass and hyperfine splitting. Table XI gives the spin-averaged mass in lattice units. The uncertainty σ_{PDG} is propagated to κ using the standard error formula $\sigma_\kappa = \sigma_{\text{PDG}}/s$, where s is the slope used in the interpolation. Table XII gives the error budget for κ_c and κ_b , and Table XIII lists the final tuned results.

TABLE X: PDG values of the pseudoscalar and vector masses for the D_s and B_s mesons and the hyperfine splitting Δ [45]. Also listed is the derived quantity \bar{M} , the spin-averaged mass.

	M (GeV)	M^* (GeV)	\bar{M} (GeV)	Δ (MeV)
D_s	1.96849(34)	2.1123(5)	2.0763(4)	143.9(4)
B_s	5.3661(6)	5.4120(12)	5.4005(9)	46.1(1.5)

TABLE XI: Spin-averaged PDG masses converted to lattice units with an error from the uncertainty in the lattice spacing a . Values of a used in the conversion can be found in Table I.

Ensemble	$a\bar{M}_{D_s}$	$a\bar{M}_{B_s}$
Fine (0.0062, 0.031)	$0.884^{+0.009}_{-0.023}$	$2.299^{+0.023}_{-0.060}$
Coarse (0.007, 0.050)	$1.242^{+0.012}_{-0.032}$	$3.230^{+0.031}_{-0.083}$
Medium-coarse (0.0097, 0.0484)	$1.529^{+0.015}_{-0.039}$	$3.977^{+0.038}_{-0.102}$

TABLE XII: Percent errors in the tuned κ and the total error. For several sources of uncertainty, we determined that the error was smaller than the precision of these calculations. This is indicated by an entry of “0.0” in the table.

Uncertainty	Charm			Bottom		
	Fine	Coarse	Medium-coarse	Fine	Coarse	Medium-coarse
Statistical	1.26	0.57	0.53	5.0	9.1	5.6
Discretization	(0, -0.86)	(0, -2.0)	(0, -3.46)	(0, -2.6)	(0, -4.4)	(0, -7.56)
Sea-quark masses	0.0	0.0	0.0	0.0	0.0	0.0
am_s mistuning	0.0	0.0	0.0	0.0	0.0	0.0
Unit conversion (a)	(+0.90, -0.35)	(+0.49, -0.19)	(+0.77, -0.30)	(+1.7, -0.64)	(+1.9, -0.72)	(+1.76, -0.66)
Total	(1.5, 1.6)	(+0.75, -2.1)	(+0.93, -3.5)	(+5.3, -5.7)	(+9.3, -10.1)	(+5.9, -9.4)

B. The rest mass and hyperfine splitting

In this section, we discuss the uncertainties in our calculation of the hyperfine splitting and compare our final results, for the B_s and D_s systems, with the PDG values. To support the discussion, we tabulate our results for the pseudoscalar and vector meson rest masses and the hyperfine splitting, aM , aM^* , $a\Delta_1$, $r_1\Delta_1$, in Tables XXI–XXIII in Appendix C. Statistical errors in these tables are the average 68% bootstrap errors described in Sec. IV A. The other errors we consider are the mistuning of the valence strange-quark mass, unphysical sea-quark masses, the uncertainty in the tuning of κ , discretization effects, and the conversion to physical units. For the central value, at each lattice spacing, we take $a\Delta_1$ at the tuned values of κ_c and κ_b , linearly interpolating in κ when necessary.

PDG results for the hyperfine splitting show a weak dependence on the light-quark valence mass, so we expect the mistuning in the simulated valence strange-quark mass to have a negligible effect.³ The simulation valence masses $am'_q = 0.0272, 0.03, 0.0484$ for the fine, coarse, and medium-coarse lattices, respectively, differ from the physical am_s given in Table I by 0.0020, 0.0044, 0.0058, respectively. Tables XXI–XXIII show that, indeed, these small mistunings have a negligible effect on the hyperfine splitting. Hence, we do not interpolate to am_s ; rather, we take $a\Delta_1$ at the valence masses am'_q listed above as the result at the physical strange valence-quark mass and take the error for this approximation to be negligible.

To estimate the error due to the non-physical values of the sea-quark masses we use partially-quenched chiral perturbation theory. The needed expression is derived in Appendix D and we repeat Eq. (D1) here for convenience. The hyperfine splitting $M_x^* - M_x$ of a heavy-light meson with light-valence quark x is

$$M_x^* - M_x = \Delta - \frac{\Delta g_\pi^2}{8\pi^2 f^2} \delta_{\log} + 2\Delta^{(\sigma)}(2m_l + m_s) + 2\Delta^{(a)}m_x , \quad (6.1)$$

where δ_{\log} contains the chiral logs, m_l and m_s are the light and strange sea-quark masses, and $\Delta^{(\sigma)}$ and $\Delta^{(a)}$ are counter terms which must be determined from the lattice data. Working at a fixed value of m_x , we can use the difference of splittings at different values of m_l to determine $\Delta^{(\sigma)}$. Given $\Delta^{(\sigma)}$, we can find the difference between the splitting at simulation values of (m'_l, m'_s) and the physical values $(m_{l,\text{phys}}, m_{s,\text{phys}})$. We take this difference as the error due to the non-physical sea-quark masses.

We have tabulated values of the hyperfine splitting in physical units, $r_1\Delta_1$, in Appendix C 2. Figure 7 shows how $r_1\Delta_1$ varies with the light sea-quark mass on fine and coarse lattices. From Fig. 7, it is clear that, due to statistical variation in the splitting, using the difference in the central values of splittings from any two points will yield different values for $\Delta^{(\sigma)}$. For the fine and coarse ensembles, we look only at the $am_l/am_s = 0.4$ to 0.1 and $am_l/am_s = 0.4$ to 0.2 differences and take the one that gives the larger error; for medium coarse, we have no $am_l/am_s = 0.1$ data and so take the error from the $am_l/am_s = 0.4$ to 0.2 difference.

For the error estimate, we take $f = 131$ MeV and $g_\pi = 0.51$ [48]. We relate meson to quark masses by

$$M_{xy}^2 = B_0(m_x + m_y) \quad (6.2)$$

where B_0 is determined empirically with $r_1B_0 = 6.38, 6.23, 6.43$ on the fine, coarse, and medium-coarse lattices, respectively. These values of B_0 come from tree-level fits to MILC light-meson data, as described in Refs. [2, 11, 35]. We calculate $\Delta^{(\sigma)}$ for each meson type, B_s and D_s , at each lattice spacing. We then calculate the difference

$$(M_x^* - M_x)_{\text{sim}} - (M_x^* - M_x)_{\text{phys}} \quad (6.3)$$

where the subscript “sim” (“phys”) denotes simulation (physical) sea-quark mass inputs (am_l, am_s) . For the physical masses, we use $(am_{l,\text{phys}}, am_{s,\text{phys}}) = (0.00092, 0.0252), (0.00125, 0.0344), (0.00154, 0.0426)$ for the fine, coarse, and medium-coarse lattices, respectively. These values of the quark masses are taken from Ref. [11], after adjustment for the r_1 scale used here.

TABLE XIII: Final tuned results for κ_c and κ_b with the total error.

	Fine	Coarse	Medium-coarse
κ_c	0.127(2)	0.1219^{+9}_{-25}	0.122^{+1}_{-4}
κ_b	0.090(5)	0.082(8)	0.077^{+5}_{-7}

³ For $X = B$ or D , the difference between the $M_{X_s^*}-M_{X_s}$ splitting and the $M_{X^*}-M_X$ splitting is measured to be about 1% or less [45].

The simulation masses are those on the the (0.0062, 0.031) fine, (0.007, 0.050) coarse, and (0.097, 0.0484) medium-coarse ensembles. The error calculated in this manner is labeled “sea-quark masses” in Tables XIV and XV.

For the uncertainty in $a\Delta_1$ due to the error in κ , recall that the non-negligible sources of error in κ , from Table XII in Sec. VI A, are statistics, units conversion, and discretization error in M_2 . Because we want to consider discretization errors separately from all others, we start by considering only the κ -tuning error that comes from statistics and units-conversion. To convert the error in κ to an error in $a\Delta_1$, we look at the change in $a\Delta_1$ between two values of κ on the (0.0062, 0.031) fine, (0.007, 0.050) coarse, and (0.097, 0.0484) medium-coarse ensembles; specific values can be found in Tables XXI–XXIII. This is the error labeled “ κ tuning” in Tables XIV and XV.

For the D_s (B_s) meson, Table XIV (XV) gives the error budget for $a\Delta_1$ at each lattice spacing, from all sources *except* discretization. These are statistics, valence-mass mistuning, unphysical sea-quark masses, and κ tuning. In Fig. 8, these values are plotted as black, filled dots.

We now consider the three, distinct sources of discretization error in $a\Delta_1$. The first is indirect, coming from the discretization error in aM_2 , which is propagated to an error on κ as discussed in Sec. VI A. This error can be traced to a mismatch between the spin-independent $O(p^4)$ terms in Eq. (2.8) (not given explicitly) and the corresponding terms in the effective Lagrangian for continuum QCD. These terms contribute to $a\bar{M}_2$ as discussed in Appendix A. The second source of discretization error is a direct result of the lattice-continuum mismatch of the dimension-seven operator $\{i\sigma \cdot \mathbf{B}, \mathbf{D}^2\}$ [23].⁴ The third source of discretization error is the $O(\alpha_s)$ mismatch in the coefficient of the $i\sigma \cdot \mathbf{B}$ operator in Eq. (2.10). For the discussion of error estimates below, it is useful to recall that the heavy-quark dynamics associate m_2 with the physical quark mass. Mismatches between m_2 and the generalized masses associated with other operators capture the heavy-quark discretization effects. We now give numerical estimates of the error from each source.

Our estimate of discretization error in $a\bar{M}_2$ and its inclusion in the error on κ is discussed in Sec. VI A. In Fig. 8, the value of $r_1\Delta_1$ with an error that includes *only* the uncertainty due to the discretization error on κ is shown as an open (blue) circle with a dashed error bar. Note, as described in Sec. V B, this uncertainty estimate depends on one’s choice of Λ_{QCD} . In this paper, we use $\Lambda_{\text{QCD}} = 0.7$ GeV. Choosing $\Lambda_{\text{QCD}} = 0.5$ GeV would cut the error on κ in half and decrease the error on $r_1\Delta_1$.

Next we estimate the contribution from the dimension-seven operator $\{i\sigma \cdot \mathbf{B}, \mathbf{D}^2\}$. Using the notation of Ref. [23], summarized in Sec. A 4, this operator’s contribution to the hyperfine splitting has a coefficient

$$\frac{1}{(m_{B'}a)^3} = \frac{1}{(m_4a)^3}, \quad (6.4)$$

where the equality holds at the tree level for the choices of parameters in our action. The difference between am_4 and am_2 captures the discretization error. The fractional error in the hyperfine splitting due to this mismatch is

$$(a\Lambda_{\text{QCD}})^2 2am_2 \left[\frac{1}{(2am_4)^3} - \frac{1}{(2am_2)^3} \right]. \quad (6.5)$$

This error is plotted as a (green) dash-dot line on an X in Fig. 8. It would be added in quadrature with the error on the filled dot, if it were to be included in the total error. Again we take $\Lambda_{\text{QCD}} = 0.7$ GeV, but choosing $\Lambda_{\text{QCD}} = 0.5$ would cut these error bars in half. The error from Eq. (6.5) is small for the D_s splitting at the fine lattice spacing, but increasingly large and non-negligible at the coarse and medium-coarse lattice spacings; for the B_s splitting, the error is negligible.

Finally, we turn to the effects of the $O(\alpha_s)$ mistuning in c_B , which leads to an $O(\alpha_s)$ mismatch between m_Ba and m_2a . Ideally, c_B should be adjusted so the coefficient of $\bar{h}^{(+)} i\sigma \cdot \mathbf{B} h^{(+)}$ equals $Z_B/2m_2$, where Z_B is a coefficient with an anomalous dimension, such that $Z_B \bar{h}^{(+)} i\sigma \cdot \mathbf{B} h^{(+)}$ is scale and scheme independent [49]. In practice, c_B is chosen in some approximation, in our case the tadpole-improved tree level of perturbation theory.

Given a value of c_B , our simulations produce

$$M_1^* - M_1 = \Delta_1 = \frac{4\lambda_2}{2m_B(c_B)}. \quad (6.6)$$

From Eq. (A26), we see that $1/am_B$ has a contribution $c_B/(1+m_0a)$. Hence, to include the leading correction to the hyperfine splitting, we shift

$$4\lambda_2 a \left[\frac{1}{2am_B(c_B)} \right] \rightarrow 4\lambda_2 a \left[\frac{1}{2am_B(c_B)} + \frac{c_B^{\text{ideal}} - c_B}{2(1+m_0a)} \right] \quad (6.7)$$

⁴ Other dimension-six and -seven operators are either redundant, loop-suppressed, or known to have small coefficients [23].

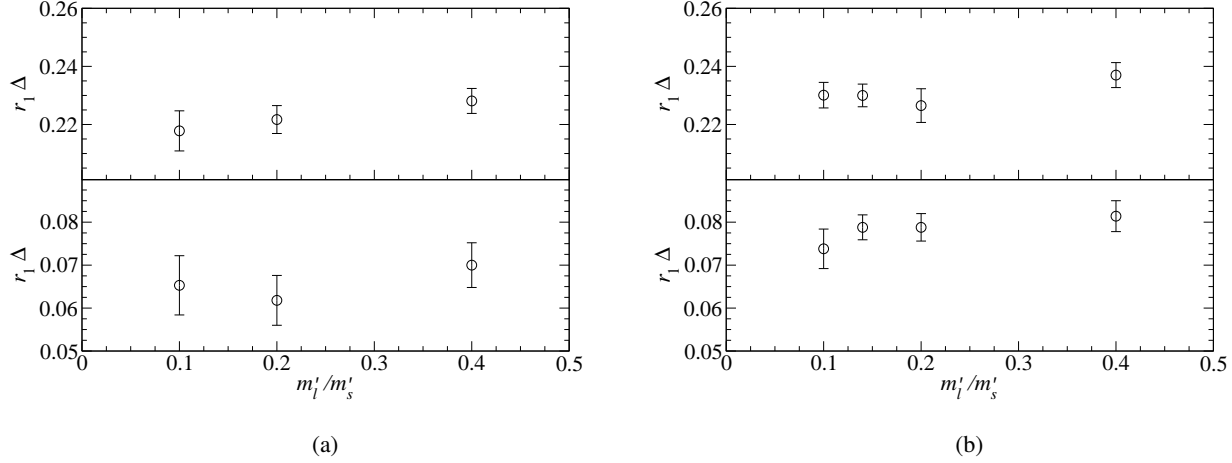


FIG. 7: The hyperfine splitting, in units of r_1 , versus the ratio of the light to strange sea-quark masses m_l'/m_s' on (a) fine and (b) coarse ensembles. Errors are the average 68% bootstrap error. The upper panel in each plot is for charm-like splittings and the lower panel is for bottom-like splittings. Values of κ are 0.127, 0.0923 for the fine ensembles and 0.122, 0.086 for coarse ensembles. Values of am_q' are 0.0272 and 0.0415 for the fine and coarse ensembles, respectively.

where c_B^{ideal} is the ideal choice. (Because loop corrections to $1/am_B$ depend on c_B , subleading corrections also exist.) To estimate the error in Δ_1 , we have to estimate $c_B^{\text{ideal}} - c_B$. In fact, Eq. (6.7) can also be used to shift the central value of the hyperfine splitting.

Reference [50] describes preliminary work on a calculation of the one-loop corrections to $c_B^{[1]}$, as a function of the bare quark mass. For all relevant values of m_0a , the one-loop effects are a small correction to the tadpole-improved Ansatz $c_B = u_0^{-3}$, provided that u_0 is the average link in Landau gauge. On the coarse ensembles, we chose u_0 this way, and we can estimate the remaining correction directly from the calculation in Ref. [50]. Given further uncertainties from higher orders, we take this small correction as an uncertainty estimate. On the medium-coarse and fine ensembles, however, we chose u_0^4 to be the average plaquette. In those cases, the leading correction to c_B comes from,

$$c_B^{\text{ideal}} - c_B = u_{0,\text{LL}}^{-3} - u_{0,\text{plaq}}^{-3} \quad (6.8)$$

where the labels refer to ‘‘Landau-gauge link’’ and ‘‘plaquette.’’ Equation (6.8) leads to significant corrections to the hyperfine splitting, so we shift Δ_1 on the medium-coarse and fine ensembles by the amount corresponding to Eq. (6.7) and (6.8). These shifts put Δ_1 at the medium-coarse and fine lattice spacings on the same footing as those at the coarse spacing. Empirically, they flatten the lattice-spacing dependence.

For the medium-coarse and fine data, we use the values of u_0 given in Table XVI to calculate the shift described above. It is displayed in Fig. 8 as a (pink) star with a single-sided, positive error bar. To obtain an error bar corresponding to the one-loop correction to c_B in Ref. [50], we take $\alpha_s(0.09 \text{ fm}) = 1/3$ and use one-loop running to obtain values of α_s for the coarse and medium-coarse lattices. These corrections are shown in in Fig. 8 as a (red) triangle with a solid error bar.

In summary, discretization errors in the hyperfine splitting are small at the fine lattice spacing; therefore, we take as our final results the splittings calculated on the fine lattice. In addition, since the effect of the leading $O(\alpha_s)$ mistuning of c_B can be quantified, we shift our final central values by this amount. All other discretization errors are included in our final error. We convert our results to physical units using the values of r_1/a and r_1 as listed in Table I. After including the error from the units conversion in the total, our final results for the hyperfine splittings are

$$\Delta_{D_s} = 145 \pm 15 \text{ MeV} \quad (6.9)$$

$$\Delta_{B_s} = 40 \pm 9 \text{ MeV} \quad (6.10)$$

These results are in good agreement with the PDG values of $143.9 \pm 0.4 \text{ MeV}$ and $46.1 \pm 1.5 \text{ MeV}$, respectively.

C. The critical hopping parameter κ_{crit}

In principle, it is possible to carry out a suite of nonperturbative heavy-quark calculations without knowing κ_{crit} , but in practice κ_{crit} is useful. In particular, it enters the construction of improved bilinear and 4-quark operators via m_0a Eq. (2.5). It

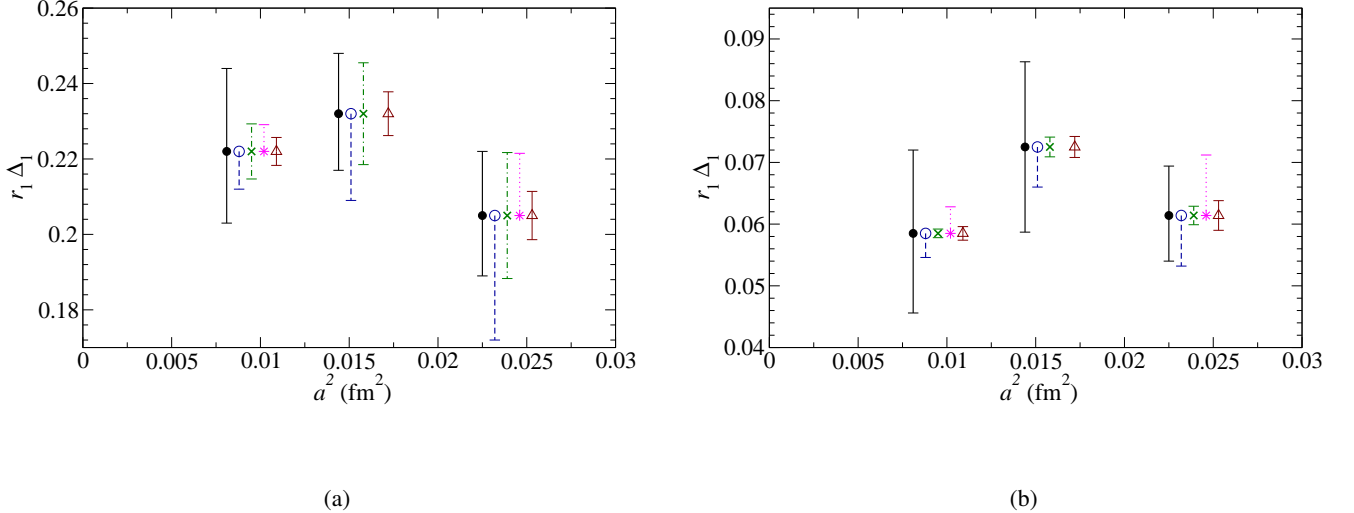


FIG. 8: Hyperfine splittings in r_1 units versus the squared lattice spacing a^2 (fm^2) for the (a) D_s meson and (b) B_s meson. Filled (black) dots with a solid error bar show the splitting with an error from all sources *except* discretization. Open (blue) circles with a dashed error bar show the splitting with an error that also includes discretization error effects in κ . (Green) X's with dash-dotted error bars show the estimated size of discretization effects from the lattice-continuum mismatch of the dimension-7 operator $\{i\sigma \cdot \mathbf{B}, \mathbf{D}^2\}$ — the errors are barely visible for the B_s system. (Pink) stars with a dotted error bar show the $O(\alpha_s)$ discretization error from the 1-loop mismatch between m_2 and m_B . For the difference between the $O(\alpha_s)$ discretization effects on the coarse lattice versus the fine and medium-coarse lattices, see the text.

also enters the computation of matching factors such as Z_V and Z_A [18]. Note that these all amount to small corrections, so we do not need a very precise determination of κ_{crit} . Equation (2.5) shows that it does not have to be much better determined than κ_c and κ_b .

A nonperturbative definition of κ_{crit} is the value of κ such that the mass of a pseudoscalar meson consisting of two Wilson quarks (with the clover action) vanishes. The computation of these light-light pseudoscalar meson masses shares code with the

TABLE XIV: Percent errors in the hyperfine splitting, $a\Delta_1$, of D_s *not* including discretization effects.

Uncertainty	Fine	Coarse	Medium-coarse
Statistical	2.2	1.9	1.9
κ tuning	(8.8, -7.5)	(4.0, -3.1)	(4.0, -2.7)
Valence m_s	0	0	0
Sea-quark masses	3.6	5.4	6.9
Total	(10, -9)	(7, -7)	(8, -8)

TABLE XV: Percent errors in the hyperfine splitting, $a\Delta_1$, of B_s *not* including discretization effects.

Uncertainty	Fine	Coarse	Medium-coarse
Statistical	9.5	4.0	5.6
κ tuning	(12, -11)	(17, -17)	(11, -10)
Valence m_s	0	0	0
Sea-quark masses	17	7.8	2.6
Total	(23, -22)	(19, -19)	(13, -12)

TABLE XVI: Tadpole-improvement factors for the estimate of the $O(\alpha_s)$ discretization error shown in Fig. 8.

ensemble	$u_{0,\text{plaquette}}$	$u_{0,\text{Landau}}$
fine (0.0062, 0.031)	0.878	0.854
medium-coarse (0.0097, 0.0484)	0.860	0.822

TABLE XVII: Values of κ_{crit} by ensemble. “ u_0 used” gives the origin of the u_0 value used in the κ_{crit} determination. κ_{crit} values are given in two columns. The first κ_{crit} column contains values which were determined by a fit. The second κ_{crit} column contains values which were estimated from fitted values at the same (approximate) lattice spacing. The last column gives the fit method used in the determination, explained in the text.

Lattice	(am'_l, am'_s)	u_0 used	κ_{crit}		
			Iterated fit	Direct fit	Estimated
Fine	(0.0031, 0.031)	Landau-gauge link		0.1372	
	(0.0062, 0.031)	Landau-gauge link	0.1372		
	(0.0062, 0.031)	plaquette	0.1391		
	(0.0124, 0.031)	Landau-gauge link	0.1372		
Coarse	(0.005, 0.050)	Landau-gauge link		0.1379	
	(0.007, 0.050)	Landau-gauge link		0.1379	
	(0.010, 0.050)	Landau-gauge link	0.1379		
	(0.020, 0.050)	Landau-gauge link	0.1378		
	(0.030, 0.050)	Landau-gauge link	0.1377		
Medium-coarse	(0.0097, 0.0484)	plaquette		0.1424	
	(0.0194, 0.0484)	plaquette		0.1424	
	(0.0290, 0.0484)	plaquette		0.1423	

work reported here and in Ref. [8], and it is convenient to report the analysis here. The value of κ_{crit} depends on u_0 via our choice of clover coupling, $c_B = c_E = u_0^{-3}$. In this and other work [3–8], u_0 has been set sometimes from the average plaquette and sometimes from the average link in Landau gauge. The prescription for u_0 used in each κ_{crit} determination is given in column four of Table XVII.

The determination of κ_{crit} is carried out on a subset of the available configurations, 50–100 configurations for the fine ensembles and 400–600 for the coarse and medium-coarse. We compute two-point correlators for a range of κ that yields meson masses of about $M_{\text{PS}} = 450$ –900 MeV on the fine ensembles, 650–1100 MeV on the coarse ensembles, and 550–950 MeV on the medium-coarse ensembles. It is impractical to push to lower M_{PS} due to exceptional configurations. M_{PS} is a function of the quark mass, which we parametrize as the tree-level, tadpole-improved kinetic or rest mass. In the relevant region, $m_{1,2}a = m_0a[1 - \frac{1}{2}m_0a] + O((m_0a)^3)$, so both pertain equally well. The meson masses can be fit to a polynomial ansatz

$$a^2 M_{\text{PS}}^2(\kappa) = A + B a m_2(\kappa, \kappa_{\text{crit}}) + C a^2 m_2^2(\kappa, \kappa_{\text{crit}}) \quad (6.11)$$

(or m_1 instead of m_2), where $A = 0$ when κ_{crit} is correctly adjusted.

We use two techniques to determine κ_{crit} . One method starts with a reasonable value of κ_{crit} and fits Eq. (6.11) to obtain A , B , and C , which depend implicitly on κ_{crit} . A better trial value of κ_{crit} is chosen, and the process is iterated until a κ_{crit} is found such that $A = 0$. We call this the “iterated fit”. The second method freezes A to zero, and then B , C , and κ_{crit} are the fit parameters. We call this the “direct fit”. On several ensembles the κ_{crit} values were simply estimated from the other ensembles with the same (approximate) lattice spacing, these are labeled as “estimated”.

Table XVII contains our results for κ_{crit} , indicating the method used. The table does not include error bars for κ_{crit} , but we believe that the results are correct to the number of significant figures shown, even though the range of M_{PS} is high. We carried out several tests to verify this accuracy. We compared linear iterated fits [i.e., $C = 0$ in Eq. (6.11)] to the baseline quadratic. We also compared direct fits with and without the (continuum) chiral log. These test show that higher order or log contributions do not alter our values of κ_{crit} significantly. We fit comparable data with staggered valence quarks allowing $(m_0a)_{\text{crit}} \neq 0$, thereby testing whether a range of such large M_{PS} skews the results. None of these tests suggests an error larger than a few in the fourth digit. Such errors are negligible compared to those for κ_c and κ_b —see Tables XII and XIII—when forming m_0a with Eq. (2.5).

VII. SUMMARY AND OUTLOOK

An accurate and precise determination of κ_c and κ_b is important for all calculations using the Fermilab action [3–8]. In this analysis, the error on κ_b is dominated by statistics, and the error on κ_c receives approximately equal contributions from statistics and discretization effects. These errors play a significant role on quantities as diverse as D - and B -meson decay constants [3] and the quarkonium hyperfine splitting [8]. Our final results for κ_c and κ_b are given in Table XIII.

Another ingredient that is useful for matrix elements [3–5] is the additive renormalization of the bare quark mass or, equivalently, κ_{crit} . The improvement and matching of the operators needed to compute these matrix elements depends mildly on κ_{crit} via m_0a [18]. Our final results for κ_{crit} are given in Table XVII.

The key ingredient needed to determine κ_c and κ_b is a computation of the pseudoscalar and vector heavy-strange meson masses. These can be combined to yield the hyperfine splitting for D_s and B_s mesons. Our final results for the hyperfine

splittings are given in Eqs. (6.9) and (6.10). Both are in good agreement with the corresponding PDG averages. These results bolster confidence in the tuning of κ_c and κ_b , as well as the choice $c_B = u_0^{-3}$. Further tests of these choices come from related calculations of the quarkonium spectrum [8]. With detailed attention given to the connection between action parameters and mass splittings, those results are found to be consistent with experiment within the expected uncertainties.

Improved determinations of κ_c , κ_b , and κ_{crit} for the medium-coarse, coarse, and fine ensembles are underway with higher statistics, as well as calculations on the new superfine ($a \approx 0.06$ fm), and ultrafine ($a \approx 0.045$ fm) lattices. The increased statistics will also allow us to use higher momentum data and fit to the $O(p^4)$ terms in the dispersion relation. Refinements in the determination and use of r_1/a are allowing for a better understanding of sea-quark effects which will be needed as the statistical error on aM_2 decreases. We are also investigating the use of twisted boundary conditions [51] which will allow us to obtain data points at lower momenta.

As uncertainties in M_2 and M_1 decrease, there will be a need for a better understanding of the chiral behavior of these masses. One-loop, $O(\Lambda/m_Q)$ chiral perturbation theory results exist for continuum QCD [47]. The extension to staggered chiral perturbation theory should be straightforward, and would allow us to extrapolate the light-valence mass to the physical up/down quark mass and determine the hyperfine splittings of the B^\pm and D^\pm mesons. In this paper, we have included the partially quenched expression for the hyperfine splitting in Appendix D, since it is useful in estimating uncertainties from the unphysical sea-quark masses.

In addition, tuned values of κ_c , κ_b , and κ_{crit} combined with one-loop (lattice) perturbation theory can yield determinations of the pole masses m_1 and m_2 for both charmed and bottom quarks⁵, which can be converted to the potential-subtracted, $\overline{\text{MS}}$, and other schemes [6]. Quark masses combined with staggered chiral perturbation theory for the B^\pm and D^\pm mesons, can yield *ab initio* calculations of HQET matrix elements [22, 52], which are used to calculate the Cabibbo-Kobayashi-Maskawa matrix element $|V_{cb}|$ via inclusive decay measurements. Finally, improved determinations of the oscillating-state energy E^p could make determinations of the experimentally accessible masses of the positive parity states, $D_{s0}^*(2317)$ and $D_{s1}(2460)$ [53] a viable option [54].

Acknowledgments

Computations for this work were carried out on facilities of the USQCD Collaboration, which are funded by the Office of Science of the U.S. Department of Energy. This work was supported in part by the U.S. Department of Energy under Grants No. DE-FC02-06ER41446 (C.D., L.L.), No. DE-FG02-91ER40661 (S.G.), No. DE-FG02-91ER40677 (A.X.K., E.G., R.T.E.), No. DE-FG02-91ER40628 (C.B., E.D.F.), No. DE-FG02-04ER-41298 (D.T.); the National Science Foundation under Grants No. PHY-0555243, No. PHY-0757333, No. PHY-0703296 (C.D., L.L.), No. PHY-0757035 (R.S.), No. PHY-0704171 (J.E.H.) and No. PHY-0555235 (E.D.F.); URA visiting scholars awards (E.G., R.T.E.), and the M. Hildred Blewett Scholarship of the American Physical Society (E.D.F.). This manuscript has been co-authored by an employee of Brookhaven Science Associates, LLC, under Contract No. DE-AC02-98CH10886 with the U.S. Department of Energy. R.S.V. acknowledges support from BNL via the Goldhaber Distinguished Fellowship. Fermilab is operated by Fermi Research Alliance, LLC, under Contract No. DE-AC02-07CH11359 with the U.S. Department of Energy.

Appendix A: Discretization Error in the Kinetic Meson Mass

In this appendix, we present a semi-quantitative estimation of the discretization error in the kinetic mass of heavy-light hadrons. We use a formalism that applies when both quarks are non-relativistic, even though this approximation is not good for the light quark in a heavy-light meson. *A posteriori*, we examine two ways to re-interpret the resulting formula for a relativistic light quark. Both estimates are numerically the same, so we proceed to use the formula in Sec. V B.

In what follows, the generalized masses m_1, m_2, m_4 and the coefficient w_4 are used to describe the discretization errors. Expressions for them when using the Fermilab action are in Refs. [14] or [23] and are given at the end of this appendix for convenience. We assume that the light quark (s) has a mass in lattice units $m_s a \ll 1$ and makes no significant contribution to the discretization error.

The bound state's kinetic mass can be read off from its kinetic energy (by definition). It will have a kinematic contribution, from the constituents' kinetic energy, and a dynamical contribution, from the interaction that binds the constituents. We consider each in turn.

⁵ The determination of the quark mass from m_1 requires a non-perturbative calculation of the binding energy as defined by $M_1 - m_1$ [6].

1. Contributions from constituents' kinetic energy

The hadron of interest is a heavy-strange meson, a bound state of a heavy quark Q (momentum \mathbf{Q}) and a strange antiquark s (momentum \mathbf{s}). The non-relativistic kinetic energy is

$$T = m_{1Q} + \frac{\mathbf{Q}^2}{2m_{2Q}} - \frac{(\mathbf{Q}^2)^2}{8m_{4Q}^3} - \frac{1}{6}w_{4Q}a^3 \sum_i Q_i^4 + m_{1s} + \frac{\mathbf{s}^2}{2m_{2s}} - \frac{(\mathbf{s}^2)^2}{8m_{4s}^3} - \frac{1}{6}w_{4s}a^3 \sum_i s_i^4. \quad (\text{A1})$$

The binding energy is communicated to the bound-state kinetic mass via the terms quartic in the momenta and via corrections to the potential, given below. In general, the lattice breaks relativistic invariance, so $m_1 \neq m_2 \neq m_4, w_4 \neq 0$. Re-writing the kinetic energy in center-of-mass coordinates

$$\mathbf{Q} = \frac{m_{2Q}}{m_{2Q} + m_{2s}} \mathbf{P} + \mathbf{p}, \quad (\text{A2})$$

$$\mathbf{s} = \frac{m_{2s}}{m_{2Q} + m_{2s}} \mathbf{P} - \mathbf{p}, \quad (\text{A3})$$

$$\mathbf{P} = \mathbf{Q} + \mathbf{s}, \quad (\text{A4})$$

$$\mathbf{p} = \frac{m_{2s}\mathbf{Q} - m_{2Q}\mathbf{s}}{m_{2Q} + m_{2s}}, \quad (\text{A5})$$

one finds

$$\begin{aligned} T &= m_{1Q} + m_{1s} + \frac{\mathbf{P}^2}{2(m_{2Q} + m_{2s})} + \frac{\mathbf{p}^2}{2\mu_2} - \frac{\mathbf{P}^2 \mathbf{p}^2 + 2(\mathbf{P} \cdot \mathbf{p})^2}{4(m_{2Q} + m_{2s})^2} \left[\frac{m_{2Q}^2}{m_{4Q}^3} + \frac{m_{2s}^2}{m_{4s}^3} \right] \\ &\quad - a^3 \sum_i \frac{P_i^2 p_i^2}{(m_{2Q} + m_{2s})^2} (w_{4Q} m_{2Q}^2 + w_{4s} m_{2s}^2) + \dots, \end{aligned} \quad (\text{A6})$$

$$\frac{1}{\mu_2} = \frac{1}{m_{2Q}} + \frac{1}{m_{2s}}. \quad (\text{A7})$$

The only quartic terms shown are those quadratic in \mathbf{P} ; the omitted terms are not smaller; they just do not contribute to the bound state's kinetic energy. The objective is to collect all terms quadratic in \mathbf{P} , because their overall coefficient will yield the bound state's kinetic mass.

2. Contribution from the interaction: Breit equation

To obtain the two-particle system's potential energy, one has to work out the scattering amplitude from one-gluon exchange, obtaining an expression called the Breit equation [46, 55].

In momentum space, for the color-singlet channel

$$\begin{aligned} V(\mathbf{K}) &= -C_F g^2 D_{\mu\nu}(K) \mathcal{N}_Q(\mathbf{Q} + \mathbf{K}) \bar{u}(\xi', \mathbf{Q} + \mathbf{K}) \Lambda_Q^\mu(Q + K, Q) u(\xi, \mathbf{Q}) \mathcal{N}_Q(\mathbf{Q}) \\ &\quad \times \mathcal{N}_s(\mathbf{s}) \bar{v}(\xi, \mathbf{s}) \Lambda_s^\nu(s, s - K) v(\xi', \mathbf{s} - \mathbf{K}) \mathcal{N}_s(\mathbf{s} - \mathbf{K}), \end{aligned} \quad (\text{A8})$$

where $D_{\mu\nu}$ is the (lattice) gluon propagator, Λ_q^μ is the lattice vertex function (for $q = Q, s$), and \mathcal{N}_q is an external-line factor needed with the normalization conditions on spinors employed here [14, 23]. (In continuum field theory, $\mathcal{N} = \sqrt{m/E}$.)

To the accuracy needed here, the gluon propagator can be replaced with the continuum propagator. The heavy-quark line is

$$\begin{aligned} J_Q^4 &= \mathcal{N}_Q(\mathbf{Q} + \mathbf{K}) \bar{u}(\xi', \mathbf{Q} + \mathbf{K}) \Lambda_Q^4(Q + K, Q) u(\xi, \mathbf{Q}) \mathcal{N}_Q(\mathbf{Q}) \\ &= \bar{u}(\xi', \mathbf{0}) \left[1 - \frac{\mathbf{K}^2 - 2i\boldsymbol{\Sigma} \cdot (\mathbf{K} \times \mathbf{Q})}{8m_{EQ}^2} + \dots \right] u(\xi, \mathbf{0}), \end{aligned} \quad (\text{A9})$$

$$\begin{aligned} \mathbf{J}_Q &= \mathcal{N}_Q(\mathbf{Q} + \mathbf{K}) \bar{u}(\xi', \mathbf{Q} + \mathbf{K}) \Lambda_Q(Q + K, Q) u(\xi, \mathbf{Q}) \mathcal{N}_Q(\mathbf{Q}) \\ &= -i\bar{u}(\xi', \mathbf{0}) \left[\frac{\mathbf{Q} + \frac{1}{2}\mathbf{K}}{m_{2Q}} + \frac{i\boldsymbol{\Sigma} \times \mathbf{K}}{2m_{BQ}} + \dots \right] u(\xi, \mathbf{0}), \end{aligned} \quad (\text{A10})$$

and, to the extent that the strange antiquark is non-relativistic, one has a similar expression for the antiquark line $J_s^\nu = \mathcal{N}_s(\mathbf{s}) \bar{v}(\xi, \mathbf{s}) \Lambda_s^\nu(s, s - K) v(\xi', \mathbf{s} - \mathbf{K}) \mathcal{N}_s(\mathbf{s} - \mathbf{K})$.

In Coulomb gauge,

$$D_{44}(K) = \frac{1}{\mathbf{K}^2}, \quad D_{ij}(K) = \frac{1}{\mathbf{K}^2} \left(\delta^{ij} - \frac{K^i K^j}{\mathbf{K}^2} \right), \quad (\text{A11})$$

and the other components vanish. Thus, noting that $K_4 = i[(\mathbf{Q} + \mathbf{K})^2 - \mathbf{Q}^2]/2m_Q$ is subleading,

$$\begin{aligned} V(\mathbf{K}) &= -C_F g^2 \left[\frac{1}{\mathbf{K}^2} - \left(\frac{1}{8m_{EQ}^2} + \frac{1}{8m_{Es}^2} \right) - \frac{1}{m_{2Q} m_{2s}} \left(\mathbf{Q} \cdot \mathbf{s} - \frac{\mathbf{Q} \cdot \mathbf{K} \mathbf{K} \cdot \mathbf{s}}{\mathbf{K}^2} \right) \frac{1}{\mathbf{K}^2} \right] \\ &\quad + \text{spin-dependent terms.} \end{aligned} \quad (\text{A12})$$

Let us discuss each part of the bracket in turn. The leading term yields, after Fourier transforming to position space, the $1/r$ potential. The second yields a contact term proportional to $\delta(\mathbf{r})$: it is a relativistic correction to the bound state's *rest* mass, so it is of no further interest here. Similarly, the spin-dependent terms do not contribute to the bound state's kinetic energy, so they are not written out. The remaining exhibited contributions do contribute to the bound state's kinetic energy, when \mathbf{Q} and \mathbf{s} are eliminated in favor of \mathbf{P} and \mathbf{p} .

Next we Fourier transform from \mathbf{K} to \mathbf{r} using

$$\int \frac{d^3 K}{(2\pi)^3} \frac{e^{i\mathbf{r} \cdot \mathbf{K}}}{\mathbf{K}^2} = \frac{1}{4\pi r}, \quad (\text{A13})$$

$$\int \frac{d^3 K}{(2\pi)^3} \frac{K_i K_j e^{i\mathbf{r} \cdot \mathbf{K}}}{(\mathbf{K}^2)^2} = \frac{1}{2} (\delta_{ij} + r_i \nabla_j) \int \frac{d^3 K}{(2\pi)^3} \frac{e^{i\mathbf{r} \cdot \mathbf{K}}}{\mathbf{K}^2}. \quad (\text{A14})$$

Following with the substitution of \mathbf{P} and \mathbf{p} for \mathbf{Q} and \mathbf{s} this yields

$$V(\mathbf{r}, \mathbf{P}, \mathbf{p}) = -\frac{C_F \alpha_s}{r} \left[1 - \frac{\mathbf{P}^2}{2(m_{2Q} + m_{2s})^2} \right] - r_i \nabla_j \frac{C_F \alpha_s}{r} \frac{P_i P_j}{2(m_{2Q} + m_{2s})^2} + \dots, \quad (\text{A15})$$

where the omitted terms do not influence the bound state's kinetic energy.

Note that \mathbf{K} changes \mathbf{p} but not \mathbf{P} , so \mathbf{r} is conjugate to \mathbf{p} . To take expectation values, we use the virial theorem

$$\langle r_i \nabla_j V(\mathbf{r}) \rangle = \frac{\langle p_i p_j \rangle}{\mu_2}, \quad (\text{A16})$$

so the total energy of the bound state, $E(\mathbf{P}) = \langle T + V \rangle$, is

$$\begin{aligned} E(\mathbf{P}) &= m_{1Q} + m_{1s} + \frac{\langle \mathbf{p}^2 \rangle}{2\mu_2} - \left\langle \frac{C_F \alpha_s}{r} \right\rangle \\ &\quad + \frac{\mathbf{P}^2}{2(m_{2Q} + m_{2s})} \left[1 - \frac{\langle \mathbf{p}^2 \rangle}{2\mu_2(m_{2Q} + m_{2s})} + \frac{1}{(m_{2Q} + m_{2s})} \left\langle \frac{C_F \alpha_s}{r} \right\rangle \right] \\ &\quad + \frac{\mathbf{P}^2}{2(m_{2Q} + m_{2s})^2} \frac{\langle \mathbf{p}^2 \rangle}{2\mu_2} \left[1 - \mu_2 \left(\frac{m_{2Q}^2}{m_{4Q}^3} + \frac{m_{2s}^2}{m_{4s}^3} \right) \right] \\ &\quad + \frac{P_i P_j}{(m_{2Q} + m_{2s})^2} \frac{\langle p_i p_j \rangle}{2\mu_2} \left[1 - \mu_2 \left(\frac{m_{2Q}^2}{m_{4Q}^3} + \frac{m_{2s}^2}{m_{4s}^3} \right) \right] \\ &\quad - a^3 \sum_i \frac{P_i^2 \langle p_i^2 \rangle}{(m_{2Q} + m_{2s})^2} (w_{4Q} m_{2Q}^2 + w_{4s} m_{2s}^2) + \dots. \end{aligned} \quad (\text{A17})$$

The first line of Eq. (A17) shows the binding energy adding to the quarks' rest masses to form the bound state's rest mass,

$$M_1 = m_{1Q} + m_{1s} + \frac{\langle \mathbf{p}^2 \rangle}{2\mu_2} - \left\langle \frac{C_F \alpha_s}{r} \right\rangle. \quad (\text{A18})$$

The second line shows the same binding energy modifying the kinetic energy. The remaining terms are discretization errors. In general they are a bit messy, but they simplify for the S -wave states we use to tune κ . Then $\langle p_i p_j \rangle = \frac{1}{3} \delta_{ij} \langle \mathbf{p}^2 \rangle$, whence

$$E(\mathbf{P}) = M_1 + \frac{\mathbf{P}^2}{2M_2} + \dots, \quad (\text{A19})$$

where

$$\begin{aligned} M_2 = & m_{2Q} + m_{2s} + \frac{\langle \mathbf{p}^2 \rangle}{2\mu_2} - \left\langle \frac{C_F \alpha_s}{r} \right\rangle \\ & + \frac{5}{3} \frac{\langle \mathbf{p}^2 \rangle}{2\mu_2} \left[\mu_2 \left(\frac{m_{2Q}^2}{m_{4Q}^3} + \frac{m_{2s}^2}{m_{4s}^3} \right) - 1 \right] + \frac{4}{3} a^3 \frac{\langle \mathbf{p}^2 \rangle}{2\mu_2} \mu_2 (w_{4Q} m_{2Q}^2 + w_{4s} m_{2s}^2) + \dots \end{aligned} \quad (\text{A20})$$

The last line exhibits the discretization errors, which would vanish if $m_4 = m_2$, $w_4 = 0$.

The error can be re-written

$$\delta M_2 = \frac{1}{3} \frac{\langle \mathbf{p}^2 \rangle}{2\mu_2} \left\{ 5 \left[\mu_2 \left(\frac{m_{2Q}^2}{m_{4Q}^3} + \frac{m_{2s}^2}{m_{4s}^3} \right) - 1 \right] + 4a\mu_2 [w_{4Q}(m_{2Q}a)^2 + w_{4s}(m_{2s}a)^2] \right\}, \quad (\text{A21})$$

which is equivalent to Eq. (14) of Ref. [46]. Note that the error ends up being proportional to the internal kinetic energy of the bound state, $\langle \mathbf{p}^2 \rangle / 2\mu_2$.

3. Relativistic light degrees of freedom

For asqtad light quarks, the discretization errors are $O(\alpha_s m_s^2 a^2)$ and $O(m_s^4 a^4)$. So, for a semi-quantitative estimate of the discretization error, it should be safe to assume $m_{4s} = m_{2s} = m_{1s} = m_s$, $a^3 w_{4s} = 0$. Equation (A21) is then

$$\delta M_2 = \frac{1}{3m_{2Q}} \frac{\langle \mathbf{p}^2 \rangle}{2\mu_2} \mu_2 \left[5 \left(\frac{m_{2Q}^3}{m_{4Q}^3} - 1 \right) + 4w_{4Q}(m_{2Q}a)^3 \right]. \quad (\text{A22})$$

To use this formula we need a value for $\langle \mathbf{p}^2 \rangle$, and we consider two possibilities. The first is to replace $\langle \mathbf{p}^2 \rangle$ with $\bar{\Lambda}^2$. The reduced mass μ_2 then cancels, yielding a sensible limit even when $m_s \rightarrow 0$. The second is to replace the non-relativistic kinetic energy $\langle \mathbf{p}^2 \rangle / 2\mu_2$ with a relativistic version, namely $\bar{\Lambda}$. If we take a constituent quark mass $m_s = \frac{1}{2}\bar{\Lambda}$, then this discretization-error estimate equals that of the first approach to $O(m_s/m_Q)$.

4. The generalized masses and w_4

General tree-level expressions for the quark masses and w_4 were originally given in Ref. [14] and succinctly recapitulated in Ref. [23]. For convenience we give them here with parameters $\zeta = 1 = r_s$ as in our simulations

$$m_0 a = \frac{1}{u_0} \left(\frac{1}{2\kappa} - \frac{1}{2\kappa_{\text{crit}}} \right), \quad (\text{A23})$$

$$m_1 a = \ln(1 + m_0 a) \quad (\text{A24})$$

$$\frac{1}{m_2 a} = \frac{2}{m_0 a(2 + m_0 a)} + \frac{1}{1 + m_0 a}, \quad (\text{A25})$$

$$\frac{1}{m_B a} = \frac{2}{m_0 a(2 + m_0 a)} + \frac{c_B}{1 + m_0 a}, \quad (\text{A26})$$

$$\frac{1}{4m_E^2 a^2} = \frac{1}{[m_0 a(2 + m_0 a)]^2} + \frac{c_E}{m_0 a(2 + m_0 a)}, \quad (\text{A27})$$

$$\frac{1}{m_4^3 a^3} = \frac{8}{[m_0 a(2 + m_0 a)]^3} + \frac{4 + 8(1 + m_0 a)}{[m_0 a(2 + m_0 a)]^2} + \frac{1}{(1 + m_0 a)^2}, \quad (\text{A28})$$

$$w_4 = \frac{2}{m_0 a(2 + m_0 a)} + \frac{1}{4(1 + m_0 a)}. \quad (\text{A29})$$

These expressions and Eq. (A22) are used to obtain Table IX.

Appendix B: Tables of the kinetic mass

In this appendix, we tabulate values of the pseudoscalar, vector, and spin-averaged kinetic mass, aM_2 , aM_2^* , and $a\bar{M}_2$, respectively. Values are given for all combinations of κ and am'_q on the ensembles used for tuning κ . χ^2/dof and the p value, one minus the χ^2 cumulative distribution [45], from the dispersion relation fits are also given.

κ	aM_2	aM_2^*	$a\bar{M}_2$	aM_2	aM_2^*	χ^2/dof (p)
$am'_q = 0.0272$	0.090	2.30(17)	2.31(25)	2.31(21)	0.21 (0.81)	0.24 (0.79)
	0.0923	2.19(15)	2.22(22)	2.21(19)	0.22 (0.80)	0.35 (0.71)
	0.093	2.16(14)	2.19(22)	2.18(18)	0.22 (0.80)	0.37 (0.69)
	0.1256	0.860(19)	0.936(42)	0.917(32)	0.09 (0.92)	0.14 (0.87)
	0.127	0.819(15)	0.912(39)	0.889(30)	0.36 (0.70)	0.00 (1.0)
$am'_q = 0.031$	0.0923	2.22(14)	2.22(21)	2.22(18)	0.18 (0.84)	0.31 (0.73)
	0.1256	0.871(18)	0.947(38)	0.928(30)	0.14 (0.87)	0.16 (0.85)
	0.127	0.828(15)	0.918(37)	0.895(29)	0.40 (0.67)	0.00 (1.0)

TABLE XVIII: The kinetic meson mass for bottom- and charm-type mesons on the (0.0062, 0.031) fine ensemble from fits to $E^2(\mathbf{p}) - E^2(\mathbf{0})$ using $|\mathbf{n}| \leq \sqrt{3}$. Fits are done to obtain aM_2 and aM_2^* and the results are then spin averaged. Uncertainties are the average 68% bootstrap error. χ^2/dof with the p value in parentheses is also given. The p value is one minus the χ^2 cumulative distribution [45].

κ	aM_2	aM_2^*	$a\bar{M}$	aM_2	aM_2^*	χ^2/dof (p)
$am'_q = 0.03$	0.074	3.78(49)	3.64(54)	3.67(50)	1.12 (0.33)	0.17 (0.84)
	0.086	2.93(21)	3.03(33)	3.01(29)	0.28 (0.76)	0.21 (0.81)
	0.093	2.50(14)	2.66(24)	2.62(21)	0.05 (0.95)	0.11 (0.90)
	0.119	1.263(16)	1.402(43)	1.368(34)	0.84 (0.43)	0.20 (0.82)
	0.122	1.132(17)	1.270(46)	1.236(37)	0.35 (0.70)	0.34 (0.71)
	0.124	1.038(16)	1.161(43)	1.130(33)	0.28 (0.76)	0.52 (0.60)
$am'_q = 0.0415$	0.074	3.66(35)	3.75(53)	3.73(48)	0.26 (0.77)	0.23 (0.79)
	0.086	2.99(19)	3.09(28)	3.06(25)	0.46 (0.63)	0.48 (0.62)
	0.093	2.57(13)	2.75(25)	2.70(21)	0.14 (0.87)	0.31 (0.73)
	0.119	1.292(15)	1.456(41)	1.415(33)	0.88 (0.41)	0.38 (0.69)
	0.122	1.157(17)	1.310(44)	1.272(36)	0.19 (0.83)	0.24 (0.79)
	0.124	1.065(15)	1.200(43)	1.166(34)	0.15 (0.86)	0.47 (0.63)

TABLE XIX: Same as Table XVIII but for mesons on the (0.007, 0.050) coarse ensemble.

κ	aM_2	aM_2^*	$a\bar{M}$	aM_2	aM_2^*	χ^2/dof (p)
$am'_q = 0.0484$	0.070	4.54(32)	4.53(45)	4.53(41)	0.55 (0.58)	0.78 (0.46)
	0.080	3.79(19)	3.77(27)	3.78(24)	0.54 (0.58)	1.19 (0.31)
	0.115	1.747(25)	1.825(47)	1.805(37)	1.32 (0.27)	0.36 (0.70)
	0.125	1.304(12)	1.415(32)	1.387(26)	1.23 (0.29)	0.05 (0.95)
$am'_q = 0.0387$	0.070	4.47(35)	4.44(50)	4.44(46)	0.47 (0.63)	0.72 (0.49)
	0.080	3.73(21)	3.70(31)	3.71(28)	0.53 (0.59)	1.07 (0.34)
	0.115	1.725(28)	1.804(58)	1.784(47)	1.06 (0.43)	0.04 (0.96)
	0.125	1.282(13)	1.388(37)	1.361(29)	0.89 (0.41)	0.07 (0.93)

TABLE XX: Same as Table XVIII but for mesons on the (0.0097, 0.0484) medium-coarse ensemble.

Appendix C: Tables of $M_1 = E(0)$ and the hyperfine splitting

In this appendix, we tabulate the hyperfine splitting $a\Delta_1$ and $r_1\Delta_1$ discussed in Sec. VI B.

1. The hyperfine splitting in lattice units $a\Delta_1$

In this subsection, we tabulate values of $a\Delta_1$ relevant to the discussion in Sec. VI B of the uncertainty in the hyperfine splitting due to statistics, κ tuning, and the light valence mass.

κ	ensemble	aM_1	aM_1^*	$a\Delta_1$
$am'_q = 0.0272$	0.090 (0.0062, 0.031)	1.7387(13)	1.7546(19)	0.0158(15)
	0.0923 (0.0031, 0.031)	1.6877(21)	1.7054(25)	0.0177(19)
	0.0923 (0.0062, 0.031)	1.6870(13)	1.7037(20)	0.0167(16)
	0.0923 (0.0124, 0.031)	1.6835(16)	1.7024(19)	0.0188(14)
	0.1256 (0.0062, 0.031)	0.8408(8)	0.8968(16)	0.0561(15)
	0.127 (0.0031, 0.031)	0.7944(9)	0.8534(19)	0.0590(19)
	0.127 (0.0062, 0.031)	0.7946(7)	0.8544(15)	0.0599(13)
	0.127 (0.0124, 0.031)	0.7901(7)	0.8514(11)	0.0613(12)
$am'_q = 0.031$	0.090 (0.0062, 0.031)	1.7441(13)	1.7601(17)	0.0159(14)
	0.0923 (0.0062, 0.031)	1.6926(12)	1.7093(18)	0.0167(14)
	0.1256 (0.0062, 0.031)	0.8470(8)	0.9030(14)	0.0560(13)
	0.127 (0.0062, 0.031)	0.8009(7)	0.8606(14)	0.0597(12)

TABLE XXI: Fine-ensemble values of the rest mass $M_1 = E(0)$ and hyperfine splitting Δ_1 . $am'_q = 0.0272$ and 0.031 . Uncertainties are the average 68% bootstrap error.

κ	ensemble	aM_1	aM_1^*	$a\Delta_1$
$am'_q = 0.0415$	0.074 (0.007, 0.050)	2.2394(22)	2.2618(25)	0.0224(09)
	0.086 (0.005, 0.050)	1.9662(17)	1.9941(27)	0.0279(18)
	0.086 (0.007, 0.050)	1.9644(17)	1.9943(21)	0.0299(11)
	0.086 (0.010, 0.050)	1.9676(16)	1.9978(21)	0.0301(12)
	0.086 (0.020, 0.050)	1.9584(16)	1.9891(21)	0.0307(14)
	0.122 (0.005, 0.050)	1.0529(10)	1.1399(22)	0.0870(17)
	0.122 (0.007, 0.050)	1.0520(7)	1.1393(17)	0.0873(15)
	0.122 (0.010, 0.050)	1.0549(10)	1.1414(26)	0.0865(22)
	0.122 (0.020, 0.050)	1.0446(9)	1.1339(16)	0.0894(16)
	0.124 (0.007, 0.050)	0.9871(7)	1.0819(17)	0.0948(15)
$am'_q = 0.030$	0.074 (0.007, 0.050)	2.2241(26)	2.2466(29)	0.0225(11)
	0.086 (0.007, 0.050)	1.9488(21)	1.9787(25)	0.0299(14)
	0.122 (0.007, 0.050)	1.0339(08)	1.1220(20)	0.0881(17)

TABLE XXII: Same as Table XXI but for the coarse ensembles with $am'_q = 0.0415$ and 0.03.

κ	ensemble	aM_1	aM_1^*	$a\Delta_1$
$am'_q = 0.0484$	0.076 (0.0097, 0.0484)	2.3192(27)	2.3472(36)	0.0280(17)
	0.076 (0.0194, 0.0484)	2.3153(30)	2.3424(47)	0.0270(26)
	0.076 (0.0290, 0.0484)	2.3137(23)	2.3445(21)	0.0308(16)
	0.080 (0.0097, 0.0484)	2.2298(24)	2.2606(34)	0.0308(17)
	0.122 (0.0097, 0.0484)	1.2427(8)	1.3390(21)	0.0963(19)
	0.122 (0.0194, 0.0484)	1.2397(8)	1.3400(17)	0.1004(14)
	0.122 (0.0290, 0.0484)	1.2364(7)	1.3402(17)	0.1038(14)
	0.125 (0.0097, 0.0484)	1.1565(8)	1.2634(21)	0.1069(20)
$am'_q = 0.0387$	0.076 (0.0097, 0.0484)	2.3060(31)	2.3341(40)	0.0281(19)
	0.122 (0.0097, 0.0484)	1.2271(9)	1.3237(25)	0.0966(24)

TABLE XXIII: Same as Table XXI but for medium-coarse ensembles with $am'_q = 0.0484$ and 0.0387.

2. The hyperfine splitting in physical units $r_1\Delta_1$

In this subsection, we tabulate values of $r_1\Delta_1$ relevant to the discussion in Sec. VI B of the dependence of the hyperfine splitting on the sea-quark masses.

ensemble	$r_1\Delta_1$
$\kappa = 0.0923$ (0.0031, 0.031)	0.0653(69)
(0.0062, 0.031)	0.0618(58)
(0.0124, 0.031)	0.0700(52)
$\kappa = 0.127$ (0.0031 0.031)	0.2178(69)
(0.0062, 0.031)	0.2217(48)
(0.0124, 0.031)	0.2281(43)

TABLE XXIV: Fine-ensemble values of the hyperfine splitting Δ_1 in units of r_1 . $am'_q = 0.0272$. Uncertainties are the average 68% bootstrap error.

ensemble	$r_1\Delta_1$
$\kappa = 0.086$ (0.005, 0.050)	0.0738(46)
(0.007, 0.050)	0.0788(29)
(0.010, 0.050)	0.0788(32)
(0.020, 0.050)	0.0814(36)
$\kappa = 0.122$ (0.005, 0.050)	0.2301(44)
(0.007, 0.050)	0.2300(39)
(0.010, 0.050)	0.2265(58)
(0.020, 0.050)	0.2370(43)

TABLE XXV: Same as Table XXIV but for the coarse-ensembles with $am'_q = 0.0415$.

ensemble	$r_1\Delta_1$
$\kappa = 0.076$ (0.0097, 0.0484)	0.0616(37)
(0.0194, 0.0484)	0.0603(57)
(0.0290, 0.0484)	0.0699(37)
$\kappa = 0.122$ (0.0097, 0.0484)	0.2117(41)
(0.0194, 0.0484)	0.2244(30)
(0.0290, 0.0484)	0.2357(39)

TABLE XXVI: Same as Table XXIV but for medium-coarse-ensembles with $am'_q = 0.0484$.

Appendix D: Partially quenched chiral perturbation theory for the heavy-light hyperfine splitting

For full (unquenched) QCD, Jenkins [47] has calculated the hyperfine splitting at one loop in heavy-meson chiral perturbation theory. It is not difficult to take her result (Eq. (A.10) of Ref. [47]) and extend it to partially quenched QCD. The further step of including staggered taste-violations (*i.e.*, doing staggered chiral perturbation theory) would also be fairly straightforward, but we do not take it here because the continuum partially quenched form is sufficient for estimating the small systematic effect due to the mistuning of sea quark masses. Unlike Jenkins, we neglect electromagnetic and isospin-violating effects.

At the quark-flow level, the relevant diagrams are the self-energy diagrams shown in Fig. 5(a) [left] of Ref. [56] (the “connected diagram”) and in Figs. 5(b),(c) [left] of Ref. [56] (the “disconnected diagram”).⁶ One simply needs to determine how much of Jenkins’s result comes from each of these two diagrams. This is accomplished by noting that, when the light valence quark is a u ($a = 1$ in Jenkins’s notation), an internal kaon only appears in the connected diagram, when the quark in the virtual loop is an s . This fixes the normalization of the connected diagram. Using the methods described in Refs. [56–58] (but dropping the taste violations and indeed the taste degree of freedom itself), the disconnected diagram is easily calculated. Its normalization can then be fixed so that it supplies the remainder of the $a = 1$ result in Ref. [47].

There are ample checks of this reasoning. First, the same normalizations must apply for any choice of the valence mass. The η contributes in each case only through the disconnected diagram, while the pion contributions come from both connected and disconnected diagrams for valence u or d ($a = 1, 2$), and must be absent for valence s ($a = 3$). Finally the contribution from the unphysical $s\bar{s}$ state, which appears in each diagram for $a = 3$, should cancel.

It is then immediate to write down the partially quenched version. Let the light valence quark be x , with mass m_x , and let the sea quarks be u, d, s with masses $m_u = m_d = m_l$ and m_s . With the light meson decay constant f normalized so that $f \approx f_\pi \approx 130$ MeV, the hyperfine splitting $M_x^* - M_x$ is given by

$$M_x^* - M_x = \Delta - \frac{\Delta g_\pi^2}{8\pi^2 f^2} \delta_{\log} + 2\Delta^{(\sigma)}(2m_l + m_s) + 2\Delta^{(a)}m_x , \quad (\text{D1})$$

where Δ is the splitting in the (three-flavor) chiral limit, and $\Delta^{(\sigma)}$ and $\Delta^{(a)}$ are LECs that start at order $1/m_Q$ in the heavy quark expansion. The non-analytic chiral logarithms δ_{\log} are

$$\delta_{\log} = \sum_{F=u,d,s} \ell(M_{xF}^2) - \frac{1}{3} R_X^{[2,2]}(\{m\}, \{\mu\}) \tilde{\ell}(M_X^2) - \frac{1}{3} \sum_{j=X,\eta} D_{j,X}^{[2,2]}(\{m\}, \{\mu\}) \ell(M_j^2) . \quad (\text{D2})$$

Here M_X is the mass of the valence $x\bar{x}$ meson, and M_{xF} is the mass of the mixed valence-sea $x\bar{F}$ meson. The residue functions $R_j^{[n,k]}$ and $D_{j,i}^{[n,k]}$, as well as the chiral logarithm functions $\ell(m^2)$ and $\tilde{\ell}(m^2)$, are defined in Refs. [57, 58]. The term with the sum over F comes from the connected diagram, while those with the residue functions come from the disconnected diagram, which has a double pole at M_X^2 in the partially quenched case. The denominator ($\{m\}$) and numerator ($\{\mu\}$) mass sets are

$$\{m\} = \{M_X, M_\eta\} , \quad \{\mu\} = \{M_U, M_S\} \quad (\text{D3})$$

with M_U and M_S the masses of the $u\bar{u}$ and $s\bar{s}$ mesons, respectively.

- [1] C. T. Davies *et al.* [HPQCD, MILC, and Fermilab Lattice Collaborations], Phys. Rev. Lett. **92**, 022001 (2004) [arXiv:hep-lat/0304004];
- [2] C. Aubin *et al.* [HPQCD, MILC, and UKQCD Collaborations], Phys. Rev. D **70**, 031504(R) (2004) [arXiv:hep-lat/0405022]; C. Aubin *et al.* [MILC Collaboration], Phys. Rev. D **70**, 114501 (2004) [arXiv:hep-lat/0407028].
- [3] C. Aubin *et al.* [Fermilab Lattice, MILC, and HPQCD Collaborations], Phys. Rev. Lett. **95**, 122002 (2005) [arXiv:hep-lat/0506030]. C. Bernard *et al.* [Fermilab Lattice and MILC Collaborations], PoS **LATTICE2008**, 278 (2008) [arXiv:0904.1895 [hep-lat]].
- [4] C. Aubin *et al.* [Fermilab Lattice, MILC, and HPQCD Collaborations], Phys. Rev. Lett. **94**, 011601 (2005) [arXiv:hep-ph/0408306]; M. Okamoto *et al.* [Fermilab Lattice and MILC Collaborations], Nucl. Phys. B Proc. Suppl. **140**, 461 (2005) [arXiv:hep-lat/0409116]; C. Bernard *et al.* [Fermilab Lattice and MILC Collaborations], Phys. Rev. D **79**, 014506 (2009) [arXiv:0808.2519 [hep-lat]]; J. A. Bailey *et al.* [Fermilab Lattice and MILC Collaborations], Phys. Rev. D **79**, 054507 (2009) [arXiv:0811.3640 [hep-lat]]; C. Bernard *et al.* [Fermilab Lattice and MILC Collaborations], Phys. Rev. D **80**, 034026 (2009) [arXiv:0906.2498 [hep-lat]].
- [5] R. T. Evans *et al.* [Fermilab Lattice and MILC collaborations], PoS **LATTICE 2008** 052 (2008); R. T. Evans, E. Gámiz, A. El-Khadra and A.S. Kronfeld [Fermilab Lattice and MILC Collaborations], PoS **LATTICE 2009** 245 (2009) [arXiv:0911.5432 [hep-lat]].

⁶ One should ignore the solid square in each of the figures from Ref. [56] because it represents a current insertion, not relevant here.

- [6] E. D. Freeland, A. S. Kronfeld, J. N. Simone and R. S. Van de Water [Fermilab Lattice and MILC Collaborations], PoS **LAT2007**, 243 (2007) [arXiv:0710.4339 [hep-lat]].
- [7] I. F. Allison *et al.* [HPQCD and Fermilab Lattice Collaborations], Phys. Rev. Lett. **94**, 172001 (2005) [arXiv:hep-lat/0411027].
- [8] T. Burch *et al.* [Fermilab Lattice and MILC Collaborations], Phys. Rev. D **81**, 034508 (2010) [arXiv:0912.2701 [hep-lat]].
- [9] C. W. Bernard *et al.*, Phys. Rev. D **64**, 054506 (2001) [arXiv:hep-lat/0104002].
- [10] C. Aubin *et al.*, Phys. Rev. D **70**, 094505 (2004) [arXiv:hep-lat/0402030].
- [11] A. Bazavov *et al.*, Rev. Mod. Phys., to be published [arXiv:0903.3598 [hep-lat]].
- [12] C. W. Bernard *et al.*, Phys. Rev. D **62**, 034503 (2000) [arXiv:hep-lat/0002028]; R. Sommer, Nucl. Phys. B **411**, 839 (1994) [arXiv:hep-lat/9310022].
- [13] T. Blum *et al.*, Phys. Rev. D **55**, R1133 (1997) [arXiv:hep-lat/9609036]; K. Orginos and D. Toussaint [MILC Collaboration], Phys. Rev. D **59**, 014501 (1998) [arXiv:hep-lat/9805009]; J. F. Lagaë and D. K. Sinclair, Phys. Rev. D **59**, 014511 (1998) [arXiv:hep-lat/9806014]; G. P. Lepage, Phys. Rev. D **59**, 074502 (1999) [arXiv:hep-lat/9809157]; K. Orginos, D. Toussaint and R. L. Sugar [MILC Collaboration], Phys. Rev. D **60**, 054503 (1999) [arXiv:hep-lat/9903032]; C. W. Bernard *et al.* [MILC Collaboration], Phys. Rev. D **61**, 111502(R) (2000) [arXiv:hep-lat/9912018].
- [14] A. X. El-Khadra, A. S. Kronfeld and P. B. Mackenzie, Phys. Rev. D **55**, 3933 (1997) [arXiv:hep-lat/9604004].
- [15] B. Sheikholeslami and R. Wohlert, Nucl. Phys. B **259**, 572 (1985).
- [16] K. G. Wilson, in *New Phenomena in Subnuclear Physics*, edited by A. Zichichi (Plenum, New York, 1977).
- [17] A. S. Kronfeld, Phys. Rev. D **62**, 014505 (2000) [arXiv:hep-lat/0002008].
- [18] J. Harada, S. Hashimoto, K. I. Ishikawa, A. S. Kronfeld, T. Onogi and N. Yamada, Phys. Rev. D **65**, 094513 (2002) [Erratum-ibid. D **71**, 019903 (2005)] [arXiv:hep-lat/0112044]; J. Harada, S. Hashimoto, A. S. Kronfeld and T. Onogi, Phys. Rev. D **65**, 094514 (2002) [arXiv:hep-lat/0112045].
- [19] K. Symanzik, in *Recent Developments in Gauge Theories*, edited by G. 't Hooft *et al.* (Plenum, New York, 1980); in *Mathematical Problems in Theoretical Physics*, edited by R. Schrader *et al.* (Springer, New York, 1982); Nucl. Phys. B **226**, 187, 205 (1983).
- [20] G. P. Lepage and P. B. Mackenzie, Phys. Rev. D **48**, 2250 (1993) [arXiv:hep-lat/9209022].
- [21] B. P. G. Mertens, A. S. Kronfeld and A. X. El-Khadra, Phys. Rev. D **58**, 034505 (1998) [arXiv:hep-lat/9712024].
- [22] A. S. Kronfeld and J. N. Simone, Phys. Lett. B **490**, 228 (2000) [Erratum-ibid. B **495**, 441 (2000)] [arXiv:hep-ph/0006345].
- [23] M. B. Oktay and A. S. Kronfeld, Phys. Rev. D **78**, 014504 (2008) [arXiv:0803.0523 [hep-lat]].
- [24] M. G. Alford, W. Dimm, G. P. Lepage, G. Hockney and P. B. Mackenzie, Phys. Lett. B **361**, 87 (1995) [arXiv:hep-lat/9507010].
- [25] C. W. Bernard *et al.* [MILC Collaboration], Phys. Rev. D **58**, 014503 (1998) [arXiv:hep-lat/9712010]; M. Lüscher and P. Weisz, Commun. Math. Phys. **97**, 59 (1985) [Erratum-ibid. **98**, 433 (1985)]; M. Lüscher and P. Weisz, Phys. Lett. B **158**, 250 (1985).
- [26] Y. Shamir, Phys. Rev. D **71**, 034509 (2005) [arXiv:hep-lat/0412014]; Phys. Rev. D **75**, 054503 (2007) [arXiv:hep-lat/0607007].
- [27] C. Bernard, Phys. Rev. D **73**, 114503 (2006) [arXiv:hep-lat/0603011].
- [28] C. Bernard, M. Golterman and Y. Shamir, Phys. Rev. D **77**, 074505 (2008) [arXiv:0712.2560 [hep-lat]].
- [29] S. Dürr, PoS **LAT2005**, 021 (2006) [arXiv:hep-lat/0509026]; S. R. Sharpe, PoS **LAT2006**, 022 (2006) [arXiv:hep-lat/0610094]; M. Golterman, PoS **CONFINEMENT8**, 014 (2008) [arXiv:0812.3110 [hep-ph]].
- [30] A. S. Kronfeld, PoS **LAT2007**, 016 (2007) [arXiv:0711.0699 [hep-lat]].
- [31] For m_s and r_1/a , we use the fitting methods described in Ref. [11] as applied to the data available in June, 2007 [32]. Specifically, to smooth r_1/a , $\ln(r_1/a)$ is fit to a polynomial in β and $2am'_l + am'_s$. Values of u_0 can also be found in this reference.
- [32] C. Bernard *et al.* [MILC Collaboration], PoS **LAT2007**, 137 (2007) [arXiv:0711.0021 [hep-lat]].
- [33] A. Gray, I. Allison, C. T. H. Davies, E. Gulez, G. P. Lepage, J. Shigemitsu and M. Wingate, Phys. Rev. D **72**, 094507 (2005) [arXiv:hep-lat/0507013].
- [34] C. Bernard *et al.* [MILC Collaboration], PoS **LAT2005**, 025 (2006) [arXiv:hep-lat/0509137].
- [35] C. Bernard *et al.*, PoS **LAT2007**, 090 (2007) [arXiv:0710.1118 [hep-lat]].
- [36] C. T. H. Davies, E. Follana, I. D. Kendall, G. P. Lepage and C. McNeile, [arXiv:0910.1229 [hep-lat]].
- [37] D. P. Menscher, “Charmonium and charmed mesons with improved lattice QCD,” (University of Illinois Ph. D. thesis, 2005).
- [38] J. L. Richardson, Phys. Lett. B **82**, 272 (1979).
- [39] M. Wingate, J. Shigemitsu, C. T. H. Davies, G. P. Lepage and H. D. Trottier, Phys. Rev. D **67**, 054505 (2003) [arXiv:hep-lat/0211014].
- [40] M. F. L. Golterman, Nucl. Phys. B **278**, 417 (1986).
- [41] F. Glouzzi, Nucl. Phys. B **204**, 419 (1982).
- [42] H. Kluberg-Stern, A. Morel, O. Napol and B. Petersson, Nucl. Phys. B **220**, 447 (1983).
- [43] G. P. Lepage, B. Clark, C. T. H. Davies, K. Hornbostel, P. B. Mackenzie, C. Morningstar and H. Trottier, Nucl. Phys. Proc. Suppl. **106**, 12 (2002) [arXiv:hep-lat/0110175]; C. Morningstar, Nucl. Phys. Proc. Suppl. **109A**, 185 (2002) [arXiv:hep-lat/0112023].
- [44] For a pedagogical introduction see D. S. Sivia, *Data Analysis: A Bayesian Tutorial* (Oxford University Press, USA, 1996); a review can be found in K. Nakamura *et al.* (Particle Data Group), J. Phys. G **37**, 075021 (2010).
- [45] W. M. Yao *et al.* [Particle Data Group], J. Phys. G **33**, 1 (2006) and 2007 partial update for edition 2008 (URL: <http://pdg.lbl.gov>). The 2009-10 updates for the D_s hyperfine splitting have not changed its value. For the B_s hyperfine splitting, the “average value” of 46.1(1.5) has remained consistent; the “fit” value has increased slightly to 49.0(1.5).
- [46] A. S. Kronfeld, Nucl. Phys. B Proc. Suppl. **53**, 401 (1997) [arXiv:hep-lat/9608139].
- [47] E. E. Jenkins, Nucl. Phys. B **412**, 181 (1994) [arXiv:hep-ph/9212295].
- [48] C. M. Arnesen, B. Grinstein, I. Z. Rothstein and I. W. Stewart, Phys. Rev. Lett. **95**, 071802 (2005) [arXiv:hep-ph/0504209].
- [49] E. Eichten and B. R. Hill, Phys. Lett. B **243**, 427 (1990).
- [50] M. Nobes and H. Trottier, PoS **LAT2005**, 209 (2006) [arXiv:hep-lat/0509128]; M. Nobes, “Automated Lattice Perturbation Theory for Improved Quark and Gluon Actions,” (Simon Fraser University) Ph. D. thesis, 2004.
- [51] C. T. Sachrajda and G. Villadoro, Phys. Lett. B **609**, 73 (2005) [arXiv:hep-lat/0411033]; P. F. Bedaque, Phys. Lett. B **593**, 82 (2004)

- [arXiv:nucl-th/0402051].
- [52] E. D. Freeland, A. S. Kronfeld, J. N. Simone and R. S. Van de Water [for the Fermilab Lattice and MILC Collaborations], PoS **LAT2006**, 083 (2006) [arXiv:hep-lat/0610108].
- [53] B. Aubert *et al.* [BABAR Collaboration], Phys. Rev. D **74**, 032007 (2006) [arXiv:hep-ex/0604030].
- [54] M. Di Pierro *et al.*, Nucl. Phys. Proc. Suppl. **129**, 328 (2004) [arXiv:hep-lat/0310045].
- [55] V. I. Berestetskii, E. M. Lifshitz, and L. P. Pitaevskii, *Relativistic Quantum Theory* (Pergamon, Oxford, 1971).
- [56] C. Aubin and C. Bernard, Phys. Rev. D **73**, 014515 (2006) [arXiv:hep-lat/0510088].
- [57] C. Aubin and C. Bernard Phys. Rev. D **68** (2003) 034014 [arXiv:hep-lat/0304014].
- [58] C. Aubin and C. Bernard, Phys. Rev. D **68** (2003) 074011 [arXiv:hep-lat/0306026].

mc4qcd: Online Analysis Tool for Lattice QCD

Massimo Di Pierro*

School of Computing - DePaul University - Chicago

E-mail: mdipierro@cs.depaul.edu

Yaoqian Zhong

School of Computing - DePaul University - Chicago

E-mail: ati_zhong@hotmail.com

Brian Schinazi

School of Computing - DePaul University - Chicago

E-mail: schinazi@gmail.com

mc4qcd is a web based collaboration tool for analysis of Lattice QCD data. Lattice QCD computations consists of a large scale Markov Chain Monte Carlo. Multiple measurements are performed at each MC step. Our system acquires the data by uploading log files, parses them for results of measurements, filters the data, mines for required information by aggregating results, represents the results as plots and histograms, and it further allows refining and interaction by fitting the results. The system computes moving averages and autocorrelations, builds bootstrap samples and bootstrap errors, and allows modeling the data using Bayesian correlated constrained linear and non-linear fits. It can be scripted to allow real time visualization of results form an ongoing computation. The system is modular and it can be adapted to automating the analysis workflow of different types of MC computations.

*13th International Workshop on Advanced Computing and Analysis Techniques in Physics Research,
ACAT2010
February 22-27, 2010
Jaipur, India*

*Speaker.

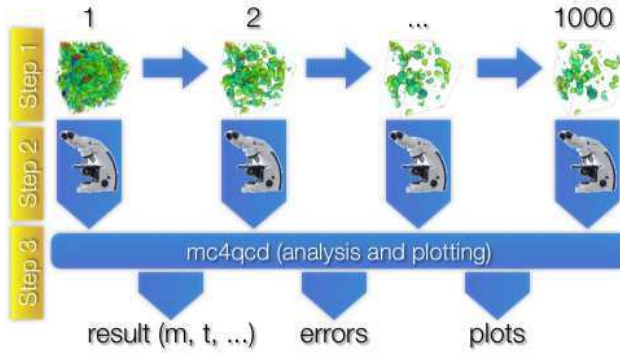


Figure 1: The typical three steps of a lattice computation.

1. Introduction

Lattice QCD is a numerical approach to Quantum Chromodynamics. Its primary goals are to describe the non-perturbative behaviour of quarks and to compute properties of hadronic matter. Typical Lattice QCD computations are comprised of three steps (fig.1). Step 1 consists of a Markov Chain Monte Carlo that generates *gauge configurations*, i.e. datasets that represent possible evolutions of the gluonic field. Step 2 consists of performing measurements on each of these gauge configurations, typically measurements of correlation functions between different operators at different locations in space and time. Step 3 consists of averaging the results of step 2 and performing a statistical analysis of the result. The outputs of step 3 may include values such as the masses and lifetimes of mesons and baryons.

In this procedure, Step 1 is the most computationally expensive, but it is also the most automated. Step 2 is also computationally intensive, of magnitude dependent on the type of question that one is trying to answer. Typically, multiple measurements are performed on each gauge configuration such that one can answer multiple questions by aggregating them in different ways in Step 3. This final step is relatively inexpensive from a computational point of view, but it is where most physicists spend their time: analyzing data and generating plots. The mc4qcd software aims to automate this process.

The data communicated between Step 1 and Step 2 is highly structured, using one of a small set of file formats that scientists have agreed on. Conversely, there is no standard format for encoding the data communicated between Step 2 and Step 3. Such standardization would be very difficult because the data is unstructured and is rarely communicated between different research groups. Additionally, the data is normally stored in flat text files with no metadata, save occasional comments printed in the output that are meant for human, not machine, consumption.

The mc4qcd application is specifically designed to ameliorate this situation.

The software performs the following basic operations:

- Import: Data can be uploaded either via a web interface or by means of web services.
- Extraction and transformation: The application parses the output text files from Step 2 computations and uses regular expressions to identify important variables. The regular expres-



Figure 2: A collection of screenshots of the mc4qcd program.

sions provide a template for transforming the original files into a structured dataset (in the form a collection of tables).

- **Filtering:** In addition to regular expressions, the user can apply mathematical constraints to filter data.
- **Mining:** mc4qcd aggregates data by computing expressions of interest and performing standard statistical analysis.
- **Visualization:** It produces plots that physicists normally look at to better read the information, including moving averages, autocorrelations, and bootstrap error.
- **Exploration:** It allows users to explore their data by zooming plots and interactively applying addition filters.
- **Fitting:** mc4qcd performs non-linear, constrained, correlated, and Bayesian fits, or combinations thereof.
- **Output:** Data, results, and plots can be exported.
- **Administration:** The software provides several administrative features, including web-based collaboration and commenting, traceability, ownership and permissions, public and private datasets, logging, storage of results, and annotations using LaTeX.

None of the above operations are new or exceedingly original. Physicists already perform them using other programs and plotting tools. The limitation of the current solutions is that they are not sufficiently general, and they require *ad hoc* programming.

The added value of mc4qcd lies in its generality, automation capabilities, ease of use, collaborative features, and its enforcement of a workflow (fig. 2).

2. Architecture

mc4qcd is written in Python. It consists of three core modules, which can be accessed either using its web interface or through shell scripting:

- **ibootstrap**: This module is responsible for reading a log file from a lattice computation, extracting the data contained therein, and performing aggregations and statistical analysis. The required inputs to this module are: the name of the log file, the regular expressions required to extract values, the expression to be computed with those values, and optional constraints. Once configured, it loops over these tasks and generates multiple output files in CSV format.
- **iplot**: This module reads the output of ibootstrap and generates corresponding plots.
- **ifit**: This module implements various fitting algorithms that can read the output of ibootstrap and cooperate with iplot to include fitting results in plots.

The web application is built around these three modules using the web2py framework. The framework provides Application Program Interfaces to perform the following tasks: concurrency handling, generation of dynamic web pages, web services, streaming of large files both in and out, security (authentication, authorization, XSS and Injection prevention), connecting to a database for storage (web2py supports 10 different database engines), maintaining state through user sessions and cookies, caching results of recurrent operations (for speed), and internationalization capabilities.

Plotting is done using the matplotlib library.

3. Example

A typical example of medium complexity consists of the computation of a meson's mass. This value can be computed (after Wick rotation to Euclidean time) by fitting a two point correlation

$$C_2(t_x - t_y) \equiv FT_{\mathbf{xy}} \langle 0 | j(\mathbf{x}, t_x) j^\dagger(\mathbf{y}, t_y) | 0 \rangle \quad (3.1)$$

with a sum of exponentials

$$C_2(t) = \sum_i A_i e^{-m_i t} \quad (3.2)$$

Here $FT_{\mathbf{xy}}$ is a zero momentum spatial Fourier transform (in \mathbf{x} and \mathbf{y}), and $j(\mathbf{x}, t_x)$ is a creation operator with the same quantum numbers as the meson we are interested in. The expectation value is computed numerically on the lattice in Step 2, as described in the introduction.

The m_i parameters are the masses of those states with the same quantum numbers as j . They can be extracted from the fit. The smaller of mass m_0 is the ground state for the meson created by the operator j .

Assume we have multiple measures for $C_2(t)$, along with other measurements, one for each gauge configuration, and that their values are stored in a flat text file as in the following:

```

loading gauge configuration 1
C2[00] = 1.913939
C2[01] = 1.537977
C2[10] = -1.029914
C2[11] = 0.000000
C2[12] = 0.000000
C2[13] = 0.000000
C2[14] = 0.000000
C2[15] = -1.029914
C3[00][00] = 5.203888
C3[00][01] = 4.372049
C3[01][00] = 4.372049
C3[01][01] = 4.372049
C3[10][00] = 4.372049
C3[10][01] = 4.372049
C3[11][00] = 4.372049
C3[11][01] = 4.372049
C3[12][00] = 4.372049
C3[12][01] = 4.372049
C3[13][00] = 4.372049
C3[13][01] = 4.372049
C3[14][00] = 4.372049
C3[14][01] = 4.372049
C3[15][00] = 4.372049
C3[15][01] = 4.372049

compton

```

In this case $C2[t]$ is just an arbitrary label – any name could be used. The index in square brackets is the value for t . For each t there are as many measurements as there are gauge configurations. The file may also contain additional text and comments. The different pages in the figure correspond to different gauge configurations and their output is in the same file.

We upload this file into mc4qcd and then ask it to compute the following expression:

```
1 "C2[<t>]"
```

which means: *look for all variables labeled $C2[<t>]$ where t is an index implicitly defined*. Everything inside double quotes identify variables via their corresponding pattern. Everything outside double quotes must be a valid Python expression, which can use all functions from the Python math module (such as \log , \exp , \sin , etc.), as well as user defined functions.

The program, for each t , extracts all values from the file, computes simple averages, moving averages, autocorrelations, bootstrap errors and sample distributions (some sample plots are shown in fig. 3).

Next, to fit this with an exponential we simply type:

```
1 a*exp(-m*t)@a=1,a_bu=0.2,m=0.1
```

Here mc4qcd understands that t is the parameter defined implicitly when parsing the data, while a and m are arbitrary unknown parameters that will be determined in the fit. The initial values used for fitting (priors) are specified on the right-hand side of the $@$ symbol. a_{bu} is the Bayesian uncertainty of the prior a . In this case, we performed a single mass fit, because this term dominates for large t . Multimass fits are also supported by mc4qcd.

The results of the fit are shown, superimposed to the data, in fig. 3. The fitting results and the Hessian describing the correlation between the fitting parameters (a and m) are displayed under the plot.

mc4qcd also allows more complex expression. Here are some examples:

```
1 log("C2[<t2>]"/"C2[<t2>]") for t1==t2+1
2 0.5*("C2[<t1>]"+"C2[<t2>]") for t1==32-t2 and t1>16
3 "C3[<t1>][<t2>]"/"C2[<t1>]"/"C2[<t2>]"
```

The latter example extracts a matrix element from a 3 point correlation function C_3 .

The fitting module also allows for complex expressions such as correlated Bayesian fits:

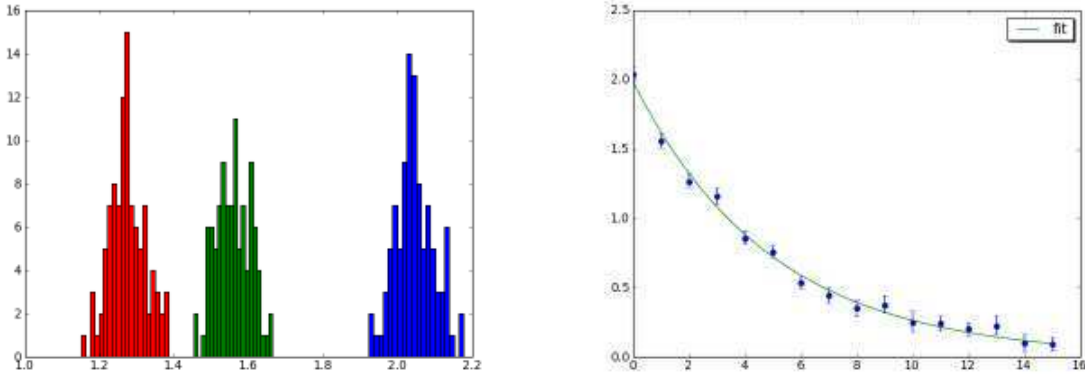


Figure 3: The figure on the left shows the distribution of bootstrap samples for $C_2(t)$ at three different values of t . The figure on the right shows the two point correlation function at different t with its bootstrap errors, fitted by an exponential function.

```
1 { 1:a , 2:b }[ t1 ]* exp( -m* t1 ) @a=1 , a_bu=0.2 , b=2 , m=0.1
```

(an exponential fit in t_1 with different coefficients depending on t_2).

4. Conclusions

mc4qcd is a new tool designed specifically for Lattice QCD analysis. It is very general, with certain limitations. For example, even though it can read unstructured data, it still often requires that the data be tagged by strings that can be recognized by the regular expression parser. Planned future enhancements include extending mc4qcd to give it the ability to learn more complex templates and handle more use cases.

Another limitation is the restricted ability to customize plots. Because all of the work is carried out automatically, it generates good quality images for screen presentation, but does not allow as much customization as is sometimes required for publication in scientific journals.

Despite this, mc4qcd can be a valuable tool for increasing collaboration between scientists working in this field and automating some of their daily tasks.

mc4qcd is distributed as a web2py package with a single dependence (the matplotlib library). It can be demoed and downloaded from <http://latticeqcd.org>

Acknowledgements This work has been supported by the US Department of Energy under grant DEFC02-06ER41441.

References

- [1] M. Di Pierro, Int. J. of Mod. Phys. A, Vol. 21, Num. 3, (2006)
- [2] Sandro Tosi, Matplotlib, Packt Publishing (2009)
- [3] M. Di Pierro, web2py Manual, 2nd Ed., Wiley (2009)

Making QCD Lattice Data Accessible and Organized through Advanced Web Interfaces

Massimo Di Pierro*

School of Computing - DePaul University - Chicago

E-mail: mdipierro@cs.depaul.edu

James Hetrick

University of the Pacific

E-mail: jhetrick@pacific.edu

Shreyas Cholia

Lawrence Berkely Laboratory

E-mail: scholia@lbl.gov

David Skinner

Lawrence Berkely Laboratory

E-mail: deskinner@lbl.gov

The Gauge Connection at qcd.nersc.gov is one of the most popular repositories of QCD lattice ensembles. It is used to access 16TB of archived QCD data from the High Performance Storage System (HPSS) at the National Energy Research Scientific Computing Center (NERSC). Here, we present a new web interface for qcd.nersc.gov which allows physicists to browse and search the data, as well as download individual files or entire ensembles in batch. Our system distinguishes itself from others because of its ease of use and web based workflow.

*XXIX International Symposium on Lattice Field Theory
July 10-16 2011
Squaw Valley, Lake Tahoe, California*

*Speaker.

1. Introduction

The Gauge Connection Lattice QCD data archive has been operated by the National Energy Research Scientific Computing [6] (NERSC) center since 1998. With over 16TBytes of data, the NERSC archive is one of the largest public repositories of lattice gauge ensembles. Its popularity has largely been due to the ease-of-use of its web interface compared to more complex grid based tools.

We are now updating the Gauge Connection to provide a number of modern features, while maintaining the simplicity and ease-of-use of the original. We are adding the ability to search data using tags. We are also providing capabilities to move data easily between the archive and the user's computer, or between two remote computers using both web and grid tools. The archive is now database driven and its pages are dynamically generated in order to facilitate access to the most recent local and remote data. It provides some visualization of the data. New data can easily be uploaded to the archive where it is automatically discovered and cataloged.

The archive can now deliver data in a variety of file formats (including ILDG [5], single and double precision, and FermiQCD [3]) by translating data on the fly after download. We have designed the new website to provide additional capabilities beyond data access, including wiki capabilities to annotate the data and link external work derived from archive data (derived data, software, tutorials, and publications).

Each gauge ensemble is also associated with a discussion forum allowing registered users to add their own comments. The archive has a more sophisticated access control mechanism and users can have four possible roles: administrators (can manage every aspect), editors (can edit the wiki pages linked to the data), registered users (can download data and comment) and anonymous visitors (can browse the wiki pages and query the data by tags). User management is greatly simplified through the use of a single-sign-on service that allows the user to log in with an existing identity from an external OpenID provider like Google or Yahoo.

2. Backend Architecture

The NERSC data is stored on the High Performance Storage System (HPSS), a hierarchical tape storage system designed to manage and access multiple petabytes of data at high speeds [?]. HPSS stores 16 terabytes of Lattice QCD data, mostly generated by the MILC [4] Collaboration. HPSS exposes different data access interfaces including a custom command line client (HSI), a C API, an FTP interface, a parallel FTP interface, as well as a GridFTP interface that can be used via Globus Online. We leverage the HPSS FTP interface to provide web access to the Lattice QCD data.

The system performs nightly introspection of the folder structure (through the HSI and FTP interfaces), reproduces this folder structure in the database, automatically tags data by parsing the file names, groups files with similar name patterns, and publishes the data online. For each folder in HPSS a corresponding web page is generated dynamically. The web structure has the same hierarchy as the folder structure on the HPSS backend.

The new web interface is designed to mimic the iPhone interface and works on both regular browsers and mobile devices.



Figure 1: The main web page for `qcd.nerc.gov` allows browsing and searching for gauge ensembles.

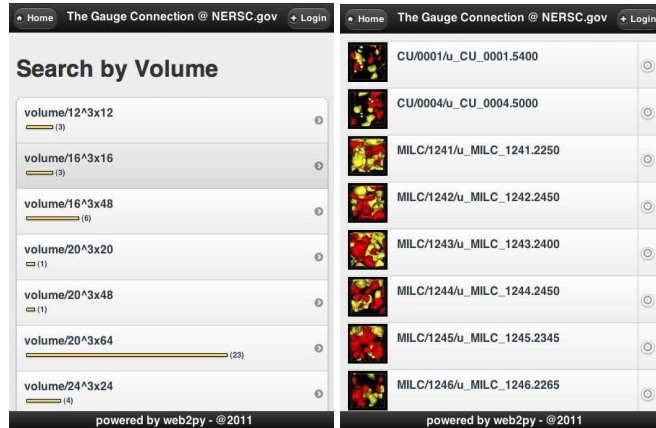


Figure 2: The left image show statics by tags. The right image shows topological change images from representative elements of various selected ensembles.



Figure 3: The image shows the page corresponding to a folder. The name of the folder is on top, followed by a folder description (optional) and by the tags applied to the folder. Files in the folder are grouped by their prefix (pattern). Patterns are shown at the bottom, above users' comments.

Every page on the QCD site is editable using a wiki syntax similar to wikipedia and registered users can comment on the pages. Both the wiki and comments allow Latex syntax for formulas. Gauge ensembles can be searched by direct browsing of the folder structure or by tag (contributing collaboration, lattice size, beta value, dynamical quark masses, etc.). The system generates interactive charts with statistics by tags.

Some ensembles have been processed off-line to generate meta-data such as a topological charge densities and have been linked to images and movies of said topological charge density. The system is data agnostic and can, in principle, store other data besides gauge ensembles. For example, it can store quark propagators and eigenvalues, examples of which are already in the system. The system uses standard third party web analytics tools to track usage and to geo-tag visitors on a map.

Here is how a simple file access workflow works. The user logs in to the Gauge Connection website (fig. 1) and searches for a desired dataset (fig. 2). When the user finds the ensemble that he/she wants (fig. 3), the user click on the appropriate file to download it. The system checks that the user is logged in, and then pulls the data from tape through the HPSS FTP server. Once the data is available (the tape has been mounted in HPSS), it is streamed back directly to the client browser. Alternatively the user can copy the link to the page for the entire ensemble and pass it to a command line script (provided) that will download every file in the ensemble, one by one, in batch, converting on the fly to the desired format.

3. Frontend Architecture

The system is based on web2py [2], a framework for rapid development of secure database driven web applications. It is written in Python and supports many standard databases including Sqlite, MySQL, PostgreSQL, Oracle, MSSQL, Informix, DB2, Sybase, Firebird, and Google Bit Table using a Database Abstraction Layer (DAL). The DAL generates SQL dynamically and as needed.

The system uses jQuery Mobile for page layout and a custom JavaScript library for charting. It uses the Google Chart API for Latex rendering and the Janrain web service for Single Sign On.

The visualizations of topological charge density are produced offline using Visit (LLNL) and the FermiQCD Visualization Toolkit.

The system has a modular Model-View-Controller design which separates the data representation from the data presentation and from the application workflow. This makes the code compact and easy to maintain. It includes a web based IDE, a web based database management tool and internationalization capabilities.

The complete model for the system consists of just a few lines of code used to describe the data that is stored:

```

1 # represents a folder in HPSS
2 db.define_table('catalog_folder',
3     Field('root_id', 'reference catalog_folder'),
4     Field('path'),
5     Field('title'),
6     Field('header', 'text'),
7     Field('footer', 'text'),
8     Field('pattern_ignore'),
9     Field('pattern_group'),
10    Field('comments', 'boolean', default=True))
11
12 # a tag to be applied to a folder
13 db.define_table('tag',
14     Field('name'),
15     Field('root_id', 'reference catalog_folder'))
16
17 # a file contained in a folder
18 db.define_table('catalog_file',
19     Field('root_id', 'reference catalog_folder'),
20     Field('filename'),
21     Field('md5'),
22     Field('pattern'),
23     Field('extension'),
24     Field('size', 'decimal(20,0)'),
25     Field('mtime', 'datetime'))
```

Each Field has a name and a type.

A dispatcher function maps web pages into function calls. These functions are defined in the controller. For example, all web pages of the form

`http://.../root/<path>`

Correspond to a <path> in the file system and they are mapped into the following function:

```

1 @cache(request.env.path_info, 60)
2 def root():
3     path = '/'.join(request.args)
4     (d,t,f) = (db.catalog_folder, db.tag, db.catalog_file)
5     query = (d.path==path) if path else (d.root_id==0)
6     page = db(query).select().first() or redirect(URL('error'))
7     tags = db(t.root_id==page.id).select()
8     subfolders = db(d.root_id==page.id).select()
9     patterns = db(f.root_id==page.id).select(
10         f.pattern,f.id.count(),f.size.sum(),
11         f.mtime.year(), groupby=f.pattern,orderby=f.pattern)
12
13     return locals()
```

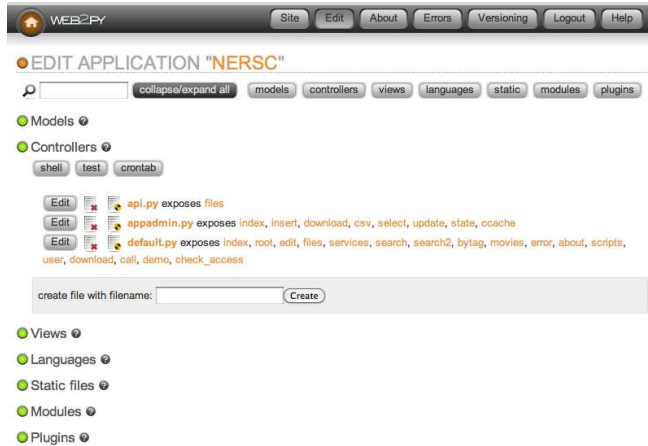


Figure 4: The system administrative interface.

This code parses the URL in the request for the path, defines some local variables (`d, t, f`) referencing the tables, builds a query to fetch the content of the folder: the path, the tags, the subfolders and the patterns (i.e. groups of files with the same prefix). At statements follow the DAL syntax:

```
1 variable = db(query).select(what,how)
```

The `@cache(...)` decorator instructs the framework to cache each page for 60 seconds. This means the if a page is requested more than once every 60 seconds, it will not hit the database more than one time. This results in better performance.

The system enforces different types of access control. It provides a web based administrative interface only accessible to managers (fig. 4). All downloads require user login.

The system itself is not domain specific and has no knowledge about QCD files and conventions. The domain specific knowledge is in a separate script that runs in background and populates the database from the file/folder structure. This means the system can be used to publish data of a different nature with minimal work. The system retains the original ability to download individual files using the web interface. Since these files can be big, the download requires login in order to prevent Denial of Service attacks.

The system exposes RESTful web services APIs based on the JSON protocol which can be used to access the data programmatically. Some gauge ensembles are comprised of thousands of files. To download them in batch we provide a script `qcdutils_get.py`, written in Python with no dependencies, available from [1].

In this example we use the script to download all files in the `demo` ensemble:

```
1 $ qcdutils_get.py http://qcd.nercsc.gov/nercsc/api/files/demo
2 http://qcd.nercsc.org/nercsc/api/files/demo
3 target folder: demo
4 total files to download: 1
5 downloading demo.nercsc
```

```
6 demo.nersc 100% |#####| Time: 00:00:00 654.52 K/s
7 completed download: 1/1
```

We now ask the script to convert all data from NERSC to ILDG(32bits):

```
1 $ qcdutils_get.py --convert ildg --float demo/demo.nersc
2 converting: demo/demo.nersc -> demo/demo.nersc.ildg
3   (precision: f, size: 4x8x8x8)
4 100% |#####|
```

`qcdutils` keeps an internal log of all the operations completed to avoid duplication of work. It remembers what was downloaded/converted and where things are. We can ask `qcdutils` for a log of the completed tasks:

```
1 $ qcdutils_get.py demo/qcdutils.catalog.db
2 demo.nersc created on 2011-06-17T13:42:30.876812
3   [14e7cf9106bfcc16388aeac285ccad9]
4 demo.nersc.ildg created on 2011-06-17T13:42:34.424604
5   [5a1ae13ddd5cab7ddfe1b17454822ff5]
```

4. Conclusions and Outlook

The system allows the user to register any URL and dynamically generates buttons that, when pressed, pass a link to the data at the associated URL. This allows for the creation of third party web services that can feed data directly from the new NERSC web interface allowing for decentralization of services. We can provide tools to help create such services. For example, we can build workflows that interface the data archive with a batch queue on a large computational system.

We envision a future when the different research groups will provide their computing capabilities and their lattice QCD algorithms as web services for the consumption of other members in the collaboration. The NERSC site provides more than just data for these collaborations - it also offers an infrastructure to register those third party services in a transparent way.

Acknowledgements

This work was funded by Department of Energy grant DEFC02-06ER41441 and by National Science Foundation grant 0970137.

References

- [1] Massimo Di Pierro. `qcdutils`, 2010.
- [2] Massimo Di Pierro. `web2py` website, 2010.
- [3] Massimo Di Pierro and Jonthan M. Flynn. Lattice QFT with FermiQCD. *PoS*, LAT2005:104, 2006.
- [4] S. Gottlieb. Benchmarking and tuning the MILC code on clusters and supercomputers. *Nuclear Physics B Proceedings Supplements*, 106:1031–1033, 2001.
- [5] C. Maynard. International Lattice Data Grid: Turn on, plug in, and download. In *Symposium on Lattice Field Theory*, 2009.
- [6] U.S. DOE. Nersc website, 2010.

***B-* and *D*-meson decay constants from three-flavor lattice QCD**

A. Bazavov,¹ C. Bernard,² C.M. Bouchard,^{3,4,5} C. DeTar,⁶ M. Di Pierro,⁷
 A.X. El-Khadra,³ R.T. Evans,³ E.D. Freeland,^{3,8} E. Gámiz,^{4,9}
 Steven Gottlieb,¹⁰ U.M. Heller,¹¹ J.E. Hetrick,¹² R. Jain,³ A.S. Kronfeld,⁴
 J. Laiho,¹³ L. Levkova,⁶ P.B. Mackenzie,⁴ E.T. Neil,⁴ M.B. Oktay,⁶
 J.N. Simone,⁴ R. Sugar,¹⁴ D. Toussaint,¹⁵ and R.S. Van de Water^{1,*}

(Fermilab Lattice and MILC Collaborations)

¹*Physics Department, Brookhaven National Laboratory, Upton, NY, USA*

²*Department of Physics, Washington University, St. Louis, Missouri, USA*

³*Physics Department, University of Illinois, Urbana, Illinois, USA*

⁴*Fermi National Accelerator Laboratory, Batavia, Illinois, USA*

⁵*Department of Physics, The Ohio State University, Columbus, OH, USA*

⁶*Physics Department, University of Utah, Salt Lake City, Utah, USA*

⁷*School of Computing, DePaul University, Chicago, Illinois, USA*

⁸*Department of Physics, Benedictine University, Lisle, Illinois, 60532, USA*

⁹*CAFPE and Depto. de Física Teórica y del Cosmos,*

Universidad de Granada, Granada, Spain

¹⁰*Department of Physics, Indiana University, Bloomington, Indiana, USA*

¹¹*American Physical Society, Ridge, New York, USA*

¹²*Physics Department, University of the Pacific, Stockton, California, USA*

¹³*SUPA, School of Physics and Astronomy,*

University of Glasgow, Glasgow, UK

¹⁴*Department of Physics, University of California, Santa Barbara, California, USA*

¹⁵*Department of Physics, University of Arizona, Tucson, Arizona, USA*

(Dated: December 15, 2011)

Abstract

We calculate the leptonic decay constants of $B_{(s)}$ and $D_{(s)}$ mesons in lattice QCD using staggered light quarks and Fermilab bottom and charm quarks. We compute the heavy-light meson correlation functions on the MILC asqtad-improved staggered gauge configurations which include the effects of three light dynamical sea quarks. We simulate with several values of the light valence- and sea-quark masses (down to $\sim m_s/10$) and at three lattice spacings ($a \approx 0.15, 0.12$, and 0.09 fm) and extrapolate to the physical up and down quark masses and the continuum using expressions derived in heavy-light meson staggered chiral perturbation theory. We renormalize the heavy-light axial current using a mostly nonperturbative method such that only a small correction to unity must be computed in lattice perturbation theory and higher-order terms are expected to be small. We obtain $f_{B^+} = 196.9(8.9)$ MeV, $f_{B_s} = 242.0(9.5)$ MeV, $f_{D^+} = 218.9(11.3)$ MeV, $f_{D_s} = 260.1(10.8)$ MeV, and the SU(3) flavor-breaking ratios $f_{B_s}/f_B = 1.229(26)$ and $f_{D_s}/f_D = 1.188(25)$, where the numbers in parentheses are the total statistical and systematic uncertainties added in quadrature.

PACS numbers: 12.38.Gc, 13.20.Fc, 13.20.He

* E-mail contact: ruthv@bnl.gov

I. INTRODUCTION

Leptonic decays of B and D mesons, in which the hadron annihilates weakly to a W boson, are important probes of heavy-to-light quark flavor-changing interactions. When combined with a nonperturbative lattice QCD calculation of the heavy-light pseudoscalar meson decay constant, f_B or f_D , a precise experimental measurement of the leptonic decay width allows the determination of the Cabibbo-Kobayashi-Maskawa (CKM) quark-mixing matrix element $|V_{ub}|$ or $|V_{cd}|$. Conversely, if the relevant CKM matrix element is known from an independent process such as semileptonic decay or from CKM-unitarity constraints, a comparison of the decay constant from lattice QCD simulations with that measured by experiment provides a straightforward test of the Standard Model. As the lattice and experimental determinations become more precise, this test will become more sensitive and may ultimately reveal, through the appearance of a discrepancy, the presence of new physics in the quark flavor sector.

Improved determinations of the B meson decay constant f_B are of particular importance given the current, approximately 3σ tension in the CKM unitarity triangle that may indicate the presence of new physics in B_d -mixing or $B \rightarrow \tau\nu$ decay [1–3]. The experimental uncertainty in the branching fraction $\mathcal{B}(B \rightarrow \tau\nu)$ is at present $\sim 30\%$ [4, 5], but this error is expected to be reduced to $\sim 10\%$ by Belle II at KEK- B in as little as five or six years [6, 7], at which point even modest improvements in the determination of f_B will significantly help constrain the apex of the CKM unitarity triangle and isolate the source of new physics [8].

Because leptonic decays are “gold-plated” processes in numerical lattice QCD simulations (they have a single stable hadron in the initial state and no hadrons in the final state [9]), they can be determined accurately using present lattice methods. Currently all realistic lattice calculations of $f_{D_{(s)}}$ and $f_{B_{(s)}}$ that include the effects of three light dynamical quarks use staggered lattice fermions [10, 11] for the up, down, and strange quarks. Because staggered fermions are computationally cheaper than other lattice fermion formulations, they allow for QCD simulations with dynamical quarks as light as $0.05m_s$, several lattice spacings, down to $a \approx 0.045$ fm, large physical volumes, and high statistics. This enables lattice determinations of many light-light and heavy-light meson quantities with controlled systematic uncertainties. The results of staggered lattice calculations are largely in excellent numerical agreement with experimental results [9]. This includes both postdictions, such as the pion and kaon decay constants [12], and predictions, as in the case of the B_c meson mass [13]. Such successes give confidence that further calculations using the same methods are reliable. This is essential if lattice QCD calculations of hadronic weak matrix elements are to be used to test the Standard Model and search for new physics.

The staggered dynamical quark simulations used here employ the fourth-root procedure (“rooting”) for eliminating unwanted extra quark degrees of freedom that arise from lattice fermion doubling. The rooting method is not standard quantum field theory, and at nonzero lattice spacing it leads to violations of unitarity [14–17] that can be considered nonlocal [18]. Nevertheless, there are strong arguments [19, 20] that the desired local, unitary theory of QCD is reproduced by the rooted staggered lattice theory in the continuum limit. Further, one can show [15, 21] that the unitarity-violating lattice artifacts in the pseudo-Goldstone boson sector can be described, and hence removed, using rooted staggered chiral perturbation theory (rS χ PT), which is a low-energy effective description of the rooted staggered lattice theory [22–24]. When coupled with other analytical and numerical evidence (see Refs. [25–28] for reviews and Ref. [29] for a recent study), this gives us confidence that the rooting procedure is valid. Indeed, the validity of the rooted staggered lattice simulations is of critical

importance to flavor physics phenomenology, since a majority of the unquenched, three-flavor lattice results for hadronic weak matrix elements used to determine CKM matrix elements and as inputs to constraints on the CKM unitarity triangle come from such simulations [30].

In this paper, we present new results for the leptonic decay constants of heavy-light mesons containing bottom and charm quarks. We use the “2+1” flavor asqtad-improved gauge configurations made publicly-available by the MILC Collaboration [31]. These ensembles include the effects of three light, dynamical sea-quark flavors: one with mass m_h near m_s (the physical strange-quark mass) and the other two with mass m_l as small as $0.1m_h$. We generate light valence quarks for the B and D mesons using the same staggered action as in the sea sector, and generate heavy bottom and charm quarks using the clover action [32] with the Fermilab interpretation [33]. Because the Fermilab method uses knowledge of the heavy-quark limit of QCD to systematically eliminate heavy-quark discretization errors, exploiting ideas of Symanzik [34, 35] and of heavy-quark effective theory (HQET) [36–38], it is well-suited for both bottom and charm quarks. We simulate with many values for the light up/down quark mass (the mass of our lightest pion in both the sea and valence sectors is ≈ 250 MeV), and at three lattice spacings ranging from $a \approx 0.09$ fm to $a \approx 0.15$ fm. We then extrapolate our numerical lattice data to the physical up and down quark masses and continuum guided by expressions derived in staggered chiral perturbation theory for heavy-light mesons (HMS χ PT) [39–41].

We renormalize the heavy-light axial current with a mostly nonperturbative approach, computing the flavor-diagonal (heavy-heavy and light-light) renormalization factors nonperturbatively and then calculate the remaining flavor off-diagonal correction factor ($\rho_{A_{Qq}^4}$) in lattice perturbation theory [37, 42, 43]. This procedure has the advantage that $\rho_{A_{Qq}^4}$ is close to unity. Furthermore, tadpole diagrams cancel in the ratio needed to obtain $\rho_{A_{Qq}^4}$, thereby improving the convergence of the perturbative series. Empirically, the size of the 1-loop contribution to $\rho_{A_{Qq}^4}$ is found to be small.

Our results for the charmed-meson decay constants improve upon our published results for f_D and f_{D_s} in Ref. [44] in several ways. The coarsest lattices used in this work have a smaller lattice spacing ($a \approx 0.15$ fm) than those used in our previous work ($a \approx 0.18$ fm). The number of configurations in the two most chiral ensembles with $a \approx 0.12$ fm has been increased, approximately by factors of 1.4 (sea $m_l = 0.1m_h$) and 1.7 (sea $m_l = 0.14m_h$). We have added new data on a new $a \approx 0.09$ fm sea-quark ensemble with a light quark mass of $0.1m_h$. We now obtain our results from a combined analysis of our entire data set (all partially-quenched mass combinations and lattice spacings). Furthermore, we now compute the bottom meson decay constants f_B and f_{B_s} . We have presented reports on this project at several conferences [45–49]; in our final analysis of this data set we also improve upon bottom and charm quark mass-tuning, with increased statistics and a more sophisticated analysis of heavy-quark discretization effects.

This paper is organized as follows. In Sec. II, we present an overview of the calculation, including the gluon and light-quark actions used in generating the gauge configurations and the light- and heavy-quark actions used in constructing the heavy-light meson correlators. We also introduce the mostly nonperturbative method for matching the lattice heavy-light current to the continuum, and the treatment of heavy-quark discretization errors from the Fermilab action within our chiral-continuum extrapolation. Next, in Sec. III, we describe the details of our numerical simulations and we present the parameters used, such as the light-quark masses and lattice spacings. We also describe the procedure for tuning the hopping

TABLE I. Flavor content of the axial vector current and associated CKM matrix element.

H	\mathcal{A}^μ	V
D	$\bar{d}\gamma^\mu\gamma^5 c$	V_{cd}^*
D_s	$\bar{s}\gamma^\mu\gamma^5 c$	V_{cs}^*
B	$\bar{b}\gamma^\mu\gamma^5 u$	V_{ub}
B_s	$\bar{b}\gamma^\mu\gamma^5 s$	—

parameter in the clover action so that it corresponds to b and c quarks. In Sec. IV, we define the two-point correlation functions used to extract the decay constant at each value of the light-quark mass and lattice spacing. We use two different fitting procedures to obtain the decay constants that differ in their treatment of the statistical errors, choice of fit ranges and number of states, and choice of input correlators. We include the difference between the two in our estimate of the fitting systematic uncertainty. Next, we present the numerical details of the calculation of the heavy-light axial-current renormalization factor in Section V. Putting the results of the two previous sections together, in Sec. VI, we extrapolate the renormalized decay constant data at unphysical quark masses and nonzero lattice spacing to the physical light quark masses and zero lattice spacing using $\text{HMS}\chi\text{PT}$. In Sec. VII, we estimate the contributions of the various systematic uncertainties to the decay constants, discussing each item in our error budget separately. We present the final results for the decay constants in Sec. VIII, and compare them to other lattice QCD calculations and to experiment. We describe the impact of our results for current flavor physics phenomenology and then conclude by discussing the ongoing improvements to our calculations, and their future impact on searches for new physics in the quark flavor sector.

Appendix A applies HQET to the Fermilab action to obtain explicit expressions for heavy-quark discretization effects. Appendix B contains the complete set of fit results for the heavy-light pseudoscalar meson mass and renormalized decay constant for all combinations of sea-quark mass, light valence-quark mass, and heavy-quark mass used in the chiral-continuum extrapolation. These results will be included as an EPAPS attachment upon publication.

II. METHODOLOGY

The decay rate for a charged pseudoscalar meson H (with flavor content Q and \bar{q}) to leptons is, in the Standard Model,

$$\Gamma(H \rightarrow \ell\nu) = \frac{M_H}{8\pi} f_H^2 |G_F V_{Qq}^* m_\ell|^2 \left(1 - \frac{m_\ell^2}{M_H^2}\right)^2, \quad (2.1)$$

where M_H is the mass of the meson H , G_F is the Fermi constant, and V_{Qq} is the pertinent element of the CKM matrix. The decay constant f_H parameterizes the pseudoscalar-to-vacuum matrix element of the axial vector current,

$$\langle 0 | \mathcal{A}^\mu | H(p) \rangle = i p^\mu f_H, \quad (2.2)$$

where p^μ is the 4-momentum of the pseudoscalar meson. The flavor contents of the associated vector current and CKM matrix element are given in Table I. Note that the neutral B_s decays to a charged lepton pair with an amplitude proportional to f_{B_s} ; hence the CKM

factor in the decay rate involves more than one CKM matrix element. Because this process is loop-suppressed in the Standard Model, it is potentially sensitive to new physics effects. These formulas hold for all pseudoscalar mesons; in the normalization convention used here, $f_\pi(|V_{ud}|/0.97425) = 130.41 \pm 0.20$ MeV [50].

In Eq. (2.2), the 1-particle state assumes the relativistic normalization convention. For mesons containing a heavy quark, however, it is more convenient to pull out factors of M_H to ensure a smooth $M_H \rightarrow \infty$ limit:

$$\langle 0 | \mathcal{A}^\mu | H(p) \rangle (M_H)^{-1/2} = i(p^\mu/M_H)\phi_H. \quad (2.3)$$

In lattice QCD, the normalization of states on the left-hand side falls out of correlation functions more naturally. Thus, most of our analysis, including error analysis, focuses on ϕ_H . We then obtain $f_H = \phi_H/\sqrt{M_H}$ using the experimentally measured value of the meson mass [51].

To compute the decay constants with lattice gauge theory, we must choose a discretization for the heavy quark, the light quark, and the gluons. As in previous work [44, 52–55], we choose the Fermilab method for heavy quarks [33] and staggered quarks with the asqtad action [56] for the light (valence) quark. The gauge action is Symanzik improved, with couplings chosen to remove order $\alpha_s a^2$ errors from gluon loops [57], but not those from quark loops [58] (which became available only after the gauge-field generation was well underway).

For heavy bottom and charm quarks, we use the Sheikholeslami-Wohlert (SW) clover action [32] with the Fermilab interpretation [33], which connects to the continuum limit as $am_Q \rightarrow 0$. This is an extension of the Wilson action [59], which retains the Wilson action's smooth limit as $am_Q \rightarrow \infty$ and also remains well behaved for $m_Q a \approx 1$. Because this lattice action respects heavy-quark spin-flavor symmetry, one can apply HQET to organize the discretization effects. In essence, one uses HQET to develop the $1/m_Q$ expansion both for continuum QCD and for lattice gauge theory (LGT) [36–38]. Discretization effects are then captured order-by-order in the heavy-quark expansion by the difference of the short-distance coefficients in the descriptions of QCD and LGT. Thus, in principle, the lattice heavy-quark action can be improved to arbitrarily high orders in $1/m_Q$ by adjusting a sufficiently large number of parameters in the lattice action. (See Ref. [60] for details at dimension 6 and 7. In principle, the adjustment can be done nonperturbatively, such as in the scheme of Ref. [61].) In practice, we tune the hopping parameter κ and the clover coefficient c_{SW} of the SW action, to remove discretization effects through order $1/m_Q$ in the heavy-quark expansion.

The HQET analysis of cutoff effects could be applied to any lattice action with heavy-quark symmetry, such as the action of lattice NRQCD [62]. In the latter case, it is simply a different perspective on the usual approach to lattice NRQCD, which derives the heavy-quark Lagrangian formally, and then replaces derivatives with difference operators. A key feature of the Wilson, SW, Fermilab and OK [60] actions is their well-behaved continuum limit, which is especially important for charm. For $m_Q a < 1$, one can analyze the cutoff effects in a complementary way with the Symanzik effective action [34, 35]. This two-pronged attack shows that the difference of short-distance coefficients, mentioned above, vanishes as a suitable power of lattice spacing a . In this paper, we shall use our knowledge of this behavior to constrain heavy-quark discretization effects in several steps of our analysis. See Secs. III B, VI, and Appendix A for details.

The lattice and continuum currents are related by a matching factor Z_{A^μ} [37]:

$$Z_{A^\mu} A^\mu \doteq \mathcal{A}^\mu + \mathcal{O}(\alpha_s a \Lambda f_i(m_Q a)) + \mathcal{O}(a^2 \Lambda^2 f_j(m_Q a)), \quad (2.4)$$

where \doteq denotes equality of matrix elements, and the functions $f_{i,j}$ that depend on $m_Q a$ stem from the difference in the HQET short-distance coefficients. In the Fermilab method, they remain of order 1 for all values of $m_Q a$ [33, 60], and they are given explicitly in Appendix A. In this work, we compute Z_{A^μ} mostly nonperturbatively [42] and partly in one-loop perturbation theory. As shown in the analysis of Ref. [37], many of the Feynman diagrams in the perturbative expansion of $Z_{A_{Qq}^4}$ are common or similar to those in the flavor-conserving renormalization factors $Z_{V_{QQ}^4}$ and $Z_{V_{qq}^4}$, which can be computed nonperturbatively. Therefore, we define $\rho_{A_{Qq}^4}$ by

$$Z_{A_{Qq}^4} = \rho_{A_{Qq}^4} \sqrt{Z_{V_{qq}^4} Z_{V_{QQ}^4}}, \quad (2.5)$$

evaluating only $\rho_{A_{Qq}^4}$ in lattice perturbation theory.

The flavor-conserving factors account for most of the value of the heavy-light renormalization factor $Z_{A_{Qq}^4}$. They are obtained by enforcing the normalization condition, at zero momentum transfer,

$$1 = Z_{V_{qq}^4} \langle H_q | V_{qq}^4 | H_q \rangle, \quad (2.6)$$

where H_q is a hadron containing a single quark of flavor q , and V_{qq}^μ is the lattice version of the degenerate vector current. This condition holds for all discretizations and quark masses and, hence, the heavy quark (*i.e.*, $Z_{V_{QQ}^4}$) as well. The remaining correction factor $\rho_{A_{Qq}^4}$ is close to unity due to the cancellation of most of the radiative corrections including tadpole graphs. Although such cancellations have only been explicitly shown at 1-loop in lattice perturbation theory [37, 43], we expect similar cancellations to persist at higher orders. Therefore, the perturbative truncation error in the heavy-light renormalization factor is subdominant.

III. LATTICE SIMULATION DETAILS

A. Parameters

Table II lists the subset of the ensembles of lattice gauge fields generated by the MILC Collaboration [28] used in this analysis. We now describe each entry in the table.

We analyze data at three lattice spacings: $a \approx 0.15$ fm, $a \approx 0.12$ fm, and $a \approx 0.09$ fm. The ensembles contain 2+1 flavors of sea quarks, using the asqtad-improved staggered action [56], and the square (fourth) root of the staggered determinant for the two degenerate light sea quarks (one strange sea quark). The sea contains one flavor with mass m_h close to the physical strange quark mass and two degenerate lighter flavors of mass m_l . The tadpole improvement factor u_0 is a parameter of the gauge and asqtad staggered (sea) quark action and is determined from the fourth root of the average plaquette. We calculate the two-point correlation functions on each ensemble from an average over four different time sources.

The relative lattice scale is determined by calculating r_1/a on each ensemble, where r_1 is related to the force between static quarks, $r_1^2 F(r_1) = 1.0$ [63, 64]. Table II lists r_1/a values for each of the ensembles that result from fitting the calculated r_1/a to a smooth function [65], as explained in Eqs. (115) and (116) of Ref. [28].

TABLE II. The MILC three-flavor lattices and valence asqtad quark masses used in this work. All of the valence masses were used in version II of the correlator fits (Sec IV C), while only the ones in bold print were used in version I (Sec IV B).

$\approx a$ [fm]	am_h	am_l	u_0	r_1/a	$n_{\text{conf}} \times n_{\text{src}}$	valence am_q
0.09	0.031	0.0031	0.8779	3.69	435×4	0.0031 , 0.0037, 0.0042, 0.0044 , 0.0052, 0.0062 , 0.0087 , 0.0124 , 0.0186 , 0.0272 , 0.031
		0.0062	0.8782	3.70	557×4	0.0031 , 0.0037, 0.0044 , 0.0052, 0.0062 , 0.0087 , 0.0124 , 0.0186 , 0.0272 , 0.031
		0.0124	0.8788	3.72	518×4	0.0031 , 0.0042 , 0.0062 , 0.0087 , 0.0124 , 0.0186 , 0.0272 , 0.031
	0.05	0.005	0.8678	2.64	678×4	0.005 , 0.006, 0.007 , 0.0084, 0.01 , 0.012, 0.014 , 0.017, 0.02 , 0.024, 0.03 , 0.0415
		0.007	0.8678	2.63	833×4	0.005 , 0.006, 0.007 , 0.0084, 0.01 , 0.012, 0.014 , 0.017, 0.02 , 0.024, 0.03 , 0.0415
		0.01	0.8677	2.62	592×4	0.005 , 0.006, 0.007 , 0.0084, 0.01 , 0.012, 0.014 , 0.017, 0.02 , 0.024, 0.03 , 0.0415
	0.02	0.02	0.8688	2.65	460×4	0.005 , 0.006, 0.007 , 0.0084, 0.01 , 0.012, 0.014 , 0.017, 0.02 , 0.024, 0.03 , 0.0415
		0.03	0.8696	2.66	549×4	0.005 , 0.006, 0.007 , 0.0084, 0.01 , 0.012, 0.014 , 0.017, 0.02 , 0.024, 0.03 , 0.0415
		0.0484	0.0097	0.8604	2.13×4	0.0048 , 0.007 , 0.0097 , 0.013, 0.0194 , 0.0242, 0.029 , 0.0387, 0.0484
	0.15	0.0194	0.8609	2.13	631×4	0.0048 , 0.007 , 0.0097 , 0.013, 0.0194 , 0.0242, 0.029 , 0.0387, 0.0484
		0.029	0.8614	2.13	576×4	0.0048 , 0.007 , 0.0097 , 0.013, 0.0194 , 0.0242, 0.029 , 0.0387, 0.0484

In order to fix the absolute lattice scale, one must compute a physical quantity which can be compared directly to experiment. The combination of the PDG’s value of f_π with MILC’s 2009 determination of $r_1 f_\pi$ [66] yields $r_1 = 0.3117(6)(^{+12}_{-31})$ fm. From an average of three methods for scale setting, including one based on Υ splittings, the HPQCD collaboration obtains $r_1 = 0.3133(23)(3)$ fm [67], consistent with MILC. Symmetrizing MILC’s error range gives $r_1 = 0.3108(21)$ fm, and a straightforward average with the HPQCD result then yields $r_1 = 0.3120(16)$ fm. This average omits likely correlations, due to the use of MILC sea-quark configurations by both groups. Conservatively assuming a 100% correlation, we inflate the error to 0.0022 fm. Finally, for convenience, we also shift the central value slightly, back to the 2009 MILC central value. We thus take $r_1 = 0.3117(22)$ fm in this paper.

The complete list of light (asqtad) valence quark masses m_q simulated in this analysis is also given in Table II. The mass values are selected to be roughly logarithmically spaced, but to also include the set of light sea quark masses simulated at each lattice spacing. We use a multimass solver to compute the valence quark propagators. The marginal numerical cost of including masses heavier than our lightest $m_q \sim 0.1 m_s$ is small and logarithmic spacing is designed to constrain the chiral logarithms.

TABLE III. Table of clover coefficients and κ values for charm and bottom used in heavy-light two-point simulations.

$\approx a$ [fm]	am_l/am_h	κ_{sim}		
		c_{SW}	charm	bottom
0.09	0.0031/0.031	1.478	0.127	0.0923
	0.0062/0.031	1.476		
	0.0124/0.031	1.473		
0.12	0.005/0.05	1.72	0.122	0.086
	0.007/0.05	1.72		
	0.01/0.05	1.72		
	0.02/0.05	1.72		
	0.03/0.05	1.72		
0.15	0.0097/0.0484	1.570	0.122	0.076
	0.0194/0.0484	1.567		
	0.0290/0.0484	1.565		

In Table III, we show the coefficient of the Sheikholeslami-Wohlert term c_{SW} of the clover action and the κ values used to compute heavy-light two-point functions. The coefficient of the clover term is set to the tadpole-improved tree-level value $c_{SW} = u_0^{-3}$. For the $a \approx 0.09$ and 0.15 ensembles the tadpole coefficient is taken from the average plaquette. We note, however, that at lattice spacing $a \approx 0.12$ fm the tadpole coefficient u_0 appearing in both the valence asqtad action and the heavy quark clover action is taken from the average of the Landau link evaluated on the $am_l/am_h = 0.01/0.05$ ensemble. Hence, in our $a \approx 0.12$ fm lattice data there is a mismatch between light valence and sea quark mass definitions. As discussed in Sec. VII, this (inadvertent) choice leads to a small error in the decay constants. We have remedied this mismatch by using the plaquette u_0 everywhere in new runs started while this analysis was underway.

The charm and bottom kappa values listed in Table III are based on our initial kappa tuning analysis using about one fourth of our final statistics. We then used a larger data set to refine our determination of the κ values corresponding to bottom and charm as described in the next subsection. We adjust our data post-facto to correspond to tuned values of κ_c and κ_b using the measured value of the derivative $\delta\phi/\delta\kappa$.

B. Input quark masses m_c and m_b

Our method for tuning κ for charm and bottom quarks closely follows that of Ref. [55], where further details can be found. We start with the dispersion relation for a heavy particle on the lattice [33]

$$E^2(\mathbf{p}) = M_1^2 + \frac{M_1}{M_2} \mathbf{p}^2 + \frac{1}{4} A_4 (a\mathbf{p}^2)^2 + \frac{1}{3} A_4' a^2 \sum_{j=1}^3 |p_j|^4 + \dots, \quad (3.1)$$

where

$$M_1 \equiv E(\mathbf{0}) \quad (3.2)$$

TABLE IV. Hopping-parameter values used to compute the dispersion relation.

$\approx a$ [fm]	$n_{\text{conf}} \times n_{\text{src}}$	charm	κ_Q
0.09	1912×4	0.1240, 0.1255, 0.1270	bottom 0.090, 0.092, 0.094
0.12	592×4	0.114, 0.117, 0.119, 0.122, 0.124	0.074, 0.086, 0.093, 0.106
0.15	631×8	0.100, 0.115, 0.122, 0.125	0.070, 0.076, 0.080, 0.090

is called the rest mass, and the kinetic mass is given by

$$M_2^{-1} \equiv \left. \frac{\partial E(\mathbf{p})}{\partial p_j^2} \right|_{\mathbf{p}=0}. \quad (3.3)$$

These meson masses differ from corresponding quark masses, m_1 and m_2 , by binding-energy effects. The bare mass or, equivalently, the hopping parameter κ must be adjusted so that these masses reproduce an experimental charmed or b -flavored meson mass. When they differ, as they do when $m_Q a \ll 1$, one must choose. Decay constants are unaffected by the heavy-quark rest mass m_1 [36], so it does not make sense to adjust the bare mass to M_1 . We therefore focus on M_2 , adjusting κ to the strange pseudoscalars D_s and B_s , both because the signal degrades for lighter spectator masses and because this avoids introducing an unnecessary systematic uncertainty due to a chiral extrapolation.

The first step is to compute the correlator $C_2^{(S_1 S_2)}(t, \mathbf{p})$ in Eq. (4.8) (below) for several 3-momenta \mathbf{p} and several values of κ and light quark mass, bracketing charm and bottom, and strange, respectively. We use all momenta such that $|\mathbf{p}| \leq 4\pi/L$. Second, we fit the time dependence of the multichannel correlation matrix $C_2^{(S_1 S_2)}$ to a sum of exponentials—including the usual staggered-fermion oscillating terms—and extract the ground state energy $aE(\mathbf{p})$ by minimization of an augmented χ^2 [55, 68, 69]. Third, we fit the energies to the dispersion relation given in Eq. (3.1), through $O(p_i^4)$. The output of this fit is aM_1 , M_1/M_2 , A_4 , and $A_{4'}$, all as functions of κ . Fourth, we form $M_2(\kappa)$ from the first two fit outputs and r_1/a , propagating the error with a single-elimination jackknife. Finally, we obtain our tuned κ_c and κ_b by interpolating in κ so that $M_2(\kappa)$ matches the experimentally known D_s and B_s masses. The κ values used to compute M_2 are listed in Table IV. For each of the lattice spacings listed, we used the ensemble with light-to-strange sea-quark mass ratio $am_l/am_h = 0.2$. The resulting tuned values of κ_c and κ_b are shown with errors in Table V.

We constrain the coefficients A_4 and $A_{4'}$ with Gaussian priors derived from the HQET theory of cutoff effects, adding the contribution of the priors to the χ^2 in the minimization procedure [68, 69]. (In principle, we could include such priors for M_1 and M_1/M_2 too, but in practice we take priors so wide that these fit parameters are solely data-driven.) Neglecting binding energies, we have exact tree-level expressions for a_4 and $a_{4'}$, the quark analogs of A_4 and $A_{4'}$. The differences $A_4 - a_4^{[0]}$ and $A_{4'} - a_{4'}^{[0]}$ stem from both perturbative and nonperturbative effects. The asymptotics of the former can be estimated along the lines of Appendix A 3, and the latter can be deduced following the methods of Refs. [36, 70]. Briefly, we constrain $A_n(\kappa)$, $n \in \{4, 4'\}$, to a Gaussian with central value

$$a_n^{[0]}(m_0 a) + \alpha_s a_n^{[1]}(m_0 a) + \bar{\Lambda} a A'_n(m_0 a). \quad (3.4)$$

Here $a_n^{[0]}$ is the exact tree-level contribution, $a_n^{[1]}$ is an estimate of the one-loop contribution, and A'_n is an expression for the binding-energy contribution. The width of the Gaussian is

TABLE V. Hopping parameter values κ_c and κ_b corresponding to charm and bottom. The outputs of the tuning are labeled κ_{tuned} , where the first error is from statistics and the second is from r_1 , which enters through matching to the experimentally-measured D_s and B_s meson masses. The derivative $d\phi/d\kappa$ is used to correct the values of ϕ obtained with the simulated values κ_{sim} listed in Table III to the tuned values given below.

$\approx a$ [fm]	charm		bottom	
	κ_{tuned}	$d\phi/d\kappa$	κ_{tuned}	$d\phi/d\kappa$
0.09	0.12691(18)(13)	-21.66	0.0959(13)(3)	-7.41
0.12	0.12136(37)(19)	-18.23	0.0856(19)(3)	-6.82
0.15	0.12093(36)(24)	-15.40	0.0788(11)(3)	-6.07

determined by combining in quadrature the chosen widths of the separate contributions, as outlined in Appendix A 3.

The details of the κ_c and κ_b determination differ from that of Ref. [55] in two respects. First, we use the pseudoscalar meson masses rather than the spin average of pseudoscalar and vector meson masses, leading to a modest reduction of the statistical error. Second, we include the quartic terms in Eq. (3.1), allowing us to fold discretization effects directly into the dispersion-relation fit. Although we consider these two changes improvements, the change in the tuned κ values as compared to Ref. [55] stems primarily from the substantial increase in statistics on key ensembles.

The computations of the correlation functions needed to extract ϕ_D and ϕ_B have been carried out using the fiducial values listed in Table III. These simulation κ 's were obtained near the beginning of the project, but while the runs were in progress, we redetermined the hopping parameters utilizing increased statistics and reflecting an updated value of r_1 [66]. The resulting improved determinations of κ_c and κ_b differ slightly from the simulation values. In order to adjust ϕ from the simulated value κ_{sim} to the tuned value κ_{tuned} , we write

$$\phi_{\text{tuned}} = \phi_{\text{sim}} + \frac{d\phi}{d\kappa}(\kappa_{\text{tuned}} - \kappa_{\text{sim}}), \quad (3.5)$$

where the derivatives $d\phi/d\kappa$ listed in Table V are obtained from tuning runs with nearby κ values. As explained in Sec. VII, these derivatives are also used to propagate to the decay constants the statistical and scale uncertainties on κ_{tuned} listed in Table V.

IV. TWO-POINT CORRELATOR FITS

We obtain the unrenormalized decay amplitude for every combination of heavy-quark mass, light-quark mass, and sea-quark ensemble by fitting the heavy-light meson two-point correlation functions, described in Sec. IV A. We use two independent fitting procedures, which we refer to as ‘‘Analysis I’’ and ‘‘Analysis II’’. These procedures differ in several respects. In Analysis I, we use a jackknife procedure for estimating errors, while in Analysis II, we use a bootstrap procedure. The two analyses also differ in their methods for handling autocorrelations in the data and in their choices of fit ranges, priors for masses and amplitudes, and numbers of states included. In the end, we use Analysis I (Sec. IV B) to obtain central values, and use differences from fits with different distance ranges and/or number

of states included, and from Analysis II (Sec. IV C) to estimate the systematic error due to choices made in the fit procedure.

A. Lattice correlators

The lattice axial-vector current is given by

$$A_a^4(x) = [\bar{\Psi}(x)\gamma^4\gamma^5\Omega(x)]_a\chi(x), \quad (4.1)$$

where $\chi(x)$ is the one-component field appearing in the staggered action, and $\Omega(x) = \gamma_1^{x_1/a}\gamma_2^{x_2/a}\gamma_3^{x_3/a}\gamma_4^{x_4/a}$ is the transformation connecting naive and staggered fields [71]. The heavy-quark field Ψ is a four-component (Dirac) spinor field, and the remaining free Dirac index is interpreted as a taste label.

To remove tree-level discretization errors in the lattice axial current, the heavy-quark field Ψ is “rotated”:

$$\Psi = [1 + ad_1\boldsymbol{\gamma} \cdot \mathbf{D}]\psi, \quad (4.2)$$

where ψ is the field appearing in the clover action. Tree-level improvement is obtained when

$$d_1 = \frac{1}{2 + m_0a} - \frac{1}{2(1 + m_0a)}, \quad (4.3)$$

where

$$m_0a = \frac{1}{u_0} \left(\frac{1}{2\kappa} - \frac{1}{2\kappa_{\text{crit}}} \right) \quad (4.4)$$

is the tadpole-improved bare mass. The critical hopping parameter κ_{crit} is the one for which the clover-clover pion mass vanishes.

As usual in lattice gauge theory, we obtain the matrix element in (2.3) from two-point correlation functions. We introduce pseudoscalar operators

$$\mathcal{O}_a^{(S)}(x) = \sum_y [\bar{\psi}(y)S(y, x)\gamma^5\Omega(x)]_a\chi(x), \quad (4.5)$$

depending on a “smearing” function S . In this work, we use two functions, the local (or unsmeared) source $S(x, y) = \delta_{xy}$, and the smeared source (in Coulomb gauge)

$$S(x, y) = \delta_{x_4y_4}S(\mathbf{x} - \mathbf{y}), \quad (4.6)$$

where $S(\mathbf{r})$ is the $1S$ solution of the Richardson potential for the quarkonium systems [72]. We obtain $S(\mathbf{x} - \mathbf{y})$ by scaling the radial Richardson wavefunction to lattice units, interpolating it to lattice sites, and then using it as the spatial source for the heavy-quark propagators [73].

We introduce two-point correlation functions

$$\Phi_2^{(S)}(t) = \sum_{a=1}^4 \sum_{\mathbf{x}} \left\langle A_a^{4\dagger}(t, \mathbf{x})\mathcal{O}_a^{(S)}(0) \right\rangle, \quad (4.7)$$

$$C_2^{(S_1 S_2)}(t, \mathbf{p}) = \sum_{a=1}^4 \sum_{\mathbf{x}} e^{i\mathbf{p} \cdot \mathbf{x}} \left\langle \mathcal{O}_a^{(S_1)\dagger}(t, \mathbf{x})\mathcal{O}_a^{(S_2)}(0) \right\rangle, \quad (4.8)$$

where $\langle \bullet \rangle$ now represents the ensemble average. For large time separations, $\Phi_2^{(S)}$ is proportional to the matrix element ϕ_H , and the proportionality is determined from $C_2^{(SS)}(t, \mathbf{0})$. Each two-point function is constructed from a staggered quark propagator with local (δ) sources and sinks. We compute C_2 functions for all (four) combinations $S_1, S_2 = \delta$ and 1S, requiring heavy clover quark propagators with all combinations of 1S smeared and local sources and sinks. Only the local sink clover propagators are needed to compute the Φ_2 functions. With the sum over tastes in Eqs. (4.7) and (4.8), the correlation functions Φ_2 and C_2 can also be cast in a heavy-naive formalism [74].

The staggered light quarks in the axial-current and pseudoscalar two-point correlation functions lead to the presence of opposite-parity states that oscillate in time as $(-1)^t$. Hence the two-point functions take the following forms:

$$\begin{aligned} \Phi_2^{(S)}(t) &= A_\Phi^{(S)} (e^{-Mt} + e^{-M(T-t)}) + \tilde{A}_\Phi^{(S)} (-1)^t (e^{-\tilde{M}t} + e^{-\tilde{M}(T-t)}) \\ &\quad + A'_\Phi^{(S)} (e^{-M't} + e^{-M'(T-t)}) + \dots, \end{aligned} \quad (4.9)$$

$$\begin{aligned} C_2^{(S_1 S_2)}(t, \vec{p} = 0) &= A^{(S_1)} A^{(S_2)} (e^{-Mt} + e^{-M(T-t)}) + \tilde{A}^{(S_1)} \tilde{A}^{(S_2)} (-1)^t (e^{-\tilde{M}t} + e^{-\tilde{M}(T-t)}) \\ &\quad + A'^{(S_1)} A'^{(S_2)} (e^{-M't} + e^{-M'(T-t)}) + \dots, \end{aligned} \quad (4.10)$$

where a prime denotes a standard excited state of the same parity and a tilde denotes the mass or amplitude of an opposite-parity state. The oscillating behavior is visible throughout the entire lattice temporal extent, and must be included in fits to extract the ground-state mass and amplitudes.

We then obtain the renormalized decay amplitude in lattice units from the ratio

$$a^{3/2} \phi_H = \sqrt{2} \frac{Z_{A_{Qq}^4} A_\Phi^{(S)}}{A^{(S)}}, \quad (4.11)$$

where $A_\Phi^{(S)}$ and $A^{(S)}$ are the amplitudes of the ground state exponentials defined in Eqs. (4.9) and (4.10), and the renormalization factor $Z_{A_{Qq}^4}$ is discussed in Sec. V.

B. Analysis I

Our primary analysis of two-point correlation functions $\Phi_2^{(S)}$ and $C_2^{(S_1 S_2)}$ —“Analysis I”—proceeds as follows. The amplitudes $A_\Phi^{(S)}$ and $A^{(S)}$ in Eq. (4.11) are determined from fits to multiple correlators using the full data correlation matrix. In Analysis I, we start by fitting combinations A, B, C and D in Table VI. We find combination A, which uses the axial-current correlator with a 1S smeared source and the pseudoscalar correlator with a 1S smeared source and sink, to be suitable. The extra complexity of combinations of three correlators (C and D) give little benefit, and the errors from combination A are somewhat smaller than those from combination B.

For fits to charm-light meson correlators, we include just one simple exponential (the desired state) and one oscillating exponential, which we call a “1+1 state fit”. We choose the minimum distance, t_{min} , such that contributions from excited states are small compared to our statistical errors. Because we fit two propagators simultaneously while imposing the constraint that the masses be equal, this is a six parameter fit: two amplitudes for each

TABLE VI. Combinations of two-point functions that can be used to extract $a^{3/2}\phi_H$. All combinations of two and three correlators are shown. Additional combinations of four or more correlators are not enumerated.

two-point function	fit combination					
	A	B	C	D	E	F
$\Phi_2^{(1S)}(t)$	•	•	•	•	•	
$\Phi_2^{(\delta)}(t)$		•	•	•	•	•
$C_2^{(1S,1S)}(t)$	•			•	•	
$C_2^{(\delta,\delta)}(t)$		•		•		
$C_2^{(\delta,1S)}(t)$		•			•	
$C_2^{(1S,\delta)}(t)$			•			

propagator and a common mass for each of the simple and oscillating exponentials. To help stabilize the fit, the amplitudes and mass of the oscillating state are weakly constrained by Gaussian priors, which are incorporated as additional terms in χ^2 in the fitting procedure [68, 69]. The central values for these priors are determined by a trial fit where the prior for the opposite parity mass is set to 500 ± 250 MeV above the ground state mass and the amplitudes are unconstrained. Then the jackknife fits use central values for the opposite parity state amplitudes and mass determined by the trial fit, with widths (Gaussian) that are typically three to ten times the error estimates on these parameters, so in the end the priors make a negligible contribution to χ^2 . (Although 500 MeV is a reasonable guess for the mass gap to the first excited state of the meson, we actually expect that this excited state in the fit approximates the contributions of a number of physical states, likely including both single and multiparticle channels.) Empirically, the width of the prior is made narrow enough to insure that the fits converge to sensible values. We propagate the uncertainties in the correlator fits to the subsequent chiral-continuum extrapolation with a jackknife procedure. In the jackknife resamples, we center the priors at the values found in the fit to the full ensemble, again with widths that are typically three to ten times the error estimates on these parameters.

The bottom meson correlators fall off much more rapidly with t , so it is difficult to take a large enough minimum distance to insure that excited state contributions are negligible. Therefore we use a fit with two simple exponentials and one oscillating exponential or a “2+1 state fit”. The mass of this excited state is also weakly constrained by priors in the same way that the opposite parity mass is, except that the width of the prior on the excited state mass is set to 200 MeV.

Figure 1 shows the heavy-light pseudoscalar mass as a function of the minimum time used in the fit. The left-hand plots show sample fits to bottom correlators, while the right-hand plots show sample fits to charm correlators. We select fitting ranges to give reasonable fits for all sea-quark ensembles and all valence-quark masses. We quantify the goodness-of-fit with the “ p value” [51], which is the probability that a fit with this number of degrees of freedom would have a χ^2 larger than this value. Table VII gives the fit ranges for charm-light and bottom-light correlators on the three lattice spacings, both for the fits used for the central values and for alternate fits used in estimating systematic errors from choices of fit parameters. The meson masses, $a^{3/2}\phi_H$ values, and p values for the data set used in

TABLE VII. Numbers of states and time ranges used in two-point Analysis I. In the number of states, “1+1” means one simple exponential and one oscillating state (opposite parity). The fits in columns two through five were used for the central values, while the fits in columns six through nine were used in estimating systematic errors from the choice of fit ranges (see Sec. VII C).

$\approx a$ [fm]	central fits				alternate fits			
	charm		bottom		charm		bottom	
	n_{states}	t range						
0.15	1+1	11–23	2+1	4–20	1+1	12–23	1+1	9–20
0.12	1+1	14–31	2+1	5–22	1+1	16–31	1+1	12–22
0.09	1+1	21–47	2+1	7–30	1+1	23–47	1+1	16–30

Analysis I are tabulated in Appendix B.

The decay amplitude $a^{3/2}\phi_H$ is highly correlated among different light valence-quark masses on the same ensemble. To propagate the correlations among the different valence masses to the subsequent chiral-continuum extrapolation, in Sec. VI, we use a single-elimination jackknife procedure to estimate the covariance matrix of $a^{3/2}\phi_H$ for the selected valence quark masses. This is done by computing the covariance matrix of the single elimination jackknife samples, and multiplying by $(N - 1)^2$, where N is the number of configurations in the ensemble. In fact, when all valence quark masses are kept, the covariance matrices are close enough to singular to be unmanageable. This reflects the fact that the correlators for intermediate valence masses can be very accurately predicted from the correlators for nearby masses, so some of the correlators provide very little new information. Therefore, we omit some valence quark masses, using only those set in bold in Table II.

We use a single elimination jackknife rather than an omit- J jackknife because a large number of samples are needed to compute a reliable covariance matrix. Successive configurations in the ensemble are not independent, however, so we must take autocorrelations into account. We do so by repeating the calculation after first blocking the data by a factor of four. (This block size of four is determined from tests on the $a \approx 0.12$ fm lattices using fit Analysis II, for which it gives a reasonable compromise between suppressing autocorrelations and leaving enough data points for the statistical analysis.) We then compute, for each valence-quark mass i , the ratio R_i of the diagonal element of the covariance matrix with a block size of four to the same element of the unblocked covariance matrix:

$$R_i = \sigma_{ii}^{(4)} / \sigma_{ii}, \quad (4.12)$$

where the superscript denotes the block size. The rescaled covariance matrix for $a^{3/2}\phi_H$ is given by

$$C_{ij}^{(4)} = C_{ij} \sqrt{R_i R_j}, \quad (4.13)$$

which preserves the eigenvalue structure of the covariance matrix, whereas simply using the covariance matrix of the blocked data would be more likely to produce spurious small eigenvalues. The rescaling factors R_i themselves have errors, and in many cases turn out to be less than one. In such cases, we do not replace the R_i by one, despite the fact that this would likely be a better estimate of the individual R_i . Doing so would yield a covariance matrix with a bias toward larger errors, and could produce misleading estimates of goodness-of-fit in the later analysis.

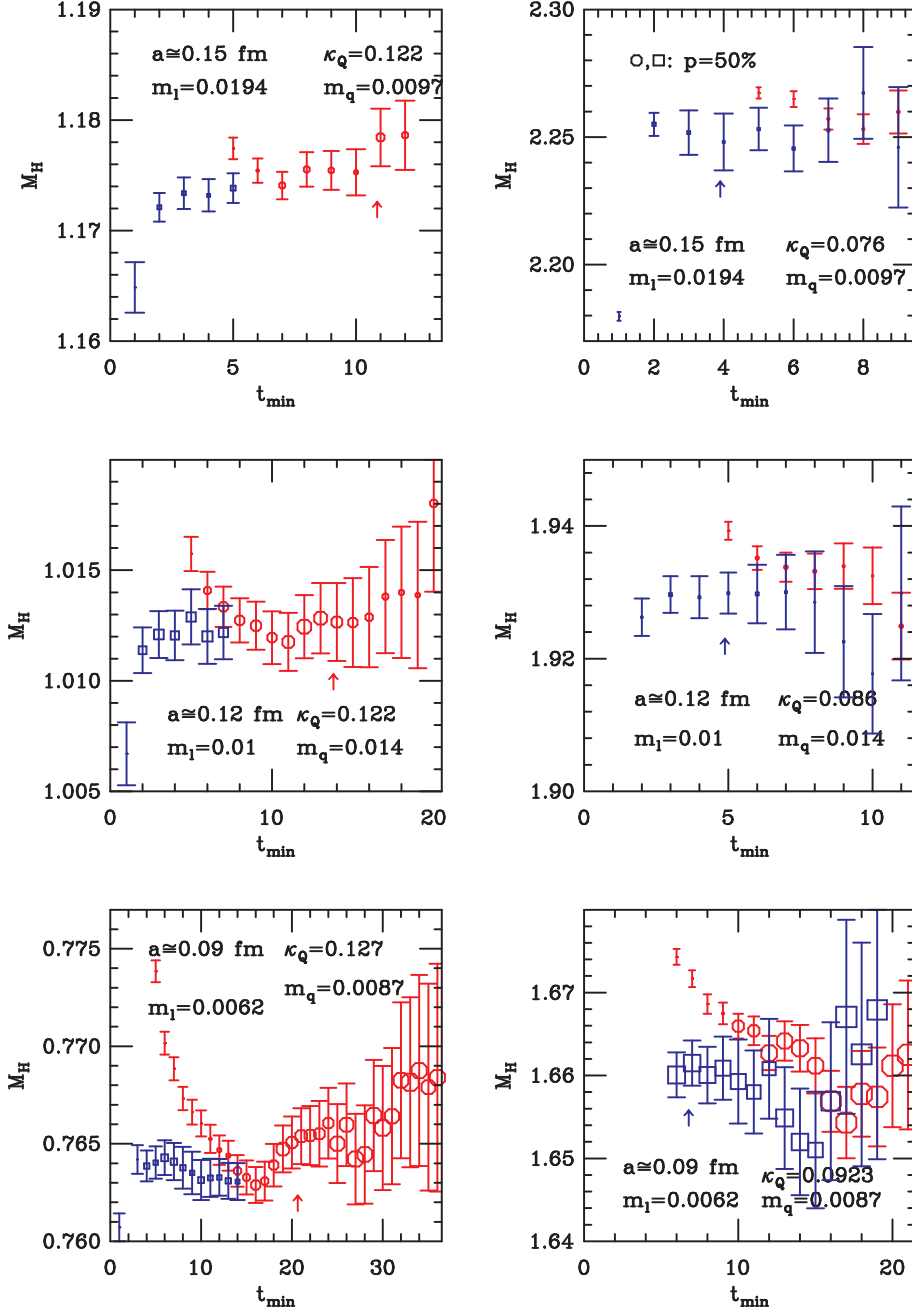


FIG. 1. Ground-state rest mass M_H versus minimum distance t_{min} included in the fit. For each lattice spacing, we show an ensemble with the dynamical light-quark mass m_l in the middle of the range. Similarly, we show correlators with a valence quark mass m_V in the center of the ranges used. The top two panels are at $a \approx 0.15$ fm, the middle two at $a \approx 0.12$ fm and the bottom two at $a \approx 0.09$ fm. In each row the left panel shows results for charm and the right-panel shows results for bottom. The size of each plot symbol is proportional to the p value (confidence level) of the fit, with the symbol size in the legends of the upper right panel corresponding to $p = 50\%$. The red octagons are for fits including one state of each parity ("1+1 fits") and the blue squares are for fits including an excited state of the same parity as the ground state ("2+1 fits"). In each panel, the arrow indicates the fit that is used in Sec. VI.

Finally, we combine the covariance matrices from all of the individual ensembles into larger covariance matrices, one each for the charm and bottom $a^{3/2}\phi_H$. Since different ensembles are statistically independent, these large covariance matrices are block diagonal, with each block containing the correlations among different light valence-quark masses on a single sea-quark ensemble.

C. Analysis II

Analysis II is a second, independent analysis of the two-point correlators that uses the bootstrap method to propagate correlated errors from the two-point analysis through to the chiral extrapolations. In Analysis II, we block average the two-point correlator data over four sequential configurations (which themselves are spaced by more than four trajectories) before the analysis. In the bootstrap procedure, we resample the data (with replacement), taking the number of sampled configurations to be equal to the number of blocked configurations in each bootstrap ensemble. For each bootstrap ensemble, we recompute the covariance matrix. During the bootstrap process, we randomly draw from a gaussian distribution new prior mean values of each constrained parameter belonging to an excited state while keeping the widths fixed. The ground state parameters are given loose priors so that the fitted values are determined by the data. To help stabilize the fits, the ground state prior means are not randomized in the bootstrap. Prior values for the energy splittings are taken from a chiral quark model calculation for the D and B meson systems [75]. Prior widths are taken to be about 200 MeV for excited states. Excited state amplitudes $\log(A^{(S)})$ have a prior width $\sigma_{\log A} = 2$.

On each gauge ensemble, the same sequence of gauge resamplings is taken for all valence m_q to preserve correlations among $a^{3/2}\phi_H$ values. Our final results are based upon 4,000 bootstrap replications of the data. We use the central values of $a^{3/2}\phi_H$ from the fits to the entire ensemble in the chiral-continuum extrapolation, and use the bootstrap values to obtain the covariance matrix.

To optimize the determination of $a^{3/2}\phi_H$, we compare simultaneous fits of up to six two-point functions; the various combinations of up to four functions are listed in Table VI. At a minimum, one axial-current correlator must be paired with one propagator (combinations A or B in Table VI) to extract $a^{3/2}\phi_H$. Combination A, using smeared operators, is used in Analysis I, described above. Because fits of four or more two-point functions over a wide time range can lead to a poorly determined data covariance matrix having large rank relative to the number of available configurations, we focus on combinations having two or three correlators. Unlike combination A, combination B does not take advantage of smeared sources and the ratio does not show convincing plateaus over the range of times with decent signal to noise. Comparing combination C to D, the smeared source in C is less noisy than the smeared sink in D.

Given these considerations, for fits to charm correlators, we use two-point function combination C to obtain $a^{3/2}\phi_H$ which uses both of the axial current functions. We look for stability of the ground-state mass and amplitude when varying t_{min} , t_{max} , and the number of excited states included in the fit. We also compare fit results from other combinations of correlators to check that we have isolated the correct ground-state energy and matrix element. Our final results come from fits accounting for two pseudoscalar states and two (oscillating) opposite-parity states.

For fits to bottom correlators, we use combination B for our final results; this is the same

set used in Analysis I. Combination C gives fits with rather low confidence levels for the B meson and tends to result in larger errors for $a^{3/2}\phi_H$. Again, we examine fits varying the time range; we also try fits with up to three pseudoscalar states plus three oscillating opposite parity states. We use these fits and fits to alternate combinations of two-point correlators as a consistency check.

The fit results from the two different analyses are consistent with each other for most cases, but there are a few cases where they differ by a standard deviation or more (see Figure 11). The $a^{3/2}\phi_H$ results from the two analyses are propagated through the chiral-continuum extrapolations in Secs. VI B and VI C. The resulting differences in the extrapolated results in turn provide the basis for our systematic error analysis due to fit choices given in Sec. VII C.

V. HEAVY-LIGHT CURRENT MATCHING

In this section, we discuss in more detail the ingredients of Eq. (2.5), which allow a “mostly nonperturbative” matching procedure [42].

A. Perturbative calculation of $\rho_{A_{Qq}^4}$

The perturbative expansion of $\rho_{A_{Qq}^4}$ can be written as

$$\rho_{A_{Qq}^4} = 1 + \alpha_s(q^*)\rho_{A_{Qq}^4}^{[1]}(m_Qa, m_qa) + \dots \quad (5.1)$$

where α_s is the strong coupling and $\rho_{A_{Qq}^4}^{[1]}$ is the one-loop coefficient. The one-loop coefficient is calculated in Ref. [43] using lattice perturbation theory, where we see explicitly that $\rho_{A_{Qq}^4}^{[1]}$ is small because most of the one-loop corrections cancel. The self-energy contributions cancel exactly (to all orders, in fact), and, in practice, we are in a region where $\rho_{A_{Qq}^4}^{[1]}(m_Qa, m_qa)$, viewed as a function of m_Qa , has two zeroes. Therefore the renormalization factor $\rho_{A_{Qq}^4}$ is close to unity for both bottom and charm.

The perturbative calculation of $\rho_{A_{Qq}^4}$ in Eq. (5.1) proceeds as follows. We use $\alpha_s(q^*)$ defined in the V scheme [76] as determined in Ref. [77], and take $q^* = 2/a$, which is close to the optimal choice of Refs. [76, 78] for a wide range of quark masses. The one-loop coefficients $\rho_{A_{Qq}^4}^{[1]}$ are computed for light-quark masses $am_q = 0.001, 0.01, 0.04$ to cover the range used in this analysis. From these we obtain $\rho_{A_{Qq}^4}$ at other light-quark masses by linear interpolation in am_q . For illustration, Table VIII lists $\rho_{A_{bq}^4}$ and $\rho_{A_{cq}^4}$ evaluated at the light valence mass $am_q = 0.01$ for the eleven sea-quark ensembles used in this work. Note that the sea-quark mass dependence is indirect, via the plaquette used to determine $\alpha_s(q^*)$. The dependence on the light-quark mass in the current is very mild: for bottom, $\rho_{A_{bq}^4}$ changes with am_q by 0.07–0.2%, depending on lattice spacing, and for charm, $\rho_{A_{cq}^4}$ changes by around 0.1%. On the fine ensembles, the am_q dependence is almost as large as the total one-loop correction because the overall cancellation, especially in $\rho_{A_{cq}^4}$, is so fortuitously good.

TABLE VIII. The perturbative correction factor $\rho_{A_{Qq}^4}$ for the heavy-light current A^4 at the simulated charm and bottom heavy quark κ values given in Table III and at $am_q = 0.01$ for the different sea-quark ensembles. The statistical errors associated with the numerical integration are negligible.

$\approx a$ [fm]	am_l/am_h	$\rho_{A_{bq}^4}$	$\rho_{A_{cq}^4}$
0.09	0.0031/0.031	1.0026	1.0000
	0.0062/0.031	1.0026	1.0000
	0.0124/0.031	1.0026	1.0000
0.12	0.005/0.05	1.0081	0.9959
	0.007/0.05	1.0081	0.9959
	0.010/0.05	1.0081	0.9959
	0.020/0.05	1.0080	0.9960
	0.030/0.05	1.0079	0.9961
0.15	0.0097/0.0484	1.0270	0.9937
	0.0194/0.0484	1.0267	0.9938
	0.0290/0.0484	1.0265	0.9938

B. Nonperturbative computation of $Z_{V_{qq}^4}$ and $Z_{V_{QQ}^4}$

The nonperturbative part of the matching factor $Z_{A_{Qq}^4}$ is obtained from the temporal components of the clover-clover and staggered-staggered vector currents. At zero-momentum transfer, the (correctly normalized) vector current simply counts flavor-number, so it is possible to obtain Z_{V^4} nonperturbatively for any discretization and any mass [42].

For the staggered-staggered current, we compute

$$C_3^{(S_1 S_2)}(t_2, 0, t_1) = \sum_{ab} \sum_{\mathbf{x}, \mathbf{y}} \left\langle \mathcal{O}_a^{(S_1)}(t_2, \mathbf{y}) V_{ab}^4(0) \mathcal{O}_b^{(S_2)\dagger}(t_1, \mathbf{x}) \right\rangle, \quad (5.2)$$

where, as in Eq. (4.5), $\mathcal{O}_a^{(S)}$ is a smeared or local clover-staggered meson operator with mass chosen to optimize the signal, and

$$V_{ab}^4(x) = \bar{\chi}(x) [\Omega^\dagger(x) \gamma^4 \Omega(x)]_{ab} \chi(x) \quad (5.3)$$

is the temporal component of the staggered-staggered vector current. The three-point functions C_3 are computed from the same staggered quarks used for the clover-staggered two point functions. The staggered quark is transformed into an improved naive quark by applying the Ω matrix; this naive quark at time t_1 is then used as the source term when computing the charm propagator. We smear the source at t_1 so that $S_1 = S_2$.

We compute $Z_{V_{qq}^4}$ using a D_q meson [*cf.* Eq. (4.5)], which provides a good signal. The three-point function $C_3^{(S_1 S_2)}(t_2, 0, t_1)$ contains states of both the desired and the opposite parity, with the latter carrying oscillating $(-1)^t$ dependence. We construct $C_3^{(S_1 S_2)}(t_2, 0, t_1)$ with local sources $S_1 = S_2 = \delta$ and compute it at multiple even and odd values of t_1 and t_2 in order to disentangle the ground-state amplitude from the other contributions.

TABLE IX. Light-light vector current renormalization factor $Z_{V_{qq}^4}$. Values in bold are used in computing the heavy-light current renormalizations. With our conventions, the tree-level value of $Z_{V_{qq}^4}$ is 2. A colon is used to represent the range of time values included in the fit.

$\approx a$ [fm]	am_l/am_h	n_{conf}	$-t_1$	t_2	am_q	$Z_{V_{qq}^4}$
0.09	0.0124/0.031	518	23:12	11:13	0.0272	1.868(49)
				23:12	11:13	0.0124 1.883(69)
0.12	0.01/0.05	592	15:9	7:11	0.03	1.853(45)
			0.007/0.05	523	20:7	7:12 0.03 1.882(56)
0.15	0.0097/0.0484	631	20:5	4:12	0.0484	1.704(34)
				20:5	4:12	0.029 1.709(40)
				20:5	4:12	0.0242 1.711(42)
				20:5	4:12	0.0194 1.707(45)
				20:5	4:12	0.0097 1.662(55)

Within the time range $t_1 < 0 < t_2$ and in the limit of large separations, $|t_1|, t_2 \gg a$,

$$\begin{aligned} C_3^{(\delta,\delta)}(t_2, 0, t_1) = & Z_{V_{qq}^4}^{-1} A^2 \exp(-E(t_2 - t_1)) \\ & + Z' AB \left[(-1)^{t_1} \exp(E't_1 - Et_2) + (-1)^{t_2} \exp(Et_1 - E't_2) \right] \\ & + Z'' B^2 (-1)^{(t_1+t_2)} \exp(-E'(t_2 - t_1)) + \dots, \end{aligned} \quad (5.4)$$

neglecting contributions from excited states. We extract $Z_{V_{qq}^4}$ from a minimum χ^2 fit to the three-point function using the right-hand side of Eq. (5.4) as the model function. The fit is linear in the free parameters $Z_{V_{qq}^4}^{-1}$, Z'' and Z' , while we fix the ground-state energies E and E' , and the operator overlaps A and B to the values determined by fitting the two-point function $C_2^{(\delta)}(t, \mathbf{0})$. We use a single-elimination jackknife procedure to compute the data covariance matrix.

Table IX presents our results for $Z_{V_{qq}^4}$ on the ensembles used in this work. The three-point functions for the $Z_{V_{qq}^4}$ calculation are generated at a single source time, $t_{\text{src}} = 0$ (instead of the four used for two-point functions $\Phi_2^{(S)}$ and $C_2^{(S_1 S_2)}$). At $a \approx 0.12$ fm we have results at two values of the sea quark masses which are consistent within errors. At $a \approx 0.09$ and 0.15 fm we have results for several values of m_q . We do not see evidence for a dependence upon m_q with current statistics. The errors, however, increase at smaller quark mass. Hence, we use the $Z_{V_{qq}^4}$ corresponding to $m_q \sim m_s$ in Eq. (4.11). In the table, they are set in **bold**.

For the clover-clover current, we compute

$$\tilde{C}_3^{(S_1 S_2)}(t_2, t_1, 0) = \sum_{\mathbf{x}, \mathbf{y}} \left\langle \tilde{\mathcal{O}}^{(S_1)\dagger}(t_2, \mathbf{y}) V_{QQ}^4(t_1, \mathbf{x}) \tilde{\mathcal{O}}^{(S_2)}(0) \right\rangle, \quad (5.5)$$

where

$$V_{QQ}^4(x) = \bar{\Psi}(x) \gamma^4 \Psi(x) \quad (5.6)$$

is the temporal component of the (rotated) clover-clover vector current. The clover-clover bilinear

$$\tilde{\mathcal{O}}^{(S)}(x) = \sum_y \bar{\psi}(y) S(x, y) \gamma^5 s(x) \quad (5.7)$$

TABLE X. Heavy-heavy vector current renormalization factor $Z_{V_{QQ}^4}$ computed at several κ values, covering the charm and bottom quark masses, for three lattice spacings.

$\approx a$ [fm]	am_l/am_h	$n_{\text{conf}} \times n_{\text{src}}$	κ_Q	$Z_{V_{QQ}^4}$
0.09	0.0062/0.031	1912×2	0.1283	0.2749(4)
			0.127	0.2830(4)
			0.110	0.3856(6)
			0.0950	0.4730(8)
			0.0931	0.4840(9)
0.12	0.007/0.05	2110×2	0.124	0.2899(4)
			0.122	0.3028(4)
			0.116	0.3410(5)
			0.098	0.4507(7)
			0.086	0.5209(10)
			0.074	0.5894(15)
0.15	0.0194/0.0484	631×2	0.122	0.3195(14)
			0.118	0.3440(16)
			0.088	0.5195(48)
			0.076	0.5898(81)

consists of a heavy-quark field corresponding to charm or bottom, as the case may be, and a light clover-quark field s with mass chosen to provide a good signal. At large time separations, these three-point functions are proportional to $Z_{V_{QQ}^4}^{-1}$, with the proportionality coming from

$$\tilde{C}_2^{(S_1 S_2)}(t) = \sum_{\mathbf{x}} \left\langle \tilde{\mathcal{O}}^{(S_1)\dagger}(t, \mathbf{x}) \tilde{\mathcal{O}}^{(S_2)}(0) \right\rangle. \quad (5.8)$$

We compute $Z_{V_{QQ}^4}$ using a $\bar{Q}s$ meson, where the strange quark is simulated with the clover action to circumvent oscillating opposite-parity states [*cf.* Eq. (5.7)]. We restrict our calculation of $\tilde{C}_{2,3}$ to $S = S_1 = S_2$ using both local and 1S smearing functions. The function \tilde{C}_2 combines a local-local clover quark with mass around m_s and a heavy clover quark propagator with source and sink S . The function \tilde{C}_3 requires the same heavy- and light-quark propagators as needed in \tilde{C}_2 . An additional heavy-quark propagator originating from t_2 has as its source the light quark propagator restricted to t_2 , multiplied by γ_5 and convolved with smearing function S .

In Eq. (5.7), we use a random color wall source with three dilutions for both the heavy and light spectator quarks that originate from $t = 0$. We generate two- and three-point functions for both local-local and smeared-smeared source-sink combinations where the smearing is applied to the heavy quark. We compute the 2- and 3-point functions at several values of κ spanning a range from around the charm quark to the bottom quark. We determine $Z_{V_{QQ}^4}$ from a fit to the plateaus in the jackknifed ratio of the three-point and two-point functions. Our results are summarized in Table X.

In order to properly normalize the derivative $d\phi/d\kappa_Q$ (see Eq. (3.5)), we need values of $Z_{V_{QQ}^4}$ at κ values other than those used in the $Z_{V_{QQ}^4}$ simulations. We therefore fit the

TABLE XI. Heavy-heavy vector current renormalization factor $Z_{V_{QQ}^4}$ corresponding to the charm and bottom κ_{sim} values used in the decay constant simulations.

$\approx a$ [fm]		charm		bottom
κ_Q	$Z_{V_{QQ}^4}$	κ_Q	$Z_{V_{QQ}^4}$	
0.09	0.127	0.2829(4)	0.0923	0.4891(9)
0.12	0.122	0.3029(4)	0.086	0.5216(10)
0.15	0.122	0.3199(14)	0.076	0.5868(81)

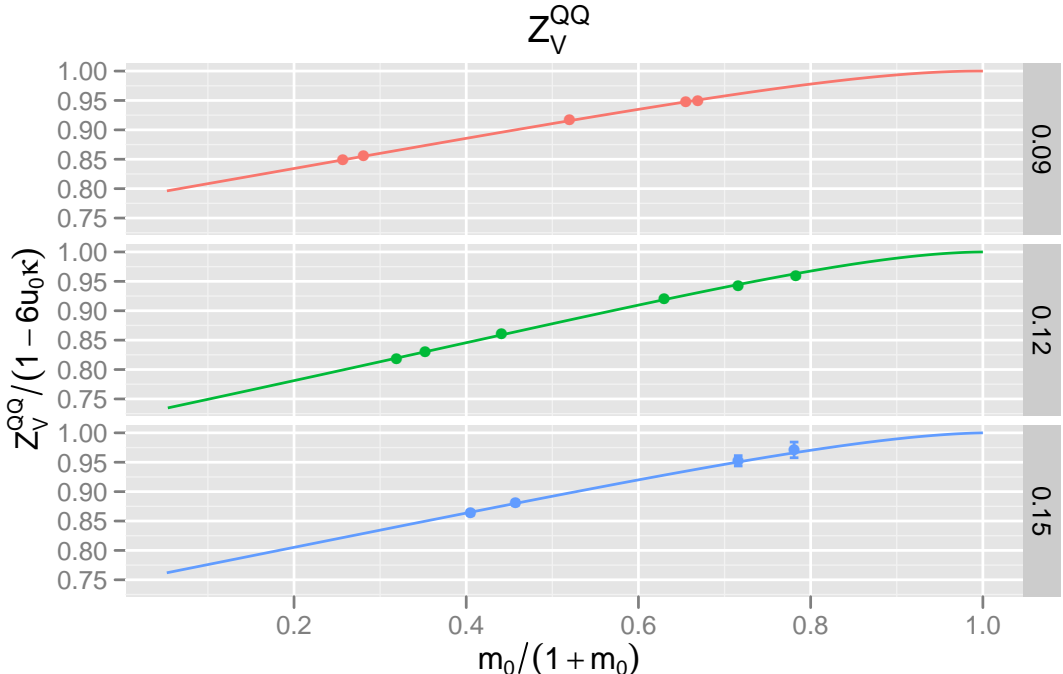


FIG. 2. Plot of $Z_{V_{QQ}^4} / (1 - 6u_0 \kappa)$ vs. $m_0 a / (1 + m_0 a)$ for the three lattice spacings.

simulation results to the interpolating quartic polynomial

$$Z_{V_{QQ}^4}(\kappa) = 1 + \sum_{j=1}^4 c_j \kappa^j \quad (5.9)$$

which reproduces the infinite mass limit $Z_{V_{QQ}^4} \rightarrow 1$. Our codes employ the hopping parameter version of the action; so, at tree level $c_1 = -6u_0$ and for $j > 1$, $c_j = 0$. We constrain the interpolation parameters to the tree-level values taking $\sigma_j = 4$ as the widths. Table XI shows values for $Z_{V_{QQ}^4}$ interpolated to the nominal charm and bottom κ_{sim} used in our decay constant runs. Figure 2 plots the data in Table X together with the interpolation of Eq. (5.9). To aid perturbative intuition, the values of $Z_{V_{QQ}^4}$ in the figure are scaled by the tree-level expression $1 - 6u_0 \kappa$; the relation between κ and $m_0 a / (1 + m_0 a)$ can be inferred from Eq. (4.4).

VI. CHIRAL AND CONTINUUM EXTRAPOLATION

In this section, we present the combined chiral and continuum extrapolations used to obtain the physical values of the $B_{(s)}$ and $D_{(s)}$ meson decay constants. We first discuss the use of $SU(3)$ chiral perturbation theory for heavy-light mesons in Sec. VI A, giving the formulas used for the chiral fits and describing our method for incorporating heavy-quark and light-quark discretization effects into the extrapolation. We then show the chiral fits for the D system in Sec. VI B, and for the B system in Sec. VI C.

A. Chiral Perturbation Theory framework

The errors introduced by the chiral and (light-quark) continuum extrapolations are controlled with rooted staggered chiral perturbation theory (rS χ PT) [22, 23] applied to heavy-light mesons. In Ref. [39], the heavy-light decay constant was calculated to one-loop in rS χ PT at leading order in the heavy-quark expansion $[(1/M_H)^0]$, where M_H is a generic heavy-light meson mass. A replica trick is used in rS χ PT to take into account the effect of the fourth root of the staggered determinant [15, 21].

In addition to using the form calculated in Ref. [39], we also use a chiral fit form that includes, in the loops, the effects of hyperfine splittings (*e.g.*, $M_B^* - M_B$) and flavor splittings (*e.g.*, $M_{B_s} - M_B$). These splittings are ~ 100 MeV, and so not much smaller than M_π , despite the fact that they are formally of order $1/M_H$. Since the lightest pseudoscalar meson masses in our simulations are ~ 225 MeV, it is not immediately obvious that including the splittings is necessary or useful. Their inclusion is motivated, first of all, by the observation of Arndt and Lin [79] that finite-volume effects in the one-loop diagrams can be substantially larger with the splittings present. This is mainly due to the fact that accidental cancellations in finite volume effects between different diagrams at $(1/M_H)^0$ disappear once splittings are included. As described below, it is not difficult to include the splitting effects into the calculation of Ref. [39]. We also discuss the extent to which including the splittings, but not other effects that could occur at order $1/M_H$, is a systematic approximation. In practice, we do fits both including and omitting the splittings, and use the difference as one estimate of the chiral extrapolation error. For central values, we include the splittings, because this yields a more conservative estimate of finite-volume effects.

With staggered quarks, the (squared) pseudoscalar meson masses are

$$M_{ab,\xi}^2 = B_0(m_a + m_b) + a^2 \Delta_\xi, \quad (6.1)$$

where m_a and m_b are quark masses, B_0 is a parameter of χ PT, and the representation of the meson under the taste symmetry group is labeled by $\xi = P, A, T, V, I$ [22]. The exact non-singlet chiral symmetry of staggered quarks as $m_a, m_b \rightarrow 0$ ensures that $\Delta_P = 0$. All of these pseudoscalars appear in the “pion” cloud around the heavy-light meson in the simulation, and all of them therefore affect the decay constant.

Working at leading order $[(1/M_H)^0]$ in the heavy-quark expansion and at one loop, or next-to-leading order (NLO), in the chiral expansion, the rS χ PT expression for the decay

constant with light valence quark q takes the form [39]

$$\begin{aligned} \phi_{H_q} = \phi_H^0 & \left[1 + \frac{1}{16\pi^2 f^2} \frac{1+3g_\pi^2}{2} \left\{ -\frac{1}{16} \sum_{e,\xi} \ell(M_{eq,\xi}^2) \right. \right. \\ & - \frac{1}{3} \sum_{j \in \mathcal{M}_I^{(2,q)}} \frac{\partial}{\partial M_{Q,I}^2} \left[R_j^{[2,2]}(\mathcal{M}_I^{(2,q)}; \mu_I^{(2)}) \ell(M_j^2) \right] \\ & - \left(a^2 \delta'_V \sum_{j \in \hat{\mathcal{M}}_V^{(3,q)}} \frac{\partial}{\partial M_{Q,V}^2} \left[R_j^{[3,2]}(\hat{\mathcal{M}}_V^{(3,q)}; \mu_V^{(2)}) \ell(M_j^2) \right] + [V \rightarrow A] \right) \Big\} \\ & \left. + p(m_q, m_l, m_h, a^2) \right], \end{aligned} \quad (6.2)$$

where m_q is the light valence-quark mass, e runs over the sea quarks, the lighter two of which have masses m_l , and the heavier, m_h .¹ The parameter ϕ_H^0 is independent of the light masses, and p is an analytic function. We fit the charm and bottom systems separately, so ϕ_H^0 depends, in practice, on the heavy-quark mass. The meson mass $M_{Q,\xi}$ is similar to $M_{ab,\xi}$ in Eq. (6.1), but constructed from a valence quark-antiquark, $q\bar{q}$. The light-meson decay constant $f \approx f_\pi \cong 130.4$ MeV and the H - H^* - π coupling g_π controls the size of the one-loop effects. Taste-violating hairpin diagrams, which arise only at non-zero lattice spacing, are parameterized by δ'_A and δ'_V . The residue functions $R_j^{[n,k]}(\{M\}, \{\mu\})$ are defined in Ref. [23]. Chiral logarithms are written in terms of the functions $\ell(M^2)$ [80]:

$$\ell(M^2) = M^2 \ln \frac{M^2}{\Lambda_\chi^2} \quad [\text{infinite volume}], \quad (6.3)$$

$$\ell(M^2) = M^2 \left(\ln \frac{M^2}{\Lambda_\chi^2} + \delta_1(ML) \right) \quad [\text{spatial volume } L^3], \quad (6.4)$$

$$\delta_1(ML) \equiv \frac{4}{ML} \sum_{\mathbf{r} \neq \mathbf{0}} \frac{K_1(|\mathbf{r}|ML)}{|\mathbf{r}|}. \quad (6.5)$$

Here Λ_χ is the chiral scale, K_1 the Bessel function of imaginary argument, and \mathbf{r} any non-zero three-vector with integer components. The mass sets in the residue functions of Eq. (6.2) are

$$\mu^{(2)} = \{M_U^2, M_S^2\}, \quad (6.6)$$

$$\mathcal{M}^{(2,q)} = \{M_Q^2, M_\eta^2\}, \quad (6.7)$$

$$\hat{\mathcal{M}}^{(3,q)} = \{M_Q^2, M_\eta^2, M_{\eta'}^2\}, \quad (6.8)$$

where M_U (M_S) is the mass of the pseudoscalar $l\bar{l}$ ($h\bar{h}$) meson.

The salient feature of the chiral extrapolation of ϕ_{H_q} is that the chiral logs have a characteristic curvature as $m_q \rightarrow 0$ [81]. At non-zero lattice spacing, the presence of the additive splittings $a^2 \Delta_\xi$ in the meson masses reduces the curvature of the chiral logarithms. The characteristic curvature returns, however, as the continuum limit is approached.

¹ The physical values of the average up-down quark mass and of the strange-quark mass are denoted by $\hat{m} = (m_u + m_d)/2$ and m_s , respectively.

To combine data from several lattice spacings into one chiral extrapolation, it is necessary to convert lattice units to (some sort of) physical units. As mentioned in Sec. III A, we convert in two steps, first by canceling lattice units with the appropriate power of r_1/a . In particular, pseudoscalar meson masses [*cf.* Eq. (6.1)] become $r_1^2 M_{ab,\xi}^2 = (r_1/a)^2 (a M_{ab,\xi})^2$, and the decay constant [*cf.* Eq. (6.2)] becomes $r_1^{3/2} \phi_H = (r_1/a)^{3/2} (a^{3/2} \phi_H)$, with $a^{3/2} \phi_H$ determined from Analyses I or II (*cf.* Sec. IV). Strictly speaking, one must take the quark mass dependence of r_1 into account, either separately or by modifying the right-hand side of Eq. (6.2) accordingly. At the present level of accuracy, we ignore this subtlety, canceling units ensemble-by-ensemble with the computed r_1/a . Since r_1 is expected to depend smoothly on m_l and m_h , we are unlikely to introduce an uncontrolled error into the extrapolated decay constants. (After completing the chiral-continuum extrapolation in r_1 units, we then use $r_1 = 0.3117(22)$ fm (*cf.* Sec. III A) to convert to MeV.)

To quantify the size of NLO (and higher) corrections to χ PT, it is useful to define dimensionless parameters x_q , x_l and x_h proportional to the quark masses m_q , m_l and m_h :

$$x_{q,l,h} \equiv \frac{(r_1 B_0)(r_1/a)(2am_{q,l,h})}{8\pi^2 f_\pi^2 r_1^2}.$$

Since the splittings $a^2 \Delta_\xi$ are added to the quark mass terms in Eq. (6.1), it is similarly useful to define

$$x_{\Delta_\xi} \equiv \frac{r_1^2 a^2 \Delta_\xi}{8\pi^2 f_\pi^2 r_1^2}, \quad (6.9)$$

$$x_{\bar{\Delta}} \equiv \frac{r_1^2 a^2 \bar{\Delta}}{8\pi^2 f_\pi^2 r_1^2}, \quad (6.10)$$

where $\bar{\Delta}$ is the average pion splitting

$$\bar{\Delta} = \frac{1}{16} (\Delta_P + 4\Delta_A + 6\Delta_T + 4\Delta_V + \Delta_I). \quad (6.11)$$

The x_i are in “natural” units for χ PT, in the sense that one expects that chiral corrections, when written as series in the x_i , have coefficients [or low-energy constants (LECs)] that are of order 1.

We then take the analytic function p in Eq. (6.2) to have the following form at NLO

$$L_{\text{val}}(x_q + x_{\Delta_{\text{val}}}) + L_{\text{sea}}(2x_l + x_h + 3x_{\Delta_{\text{sea}}}) + L_a \frac{a^2}{16\pi^2 f_\pi^2 r_1^4}, \quad (6.12)$$

where L_{val} , L_{sea} and L_a are quark-mass-independent LECs that we fit from our data, and we define

$$x_{\Delta_{\text{val}}} \equiv \frac{9}{5} x_{\bar{\Delta}} - \frac{4}{5} x_{\Delta_I}, \quad (6.13)$$

$$x_{\Delta_{\text{sea}}} \equiv \frac{9}{11} x_{\bar{\Delta}} + \frac{2}{11} x_{\Delta_I}, \quad (6.14)$$

The low-energy constants L_{val} , L_{sea} and L_a depend implicitly on the chiral scale Λ_χ , so that the complete expression, Eq. (6.2), is independent of Λ_χ . As in Ref. [39], we choose to include the a^2 dependent terms $x_{\Delta_{\text{sea}}}$ and $x_{\Delta_{\text{val}}}$ in the coefficients of L_{val} and L_{sea} so that

these coefficients represent those combinations of meson masses that arise naturally under a change of Λ_χ in the chiral logarithms.

The LEC L_a arises from analytic taste-violating effects; it serves as a counterterm to absorb changes proportional to the taste-violating hairpins δ'_A and δ'_V under a change in chiral scale. As such, we take the a^2 coefficient of L_a in Eq. (6.12) to vary with lattice spacing like $x_{\Delta_{\text{val}}}$. As long as L_a then appears as an independent fit parameter, the introduction of the $x_{\Delta_{\text{sea}}}$ and $x_{\Delta_{\text{val}}}$ terms in the coefficients of L_{val} and L_{sea} in Eq. (6.12) has a negligible effect on the results from the chiral fits. However, we find that the introduction of these terms significantly reduces the magnitude of L_a ; in other words, most of the discretization error from the light quarks appears to be due to the a^2 dependence of the light meson masses in the chiral loops. We leave L_{val} , L_{sea} and L_a unconstrained in the fits that determine central values; their size is of $O(1)$ as expected (and is in fact ≤ 0.6).

In the region of the strange-quark mass, the data for the decay constants show some curvature, and at least some quadratic terms in the quark masses (NNLO effects) must in general be added in order to obtain acceptable ($p > 0.01$) fits. There are four such LECs, giving a NNLO contribution to p of the form

$$Q_1 x_q^2 + Q_2 (2x_l + x_h)^2 + Q_3 x_q (2x_l + x_h) + Q_4 (2x_l^2 + x_h^2). \quad (6.15)$$

Fits omitting the Q_1 and Q_3 terms give poor confidence levels and are rejected; adding the Q_2 and Q_4 terms does not change the fit results much, but increases over-all errors by up to 30%. To be conservative, we include all four terms in fits for central values; other acceptable fits (for example, fixing Q_2 or Q_4 or both to zero) are included among the alternatives used to estimate the systematic error of the chiral extrapolation.

For the central-value fits, the Q_i are mildly constrained by Gaussian priors with central value 0 and width 0.5, since that is roughly the expected size in natural units. After fitting, the posterior values satisfy $|Q_i| \leq 0.5$, and Q_1 and Q_3 have errors ≈ 0.05 (much less than the prior width), indicating that they are constrained by the data. Q_2 and Q_4 have errors ~ 0.5 , indicating that they are largely constrained by the priors. Changing the prior widths for the Q_i to 1.0 has a negligible effect on central values and errors of the decay constants, although the posterior Q_2 and Q_4 typically increase in size and error, as expected.

While the chiral form introduced so far gives acceptable simultaneous fits to our data from all available lattice spacings, we still need to estimate the size of heavy-quark and generic light-quark discretization errors. Following the Bayesian approach advocated in Refs. [68, 69], we add constrained lattice-spacing-dependent terms to the fit function until the statistical errors of the results cease to increase appreciably. For the heavy quark, we take up to six such terms, $f_E(m_0a)$, $f_X(m_0a)$, $f_Y(m_0a)$, $f_B(m_0a)$, $f_3(m_0a)$, and $f_2(m_0a)$, where m_0 is the heavy quark bare mass. Details about the origin and form of these six functions are given in Appendix A. These functions estimate fractional (not absolute) errors, and as such are included within the square brackets in Eq. (6.2) (or its equivalent, Eq. (6.20) below). The first three are $O(a^2)$ corrections and are added to the fit with coefficients $z_i(a\Lambda)^2$, $i \in \{E, X, Y\}$, where Λ is a scale characteristic of the heavy-quark expansion, and the z_i are parameters with prior value 0 and prior width 1 (for f_Y) or $\sqrt{2}$ (for f_E and f_X , since they each appear twice in the analysis of Appendix A). The next two terms are $O(\alpha_s a)$ corrections, added with coefficients $z_i \alpha_s a \Lambda$, $i \in \{B, 3\}$, with z_i taken to have prior value 0 and prior width 1 (for f_B) or $\sqrt{2}$ (for f_3 , again because it appears twice). The final term arises from the propagation to the decay constants of heavy-quark errors in the tuning of the heavy-quark hopping parameter, κ . It comes in with coefficient $z_2(a\Lambda)^3$, with z_2 having

prior value 0 and prior width 1. We take a large value $\Lambda = 700$ MeV, which provides conservatively wide priors, especially for the first five terms. Once one of each of the first two types of terms is added, the errors already reach $\sim 80\%$ of their values with all six added.

Similar terms representing generic light-quark errors, which are not automatically included in the fit function (unlike taste-violating terms), may also be added. With the asqtad staggered action, generic discretization effects are of $O(\alpha_s a^2)$. We allow the physical LECs ϕ_H^0 , L_{val} , L_{sea} , Q_1 , Q_2 , Q_3 , and Q_4 , to have small relative variations with lattice spacing with coefficients $C_i \alpha_s (a\Lambda)^2$, where i stands for any of the seven physical LECs, Λ is again taken to be 700 MeV, and the C_i have prior value 0 with prior width 1. This corresponds to a maximum of about a 3% difference for a given LEC between the $a \approx 0.12$ fm and the $a \approx 0.09$ fm ensembles. Once several heavy-quark discretization terms have been introduced, these light-quark terms further increase the total error of individual decay constants by less than 10%. However, the errors on the decay constant ratios f_{D_s}/f_{D^+} and f_{B_s}/f_{B^+} are significantly increased by light-quark discretization effects, because the heavy-quark effects on the ratios cancel to first approximation. For our central values, we include all six heavy-quark and all seven light-quark terms, so the total error from a given fit should estimate all (taste-conserving) discretization errors, as well as normal statistical effects. To estimate “heavy-quark” and “light-quark” discretization effects separately, we set to zero the light- or heavy-quark discretization terms, respectively, and then subtract the statistical errors in quadrature. Such separate errors are not relevant to any final results quoted below, but are included as separate lines in the error budget for informational purposes.

As mentioned above, our preferred fit form modifies Eq. (6.2) by including the effects of hyperfine and flavor splittings of the heavy-light mesons in one-loop diagrams. We now briefly describe how one may adjust the results of Ref. [39] to include these splittings. In Eq. (6.2), the contributions proportional to g_π^2 come from diagrams with internal H^* propagators, namely the left-hand diagrams in Fig. 5 of Ref. [39]. Contributions with no factor of g_π^2 come from diagrams with light-meson tadpoles, namely the right-hand diagrams in Fig. 5 of Ref. [39]. The latter have no internal heavy-light propagators, so are unaffected by any heavy-light splittings. The splittings in the former diagrams depend on whether the light-meson line is connected (Fig. 5a, left, of Ref. [39]), or disconnected (Fig. 5b, left). In the disconnected case, the H^* in the loop always has the same flavor (q) as the external H_q , so there is no flavor splitting between the two, only a hyperfine splitting. In the connected case, the H^* in the loop has the flavor of the virtual sea quark loop (which we labeled by e in Eq. (6.2)), so there is flavor splitting with the external H_q , in addition to the hyperfine splitting.

Let Δ^* be the (lowest-order) hyperfine splitting, and δ_{eq} be the flavor splitting between a heavy-light meson with light quark of flavor e and one of flavor q . At lowest order, δ_{eq} is proportional to the quark-mass difference (or light-meson squared mass difference), which can be written in terms of a parameter λ_1 :

$$\delta_{eq} \cong 2\lambda_1 B_0(m_e - m_q) \cong \lambda_1(M_E^2 - M_Q^2), \quad (6.16)$$

where M_E is the mass of an $e\bar{e}$ light meson. Here we have used the notation of Arndt and Lin [79] and included a factor of B_0 in the middle expression; B_0 is omitted in the notation of Ref. [82], Eq. (16), and of Ref. [39], Eq. (45).

By convention, the mass of the external H is removed in the heavy quark effective theory, so the mass shell is at $\mathbf{k} = \mathbf{0}$, where \mathbf{k} is the external three-momentum. When there

is no splitting, the internal H^* has its pole at the same place, which makes the integrals particularly simple, giving the chiral log function $\ell(M^2)$, Eq. (6.3). If a splitting Δ is present, the integrals involve a significantly more complicated function, which we denote

$$J(M, \Delta) = (M^2 - 2\Delta^2) \log(M^2/\Lambda^2) + 2\Delta^2 - 4\Delta^2 F(M/\Delta) \quad [\text{infinite volume}]. \quad (6.17)$$

Here the function F is most simply expressed [83, 84]

$$F(1/x) = \begin{cases} -\frac{\sqrt{1-x^2}}{x} \left[\frac{\pi}{2} - \tan^{-1} \frac{x}{\sqrt{1-x^2}} \right], & \text{if } |x| \leq 1, \\ \frac{\sqrt{x^2-1}}{x} \ln(x + \sqrt{x^2-1}), & \text{if } |x| \geq 1, \end{cases} \quad (6.18)$$

which is valid for all x .

It is then straightforward to write down the generalization of Eq. (6.2) to include splittings. The basic rule is to replace

$$\ell(M^2) \rightarrow J(M, \Delta) \quad (6.19)$$

in the terms proportional to g_π^2 . It is not hard to show that $J(M, 0) = \ell(M^2)$, so this replacement is consistent with the original result neglecting the splittings. In making the replacements, one must choose the correct value of the splitting Δ in each term. As mentioned above, in terms that come from the diagram with a disconnected light-meson propagator, one must put $\Delta = \Delta^*$. But in terms that come from the diagram with a connected light-meson propagator, one must put $\Delta = \Delta^* + \delta_{eq}$, because the internal heavy-light meson is a H_e^* , while the external meson is an H_q . The result for the heavy-light meson decay amplitude including the splittings is then

$$\begin{aligned} \phi_{H_q} = \phi_H^0 &= \phi_H^0 \left[1 + \frac{1}{16\pi^2 f^2} \frac{1}{2} \left\{ -\frac{1}{16} \sum_{e, \Xi} \ell(M_{eq, \Xi}^2) \right. \right. \\ &\quad - \frac{1}{3} \sum_{j \in \mathcal{M}_I^{(2,x)}} \frac{\partial}{\partial M_{X,I}^2} \left[R_j^{[2,2]}(\mathcal{M}_I^{(2,x)}; \mu_I^{(2)}) \ell(M_j^2) \right] \\ &\quad - \left(a^2 \delta'_V \sum_{j \in \hat{\mathcal{M}}_V^{(3,x)}} \frac{\partial}{\partial M_{X,V}^2} \left[R_j^{[3,2]}(\hat{\mathcal{M}}_V^{(3,x)}; \mu_V^{(2)}) \ell(M_j^2) \right] + [V \rightarrow A] \right) \\ &\quad - 3g_\pi^2 \frac{1}{16} \sum_{e, \Xi} J(M_{eq, \Xi}, \Delta^* + \delta_{eq}) \\ &\quad - g_\pi^2 \sum_{j \in \mathcal{M}_I^{(2,x)}} \frac{\partial}{\partial M_{X,I}^2} \left[R_j^{[2,2]}(\mathcal{M}_I^{(2,x)}; \mu_I^{(2)}) J(M_j, \Delta^*) \right] \\ &\quad - 3g_\pi^2 \left(a^2 \delta'_V \sum_{j \in \hat{\mathcal{M}}_V^{(3,x)}} \frac{\partial}{\partial M_{X,V}^2} \left[R_j^{[3,2]}(\hat{\mathcal{M}}_V^{(3,x)}; \mu_V^{(2)}) J(M_j, \Delta^*) \right] + [V \rightarrow A] \right) \Big\} \\ &\quad \left. + p(m_q, m_l, m_h, a^2) \right]. \end{aligned} \quad (6.20)$$

It is also straightforward to include finite-volume effects into Eq. (6.20). One simply replaces

$$J(M, \Delta) \rightarrow J(M, \Delta) + \delta J(M, \Delta, L), \quad (6.21)$$

where $\delta J(M, \Delta, L)$ is the finite-volume correction in a spatial volume L^3 . The correction can be written in terms of functions defined in Refs. [41, 79]:

$$\delta J(M, \Delta, L) = \frac{M^2}{3} \delta_1(ML) - 16\pi^2 \left[\frac{2\Delta}{3} J_{FV}(M, \Delta, L) + \frac{\Delta^2 - M^2}{3} K_{FV}(M, \Delta, L) \right], \quad (6.22)$$

with

$$K_{FV}(M, \Delta, L) \equiv \frac{\partial}{\partial \Delta} J_{FV}(M, \Delta, L), \quad (6.23)$$

and $\delta_1(ML)$ as given in Eq. (6.5).

Before turning to the fit details and results, we briefly discuss the extent to which including the splittings as in Eq. (6.20), and not other possible $1/M_H$ effects, is a systematic improvement on Eq. (6.2). In fact, in a parametric sense within the power counting introduced by Boyd and Grinstein [82], this is a systematic improvement, as long as we make some further specifications as to how Eq. (6.20) should be applied. As we detail below, however, the power counting of Ref. [82] is only marginally applicable to our data. For that reason we ultimately fit to both Eq. (6.20) and Eq. (6.2) and take the difference as one measure of the chiral extrapolation error.

For the following discussion, let Δ be a generic splitting (Δ^* or δ_{eq} or a linear combination of the two), and M be a generic light pseudoscalar mass. The power counting introduced in Ref. [82] takes

$$\frac{\Delta^2, \Delta M, M^2}{M_H} \ll \Delta \sim M. \quad (6.24)$$

For our data, treating Δ and M as the same size is not dangerous, even though Δ is significantly smaller than our simulation M values—at worst this means that we include some terms unnecessarily. The condition $M^2/M_H \ll \Delta$, which is necessary to drop other $1/M_H$ contributions as still higher order, is marginally valid, however. For the D system, $M_K^2/M_D \approx 130$ MeV, which is roughly of the same size as Δ^* and δ_{sd} . For the B system, $M_K^2/M_B \approx 47$ MeV, of the same size as Δ^* but somewhat less than δ_{sd} . For the purposes of the chiral extrapolation, however, what matters is the applicability of the power counting at the lowest simulated light meson masses, not its applicability at M_K .² For our lightest simulated pions with mass $\sim M_K/2$, we can reduce the left hand side of the inequality in Eq. (6.24) by a factor of four, at which point it becomes reasonably applicable.

Having tentatively accepted the power counting of Eq. (6.24), it is clear that $F(M/\Delta)$ in Eq. (6.17) should be treated as $O(1)$. Then the difference between $J(M, \Delta)$ and the chiral logarithm it replaces, $\ell(M^2)$ is of the same order as $\ell(M^2)$ itself, so including the splittings becomes mandatory at the one-loop order to which we are working. The next question is whether Eq. (6.2) includes *all* effects to this order. As discussed by Boyd and Grinstein, the key issue is whether operators with two or more derivatives (two or more powers of residual momentum \mathbf{k}) on the heavy fields can contribute. Such operators are suppressed by $1/M_H$ relative to the leading-order heavy-light Lagrangian, which has a single derivative. Since we are keeping Δ^* , which is also in principle a $1/M_H$ effect, one might worry that such operators could contribute at the same order. The power counting implies, however, that the relevant diagrams pick up a factor of $(\Delta, M)/M_H$ relative to the terms being kept in

² We assume here that the fit to the data is good over the full mass range simulated. It is not important for the chiral extrapolation that the fit be systematic in the region around M_K , but it must describe the data in that range so that we can correctly interpolate to the physical kaon mass.

Eq. (6.20). The reason for the difference is that the explicit extra factor of \mathbf{k} turns into Δ or M —the only dimensional constants available—after integration. In the term that generates the hyperfine splitting itself, in contrast, the dimensional quantity balanced against $1/M_H$ is Λ —a heavy-quark QCD scale—rather than M . The power counting in Eq. (6.24) effectively treats Λ as larger than M (so that $\Delta \sim \Lambda^2/M_H \sim M$). Similarly, the term that generates the flavor splittings has a single factor of m_q and no residual momentum, and Eq. (6.24) effectively takes $m_q \sim \mathbf{k}$ in such terms.

Boyd and Grinstein do find some other contributions at the same order as Eq. (6.20), but most come from terms that are simply Λ/M_H times terms in the leading-order heavy-light Lagrangian or current, and thus give simply an overall factor times the result without them. The exceptions are the terms multiplied by g_2 in Eq. (15) of Ref. [82] and by ρ_2 in Eq. (18) of Ref. [82]. These are operators that have the same dimension as the original Lagrangian current operators, but that violate heavy-quark spin symmetry, and therefore give different contributions to the pseudoscalar and vector meson decay constants at this order. Since we are only looking at pseudoscalar meson decay constants here, however, and since these effects are flavor-independent, we can also absorb all of the $1/M_H$ effects into (1) the effects of the splittings in the loop, described by Eq. (6.20), and (2) an overall factor in front of the full one-loop result.

The overall factor in Eq. (6.20) is $1/(16\pi^2 f^2)$. Since f is not fixed at one loop, one should in any case allow it to vary over a reasonable range, which we take to be f_π to f_K . We allow such variations even when we fit to the form without splittings, Eq. (6.2). The difference between using f_π and f_K corresponds to a 45% change in the size of the one-loop coefficient, but produces only a 1 to 3 MeV change in the decay constants.³ We therefore assume that any further $1/M_H$ uncertainty in $1/(16\pi^2 f^2)$ has negligible effects on our results.

Finally, there is a question of whether terms coming from taste violations contribute something new at the same order in which we include splittings. Since taste-violating terms in the Lagrangian can enter just like light-quark masses, this is a possibility in principle. Corresponding to the terms in the quark masses that generate flavor splittings of heavy-light mesons (*cf.* Eq. (45) of Ref. [39]), there are taste-violating terms given in Eq. (51) of that paper. Just as for the quark-mass terms, however, we are only interested here in contributions that change the heavy-light meson mass, not ones coupling the mesons to pion fields. When the pion fields are set to zero, all the terms in Eq. (51) of Ref. [39] just give a constant heavy-light meson mass term proportional to a^2 that contributes equally to the H and H^* masses of all valence flavors. Terms that produce a hyperfine splitting would have to also violate heavy quark spin symmetry, and hence be of order $a^2\Lambda/M_H$. Similarly, terms that produce flavor splitting would need to violate flavor symmetry, and hence be of order a^2m_q/Λ_χ . Both such contributions are higher order in our power-counting. Since there is no splitting, there is no contribution to the decay constants because the effect will vanish when we put the external B or D meson on mass shell.

In our chiral fits, we take the physical light-quark masses, as well as the parameters B_0 , $a^2\Delta_\xi$, δ'_A , and δ'_V , from the MILC Collaboration’s results of rS χ PT fits to light pseudoscalars masses and decay constants [12, 85] on ensembles that include lattice spacing $a \approx 0.15$ fm through $a \approx 0.06$ fm. Table XII shows the values used. In general, we use older MILC determinations since newer versions, *e.g.*, those in Ref. [66], do not cover the full range of lattice spacings employed here (but are consistent where they overlap). The exceptions are

³ Most of the change in the size of the overall coefficient is compensated by a change in the LECs that come from the fit to our data.

TABLE XII. Inputs to our heavy-light chiral fits taken from the MILC Collaboration’s light-meson chiral fits [12, 85]. The physical bare-quark masses m_u , m_d , $\hat{m} \equiv (m_u + m_d)/2$, and m_s are determined by demanding that the charged pion and kaons take their physical masses after the removal of electromagnetic effects. Errors in the masses are due to statistics, chiral extrapolation systematics, scale determination, and (for m_d and m_u) the estimate of electromagnetic effects, respectively. “Continuum” values are found from chiral fits that have been extrapolated to the continuum, but masses are still in units of the “fine” ($a \approx 0.09$ fm) lattice spacing, and with the fine-lattice value of the mass renormalization. Values for $r_1^2 a^2 \delta'_A$ and $r_1^2 a^2 \delta'_V$ take into account newer MILC analyses [66] as noted in the text. The light-meson analysis determining these quantities assumes that they scale like the taste-violating splittings Δ_ξ and are larger by a factor of 1.68 on the 0.15 fm lattices than on the 0.12 fm lattices, and smaller by a factor 0.35 on the 0.09 fm lattices than on the 0.12 fm lattices. The statistical and systematic errors on $r_1 B_0$ and $r_1^2 a^2 \Delta_\xi$ are not given here; such errors have negligible effect on the heavy-light decay constants.

Quantity	Lattice spacing			
	$a \approx 0.15$ fm	$a \approx 0.12$ fm	$a \approx 0.09$ fm	“continuum”
$am_s \times 10^2$	4.29(1)(8)(6)	3.46(1)(10)(5)	2.53(0)(6)(4)	2.72(1)(7)(4)
$a\hat{m} \times 10^3$	1.55(0)(3)(2)	1.25(0)(4)(2)	0.927(2)(27)(13)	0.997(2)(32)(14)
$am_d \times 10^3$	2.20(0)(4)(3)(5)	1.78(0)(6)(3)(4)	1.31(0)(4)(2)(3)	1.40(0)(5)(2)(3)
$am_u \times 10^4$	8.96(2)(17)(13)(49)	7.31(2)(23)(10)(40)	5.47(1)(16)(8)(30)	5.90(1)(19)(9)(32)
$r_1 B_0$	6.43	6.23	6.38	6.29
$r_1^2 a^2 \Delta_A$	0.351	0.205	0.0706	0
$r_1^2 a^2 \Delta_T$	0.555	0.327	0.115	0
$r_1^2 a^2 \Delta_V$	0.721	0.439	0.152	0
$r_1^2 a^2 \Delta_I$	0.897	0.537	0.206	0
$r_1^2 a^2 \delta'_A$	—	-0.28(6)	—	0
$r_1^2 a^2 \delta'_V$	—	0.00(7)	—	0

the values of the taste-violating hairpin parameters $r_1^2 a^2 \delta'_A$ and $r_1^2 a^2 \delta'_V$. For them, the newer analysis including two-loop chiral logarithms gives larger systematic errors and a changed sign of the central value of $r_1^2 a^2 \delta'_V$, which has always been consistent with zero. For these parameters, we therefore use the wider ranges listed in Table XII, which encompasses both types of analyses. For comparison, the results of the analysis of Ref. [85] were $r_1^2 a^2 \delta'_A = -0.30(1)(4)$ and $r_1^2 a^2 \delta'_V = -0.05(2)(4)$.

In order to fit Eq. (6.20) to our lattice data, it is also necessary to input values for the hyperfine splitting Δ^* and for λ_1 in Eq. (6.16). For B mesons, we have [51]

$$\Delta^* = M_{B^*} - M_B \approx 45.8 \text{ MeV}, \quad (6.25)$$

$$\delta_{sd} = M_{B_s} - M_B \approx 87.0 \text{ MeV}, \quad (6.26)$$

$$\lambda_1 \approx 0.192 \text{ GeV}^{-1}, \quad (6.27)$$

where we use $M_E = M_S = 0.6858(40)$ GeV [67] and $M_Q = M_{\pi^0} \approx 135.0$ MeV to obtain λ_1

from the experimental data. Similarly, for D mesons, we have

$$\Delta^* = M_{D_0^*} - M_{D_0} \approx 142.1 \text{ MeV}, \quad (6.28)$$

$$\delta_{sd} = M_{D_s} - M_{D_\pm} \approx 98.9 \text{ MeV}, \quad (6.29)$$

$$\lambda_1 \approx 0.219 \text{ GeV}^{-1}. \quad (6.30)$$

In the chiral fit, we input the relevant physical Δ^* and λ_1 from either Eqs. (6.25)–(6.27) or (6.28)–(6.30), and then use Eq. (6.16) with the actual m_e and m_q from each data point, and B_0 the slope for a given ensemble, from Table XII. We emphasize here that B_0 comes from a simple tree-level chiral fit of light meson masses to Eq. (6.1). This is adequate for our purposes, since the resulting meson masses are only used within the one-loop chiral logarithms.

We can now present the actual chiral fits and show how we extract results and systematic errors from them. Recall that we compute ϕ_{H_q} for many combinations of the valence and light sea-quark masses, and at three lattice spacings: $a \approx 0.15, 0.12,$ and 0.09 fm . We fit all the decay constant data to the form given either by Eq. (6.20) or by Eq. (6.2). One-loop finite-volume effects are included through Eq. (6.21) or Eq. (6.4). There are four unconstrained free parameters in our fits: the LO parameter ϕ_H^0 , and the one-loop LECs L_{val} , L_{sea} , L_a [Eq. (6.12)]. The central fit fixes the chiral coupling f at f_π , but a range of couplings are considered in alternative fits, as described in more detail in Sec. VII. Similarly, the H - H^* - π coupling g_π , which is poorly constrained by our data, is taken in the range 0.51 ± 0.20 . This encompasses a range of phenomenological and lattice determinations [83, 86–91], as discussed in Ref. [53]. In the central fit, g_π is held fixed at 0.51, while it is varied in alternative fits described in Sec. VII. Although changing g_π is equivalent to changing f when splittings are omitted [*cf.* Eq. (6.2)], the effects are inequivalent when splittings are included [*cf.* Eq. (6.20)]. This is especially true of the finite-volume effects, for which the splittings have the potential to produce significant changes [79].

Some additional parameters constrained by Bayesian priors are also included in the chiral fits, as discussed above. The taste-violating hairpin parameters δ'_V and δ'_A are given by the ranges in Table XII. In addition, up to six heavy-quark and up to seven light-quark lattice-spacing dependent terms, are added for investigation of discretization effects. Except where otherwise noted, all twelve such terms are included in the fits plotted below: this gives errors that include true statistical errors plus our estimate of discretization effects from the heavy quarks and generic (taste non-violating) discretization errors from the light quarks. In addition, some or all of the (mildly) constrained NNLO LECs, Q_1, \dots, Q_4 , are included. Again, unless otherwise noted, the fits below include all four such parameters; such fits tend to give larger (and hence more conservative) errors than fits that restrict the number of these parameters. In total, there are 23 fit parameters in the central fits: the 19 constrained parameters listed in this paragraph, and the 4 unconstrained parameters listed in the previous paragraph.

B. Chiral fits and extrapolations for the D system

Figure 3 shows our central chiral fit to $r_1^{3/2}\phi_{D^+}$ and $r_1^{3/2}\phi_{D_s}$. Data from ensembles at $a \approx 0.15 \text{ fm}$, $a \approx 0.12 \text{ fm}$ and $a \approx 0.09 \text{ fm}$ are shown, but the $a \approx 0.15 \text{ fm}$ ensembles are not included in the fit. The points and covariance matrix are obtained from Analysis I

(Sec. IV B) of the two-point functions. For clarity, only the unitary (full QCD) points are shown for ϕ_D (and approximately unitary for ϕ_{D_s}), but the fit is to all the partially-quenched data on the $a \approx 0.12$ fm and $a \approx 0.09$ fm ensembles. The fit properly takes into account the covariance of the data; χ^2/dof and the p value (goodness of fit) are reasonable, as shown. The points in Fig. 3 are plotted as a function of mass m_x , where, for ϕ_{D+} , the light valence mass m_q and the light sea mass m_l are given by $m_q = m_l = m_x$. For ϕ_{D_s} , only $m_l = m_x$ varies, while m_q is held fixed at the value m_{s_v} near the physical strange mass m_s .⁴ In order to be able to compare ensembles at different lattice spacings, we have adjusted the bare quark masses by the ratio $Z_m/Z_m^{0.09\text{fm}}$, where Z_m is the (one-loop) mass renormalization constant [92], and $Z_m^{0.09\text{fm}}$ is its value on the $a \approx 0.09$ fm ensembles.

The continuum extrapolation is carried out by taking the fitted parameters and setting $a^2 = 0$ in all taste-violating terms (parameterized by Δ_ξ , δ'_A , δ'_V , and L_a), all heavy-quark discretization effects (parameterized by z_E , z_X , z_Y , z_B , z_3 , and z_2) and all generic light-quark discretization effects (parameterized by C_i). The red lines (solid for ϕ_{D+} , dotted for ϕ_{D_s})

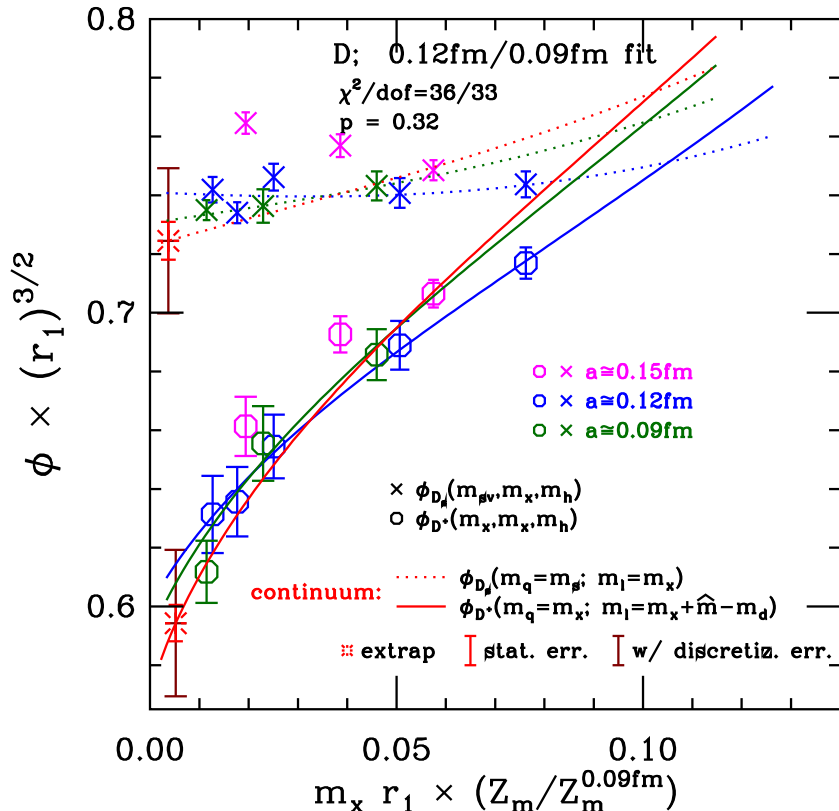


FIG. 3. Central chiral fit for the D system, based on Analysis I of the fits to 2-point correlators. Only (approximately) unitary points are shown. Data from ensembles at $a \approx 0.15$ fm, $a \approx 0.12$ fm and $a \approx 0.09$ fm are shown, but the $a \approx 0.15$ fm ensembles are not included in the fit. The bursts show extrapolated values for ϕ_{D_s} and ϕ_{D+} , with the purely statistical errors in bright red and the statistical plus discretization errors in darker red. The physical strange-quark mass corresponds to an abscissa value of $m_x \approx 0.1$.

⁴ On the $a \approx 0.15$ fm ensembles, m_{s_v} is equal to the value of the strange sea quark mass m_h ($am_{s_v} = 0.0484$), but on the other two ensembles we take it lower than m_h , because m_h has been chosen somewhat larger than the physical strange mass. In the figure, $am_{s_v} = 0.415$ for the $a \approx 0.12$ fm ensembles and $am_{s_v} = 0.272$ for the $a \approx 0.09$ fm ensembles.

show the effect of extrapolating to the continuum and setting the strange quark mass (both sea, m_h , and valence, m_{s_v}) to the physical value m_s .

Finally, the bursts give the result after the chiral extrapolation in the continuum, *i.e.*, setting $m_x = m_d$ for ϕ_{D^+} , and $m_x = \hat{m}$ for ϕ_{D_s} . The larger, dark red, error bars on the bursts show the total error from the fit, which includes heavy-quark and generic light-quark discretization errors using Bayesian priors, as described above. The smaller, bright red error bars, show purely statistical errors, which are computed by a fit with all the discretization prior functions turned off. In plotting the red line for ϕ_{D^+} , the light sea mass is shifted slightly ($m_l = m_x + \hat{m} - m_d$) so that it takes its proper mass when $m_x = m_d$. (We neglect isospin violations in the sea.) The small mass differences between \hat{m} and m_d (and the corresponding difference between \hat{m} and m_u for the B^+) produce changes in ϕ that are much smaller than our current errors, but we include them here with an eye to future work, where the precision will improve.

The trend of the data for the coarsest lattice spacing ($a \approx 0.15$ fm, the magenta points in Fig. 3) tends to be rather different than for the finer lattice spacings, especially for the D_s , which is why we exclude the $a \approx 0.15$ fm data from the central fit. This trend is even more exaggerated for the B system, but with particularly large statistical errors; see Fig. 6 below. Nevertheless, the effect of including the $a \approx 0.15$ fm points in the fit is a rough indication of the size of discretization errors. Figure 4 shows what happens to the fit when these points are included: ϕ_{D^+} and ϕ_{D_s} each move up an amount comparable to (but less than) the size of the larger (dark red) error bars, which represent heavy and generic light quark discretization errors (as well as statistical errors, which are smaller). The consistency is reassuring.

As discussed in Sec. IV, we also examine Analysis II of the 2-point functions. Figure 5 shows the effect of using Analysis II in the chiral fits. The differences in the decay constant results between Fig. 3 and Fig. 5 are included in the decay-constant error budgets as a “fitting error”. Note that the covariance matrix calculation in Analysis II results in an apparent underestimate of χ^2 (and, consequently, a high apparent p value). We believe that this stems from binning of the data to remove autocorrelation effects, which has the disadvantage of reducing the number of samples used to compute the covariance matrix. It is then difficult to determine small eigenvalues accurately. Indeed the eigenvalues of the (normalized) correlation matrix tend to have a lower bound of $\sim 10^{-4}$ to 10^{-3} with this approach, whereas they typically go down to 10^{-5} in Analysis I. [Recall that in Analysis I we keep all samples, and deal with autocorrelation effects by Eq. (4.13).] Nevertheless, the difficulty with small eigenvalues explains only a small fraction of the difference between the results from Analyses I and II. For example, f_D is changed by only 0.2 MeV when we smooth eigenvalues from Analysis I that are less than 10^{-3} , following the method of Ref. [93]. This may be compared to the total difference between f_D in Analyses I and II, which is 1.7 MeV.

C. Chiral fits and extrapolations for the B system

Results for the B system closely resemble those for the D system in most respects. One important difference is that the signal-to-noise ratio is worse for the B system because the mass difference that controls the noise, $2m_B - m_{\eta_b} - m_\pi$, increases with the mass of the heavy quark [94]. Therefore, the preferred fit in Analysis I for the charm case (1 simple exponential + 1 oscillating exponential at large t_{min}) is too noisy here, and we must use fits with an extra excited state and smaller t_{min} (see Sec. IV B). Consequently, our B -system

results have larger statistical errors. On the other hand, heavy-quark discretization errors are smaller in the B system. In the HQET analysis of discretization effects they appear in the heavy-quark expansion, which works better for B 's to begin with [60].

Figure 6 shows, for unitary points only, our central chiral fit for the B system. This is based on Analysis I of the 2-point functions. As in Fig. 3, the red lines (solid for ϕ_{B^+} , dotted for ϕ_{B_s}) show the effect of extrapolation to the continuum and setting the strange quark mass to its physical value m_s . For the solid red line, the light sea mass is again shifted slightly, but now $m_l = m_x + \hat{m} - m_u$, so that it takes its proper mass when $m_x = m_u$. The bursts show the final results, and come from setting $m_x = m_u$ for ϕ_{B^+} and $m_x = \hat{m}$ for ϕ_{B_s} . As before, the smaller, bright red, error bars, show purely statistical errors, and the larger, dark red, error bars come from the fit with Bayesian priors and include heavy-quark and generic light-quark discretization errors as well as statistical errors.

In Fig. 6, the $a \approx 0.15$ fm data are both noisy and far from those of the finer lattice spacings. Therefore, these ensembles are again dropped from the central fit. Figure 7 shows the effect of including the $a \approx 0.15$ fm points. Note that the resulting continuum-extrapolated line for ϕ_{B_s} (dotted red line) now has what appears to be a rather unphysical shape, showing a significant initial increase as the light sea-quark mass is decreased, starting at the right side of the graph. Hence, the differences caused by including the $a \approx 0.15$ fm points is 10 to 20% larger than the dark red error bars in Fig. 6, and 40 to 60% larger than discretization errors estimated by removing the statistical errors from the dark red bars. Because the trend for $a \approx 0.15$ fm is so different from the other spacings, and because of the unphysical behavior when these points are included in the fit, we believe this difference

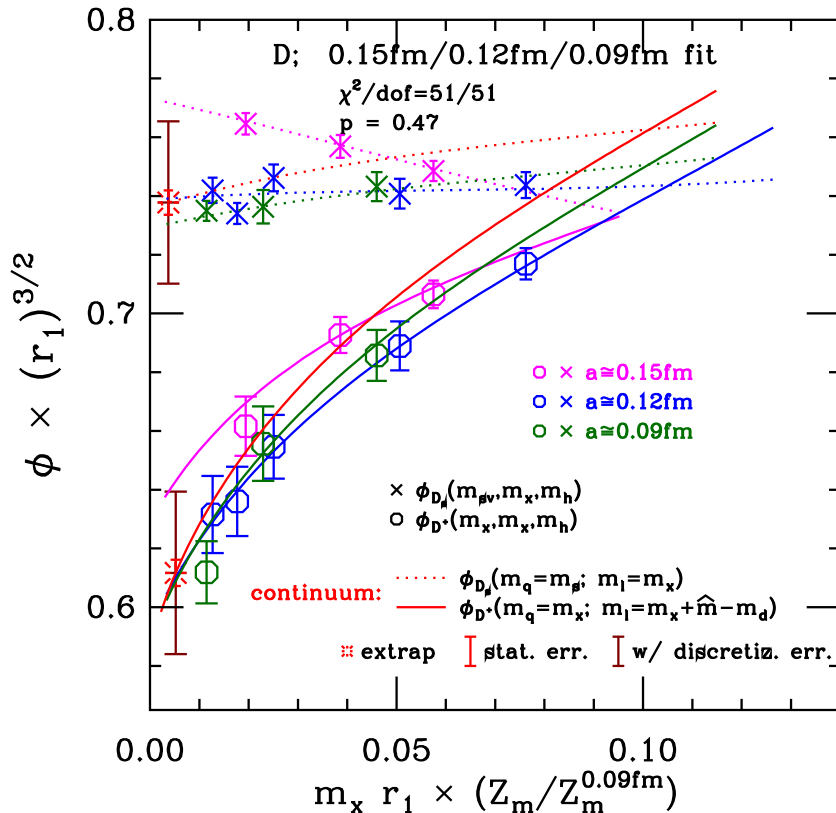


FIG. 4. Same as Fig. 3, but including points at $a \approx 0.15$ fm in the chiral-continuum fit.

overestimates the true discretization error, and we do not enlarge the errors coming from the fit.

Figure 8 shows the effect of using Analysis II of the correlation functions. In order to make these comparisons as direct as possible, we first turn off all the Bayesian discretization terms in the fits. Compared to the results from Fig. 6, this fit gives a value of f_{B_s} about 1 MeV higher and a value of f_{B^+} about 2 MeV lower. These differences are included in our estimate of the fitting errors due to excited state contamination in Sec. VII.

VII. ESTIMATION OF SYSTEMATIC ERRORS

In this section, we present a careful, quantitative accounting for the uncertainties in our calculation. We consider in turn discretization errors, fitting errors, errors from inputs r_1 and quark-mass tuning, renormalization, and finite-volume effects. Table XIII details our error budget.

A. Heavy-quark and generic light-quark discretization effects

As described in Sec. VI and Appendix A, we parameterize possible heavy-quark and generic light-quark discretization effects and follow a Bayesian approach in including such effects in our chiral fitting function. Consequently, the raw “statistical” error that comes from our fits is not a pure statistical error but includes an estimate of the errors coming

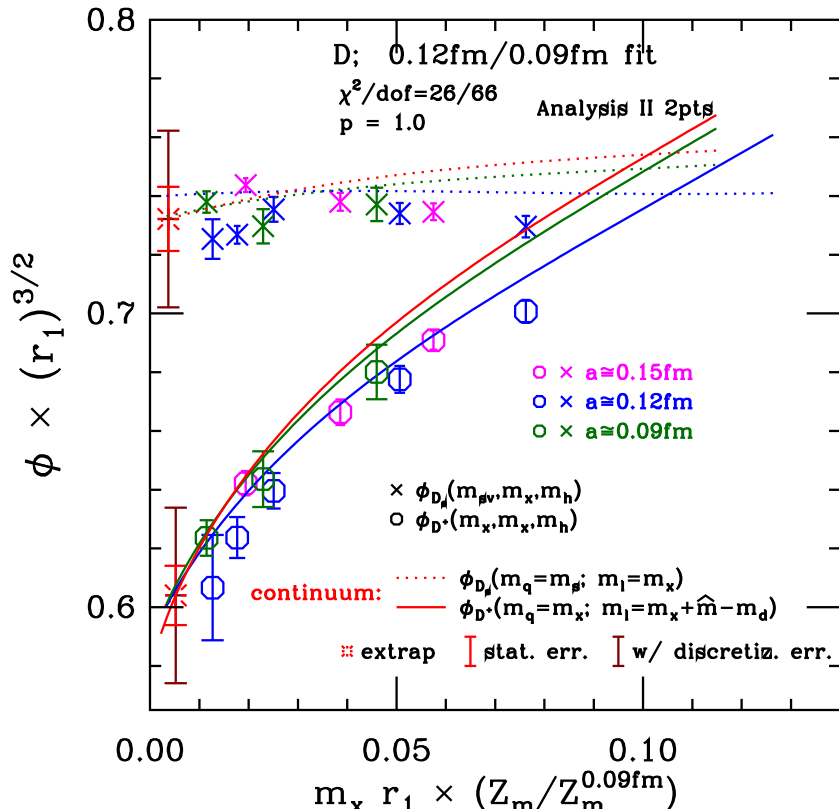


FIG. 5. Same as Fig. 3, but using Analysis II of the 2-point function.

from the discretization effects. This inclusive error is shown with the dark red error bars in the plots in Sec. VI, and is listed in the first line of Table XIII.

For informational purposes, it is useful to break down this inclusive error into its component parts, at least approximately. We can see what errors to expect and, hence, target for improvement in future simulations. In particular, with our current actions, the light-quark and heavy-quark discretization errors should behave differently as a function of lattice spacing, with heavy-quark errors decreasing more slowly as a is reduced. To extract the pure statistical errors, we rerun the fits with all the Bayesian discretization terms set to zero. We then find the pure heavy-quark (or pure light-quark) discretization contributions, by turning back on the heavy-quark (light-quark) terms, and then subtracting in quadrature the pure statistical errors from the resulting raw errors. These individual errors are shown in Table XIII in parentheses. Note that the total error at the bottom of the table includes the error on the first line, not the sum of the three errors in parentheses, when these differ. Note also that the discretization errors are similar to what we would have obtained with less sophisticated power counting.

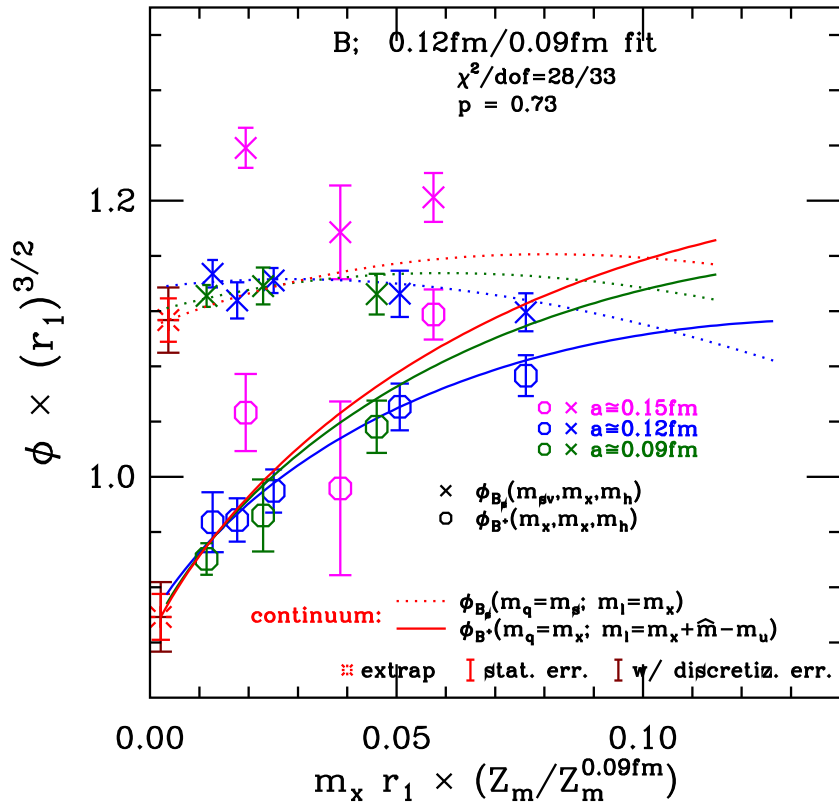


FIG. 6. Central chiral fit for the B system, with data from Analysis I of the 2-point functions. Only (approximately) unitary points are shown. Data from ensembles at $a \approx 0.15$ fm, $a \approx 0.12$ fm, and $a \approx 0.09$ fm are shown, but the $a \approx 0.15$ fm ensembles are not included in the fit. The bursts show extrapolated values for ϕ_{B_s} and ϕ_{B^+} , with the purely statistical errors in bright red and the statistical plus discretization errors in darker red. The physical strange-quark mass corresponds to an abscissa value of $m_x \approx 0.1$.

B. Chiral extrapolation and taste-violating light-quark discretization effects

As described in Sec. VI, we modify the chiral fit function in a variety of ways to estimate the error associated with the chiral extrapolation:

- $\chi 1$. Set the chiral coupling f to f_K instead of f_π .
- $\chi 2$. Allow the chiral coupling f to be a Bayesian fit parameter, with prior value f_π and prior width equal to $f_K - f_\pi$.
- $\chi 3$. Replace the H - H^* - π coupling g_π (which is 0.51 in the central fit) with 0.31 or 0.71, which are the extremes of the range discussed in Sec. VI.
- $\chi 4$. Allow g_π to be a constrained fit parameter, with prior value 0.51 and prior width 0.20.
- $\chi 5$. Fix to zero those NNLO analytic terms [Q_2 and/or Q_4 in Eq. (6.15)] that may be eliminated without making the fit unacceptably poor.
- $\chi 6$. Use the chiral function without hyperfine and flavor splittings, *i.e.*, use Eq. (6.2) instead of Eq. (6.20).
- $\chi 7$. Use combinations of modifications $\chi 1$ and $\chi 3$ or modifications $\chi 2$ and $\chi 3$. These choices can produce significantly larger deviations since changes in g_π have a similar effect on the fit function as changes in f .

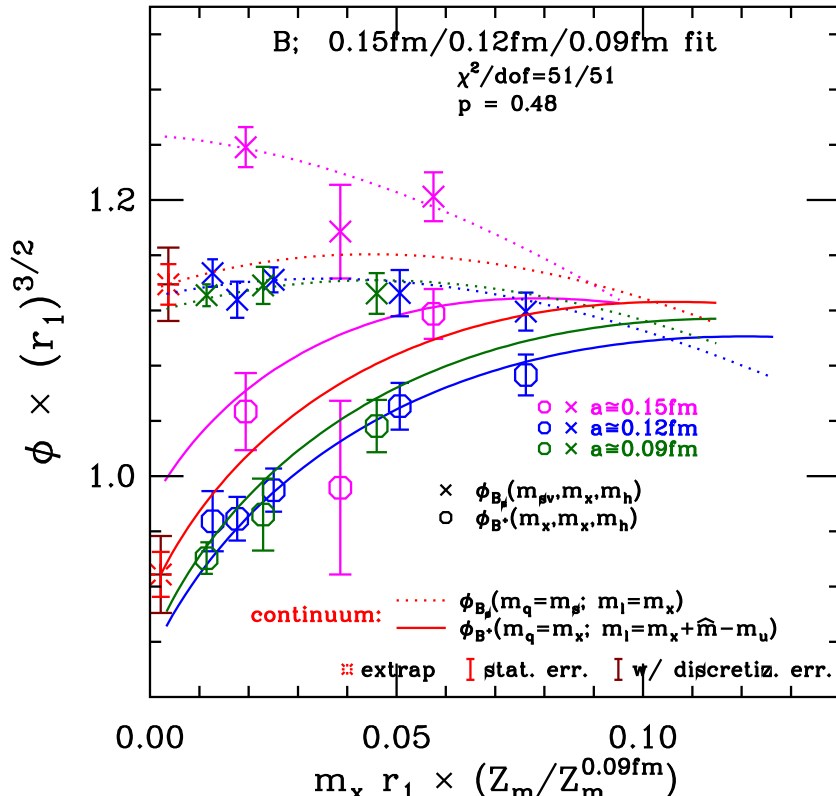


FIG. 7. Same as Fig. 6, but including points at $a \approx 0.15$ fm in the fit.

These modifications typically change the decay constant by 1–3 MeV, and the ratios by 1–1.5%. We take the chiral extrapolation error of a given quantity to be the largest change (of either sign) under the above modifications, and list it in Table XIII. In several cases, (f_{D^+} , f_{D_s}/f_{D^+} , and f_{B_s}/f_{B^+}) the largest change comes from modification $\chi 6$, eliminating the heavy-light splittings. The fit without the splittings is shown for the D system in Fig. 9. It may be compared to Fig. 3 to see the effects: the curvature at small mass for ϕ_{D^+} is slightly greater without the splittings, which results in a decrease of f_{D^+} of 3.2 MeV. Note that the p values of the two fits are almost identical, so the goodness-of-fit cannot be used to choose one version of the chiral extrapolation over the other.

Modifications of f and/or g_π produce the largest changes in the other quantities, namely f_{D_s} , f_{B^+} and f_{B_s} . In particular, putting $f = f_K$ and $g_\pi = 0.31$ results in an increase of +2.9 for f_{B^+} and +2.8 MeV for f_{B_s} . The modified fit is shown in Fig. 10, and may be compared with Fig. 6 to see the effects of the changes. Increasing f and decreasing g_π both suppress the chiral logarithms [cf. Eq. (6.20)] and give fit functions with less curvature and smaller slope at low quark mass.

Since the rS χ PT fit functions in Eqs. (6.2) and (6.20) explicitly include one-loop discretization effects coming from taste violations in the (rooted) staggered light quark action, the chiral error estimates we describe here inherently include taste-violating discretization errors. However, it seems unlikely that the current data can accurately distinguish between such taste-violating errors of order $\alpha_s^2 a^2$ and generic light-quark discretization effects of order $\alpha_s a^2$, or even heavy-quark discretization effects. Indeed, the taste-violating LEC L_a [cf. Eq. (6.12)] is not well constrained by our fits and is consistent with zero within large errors.

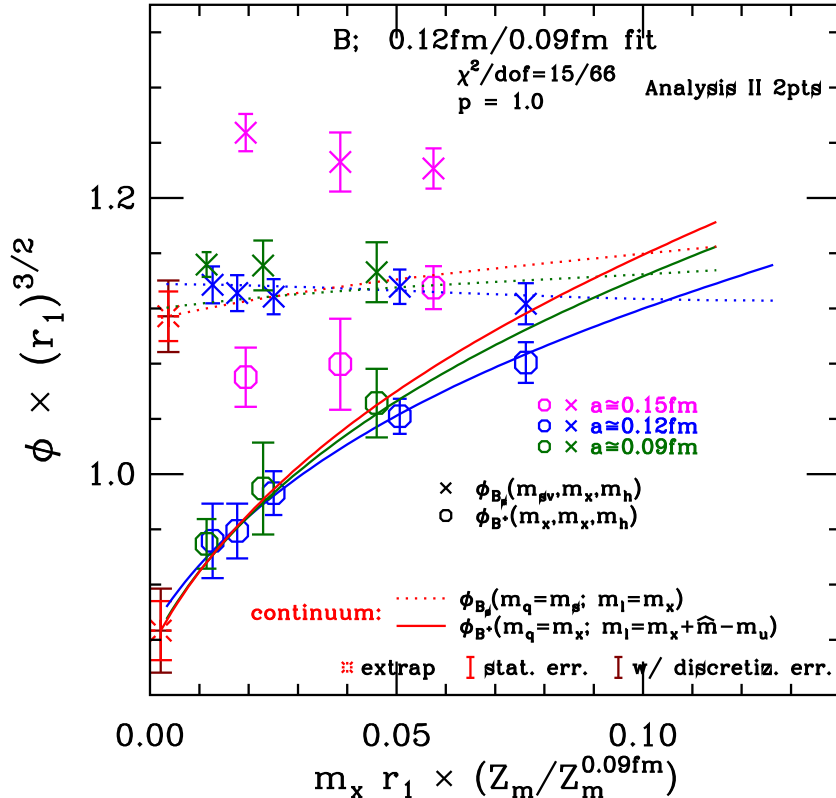


FIG. 8. Same as Fig. 6, but using Analysis II of the 2-point functions.

TABLE XIII. Total error budget for the heavy-light decay constants. Uncertainties are in MeV for decay constants. The total combines errors in quadrature. The first row includes statistics, heavy-quark discretization errors, and generic light-quark discretization errors, as explained in the text. Errors in parentheses are approximate sub-parts of errors that are computed in combination.

Source	f_{D^+} (MeV)	f_{D_s} (MeV)	f_{D_s}/f_{D^+}	f_{B^+} (MeV)	f_{B_s} (MeV)	f_{B_s}/f_{B^+}
Statistics \oplus discretization	9.2 (statistics) (heavy-quark disc.) (light-quark disc.)	8.9 (2.3) (8.2) (2.9)	0.014 (0.005) (0.007) (0.012)	5.5 (3.6) (3.7) (2.5)	5.1 (3.4) (3.8) (2.1)	0.013 (0.010) (0.004) (0.007)
Chiral extrapolation	3.2	2.2	0.014	2.9	2.8	0.014
Two-point functions	3.3	1.6	0.013	3.0	4.1	0.015
Scale (r_1)	1.0	1.0	0.001	1.0	1.4	0.001
Light quark masses	0.3	1.4	0.005	0.1	1.3	0.006
Heavy quark tuning	2.8	2.8	0.003	3.9	3.9	0.005
u_0 adjustment	1.8	2.0	0.001	2.5	2.8	0.001
Finite volume	0.6	0.0	0.003	0.5	0.1	0.003
$Z_{V_{QQ}^4}$ and $Z_{V_{q\bar{q}}^4}$	2.8	3.4	0.000	2.6	3.1	0.000
Higher-order $\rho_{A_4}^{Qq}$	1.5	1.8	0.001	1.4	1.7	0.001
Total Error	11.3	10.8	0.025	8.9	9.5	0.026

The central fits give

$$L_a = +0.6 \pm 6.5 \quad (\text{D system}), \quad (7.1)$$

$$L_a = -1.9 \pm 8.8 \quad (\text{B system}), \quad (7.2)$$

where the error is the raw statistical error. (Note that we do not constrain L_a by any prior width.) The errors in L_a decrease by about 10% if Bayesian parameters for generic light-quark errors are removed, and an additional 10% if the parameters for heavy-quark errors are removed. Thus, there is “cross talk” between various error sources, making it difficult to completely distinguish the various types of discretization errors. Future work, with more and finer lattice spacings, should make a cleaner separation possible.

C. Fitting errors

The “fitting errors” are the errors introduced in the analysis of the two-point correlators. They represent the effects of various choices of fit ranges and fitting functions, and are an estimate of the systematic effect of the contamination by excited states. We compare results from the three choices of two-point fitting (see Sec. IV): Analysis I, Analysis II, and a modified Analysis I using 1 simple + 1 oscillating state, but values of t_{min} larger than those described in Sec. IVB.

Some of these differences may, in fact, be due simply to statistical effects, and hence already included in the statistical error. Figure 11 shows the differences between values of ϕ_{B_q} in Analyses I and II, divided by the average statistical error for each of the common partially quenched data points. Only 10 of 74 differences are greater than 1 statistical σ .

Nevertheless, there appears to be some significant systematic trend in that 46 of 74 points are positive. To be conservative, we take the largest difference between the Analysis-I fits and the other two fits as the fitting error for each physical quantity, and list it in Table XIII. For f_{D_s} and f_{B_s} , the difference is largest for chiral fits based on 2-point Analysis II, while, for the other four quantities, the difference is largest for the modified Analysis I.

D. Scale uncertainty

We use the scale $r_1 = 0.3117(22)$ fm to tune the values of the quark masses and convert the decay constants into physical units (see Sec. III A). To find the scale errors on the final results, we shift r_1 to 0.3139 fm or 0.3095 fm and redo the analysis. Although ϕ_H scales like $r_1^{-3/2}$, the change in the results under a change in r_1 is smaller than pure dimensional analysis would imply, because our estimates of the physical light masses and the heavy-quark κ_c and κ_b also shift, producing partially compensating changes in ϕ_H . At $r_1 = 0.3139$ fm, we shift the light masses in Table XII upward by the scale error shown in that table. [The lattice light-quark masses scale like r_1^2 , because they are approximately linear in the squared meson masses $(r_1 m_\pi)^2$ and $(r_1 m_K)^2$.] Similarly, we shift the tuned κ_c and κ_b downward by the scale error in Table V because the bare heavy quark mass increases with r_1 . We then adjust $\phi_{B(s)}$ and $\phi_{D(s)}$ at each lattice spacing using Eq. (3.5) and the values of $d\phi/d\kappa$ given in Table V. Redoing the preferred chiral fits shown in Figs. 3 and 6, extrapolating to the

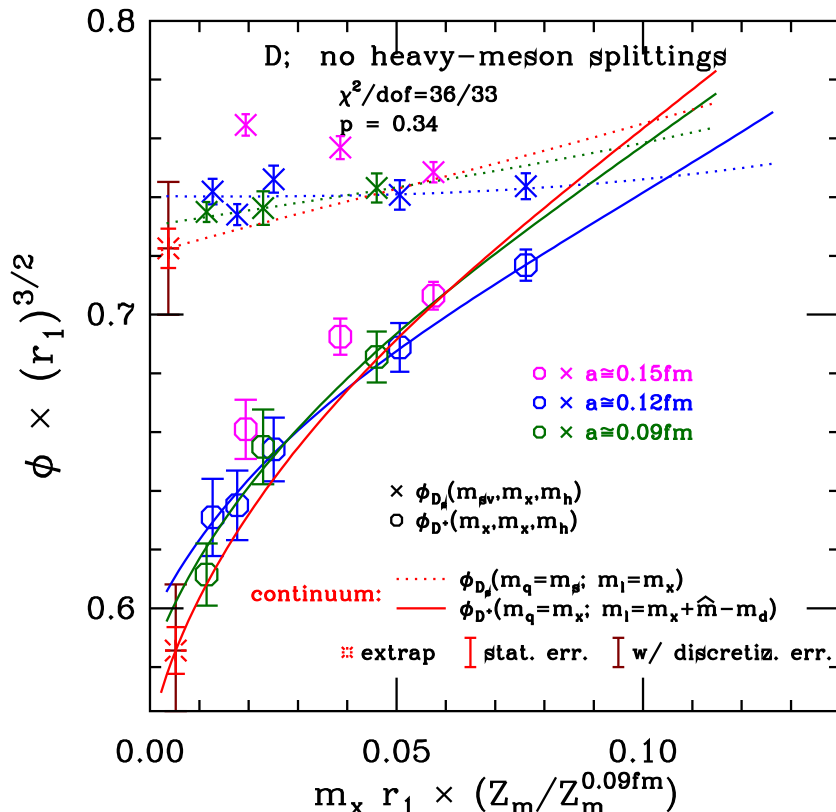


FIG. 9. Same as Fig. 3 but omitting heavy-light hyperfine and flavor splittings in the chiral fit function.

continuum, and plugging in the adjusted continuum light quark masses gives the scale error listed in Table XIII.

E. Light-quark mass determinations

To estimate the error from the light-quark mass determination, we follow a similar procedure to that in the scale-error case. We shift the continuum light quark masses in Table XII by the sum in quadrature of all errors except scale errors. This includes the statistical errors, the chiral errors and, where relevant, the electromagnetic errors. We then plug the new masses into the continuum-extrapolated chiral fits and take the difference from the central results to give the errors listed in Table XIII. The relative direction of shifts on different masses makes little difference in the size of the errors on the decay constants f_{D_s} , f_{D^+} , f_{B_s} , and f_{B^+} , since they are sensitive primarily to the valence quark masses. However, it does affect the error of the ratios f_{D_s}/f_{D^+} and f_{B_s}/f_{B^+} . The largest effect clearly occurs when the strange mass is shifted in the opposite direction from the lighter masses. To be conservative, we take the size of change of the ratios in this case as the error, but this is almost certainly an overestimate because the statistical and chiral extrapolation errors on the light quark masses are positively correlated between the strange mass and the other masses.

Note that the errors from the light-quark masses in Table XIII are much larger for f_{D_s} and f_{B_s} than for f_{D^+} and f_{B^+} . That simply reflects the facts that the decay constants have a nonzero limit when the quark masses vanish, and that the dependence on the quark masses is reasonably linear. Thus a given percent error in the strange mass produces a much larger

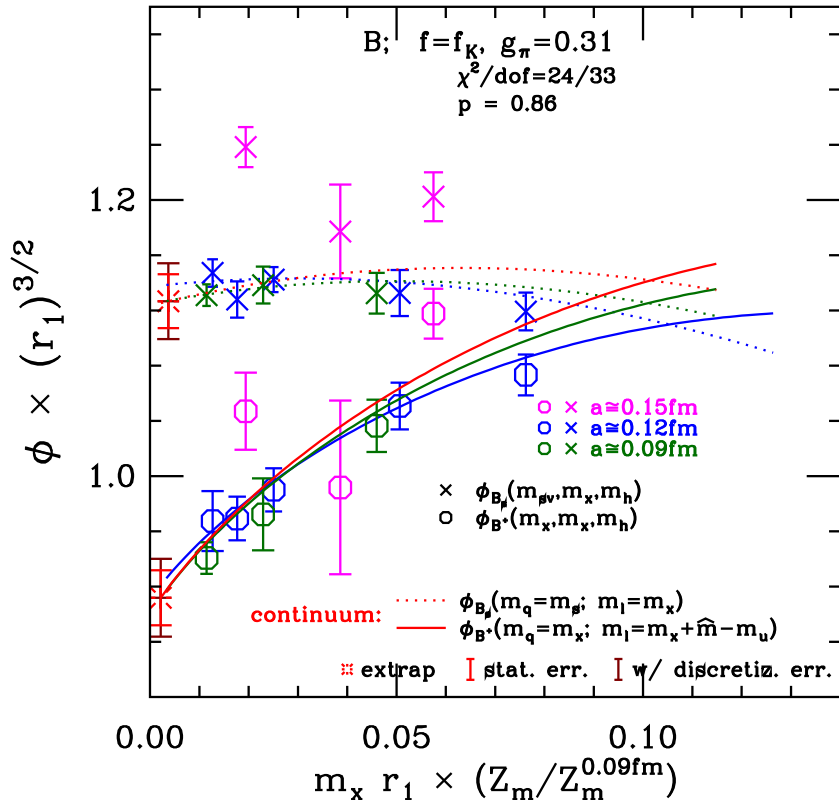


FIG. 10. Same as Fig. 6 but with $f = f_K$ and $g_\pi = 0.31$ in the chiral fit function.

percent difference in f_{D_s} and f_{B_s} , than the same percent error in the d or u mass does in f_{D^+} and f_{B^+} .

F. Bottom and charm quark mass determinations

The propagation of statistical errors in the tuned κ_c and κ_b to the decay constants is complicated by the fact that the independent errors at each lattice spacing affect the final results in a nontrivial way through the continuum and chiral extrapolations. At each lattice spacing, we choose 200 gaussian-distributed ensembles of trial κ values with central value equal to the tuned values, and standard deviation equal to the statistical error, taken from Table V. For a given choice of trial κ values at each lattice spacing, we produce an adjusted trial data sample by shifting the ϕ_H values according to Eq. (3.5), but with the trial values replacing the tuned values. We then perform the complete chiral fit and extrapolation

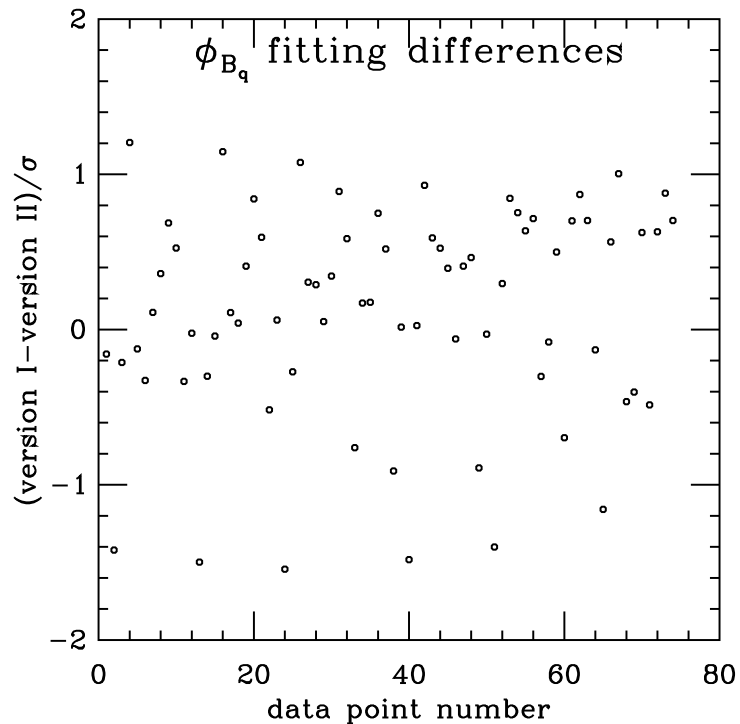


FIG. 11. Difference of ϕ_{B_q} values from Analyses I and II, divided by the average statistical error at each of the common valence and sea mass points. The order along the abscissa is arbitrary.

procedure on each of the 200 trial data sets. The standard deviation over trials of a given decay constant or decay constant ratio is taken to be the heavy quark tuning error, and is listed in Table XIII.

G. Tadpole factor (u_0) adjustment

In order to improve the convergence of lattice perturbation theory, we use tadpole-improved actions for the gluons, light quarks, and heavy quarks [76]. For the gluon and sea-quark actions we take the tadpole factor u_0 from the average plaquette. On the $a \approx 0.15$ fm and $a \approx 0.09$ fm lattices we use the same choice for the light valence and heavy-quark actions. On the $a \approx 0.12$ fm lattices, however, we use the tadpole factor u_0 taken from the Landau link in the valence-quark action and in the clover term in the heavy-quark action. This results in a slight mismatch between the light valence and sea-quark actions on these ensembles, and also affects the values obtained for the tuned bottom- and charm-quark masses κ_b and κ_c . The difference between u_0 obtained from the average plaquette and the Landau link is approximately 3–4% on the $a \approx 0.12$ fm ensembles.

We propagate this difference through the chiral/continuum extrapolation as follows. First, we compute the heavy-strange meson decay amplitudes ϕ_{B_s} and ϕ_{D_s} with both choices for u_0 on the ensemble with $am_l/am_h = 0.01/0.05$, $a \approx 0.12$ fm. For each choice of u_0 , we compute ϕ_{B_s} and ϕ_{D_s} directly at the tuned values of κ_b and κ_c , thereby avoiding an interpolation in κ . Next, we renormalize the lattice decay amplitudes using the nonperturbative, flavor-diagonal current renormalization factors $Z_{V_{qq}^4}$ and $Z_{V_{QQ}^4}$ obtained for each case. (We neglect the slight difference in the perturbative correction $\rho_{A_{Qq}^4}$.) Then, we calculate the ratio of the renormalized decay amplitudes, finding no difference within errors:

$$\phi_c^{\text{plaquette}}/\phi_c^{\text{Landau}} = 1.005(13), \quad (7.3)$$

$$\phi_b^{\text{plaquette}}/\phi_b^{\text{Landau}} = 1.014(20). \quad (7.4)$$

As expected, the u_0 dependence from the bare current and renormalization factors mostly cancels. Finally, we repeat the chiral/continuum extrapolation shifting ϕ_c and ϕ_b on the $a \approx 0.12$ fm ensembles by the statistical errors reported in Eqs. (7.3)–(7.4). We find that these percent-level errors in ϕ_c and ϕ_b lead to approximately 1% errors in the extrapolated decay constants and approximately 0.1% errors in the decay-constant ratios. These errors are listed as “ u_0 adjustment” in the error budget in Table XIII.

H. Heavy-light current renormalization

There are two sources of systematic error in our heavy-light current renormalization. The first is due to the perturbative calculation of $\rho_{A_{Qq}^4}$ and the second is due to the nonperturbative calculation of $Z_{V_{QQ}^4}$ and $Z_{V_{qq}^4}$.

The perturbative calculation of $\rho_{A_{Qq}^4}$ has been carried out to one-loop order. Since $\rho_{A_{Qq}^4}$ is defined from a ratio of renormalization factors [see Eq. (2.5)], its perturbative corrections are small by construction. Indeed, as can be seen from the results for $\rho_{A_{Qq}^4}$ given in Table VIII, we observe very small corrections. For bottom they range from 0.3% at $a \approx 0.09$ fm to 0.8% at $a \approx 0.12$ fm and 2.8% at $a \approx 0.15$ fm. For charm they range from less than 0.08% at $a \approx 0.09$ fm to 0.4% at $a \approx 0.12$ fm and 0.6% at $a \approx 0.15$ fm. As shown in Ref. [43] the

perturbative corrections to the ρ -factors for the spatial currents, while still small, tend to be bigger than those for the temporal currents A^4 and V^4 . We therefore estimate the error due to neglecting higher order terms as $\rho_{V_{Qq}^1}^{[1]} \alpha_s^2$. We take α_s at $a \approx 0.09$ fm and $\rho_{V_{Qq}^1}^{[1]} \approx 0.1$, which is the largest one-loop coefficient for $\rho_{V_{Qq}^1}$ in the mass range $m_Q a \leq 3$. This procedure yields a systematic error of 0.7%, which we take for both charm and bottom decay constants.

The decay constant ratios f_{B_s}/f_{B^+} and f_{D_s}/f_{D^+} depend on the corresponding ratios of $\rho_{A_{Qs}^4}/\rho_{A_{Qq}^4}$. These ratios differ from unity only because of the small variation of the $\rho_{A_{Qq}^4}$ with light valence mass, which is described in Sec. V. We take the variation of the $\rho_{A_{Qq}^4}$ with light valence mass at $a \approx 0.09$ fm as the error. This yields an error of 0.1% for both bottom and charm.

The dominant corrections in the heavy-light renormalization factor as defined in Eq. (2.5) are due to $Z_{V_{QQ}^4}$ and $Z_{V_{qq}^4}$ which are calculated nonperturbatively. The values (and errors) for $Z_{V_{qq}^4}$ and $Z_{V_{QQ}^4}$ are listed in Tables IX and XI, respectively. To obtain the error in $Z_{V_{Qq}^4} = \sqrt{Z_{V_{qq}^4} Z_{V_{QQ}^4}}$ we add the statistical errors in $Z_{V_{qq}^4}$ and $Z_{V_{QQ}^4}$ in quadrature. The error on $Z_{V_{Qq}^4}$ is dominated by the error on $Z_{V_{qq}^4}$. The errors are largest, 1.3%, on the $a \approx 0.09$ fm ensemble and they are about the same for both charm and bottom on the two finest ensembles used to obtain our main decay constant results. Hence we use 1.3% as our estimate for the uncertainty in $Z_{V_{Qq}^4}$.

I. Finite volume effects

To study finite volume effects, we use the chiral fit function with heavy-light hyperfine and flavor splittings included (Eq. (6.20)), since the effects are known to be larger with the splittings than without [79]. The central fit includes the (one-loop) finite volume corrections, Eq. (6.21), on the lattice data, and then takes the infinite volume limit when extracting the final results for the decay constants. We then take the larger of the following two values as our estimate of the finite volume error:

- V1. The difference between the central result and the result from a chiral fit in which the finite volume corrections are omitted.
- V2. The largest finite volume correction to the relevant data points, as determined by the central fit. For ϕ_{D^+} and ϕ_{B^+} , the “relevant data points” are the ones on each ensemble with the lightest valence mass, *i.e.*, those closest to the chirally extrapolated point. For ϕ_{D_s} and ϕ_{B_s} , the relevant points are the ones on each ensemble with valence mass closest to m_s .

Method V1 gives a larger difference for ϕ_{D_s} and ϕ_{B_s} ; method V2 for ϕ_{D^+} and ϕ_{B^+} and the ratios. The resulting values are shown in Table XIII. Note that our choices are conservative because we correct for the (one-loop) finite volume errors, but nevertheless take the full size of these effects as our error.

VIII. RESULTS AND CONCLUSIONS

After adding the error estimates described in the previous section in quadrature, we obtain:

$$f_{B^+} = 196.9(8.9) \text{ MeV}, \quad (8.1)$$

$$f_{B_s} = 242.0(9.5) \text{ MeV}, \quad (8.2)$$

$$f_{B_s}/f_{B^+} = 1.229(0.026), \quad (8.3)$$

$$f_{D^+} = 218.9(11.3) \text{ MeV}, \quad (8.4)$$

$$f_{D_s} = 260.1(10.8) \text{ MeV}, \quad (8.5)$$

$$f_{D_s}/f_{D^+} = 1.188(0.025). \quad (8.6)$$

Since our most reliable method of determining discretization errors combines them with statistical errors, we do not quote separate statistical and systematic errors.

Figure 12 shows a comparison of our results for charmed decay constants with other lattice QCD calculations and with experiment. Our results agree with the only other three-flavor lattice QCD determination from the HPQCD collaboration [95], which is obtained with HISQ staggered valence quarks and asqtad staggered sea quarks. (The difference in f_{D_s} is a bit greater than 1σ .) They are also consistent with the two-flavor results of the ETM Collaboration using twisted-mass Wilson fermions [96], although the ETM error budget does not include an estimate of the uncertainty due to quenching the strange quark. One can also compare with “experimental” determinations of f_D and f_{D_s} if one assumes CKM unitarity to obtain the matrix elements $|V_{cd}|$ and $|V_{cs}|$. For the D meson, Rosner and Stone combine CLEO’s measurement of branching fraction $\mathcal{B}(D^+ \rightarrow \mu^+\nu)$ [97] with the latest determination of $|V_{cd}|$ from the PDG [51] to obtain $f_D = 206.7(8.9) \text{ MeV}$ [50]. For the D_s meson, they average CLEO and Belle results for $\mathcal{B}(D_s^+ \rightarrow \mu^+\nu)$ [98, 99] with CLEO and BABAR results for $\mathcal{B}(D_s^+ \rightarrow \tau^+\nu)$ [98, 100–102] to obtain a combined average for the two decay channels of $f_{D_s} = 257.5(6.1) \text{ MeV}$ [50]. The Heavy Flavor Averaging Group obtains a similar average, $f_{D_s} = 257.3(5.3) \text{ MeV}$ [103]. Our results are consistent with these values, confirming Standard Model expectations at the $\sim 5\%$ level.

Figure 13 shows a similar comparison of our results for bottom meson decay constants with other lattice QCD calculations. Our results agree with the published three-flavor determination using NRQCD b -quarks and Asqtad staggered light quarks of the HPQCD collaboration [105], but are only marginally consistent with HPQCD’s more recent calculation of f_{B_s} using HISQ light valence quarks [104]. Our results are also consistent with the two-flavor results of the ETM collaboration [96], who use Wilson heavy quarks and interpolate between the charm-mass region and the static limit to obtain results for bottom. Further, our result for the ratio f_{B_s}/f_B also agrees with the significantly less precise three-flavor determination using static b -quarks and domain-wall light quarks by the RBC and UKQCD Collaborations [106].

For the D system the largest uncertainties in our current calculation stem from heavy-quark discretization, while the chiral extrapolation, the Z_V factors, excited states, heavy-quark tuning, and the chiral-continuum extrapolation play important but subdominant roles. For the B system, heavy-quark tuning, statistics, and excited states are the sources of the largest errors, while the Z_V factors and the chiral-continuum extrapolation (incorporating our estimate of heavy-quark discretization effects) are next in size. Recall that a novel feature of our work is the treatment of heavy-quark discretization effects, via the functions

f_i in Eq. (2.4), and priors constraining the chiral-continuum fits to follow this form. At tree level, we have explicit calculations of the mismatch, some of which appeared already in Ref. [33] and all of which are compiled in Ref. [60]. Beyond the tree level, the continuum and static limits can be used to constrain the functional form. That said, the theoretical guidance of the priors cannot be highly effective in an analysis, such as this, with only two lattice spacings. Indeed, the quoted heavy-quark discretization errors are similar to less sophisticated power-counting estimates.

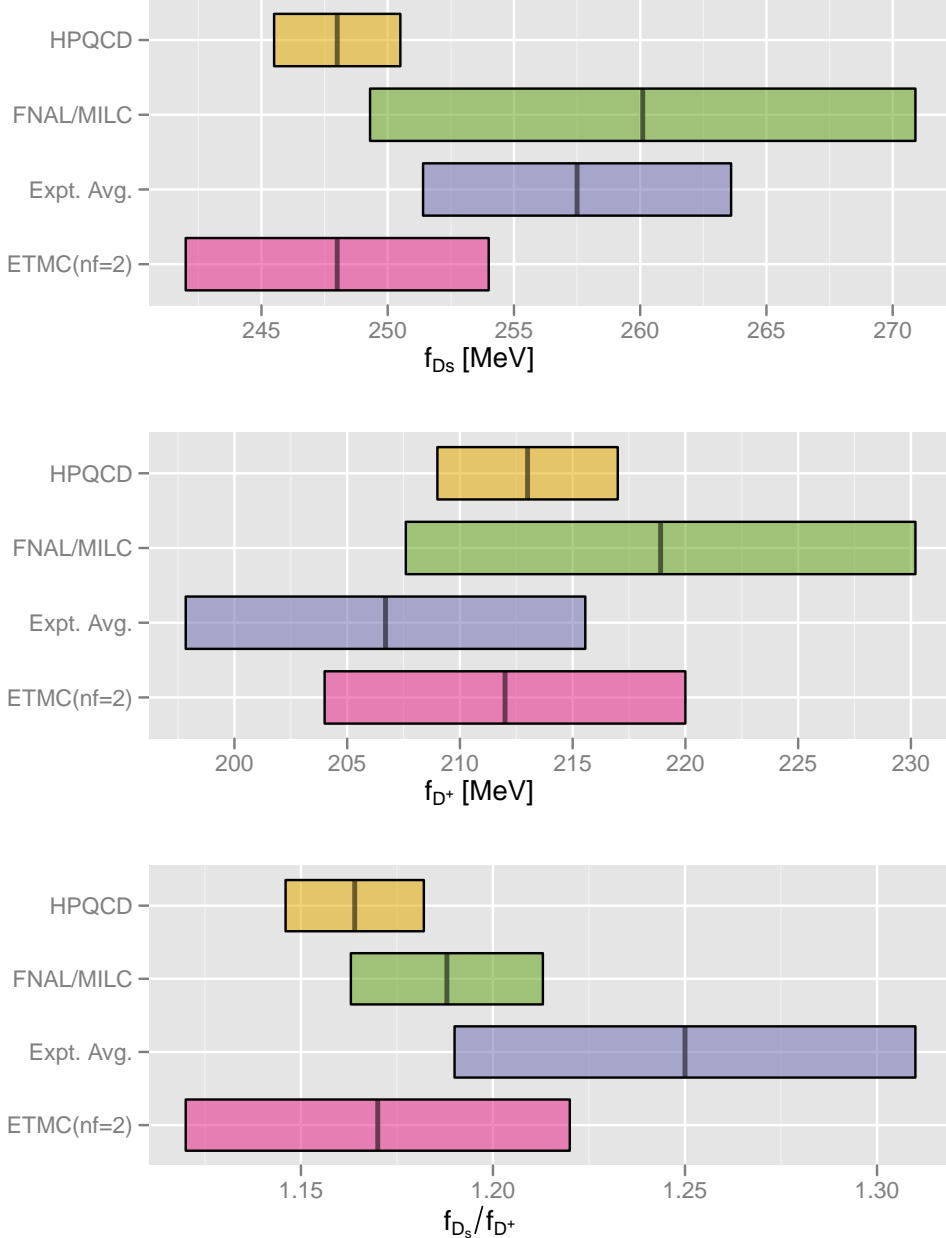


FIG. 12. Comparison of f_D and f_{D_s} with other two- and three-flavor lattice QCD calculations and with experiment. Results shown come from Refs. [50, 95–102]. The HPQCD f_D value is computed from their update to f_{D_s} and their earlier result for the ratio f_{D_s}/f_D .

While completing this analysis, we have begun runs to generate data that will address the main sources of uncertainty reported here. The new data set will contain four times the configurations used here to reduce the statistical errors in the correlation functions and, thus, directly improve the decay amplitudes, the determinations of the hopping-parameters

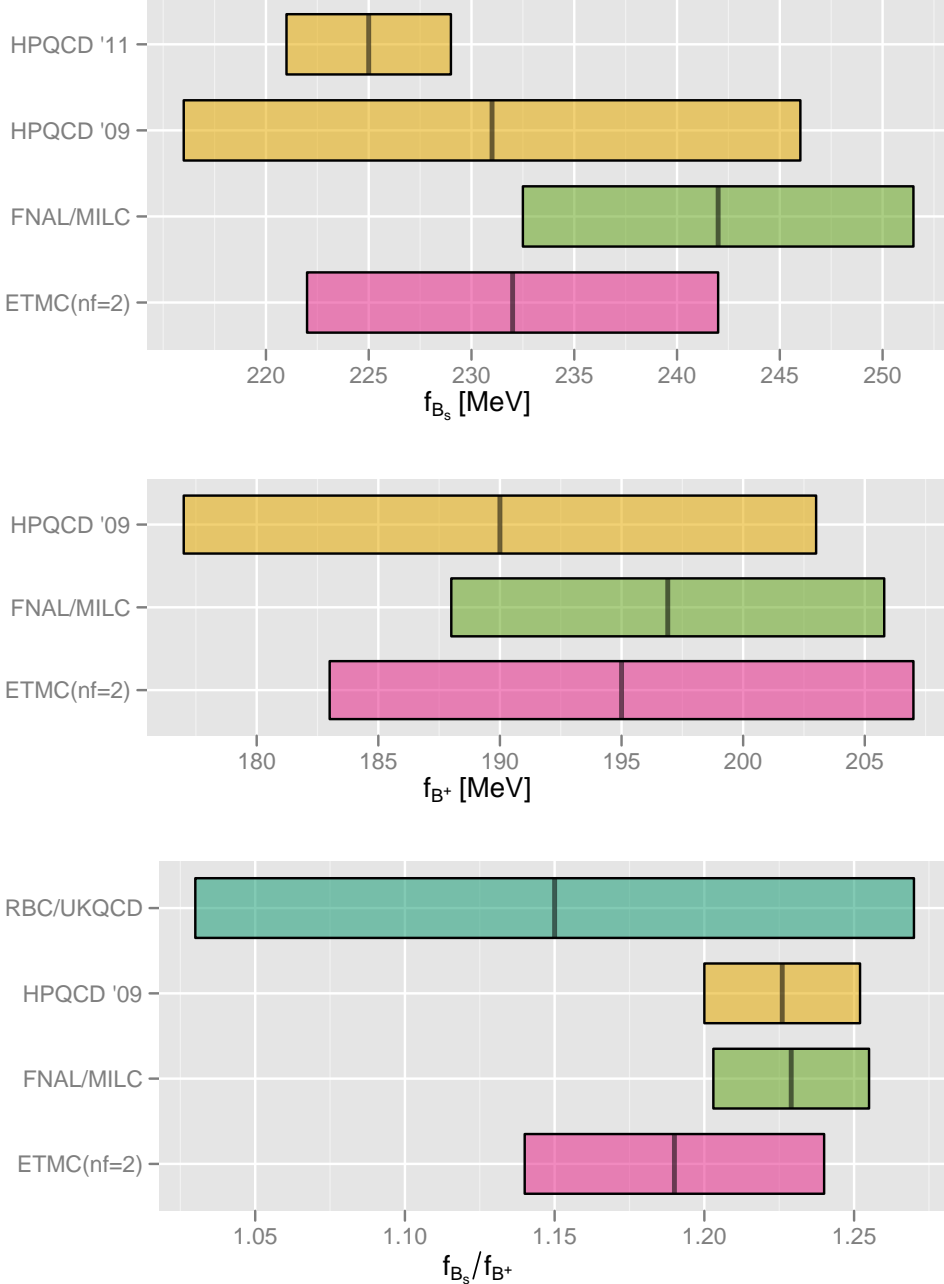


FIG. 13. Comparison of f_B and f_{B_s} with other two- and three-flavor lattice QCD calculations. Results shown come from Refs. [96, 104–106]. In the case of f_{B_s} , HPQCD has two separate calculations using NRQCD b quarks and using HISQ b quarks; we show both the published NRQCD result (HPQCD '09) and the more recent HISQ result (HPQCD '11) in the plot above.

κ_c and κ_b , and the renormalization factors $Z_{V_{qq}^4}$ and $Z_{V_{QQ}^4}$, all of which feed into the decay constant. Our new data will also encompass two finer lattice spacings of $a \approx 0.06$ fm and $a \approx 0.045$ fm, in order to explicitly reduce light- and heavy-quark discretization errors and better control the continuum extrapolation. With four lattice spacings, our new method of heavy-quark discretization priors will be put to a more stringent test. The new runs will also include light valence- and sea-quark masses down to $\sim m_s/20$ in order to better control the chiral extrapolation to the physical d and u quark masses.

In order to reduce errors further, we will have to eliminate the errors from the matching factors and from quenching the charmed quark. The MILC Collaboration [107] is generating ensembles with 2+1+1 flavors of sea quarks with the HISQ action, with plans to provide a range of lattice spacings and sea quark masses equal to or more extensive than the 2+1 asqtad ensembles. Use of the HISQ action for the charm valence quark will allow us to further reduce many of the uncertainties, and provides the particularly nice advantage that one can use the local pseudoscalar density without multiplicative renormalization to obtain the continuum matrix element [108]. In several years, once the full suite of HISQ ensembles with several sea-quark masses and lattice spacings has been analyzed, we expect to obtain percent-level errors for both B - and D -meson decay constants. This will enable precise tests of the Standard Model and may help to reveal the presence of new physics in the quark-flavor sector.

ACKNOWLEDGMENTS

We thank David Lin for his finite-volume chiral-log *Mathematica* code, upon which our own code is based. Computations for this work were carried out with resources provided by the USQCD Collaboration, the Argonne Leadership Computing Facility, the National Energy Research Scientific Computing Center, and the Los Alamos National Laboratory, which are funded by the Office of Science of the U.S. Department of Energy; and with resources provided by the National Institute for Computational Science, the Pittsburgh Supercomputer Center, the San Diego Supercomputer Center, and the Texas Advanced Computing Center, which are funded through the National Science Foundation’s Teragrid/XSEDE Program. This work was supported in part by the U.S. Department of Energy under Grants No. DE-FC02-06ER41446 (C.D., L.L., M.B.O.), No. DE-FG02-91ER40661 (S.G.), No. DE-FG02-91ER40677 (C.M.B., R.T.E., E.D.F., E.G., R.J., A.X.K.), No. DE-FG02-91ER40628 (C.B.), No. DE-FG02-04ER-41298 (D.T.); by the National Science Foundation under Grants No. PHY-0555243, No. PHY-0757333, No. PHY-0703296 (C.D., L.L., M.B.O.), No. PHY-0757035 (R.S.), No. PHY-0704171 (J.E.H.); by the URA Visiting Scholars’ program (C.M.B., R.T.E., E.G., M.B.O.); by the Fermilab Fellowship in Theoretical Physics (C.M.B.); by the M. Hildred Blewett Fellowship of the American Physical Society (E.D.F.); and by the Science and Technology Facilities Council and the Scottish Universities Physics Alliance (J.L.). This manuscript has been co-authored by employees of Brookhaven Science Associates, LLC, under Contract No. DE-AC02-98CH10886 with the U.S. Department of Energy. R.S.V. acknowledges support from BNL via the Goldhaber Distinguished Fellowship. Fermilab is operated by Fermi Research Alliance, LLC, under Contract No. DE-AC02-07CH11359 with the United States Department of Energy.

Appendix A: Heavy-quark Discretization Effects

We are using the heavy-quark Lagrangian as given in [33], with $\kappa_t = \kappa_s$ (or, equivalently, $\zeta = 1$), $r_s = 1$, and $c_B = c_E = c_{\text{SW}}$. This amounts to the Sheikholeslami-Wohlert Lagrangian [32] for Wilson fermions [59]. The current has a heavy quark of this type, rotated as in Eq. (4.2) (*cf.* Eqs. (7.8)–(7.10) of Ref. [33]), and a staggered light quark. At the tree level, the heavy-quark rotation is the same no matter what the other quark is. The discretization effects are estimated from a (continuum) effective field theory [36–38], as shown explicitly for decay constants in Eqs. (8.7)–(8.12) of Ref. [36].

1. Theory

Both QCD and lattice gauge theory can be described via

$$\mathcal{L}_{\text{QCD}} \doteq \mathcal{L}_{\text{HQET}} = \sum_i \mathcal{C}_i^{\text{cont}}(m_Q) \mathcal{O}_i, \quad (\text{A1})$$

$$\mathcal{L}_{\text{LGT}} \doteq \mathcal{L}_{\text{HQET}(m_0a)} = \sum_i \mathcal{C}_i^{\text{lat}}(m_Q, m_0a) \mathcal{O}_i, \quad (\text{A2})$$

where the \mathcal{C}_i are short-distance coefficients and the \mathcal{O}_i are operators describing the long-distance physics. The coefficients have dimension $4 - \dim \mathcal{O}_i$. For lattice gauge theory, they depend on m_0a , which is a ratio of short distances a and $1/m_Q$. The effective-theory operators \mathcal{O}_i in Eqs. (A1) and (A2) are the same.

The error from each term is simply the difference

$$\text{error}_i = |[\mathcal{C}_i^{\text{lat}}(m_Q, m_0a) - \mathcal{C}_i^{\text{cont}}(m_Q)] \mathcal{O}_i|. \quad (\text{A3})$$

The relative error in our matrix elements can be estimated by setting $\langle \mathcal{O}_i \rangle \sim \Lambda_{\text{QCD}}^{\dim \mathcal{O}_i - 4}$; choices for the QCD scale Λ_{QCD} are discussed below. The coefficient mismatch can be written

$$\mathcal{C}_i^{\text{lat}}(m_Q, m_0a) - \mathcal{C}_i^{\text{cont}}(m_Q) = a^{\dim \mathcal{O}_i - 4} f_i(m_0a). \quad (\text{A4})$$

This recovers the usual counting of powers of a (familiar from Symanzik [34, 35]), but maintaining the full m_0a dependence. The final expression for the discretization errors is then

$$\text{error}_i \propto f_i(m_0a) (a \Lambda_{\text{QCD}})^{\dim \mathcal{O}_i - 4}. \quad (\text{A5})$$

For Wilson fermions, $\lim_{m_0a \rightarrow 0} f_i = \text{constant}$ (whereas in lattice NRQCD without fine tuning this is not the case). We have explicit calculations of the f_i for the $O(a)$ and $O(a^2)$ errors at the tree level [33, 60]. The next subsection discusses how to use them to guide a continuum-limit extrapolation the $O(\alpha_s a)$ and $O(a^2)$ errors.

Equations (A1) and (A2) can be generalized to currents. For the axial-vector current,

$$\mathcal{A}^\mu \doteq C_{A_\perp}^{\text{cont}}(m_Q) \bar{q} i \gamma_\perp^\mu \gamma_5 h_v - C_{A_\parallel}^{\text{cont}}(m_Q) v^\mu \bar{q} \gamma_5 h_v - \sum_i B_{Ai}^{\text{cont}}(m_Q) \mathcal{Q}_{Ai}^\mu, \quad (\text{A6})$$

$$A_{\text{lat}}^\mu \doteq C_{A_\perp}^{\text{lat}}(m_Q, m_0a) \bar{q} i \gamma_\perp^\mu \gamma_5 h_v - C_{A_\parallel}^{\text{lat}}(m_Q, m_0a) v^\mu \bar{q} \gamma_5 h_v - \sum_i B_{Ai}^{\text{lat}}(m_Q, m_0a) \mathcal{Q}_{Ai}^\mu, \quad (\text{A7})$$

and \doteq again means in the sense of matrix elements. Here v^μ selects the temporal component and \perp the spatial, and the list of dimension-4 operators \mathcal{Q} can be found in Refs. [37].

The matrix element of the temporal component of the axial-vector current [*cf.* Eq. (4.7)] is normalized by multiplying with $Z_{A^4} = C_{A_\parallel}^{\text{cont}}/C_{A_\parallel}^{\text{lat}}$. The current mismatch then leads to errors

$$a^{\dim \mathcal{Q}_i - 3} f_i(m_0 a) = Z_{A^4} B_{A_i}^{\text{lat}} - B_{A_i}^{\text{cont}}, \quad (\text{A8})$$

with the sum running over the two operators \mathcal{Q} that point in the temporal direction [37].

2. Error Estimation

The total error from heavy-quark discretization effects is then

$$\text{error} = \sum_i z_i (a\Lambda_{\text{QCD}})^{s_i} f_i(m_0 a) \quad (\text{A9})$$

where the sum runs over Lagrangian operators \mathcal{O}_i of dimension 5 and 6 and current operators \mathcal{Q}_i of dimension 4 and 5, $s_i = \dim \mathcal{O}_i - 4$ or $\dim \mathcal{Q}_i - 3$, and the z_i are unknown coefficients. The functions f_i (summarized below) have been computed for $\mathcal{O}(a^2)$ and estimated for $\mathcal{O}(\alpha_s a)$. We omit contributions of order $\alpha_s^l a^2$, whether from extra operators or from iterating to second order operators with coefficients of order $\alpha_s a$.

In the past, we have taken a very conservative $\Lambda_{\text{QCD}} = 700$ MeV and assumed a Gaussian distribution for the z_i centered on 0 and of width 1. This amounts to treating the discretization errors as independent and adding them in quadrature. It also implicitly assumes that the data have nothing to say about the size or relative importance of the terms.

Here, however, we incorporate these errors into the chiral-continuum extrapolation, discussed in Sec. VI. This means that the z_i are now constrained fit parameters, with prior constraints discussed in Sec. VI.

The f_i are collected next.

a. $\mathcal{O}(a^2)$ errors

We start with these, because explicit expressions for the functions $f_i(m_0 a)$ are available. The Lagrangian leads to two bilinears, $\bar{h}\mathbf{D} \cdot \mathbf{E} h$ and $\bar{h}i\boldsymbol{\Sigma} \cdot [\mathbf{D} \times \mathbf{E}]h$, and many four-quark operators. At the tree level the coefficients of all four-quark operators vanish. At the tree level the coefficients of the two bilinears are the same, and the mismatch function is

$$f_E(m_0 a) = \frac{1}{8m_E^2 a^2} - \frac{1}{2(2m_2 a)^2}. \quad (\text{A10})$$

Using explicit expressions for $1/m_2$ [33] and $1/m_E^2$ [60], one finds

$$f_E(m_0 a) = \frac{1}{2} \left[\frac{c_E(1 + m_0 a) - 1}{m_0 a(2 + m_0 a)(1 + m_0 a)} - \frac{1}{4(1 + m_0 a)^2} \right]. \quad (\text{A11})$$

We are using $c_E = 1$, so

$$f_E(m_0 a) = \frac{2 + 3m_0 a}{8(2 + m_0 a)(1 + m_0 a)^2}. \quad (\text{A12})$$

With no further assumptions, this term enters twice independently, so we take the width of this prior to be $\sqrt{2}$ rather than 1.

The current leads to three more terms with non-zero coefficients, $\bar{q}\Gamma\mathbf{D}^2h$, $\bar{q}\Gamma i\boldsymbol{\Sigma}\cdot\mathbf{B}h$, and $\bar{q}\Gamma\boldsymbol{\alpha}\cdot\mathbf{E}h$, which can be deduced from Eq. (A17) of Ref. [33]. Their coefficients can be read off from Eq. (A19). When $c_B = r_s$ the first two share the same coefficient

$$\begin{aligned} f_X(m_0a) &= \frac{1}{8m_X^2a^2} - \frac{\zeta d_1(1+m_0a)}{m_0a(2+m_0a)} - \frac{1}{2(2m_2a)^2}, \\ &= \frac{1}{2} \left[\frac{1}{(2+m_0a)(1+m_0a)} + \frac{1}{2(1+m_0a)} - \frac{1}{4(1+m_0a)^2} - \frac{1}{(2+m_0a)^2} \right], \\ &= \frac{1}{2} \left[\frac{1}{2(1+m_0a)} - \left(\frac{m_0a}{2(2+m_0a)(1+m_0a)} \right)^2 \right], \end{aligned} \quad (\text{A13})$$

where the last term on the second line comes from using the tree-level d_1 (as we do in the simulations). Because of the two-fold appearance, we again take the prior width to be $\sqrt{2}$.

For $\bar{q}\Gamma\boldsymbol{\alpha}\cdot\mathbf{E}h$

$$\begin{aligned} f_Y(m_0a) &= \frac{1}{2} \left[\frac{d_1}{m_2a} - \frac{\zeta(1-c_E)(1+m_0a)}{m_0a(2+m_0a)} \right], \\ &= \frac{2+4m_0a+(m_0a)^2}{4(1+m_0a)^2(2+m_0a)^2}, \end{aligned} \quad (\text{A14})$$

where the last line reflects the choices made for c_E and d_1 .

b. $\mathcal{O}(\alpha_s a)$ and $\mathcal{O}(a^3)$ errors

Here the mismatch functions $f_i(m_0a)$ start at order α_s , and we do not have explicit expressions for them. We take unimproved tree-level coefficients as a guide to the combinatoric factors and the asymptotic behavior as $m_0a \rightarrow 0$ and $m_0a \rightarrow \infty$.

The Lagrangian leads to two bilinears, the kinetic energy $\mathcal{O}_2 = \bar{h}\mathbf{D}^2h$ and the chromomagnetic moment $\mathcal{O}_B = \bar{h}i\boldsymbol{\Sigma}\cdot\mathbf{B}h$. We match the former nonperturbatively, by identifying the meson's kinetic mass with the physical mass; the discretization error f_2 stems, therefore, from discretization effects in M_2 .

The computed kinetic meson mass is

$$M_2 = m_2(\kappa) + \text{continuum binding energy} + \delta M_2, \quad (\text{A15})$$

where [55]

$$\delta M_2 = \frac{\bar{\Lambda}^2}{6m_Q} \left[5 \left(\frac{m_2^3}{m_4^3} - 1 \right) + 4w_4(m_2a)^3 \right], \quad (\text{A16})$$

and m_2 , m_4 , and w_4 are functions of m_0a and, hence, κ . (See Refs. [33, 60] for explicit expressions.) Equating M_2 to a physical meson mass means that we choose κ such that $m_2(\kappa) + \delta M_2 = m_Q$, thereby making in ϕ a relative error

$$\text{error}_2 = \bar{\Lambda} \left(\frac{1}{2m_2} - \frac{1}{2m_Q} \right) = \bar{\Lambda} \left(\frac{1}{2m_Q - 2\delta M_2} - \frac{1}{2m_Q} \right) \approx \bar{\Lambda} \frac{\delta M_2}{2m_Q^2}. \quad (\text{A17})$$

The right-most expression is $(a\bar{\Lambda})^3 f_2(m_0a)$, $f_2 = []/12(m_2a)^3$, where $[]$ is the bracket in Eq. (A16). It is formally smaller than the other errors considered here— f_2 is of order 1 for all m_0a . Numerically, however, it is not much smaller.

At the tree level the chromomagnetic mismatch is

$$f_B^{[0]}(m_0a) = \frac{c_B - 1}{2(1 + m_0a)}. \quad (\text{A18})$$

This has the right asymptotic behavior in both limits, so our Ansatz for the one-loop mismatch function is simply

$$f_B(m_0a) = \frac{\alpha_s}{2(1 + m_0a)}, \quad (\text{A19})$$

and error_B is this function multiplied by $a\Lambda$. We take $\alpha_s = 0.288$ on the $a \approx 0.12$ fm ensembles, which is the value determined for α_V from the plaquette [76] with one-loop running to scale $q^* = 2.5/a$. On other ensembles, α_s is found by assuming that the measured average taste splitting goes like $\alpha_s^2 a^2$ (with a determined from r_1/a). This gives α_s values that track $\alpha_V(q^* = 2.5/a)$ quite well, which is why we make that q^* choice. The results are rather insensitive to the details here. For example, using $\alpha_s = 0.325$ on the $a \approx 0.12$ fm ensembles, which corresponds to $q^* = 2.0/a$, increases the error estimate by less than 0.6 MeV for f_{D^+} , and less than 0.25 MeV for f_{B^+} .

The current leads to one more term, with tree-level mismatch function

$$f_3^{[0]}(m_0a) = \frac{m_0a}{2(2 + m_0a)(1 + m_0a)} - d_1, \quad (\text{A20})$$

and the tree-level d_1 is chosen so that $f_3^{[0]} = 0$. As with the mismatch function f_B , we would like to anticipate $f_3^{[1]}$ by setting $d_1^{[1]} = 0$ and multiplying the rest with α_s . But it is not generic that this vanishes as $m_0a \rightarrow 0$. Therefore, we take

$$f_3(m_0a) = \frac{\alpha_s}{2(2 + m_0a)}, \quad (\text{A21})$$

which has the right asymptotic behavior. We take the prior width as $\sqrt{2}$, because A^4 has two such corrections [37].

3. Dispersion relation, Eq. (3.1)

We take a similar approach to the dispersion relation, Eq. (3.1), with the difference that we now know the sign of the leading effect.

The tree-level functions are

$$a_4^{[0]} = \frac{1}{(m_2^{[0]}a)^2} - \frac{m_1^{[0]}a}{(m_4^{[0]}a)^3}, \quad (\text{A22})$$

$$a_{4'}^{[0]} = m_1^{[0]}a w_4^{[0]}. \quad (\text{A23})$$

The binding energy enters A_4 and $A_{4'}$ via the meson's kinetic energy. Hence, the binding contributions are

$$A'_4 = \frac{3m_1^{[0]}a}{m_2^{[0]}a(m_4^{[0]}a)^3} - \frac{2}{(m_2^{[0]}a)^3} - \frac{1}{(m_4^{[0]}a)^3}, \quad (\text{A24})$$

$$A'_{4'} = w_4^{[0]} \left(1 - \frac{m_1^{[0]}a}{m_2^{[0]}a} \right), \quad (\text{A25})$$

and in Eq. (3.4) the binding energy floats within a Gaussian prior described by $(\bar{\Lambda}, \sigma_{\bar{\Lambda}}) = (600, 400)$ MeV. This choice conservatively brackets the binding energy of a heavy-strange meson. For the higher-order perturbative contribution to the coefficients, we take the Ansätze based on the asymptotic behavior:

$$a_4^{[1]} = \frac{y_4 + z_4 \ln(1 + m_0 a)}{(1 + m_0 a)^2}, \quad (\text{A26})$$

$$a_{4'}^{[1]} = \frac{y_{4'} m_0 a + z_{4'} \ln(1 + m_0 a)}{1 + m_0 a}, \quad (\text{A27})$$

where the y s and z s float within Gaussian priors described by $(y_4, \sigma_{y_4}) = (3, 5)$, $(z_4, \sigma_{z_4}) = (1, 2)$, $(y_{4'}, \sigma_{y_{4'}}) = (0, 0)$, and $(z_{4'}, \sigma_{z_{4'}}) = (0, 2)$. The terms proportional to y_i stem from the $m_0 a \rightarrow 0$ limit, in which the renormalization of m_4 must coincide with that of m_1 , and $a_4 = m_1 a w_4$ must vanish like $m_0 a$. The terms proportional to z_i stem from the $m_0 a \rightarrow \infty$ limit, where the static limit is obtained. Except for $y_{4'}$, the numerical values have been chosen consistent with one-loop experience for m_1 and m_2 [109]. We have set $y_{4'} \equiv 0$, because at small $m_0 a$ it is indistinguishable from the other term in $a_{4'}^{[1]}$, and our range of $m_0 a$ does not reach far into the region $m_0 a \gg 1$.

Appendix B: Two point fit results from Analysis I

TABLE XIV. Heavy-light pseudoscalar meson masses and renormalized decay amplitudes obtained from Analysis I fits of the charm correlators at lattice spacing $a \approx 0.09$ fm.

am_l/am_s	am_q	aM_H	$a^{3/2}\phi_H$	χ^2/dof	p
0.0031/0.031	0.0031	0.7523(0.0016)	0.0857(0.0015)	58/48	0.23
0.0031/0.031	0.0044	0.7553(0.0014)	0.0873(0.0013)	56/48	0.28
0.0031/0.031	0.0062	0.7589(0.0011)	0.0890(0.0011)	55/48	0.33
0.0031/0.031	0.0087	0.7634(0.0009)	0.0910(0.0009)	53/48	0.38
0.0031/0.031	0.0124	0.7699(0.0007)	0.0936(0.0007)	53/48	0.41
0.0031/0.031	0.0186	0.7807(0.0005)	0.0978(0.0006)	52/48	0.44
0.0031/0.031	0.0272	0.7954(0.0004)	0.1030(0.0005)	50/48	0.5
0.0031/0.031	0.031	0.8018(0.0004)	0.1052(0.0004)	50/48	0.5
0.0062/0.031	0.0031	0.7541(0.0030)	0.0875(0.0027)	56/48	0.37
0.0062/0.031	0.0044	0.7577(0.0023)	0.0899(0.0021)	52/48	0.49
0.0062/0.031	0.0062	0.7613(0.0019)	0.0917(0.0018)	50/48	0.58
0.0062/0.031	0.0087	0.7654(0.0015)	0.0933(0.0015)	58/51	0.43
0.0062/0.031	0.0124	0.7712(0.0012)	0.0952(0.0012)	52/48	0.48
0.0062/0.031	0.0186	0.7810(0.0009)	0.0985(0.0010)	56/48	0.37
0.0062/0.031	0.0272	0.7952(0.0006)	0.1032(0.0008)	59/48	0.28
0.0062/0.031	0.031	0.8015(0.0005)	0.1052(0.0007)	60/48	0.25
0.0124/0.031	0.0031	0.7551(0.0038)	0.0930(0.0036)	60/48	0.27
0.0124/0.031	0.0042	0.7554(0.0031)	0.0926(0.0028)	65/48	0.15
0.0124/0.031	0.0062	0.7574(0.0023)	0.0929(0.0021)	65/48	0.16
0.0124/0.031	0.0087	0.7608(0.0017)	0.0938(0.0015)	59/48	0.28
0.0124/0.031	0.0124	0.7666(0.0013)	0.0957(0.0012)	49/48	0.63
0.0124/0.031	0.0186	0.7766(0.0008)	0.0991(0.0009)	42/48	0.85
0.0124/0.031	0.0272	0.7907(0.0006)	0.1038(0.0007)	48/48	0.64
0.0124/0.031	0.031	0.7969(0.0005)	0.1058(0.0006)	53/48	0.47

TABLE XV. Heavy-light pseudoscalar meson masses and renormalized decay amplitudes obtained from Analysis I fits of the charm correlators at lattice spacing $a \approx 0.12$ fm.

am_l/am_s	am_q	aM_H	$a^{3/2}\phi_H$	χ^2/dof	p
0.005/0.050	0.005	0.9943(0.0032)	0.1436(0.0030)	30/30	0.52
0.005/0.050	0.007	0.9977(0.0024)	0.1453(0.0024)	29/30	0.6
0.005/0.050	0.01	1.0026(0.0018)	0.1477(0.0019)	28/30	0.64
0.005/0.050	0.014	1.0090(0.0016)	0.1508(0.0017)	28/30	0.64
0.005/0.050	0.02	1.0186(0.0013)	0.1551(0.0015)	29/30	0.58
0.005/0.050	0.03	1.0345(0.0010)	0.1620(0.0012)	33/30	0.42
0.005/0.050	0.0415	1.0526(0.0008)	0.1694(0.0010)	36/30	0.27
0.007/0.050	0.005	0.9948(0.0035)	0.1442(0.0035)	17/30	0.98
0.007/0.050	0.007	0.9975(0.0027)	0.1455(0.0028)	19/30	0.95
0.007/0.050	0.01	1.0019(0.0021)	0.1476(0.0021)	22/30	0.89
0.007/0.050	0.014	1.0081(0.0016)	0.1504(0.0017)	24/30	0.83
0.007/0.050	0.02	1.0178(0.0012)	0.1547(0.0014)	23/30	0.85
0.007/0.050	0.03	1.0338(0.0009)	0.1615(0.0010)	20/30	0.94
0.007/0.050	0.0415	1.0520(0.0007)	0.1687(0.0008)	19/30	0.95
0.010/0.050	0.005	0.9958(0.0039)	0.1461(0.0041)	15/30	0.99
0.010/0.050	0.007	1.0000(0.0031)	0.1486(0.0032)	20/30	0.94
0.010/0.050	0.01	1.0057(0.0024)	0.1516(0.0026)	26/30	0.75
0.010/0.050	0.014	1.0126(0.0019)	0.1549(0.0021)	29/27	0.41
0.010/0.050	0.02	1.0226(0.0015)	0.1594(0.0017)	33/30	0.39
0.010/0.050	0.03	1.0387(0.0011)	0.1662(0.0014)	31/30	0.5
0.010/0.050	0.0415	1.0567(0.0008)	0.1733(0.0011)	27/30	0.68
0.020/0.050	0.005	0.9942(0.0046)	0.1537(0.0050)	49/30	0.036
0.020/0.050	0.007	0.9959(0.0036)	0.1533(0.0039)	49/30	0.036
0.020/0.050	0.01	0.9987(0.0027)	0.1532(0.0031)	48/30	0.051
0.020/0.050	0.014	1.0037(0.0021)	0.1543(0.0024)	45/30	0.075
0.020/0.050	0.02	1.0124(0.0016)	0.1575(0.0019)	43/30	0.11
0.020/0.050	0.03	1.0274(0.0011)	0.1632(0.0014)	37/30	0.27
0.020/0.050	0.0415	1.0447(0.0009)	0.1695(0.0012)	32/30	0.48
0.030/0.050	0.005	0.9830(0.0042)	0.1475(0.0042)	33/30	0.39
0.030/0.050	0.007	0.9853(0.0033)	0.1485(0.0033)	33/30	0.4
0.030/0.050	0.01	0.9897(0.0025)	0.1505(0.0025)	32/30	0.47
0.030/0.050	0.014	0.9960(0.0020)	0.1534(0.0020)	31/30	0.53
0.030/0.050	0.02	1.0054(0.0015)	0.1574(0.0016)	32/30	0.46
0.030/0.050	0.03	1.0205(0.0011)	0.1633(0.0012)	37/30	0.27
0.030/0.050	0.0415	1.0376(0.0009)	0.1695(0.0010)	40/30	0.15

TABLE XVI. Heavy-light pseudoscalar meson masses and renormalized decay amplitudes obtained from Analysis I fits of the charm correlators at lattice spacing $a \approx 0.15$ fm.

am_l/am_s	am_q	aM_H	$a^{3/2}\phi_H$	χ^2/dof	p
0.0097/0.0484	0.0048	1.1659(0.0044)	0.1979(0.0052)	20/20	0.5
0.0097/0.0484	0.007	1.1710(0.0034)	0.2017(0.0040)	22/20	0.37
0.0097/0.0484	0.0097	1.1768(0.0027)	0.2054(0.0032)	25/20	0.26
0.0097/0.0484	0.0194	1.1951(0.0016)	0.2159(0.0020)	25/20	0.26
0.0097/0.0484	0.029	1.2117(0.0012)	0.2242(0.0015)	20/20	0.51
0.0097/0.0484	0.0484	1.2432(0.0009)	0.2385(0.0012)	15/20	0.79
0.0194/0.0484	0.0048	1.1726(0.0046)	0.2106(0.0052)	23/20	0.35
0.0194/0.0484	0.007	1.1749(0.0036)	0.2105(0.0041)	23/20	0.35
0.0194/0.0484	0.0097	1.1785(0.0028)	0.2113(0.0031)	23/20	0.32
0.0194/0.0484	0.0194	1.1935(0.0016)	0.2174(0.0020)	30/20	0.092
0.0194/0.0484	0.029	1.2091(0.0013)	0.2244(0.0016)	32/20	0.055
0.0194/0.0484	0.0484	1.2400(0.0010)	0.2381(0.0013)	27/20	0.17
0.0290/0.0484	0.0048	1.1613(0.0044)	0.1975(0.0049)	17/20	0.72
0.0290/0.0484	0.007	1.1660(0.0034)	0.2010(0.0040)	18/20	0.64
0.0290/0.0484	0.0097	1.1717(0.0026)	0.2049(0.0031)	21/20	0.47
0.0290/0.0484	0.0194	1.1896(0.0015)	0.2151(0.0019)	24/20	0.3
0.0290/0.0484	0.029	1.2058(0.0011)	0.2229(0.0015)	23/20	0.32
0.0290/0.0484	0.0484	1.2368(0.0008)	0.2364(0.0011)	20/20	0.49

TABLE XVII. Heavy-light pseudoscalar meson masses and renormalized decay amplitudes obtained from Analysis I fits of the bottom correlators at lattice spacing $a \approx 0.09$ fm.

am_l/am_s	am_q	aM_H	$a^{3/2}\phi_H$	χ^2/dof	p
0.0031/0.031	0.0031	1.6509(0.0018)	0.1359(0.0016)	41/39	0.48
0.0031/0.031	0.0044	1.6532(0.0016)	0.1378(0.0015)	40/39	0.51
0.0031/0.031	0.0062	1.6562(0.0015)	0.1402(0.0014)	40/39	0.49
0.0031/0.031	0.0087	1.6601(0.0013)	0.1433(0.0014)	42/39	0.42
0.0031/0.031	0.0124	1.6659(0.0012)	0.1475(0.0013)	45/39	0.31
0.0031/0.031	0.0186	1.6752(0.0011)	0.1542(0.0012)	47/39	0.23
0.0031/0.031	0.0272	1.6879(0.0009)	0.1628(0.0011)	49/39	0.19
0.0031/0.031	0.031	1.6934(0.0009)	0.1664(0.0011)	49/39	0.18
0.0062/0.031	0.0031	1.6539(0.0046)	0.1358(0.0051)	40/39	0.56
0.0062/0.031	0.0044	1.6557(0.0039)	0.1377(0.0044)	37/39	0.68
0.0062/0.031	0.0062	1.6584(0.0032)	0.1402(0.0037)	34/39	0.77
0.0062/0.031	0.0087	1.6620(0.0027)	0.1434(0.0031)	34/39	0.8
0.0062/0.031	0.0124	1.6675(0.0022)	0.1480(0.0026)	36/39	0.72
0.0062/0.031	0.0186	1.6767(0.0018)	0.1550(0.0022)	41/39	0.53
0.0062/0.031	0.0272	1.6892(0.0014)	0.1637(0.0019)	45/39	0.37
0.0062/0.031	0.031	1.6946(0.0014)	0.1672(0.0018)	45/39	0.35
0.0124/0.031	0.0031	1.6532(0.0036)	0.1387(0.0038)	52/39	0.16
0.0124/0.031	0.0042	1.6550(0.0033)	0.1407(0.0034)	48/39	0.27
0.0124/0.031	0.0062	1.6576(0.0030)	0.1432(0.0031)	40/39	0.55
0.0124/0.031	0.0087	1.6606(0.0027)	0.1456(0.0029)	35/39	0.77
0.0124/0.031	0.0124	1.6650(0.0024)	0.1488(0.0027)	33/39	0.84
0.0124/0.031	0.0186	1.6730(0.0019)	0.1544(0.0023)	36/39	0.73
0.0124/0.031	0.0272	1.6847(0.0016)	0.1623(0.0021)	42/39	0.48
0.0124/0.031	0.031	1.6900(0.0015)	0.1657(0.0020)	45/39	0.38

TABLE XVIII. Heavy-light pseudoscalar meson masses and renormalized decay amplitudes obtained from Analysis I fits of the bottom correlators at lattice spacing $a \approx 0.12$ fm.

am_l/am_s	am_q	aM_H	$a^{3/2}\phi_H$	χ^2/dof	p
0.005/0.050	0.005	1.9170(0.0044)	0.2236(0.0050)	45/27	0.03
0.005/0.050	0.007	1.9197(0.0039)	0.2263(0.0046)	46/27	0.022
0.005/0.050	0.01	1.9235(0.0033)	0.2300(0.0040)	46/27	0.021
0.005/0.050	0.014	1.9287(0.0029)	0.2347(0.0036)	45/27	0.027
0.005/0.050	0.02	1.9367(0.0024)	0.2418(0.0031)	43/27	0.046
0.005/0.050	0.03	1.9503(0.0020)	0.2532(0.0026)	39/27	0.096
0.005/0.050	0.0415	1.9657(0.0017)	0.2654(0.0023)	36/27	0.17
0.007/0.050	0.005	1.9147(0.0036)	0.2224(0.0039)	37/27	0.12
0.007/0.050	0.007	1.9177(0.0033)	0.2254(0.0037)	35/27	0.17
0.007/0.050	0.01	1.9219(0.0030)	0.2292(0.0036)	34/27	0.2
0.007/0.050	0.014	1.9272(0.0028)	0.2337(0.0037)	35/27	0.19
0.007/0.050	0.02	1.9351(0.0026)	0.2401(0.0037)	36/27	0.15
0.007/0.050	0.03	1.9485(0.0022)	0.2508(0.0035)	38/27	0.096
0.007/0.050	0.0415	1.9638(0.0019)	0.2628(0.0031)	40/27	0.07
0.010/0.050	0.005	1.9182(0.0047)	0.2254(0.0047)	30/27	0.4
0.010/0.050	0.007	1.9207(0.0041)	0.2284(0.0042)	32/27	0.29
0.010/0.050	0.01	1.9250(0.0035)	0.2328(0.0037)	36/27	0.18
0.010/0.050	0.014	1.9307(0.0030)	0.2383(0.0033)	39/27	0.097
0.010/0.050	0.02	1.9391(0.0025)	0.2457(0.0028)	43/27	0.048
0.010/0.050	0.03	1.9527(0.0020)	0.2569(0.0024)	47/27	0.02
0.010/0.050	0.0415	1.9682(0.0017)	0.2689(0.0021)	51/27	0.0092
0.020/0.050	0.005	1.9136(0.0060)	0.2278(0.0069)	33/27	0.27
0.020/0.050	0.007	1.9163(0.0050)	0.2305(0.0059)	33/27	0.28
0.020/0.050	0.01	1.9200(0.0042)	0.2340(0.0050)	31/27	0.36
0.020/0.050	0.014	1.9249(0.0036)	0.2381(0.0043)	29/27	0.47
0.020/0.050	0.02	1.9322(0.0031)	0.2437(0.0039)	28/27	0.52
0.020/0.050	0.03	1.9445(0.0027)	0.2526(0.0038)	30/27	0.42
0.020/0.050	0.0415	1.9590(0.0025)	0.2627(0.0039)	33/27	0.3
0.030/0.050	0.005	1.9030(0.0058)	0.2196(0.0073)	38/27	0.12
0.030/0.050	0.007	1.9058(0.0049)	0.2223(0.0064)	32/27	0.29
0.030/0.050	0.01	1.9099(0.0041)	0.2258(0.0056)	27/27	0.56
0.030/0.050	0.014	1.9155(0.0034)	0.2306(0.0048)	23/27	0.74
0.030/0.050	0.02	1.9239(0.0028)	0.2376(0.0040)	22/27	0.77
0.030/0.050	0.03	1.9372(0.0022)	0.2479(0.0034)	25/27	0.64
0.030/0.050	0.0415	1.9518(0.0019)	0.2585(0.0032)	28/27	0.49

TABLE XIX. Heavy-light pseudoscalar meson masses and renormalized decay amplitudes obtained from Analysis I fits of the bottom correlators at lattice spacing $a \approx 0.15$ fm.

am_l/am_s	am_q	aM_H	$a^{3/2}\phi_H$	χ^2/dof	p
0.0097/0.0484	0.0048	2.2553(0.0071)	0.3311(0.0115)	36/25	0.097
0.0097/0.0484	0.007	2.2576(0.0061)	0.3341(0.0102)	37/25	0.09
0.0097/0.0484	0.0097	2.2611(0.0052)	0.3389(0.0089)	36/25	0.1
0.0097/0.0484	0.0194	2.2757(0.0036)	0.3568(0.0063)	34/25	0.16
0.0097/0.0484	0.029	2.2901(0.0030)	0.3727(0.0053)	33/25	0.16
0.0097/0.0484	0.0484	2.3175(0.0023)	0.4002(0.0046)	35/25	0.12
0.0194/0.0484	0.0048	2.2296(0.0175)	0.2743(0.0416)	32/25	0.2
0.0194/0.0484	0.007	2.2349(0.0142)	0.2823(0.0357)	34/25	0.15
0.0194/0.0484	0.0097	2.2416(0.0118)	0.2917(0.0309)	36/25	0.1
0.0194/0.0484	0.0194	2.2639(0.0072)	0.3243(0.0202)	36/25	0.1
0.0194/0.0484	0.029	2.2819(0.0054)	0.3482(0.0152)	30/25	0.27
0.0194/0.0484	0.0484	2.3124(0.0038)	0.3839(0.0109)	24/25	0.59
0.0290/0.0484	0.0048	2.2402(0.0073)	0.3101(0.0123)	29/25	0.32
0.0290/0.0484	0.007	2.2464(0.0061)	0.3199(0.0104)	30/25	0.28
0.0290/0.0484	0.0097	2.2524(0.0052)	0.3289(0.0089)	31/25	0.25
0.0290/0.0484	0.0194	2.2695(0.0036)	0.3502(0.0066)	27/25	0.42
0.0290/0.0484	0.029	2.2847(0.0030)	0.3665(0.0058)	21/25	0.72
0.0290/0.0484	0.0484	2.3125(0.0025)	0.3939(0.0057)	18/25	0.87

-
- [1] A. Lenz *et al.* (CKMfitter), *Phys. Rev.* **D83**, 036004 (2011), [arXiv:1008.1593 \[hep-ph\]](https://arxiv.org/abs/1008.1593)
- [2] E. Lunghi and A. Soni, *Phys. Lett.* **B697**, 323 (2011), [arXiv:1010.6069 \[hep-ph\]](https://arxiv.org/abs/1010.6069)
- [3] J. Laiho, E. Lunghi, and R. Van de Water, PoS **FPCP2010**, 040 (2010), [arXiv:1102.3917 \[hep-ph\]](https://arxiv.org/abs/1102.3917)
- [4] K. Hara *et al.* (Belle), *Phys. Rev.* **D82**, 071101 (2010), [arXiv:1006.4201 \[hep-ex\]](https://arxiv.org/abs/1006.4201)
- [5] P. del Amo Sanchez *et al.* (BaBar)(2010), [arXiv:1008.0104 \[hep-ex\]](https://arxiv.org/abs/1008.0104)
- [6] M. Masuzawa, in *Proceedings of IPAC 2010*, edited by K. Oide (2010) <http://accelconf.web.cern.ch/AccelConf/IPAC10/>
- [7] T. Iijima, “Search for Charged Higgs in $B \rightarrow \tau\nu$ and $D \rightarrow \tau\nu$ Decays,” (2009), <http://kds.kek.jp/materialDisplay.py?contribId=5&sessionId=2&materialId=slides&confId=2865>
- [8] E. Lunghi and A. Soni, *Phys. Rev. Lett.* **104**, 251802 (2010), [arXiv:0912.0002 \[hep-ph\]](https://arxiv.org/abs/0912.0002)
- [9] C. T. H. Davies *et al.* (HPQCD, MILC, and Fermilab Lattice), *Phys. Rev. Lett.* **92**, 022001 (2004), [arXiv:hep-lat/0304004](https://arxiv.org/abs/hep-lat/0304004)
- [10] L. Susskind, *Phys. Rev.* **D16**, 3031 (1977)
- [11] H. S. Sharatchandra, H. J. Thun, and P. Weisz, *Nucl. Phys.* **B192**, 205 (1981)
- [12] C. Aubin *et al.* (MILC), *Phys. Rev.* **D70**, 114501 (2004), [arXiv:hep-lat/0407028 \[hep-lat\]](https://arxiv.org/abs/hep-lat/0407028)
- [13] I. F. Allison *et al.* (HPQCD), *Phys. Rev. Lett.* **94**, 172001 (2005), [arXiv:hep-lat/0411027](https://arxiv.org/abs/hep-lat/0411027)
- [14] S. Prelovšek, *Phys. Rev.* **D73**, 014506 (2006), [arXiv:hep-lat/0510080](https://arxiv.org/abs/hep-lat/0510080)
- [15] C. Bernard, *Phys. Rev.* **D73**, 114503 (2006), [arXiv:hep-lat/0603011](https://arxiv.org/abs/hep-lat/0603011)
- [16] C. Bernard, C. E. DeTar, Z. Fu, and S. Prelovšek, *Phys. Rev.* **D76**, 094504 (2007), [arXiv:0707.2402 \[hep-lat\]](https://arxiv.org/abs/0707.2402)
- [17] C. Aubin, J. Laiho, and R. S. Van de Water, *Phys. Rev.* **D77**, 114501 (2008), [arXiv:0803.0129 \[hep-lat\]](https://arxiv.org/abs/0803.0129)
- [18] C. Bernard, M. Golterman, and Y. Shamir, *Phys. Rev.* **D73**, 114511 (2006), [arXiv:hep-lat/0604017 \[hep-lat\]](https://arxiv.org/abs/hep-lat/0604017)
- [19] Y. Shamir, *Phys. Rev.* **D71**, 034509 (2005), [arXiv:hep-lat/0412014](https://arxiv.org/abs/hep-lat/0412014)
- [20] Y. Shamir, *Phys. Rev.* **D75**, 054503 (2007), [arXiv:hep-lat/0607007](https://arxiv.org/abs/hep-lat/0607007)
- [21] C. Bernard, M. Golterman, and Y. Shamir, *Phys. Rev.* **D77**, 074505 (2008), [arXiv:0712.2560 \[hep-lat\]](https://arxiv.org/abs/0712.2560)
- [22] W.-J. Lee and S. R. Sharpe, *Phys. Rev.* **D60**, 114503 (1999), [arXiv:hep-lat/9905023](https://arxiv.org/abs/hep-lat/9905023)
- [23] C. Aubin and C. Bernard, *Phys. Rev.* **D68**, 034014 (2003), [hep-lat/0304014](https://arxiv.org/abs/hep-lat/0304014)
- [24] S. R. Sharpe and R. S. Van de Water, *Phys. Rev.* **D71**, 114505 (2005), [arXiv:hep-lat/0409018](https://arxiv.org/abs/hep-lat/0409018)
- [25] S. R. Sharpe, PoS **LAT2006**, 022 (2006), [arXiv:hep-lat/0610094](https://arxiv.org/abs/hep-lat/0610094)
- [26] A. S. Kronfeld, PoS **LAT2007**, 016 (2007), [arXiv:0711.0699 \[hep-lat\]](https://arxiv.org/abs/0711.0699)
- [27] M. Golterman, PoS **CONFINEMENT8**, 014 (2008), [arXiv:0812.3110 \[hep-ph\]](https://arxiv.org/abs/0812.3110)
- [28] A. Bazavov *et al.*, *Rev. Mod. Phys.* **82**, 1349 (2010), [arXiv:0903.3598 \[hep-lat\]](https://arxiv.org/abs/0903.3598)
- [29] G. C. Donald, C. T. H. Davies, E. Follana, and A. S. Kronfeld, *Phys. Rev.* **D84**, 054501 (2011), [arXiv:1106.2412 \[hep-lat\]](https://arxiv.org/abs/1106.2412)
- [30] J. Laiho, E. Lunghi, and R. S. Van de Water, *Phys. Rev.* **D81**, 034503 (2010), [arXiv:0910.2928 \[hep-ph\]](https://arxiv.org/abs/0910.2928)
- [31] C. W. Bernard *et al.*, *Phys. Rev.* **D64**, 054506 (2001), [arXiv:hep-lat/0104002](https://arxiv.org/abs/hep-lat/0104002)
- [32] B. Sheikholeslami and R. Wohlert, *Nucl. Phys.* **B259**, 572 (1985)

- [33] A. X. El-Khadra, A. S. Kronfeld, and P. B. Mackenzie, *Phys. Rev.* **D55**, 3933 (1997), [arXiv:hep-lat/9604004](#)
- [34] K. Symanzik, *Nucl. Phys.* **B226**, 187 (1983)
- [35] K. Symanzik, *Nucl. Phys.* **B226**, 205 (1983)
- [36] A. S. Kronfeld, *Phys. Rev.* **D62**, 014505 (2000), [arXiv:hep-lat/0002008](#)
- [37] J. Harada *et al.*, *Phys. Rev.* **D65**, 094513 (2002), [Erratum-ibid. **D71**, 019903 (2005)], [arXiv:hep-lat/0112044](#)
- [38] J. Harada *et al.*, *Phys. Rev.* **D65**, 094514 (2002), [arXiv:hep-lat/0112045](#)
- [39] C. Aubin and C. Bernard, *Phys. Rev.* **D73**, 014515 (2006), [arXiv:hep-lat/0510088](#)
- [40] J. Laiho and R. S. Van de Water, *Phys. Rev.* **D73**, 054501 (2006), [arXiv:hep-lat/0512007](#)
- [41] C. Aubin and C. Bernard, *Phys. Rev.* **D76**, 014002 (2007), [arXiv:0704.0795 \[hep-lat\]](#)
- [42] A. X. El-Khadra, A. S. Kronfeld, P. B. Mackenzie, S. M. Ryan, and J. N. Simone, *Phys. Rev.* **D64**, 014502 (2001), [arXiv:hep-ph/0101023](#)
- [43] A. X. El-Khadra, E. Gámiz, A. S. Kronfeld, and M. A. Nobes, PoS **LAT2007**, 242 (2007), [arXiv:0710.1437 \[hep-lat\]](#)
- [44] C. Aubin *et al.* (Fermilab Lattice and MILC), *Phys. Rev. Lett.* **95**, 122002 (2005), [arXiv:hep-lat/0506030](#)
- [45] C. Bernard *et al.* (Fermilab Lattice and MILC), PoS **LAT2006**, 094 (2006)
- [46] C. Bernard *et al.* (Fermilab Lattice and MILC), PoS **LAT2007**, 370 (2007)
- [47] C. Bernard *et al.* (Fermilab Lattice and MILC), PoS **LATTICE2008**, 278 (2008), [arXiv:0904.1895 \[hep-lat\]](#)
- [48] A. Bazavov *et al.* (Fermilab Lattice and MILC), PoS **LAT2009**, 249 (2009), [arXiv:0912.5221 \[hep-lat\]](#)
- [49] J. Simone *et al.* (Fermilab Lattice and MILC), PoS **LATTICE2010**, 317 (2010)
- [50] J. L. Rosner and S. Stone(2010), in Ref. [51], [arXiv:1002.1655 \[hep-ex\]](#)
- [51] K. Nakamura *et al.* (Particle Data Group), *J. Phys.* **G37**, 075021 (2010), and 2011 partial update for the 2012 edition
- [52] C. Aubin *et al.* (Fermilab Lattice and MILC), *Phys. Rev. Lett.* **94**, 011601 (2005), [arXiv:hep-ph/0408306](#)
- [53] C. Bernard *et al.* (Fermilab Lattice and MILC), *Phys. Rev.* **D79**, 014506 (2009), [arXiv:0808.2519 \[hep-lat\]](#)
- [54] J. A. Bailey *et al.* (Fermilab Lattice and MILC), *Phys. Rev.* **D79**, 054507 (2009), [arXiv:0811.3640 \[hep-lat\]](#)
- [55] C. Bernard *et al.* (Fermilab Lattice and MILC), *Phys. Rev.* **D83**, 034503 (2011), [arXiv:1003.1937 \[hep-lat\]](#)
- [56] G. P. Lepage, *Phys. Rev.* **D59**, 074502 (1999), [arXiv:hep-lat/9809157](#)
- [57] M. Lüscher and P. Weisz, *Phys. Lett.* **B158**, 250 (1985)
- [58] Z. Hao, G. M. von Hippel, R. R. Horgan, Q. J. Mason, and H. D. Trottier, *Phys. Rev.* **D76**, 034507 (2007), [arXiv:0705.4660 \[hep-lat\]](#)
- [59] K. G. Wilson, “Quarks and Strings on a Lattice,” in *New Phenomena In Subnuclear Physics*, edited by A. Zichichi (Plenum, New York, 1975) p. 69, cLNS-321
- [60] M. B. Oktay and A. S. Kronfeld, *Phys. Rev.* **D78**, 014504 (2008), [arXiv:0803.0523 \[hep-lat\]](#)
- [61] H.-W. Lin and N. Christ, *Phys. Rev.* **D76**, 074506 (2007), [arXiv:hep-lat/0608005](#)
- [62] G. P. Lepage, L. Magnea, C. Nakhleh, U. Magnea, and K. Hornbostel, *Phys. Rev.* **D46**, 4052 (1992), [arXiv:hep-lat/9205007](#)
- [63] R. Sommer, *Nucl. Phys.* **B411**, 839 (1994), [arXiv:hep-lat/9310022](#)

- [64] C. W. Bernard *et al.*, *Phys. Rev.* **D62**, 034503 (2000), [arXiv:hep-lat/0002028](https://arxiv.org/abs/hep-lat/0002028)
- [65] C. R. Allton(1996), [hep-lat/9610016](https://arxiv.org/abs/hep-lat/9610016)
- [66] A. Bazavov *et al.* (MILC), *PoS CD09*, 007 (2009), [arXiv:0910.2966 \[hep-ph\]](https://arxiv.org/abs/0910.2966)
- [67] C. T. H. Davies, E. Follana, I. D. Kendall, G. P. Lepage, and C. McNeile (HPQCD), *Phys. Rev.* **D81**, 034506 (2010), [arXiv:0910.1229 \[hep-lat\]](https://arxiv.org/abs/0910.1229)
- [68] G. P. Lepage *et al.*, *Nucl. Phys. Proc. Suppl.* **106**, 12 (2002), [arXiv:hep-lat/0110175](https://arxiv.org/abs/hep-lat/0110175)
- [69] C. Morningstar, *Nucl. Phys. Proc. Suppl.* **109A**, 185 (2002), [arXiv:hep-lat/0112023](https://arxiv.org/abs/hep-lat/0112023)
- [70] A. S. Kronfeld, *Nucl. Phys. Proc. Suppl.* **53**, 401 (1997), [arXiv:hep-lat/9608139](https://arxiv.org/abs/hep-lat/9608139)
- [71] N. Kawamoto and J. Smit, *Nucl. Phys.* **B192**, 100 (1981)
- [72] J. L. Richardson, *Phys. Lett.* **B82**, 272 (1979)
- [73] D. P. Menscher, “Charmonium and Charmed Mesons with Improved Lattice QCD,” (2005), PhD thesis
- [74] M. Wingate, J. Shigemitsu, C. T. H. Davies, G. P. Lepage, and H. D. Trottier, *Phys. Rev.* **D67**, 054505 (2003), [arXiv:hep-lat/0211014](https://arxiv.org/abs/hep-lat/0211014)
- [75] M. D. Pierro and E. Eichten, *Phys. Rev.* **D64**, 114004 (2001), [hep-ph/0104208](https://arxiv.org/abs/hep-ph/0104208), <http://arxiv.org/abs/hep-ph/0104208>
- [76] G. P. Lepage and P. B. Mackenzie, *Phys. Rev.* **D48**, 2250 (1993), [arXiv:hep-lat/9209022](https://arxiv.org/abs/hep-lat/9209022)
- [77] Q. Mason *et al.* (HPQCD), *Phys. Rev. Lett.* **95**, 052002 (2005), [arXiv:hep-lat/0503005](https://arxiv.org/abs/hep-lat/0503005)
- [78] K. Hornbostel, G. P. Lepage, and C. Morningstar, *Phys. Rev.* **D67**, 034023 (2003), [arXiv:hep-ph/0208224](https://arxiv.org/abs/hep-ph/0208224)
- [79] D. Arndt and C. J. D. Lin, *Phys. Rev.* **D70**, 014503 (2004), [arXiv:hep-lat/0403012](https://arxiv.org/abs/hep-lat/0403012)
- [80] C. Bernard (MILC), *Phys. Rev.* **D65**, 054031 (2002), [arXiv:hep-lat/0111051](https://arxiv.org/abs/hep-lat/0111051)
- [81] A. S. Kronfeld and S. M. Ryan, *Phys. Lett.* **B543**, 59 (2002), [arXiv:hep-ph/0206058](https://arxiv.org/abs/hep-ph/0206058)
- [82] C. G. Boyd and B. Grinstein, *Nucl. Phys.* **B442**, 205 (1995), [arXiv:hep-ph/9402340](https://arxiv.org/abs/hep-ph/9402340)
- [83] I. W. Stewart, *Nucl. Phys.* **B529**, 62 (1998), [arXiv:hep-ph/9803227](https://arxiv.org/abs/hep-ph/9803227)
- [84] D. Bećirević, S. Prelovšek, and J. Zupan, *Phys. Rev.* **D68**, 074003 (2003), [arXiv:hep-lat/0305001](https://arxiv.org/abs/hep-lat/0305001)
- [85] C. Bernard *et al.* (MILC), *PoS LATTICE2007*, 090 (2007), [arXiv:0710.1118 \[hep-lat\]](https://arxiv.org/abs/0710.1118)
- [86] R. Casalbuoni *et al.*, *Phys. Rept.* **281**, 145 (1997), [arXiv:hep-ph/9605342 \[hep-ph\]](https://arxiv.org/abs/hep-ph/9605342)
- [87] A. Anastassov *et al.* (CLEO), *Phys. Rev.* **D65**, 032003 (2002), [arXiv:hep-ex/0108043](https://arxiv.org/abs/hep-ex/0108043)
- [88] A. Abada *et al.*, *Nucl. Phys. Proc. Suppl.* **119**, 641 (2003), [arXiv:hep-lat/0209092](https://arxiv.org/abs/hep-lat/0209092)
- [89] M. C. Arnesen, B. Grinstein, I. Z. Rothstein, and I. W. Stewart, *Phys. Rev. Lett.* **95**, 071802 (2005), [arXiv:hep-ph/0504209](https://arxiv.org/abs/hep-ph/0504209)
- [90] H. Ohki, H. Matsufuru, and T. Onogi, *Phys. Rev.* **D77**, 094509 (2008), [arXiv:0802.1563 \[hep-lat\]](https://arxiv.org/abs/0802.1563)
- [91] J. Bulava, M. A. Donnellan, and R. Sommer (ALPHA), *PoS LATTICE2010*, 303 (2010), [arXiv:1011.4393 \[hep-lat\]](https://arxiv.org/abs/1011.4393)
- [92] C. Aubin *et al.* (HPQCD), *Phys. Rev.* **D70**, 031504 (2004), [arXiv:hep-lat/0405022](https://arxiv.org/abs/hep-lat/0405022)
- [93] C. Bernard *et al.* (MILC), *Phys. Rev.* **D66**, 094501 (2002), [arXiv:hep-lat/0206016](https://arxiv.org/abs/hep-lat/0206016)
- [94] G. P. Lepage, in *From actions to answers. Proceedings, Theoretical Advanced Study Institute in Elementary Particle Physics, Boulder, USA, June 5-30, 1989*, edited by T. A. DeGrand and D. Toussaint (World Scientific, 1989)
- [95] C. T. H. Davies, C. McNeile, E. Follana, G. P. Lepage, H. Na, *et al.* (HPQCD), *Phys. Rev.* **D82**, 114504 (2010), [arXiv:1008.4018 \[hep-lat\]](https://arxiv.org/abs/1008.4018)
- [96] P. Dimopoulos *et al.* (ETM)(2011), [arXiv:1107.1441 \[hep-lat\]](https://arxiv.org/abs/1107.1441)
- [97] B. I. Eisenstein *et al.* (CLEO), *Phys. Rev.* **D78**, 052003 (2008), [arXiv:0806.2112 \[hep-ex\]](https://arxiv.org/abs/0806.2112)

- [98] J. P. Alexander *et al.* (CLEO), *Phys. Rev.* **D79**, 052001 (2009), [arXiv:0901.1216 \[hep-ex\]](https://arxiv.org/abs/0901.1216)
- [99] L. Widhalm *et al.* (Belle), *Phys. Rev. Lett.* **100**, 241801 (2008), [arXiv:0709.1340 \[hep-ex\]](https://arxiv.org/abs/0709.1340)
- [100] P. Naik *et al.* (CLEO), *Phys. Rev.* **D80**, 112004 (2009), [arXiv:0910.3602 \[hep-ex\]](https://arxiv.org/abs/0910.3602)
- [101] P. U. E. Onyisi *et al.* (CLEO), *Phys. Rev.* **D79**, 052002 (2009), [arXiv:0901.1147 \[hep-ex\]](https://arxiv.org/abs/0901.1147)
- [102] J. P. Lees *et al.* (BaBar), *Phys. Rev.* **D82**, 091103 (2010), [arXiv:1003.3063 \[hep-ex\]](https://arxiv.org/abs/1003.3063)
- [103] D. Asner *et al.* (Heavy Flavor Averaging Group)(2010), http://www.slac.stanford.edu/xorg/hfag/charm/CHARM10/f_ds/results_20jan11.html with future updates at <http://www.slac.stanford.edu/xorg/hfag/charm/>, [arXiv:1010.1589 \[hep-ex\]](https://arxiv.org/abs/1010.1589)
- [104] C. McNeile, C. T. H. Davies, E. Follana, K. Hornbostel, and G. P. Lepage (HPQCD)(2011), [arXiv:1110.4510 \[hep-lat\]](https://arxiv.org/abs/1110.4510)
- [105] E. Gámiz, C. T. H. Davies, G. P. Lepage, J. Shigemitsu, and M. Wingate (HPQCD), *Phys. Rev.* **D80**, 014503 (2009), [arXiv:0902.1815 \[hep-lat\]](https://arxiv.org/abs/0902.1815)
- [106] C. Albertus *et al.* (RBC and UKQCD), *Phys. Rev.* **D82**, 014505 (2010), [arXiv:1001.2023 \[hep-lat\]](https://arxiv.org/abs/1001.2023)
- [107] A. Bazavov *et al.* (MILC), PoS **LATTICE2010**, 320 (2010), [arXiv:1012.1265 \[hep-lat\]](https://arxiv.org/abs/1012.1265)
- [108] E. Follana, C. T. H. Davies, G. P. Lepage, and J. Shigemitsu (HPQCD), *Phys. Rev. Lett.* **100**, 062002 (2008), [arXiv:0706.1726 \[hep-lat\]](https://arxiv.org/abs/0706.1726)
- [109] B. P. G. Mertens, A. S. Kronfeld, and A. X. El-Khadra, *Phys. Rev.* **D58**, 034505 (1998), [arXiv:hep-lat/9712024](https://arxiv.org/abs/hep-lat/9712024)

B and D meson decay constants from 2+1 flavor improved staggered simulations

**E. T. Neil^{a,*†}, Jon A. Bailey^{a,b}, A. Bazavov^c, C. Bernard^d, C. M. Bouchard^{e,a,g},
 C. DeTar^h, M. Di Pierroⁱ, A. X. El-Khadra^e, R. T. Evans^e, E. Freeland^{e,f}, E. Gamiz^{a,j},
 Steven Gottlieb^k, U. M. Heller^l, J. E. Hetrick^m, R. Jain^e, A. S. Kronfeld^a, J. Laihoⁿ,
 L. Levkova^h, P. B. Mackenzie^a, M. B. Oktay^h, J. N. Simone^a, R. Sugar^o,
 D. Toussaint^p, and R. S. Van de Water^c**

^a*Fermi National Accelerator Laboratory, Batavia, Illinois, USA*

^b*Department of Physics and Astronomy, Seoul National University, Seoul, ROK*

^c*Physics Department, Brookhaven National Laboratory, Upton, NY, USA*

^d*Department of Physics, Washington University, St. Louis, Missouri, USA*

^e*Physics Department, University of Illinois, Urbana, Illinois, USA*

^f*Department of Physics, Benedictine University, Lisle, Illinois, USA*

^g*Department of Physics, The Ohio State University, Columbus, OH, USA*

^h*Physics Department, University of Utah, Salt Lake City, Utah, USA*

ⁱ*School of Computing, DePaul University, Chicago, Illinois, USA*

^j*Department of Physics, University of Granada, Granada, Spain*

^k*Department of Physics, Indiana University, Bloomington, Indiana, USA*

^l*American Physical Society, Ridge, New York, USA*

^m*Physics Department, University of the Pacific, Stockton, California, USA*

ⁿ*SUPA, School of Physics and Astronomy, University of Glasgow, Glasgow, UK*

^o*Department of Physics, University of California, Santa Barbara, California, USA*

^p*Department of Physics, University of Arizona, Tucson, Arizona, USA*

[†]*E-mail:* eneil@fnal.gov

Fermilab Lattice and MILC Collaborations

We give an update on simulation results for the decay constants f_B, f_{B_s}, f_D and f_{D_s} . These decay constants are important for precision tests of the standard model, in particular entering as inputs to the global CKM unitarity triangle fit. The results presented here make use of the MILC (2+1)-flavor asqtad ensembles, with heavy quarks incorporated using the clover action with the Fermilab method. Partially quenched, staggered chiral perturbation theory is used to extract the decay constants at the physical point. In addition, we give error projections for a new analysis in progress, based on an extended data set.

*XXIX International Symposium on Lattice Field Theory
 July 10-16, 2011
 Squaw Valley, Lake Tahoe, California*

*Speaker.

1. Introduction

Within the standard model, the decay of mesons containing heavy quarks (in particular, B and D mesons) into purely leptonic final states provides an important testing ground for a number of theoretical ideas. Such decays involve both weak and strong interactions simultaneously, so that a complete understanding of the standard model is necessary to describe them. In particular, the decay width of a charged meson is proportional to both the meson decay constant (determined by strong interactions) and the CKM mixing angle,

$$\Gamma(H \rightarrow \ell v_\ell) \propto f_H^2 |V_{Qq}|^2. \quad (1.1)$$

Because this fully leptonic decay has no hadrons in the final state, the meson decay constant f_P can be readily and accurately determined by lattice simulations [1, 2, 3, 4]. Such a determination is in fact necessary in order to extract the CKM angles from experimental measurements of these decays, and precise computations of the decay constants could potentially reveal the presence of new physics through tension in the CKM unitarity triangle [5, 6, 7, 8]. In addition, certain leptonic decay channels (e.g. $B_s \rightarrow \mu^+ \mu^-$) are both loop and CKM suppressed in the standard model, and so they may be particularly sensitive to flavor-changing interactions induced by new physics [9].

2. Simulation Details

We make use of the MILC asqtad-improved staggered gauge configurations, with $2 + 1$ dynamical quarks in the sea [10]. For the light valence quarks, we make use of the same staggered action, while charm and bottom valence quarks are incorporated using the clover action with the Fermilab interpretation [11]. The particular set of ensembles used to obtain the results presented here, along with the number of configurations and other relevant information, are detailed in Table 1. Data on the coarsest lattice spacing $a \approx 0.15$ fm are shown in the analysis but are used only for the purpose of estimating the discretization errors; these points are excluded from the final fit used for chiral and continuum extrapolation.

3. Analysis and Fitting

The heavy meson decay constant is determined through the overlap of the meson wavefunction $|H\rangle$ with the axial vector current:

$$\langle 0 | \mathcal{A}^\mu | H(p) \rangle (M_H)^{-1/2} = i(p^\mu / M_H)(f_H \sqrt{M_H}) \equiv i(p^\mu / M_H)\phi_H. \quad (3.1)$$

The quantity $\phi_H \equiv f_H \sqrt{M_H}$ is thus proportional to the ground-state amplitude of the two-point function between the axial vector current and a heavy-light pseudoscalar operator \mathcal{O} . We therefore extract ϕ_H by fitting this two-point function simultaneously with the two-point pseudoscalar correlator,

$$\Phi_2^s(t) = \frac{1}{4} \sum_{a=1}^4 \langle A_a^{4\dagger}(t, \mathbf{x}) \mathcal{O}_a^{(s)}(0) \rangle, \quad (3.2)$$

$$C_2^{s,s'}(t) = \frac{1}{4} \sum_{a=1}^4 \langle \mathcal{O}_a^{(s)\dagger}(t, \mathbf{x}) \mathcal{O}_a^{(s')}(0) \rangle, \quad (3.3)$$

$\approx a$ [fm]	am_h	am_l	β	r_1/a	N_{conf}
0.09	0.031	0.0031	7.08	3.75	435
		0.0062	7.09	3.79	557
		0.0124	7.11	3.86	518
0.12	0.050	0.005	6.76	2.74	678
		0.007	6.76	2.74	833
		0.010	6.76	2.74	592
		0.020	6.79	2.82	460
		0.030	6.81	2.88	549
0.15	0.0484	0.0097	6.572	2.22	631
		0.0194	6.586	2.26	631
		0.0290	6.600	2.29	576

Table 1: Table of gauge configurations used for the full analysis to be presented. The ensembles with $a \approx 0.15$ fm (italics) are excluded from the final chiral/continuum extrapolation, as described in the text.

where a is a staggered taste index. Precise definitions of the interpolating operators A^4 and \mathcal{O} are given in Ref. [12].

For a correlation function with source type s and sink type s' , we fit to the “factorized” functional form

$$C_{ss'}(t) = \sum_{n=0}^{N_X} \left[A_{s,n} A_{s',n} \left(e^{-E_n t} + e^{-E_n(N_t-t)} \right) - (-1)^t A'_{s,n} A'_{s',n} \left(e^{-E'_n t} + e^{-E'_n(N_t-t)} \right) \right] \quad (3.4)$$

where N_X denotes the number of excited states included in the fit. The pseudoscalar source and sink type s, s' can be either point-like or smeared, so that a total of six distinct correlators are available for analysis. In the results shown here, joint fits are carried out to various combinations of correlators, with Bayesian priors imposed as constraints on the fit parameters.

From the two-point fits, we extract a bare value for the ground-state amplitude between an axial-vector current and pseudoscalar operator, which must then be renormalized in order to obtain the decay constant:

$$\phi_H = \sqrt{2} Z_{A_{Qq}^4} A_{A_{Qq}^4,0}. \quad (3.5)$$

To compute the heavy-light axial current renormalization constant $Z_{A_{Qq}^4}$, we divide it into flavor-diagonal contributions $Z_{V_{qq}^4}, Z_{V_{QQ}^4}$, which are determined non-perturbatively, and a flavor off-diagonal piece $\rho_{A_{Qq}^4}$ which is computed in lattice perturbation theory [13]. Our renormalized result for $\phi_H = f_H \sqrt{M_H}$ is thus given by

$$\phi_H = \sqrt{2} Z_{A_{Qq}^4} A_{A_{Qq}^4,0} = \sqrt{2} (\rho_{A_{Qq}^4} \sqrt{Z_{V_{qq}^4} Z_{V_{QQ}^4}}) A_{A_{Qq}^4,0}. \quad (3.6)$$

We use rooted staggered chiral perturbation theory (rS χ PT) [14] to extrapolate our results simultaneously to the continuum limit and to the physical light-quark masses. (Heavy quark masses are tuned non-perturbatively to give physical heavy-light meson masses, so no extrapolation is necessary for them. Details of the tuning procedure are given in [15].) The chiral fit functions incorporate terms describing a number of different effects, including discretization errors, finite-volume corrections, and hyperfine splittings.

Table 2: Error budget for the decay constants, as obtained in Section 4. In addition, projected improvements to the decay constant error budget for the updated analysis in progress (discussed in Section 5) are shown italicized and in brackets.

Source	f_{D^+} (MeV)	f_{D_s} (MeV)	f_{B^+} (MeV)	f_{B_s} (MeV)
Statistics	2.3 [1.1]	2.3 [1.1]	3.6 [1.8]	3.4 [1.7]
Heavy-quark disc.	8.2 [3.6]	8.3 [3.6]	3.7 [1.9]	3.8 [2.0]
Light-quark disc.	2.9 [0.7]	1.5 [0.3]	2.5 [0.6]	2.1 [0.5]
Chiral extrapolation	3.2 [1.6]	2.2 [1.1]	2.9 [1.5]	2.8 [1.4]
Heavy-quark tuning	2.8 [2.0]	2.8 [2.0]	3.9 [2.4]	3.9 [2.4]
$Z_{V_{QQ}^4}$ and $Z_{V_{qq}^4}$	2.8 [1.4]	3.4 [1.7]	2.6 [1.5]	3.1 [1.9]
u_0 adjustment	1.8 [0]	2.0 [0]	2.5 [0]	2.8 [0]
Other sources	3.8 [3.8]	3.0 [3.0]	3.5 [3.5]	4.8 [4.8]
Total [<i>projected</i>] error	11.3 [6.1]	10.8 [5.6]	8.9 [5.5]	9.5 [6.4]

4. Results

Applying the procedure outlined above, we obtain the values for ϕ shown in Figures 1 and 2, renormalized and in units of the standard scale r_1 . The chiral best-fit curve to the points is also shown, both explicitly at each lattice spacing and extrapolated to the continuum limit.

Evaluating the continuum best-fit curves at the physical points, we obtain the following values for the decay constants and their ratios:

$$f_{B^+} = 196.9(8.9) \text{ MeV}, \quad (4.1)$$

$$f_{B_s} = 242.0(9.5) \text{ MeV}, \quad (4.2)$$

$$f_{B_s}/f_{B^+} = 1.229(0.026), \quad (4.3)$$

$$f_{D^+} = 218.9(11.3) \text{ MeV}, \quad (4.4)$$

$$f_{D_s} = 260.1(10.8) \text{ MeV}, \quad (4.5)$$

$$f_{D_s}/f_{D^+} = 1.188(0.025). \quad (4.6)$$

The error bars quoted here include both statistical and systematic sources of error, which are accounted for in a detailed error budget. A summary of the full error budget for the individual decay constants is given in Table 2. We discuss the error budget further in Section 5 below, but a thorough discussion is beyond the scope of this paper. Instead, we refer the reader to Ref. [12], which contains a complete discussion of the systematic error analysis, including the full error budget for the decay-constant ratios.

5. Outlook

A new analysis following the approach outlined above is currently in progress, based on an expanded set of gauge configurations as shown in Table 3. In addition to extending the available simulations to finer lattice spacing and smaller quark mass, the “new” data set includes large increases in statistics for several ensembles.

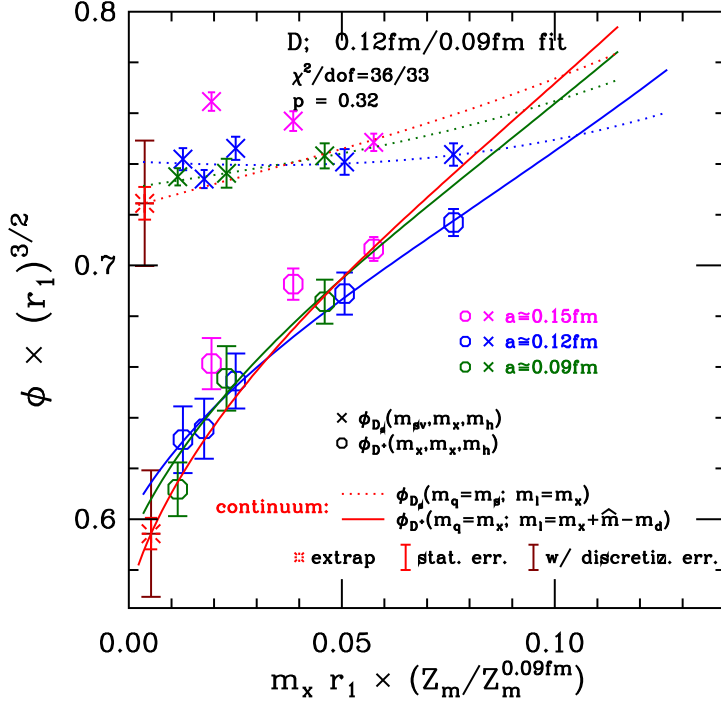


Figure 1: Extracted values of ϕ and chiral best-fit curves for the D system. Only points where valence and sea light-quark masses are equal are shown here. Data from the $a \approx 0.15$ fm ensemble are shown but not included in the fit. The red curve and symbols show the continuum extrapolation and the continuum/physical point extrapolation, respectively, for both ϕ_{D^+} and ϕ_{D_s} . For the fully extrapolated points, the inner error bars (bright red) represent statistical errors only, while the outer errors (dark red) include discretization errors.

Projected improvements in the error budget when the new data set is included are shown alongside the previous error estimates in Table 2. Statistical errors are projected to improve as $\sqrt{N_{\text{cfg}}}$, with N_{cfg} the number of gauge configurations available for a given ensemble. For the various discretization errors, the projected improvements are a result of reducing the smallest lattice spacing available from $a = 0.09$ fm to $a = 0.045$ fm. Light-quark discretization errors are estimated to scale as $\mathcal{O}(\alpha_s a^2)$; the heavy-quark discretization errors are estimated using the known functional dependence, which has several terms. The decrease in the chiral extrapolation error is projected based on the lightest available value of the quark mass in r_1 units, $m_x r_1$. The heavy-quark tuning error is based on a combination of statistical and discretization errors, and is treated as such. The “ u_0 adjustment” error is the result of using different tadpole improvement factors for the valence and sea quarks. This is rectified in the new data analysis, eliminating the associated error. Finally, the error estimates for the heavy-quark renormalization factors $Z_{V_{QQ}^4}, Z_{V_{qq}^4}$ are based on preliminary non-perturbative results for those quantities.

Acknowledgments

Computations for this work were carried out with resources provided by the USQCD Collaboration, the Argonne Leadership Computing Facility, the National Energy Research Scientific Com-

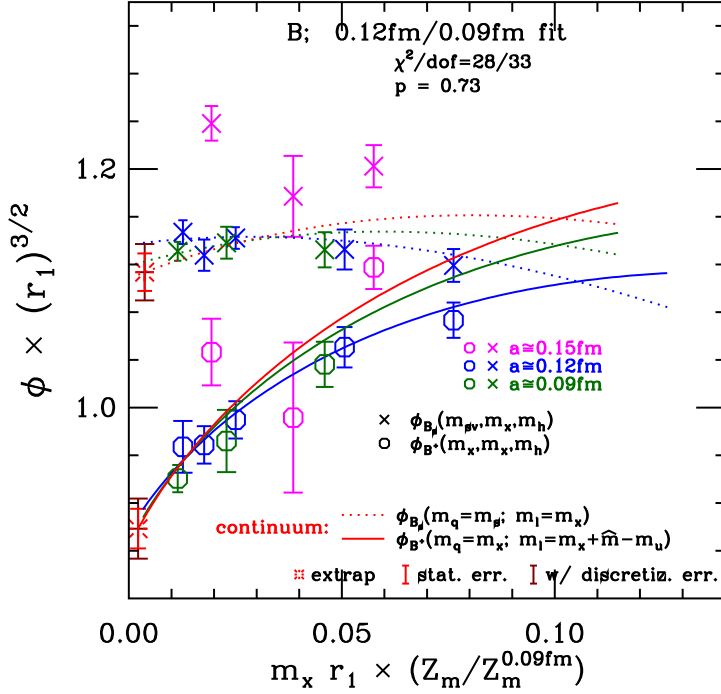


Figure 2: ϕ values and chiral best-fit curves as in Figure 1, but for the B system.

puting Center, and the Los Alamos National Laboratory, which are funded by the Office of Science of the U.S. Department of Energy; and with resources provided by the National Institute for Computational Science, the Pittsburgh Supercomputer Center, the San Diego Supercomputer Center, and the Texas Advanced Computing Center, which are funded through the National Science Foundation's Teragrid/XSEDE Program. This work was supported in part by the U.S. Department of Energy under Grants No. DE-FC02-06ER41446 (C.D., L.L., M.B.O.), No. DE-FG02-91ER40661 (S.G.), No. DE-FG02-91ER40677 (C.M.B., R.T.E., E.D.F., E.G., R.J., A.X.K.), No. DE-FG02-91ER40628 (C.B.), No. DE-FG02-04ER-41298 (D.T.); by the National Science Foundation under Grants No. PHY-0555243, No. PHY-0757333, No. PHY-0703296 (C.D., L.L., M.B.O.), No. PHY-0757035 (R.S.), and No. PHY-0704171 (J.E.H.); by the URA Visiting Scholars' program (C.M.B., R.T.E., E.G., M.B.O.); and by the Fermilab Fellowship in Theoretical Physics (C.M.B.). This manuscript has been co-authored by employees of Brookhaven Science Associates, LLC, under Contract No. DE-AC02-98CH10886 with the U.S. Department of Energy. Fermilab is operated by Fermi Research Alliance, LLC, under Contract No. DE-AC02-07CH11359 with the United States Department of Energy.

References

- [1] C. McNeile, C. T. H. Davies, E. Follana, K. Hornbostel and G. P. Lepage, arXiv:1110.4510 [hep-lat].
- [2] C. T. H. Davies *et al.*, Phys. Rev. D **82**, 114504 (2010) [arXiv:1008.4018 [hep-lat]].
- [3] P. Dimopoulos *et al.* [ETM Collaboration], arXiv:1107.1441 [hep-lat].

$\approx a$ [fm]	am_h	am_l	β	r_1/a	N_{conf} (old run)	N_{conf} (new run)
0.045	0.014	0.0028	7.81	7.21	—	800
		0.0018	7.46	5.31	—	825
		0.0025	7.465	5.33	—	800
		0.0036	7.47	5.35	—	631
		0.0072	7.48	5.40	—	591
	0.09	0.00155	7.075	3.74	—	790
		0.0031	7.08	3.75	435	577
		0.00465	7.085	3.77	—	983
		0.0062	7.09	3.79	557	1377
		0.0124	7.11	3.86	518	1476
0.12	0.050	0.005	6.76	2.74	678	1419
		0.007	6.76	2.74	833	1274
		0.010	6.76	2.74	592	1664
		0.020	6.79	2.82	460	1637
		0.030	6.81	2.88	549	—
0.15	0.0484	0.0097	6.572	2.22	631	—
		0.0194	6.586	2.26	631	—
		0.0290	6.600	2.29	576	—

Table 3: Table of gauge configurations for the updated analysis in progress. Only configurations labelled “old run” were used to obtain the results presented in Section 4. The analysis in progress will make use of all configurations from both runs combined.

- [4] F. Farchioni *et al.*, PoSLATTICE **2010**, 128 (2010) [arXiv:1012.0200 [hep-lat]].
- [5] A. Lenz *et al.* [CKMfitter Collaboration], Phys. Rev. D **83**, 036004 (2011) [arXiv:1008.1593 [hep-ph]].
- [6] E. Lunghi and A. Soni, Phys. Lett. B **697**, 323 (2011) [arXiv:1010.6069 [hep-ph]].
- [7] J. Laiho, E. Lunghi and R. Van De Water, PoSFPCP **2010**, 040 (2010) [arXiv:1102.3917 [hep-ph]].
- [8] A. J. Bevan *et al.* [UTfit Collaboration], PoS **ICHEP2010**, 270 (2010) [arXiv:1010.5089 [hep-ph]].
- [9] T. Aaltonen *et al.* [CDF Collaboration], Phys. Rev. Lett. **107**, 191801 (2011) [arXiv:1107.2304 [hep-ex]].
- [10] A. Bazavov *et al.*, Rev. Mod. Phys. **82**, 1349 (2010) [arXiv:0903.3598 [hep-lat]].
- [11] A. X. El-Khadra, A. S. Kronfeld and P. B. Mackenzie, Phys. Rev. D **55**, 3933 (1997) [hep-lat/9604004].
- [12] A. Bazavov *et al.* [Fermilab Lattice and MILC Collaborations], “B- and D-meson decay constants from three-flavor lattice QCD,” [arXiv:1112.3051 [hep-lat]].
- [13] A. X. El-Khadra *et al.*, PoSLAT **2007**, 242 (2007) [arXiv:0710.1437 [hep-lat]].
- [14] C. Aubin and C. Bernard, Phys. Rev. D **73**, 014515 (2006) [hep-lat/0510088].
- [15] C. Bernard *et al.* [Fermilab Lattice and MILC Collaborations], Phys. Rev. D **83**, 034503 (2011) [arXiv:1003.1937 [hep-lat]].

Visualization as a tool for understanding QCD evolution algorithms

This article has been downloaded from IOPscience. Please scroll down to see the full text article.

2009 J. Phys.: Conf. Ser. 180 012068

(<http://iopscience.iop.org/1742-6596/180/1/012068>)

View the [table of contents for this issue](#), or go to the [journal homepage](#) for more

Download details:

IP Address: 24.1.126.5

The article was downloaded on 23/01/2012 at 02:46

Please note that [terms and conditions apply](#).

Visualization as a tool for understanding QCD evolution algorithms

Massimo Di Pierro¹, Michael Clark², Chulwoo Jung³, James Osborn⁴, John Negele⁵, Richard Brower², Steven Gottlieb⁶, Yaoqian Zhong¹

¹ School of Computing, Depaul University; ² Physics Department, Boston University;

³ Physics Department, Brookhaven National Laboratory; ⁴ Argonne National Laboratory; ⁵ Center for Theoretical Physics, MIT; ⁶ Indiana University

Abstract. In this paper we present a project of visualizing topological charge in Lattice QCD in order to understand its evolution under the Markov Chain Monte Carlo algorithms and how to maximize its equilibration. Lattice QCD is a very computationally expensive technology for computing properties of composite particles from a few fundamental parameters such as quark masses. Our research plays an important role in validating these computations by showing that the autocorrelation length is small and it can eventually lead to even more efficient algorithms.

1. Introduction and Motivations

The Standard Model of Particle Physics provides a strikingly successful description of the structure of the matter down to scales of 10^{-18} m. The basic degrees of freedom are elementary particles including quarks and leptons which interact with each other according to strong and electro-weak interactions. Quarks play a special role in this model because their interacting are mediated by the exchange of gluons; thus, they create bound states such as the proton, the neutron and the majority of particles that constitute the richness of structures that we observe in the physical world. The part of the Standard Model that describes quarks and gluons is called Quantum Chromo Dynamics (QCD). The ability to perform computations in QCD is of critical importance in Particle and Nuclear Physics. It enables us to determine fundamental parameters of the Standard Model from experiments, compare experimental results with model predictions, and eventually find discrepancies that can shed some light into yet unknown smaller structures and laws of physics at higher energy. It enables us to calculate the equation of state, transport coefficients, and other properties of hadronic matter and the quark gluon plasma explored in relativistic heavy ion collisions at RHIC the LHC. It also enables us to calculate the spectrum, structure, and interactions of mesons and baryons from first principles and lies at the heart of explorations at Jefferson Lab, RHIC spin, and a future electron-ion collider.

Since quarks are subject to strong interactions, standard perturbative techniques are inadequate to perform many interesting computations. For computing the spectrum of the model and computing the lifetime of composite particles, the purely numerical approach known as Lattice QCD that has been the most productive[2].

Lattice QCD consists of taking a small portion of space (a cube of $\sim 10^{-15}\text{m}$ of size) for a brief time interval ($\sim 10^{-23}\text{secs}$), discretizing it on a four dimensional lattice, and simulating numerically the dynamics of QCD inside. The spatial fields do not evolve over time as in ordinary classical systems. Instead, the fields, that are defined on the four-dimensional Euclidean space-time, evolve over a fictitious MCMC time (τ). Lattice QCD computations consist of measuring correlation functions over the possible four dimensional configurations of the fields, each weighted by a number that encodes the dynamics of QCD[1]. Quantities like particles masses and lifetimes can be determined from these correlations.

In practice, the four dimensional configurations are created using Markov Chain Monte Carlo (MCMC) algorithms. Examples are the Molecular Dynamics algorithm or the Hybrid Monte Carlo algorithm. Each configuration is generated from the previous one using a transition in probability that encodes the laws of QCD dynamics.

In this paper, we describe how visualization techniques can be useful to provide information about these algorithms, about the data that is being generated.

The quark fields can be integrated out and, while they play a critical role in the inner workings of the algorithms, they are not part of the actual configurations. The latter only contain gauge degrees of freedom representing gluons, hence they are usually referred to as gauge configurations. Typical gauge configurations have sizes that range from 32×24^3 to 192×64^3 points; which correspond to a size ranging from 256 MBytes to 15 GBytes each (in single precision). A typical Lattice QCD computation generates and utilizes about 1000 of these gauge configurations, thus requiring multiple TBytes of storage. Algorithms are always parallel because of the size of the problem of Lattice QCD.

A typical problem consists in determining whether this small subset of the infinite space of all possible gauge configuration is sufficiently representative and whether the statistical uncertainty determined from the averages can be trusted. From a physical perspective the gauge configurations can be grouped into equivalence classes characterized by their topological charge density.

Our goal is to visualize this topological charge density and measure how fast/slow it evolved under the MCMC for different algorithms and different simulation parameters (the dynamic quark mass in particular). This would provide us with a proof that current Lattice QCD computation are adequately sampling the space of all possible configurations as opposed to getting stuck in one topological sector, and provide an effective tool for developing algorithms that maximize equilibration of the topological charge.

2. Visualization

Typical production gauge configurations appear to be separated by enough MCMC steps and there is no visible continuity in the topological charge. In order to measure autocorrelation in the topological charge we generated *ad hoc* gauge configurations with small trajectories for two different algorithms and different dynamical quark masses.

- **Wilson** Two sets of $24^3 \times 32$ dynamical Wilson gauge configurations with $\beta = 5.6$ and quark masses of $m_1 = 66\text{MeV}$ and $m_2 = 33\text{MeV}$ respectively. Each set consists of 1000 trajectories with a 0.1 molecular dynamics time units, saved every 2 time units ($dt = 0.2$). To integrate Hamilton's equations a multi-step 2nd order symmetric symplectic integrator was used (Omelyan) [3].
- **DWF:** One set of $24^3 \times 64$ dynamical gauge configurations generated with Domain Wall Fermions (two degenerate light ones, $m_u = 14\text{MeV}$, and one strange, $m_s = 74\text{MeV}$) and Iwasaki gauge action at $\beta = 2.13$, saved every 1/6 of a trajectory ($dt = 0.1\bar{6}$). Further details can be found in [4] and the references therein.

Each gauge configuration consists of a set of $SU(3)$ matrices $U_{x,y}$ for every pair of neighbor sites x, y on the lattice. Given a quark field q_y , the $U_{x,y}$ matrix represent the change in the quark field under parallel transport from $y \rightarrow x$, *i.e.*, $q_y \rightarrow q_x = U_{x,y}q_y$. Therefore $U_{y,x} = U_{x,y}^H$.

The topological charge is computed in three steps according to the definition:

- The gauge field was smoothed by n -iterations of a “cooling step”

$$U_{x,y} \rightarrow U_{x,y} = P_{SU(3)}(\alpha U_{x,y} + (1 - \alpha)S_{x,y}) \quad (1)$$

where $P_{SU(3)}$ is a projection operator into $SU(3)$ and $S_{x,y}$ is the average of all products of three consecutive links connecting x with y .

- We computed the chromo-electro-magnetic field defined by

$$F_{x,\mu,\nu} = \frac{1}{2}\text{Re}(A_{x,\mu,\nu} - A_{x,\mu,\nu}^H) \quad (2)$$

where $A_{x,\mu,\nu}$ is the average of the product of four consecutive links in the μ, ν plane starting and ending at point x .

- We computed the topological charge density, defined by

$$Q_x = \frac{1}{32\pi^2} \sum_{\mu\nu\rho\sigma} \epsilon_{\mu\nu\rho\sigma} \text{Tr}(F_{x,\mu,\nu} F_{x,\rho,\sigma}) \quad (3)$$

In fig. 1 we show three images of iso-surfaces of topological charge density for one gauge configuration for different numbers of cooling steps (0,10,15). In fig. 2 we show three images of iso-surfaces of topological charge density for the same number of cooling steps (20) for different consecutive gauge configurations separated by 6 trajectories.

3. Autocorrelation and Hurst Exponent

In addition to the visualization of the topological charge density we also computed the average autocorrelation $R(\tau)$ and average Hurst exponent H for each independent Markov Chain. First we computed the autocorrelation and the Hurst exponent over the MCMC time (τ) for each lattice point, then we averaged the results over all lattice points. The Hurst exponent is computed using the standard R/S technique described in ref. [5]. In fractal geometry, the Hurst exponent is also known as “index of dependence”, it measures the relative tendency of a time series to either strongly regress to the mean or cluster in a direction. H is 0.5 for white noise. H is related to the auto-correlation length via $R(\tau) \simeq \tau^{2H-2}$ and $2 - H$ is known as the “fractal dimension” of the problem.

Our results are summarized in the following table.

Action	quark masses	H
Wilson	66MeV	0.966
Wilson	33MeV	0.973
DWF	69,17MeV	0.908

The autocorrelation is plotted in fig. 3

Notice how the autocorrelation becomes negative at around 100 MCMC steps. This indicates an alternating pattern in the data, but a larger MCMC chain will be required to validate this hypothesis.

4. Conclusion

Our analysis demonstrates that the autocorrelation length of a topological charge is very small compared with the trajectory length of typical production grade Lattice QCD computations. Our work is still in progress and, as more data is analyzed, we hope to derive an empirical interpolating formula for the autocorrelation length as function of the simulation parameters.

Acknowledgments

This research is funded by the Department of Energy grant DE-FC02-06ER41441. We thank Argonne National Laboratory computing resources, the DOE Advanced Simulation and Computing Initiative (ASCI) for the VisIt software, and Brian Fox at DePaul Univ.

Bibliography

- [1] Pierro M D 2008 *Modern Physics A* **125:012067**
- [2] Kronfeld A 2006 *J. Phys. Conf. Ser.* **21-3**
- [3] Takaishi T and de Forcrand P 2006 *Phys. Rev. E* **73** 036706 (*Preprint hep-lat/0505020*)
- [4] Jung C 2007 *POS(LATTICE 2007)* **37** (*Preprint arXiv:0710.5337*)
- [5] Hurst E 1951 *Trans. Am. Soc. Civil Eng.* **116** 770

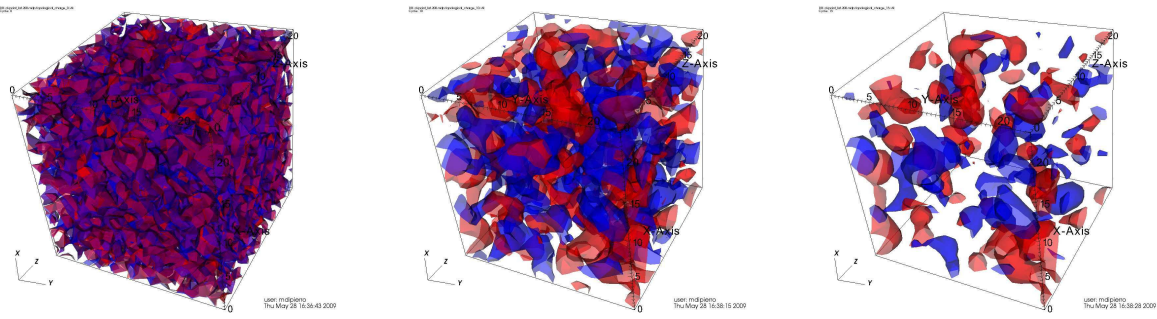


Figure 1. Iso-surfaces for a 3D slice of a topological charge density for one gauge configuration for different numbers of cooling steps (0,10, 15).

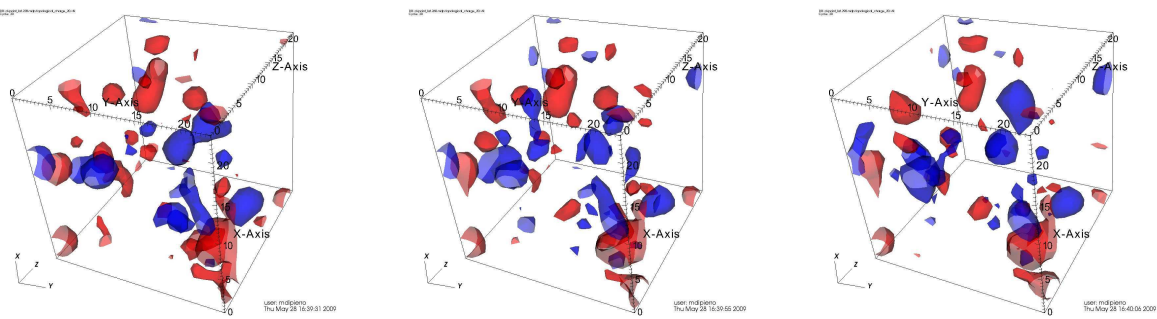


Figure 2. Iso-surfaces for a 3D slice of topological charge density for the same number of cooling steps (20) for different consecutive gauge configurations separated by 6 trajectories.

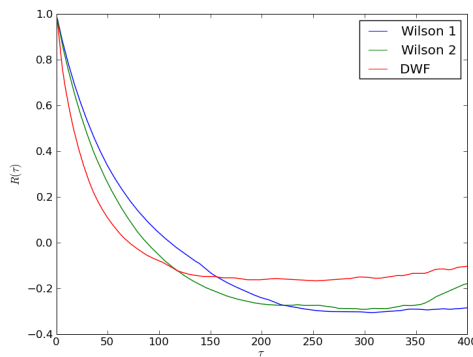


Figure 3. Autocorrelation length for the three sets of gauge configurations considered in the paper.